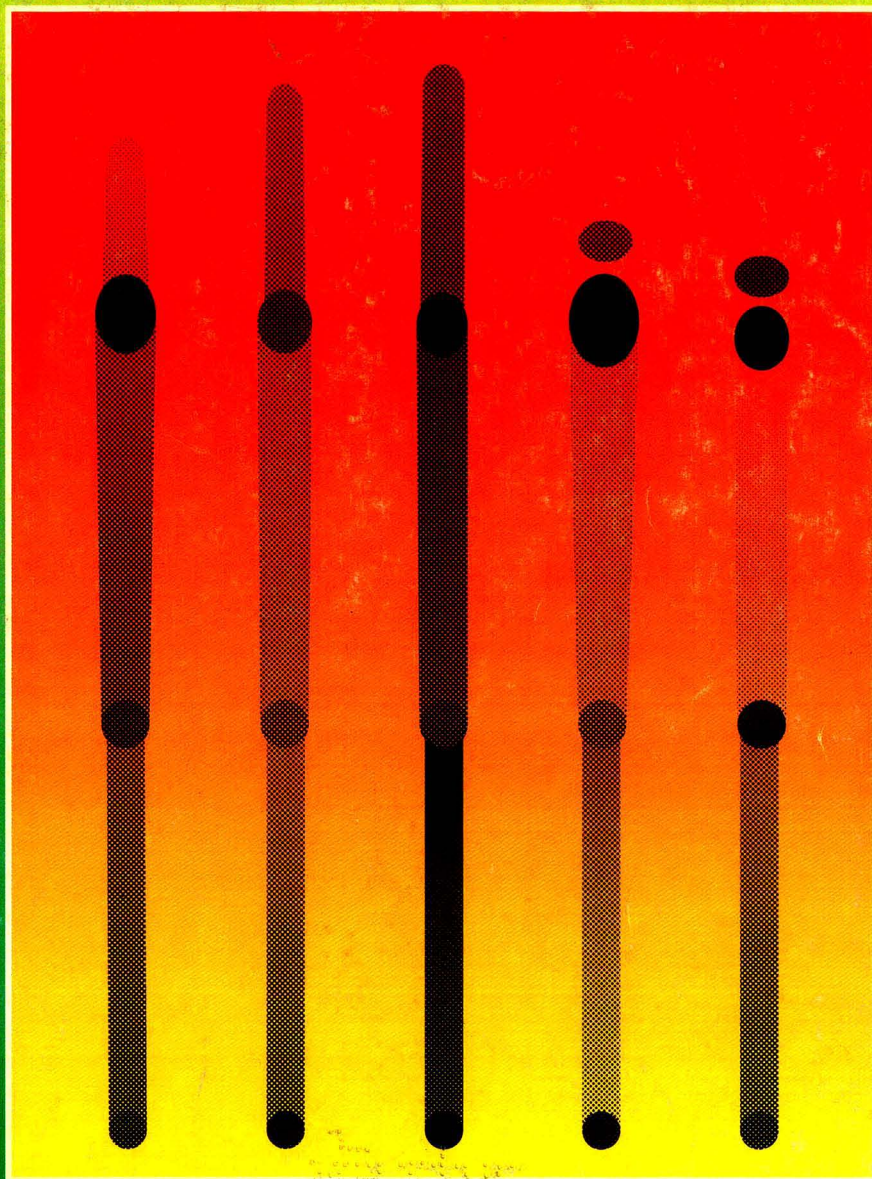


NOVEMBER 15, 1989

Analytical CHEMISTRY



MODERN THIN-LAYER CHROMATOGRAPHY

1257 A

No Glubs, Gurgles, Grumbles or Groans

Proven DD-20 is our most silent vacuum pump ever.

Listen to the quiet at working pressure with the Precision® DD-20. Our internal baffle puts a lid on noise.

An exhaust valve along with the baffle eliminates oil back-up. Your system runs quiet and clean.

Removable intake lets you adapt

to a variety of setups, quickly and precisely. Work to a low 5 micron ultimate vacuum. The DD-20 gives you a full 10 liters/minute pumping efficiency even at 100 microns. It's 16 lbs. light and 10" x 7 3/4" x 6 1/4" small to carry wherever you need.

Hear about our complete line of vacuum pumps.


Write Precision Scientific, P.O. Box 10066,

Rochester, NY 14610.

Or call 800-621-8820.

CIRCLE 127 ON
READER SERVICE CARD

*Your
Performance
Demands
Precision®*



Precision®
VACUUM PUMP
20 l/m (0.7 CFM) 5 Micron
MODEL DD 20

**Precision®
Scientific**

MEMBER
SAMA
SCIENTIFIC APPARATUS
MAKERS ASSOCIATION

If You're Shopping For A Sequential Plasma Spectrometer, Tear Out This Ad & Take It With You.

The spectrometer's galvanometer grating drive has no articulating surfaces and remains completely wear free.

Covers complete wavelength range from 160 to 350 nm.

Minimum interelement interferences with 0.008 nm resolution.

Built-in quality and reliability. Over 600 Jarrell Ash plasma spectrometers shipped to date.

Organics and other difficult samples are now analyzable with our directly coupled, autotuned 2KW RF generator.

Minimizes argon gas consumption on routine samples with low power/low flow operation; maximizes analytical results on difficult samples with high power/high flow operation.

Color graphics speeds peak selection, background and interelement correction, and other methods development tasks.

Full computer automated control of sample delivery, gas flows, RF power and observation height gives best possible accuracy and detection limits on every sample.

Fast, semiquantitative analysis of up to 72 elements with a three element standard.

Sophisticated command language provides decision making logic for complex analytical tasks—e.g. CLP protocol with autosampler operation.

Even novice technicians can get excellent results with minimal training. Menu-driven Thermo-SPEC™ software gives frequent prompts and calls for easy fill in the blanks' responses and single key commands.

In the words of our chief engineer, our *AtomScan™ 25 Spectrometer* is "everything anyone ever wanted in a sequential ICP instrument."

It's the culmination of more than three decades of developmental work, incorporating the best features—RF generator, monochromator, sample delivery and excitation, data system and software—of all previous generations of Jarrell Ash plasma spectrometers.

And whether you are a research spectroscopist or an occasional user, that simply means you are going to get better accuracy and detection limits on every

element in any sample matrix with the *AtomScan 25* than with instruments costing twice as much.

Don't take our word for it.

Tear out this ad and take it with you on your trip to see brand X. See if they offer you anywhere near as much for so little.

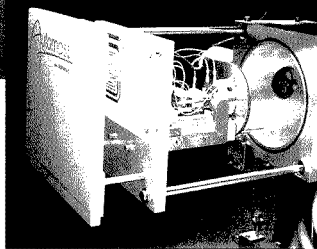
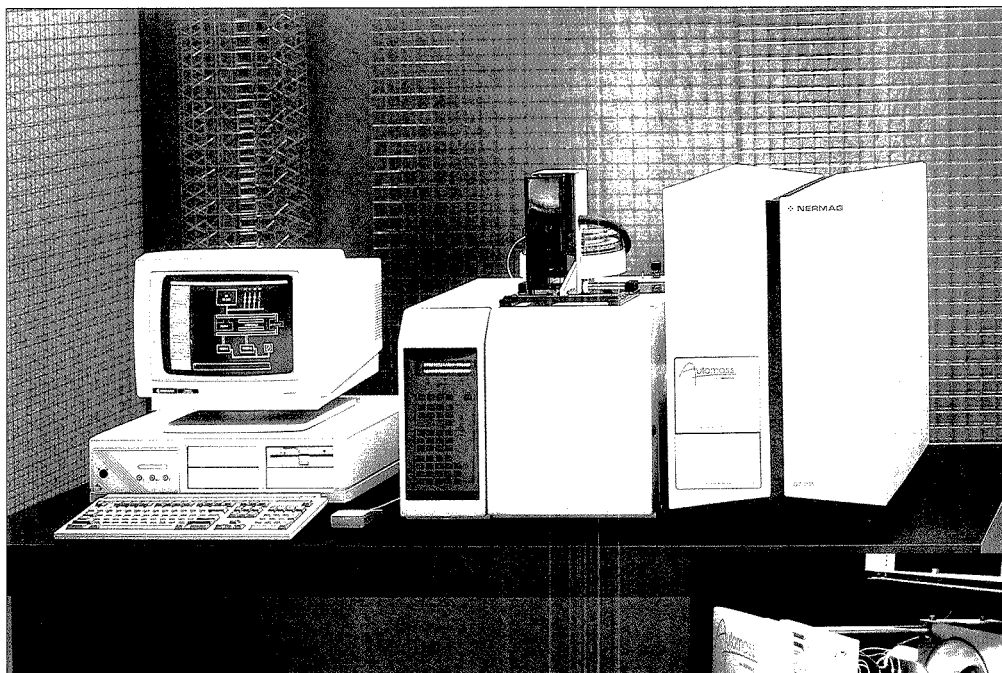
We think we'll make you a believer.

For literature or a demonstration of the *AtomScan 25*, call (508) 520-1880. Or write Thermo Jarrell Ash Corp., 8 East Forge Parkway, Franklin, MA 02038-9101.

Thermo Jarrell Ash Corporation

A Division of Thermo Instrument Systems, Inc.

CIRCLE 156 ON READER SERVICE CARD



Automass

 The Power of Original Thinking

When Nermag set out to develop the premier Automated Benchtop GC/MS Workstation, we were aware there was a need - *your need*, for more analytical power. Power that is simple to use, yet flexible enough to tackle the toughest problems. A true research-grade mass spectrometer was required, not a compromised mass analyzer camouflaged by glitzy game-show software.

Introducing Automass, the benchtop mass spectrometer that only Nermag could build, and the only one of its kind in the world today. The basis of Automass is a state of the art quadrupole with plug-in prefilters and an optimized Ionization Source for EI, CI, and negative ions. Our original Off Axis Ion - Photon Conversion Detector and patented Resolver electronics are enhanced by a differentially pumped vacuum system for real CI spectra.

Automass is controlled by our exclusive LUCY™ software. LUCY does window after window of instrument configuration setting, auto or manual tuning, calibration, mass spectra, chromatographic trace, and data reduction; while simultaneously examining the complete library and quantifying results. You'll Love LUCY.

Automass can flawlessly perform routine analysis all day virtually unattended, or help you tackle the most difficult analytical problem.

Automass advances Mass Spectrometry into the 90's.

Powerfully.

DELSI
NERMAG
I N S T R U M E N T S

France: Delsi-Nermag Instruments, 981erBlvd, Holoise, Argenteuil 9500, Tel: (1) 39 47 66 22, Fax: (1) 39 47 85 66
USA: Delsi Inc., 15701 West Hardy Rd. Houston, TX 77060, Tel: (713) 847-0811, Fax (713) 591-2132
Netherlands: Delsi Instruments BV, Gebouw adelsvelt, van Houten Ind Pk 11, 1381 Weesp, Tel: (0)2940-18611
U.K.: Delsi Instruments Ltd, 38 Thrapston Fd., Brampton, Huntingdon, Cambs PE 18 8TE, Tel: 0480 431 809
West Germany: Delsi Instruments GmbH, Jülichstr. 1 D4020 Mettmann, Tel: 02104/25086-87-88
Belgium: Intersmat, 103, Av. des Volontaires, 1160 Bruxelles, Tel: 2 733.16.32

CIRCLE 32 ON READER SERVICE CARD

Registered in U.S. Patent and Trademark Office;
Copyright 1989 by the American Chemical Society

ANALYTICAL CHEMISTRY (ISSN 0003-2700) is published semi-monthly by the American Chemical Society at 1155 16th St., N.W., Washington, DC 20036. Editorial offices are located at the same ACS address (202-872-4570; FAX 202-872-6325; TDD 202-872-8733). Second-class postage paid at Washington, DC, and additional mailing offices. Postmaster: Send address changes to ANALYTICAL CHEMISTRY Member & Subscriber Services, P.O. Box 3337, Columbus, OH 43210.

Claims for missing numbers will not be allowed if loss was due to failure of notice of change of address to be received in the time specified; if claim is dated (a) North America: more than 90 days beyond issue date, (b) all other foreign: more than one year beyond issue date, or if the reason given is "missing from files."

Copyright Permission: An individual may make a single reprographic copy of an article in this publication for personal use. Reprographic copying beyond that permitted by Section 107 or 108 of the U.S. Copyright Law is allowed, provided that the appropriate per-copy fee is paid through the Copyright Clearance Center, Inc., 27 Congress St., Salem, MA 01970. For reprint permission, write Copyright Administrator, Publications Division, ACS, 1155 16th St., N.W., Washington, DC 20036. Registered names and trademarks, etc., used in this publication, even without specific indication thereof, are not to be considered unprotected by law.

Advertising Management: Centcom, Ltd., 500 Post Rd. East, Westport, CT 06880 (203-226-7131)

1989 subscription rates include air delivery outside the U.S., Canada, and Mexico

	1 yr	2 yr
Members		
Domestic	\$ 27	\$ 45
Canada and Mexico	56	103
Europe	83	157
All Other Countries	120	231
Nonmembers		
Domestic	49	83
Canada and Mexico	78	141
Europe	135	230
All Other Countries	192	354

Three-year and other rates contact: Member & Subscriber Services, ACS, P.O. Box 3337, Columbus, OH 43210 (614-447-3776 or 800-333-9511).

Subscription orders by phone may be charged to VISA, MasterCard, Barclay card, Access, or American Express. Call toll free 800-ACS-5558 in the continental United States; in the Washington, DC, metropolitan area and outside the continental United States, call 202-872-8065. Mail orders for new and renewal subscriptions should be sent with payment to the Business Management Division, ACS, P.O. Box 57136, West End Station, Washington, DC 20037.

Subscription service inquiries and changes of address (include both old and new addresses with ZIP code and recent mailing label) should be directed to the ACS Columbus address noted above. Please allow six weeks for change of address to become effective.

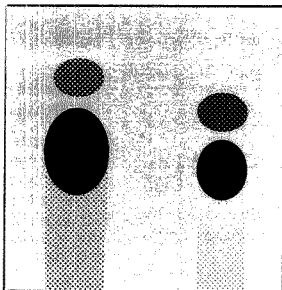
ACS membership information: Lorraine Binlin (202-872-4567)

Single issues, current year, \$7.00 except review issue and LabGuide, \$12.00; back issues and volumes and microform editions available by single volume or back issue collection. For information or to order, call 800-ACS-5558 or write the Microform & Back Issues Office at the Washington address.

Nonmembers rates in Japan: Rates above do not apply to nonmember subscribers in Japan, who must enter subscription orders with Maruzen Company Ltd., 3-10 Nihonbashi 2-chome, Chuo-ku, Tokyo 103, Japan. Tel: (03) 272-7211.

Analytical

CHEMISTRY



REPORT

1257 A

On the cover. Modern thin-layer chromatography. TLC methods are most effective for low-cost analysis of simple mixtures, for samples that remain sorbed to the separation medium, and for substances that require postchromatographic treatment prior to detection. Colin F. Poole and Salwa K. Poole of Wayne State University define the scope and limitations of TLC as an analytical tool

VIIb		VIII				Ib	
Mn	Fe	Co	Ni	Cu	Zn	Ag	Au
2	2	2	2	2	2	2	2
7.4	7.9	7.9	7.6	7.7	7.4	7.6	7.6
2	3	3	Rh	Pd	2	2	2
7.3	7.4	7.5	8.3	7.6	7.3	7.6	7.6
Re	Os	Ir	Pt	Au	Hg	Tl	Pb
2	2	2	2	2	2	2	2

INSTRUMENTATION

1271 A

Resonance ionization mass spectrometry uniquely combines the elemental or molecular selectivity of optical spectroscopy with the sensitive detection capability of mass spectrometry. J. P. Young, R. W. Shaw, and D. H. Smith of Oak Ridge National Laboratory describe the instrumentation involved and cite examples of the technique's growing usefulness

BRIEFS

1248 A

NEWS

1255 A

Coetzee given Pittsburgh Award. Pittsburgh Conference offers college grants. LANSCE provides higher neutron flux

MEETINGS

1281 A

Pittsburgh Conference. The 41st Pittsburgh Conference and Exposition on Analytical Chemistry will be held at the Jacob Javits Convention Center in New York City, March 5-9, 1990. Conferences. Call for papers. Short courses and workshops

BOOKS

1285 A

Critical reviews. Recently released books on gas, liquid, and size exclusion chromatography; tandem MS; natural products isolation; thermal analysis; and NMR spectroscopy are reviewed

FOCUS

1291 A

Chemistry in Miami. The ACS fall national meeting featured talks by the Division of Analytical Chemistry award winners as well as the French exhibit "Molecules and Society"

NEW PRODUCTS & MANUFACTURERS' LITERATURE

1294 A

AUTHOR INDEX

2465

Articles

Pulsed Amperometric Detection of Alkanolamines Following Ion Pair Chromatography 2466

Alkanolamines are determined without derivatization by PAD following ion pair chromatography. Detection limits are in the 5–10-ng range ($S/N = 3$).

William R. LaCourse*, Warren A. Jackson, and Dennis C. Johnson, Department of Chemistry, Iowa State University, Ames, IA 50011

Detection of Rat Basophilic Leukemia by Cyclic Voltammetry for Monitoring Allergic Reaction 2471

The peak current obtained from RBL-1 cells is attributed to serotonin. The method is applied to the detection of an allergic reaction.

Tadashi Matsunaga*, Akinori Shigematsu, and Noriyuki Nakamura, Department of Biotechnology, Tokyo University of Agriculture & Technology, Koganei, Tokyo 184, Japan

Room-Temperature Phosphorescence of Compounds in Mixed Organized Media: Synthetic Enzyme Model–Surfactant System 2475

A comparative study of a synthetic enzyme model compound with cyclodextrin is described in a mixed organized media, synthetic enzyme model surfactant using room-temperature phosphorescence and phosphorescence decay lifetimes.

Haidong Kim and Stanley R. Crouch*, Department of Chemistry, Michigan State University, East Lansing, MI 48824, and **Matthew J. Zabik***, Pesticide Research Center, Michigan State University, East Lansing, MI 48824

Data Analysis in the Shot Noise Limit. 1. Single Parameter Estimation with Poisson and Normal Probability Density Functions 2479

The maximum likelihood method is applied to single-parameter estimation of data obtained in the shot noise limit.

Stephen E. Bialkowski, Department of Chemistry and Biochemistry, Utah State University, Logan, UT 84322-0300

Data Analysis in the Shot Noise Limit. 2. Methods for Data Regression 2483

Equations describing multiple-parameter regression of shot-noise-limited data are derived, examined, and tested.

Stephen E. Bialkowski, Department of Chemistry and Biochemistry, Utah State University, Logan, UT 84322-0300

Simulation of Carbon-13 Nuclear Magnetic Resonance Spectra of Piperidines 2489

Linear predictive models are used to generate accurate, simulated, conformationally averaged ^{13}C NMR spectra for a set of methyl-substituted piperidines. These equations are also used to simulate low-temperature spectra.

Martha L. Ranc and Peter C. Jurs*, Department of Chemistry, The Pennsylvania State University, 152 Davey Laboratory, University Park, PA 16802

Background Illumination Filtering in Thermal Lens Spectroscopy 2496

A thermal lens spectrometer with spatial filtering of a probe beam is analyzed. Calculations of diffraction at the blocking filter are presented. Experiments show a fivefold enhancement of the ratio of useful signal to constant, signal-independent detector response.

Jerzy Slaby, Institute of Experimental Physics, Warsaw University, Hoza 69, 00-681 Warsaw, Poland

Intermolecular Processes in the Ion Trap Mass Spectrometer 2500

Compounds that show minimal fragmentation provide normal ($M + 1$)/ M ratios except under conditions of space charging, whereas substances that provide abundant alkyl ions form ($M + H$) $^+$ ions through proton transfer to neutrals.

L. K. Pannell and Q.-L. Pu, Laboratory of Bioorganic Chemistry, National Institute of Diabetes, Digestive and Kidney Diseases, National Institutes of Health, Bethesda, MD 20892, **H. M. Fales*** and **R. T. Mason**, Laboratory of Chemistry, National Heart, Lung, and Blood Institute, National Institutes of Health, Bethesda, MD 20892, and **J. L. Stephenson**, Finnigan MAT, Frederick, MD 21701

Coaxial Continuous Flow Fast Atom Bombardment in Conjunction with Tandem Mass Spectrometry for the Analysis of Biomolecules 2504

The ability to obtain on-the-fly MS/MS data makes the coaxial CF-FAB interface compatible with liquid chromatography. The constant flow of analytes into the mass spectrometer is advantageous for the acquisition of MS/MS and MS/MS/MS data.

Leesa J. Deterding, M. Arthur Moseley, and Kenneth B. Tomer*, Laboratory of Molecular Biophysics, National Institute of Environmental Health Sciences, Research Triangle Park, NC 27709, and **James W. Jorgenson***, Department of Chemistry, University of North Carolina at Chapel Hill, Chapel Hill, NC 27514

Separation of the Reagent Ions from the Reagent Gas in Ammonia Chemical Ionization Mass Spectrometry 2511

Competitive reactions occurring in ammonia CI-MS are eliminated by using a Fourier transform mass spectrometer with a dual trapped-ion cell to separate the reagent ions from the reagent gas.

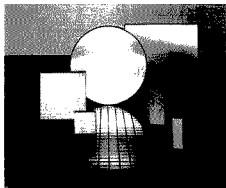
Robert B. Cody, Nicolet Analytical Instruments, 6416 Schroeder Road, Madison, WI 53711

* Corresponding author

■ Supplementary material available

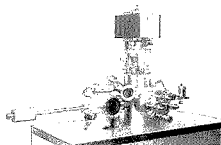
Ruled and Holographic Diffraction Gratings

Instruments SA provides a wide variety of high performance diffraction gratings. Among the many standard types available are aberration corrected blazed and ion etched concave monochromator gratings, flat field gratings for use with diode array detectors, toroidal gratings for use in the VUV and classically ruled as well as holographic plane gratings. Applications range from upper atmosphere ozone monitoring by satellite to big testing and emission spectrometers. For further information contact Jobin Yvon, Instruments SA (201) 494-8660. CIRCLE 70



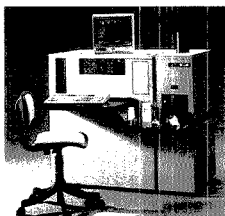
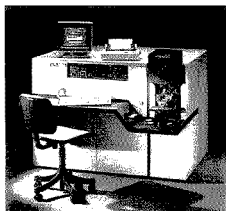
Nanoscan 50 The Field Emission Auger Microprobe

Low energy, high brightness field emission source guarantees high signal and excellent spatial resolution in SEM and SAM. Other features include video-rate SEM/SAM image accumulation, full automation, and high constant energy resolution. For further information, contact the Riber Division of Instruments SA, Inc. at (201) 494-8660. CIRCLE 71



Glow Discharge Spectroanalyzer

The GDL Excitation Source for direct solid sample analysis, uses the principle of cathodic sputtering. The conducting sample forms the cathode which is bombarded with positive argon ions to excite the sample atoms. The GDL is used for both elemental and surface analysis of metals including ferrous and non-ferrous alloys, noble metals and ceramics. For further information contact Jobin Yvon, Instruments SA (201) 494-8660. CIRCLE 72

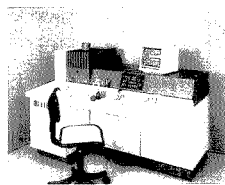
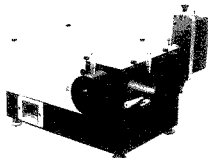


Compact Sequential ICP Spectrometer

The JY 24 has the advantages of a full featured ICP spectrometer in a single, compact, space-saving unit. By using a large surface area and high groove density holographic grating, the resolution and light gathering power of the JY 24 are unequaled for its size. For further information contact Jobin Yvon, Instruments SA (201) 494-8660. CIRCLE 73

Spectrometers

With a line of single and double spectrometers which spans from 100 to 1600 mm in focal length. Instruments SA/Jobin Yvon can furnish the ideal spectrometer for any UV, Visible or IR application. This broad range of instruments significantly reduces the need for compromise in coverage, stray light rejection or resolution when specifying a system. Each spectrometer can be automated for integration into a spectroanalytical system. For further information contact Instruments SA/Jobin Yvon (201) 494-8660. CIRCLE 74



Simultaneous and Sequential ICP Spectrometers

The JY 70 Plus consists of an integrated direct reading double polychromator — sequential spectrometer. This ICP system combines the speed of simultaneous, multi-element analysis with the versatility and flexibility of the sequential system. For further information on the JY 70 Plus or JY 38 Plus contact Jobin Yvon, Instruments SA (201) 494-8660. CIRCLE 75

INTRODUCING THE NEW JY 50 POLYSCAN FROM A WORLD LEADER IN ICP SYSTEMS

The JY 50 PolyScan not only provides all the advantages inherent in a simultaneous multi-element Spectroanalyzer but also offers spectral line selection flexibility which previously was found only in sequential ICP systems. Jobin Yvon has developed a new scanning entrance slit which furnishes 2.2 nm wavelength displacement from any of the preselected fixed analytical channels.

For more information on the JY 50 PolyScan and the complete spectrum of JY instruments, use the reader service card, or write or call today.

CIRCLE 76 ON READER SERVICE CARD

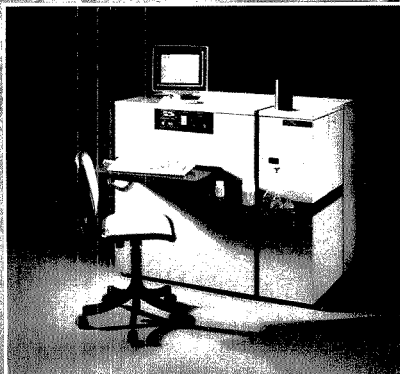
**JOBIN
YVON**



**J-Y DIVISION
Instruments SA, Inc.**

6 Olsen Avenue, Edison, NJ 08820-2419
Tel. (201) 494-8660, Telex 844516
FAX (201) 494-8796

In Europe: Jobin Yvon, 16-18 Rue du
Canal 91163 Longjumeau, France
Tel. (33) 1.69.09.34.93
Telex JOBYVON 692882F
FAX 011-331-6909-0721



Laser Mass Spectrometric Analysis of Compounds Separated by Thin-Layer Chromatography 2516

TLC combined with laser MS is applied successfully to characterize polynuclear aromatic hydrocarbons and purine bases.

Alan J. Kubis, Kasi V. Somayajula, Andrew G. Sharkey, and David M. Hercules*, Department of Chemistry, University of Pittsburgh, Pittsburgh, PA 15260

Elimination of Unexpected Ions in Electron Capture Mass Spectrometry Using Carbon Dioxide Buffer Gas 2523

Carbon dioxide buffer gas provides a means of eliminating unexpected and misleading ions that are commonly observed in high-pressure electron capture MS when methane is used as the buffer gas.

L. J. Sears and E. P. Grimsrud*, Department of Chemistry, Montana State University, Bozeman, MT 59717

Axial Magnetic Inhomogeneities and Low Energy Ion Injection in Fourier Transform Ion Cyclotron Resonance Spectrometry 2528

Magnetic field inhomogeneities are generated by the interaction of highly paramagnetic cell materials with uniform magnetic fields. These inhomogeneities are more significant as magnetic field strength is increased. Stray fields complicate trapping and detection of ions by FT-ICR spectrometry.

Eric L. Kerley, Curtiss D. Hanson, Mauro E. Castro, and David H. Russell*, Department of Chemistry, Texas A&M University, College Station, TX 77843

Measurement of Linear Alkylbenzenesulfonates in Aqueous Environmental Matrices by Liquid Chromatography with Fluorescence Detection 2534

LASs are isolated from complex matrices by sequential adsorption and recovery from C₂ and strong anion-exchange SPE cartridges. LASs in the isolated fractions are separated by HPLC and measured with a fluorescence detector. The limit of quantitation ($S/N \geq 10$) is 7–10 ppb.

Mark A. Castles, Billy L. Moore*, and Susan R. Ward, The Procter and Gamble Company, Ivorydale Technical Center, Cincinnati, OH 45217

Retention Mechanisms of Reversed-Phase Liquid Chromatography: Determination of Solute-Solvent Interaction Free Energies 2540 ■

Predictions of mean-field statistical mechanical lattice theories describing the retention mechanism in reversed-phase LC are tested against a large database. Descriptions of contact interactions of solutes with molecular neighbors in mobile and stationary phases are in good agreement with experimental results.

Peter T. Ying and John G. Dorsey*, Department of Chemistry, University of Florida, Gainesville, FL 32611, and Ken A. Dill*, Departments of Pharmaceutical Chemistry and Pharmacy, University of California, San Francisco, CA 94143

Laser-Enhanced Ionization as a Diagnostic Tool in Laser-Generated Plumes 2546

Laser-enhanced ionization is used to monitor ion formation in the laser microprobe with the use of a single dye laser. Acoustic waves generated from the laser plasma are used to normalize the ion signals for improved precision.

Ho-ming Pang and Edward S. Yeung*, Ames Laboratory—USDOE and Department of Chemistry, Iowa State University, Ames, IA 50011

Characteristics of Methods for the Simultaneous Determination of Catalysts by First-Order Inhibition Kinetics 2551

Factors that affect the simultaneous kinetic determination of catalysts based on different rates of inhibition by a common reagent are evaluated.

Carol P. Fitzpatrick and Harry L. Pardue*, Department of Chemistry, Purdue University, West Lafayette, IN 47907

Elemental Analysis Based on Chemiluminescence in the Laser Microprobe 2557

Chemiluminescence is used as a detection scheme in laser microprobe analysis, and the acoustic signal can be used as an internal standard to improve precision.

Jianzhong Zhu and Edward S. Yeung*, Ames Laboratory—USDOE and Department of Chemistry, Iowa State University, Ames, IA 50011

Measurement of the Rate of Oxidation of Iodide by Iron(III) Using Solvent Extraction 2562

(Pseudo)-first-order rate constants of $\sim 1 \text{ s}^{-1}$ are measured for the oxidation of I⁻ with Fe³⁺ by extraction of the product I₂ and deconvolution.

Lawrence Amankwa and Frederick F. Cantwell*, Department of Chemistry, University of Alberta, Edmonton, Alberta, Canada T6G 2G2

Pulsed Amperometric Detection of Glucose in Biological Fluids at a Surface-Modified Gold Electrode 2566

The direct electrochemical oxidation at a gold electrode of glucose in biological samples is accomplished. By using a bilayer polymer coating, it is possible to achieve reasonable selectivity and freedom from electrode fouling, which is not possible with a bare electrode.

Dilbir S. Bindra and George S. Wilson*, Department of Chemistry, University of Kansas, Lawrence, KS 66045

Bias and Nonlinearity of Ultraviolet Calibration Curves Measured Using Diode-Array Detectors 2571

Models and experimental results characterizing the bias and nonlinearity of measured UV fixed-wavelength absorbance indicate a fundamental behavioral distinction between two classes of diode-array detectors.

Eric V. Dose and Georges Guiochon*, Department of Chemistry, University of Tennessee, Knoxville, TN 37996, and Analytical Chemistry Division, Oak Ridge National Laboratory, Oak Ridge, TN 37831

Acrodisc: The Difference is Clear.

Clearly the Widest Selection.

Gelman Sciences Acrodiscs® are available in a wide variety of membrane types, with 0.2 μ m or 0.45 μ m pore sizes and 13mm or 25mm diameters.

Clearly Identified.

Acrodiscs are printed with identifying information, and are color-coded to the product packaging. Convenient tube containers allow you to see their contents at a glance.

Clearly the Best Performance.

Gelman Sciences is so certain you'll be satisfied with the performance of its Acrodisc syringe filters, every package is covered by a free-replacement guarantee. So order Gelman Sciences Acrodiscs today through your local laboratory products distributor.

CIRCLE 58 ON READER SERVICE CARD

 **Gelman Sciences**

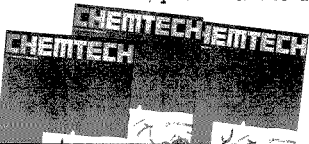
600 S. Wagner Rd. • Ann Arbor, MI 48106-1443 • 313-665-0661



Whether you are in research, development, management, or all three . . .

CHEMTECH is the publication you should be reading!

CHEMTECH is so stimulating, so wide-ranging, so idea-packed, it's guaranteed! Once you've seen an issue of CHEMTECH, you'll want to use it every day.



Countless benefits in each monthly issue!

ARTICLES

You'll welcome regular access to wide-ranging authoritative articles on people management . . . legal issues . . . new chemical technologies . . . chemical effects within the environment . . . development of new materials . . . new engineering techniques . . . education . . . business strategies . . . uses of computers and robotics . . . just to name a few.

CHEMTECH also contains regular features that will undoubtedly become your favorite reading . . .

VALUED HIGHLIGHTS

Heart Cuts point the way to new products, processes, research, or simply that odd fact you wouldn't see anywhere else. You'll also find informative highlights from current literature.

EYE-OPENING OPINIONS

View from the Top gives CEO's, university presidents, and other top-ranking industry leaders a chance to speak out. The *Guest Editorial* is one person's opinion on important issues of all kinds. And each month the founding editor, *B.J. Luberoff*, provides a provocative look at today's world.

CHEMTECH also looks at the world with a lighter eye in *The Last Word* and original cartoons. We could go on, but there just isn't enough room!

See for yourself . . . **Subscribe today!**

1989 Rates		U.S.	Canada & Mexico	Europe**	All Other Countries**
Members*	One Year	\$ 37	\$ 43	\$ 50	\$ 54
	Two Years	\$ 62	\$ 74	\$ 88	\$ 96
Nonmembers (Personal)	One Year	\$ 65	\$ 71	\$ 78	\$ 82
	Two Years	\$110	\$122	\$136	\$144
Nonmembers (Institutional)	One Year	\$282	\$288	\$295	\$299
	Two Years	\$479	\$491	\$505	\$513

*For personal use only. **Air Service included.

Foreign payment must be made in U.S. dollars by international money order, UNESCO coupons, or U.S. bank draft. Orders accepted through your subscription agency. For nonmember rates in Japan, contact Maruzen Co., Ltd.

Subscriptions to CHEMTECH will begin when order is received and will expire one year later unless specific start date is requested. Please allow 45 days for your first copy to be mailed.

To subscribe, contact: American Chemical Society, Marketing Communications Dept., 1155 Sixteenth Street, NW, Washington, DC 20036. Telex: 440159 ACSP UI or 89 2582 ACSPUBS.

In a hurry? Call TOLL FREE (800) 227-5558 (U.S. Only) and charge you order! In D.C. or outside the U.S. call (202) 872-4363. Or FAX your order: (202) 872-4615. Please send FAX to the attention of the Marketing Communications Dept.

BRIEFS

Built-in Carbon-13 Intensity Reference for Solid-State Analysis by Magic-Angle-Spinning Nuclear Magnetic Resonance Spectrometry 2579

Detailed ^{13}C relaxation and calibration experiments demonstrate that the ^{13}C NMR signal of the "built-in" Delrin resonance of a large-sample MAS system can be used as an intensity standard for absolute ^{13}C spin counting measurements.

Ming Zhang and Gary E. Maciel*, Department of Chemistry, Colorado State University, Fort Collins, CO 80523

Technical Notes

Evaporation Device for Continuous Flow Liquid Secondary Ion Mass Spectrometry 2582

Ming-chuen Shih*, Tao-Chin Lin Wang, and S. P. Markey*, Laboratory of Clinical Science, National Institute of Mental Health, Bethesda, MD 20892

Manual Headspace Method To Analyze for the Volatile Aromatics of Gasoline in Groundwater and Soil Samples 2584

Valerie D. Roe, Michael J. Lacy, and James D. Stuart*, Department of Chemistry, U-60, 215 Glenbrook Road, University of Connecticut, Storrs, CT 06269-3060 and Gary A. Robbins, Department of Geology and Geophysics, U-45, 345 Mansfield Road, University of Connecticut, Storrs, CT 06269-3045

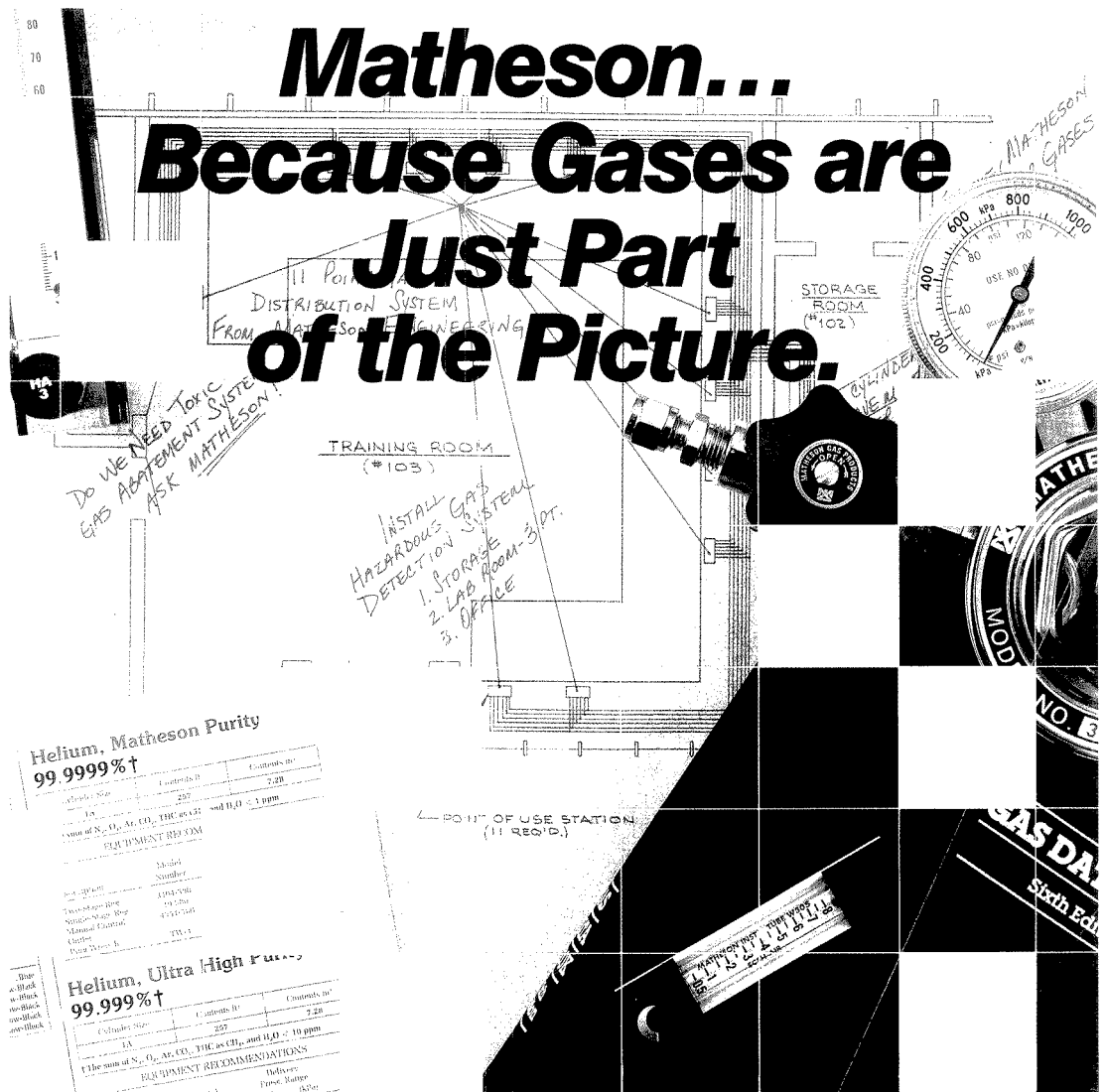
Comparison of Paraffin Oil and Poly(chlorotrifluoroethylene) Oil Carbon Paste Electrodes in High Organic Content Solvents 2585

Neil D. Danielson*, Julie Wangsa, and Margaret A. Targove, Department of Chemistry, Miami University, Oxford, OH 45056

Versatile Impedance Matching Network for Inductively Coupled Plasma Spectrometry 2589

Akbar Montaser*, Izumi Ishii, and R. H. Clifford, Department of Chemistry, George Washington University, Washington, D.C. 20052, and S. A. Sinex and S. G. Capar, Division of Contaminants Chemistry, Food and Drug Administration, Washington, D.C. 20204

Matheson... Because Gases are Just Part of the Picture.



Helium, Matheson Purity
99.9999% †

Cylinder Size	Contents (lb)	Contents (m³)
1A	257	7.28
The sum of N ₂ , O ₂ , Ar, CO ₂ , H ₂ C as CH ₄ , and H ₂ O < 1 ppm		
EQUIPMENT RECOMMENDATIONS		
Deliver	Purity	
Pressure	Range	
Flow	Rate	

Helium, Ultra High Purity
99.999% †

Cylinder Size	Contents (lb)	Contents (m³)
1A	257	7.28
The sum of N ₂ , O ₂ , Ar, CO ₂ , H ₂ C as CH ₄ , and H ₂ O < 10 ppm		
EQUIPMENT RECOMMENDATIONS		
Deliver	Purity	
Pressure	Range	
Flow	Rate	

You know Matheson as the pioneer in specialty gases; the reliable supplier of over 90 different gases in a variety of purities and sizes to suit your application.

But, did you know that Matheson offers you much more to meet today's laboratory requirements for increased efficiency and safety? Matheson engineers can provide you with gas distribution systems, hazardous gas detection instrumentation and toxic waste abatement systems customized to meet your lab's need.

Gases cannot be used alone. You need the right

Gas Distribution Systems,
select Reader Service No. 100

Toxic Waste Abatement,
select Reader Service No. 101

Gas Detection,
select Reader Service No. 102

Gases,
select Reader Service No. 103

regulators, flowmeters and other equipment to handle them properly. To select or install the right equipment to achieve maximum effectiveness, the exclusive full service back-up of Matheson is required.

Get the whole picture. Contact your Matheson office or use the Reader Service Numbers below.

Matheson
Gas Products

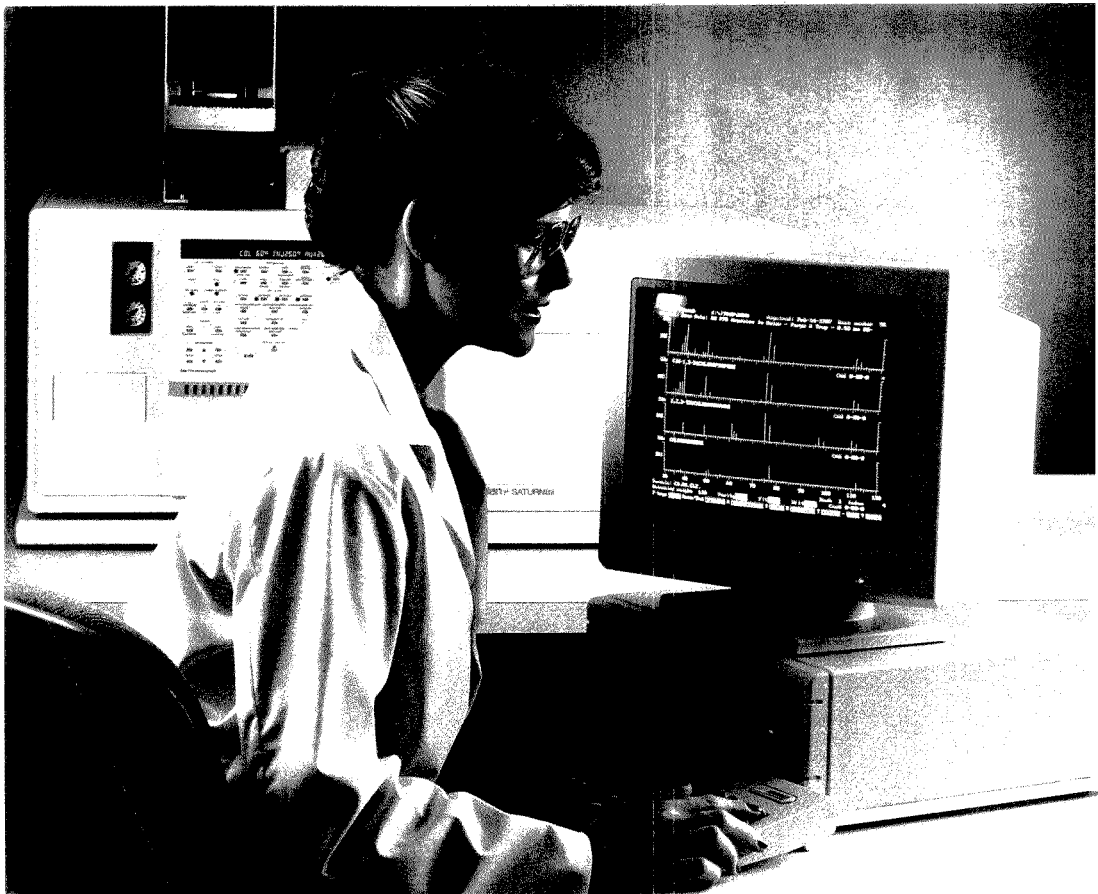
World Leader in Specialty Gases & Equipment
30 Seaview Drive, Secaucus, NJ 07096-1587

Regulators,
select Reader Service No. 104

Flowmeters,
select Reader Service No. 105

Gas Handling Equipment,
select Reader Service No. 106

Publications,
select Reader Service No. 107



THE FUTURE OF GC/MS IS WITH VARIAN.

The best GC/MS, now and in the future, starts with chromatographic excellence. After all, if you don't start with expert chromatographic techniques, how can you trust the final results? Look to the company known for its expertise — from sample handling to the most sensitive detection — Varian.

The combination of our proven 3400 Gas Chromatograph with second generation ion trap technology brings the most sensitive and reliable benchtop GC/MS to the market.

The new Varian Saturn GC/MS System gives picture perfect spectra even at picogram levels, a significant advantage over conventional benchtop quadrupoles. It's important to know that you can count on the Saturn GC/MS to give you the whole picture when you're confirming compounds, because you're doing scientific analyses that affect our environment, our health, the products we use, and must meet regulatory protocols.

Chromatographic excellence and the most sensitive mass spec detector, coupled with Varian's renowned service and support throughout the world, make this the GC/MS with a future.

Let us show you why you should invest your GC/MS future with Varian. For more information, call **800-231-8134**. In Canada, call **416-457-4130**.

VI6-5159/259 9/85

CIRCLE 170 ON READER SERVICE CARD

GC WITH A FUTURE



Coetzee Given Pittsburgh Award



The ACS Pittsburgh Section has presented its 1989 Pittsburgh Award to analytical chemist Johannes Coetzee. This annual award recognizes an individual who has made outstanding contributions to the Pittsburgh chemistry community.

Coetzee, professor of chemistry at the University of Pittsburgh, was cited for his research detailing interactions in solution—particularly among electrolytes in dipolar aprotic solvents—and his electroanalytical studies. He was also recognized for his enthusiastic teaching of analytical chemistry.

Coetzee received his B.Sc. (1944) and M.Sc. (1949) degrees from the University of the Orange Free State in his homeland of South Africa and a Ph.D. from the University of Minnesota (1956). He taught for a short time at South Africa's University of Witwatersrand before joining the Pittsburgh faculty in 1957.

Pittsburgh Conference College Grants

The Pittsburgh Conference on Analytical Chemistry and Applied Spectroscopy, Inc., the Spectroscopy Society of Pittsburgh, and the Society for Analytical Chemists of Pittsburgh will once again sponsor the Pittsburgh Conference Memorial National College Grants Award Program. Established in 1974, the program is designed to enhance science education through grants to small colleges. Ten colleges each will receive up to \$3000 for the purchase of undergraduate teaching materials (e.g., scientific equipment, audio-visual equipment, and library materials).

To be eligible, a college must have an enrollment that does not exceed 2500 students and must receive no more than 25% of its operating budget from national or state governments. Two-year community colleges sponsored by political subdivisions of a state are not bound by these requirements. Awardees are ineligible for another grant for three years following receipt of their award.

Interested faculty members should request applications from George L. Vassilaros, The Pittsburgh Conference Inc., 300 Penn Center Boulevard, Suite 322, Pittsburgh, PA 15235. The deadline for completed applications and proposals is March 1, 1990. Award winners will be announced by May 1, 1990.

Concentrated Neutrons

Improvements in the beam delivery system have boosted the peak neutron flux for Los Alamos National Laboratory's Lujan Neutron Scattering Center (LANSCE) to the highest in the world. The neutron beam intensity regularly runs approximately 20% higher than neutron beams generated at comparable facilities.

LANSCE is a national user facility dedicated to research on the fundamental structure of important materials such as polymers and superconductors. With a higher neutron flux, smaller samples can be studied and more precise data can be collected in a shorter period of time.

The center's neutron beam is generated from short, repetitive pulses of protons striking a tungsten target, each proton producing about 20 neutrons. The protons, in turn, are generated in Los Alamos's linear accelerator and stored in the neutron facility's proton storage ring. Inside this unique storage ring, protons are concentrated before striking the target. Improvements in this system have increased the beam delivery efficiency by 70%. Protons now strike the target 20 times per second with an average current of 50 μ A. Eventually, predict Los Alamos scientists, the system should reach 100- μ A currents.

For Your Information

R. Bruce Prime of IBM's General Products Division Development Laboratories in San Jose, CA, **has won the 1989 Mettler Award** for distinguished achievements in the area of thermal analysis. Prime was honored for his work characterizing the cure and composition of coatings for rigid magnetic recording disks, for which he codeveloped the TGA-APCI/MS/MS approach and applied time/temperature superposition to kinetic processes.

The American Society for Testing and Materials (ASTM) requests assistance in developing two new standards. The subcommittee on Geotechnics of Waste Management needs participants to help in the formulation of a new standard practice for the decontamination of field equipment used at low-level radioactive waste sites. For more information, contact G. David Knowles, Malcom Pirnie, 4 Corporate Plaza, Albany, NY 12203 (518-869-7257) or Bob Morgan, ASTM, 1916 Race St., Philadelphia, PA 19103 (215-299-5505). The subcommittee on Methods of Sampling and Analysis is seeking laboratories willing to test new methods for measuring Cr in welding fumes, Cr in the workplace, and ethylene oxide. For more information, contact S. D. Allen Iske, Mobay Corp., P.O. Box 4913, Kansas City, MO 64120 (816-242-2498) or George Luciw, ASTM (215-299-5571).

Bruce Lewenstein, a communication professor at Cornell University, is investigating the roles scientists, journalists, and others played in the recent University of Utah claims of **room-temperature fusion**. He is requesting that scientists send seminar, lecture, or laboratory notes; computer bulletin board notices; bibliographies; and any other documents related to cold fusion that can be archived. His address is 640 Stewart Avenue, Ithaca, NY 14850.

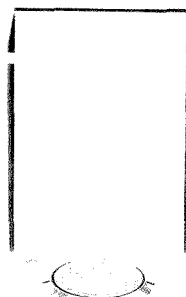
Merck has produced a **new version of *The Merck Index***, 100 years after publication of the first edition. The first copy of this centennial edition was presented to the ACS at this fall's national meeting in Miami.



Ultra Wide Range! The FR Series of Precision, Multi-functional Analytical Balances

Another first from A&D — Analytical precision balances with multi weighing units, multi-functions and optional wireless remote control.

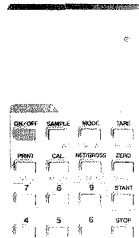
By using the latest electronic technology combined with easy-to-use multi-function features and extensive ergonomic design — the FR series will revolutionize the ways you can use an analytical balance. Multi weighing units; Comparator mode; Percentage add/subtract mode; Counting mode; Environmental conditions adjustment (including last-digit blanking during course weighing); Auto power ON; — and much, much more.



Wireless Remote Control
RS-232C
COMPARATOR

Wireless remote control with total command at the push of a single button!

Start with an optional wireless remote control that simplifies and expands operation of every feature the balance has available — then, enjoy the rest of the full range of options available for the FR Series.

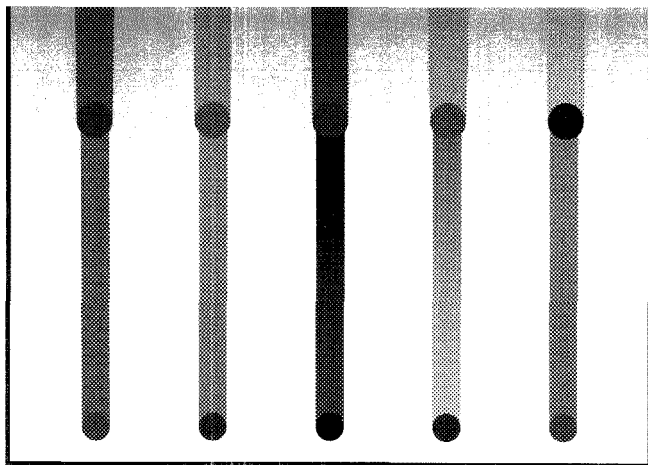


A&D

ANALYTICAL & DIGITAL
ENGINEERING, INC.

3555 McCandless Drive, Marietta, GA 30035
 Tel: (404) 233-0119 Telex: 345940 AANDD SNJ
EAST COAST BRANCH OFFICE
 2185 N. West Park Court, Stone Mountain, GA 30087
 800: 426-4480, In Georgia (404) 498-9732
 Fax: (404) 498-4877

CIRCLE 2 ON READER SERVICE CARD



MODERN THIN-LAYER CHROMATOGRAPHY

Colin F. Poole and Salwa K. Poole
Department of Chemistry
Wayne State University
Detroit, MI 48202

Thin-layer chromatography (TLC) as practiced in the 1980s is very much an instrumental technology. TLC methods are most effective for low-cost analysis of simple mixtures when the sample workload is high, for rapid analysis of simple mixtures requiring minimum sample cleanup, for analysis of samples containing components that remain sorbed to the separation medium or contain suspended microparticles, and for analysis of substances with poor detection characteristics that require postchromatographic treatment for detection.

In this REPORT we will introduce some of the important modern devel-

REPORT

opments of TLC that will make the technique useful in the next decade and define the scope and limitations of TLC as an analytical tool. Rather than claim that TLC should replace HPLC as a separation tool, we will attempt to show that the two techniques are complementary and that the experienced analyst should have both techniques at his or her disposal for problem solving and routine analysis.

Modern TLC originated in the mid-1970s with the commercial introduc-

tion of fine-particle layers optimized for fast and efficient separations with controlled sample application (1). Table I compares these small-particle plates with conventional TLC plates. The tightness of the particle size distribution is just as important as the decrease in actual particle size in the performance of the new plates (2). In many cases, they were not well received when first introduced. Too often, they were used with methods considered more appropriate for conventional plates and were overloaded with sample and developed for too long a migration length, which resulted in longer separa-

tion times and poorer resolution than for conventional plates.

Table I shows that these new layers require smaller sample sizes and shorter migration lengths to reveal their true separation potential and to deliver large savings in analysis time; better resolution; and, because spots are more compact and the optical properties of the layer more favorable for in situ detection, much better detection limits. Today, many types of fine-particle layers are available, including silica, bonded phases, and cellulose. In fact, just about all phases used for normal and reversed-phase HPLC are

Table I. Comparison of conventional and modern TLC

Parameter	Conventional TLC	Modern TLC
Plate size (cm)	20 × 20	10 × 10
Layer thickness (μm)	100–250	200
Particle size (μm)		
Average	20	Between 5 and 15
Distribution	10–60	Narrow
Sample volume (μL)	1–5	0.1–0.2
Starting spot diameter (mm)	3–6	1.0–1.5
Diameter of separated spots (mm)	6–15	2–6
Solvent migration distance (cm)	10–15	3–6
Time for development (min)	30–200	3–20
Detection limits		
Absorption (ng)	1–5	0.1–0.5
Fluorescence (pg)	50–100	5–10
Sample lanes per plate ^a	10	18–36

^a Simultaneous development from both ends to the center increases this number twofold.

available for TLC (3-5), and bonded chiral phases for the separation of enantiomers have been introduced recently (6-8).

Theory

Separations by TLC are usually achieved using the development mode with the migration velocity of the mobile phase controlled by capillary forces. For fine-particle layers it can be assumed that spot broadening in TLC is controlled entirely by molecular diffusion, resulting in a series of symmetrical, compact spots increasing uniformly in diameter with increasing migration distance (9, 10). For coarse-particle layers, contributions to the plate height from slow mass transfer can be significant and the spots can become distorted in the direction of migration. We will ignore this tendency and assume that the performance of both types of layers can be calculated assuming a Gaussian distribution of the sample within the spot according to

$$n = 16 \left[\frac{Z_s}{W_s} \right]^2 = 16 \left[\frac{R_f Z_f}{W_s} \right]^2 \quad (1)$$

where n is the number of theoretical plates, Z_s the distance migrated by the sample (spot) from its origin, W_s the spot diameter, R_f is the retardation factor (Z_s/Z_f), and Z_f is the distance moved by the mobile phase from the sample origin to the solvent front. Separated components migrate different distances through the layer; their zones are broadened to different extents and, therefore, the efficiency of the TLC plate is only constant for a specific migration distance. This differs from column chromatography using the elution mode and can be confusing when one compares the efficiency of TLC and column systems. By convention, the efficiency of a thin-layer plate is measured or calculated for a substance having an R_f value of 0.5, 1.0, or some average value (10).

If the vapor phase in contact with the layer has attained equilibrium, the speed with which the mobile phase moves through the layer when governed by capillary forces will be described by

$$(Z_f)^2 = \kappa t \quad (2)$$

and the velocity constant κ by

$$\kappa = 2K_0 d_p \left(\frac{\gamma}{\eta} \right) \cos \theta \quad (3)$$

where K_0 is the permeability constant, d_p is the average particle diameter, γ is the surface tension of the mobile phase, η is the viscosity of the mobile phase, θ is the contact angle, and t is the time

(11, 12). Experimental values for K_0 tend to vary more widely than reported values for columns, for which a value of 1×10^{-3} is generally considered to be a good approximation. Values for TLC tend to be somewhat higher, around 8×10^{-3} ; thus, the packing density may be higher in columns than that observed for layers (13). Assuming a narrow particle-size distribution, the velocity constant should increase linearly with the average particle size and thus the solvent front velocity is greater for coarse-particle layers. The velocity constant also depends linearly on the ratio of the surface tension of the solvent to its viscosity, and solvents that maximize this ratio (and not just optimize one of the parameters) are preferred for TLC (13).

Although for silica gel layers the contact angle for all common solvents is close to zero, for reversed-phase layers containing bonded, long-chain alkyl groups the contact angle of the solvent increases rapidly with increasing water content of the mobile phase and, at about 30-40% (v/v) water, $\cos \theta$ becomes smaller than 0.2-0.3 (4, 11). The mobile phase is virtually unable to ascend the thin-layer plate, and chromatography becomes impossible. To improve solvent compatibility, modern reversed-phase TLC plates are prepared from larger size particles (10-13 μm) than other high-performance plates or from sorbents with a defined degree of modification that is lower than that of exhaustively silanized sorbents. Plates with lower degrees of modification can be used without any solvent composition restrictions, and pure water may also be used. Solvent compatibility is much less of a problem for polar, bonded sorbents such as 3-aminopropylsilanized and 3-cyanopropylsilanized sorbents, which are wetted by all solvents including pure water.

If the mobile-phase velocity is controlled externally, as in forced-flow TLC, then the restrictions imposed by using capillary action for solvent migration are removed. The mobile-phase velocity can be controlled and optimized independently of the solvent migration distance and is no longer dependent on the contact angle. Two approaches to forced-flow development have been used (14). In rotational planar chromatography, centrifugal force generated by spinning the sorbent layer about a central axis is used to drive the solvent through the layer (15). The rate of solvent migration is a function of the rotation speed and the rate at which the mobile phase is supplied to the layer. Because the layer is not enclosed, the ultimate velocity of the solvent front is limited by the amount of

solvent that can be kept within the layer without floating over the surface. At high rotation speeds the migration of the solvent front as a function of time becomes approximately constant in the linear development mode. If the sorbent layer is sealed (using a flexible membrane or an optically flat rigid surface under hydraulic pressure) and the mobile phase is delivered to the layer by a mechanical pump, the mobile-phase velocity can be controlled and optimized by adjusting the output from the pump feeding the mobile phase to the layer. For a pump with a constant volume delivery using linear development mode, the migration of the solvent front will be a linear function of time.

Figure 1 demonstrates the importance of using an optimal and constant mobile-phase velocity. Under capillary flow-controlled conditions with fine-particle layers, the average plate height first passes through a minimum and then increases sharply for longer migration distances. For coarse-particle layers the plate height is less dependent on the migration distance and eventually the two curves cross, indicating that a greater number of theoretical plates can be obtained by using coarse-particle layers and long migration distances.

This contrary finding is easily explained by the relative permeability of the layers. The mobile-phase velocity for the fine-particle layer declines rapidly with the migration distance until it becomes so slow that diffusion causes the spots to broaden at a rate faster than the spot centers are migrating through the layer. The coarse-particle layer is more permeable than the fine-particle layer, and both the solvent velocity and the efficiency are higher at longer plate lengths. For fine-particle layers with a development length of 5-7 cm it should be possible to obtain up to about 5000 theoretical plates, but it is nearly impossible to exceed this number using capillary flow-controlled development. For coarse-particle layers ($d_p \approx 15 \mu\text{m}$), a development length of about 15 cm is required to obtain around 5000 theoretical plates and, although higher numbers are possible, they will lead to long separation times. Fine-particle layers are preferred for capillary flow-controlled conditions because they provide faster separations; separations that can be achieved only with more than 4000-5000 theoretical plates are too difficult to be worthwhile.

In forced-flow TLC the average plate height is largely independent of the migration distance and is more favorable for fine-particle layers than coarse ones

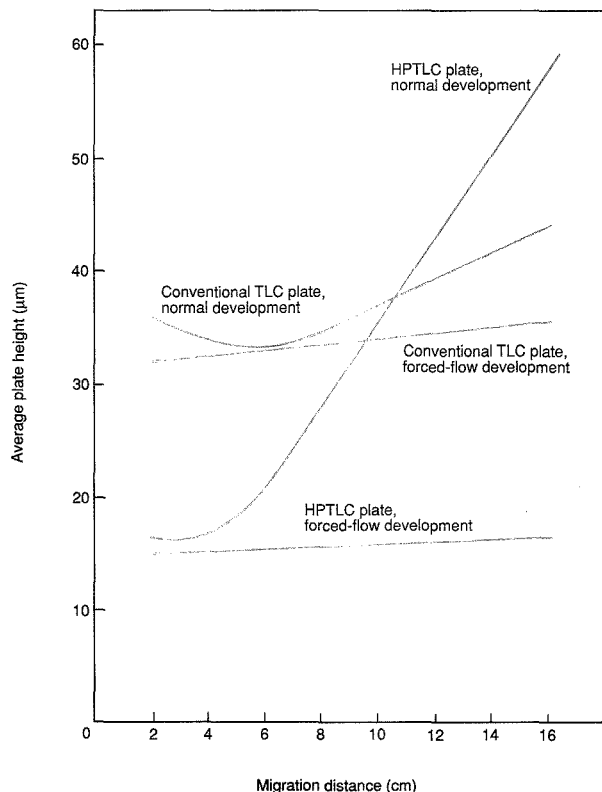


Figure 1. Variation of the efficiency (average plate height) of fine- and coarse-particle layers as a function of migration distance and development technique. (Adapted with permission from Reference 2.)

(Figure 1). The quadratic decrease in linear velocity with time is defeated, and an optimum constant linear velocity—similar to that for column chromatography—leads to the optimum plate height (10, 16). Compared with capillary flow-controlled systems, zone broadening by diffusion is now minor even for long migration distances because the optimum mobile-phase velocity is always higher than that observed for ascending development by capillary flow. Commercially available TLC layers and equipment make it possible to achieve an upper limit of about 31,000 plates ($Z_f = 25$ cm), but it will be difficult to exceed this value. However, this limit is not theoretical; the ultimate efficiency of the forced-flow system is limited only by the particle size and homogeneity of the bed, the

available bed length, and the pressure required to maintain the optimum mobile-phase velocity.

The object of any chromatographic analysis is to rapidly obtain a certain resolution between individual components of a mixture. To control resolution we must know how it varies with experimental parameters such as the layer efficiency, the ratio of the equilibrium constants governing the separation process, and the position of the zones within the chromatogram (17). This variation can be expressed approximately by Equation 4 for a single unidimensional development under capillary flow-controlled conditions:

$$R_S = \frac{\sqrt{n_f R_{f2}}}{4[(k_1/k_2) - 1][1 - R_{f2}]} \quad (4)$$

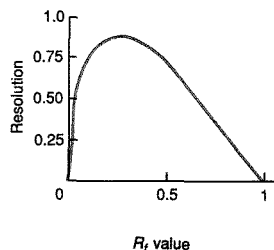


Figure 2. Change in resolution of two closely migrating spots as a function of the R_f value of the faster moving spot. (Adapted with permission from Reference 2.)

where R_S is the peak-to-peak resolution, n_f is the number of theoretical plates for a zone migrating with the solvent front, and k is the capacity factor $[(1 - R_f)/R_f]$. The subscripts 1 and 2 refer to the individual zones numbered such that the larger number corresponds to the zone with the highest R_f value. The variation of resolution with R_f is not a simple function (see Figure 2). The resolution increases with the square root of the layer efficiency, which depends linearly on the R_f value. The influence of the position of the zones in the chromatogram on resolution shows the opposite behavior to that of the layer quality. At greater values of R_{f2} , the term $1 - R_{f2}$ will decrease and the resolution will become zero at a value of $R_{f2} = 1$. Differentiation of Equation 4 indicates that the optimum resolution of two closely migrating zones will occur at an R_f value of about 0.3. Figure 2 indicates that the resolution does not change significantly for R_f values between 0.2 and 0.5; within this range, the resolution is greater than 92% of the maximum value. This R_f region is thus the target zone for solvent selection to achieve the optimum resolution of the most difficult solute pair in a mixture.

TLC separations generally can be optimized by increasing the selectivity of the system because relatively small changes in selectivity make it much easier to obtain a given separation. The total number of theoretical plates that can be made available for a separation cannot be increased sufficiently to make kinetic optimization the most worthwhile approach to improving resolution. In planar chromatography, separations are easy when $(R_{f2} - R_{f1})$ is greater than 0.1 and very difficult or impossible when $(R_{f2} - R_{f1})$ is less than or equal to 0.05 in the region of the

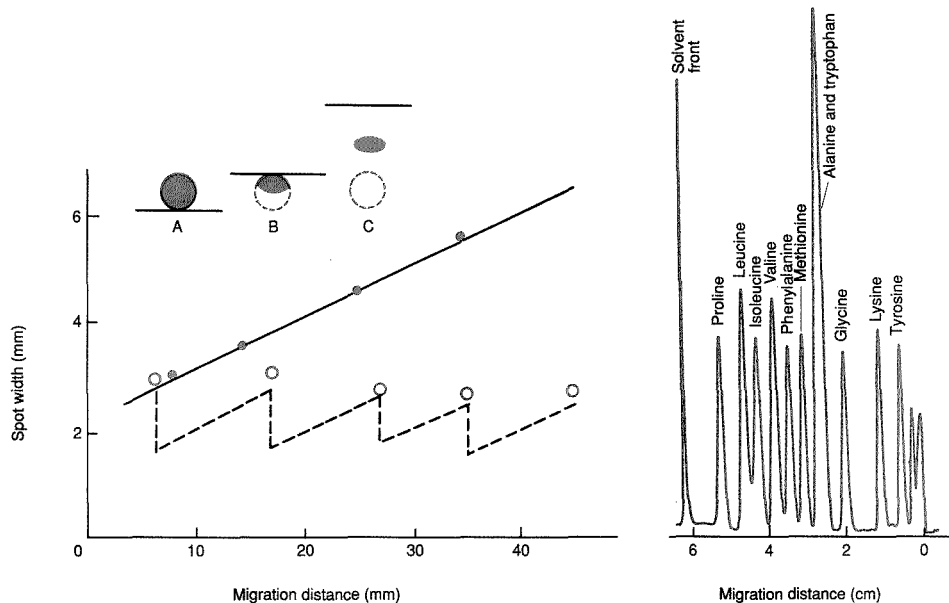


Figure 3. Separation of a mixture of PTH-amino acid derivatives by unidimensional multiple development, illustrating the spot re-concentration mechanism used to control zone broadening. (Adapted with permission from Reference 23.)

optimum R_f value for the separation. Window diagrams, simplex methods, statistical design, and the prisma method have emerged in the past few years as powerful solvent optimization strategies for TLC (18–20). These methodological guides and computational techniques minimize the number of trial-and-error experiments required to identify the most valuable solvent systems for a separation.

Under forced-flow conditions there is no maximum obtained for resolution as a function of migration distance (16). In this case, the resolution continues to increase with increasing migration distance; the upper limit is established by practical constraints such as the available sorbent length, acceptable separation time, and the inlet pressure required to maintain the optimum mobile-phase velocity.

A popular approach for improving resolution under capillary flow-controlled conditions is to use multiple development (21–23). Either unidimensional or two-dimensional separations are possible in planar chromatography. In unidimensional multiple development, the TLC plate is developed for some selected distance or time (continuous development), the plate is withdrawn from the developing chamber

and the adsorbed solvent evaporated, and the plate is returned to the developing chamber and the development process repeated. This versatile strategy for separating complex mixtures allows variation among the primary experimental components: plate length (or time), composition of the mobile phase for each development, and the number of developments.

Another unique feature of the multiple development process is the zone re-concentration mechanism, illustrated in Figure 3, which enhances the layer efficiency by counteracting the zone diffusion broadening mechanism. Each time the solvent front traverses the stationary phase, it compresses the spot in the direction of development. Initially the spot will be round, but gradually it will become more oval shaped until—if a sufficiently large number of developments are used—it will be compressed to a thin band. The compression occurs because the mobile phase first contacts the bottom edge of the spot where the sample molecules start to move forward before those molecules that are still ahead of the solvent front. Once the solvent front has reached beyond the spot, the re-concentrated spot migrates and is broadened by diffusion in the usual way. It is thus possible to

migrate a spot a substantial distance without significantly changing the zone dimensions in the direction of migration.

One disadvantage of multiple development is that for samples requiring a large number of theoretical plates (long migration length) a lot of time is wasted while the solvent level reaches the level of the lowest spot on the plate. For capillary controlled-flow conditions, the mobile-phase velocity may no longer be adequate to maintain optimum separation conditions. A solution to this problem is to position the solvent entry point higher on the plate at each development step (24, 25), thereby increasing efficiency about eightfold over that of conventional development. This method can be accomplished within a similar separation time by using 10 development steps. A theoretical framework for multiple development would be very complex and has only been solved for repetitive development without change of solvent or migration distance (17).

Multidimensional and multimodal TLC

In two-dimensional TLC the sample is spotted at the corner of the layer and developed along one edge of the plate. The solvent is then evaporated and the

plate rotated 90° and redeveloped in the orthogonal direction. If the same solvent is used for both developments, only a slight increase in resolution can be anticipated (a factor of $\sqrt{2}$). This increase will correspond to the increased migration distance for the sample. More efficient separation requires the resolved sample to be distributed over the entire plate surface, necessitating complementary separation mechanisms for the orthogonal development that may be challenging to achieve. Difficulties in scanning two-dimensional chromatograms with slit-scanning densitometers and in the construction of a two-dimensional forced-flow instrument have prevented two-dimensional TLC from reaching its true potential as a separation tool.

The potential of a chromatographic system to provide a certain separation can be estimated from its separation number, referred to as the spot capacity in TLC (i.e., the number of spots resolved with a resolution of unity that can be placed between the sample spot at the origin and the spot of an unrestrained compound) (17, 26). An exact spot capacity value is more difficult to calculate than the equivalent value for a column system because it depends on many experimental variables that are not well understood.

For a single, unidimensional development using capillary flow-controlled conditions, it is not difficult to achieve a spot capacity between 10 and 20, but it is very difficult to reach 25 and practically impossible to exceed 30. To obtain separation numbers greater than 25, very long plates and prohibitively long separation times would be needed. (In HPLC, separation numbers around 150 can be achieved; in exceptional cases, a value of 500 can be obtained.) In theory, the spot capacity of forced-flow TLC should be identical to that of column chromatography. In practice, however, shorter bed lengths and limited inlet pressures compared with those used in column chromatography set a practical limit of about 80 with commercially available equipment (with a plate length of 30 cm, a particle size of 5 μm , and a pressure drop of 36 atm). For two-dimensional TLC under capillary controlled-flow conditions it should be easy to achieve a spot capacity of 100–250, but it will be difficult to reach 400 and nearly impossible to exceed 500 except in very favorable circumstances. If forced-flow development is used in the first direction and elution in the second, a spot capacity of a few thousand is achievable. This represents an order of magnitude increase in separation potential over column systems, but the experimental difficul-

ties in implementing such a separation system are formidable (27).

The confident analysis of moderate-to-complex mixtures requires a large separation capacity that is most readily obtained by using multidimensional and multimodal separation techniques (21, 23). In multimodal separations two different separation techniques are combined via an interface that ideally allows independent and optimized use of the two separation techniques. Examples of multimodal techniques include GC/TLC, HPLC/TLC, and SFC/TLC. Spectroscopic techniques such as IR, Raman, and mass spectrometry can be used in alternative multimodal approaches in which partially separated sample zones are further resolved based on differences in their spectroscopic properties (23, 28). The TLC plate can function as a storage medium, enabling spectroscopic evaluation that is free of time constraints and time-consuming techniques such as signal averaging to improve sensitivity.

Interface requirements for coupling microcolumn HPLC or SFC to TLC are comparatively simple. With microbore HPLC columns that operate at flow rates of 5–100 $\mu\text{L}/\text{min}$, the complete

column effluent can be deposited on the TLC plate using a modified spray-jet band applicator (29, 30). For example, Jaenchen used this approach to separate a mixture of 56 pesticides by a combination of reversed-phase microbore HPLC and normal-phase automated multiple development (31). More than a decade ago, Stahl (32) described an apparatus for supercritical fluid extraction (SFE) and deposition onto a TLC plate, which used a very fine heated capillary (25–50 μm) as the interface. Decompression of the supercritical fluid occurs with rapid cooling that favors the deposition process without inhibiting the evaporation of the decompressed fluid. The current strong interest in SFE should encourage reevaluation of Stahl's early work, particularly if spectroscopic evaluation for structural identification is required. The TLC plate in this case is a much more convenient fluid elimination interface for spectroscopy than some of the on-line approaches currently under development. Certain spectroscopic techniques such as low-temperature fluorescence line-narrowing spectroscopy, surface-enhanced Raman spectroscopy, and liquid sur-

IF YOU CAN'T LIVE WITH OUR STANDARDS, WE'LL CHANGE THEM.



If your spectrometric analysis of metals in oils requires a blend of elements we don't routinely offer—we'll custom blend it for you. Conostan custom blending allows you to test for unusual combinations

and concentrations of elements with minimal interference and repeatable results. For a complete list of Conostan single and multi-element standards, write or call for our free brochure. If you don't find what you

need, we'll blend something special just for you.



Conostan Division
Conoco Specialty Products Inc.
P.O. Box 1267
Panca City, OK 74603
Phone: (405) 767-3078
Fax: (405) 767-5843

CIRCLE 28 ON READER SERVICE CARD

face ionization MS are actually enhanced by entrainment of the sample in a sorbent matrix compared to solution spectra, and their use might well increase in the future (28).

Instrumentation

Without the commercial availability of reliable instrumentation for in situ quantitation of planar separations, TLC would not have made the progress and attained the acceptance that it has. Earlier methods of quantitation, such as visual comparison of colored or chemically visualized zones or excision of separated zones from the layer followed by elution from the sorbent and spectrophotometric analysis, are too insensitive, imprecise, labor-intensive, and tedious for acceptance in a modern analytical laboratory.

At low sample concentrations in a nonabsorbing solvent matrix there is a linear relationship between the sample concentration and the intensity of absorbed monochromatic light expressed by the Beer-Lambert law. However, this simple relationship is not applicable to samples dispersed in a solid matrix capable of scattering light. Indeed, the theoretical treatment of absorption of monochromatic light by sorbent-immobilized solutes is complex. The most generally accepted theory, that of Kubelka and Munk, is often expressed in the following form (28, 33-35)

$$\frac{(1 - R_\infty)^2}{2R_\infty} = \frac{2.303aC}{S} \quad (5)$$

where R_∞ is the reflectance for an infinitely thick opaque layer, S is the scatter coefficient, a is the molar absorption coefficient of the sample, and C is the sample concentration. This is only an approximation for thin-layer plates as it is derived explicitly for a layer of infinite thickness. However, it illustrates the general effects of a solid-sorbent matrix on the observed sample response. It predicts, for example, a nonlinear relationship between signal and sample concentration in the absorption mode, an increase in response with increasing molar absorption coefficient, and an increase in response for sorbents with low scatter coefficients. Calibration curves are individual in shape, generally with a pseudolinear region at low sample concentration curving toward the concentration axis at higher concentration, as shown in Figure 4. Calibration curves are usually fitted to polynomial functions, based on the assumption that the linear region of the calibration curve is too short to suffice, but this nonlinearity causes more alarm than common sense dictates. Too often, analysts have assumed un-

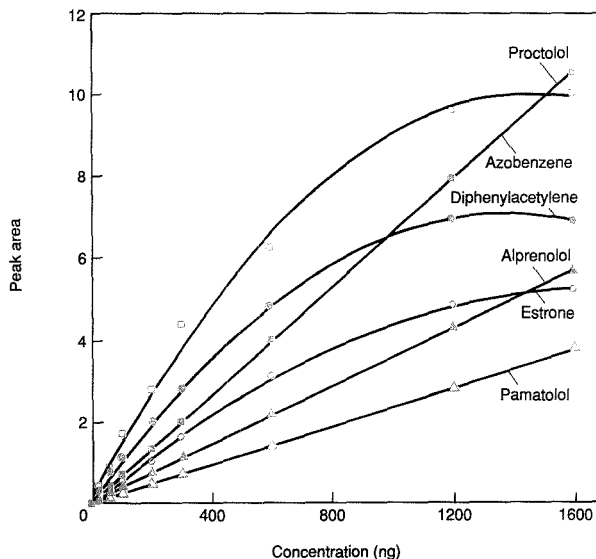


Figure 4. Typical calibration curves determined in the reflectance mode by slit-scanning densitometry at 240 nm.

(Adapted with permission from Reference 28.)

foreseen problems attributable to the curvature of some calibration curves in regions where others are linear, forgetting the individual nature of the calibration curves expressed by Equation 5.

Fluorescence measurements are fundamentally different from absorption measurements, and in this case the sample can be considered a secondary source emitting photons of low-to-moderate intensity but against a very low background. At small sample sizes the fluorescence intensity is usually a linear function of sample amount over 2-3 orders of magnitude, expressed by

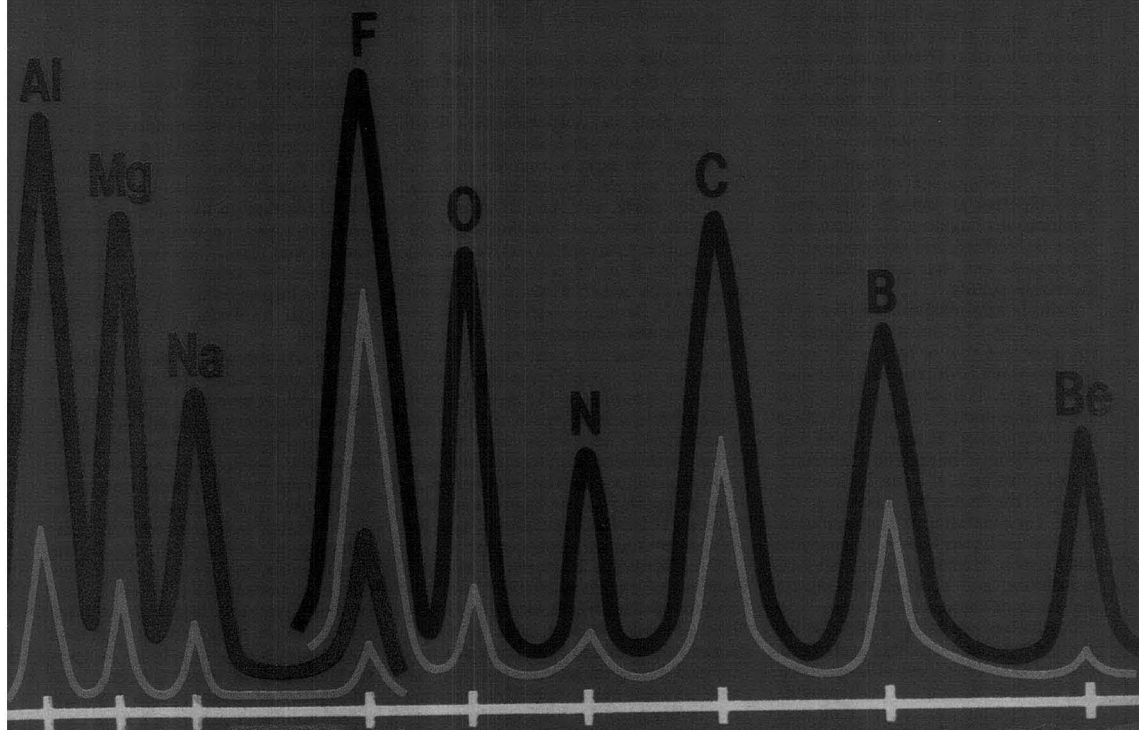
$$F = \phi I_0 abc \quad (6)$$

where F is the fluorescence flux (emission), ϕ is the quantum yield, I_0 is the intensity of the excitation source, a is the absorption coefficient, b is the thickness of the TLC layer, and c is the sample amount (28, 34-37). The magnitude of the fluorescence yield is sometimes influenced by quenching from nonradiative interactions with the sorbent, quenching from atmospheric oxygen in contact with the layer, and sorbent-catalyzed reactions, usually oxidation, to produce new products of low fluorescence yield.

These problems can often be handled by applying antioxidants or fluorescence-enhancing reagents to the sorbent layer (34, 35), and they occur far more commonly with silica gel layers than with chemically bonded silica layers. Also, pre- and postchromatographic derivatization reactions are commonly used to enhance the detection characteristics of those samples with unfavorable detection properties (weak or insignificant absorption or fluorescence in the UV-vis range) because alternative detection methods for routine quantitation of planar chromatograms are unavailable. Also, because detection is carried out in an open system over a finite time, the sample must have negligible vapor pressure at room temperature.

Progress in planar chromatography in the last decade resulted from a synergistic interaction of developments that took place in layer technology, sample application, development methods, and quantitation by densitometry. The most obvious change in the practice of TLC during this period is that the processes of sample application, chromatographic development, and chromatogram recording have become completely "instrumentalized," and often automated, procedures.

TAKE A PEAK AT OVONYX™ MULTILAYERS— YOU'LL NEVER LOOK AT CRYSTALS AGAIN.



Peak intensities 2 to 20 times higher.

When it comes to light element X-ray analysis, Ovonyx multilayers are fast replacing yesterday's Acid Phthalate crystals and Langmuir-Blodgett pseudo-crystals in WD XRF and EPMA spectrometers. With peak intensities 2 to 20 times higher than those of crystals, Ovonyx multilayers offer reflectivities previously unobtainable for light elements. So your X-ray measurements can be faster *and* more accurate.

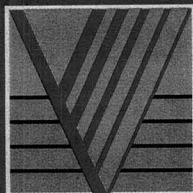
Standardized or customized.

Ovonyx multilayers have been designed for almost every WDXRF spectrometer in use, both old and new. We can also custom design multilayers to meet your particular research requirements.

So before you look into replacing your crystals, look into Ovonyx. And take advantage of today's technology.

Call us today for details at 1-800-366-1299.

 OVONYX™
 CRYSTALS



OVONYX™

Ovonic Synthetic Materials Co., Inc.
A Subsidiary of Energy Conversion Devices, Inc.
1788 Northwood Drive
Troy, MI 48084
(313) 362-1290
FAX (313) 362-4043

Equipment has surrounded the plate to the extent that modern TLC could realistically be called instrumental TLC, and workers wishing to practice modern TLC must "instrumentalize" their laboratories in the same way that those wishing to use HPLC had to acquire more than a column to realize the benefits of the improved separation technology. What at first might seem obvious has been one of the primary reasons for the slow growth of modern TLC. Many analysts wanted the benefits of high-performance TLC without the price of the instrumentation, and they practiced TLC using homemade plates, jam-jar development chambers, and glass pipettes as sample applicators. Exploration of modern TLC focused on layer technology, and this same auxiliary equipment was used, often with disastrous results.

Sample application. Samples to be analyzed by TLC must be applied to the layer as a spot or band sufficiently small so as not to degrade the efficiency of the layer. The sample aliquot must not be large enough to cause volume or mass overload of the layer. In addition, the sample must be applied in an exactly known volume, at a precise location, without mechanically damaging the layer if quantitation is contemplated. Various mechanical devices employing dosimeters, microsyringes, spray-on techniques, and solid-phase transfer devices meet these goals (38-40).

Dosimeters consist of a 100-200-nL platinum-iridium capillary sealed into a glass support capillary of larger bore. The capillary tip is polished to provide a smooth planar surface of small area (~0.05 mm²), which, when used with a mechanical applicator, does not seriously damage the plate surface. (Spotting by hand invariably damages the layer, causing the chromatogram to develop irregularly and the dosimeter to become blocked by sorbent particles from the layer [41].) Both the position and the force with which the dosimeter touch the plate can be easily controlled. A click-stop grid mechanism is used to aid in spacing the samples evenly on the plate and to provide a frame of reference for sample location during scanning densitometry. The dosimeters are self-loading and emptying and are limited to solutions that wet the capillary tubing adequately, as is the case for most common solvents and solutions of average viscosity.

Samples can also be spotted with a microsyringe. To accurately dispense nanoliter volumes, the syringe is controlled by a micrometer screw gauge and can be operated to provide various precisely selected volumes (50-230 nL) or, via a fixed lever mechanism, to re-

petitively dispense a selected constant sample volume. The microsyringe delivers the sample volume by displacement rather than capillary action and therefore does not deform the plate surface. The microsyringe needle is brought just close enough to the plate surface for the convex sample drop of the ejected liquid to touch the plate surface.

Samples can also be applied to HPTLC plates as narrow bands, of any desired length, by mechanically moving the plate on a stage beneath a fixed syringe. A controlled-nitrogen atomizer sprays the sample from the syringe, forming narrow, homogeneous bands on the plate surface. Because the spray-on technique combines sample application with sample concentration, more than 10 μ L of solution can be applied to the layer if mass overload does not occur. Bands are easier to locate for scanning densitometry by aliquot scanning (scanning with a slit width shorter than the band length), but few samples can be applied to the layer because bands occupy more space than spots. Calibration is somewhat more convenient with band applicators because different volumes of the same solution can be applied to the layer compared with a fixed volume of different sample concentrations with dosimeters.

An alternative approach to sample application that is particularly adaptable for spotting dilute, viscous, or non-homogeneous samples (such as those commonly obtained from environmental and biological sample extracts) is the Transpot applicator. This apparatus is designed for the simultaneous solventless sample application of evaporated residues at precise locations on the thin-layer plate (42, 43). The transfer medium is a fluorinated PTFE film coated with perfluorokerosene and positioned over a series of depressions in a metal platform in a line for linear chromatography or in a circle for circular development. With application of vacuum through orifices in the center of each depression, the film conforms to the contour of the platform's surface. The sample solutions, up to 100 μ L, are pipetted into these depressions, and

the solvent is evaporated by gentle heat and a flow of nitrogen. The TLC layer is then positioned over the film and, with slight pressure replacing the vacuum, the spots are all transferred simultaneously to the plate. Crystalline residues do not penetrate the sorbent layer; these must be transferred in a small volume of nonvolatile carrier solvent added to the sample solution prior to the evaporation step.

Automated sample applicators are available to minimize sample application time. The most advanced of these withdraws sample from a specified vial, applies it to the layer as a spot or band in any selected volume and to any selected position on the plate, rinses the applicator, and continues with the next sample vial. These devices are microprocessor- or computer-controlled, so they can be programmed in advance for particular analyses and calibration routines.

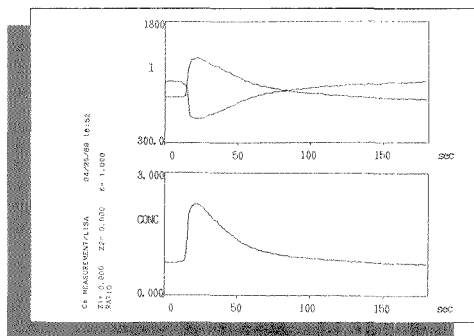
Chromatographic development. Several approaches are available for layer development, depending on whether capillary or forced-flow conditions are employed. For ascending development, small-scale chambers such as the twin trough chamber are commonly used (44). Because there is no theoretical advantage to ascending development, horizontal developing chambers are becoming more common. These chambers allow prechromatographic layer conditioning, sandwich configuration development, optional development of two sets of samples from either end simultaneously, and miserly solvent consumption (typically a few milliliters per plate). Some are even designed to be portable for field applications and can be easily used in teaching laboratories.

Although there are theoretical advantages to forced-flow development in TLC (see box), the design of instrumentation to take advantage of this operating mode is more complicated. The Rotachrom device (by Petazon in Zug, Switzerland) uses centrifugal forces by spinning the plate around a central axis to move the solvent through the layer (15). Other devices, including the Chrompres (Labor Mim, Budapest)

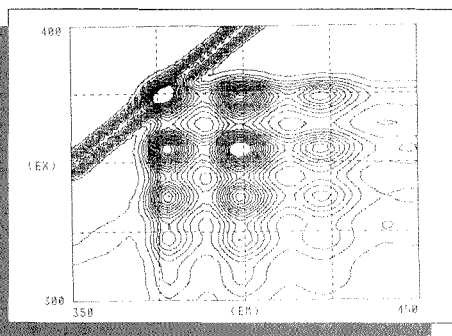
Advantages of forced-flow TLC

- Solvent velocity can be optimized independently of other experimental variables.
- Higher total efficiency can be achieved using fine-particle sorbents and longer plates than is possible with capillary-controlled systems.
- Separation times can be dramatically reduced.
- Mobile phases with poor sorbent wetting characteristics may be used.
- Solvent gradients, either step gradients or continuous gradients, can be employed to optimize the separation conditions.

Compare Our 99% Guaranteed Up-Time Before Your Next Fluorescence Purchase!



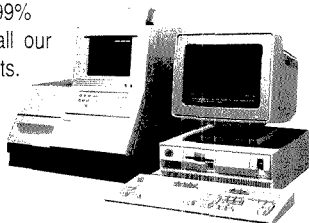
Top: Intracellular Ca^{2+} measurement of monocytes on a glass cover slip, using *Inoo-1* as the Ca^{2+} indicator. Bottom: Ca^{2+} ratio calculation of the above measurement. The Model F-2000 Intracellular Cation Measurement system consists of a complete software package and microsampling system. The software allows for simultaneous measurement of two different fluorescent probes and includes post-run calculations of concentration or ratio determination.



Contour plot of anthracene. The Model F-4010 software provides a two dimensional view of the fluorescence excitation-emission spectra in which the degree of fluorescence intensity is indicated by the density of line. Contour plots allow the user to view small changes in excitation and emission profiles.

Reliability... New Meaning for an Overused Term.

In survey after survey, Fluorescence users have indicated that reliability is the most important factor considered in a new purchase decision. Our service records confirm such outstanding dependability that we can now offer a guaranteed 99% up-time policy on all our analytical instruments. Call us now, and learn more about reliability... and its new meaning.



With each instrument you receive a certificate of "Our Pledge of Quality to You". This guarantees you a 99% up-time, or we pay the bill.



For Details...

Call us Toll-Free (800)548-9001
or write: Hitachi Instruments, Inc.
15 Miry Brook Road, Danbury, Ct 06810



Hitachi Instruments, Inc.

CIRCLE 63 ON READER SERVICE CARD

and the HPPLC 3000 (Institut für Chromatographie, Bad Dürkheim, FRG) use a mechanical pump to force solvent through the layer, which in turn is completely closed on both sides and is under pressure. The HPPLC instrument operates in the circular or anticircular mode and is limited to the use of 10×10 cm plates (45). However, no sealing of the plate edges is required and the instrument is designed to conform with strict engineering specifications. The Chrompres instrument is designed for linear development and requires the application of a sealant to the plate edges to prevent solvent leaking from the sides (14). It can also use longer plate lengths to maximize efficiency. The theoretical advantages of forced-flow development outweigh the practical problems of its implementation, and it is likely that new equipment in this area will be developed. Figure 5 illustrates a separation of equine doping agents by forced-flow TLC and is representative of the results that can be obtained.

A new apparatus for automated multiple development with all sequences under microprocessor control has also been developed (20, 23, 31). A typical separation sequence generally involves 10–25 individual developments, and each development is longer than the

previous one by about 3–5 mm. The mobile phase is removed from the developing chamber and the plate dried under vacuum between each development. Provision is also made for conditioning the layer with an atmosphere of controlled composition prior to each development. The distinctive feature of this method is that development starts with the most polar solvent (for the shortest development distance) and concludes with the least polar solvent (for the longest migration distance). The use of solvents of gradually decreasing solvent strength for the individual chromatographic steps leads to step gradients whose effect corresponds to a linear solvent gradient, provided that a sufficient number of development segments are used. Thus the automated multiple development technique is suitable for the straightforward optimization of separation conditions for samples with unknown chromatographic behavior and for the identification of isocratic solvent systems for poorly resolved samples using gradient techniques. The separation potential of automated multiple development is illustrated by the chromatogram in Figure 6. Presumably, a marriage between forced-flow TLC and automated multiple development would provide the greatest separation potential of all the development techniques if problems caused by the disturbing zone (47) could be defeated.

Detection. Commercial instruments

for scanning densitometry share many features in common (3, 28, 31, 34, 39, 40, 48). Different sources must be used to cover the entire UV–vis range: halogen or tungsten lamps for visible wavelengths, deuterium lamps for UV wavelengths, and high-intensity mercury or xenon sources for fluorescence excitation. Monochromators or filters are used to isolate the measuring wavelength or fluorescence emission. Measurements are commonly made in the reflectance mode and occasionally in the transmission mode by moving the plate on a scanning stage through the measuring beam shaped in the form of a rectangle by adjustable slits. The signal is then detected using either a photomultiplier tube or photodiode. Some instruments have a turntable-type scanning stage as an option for peripheral and radial scanning (used for circular or anticircular chromatograms) or are equipped for linear scanning in a zig-zag fashion to improve the quantitative reliability of irregular chromatograms. In modern scanning densitometry with HPTLC plates, the relative standard deviation from all errors can be maintained below 2%; the largest source of experimental error occurs in the chromatographic and sample application steps, and therefore does not reflect instrument operating capability.

Most modern densitometers are designed for automatic scanning of a complete plate. All required lane changes; spot detection; and optimiza-

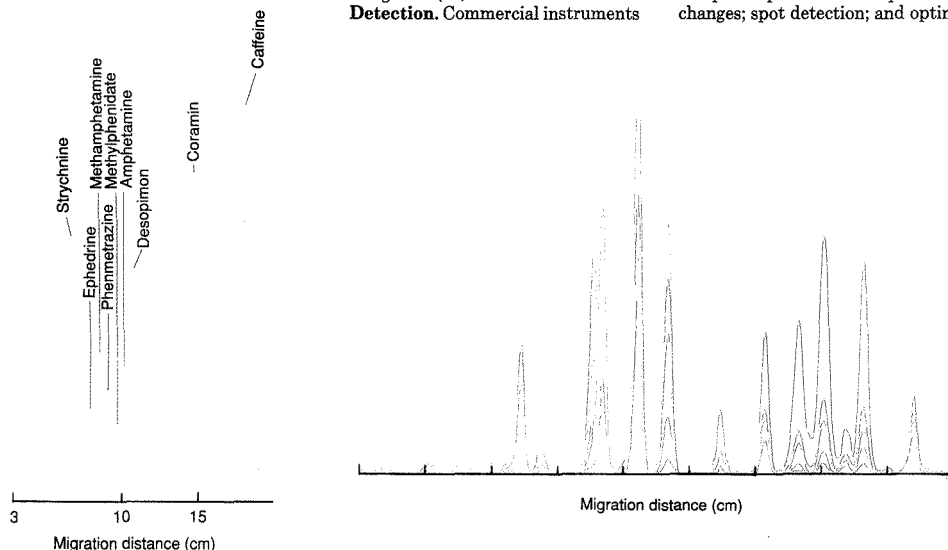
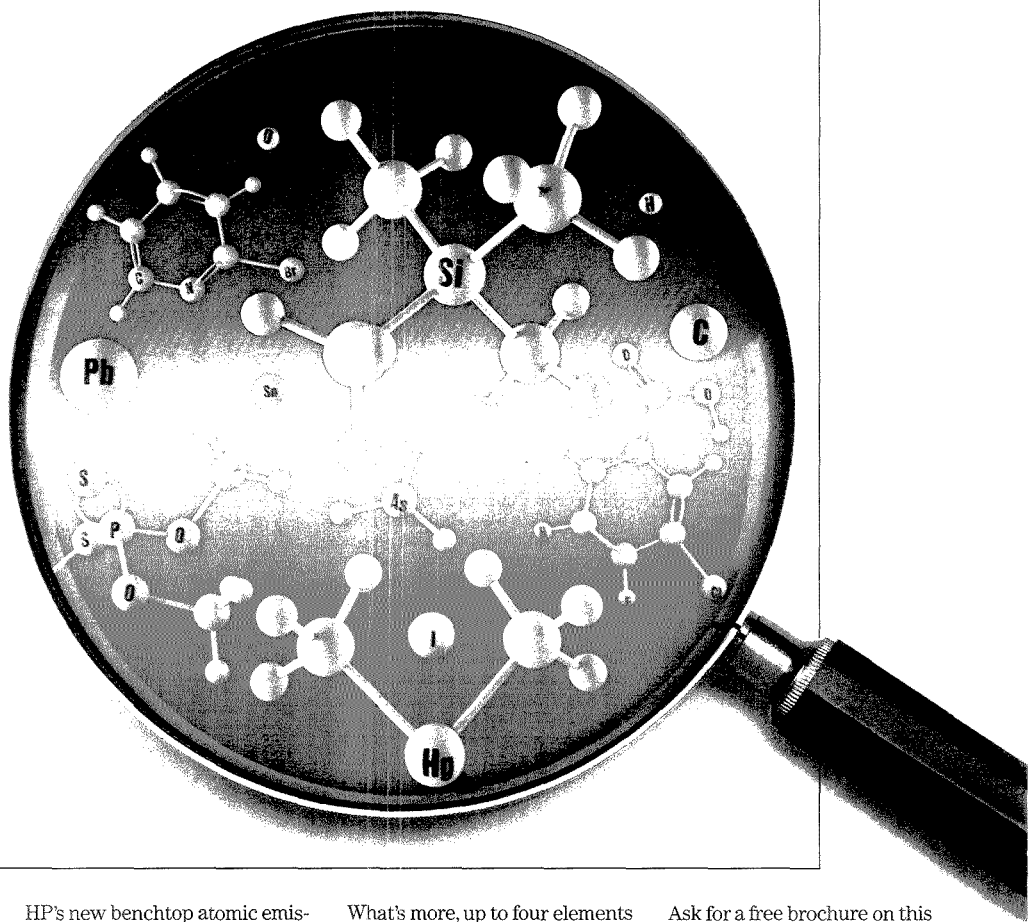


Figure 5. Separation of equine doping agents by forced-flow TLC. (Adapted with permission from Reference 46.)

Figure 6. Separation of a test mixture using automated multiple development employing a universal step gradient from acetonitrile through dichloromethane to carbon disulfide on a silica gel HPTLC plate. The chromatogram was scanned at different wavelengths to enhance the chromatographic information. (Adapted with permission from Reference 20.)

Now GC detection is more elemental.



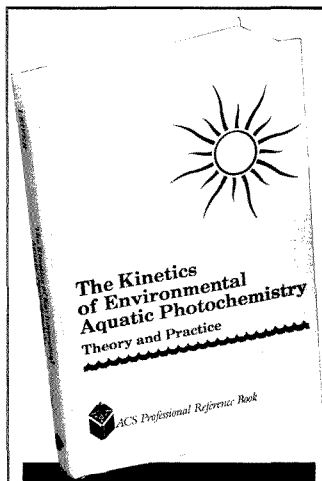
HP's new benchtop atomic emission detector enables you to selectively identify multiple elements in GC effluents. Even some that were previously difficult or impossible to detect. Like carbon. And organometallics. And it's the first GC detector to perform both qualitative *and* quantitative analysis of oxygen.

What's more, up to four elements may be simultaneously detected from a single injection. And sequencing through any number of elements is performed automatically. To confirm MSD or IRD library searches, HP's AED provides elemental information, with the convenience of single-instrument setup.

Ask for a free brochure on this exciting new product. Just call **1 800 556-1234, Ext. 10213**. In California, call **1 800 441-2345, Ext. 10213**.



**HEWLETT
PACKARD**



The Kinetics of Environmental Aquatic Photochemistry

Here at last—a single-volume source on the theory and practice of the kinetics of environmental aquatic photochemistry. Get a solid foundation on this fast developing field with easy-to-understand explanations on such topics as... Kinetics of direct and indirect (sensitized) photoreaction in aquatic media in the environment... absorption and transmission of sunlight in the atmosphere and in natural body water... measuring rates of direct and indirect aqueous photoreaction... actinometry in dilute aqueous solutions... and more.

Learn more on experimental procedures for obtaining requisite kinetic data. Become more familiar with the mathematical concepts through simple, step-by-step derivations. Examples are also provided that illustrate how to use data from experiments when estimating rates of photoreaction. Tables of solar irradiance as a function of latitude and season of the year in the northern hemisphere also are given.

Get complete and practical information on determining direct and indirect (sensitized) photoreaction rate constants and half-lives with this handy and useful reference.

by Asa Leifer, PhD

ACS Professional Reference Book
336 pages (1988) Clothbound
ISBN 0-8412-1464-6 LC 88-16718
US & Canada \$59.95 Export \$71.95

ORDER FROM

American Chemical Society
Distribution Office Dept. 96
1155 Sixteenth St., N.W.
Washington, DC 20036

or CALL TOLL FREE

800-227-5558

(in Washington D.C. 872-4363) and use your credit card!

tion of measuring conditions, calibration, and data reporting are computer-controlled (48, 49). Digital data stored on floppy disks can be recalculated numerous times without having to rerun the chromatogram. Video integration allows correct determination of the baseline under each peak as well as compensation for disturbances from matrix interferences and impurity gradients in the sorbent layer. Some progress has been made in subtracting the entire background contribution of the plate to the analytical signal with the intent of improving detection limits by an order of magnitude or more (20).

The detection process can be considered static, and all information concerning the chromatographic experiment can be made available as a three-dimensional array in which the x and y coordinates define spot position and the z direction defines the sample amount using image analysis techniques (20, 28, 50, 51). Scanning takes place electronically, and the plate is held stationary using a combination of video digitizer, light source, monochromators, and appropriate optics to homogeneously illuminate the plate and focus the image onto a vidicon tube or charged-coupled video camera. The main advantages of electronic scanning are fast acquisition of data, absence of moving parts, simple instrument design, and compatibility with data analysis of two-dimensional chromatograms that are very difficult to scan using conventional slit-scanning densitometers. On the other hand, electronic scanners cannot compare with slit-scanning densitometers in terms of cost, sensitivity, available wavelength measuring range, and dynamic signal range. With continuous advances in image analysis techniques, this situation could change. High-quality systems are available for the detection of radioisotopically labeled substances by TLC (38, 52) and for flame-ionization-based detection of chromatograms separated on sintered-layer rods (28, 53).

Separations by HPLC and TLC occur by essentially the same physical methods. Thus the two techniques often are viewed as competitors when it would be more realistic to consider them as complementary techniques (20, 28, 35). It is easier to develop a large number of theoretical plates and simpler to automate the analytical procedure using HPLC than TLC. However, in practice, most separations performed by HPLC are done with relatively few theoretical plates—typically fewer than 20,000. Unattended analysis is routine for HPLC, whereas for TLC the individual steps of sample application, development, and detection

can be automated, but manual intervention is required to move the plate from station to station. TLC offers a much higher sample throughput than HPLC because of the ability to perform separations in parallel, and cruder samples can be handled because the separation medium is used only once. The detection process in HPLC is dynamic and subject to time constraints that are not applicable to TLC. Using TLC, it is possible to apply sequential detection techniques, evaluate the chromatogram at different stages during development (as is commonly done in multiple development), and to apply chemical reagents for greater and more rapid detection sensitivity and selectivity.

References

- (1) Fennimore, D. C.; Davis, C. M. *Anal. Chem.* 1981, 53, 252 A-266 A.
- (2) Poole, C. F. *Trends Anal. Chem.* 1985, 4, 209-13.
- (3) Poole, C. F.; Schuetz, S. A. *Contemporary Practice of Chromatography*; Elsevier: Amsterdam, 1984; pp. 619-99.
- (4) Brinkman, U. A. Th. *Trends Anal. Chem.* 1986, 5, 178-82.
- (5) Jost, W.; Hauck, H. E. *Adv. Chromatogr.* 1987, 27, 129-66.
- (6) Mack, M.; Hauck, H. E.; Herbert, H. *J. Planar Chromatogr.—Modern TLC* 1988, 1, 304-8.
- (7) Mack, M.; Hauck, H. E. *Chromatographia* 1988, 26, 197-205.
- (8) Brunner, C. A.; Wainer, I. *J. Chromatogr.* 1980, 472, 277-83.
- (9) Guiochon, G.; Siouffi, A. *J. Chromatogr. Sci.* 1978, 16, 470-81.
- (10) Poole, C. F. *J. Planar Chromatogr.—Modern TLC* 1988, 1, 373-76.
- (11) Guiochon, G.; Korosi, G.; Siouffi, A. *J. Chromatogr. Sci.* 1980, 18, 324-29.
- (12) Poole, C. F. *J. Planar Chromatogr.—Modern TLC* 1989, 2, 95-98.
- (13) Geiss, F. *Fundamentals of Thin Layer Chromatography (Planar Chromatography)*; Huethig: Heidelberg, 1987.
- (14) Tyihak, E.; Mincsovcics, E. *J. Planar Chromatogr.—Modern TLC* 1988, 1, 6-19.
- (15) Nyiredy, S.; Botz, L.; Sticher, O. *J. Planar Chromatogr.—Modern TLC* 1989, 2, 53-61.
- (16) Witkiewicz, Z.; Bladec, J. *J. Chromatogr.* 1986, 373, 111-40.
- (17) Poole, C. F.; Poole, S. K. *J. Planar Chromatogr.—Modern TLC* 1989, 2, 165-68.
- (18) Nurok, D. *Chem. Rev.* 1989, 89, 363-75.
- (19) Nyiredy, S.; Dallenbach-Tolke, K.; Sticher, O. *J. Planar Chromatogr.—Modern TLC* 1988, 1, 336-42.
- (20) *Planar Chromatography*; Kaiser, R. E., Ed.; Huethig: Heidelberg, Vol. 1, 1986.
- (21) Poole, C. F.; Poole, S. K. In *Multidimensional Chromatography: Techniques and Applications*; Cortes, H. J., Ed.; Marcel Dekker: New York, 1989.
- (22) Zakaria, M.; Gonnord, M.-F.; Guiochon, G. *J. Chromatogr.* 1983, 271, 127-92.
- (23) Poole, C. F.; Poole, S. K.; Fernando, W. P. N.; Dean, T. A.; Ahmed, H. D.; Berndt, J. A. *J. Planar Chromatogr.—*

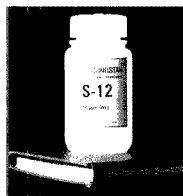
- Modern TLC* 1989, 2, in press.
- (24) Buncak, P. *Fresenius Z. Anal. Chem.* 1984, 318, 289-92.
- (25) Poole, C. F.; Butler, H. T.; Coddens, M. E.; Khatib, S.; Vandervennet, R. *J. Chromatogr.* 1984, 302, 149-58.
- (26) Guiochon, G.; Beaver, L. A.; Gonnord, M. F.; Siouffi, A. M.; Zakaria, M. *J. Chromatogr.* 1983, 255, 415-37.
- (27) Guiochon, G.; Gonnord, M. F.; Zakaria, M.; Beaver, L. A.; Siouffi, A. M. *Chromatographia* 1983, 17, 121-24.
- (28) Poole, C. F.; Poole, S. K. *J. Chromatogr.* 1989, 492, 539-84.
- (29) Hofstraat, J. W.; Griffioen, S.; van de Nesse, R. J.; Brinkman, U. A. Th.; Gooijer, C.; Velthorst, N. H. *J. Planar Chromatogr.—Modern TLC* 1988, 1, 220-26.
- (30) Fujimoto, C.; Morita, T.; Jinno, K.; Shafer, K. H. *J. High Resolut. Chromatogr.* 1988, 11, 810-14.
- (31) Jaenchen, D. E.; Issaq, H. J. *Liquid Chromatogr.* 1988, 11, 1941-65.
- (32) Stahl, E. *J. Chromatogr.* 1977, 142, 15-21.
- (33) Huf, F. A. *J. Planar Chromatogr.—Modern TLC* 1988, 1, 46-49.
- (34) Poole, C. F.; Khatib, S. In *Quantitative Analysis Using Chromatographic Techniques*; Katz, E., Ed.; Wiley: New York, 1987; pp. 193-270.
- (35) Poole, C. F.; Poole, S. K.; Dean, T. A.; Chirco, N. M. *J. Planar Chromatogr.—Modern TLC* 1989, 2, 180-89.
- (36) Berkham, E. W. *J. Planar Chromatogr.—Modern TLC* 1988, 1, 81-85.
- (37) Baeyens, W. R. G.; Ling, B. L. *J. Planar Chromatogr.—Modern TLC* 1988, 1, 198-213.
- (38) Poole, C. F.; Butler, H. T.; Coddens, M. E.; Schuette, S. A. In *Analytical and Chromatographic Techniques in Radiopharmaceutical Chemistry*; Wieland, D. M.; Tobes, M. C.; Manger, T. J., Eds.; Springer-Verlag: New York, 1986; pp. 3-37.
- (39) Touchstone, J. C. *J. Chromatogr. Sci.* 1988, 26, 645-49.
- (40) Bertsch, W.; Hara, S.; Kaiser, R. E.; Zlatkis, A., Eds.; *Instrumental HPLC*; Huethig: Heidelberg, 1980.
- (41) Kaiser, R. E. *J. Planar Chromatogr.—Modern TLC* 1988, 1, 182-87.
- (42) Fenimore, D. C.; Meyer, C. J. *J. Chromatogr.* 1979, 186, 555-61.
- (43) Malikin, G.; Lam, S.; Karman, A. *Chromatographia* 1984, 18, 253-59.
- (44) Petrin, P. *J. Chromatogr.* 1976, 123, 65-70.
- (45) Kaiser, R. E. *Einführung in die HPLC*; Huethig: Heidelberg, 1987.
- (46) Gulyas, H.; Kemeny, G.; Hollosi, I.; Pucsok, J. *J. Chromatogr.* 1984, 291, 471-75.
- (47) Nyiredy, S.; Meszaros, S. Y.; Dallenbach-Tolke, K.; Nyiredy-Mikita, K.; Sticher, O. *J. High Resolut. Chromatogr.* 1987, 10, 352-56.
- (48) Bohrer, I. M. *Topics in Cur. Chem.* 1984, 126, 95-118.
- (49) Pollak, V. A. *J. Liq. Chromatogr.* 1980, 3, 1881-99.
- (50) Pollak, V. A.; Schulze-Clewing, J. *J. Chromatogr.* 1988, 437, 97-107.
- (51) Cosgrove, J. A.; Bilhorn, R. B. *J. Planar Chromatogr.—Modern TLC* 1989, 2, in press.
- (52) *Recent Advances in Thin-Layer Chromatography*; Dallas, F.A.A.; Read, H.; Ruane, R. J.; Wilson, I. D., Eds.; Plenum Press: London, 1988.
- (53) Ranny, M. *Thin-Layer Chromatography with Flame Ionization Detection*; D. Reidel Publishing Co.: Dordrecht, The Netherlands, 1987.



Colin F. Poole received his Ph.D. in analytical chemistry from the University of Keele (U.K.) in 1975. After postdoctoral appointments at the University of Aston (U.K.), University of Ghent (Belgium), and the University of Houston, he joined the faculty of Wayne State University, where he is an associate professor of chemistry. His research interests include the application of chromatographic techniques (GC, HPLC, SFC, TLC) to environmental or biomedical problems, the solvent properties of liquid organic salts and highly fluorinated polymers, column design in SFC, and instrument design.

Salwa K. Poole received her B.S. degree from the University of Damascus (Syria) and her Ph.D. from Wayne State University in 1986. She is presently a postdoctoral research associate in the chemistry department at Wayne State University performing research in TLC, the thermodynamic properties of polar solvents, and size-exclusion LC.

WE MAKE STANDARDS BY THE BOOK.



The metal content in each Conostan oil-based calibration standard is determined by chemical assay methods with results that are traceable to NIST standards (where applicable). This traceability means Conostan

products can serve as reference standards and provide a reliable benchmark for the determination of metals in organics. For a complete list of Conostan single and multi-element standards and special blends for the analysis

of metals in oils, write for our free brochure.



Conostan Division
Conoco Specialty Products Inc.
P.O. Box 1267
Panola City, OK
Phone: (405) 767-3078
Fax: (405) 767-5843

CIRCLE 29 ON READER SERVICE CARD

Way out in front: 670 Titroprocessor



The 670 Titroprocessor typifies our latest generation of titrators: It is distinguished by a performance which reflects our many years of experience in titrating. Where until now could you determine the procedure of your methods with all auxiliary functions yourself? Do you require, for example

- intelligible dialog with the instrument via a typewriter keyboard?
- Complete problem solutions which you can easily adapt

to your needs, also for automatic titrations?

- Result outputs with designations and comments you can formulate yourself?
- Live information on the screen regarding the sequence of events during the titration?
- Printouts in A4 format on a built-in thermal printer/plotter?
- numerous automation possibilities with sample changers

- memory for 68 complete methods
 - high resolution of reagent addition:
1/10 000 of burette cylinder volume
- All this and much more is possible with the 670 Titroprocessor.

 **Metrohm**
Measurement in Chemistry
Worldwide with Metrohm.

METROHM Ltd.
CH-9101 Herisau Switzerland
Phone 071 / 53 11 33
Telefax 071 / 52 11 14
Telex 88 27 12 metr ch

Brinkmann
INSTRUMENTS, INC.
Cantiague Rd., Westbury, New York 11590
(516) 334-7500 (800) 645-3050

Resonance Ionization Mass Spectrometry

J. P. Young, R. W. Shaw, and
D. H. Smith

Analytical Chemistry Division
Oak Ridge National Laboratory
Oak Ridge, TN 37831

Resonance ionization mass spectrometry (RIMS) is an analytical technique that uses photons from lasers to resonantly excite an electron from some initial state of a gaseous atom (or molecule) through various excited states of that atom (molecule) to the continuum. The cation formed in this manner from the ion pair is mass-analyzed and detected. RIMS is derived from the parent technique, resonance ionization spectroscopy (RIS), which originally used the same optical concept but de-

tected the electron of the ion pair (1). RIS is capable of detecting single atoms in a time-resolved fashion, and such sensitivity is also theoretically possible with RIMS.

RIMS was first described around the beginning of this decade and from that time has been developed and adopted by an increasingly larger group of sci-

entists. It has been applied in fields such as chemistry, physics, geology, hydrology, and biology. The technique uniquely combines the elemental (molecular) selectivity of optical spectroscopy with the extremely sensitive detection capability of mass spectrometry. This combination yields an analytical technique that is applicable, with varying degrees of difficulty, to a number of fields.

Five optical routes, or schemes, have been formulated (1) for RIS whereby most of the elements of the periodic

INSTRUMENTATION

entists. It has been applied in fields such as chemistry, physics, geology, hydrology, and biology. The technique uniquely combines the elemental (molecular) selectivity of optical spectroscopy with the extremely sensitive detection capability of mass spectrometry. This combination yields an analytical technique that is applicable, with varying degrees of difficulty, to a number of fields.

chart can be resonantly ionized. The schemes, which involve the absorption of two or three photons to achieve ionization, are depicted in the upper left corner of Figure 1. They are based on

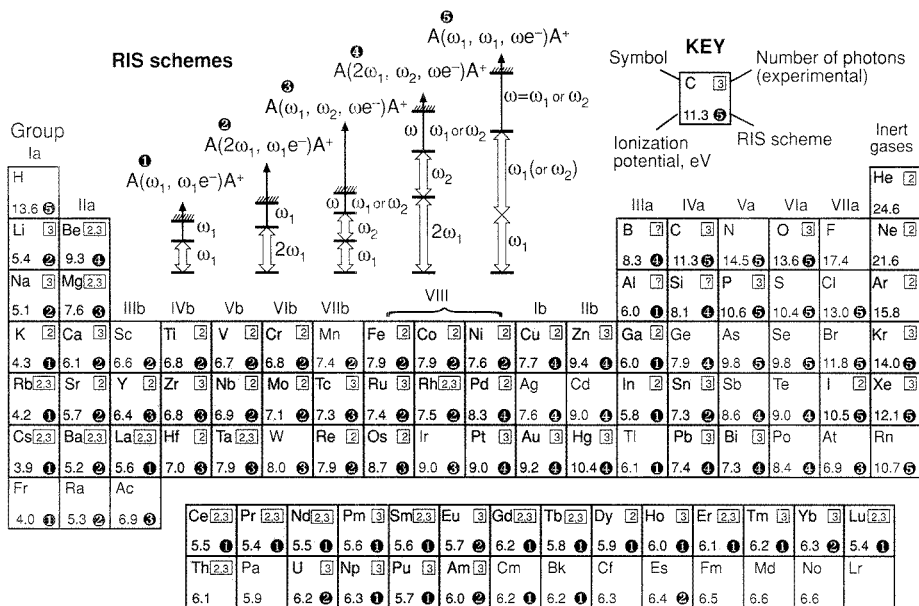


Figure 1. Applications of RIMS to the elements.

References to the experimental details are given elsewhere (4, 5). RIS schemes are described in detail elsewhere (2); ω_1 to ω_2 are photons of a particular energy (wavelength); double-headed, wide arrows denote transitions within the atomic state; single-headed arrows denote transitions to the continuum generating an electron (e^-) and an ion (A^+) from the atom (A).

optically allowed transitions between levels of the atom and are shown as wide, double-headed arrows in the figure; the term "bound-bound transition" is used in this article to describe such a process. The energies of the photons must lie within the energy range of tunable lasers; and the last photon, depicted as a single-headed arrow in the figure, must be of sufficient energy to exceed the ionization potential of the atom to promote a bound-continuum transition.

These optical routes can be represented by a notation that depicts the number of photons absorbed to make the ion pair. Schemes 1 and 2 are 1 + 1 processes; one photon excites the atom from some initial state (in this case, the ground state) to an intermediate state, and another photon ionizes the atom. Schemes 3 and 4 can be represented as 1 + 1 + 1 processes; two separate, sequential bound-bound transitions within the atom are followed by absorption of a third photon for ionization. Scheme 5 is a 2 + 1 process; that is, a two-photon step to an excited atomic state and absorption of another photon for ionization. Such summation notations will be used in this review. These photoionization processes are also known by other names such as resonant multiphoton ionization (REMPI) spectroscopy.

Two reviews of RIS have appeared in this JOURNAL (2, 3). Figure 1 shows a periodic chart that depicts 70 elements (the blue blocks) that have been studied by some form of RIMS. The fact that so many elements have been studied indicates that the development of RIMS has reached a point where a review of this technique seems timely.

We will essentially limit our discussion of RIMS to atomic applications. Both RIS and RIMS, however, can also be applied to molecules, but with correspondingly more complex problems associated with the multitudinous and overlapping energy levels characteristic of molecules. This article comprises a description of RIMS, its status, and its future directions. References are cited to lead the reader to more technical detail, but an exhaustive list is not included here. Some excellent technical reviews of RIMS and RIS have appeared recently; for technical discussions, see References 4-6.

Apparatus

RIMS instrumentation includes a source of atoms (molecules), tunable laser(s), and a mass analyzer or detector, as shown in Figure 2. Historically, these components have been applied in many variations.

Atom source. Atoms are often gen-

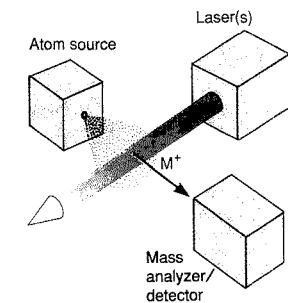


Figure 2. Generic experimental arrangement for RIMS.

erated from sources of a thermal nature; gas-phase atoms can be generated from a heated filament, a graphite furnace, an inductively coupled plasma (ICP), or by ablation from a sample surface. Atoms generated from a filament, furnace, or ICP are normally continuous in time, so there will be a coupling inefficiency when such an atom source is used with a pulsed laser.

Two types of pulsed atom sources have been developed that use either a pulsed laser or a pulsed particle beam to generate an atom plume. Either of these types of atom sources can be made to couple more efficiently than a continuous atom source to pulsed-laser excitation. Another useful atom-generating source for RIMS is a glow discharge.

Laser(s). Most types of lasers, either continuous-wave (CW) or pulsed, have been applied to RIMS. Resonant optical processes have typically included one, two, or more laser energies delivered by one or more lasers. For analytical simplicity, one laser is desirable. Using only one laser wavelength (single-color RIMS), however, requires the absorption of two or more photons, of which at least one optical process must be a bound-bound transition. There are nonresonant optical routes to ionization that can be promoted by lasers, and these are usually referred to as multiphoton ionization (MPI) routes. These latter processes will not be considered in this review.

Tunable lasers are available in all types, from those relatively easy to operate, such as dye lasers pumped by a Nd:YAG laser, an excimer laser, or a flashlamp, to those more difficult to operate, such as an argon ion stabilized ring dye laser. Easy-to-operate semiconductor diode lasers have recently

become available. Wavelength ranges available to tunable lasers are very broad; they can be easily obtained (e.g., semiconductor diode) or they can involve extreme complexity (e.g., if one wishes a wavelength in the far- or vacuum-UV). Table I lists several types of lasers and their characteristics.

Early RIMS studies were carried out with nitrogen laser-pumped or flashlamp-pumped dye lasers (7, 8). The power of these lasers, when focused in an atom plume, is adequate to saturate a two or more photon process that involves one or several bound-bound steps and a bound-continuum step (1). The last step is rate-limiting. Other lasers, CW or pulsed, have since been used alone or in various combinations to produce ionization. An ideal arrangement is to use CW lasers of relatively low power for the bound-bound steps and an additional energy source, such as a pulsed laser, high-power CO₂ laser, or electric field, for the ionization step. Such combined processes have proven to be quite satisfactory (5, 6). The use of a semiconductor diode laser in combination with another laser was recently reported (9); the former was used for excitation and the latter for ionization in the RIMS process. An instrument that incorporates a number of diode lasers with the ionization step effected by some other process is an interesting concept that could lead to a relatively small field instrument.

Mass analyzer/detector. Most of the major types of mass analyzer have been used for RIMS studies. These include magnetic sector, quadrupole, and time-of-flight (TOF) instruments, each of which has advantages and disadvantages. In the application of RIMS, it seems that the researcher uses whatever mass analyzer is available. The combination of a TOF analyzer with a pulsed laser is ideal in terms of matching duty cycle to the characteristics of the mass analyzer. The pulsed laser is capable of generating a burst of ions in a short period (see Table I) suitable for TOF separation. In terms of most measures of mass spectrometric performance (such as resolution), magnetic sector instruments are superior to TOF analyzers, but modifications of the detector system may be required if RIMS uses pulsed-laser excitation. Recent designs of quadrupole mass analyzers have demonstrated improved performance with regard to several important mass spectrometric parameters. An advantage for some applications is that these analyzers are compact and less costly than sector instruments.

The choice of mass analyzer involves the decision of whether to use CW or pulsed lasers for ion generation. For

CW lasers, the duty factor is unity, but the probability of ion generation is relatively poor; an independent source of energy for the ionization step improves the situation. For pulsed lasers, the probability of ion generation approaches unity per pulse in an appropriately focused laser volume, but detector dead time can result in errors of ion counting if too many ions arrive at the detector in a short time. Note the duty factors of pulsed lasers given in Table I; pulsed lasers are off most of the time. The pulsed-laser approach is ideal for detecting extremely small numbers of atoms, however, and has been used for such applications. In general, obtaining analytical data by RIMS requires a compromise that involves the selection of a sample atomization method, laser, mass analyzer, and detector. Various studies involving these parameters are described in the literature, and the results are summarized in review articles (4-6). No one solution is perfect in all respects, and the experimental arrangement must be considered individually for each application.

Analytical applications

Figure 1 clearly demonstrates the wide potential for analytical applications of RIMS. Each element block contains (in a counterclockwise direction from the top left) the element symbol, the ionization potential in electron volts, and a number corresponding to a predicted RIS scheme as given in an earlier article (2). A key depicting the various locations of this information for the element blocks is shown in the figure. The blue blocks represent the elements for which experimental resonance ionization data have been obtained, and the

number of photons absorbed to create an ion pair is given in the upper right corner of those blue blocks. This information is taken from results summarized in two recent technical reviews (4, 6). In some cases, more than one experimental route has been demonstrated; this fact is depicted by showing more than one number in the experimental blocks. Details of the experiments and optical route(s) are in the references cited in the reviews.

Every elemental group is represented experimentally, although the nonmetals have been studied least. Note the comparisons of RIS scheme number and the number of photons actually used in the experimental studies. In general they correspond fairly well. Notable exceptions are some of the scheme 4 elements, where it was found that ionization can be accomplished by a 2 + 1 process involving only one laser. Single-color methods have procedural advantages because only one laser is required. Such processes include the scheme 1 elements and derivations of the scheme 3 and 5 elements where only one wavelength is used.

The ultimate value of any analytical technique is related to its unique attributes that give it advantages over competitive techniques. Considering the fact that photons are used to generate ions, RIMS is a relatively noninvasive method; only a window into the sample chamber is required. RIMS has unique characteristics that involve its elemental selectivity, isotopic selectivity, sensitivity to the initial atomic or molecular state of the gaseous sample, and the ability to detect and measure extremely small amounts of analyte. The optical processes involved in atomic RIMS make it elementally or isotopically se-

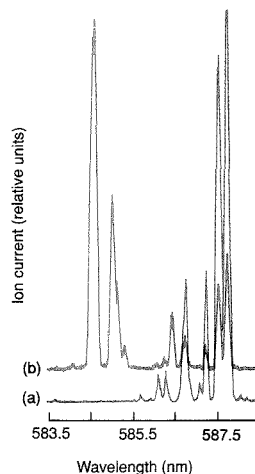


Figure 3. Determination of Pm and Sm isobars by RIMS.

(a) Ionization spectrum of ^{152}Sm and (b) ionization spectrum of mass 147 detecting both Pm and Sm. Note that the two strong lines near 584 nm are present only for Pm. (Adapted from Reference 10.)

lective. Isobaric interference (same nominal mass but different species) is thus minimized or eliminated. This selectivity has been demonstrated in many studies and holds true for elements or molecules.

An example of the elemental selectivity of RIMS for a 1 + 1 + 1 single-color process is that of ^{147}Pm and Sm (10). Pm is a man-made radioactive element that has several isotopes with the same nominal masses as those of its neighboring elements, Sm or Nd. Mass analysis of ^{147}Pm , a β^- emitting radioactive isotope, suffers from isobaric interference from its daughter, ^{147}Sm . The ability to measure either parent or daughter is demonstrated by the results shown in Figure 3. By tuning the mass analyzer (in this case, a magnetic sector instrument) to mass 152, various wavelengths at which Sm is ionized are obtained over the wavelength range of 583-588 nm (Figure 3a). By tuning the mass analyzer to mass 147, wavelengths at which either ^{147}Pm or its daughter ^{147}Sm are ionized can be observed (Figure 3b). At a wavelength of 584.6 nm, a selectivity factor of at least 1000 is reported for the ability to determine Pm in the presence of Sm.

Another example where isobaric interference is a problem that can be eliminated by RIMS is with the elements Pb and Bi (11). With natural

Table I. Typical characteristics of lasers useful for RIMS

Type	Repetition rate, pulse/s	Duty factor	Peak power, kW	Average power, W	Pulse energy, mJ	Line-width, cm^{-1}
Nd:YAG dye	10	1×10^{-7}	9000	0.7	70	0.25
Nitrogen dye	30	3×10^{-7}	90	0.03	1.0	0.3
Excimer dye	500	8×10^{-6}	2700	20	40	0.3
Flashlamp dye	30	3×10^{-5}	10	0.3	10	3.0
Copper vapor dye	10,000	2×10^{-4}	4	1	0.1	0.3
Argon ion linear dye	—	CW	—	5	—	1.4
Argon ion-stabilized ring dye	—	CW	—	1	—	3×10^{-5}
Semiconductor diode	—	CW	—	0.003-0.03	—	5×10^{-3}

PEAK QUALITY

with

Claisse Fluxes

(Borates and Phosphates)

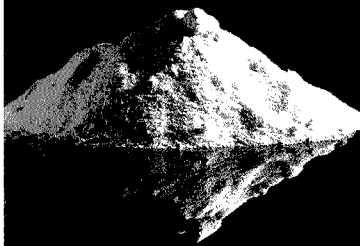
Get a new perspective on analysis and better results. The CLASSE FLUXES have exceptional qualities due to their PURITY and COARSE texture. Claisse Fluxes are Tip-Top.

FEATURES

- ▶ free-flowing crystals
- ▶ low surface area
- ▶ high density
- ▶ fused, not mixed
- ▶ popular and special compositions

CONSEQUENT ADVANTAGES

- ▶ no loss from static electricity
- ▶ no loss by splattering or foaming on heating
- ▶ very low water absorption
- ▶ no uncertainty on quantity weighed
- ▶ no segregation in containers
- ▶ FREE SAMPLE upon request



For world-wide sales, address of local agents and service information please call or write to:



corporation
scientifique
claisse inc.

2522, chemin Sainte-Foy
Sainte-Foy (Quebec)
Canada G1V 1T5
Tel: (418) 656-6453
Fax: (418) 656-1169
Telex: 051-31731

The First and Finest in Fusion.

CIRCLE 26 ON READER SERVICE CARD

INSTRUMENTATION

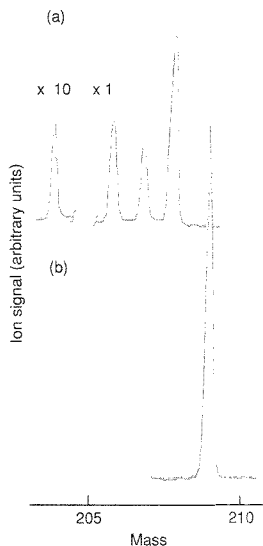


Figure 4. Resonance ionization mass spectra of (a) Pb and (b) Bi derived from a common sample.

The ionization wavelength for (a) is 450.3 nm and for (b) is 456.6 nm. (Adapted from Reference 11.)

abundance mixtures, there is no isobaric interference; Bi is monoisotopic (mass 209), and Pb has four isotopes (masses 204, 206, 207, and 208). Isobaric interferences occur with radioactive isotopes of these elements and their transmutation products. The mass spectrum of a mixture of natural Bi and Pb obtained by RIMS is shown in Figure 4. The mass spectra of Pb and Bi are obtained at wavelengths of approximately 450.3 and 465.6 nm, respectively; these wavelengths correspond to a single-color laser resonance ionization involving, in this case, $2 + 1$ optical processes for both elements. By using RIMS at these laser wavelengths, it is possible to ionize either element, circumventing the isobaric interferences in radioactive mixtures.

Studies of isotopic selectivity have been carried out by several groups (6). One example of such studies uses a CW stabilized ring dye laser to address a small subset of atomic velocities and therefore reduce Doppler broadening effects. This work was pioneered at Pacific Northwest Laboratory (12). Recently it was found that similar sub-Doppler spectral resolution can be attained in a properly designed experimental arrangement that in-

cludes a diode laser for excitation of the first bound-bound atomic excitation preceding resonant processes leading to ionization (13). Either technique can lead to enhanced isotopic selectivity for amenable atomic species.

Another feature that is unique to RIMS is selectivity for initial atomic states. Gaseous atoms as they are generated may not all be in the lowest energy (ground) state; rather, they can exist in a number of excited states. Within less than $1 \mu\text{s}$, the excited states that are coupled to lower energy states will lose energy by emission. Ultimately, in the absence of collision, the metastable states (i.e., those states that are not optically coupled to lower states) remain. It is often a very difficult problem to determine the distribution of metastable states, but it can be accomplished with RIMS. Not only the distribution, but also the lifetime and branching ratios of the individual initial states can be measured by laser resonance ionization techniques. The need to obtain this information for the helium 2S metastable state is the reason for the original development of RIS (1). Although no work seems to have been done in the area, it is also possible to determine the initial states of gaseous ions by a RIMS process that ultimately generates a divalent ion.

There is an adverse side to the presence of initial atomic-state distributions. Because gaseous atoms exist in various metastable states, the ultimate sensitivity of RIMS is reduced; a given optical excitation route will yield ions only from the atoms in one initial state. This fact needs to be addressed in future studies of the atomization process.

Earlier, we pointed out that one of the unique features of RIMS is its excellent sensitivity. Where elemental identification or determination is required for trace levels of elements in samples, RIMS has been widely applied. It has, for example, been applied to very sensitive determinations of Fe in blood serum (14). Several instruments using pulsed-ion-beam sample ablation to generate a pulsed-atom plume have been applied to trace element analysis. These specialized instruments have been used to determine various metals from aqueous samples (15) and elemental low-level impurities in semiconductor materials (16). In the latter example, these combination instruments do not compete with other types of mass analyses in sensitivity, such as secondary ion mass spectrometry, for this application; however, they do give alternate routes for determination. The RIMS technique has been elegantly applied to ultrasensitive determinations of trace elements of interest

in geochemical studies (17). Confirmation of the abrupt change in the concentration of both Rh and Ir in deposits at the Cretaceous/Tertiary geologic boundary has been obtained.

The unique characteristics of RIMS have been applied to the study, identification, and quantification of rare elements in specific samples. An example of such an application is the dating of ground water by counting ^{81}Kr atoms (18), described at the most recent international RIS conference. ^{81}Kr is a naturally occurring radioisotope produced by cosmic rays; it has a half-life of 210,000 years. Because of its inert chemical nature, it can be used to date ancient water samples, such as polar ice or underground water sources, where the water is trapped and unable to equilibrate with the atmosphere. A representative mass spectrum resulting from the RIMS determination of

^{81}Kr in an ancient ground water sample is shown in Figure 5. These data were obtained from a 50-L sample. Radioactive decay counting of ^{81}Kr is not sensitive enough for this determination because of the low concentration of Kr. With RIMS, the measurement of approximately 6200 atoms of ^{81}Kr is possible, and the results provide a date for this water sample.

Short-lived or rare isotopes synthesized in accelerators have been characterized by RIMS (19, 20). RIMS has been applied to studies of as few as 10^9 atoms. With such sensitivity RIMS can be used to identify species that are created in nuclear processes. If the experiment is properly designed with respect to such parameters as sample introduction and laser linewidth, not only can a particular isotopic species be identified, but spectral characteristics can be measured.

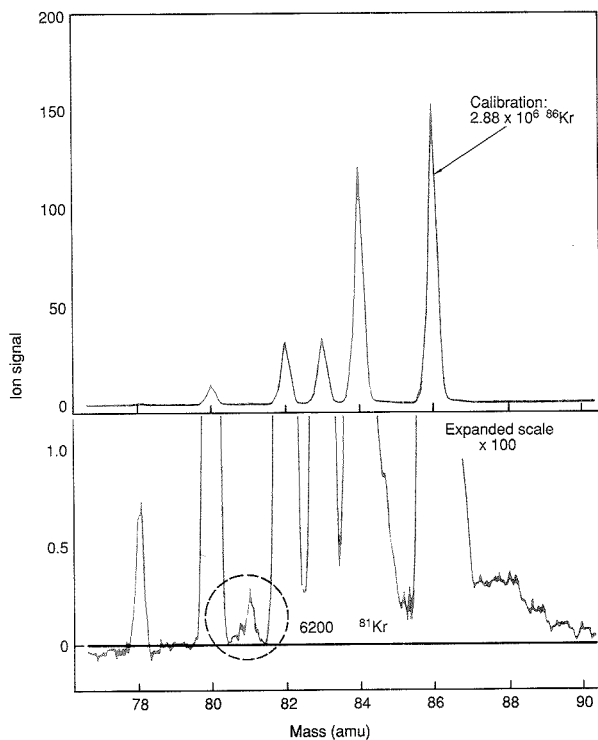


Figure 5. Mass spectrum of krypton derived from an ancient water sample showing ^{81}Kr ions.

Ions are generated by resonant optical ionization and mass-analyzed using a TOF instrument. (Adapted with permission from Reference 18.)

An example of such an experimental arrangement is shown in Figure 6 for an apparatus in operation at the ISOLDE-3 facility located at CERN (European Organization for Nuclear Research) in Switzerland. A pulsed beam containing rare atomic species is deposited on a graphite target wheel. The wheel can be rotated 180° and the deposited species desorbed by a pulsed-laser beam. The sample plume is allowed to interact with a laser beam consisting of photons of one or more energies. Atomic species of interest, if present, are resonantly ionized and determined by the TOF mass analyzer. The pulsed deflectors, shown in the TOF instrument, are time-correlated to permit passage of the isotope under investigation. To prevent background signals from radioactive emanations of the sample target wheel, the ions are deflected before detection. With this apparatus hyperfine structural and isotope shift information for ^{183}Au and ^{184}Au has been obtained (19).

As was pointed out in the introduction, RIMS of molecules is a more complex concept than is RIMS of atoms because of the nature of the molecular bond. Nevertheless, molecular RIMS

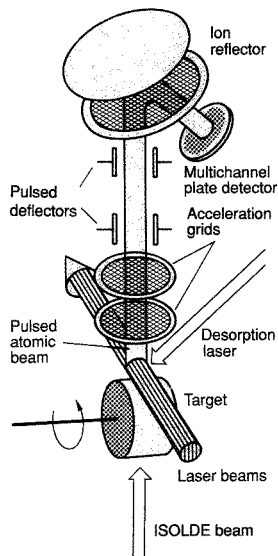


Figure 6. Apparatus for on-line RIMS at ISOLDE-3 using pulsed-laser desorption of implanted species.

(Adapted with permission from Reference 19.)

can be applied to analytical problems (4). A thorough discussion of this type of research, with examples of results, was presented at the 1988 international RIS conference. A session devoted to molecular RIMS included papers dealing with studies of simple molecules (such as hydrogen), inorganic molecules, and organic molecules. The RIMS study of molecular hydrogen (21) involved a 1 + 1 process in which the first photon was in the vacuum-UV (118 nm), and the second photon was in the visible range; a number of resonance ionization wavelengths were found as the wavelength of the second laser was varied from 400 to 700 nm. RIMS studies of the 2-butene-1-yl (i.e., 1-methylallyl) radical were described (22). The results of these studies demonstrated isomeric interference removal for molecular species. The radical was generated by abstraction of hydrogen from butene. Although the resultant optical spectrum was broad (ions were seen from 450 to 480 nm), the spectral features of the radical ions varied with the *cis*- or *trans*-butene precursor and could be used to identify a *cis*- or *trans*-radical ion.

Precision and accuracy

RIMS has proven to be an extremely sensitive technique, as evidenced by the examples given in the previous section, but as yet it is only moderately precise. A benchmark comparison can be made by considering the excellent precision of inorganic isotope ratio measurements (~0.05–0.2%) by traditional thermal ionization MS with magnetic sector instruments; that technique can be applied to samples of 1 ng or less. In one study of U and Pu by RIMS, precisions of 0.6 and 0.2%, respectively, were reported (23) for the major isotopes. Such values are not the general case, however. To date, typical precisions for RIMS determinations range from 2 to 5% for sample sizes larger than 10 ng. There also seems to be increasing evidence that bias effects are present in some isotopic ratio measurements carried out by RIMS. This effect was discussed in several papers at the recent RIS conference (24–26). This problem has become more apparent as the technique has developed into a more widely applied analytical method, and sources of bias are currently

being investigated. In thermal ionization MS, bias effects are related to sample volatility, although this would seem to be only a very small effect in comparison to those operating in resonance ionization. For one-color RIMS processes, one could assume that the biases are related to spectral mismatches that are exacerbated by the characteristics of the lasers. Bias effects for pulsed RIMS may be affected by detector saturation effects for the major isotopes. Precision and accuracy (bias) are current limitations of RIMS as an analytical tool in some applications. Keep in mind, though, that even with these limitations, RIMS has relevant applications. It is expected that further development will improve precision and accuracy.

Conclusions

RIMS is a viable, useful, unique analytical technique that should be considered for many applications. As a method for the identification, characterization, and quantification of atomic species and atomic states, it fulfills a definite need. It is extremely well suited as a spectroscopic tool to measure

**Reaching Perfection
in MS and SEM.**

*"A man's reach should
exceed his grasp..."*
Robert Browning

Galileo detectors for Mass Spectrometry and Electron Microscopy.

What silicon chips did for computers, Galileo high-performance detectors are doing for GC/MS, MS and SEM analysis.

Whether your projects involve environmental or pharmaceutical analysis, analysis of organic compounds or general spectroscopy applications, a Galileo detector will speed sample identification while providing accurate and precise analysis.

When research projects require frequent sample analysis over a long period of time, you'll want the latest and best technology backing you up. Galileo is the innovator in analytical instrument detectors. If you demand high performance and are concerned about down time, rapid analysis, dynamic range and cost, insist on Galileo scientific detectors. You'll wonder how you ever got along without us.

Write us and ask how to ensure that your instruments have Galileo scientific detectors.

Galileo Electro-Optics Corp.
Scientific Detector Products Group
P.O. Box 550, Dept. AA
Sturbridge, MA 01566
(508) 347-9191



CIRCLE 60 ON READER SERVICE CARD

spectral properties of unusual species. RIMS has advanced beyond the analytical curiosity stage and is ready for use in situations similar to those described here. Diode lasers will have a definite role in the future development of the technique. RIMS needs to be further evaluated and developed for improved quantification in the areas of precision and accuracy. Even with these limitations, however, it is proving to be useful in a variety of applications.

This research was sponsored by the U.S. Department of Energy, Office of Basic Energy Sciences, under Contract DE-AC05-84OR21400 with Martin Marietta Energy Systems, Inc. The authors also acknowledge D. L. Donohue, D. E. Goeringer, and W. H. Christie for helpful discussions.

References

- (1) Hurst, G. S.; Payne, M. G.; Kramer, S. D.; Young, J. P. *Rev. Mod. Phys.* 1979, 51, 767.
- (2) Young, J. P.; Hurst, G. S.; Kramer, S. D.; Payne, M. G. *Anal. Chem.* 1979, 51, 1050 A.
- (3) Hurst, G. S. *Anal. Chem.* 1981, 53, 1448 A.
- (4) Letokhov, V. S. *Laser Photoionization Spectroscopy*; Academic Press: New York, 1987.
- (5) Hurst, G. S.; Payne, M. G. *Principles and Applications of Resonance Ionization Spectroscopy*; Adam Hilger: Philadelphia, 1988.
- (6) Smith, D. H.; Young, J. P.; Shaw, R. W. *Mass Spectrometry Reviews* 1989, 8, 345.
- (7) Worden, E. F.; Solarz, R. W.; Paisner, J. A.; Conway, J. G. *J. Opt. Soc. Am.* 1978, 68, 52.
- (8) Beekman, D. W.; Callcott, T. A.; Kramer, S. D.; Arakara, E. T.; Hurst, G. S.; Nussbaum, E. *Int. J. Mass Spectrom. Ion Phys.* 1980, 34, 89.
- (9) Shaw, R. W.; Young, J. P.; Smith, D. H. *Anal. Chem.* 1989, 61, 695.
- (10) Shaw, R. W.; Young, J. P.; Smith, D. H. *Anal. Chem.* 1988, 60, 282.
- (11) Fearey, B. L.; Miller, C. M.; Anderson, J. E.; Rowe, M. W.; Nogar, N. S. *Anal. Chem.* 1988, 60, 1786.
- (12) Whitaker, T. *Lasers and Applications*; August 1986, p. 67.
- (13) Shaw, R. W.; Young, J. P.; Smith, D. H.; Bonano, A. S.; Dale, J. M., submitted for publication in *Phys. Rev. A*.
- (14) Fassett, J. D.; Powell, L. J.; Moore, L. J. *Anal. Chem.* 1984, 56, 2228.
- (15) Moore, L. J.; Parks, J. E.; Taylor, E. H.; Beekman, D. W.; Spaar, M. T. In *Inst. Phys. Conf. Ser. 84 (RIS-86)*; Hurst, G. S.; Morgan, C. G., Eds.; Institute of Physics: Bristol, England, 1987, p. 239.
- (16) Parks, J. E.; Spaar, M. T.; Beekman, D. W.; Moore, L. J.; Cressman, P. J. In *Inst. Phys. Conf. Ser. 94 (RIS-88)*; Lucatorto, T. B.; Parks, J. E., Eds.; Institute of Physics: Bristol, England, 1989, p. 197.
- (17) Bekov, G. I.; Letokhov, V. S. In *Inst. Phys. Conf. Ser. 94 (RIS-88)*; Lucatorto, T. B.; Parks, J. E., Eds.; Institute of Physics: Bristol, England, 1989, p. 331.
- (18) Willis, R. D.; Thonard, N.; Wright, M. C.; Lehmann, B. E.; Rauber, D. In *Inst. Phys. Conf. Ser. 94 (RIS-88)*; Lucatorto, T. B.; Parks, J. E., Eds.; Institute of

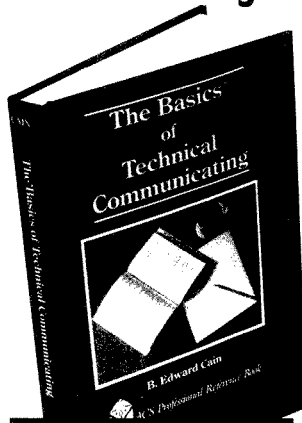
Physics: Bristol, England, 1989, p. 213.

- (19) Kroenert, U.; Becker, St.; Bollen, G.; Gerber, M.; Hilberath, Th.; Kluge, H.-J.; Passler, G. In *Inst. Phys. Conf. Ser. 94 (RIS-88)*; Lucatorto, T. B.; Parks, J. E., Eds.; Institute of Physics: Bristol, England, 1989, p. 155.
- (20) Kroenert, U.; Becker, S.; Hilberath, T.; Kluge, H.-J.; Schulz, C. *Appl. Phys. A* 1987, A44(4), 339.
- (21) McCann, M. P.; Chen, C. H.; Payne, M. G. In *Inst. Phys. Conf. Ser. 94 (RIS-88)*; Lucatorto, T. B.; Parks, J. E., Eds.; Institute of Physics: Bristol, England, 1989, p. 109.
- (22) Tsai, B. P.; Johnson, R. D., III; Hudgens, J. W. In *Inst. Phys. Conf. Ser. 94 (RIS-88)*; Lucatorto, T. B.; Parks, J. E., Eds.; Institute of Physics: Bristol, England, 1989, p. 129.
- (23) Donohue, D. L.; Smith, D. H.; Young, J. P.; McKown, H. S.; Pritchard, C. A. *Anal. Chem.* 1984, 56, 379.
- (24) Fairbank, W. M., Jr.; Spaar, M. T.; Parks, J. E.; Hutchinson, J.M.R. In *Inst. Phys. Conf. Ser. 94 (RIS-88)*; Lucatorto, T. B.; Parks, J. E., Eds.; Institute of Physics: Bristol, England, 1989, p. 293.
- (25) Miller, C. M.; Fearey, B. L.; Palmer, B. A.; Nogar, N. S. In *Inst. Phys. Conf. Ser. 94 (RIS-88)*; Lucatorto, T. B.; Parks, J. E., Eds.; Institute of Physics: Bristol, England, 1989, p. 297.
- (26) Young, J. P.; Shaw, R. W.; Goeringer, D. E.; Smith, D. H. In *Inst. Phys. Conf. Ser. 94 (RIS-88)*; Lucatorto, T. B.; Parks, J. E., Eds.; Institute of Physics: Bristol, England, 1989, p. 367.



J. P. Young (left), R. W. Shaw (center), and D. H. Smith (right) are research staff members of the Analytical Chemistry Division at Oak Ridge National Laboratory. They share a common interest in the development of RIMS as a useful analytical tool. They also have individual interests in general applications of lasers to chemical analysis, application of spectral techniques to the study of transuranium elements and their progeny, processes involved in vapor-phase deposition, and isotope ratio measurements in inorganic MS.

The Basics of Technical Communicat^{ing}



Communications skills—they're a must for successful scientists. Now you can increase your effectiveness and improve your communication skills with this new, easy-to-use reference book. With 18 chapters, this handy guide starts with the basics, such as eliminating wordiness and jargon in technical communications, using correct punctuation, and selecting appropriate verbs. From there, you'll learn how to assemble your papers and gather data for both written and oral reports. You'll learn correct documenting procedures, including footnoting and writing a bibliography. You'll cover the use of visual aids and graphics, abstract preparation, the use of computers and proofreading.

A wide variety of practical applications is covered in this volume, including laboratory and business reports, journal publications, grants and proposals, business correspondence, resumés, and memos. *The Basics of Technical Communicat^{ing}* is a convenient, essential reference—one that you'll use time and time again! It complements *The ACS Style Guide* and *Writing the Laboratory Notebook* to give scientists a complete package for professional development in technical communication skills.

by B. Edward Cain, Rochester Institute of Technology

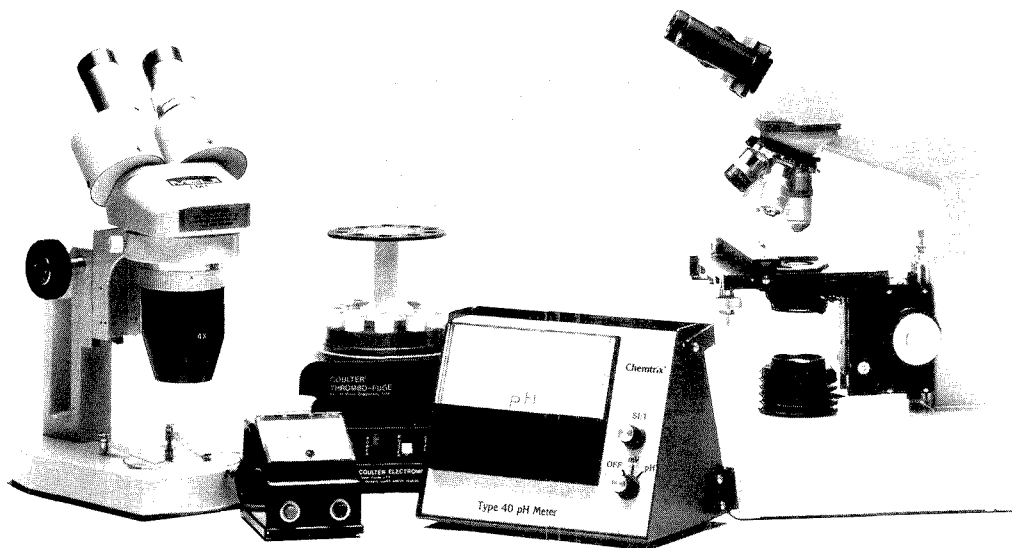
200 pages (1988)
 ISBN 0-8412-1451-4 LC 88-3325
 Clothbound:
 US & Canada \$29.95 Export \$35.95
 ISBN 0-8412-1452-2 LC 88-3325
 Paperbound:
 US & Canada \$19.95, Export \$23.95

Order from: American Chemical Society
 Distribution Office Dept. 90
 1155 Sixteenth St. NW
 Washington, D.C. 20036

or CALL TOLL FREE

800-227-5558

and use your credit card!



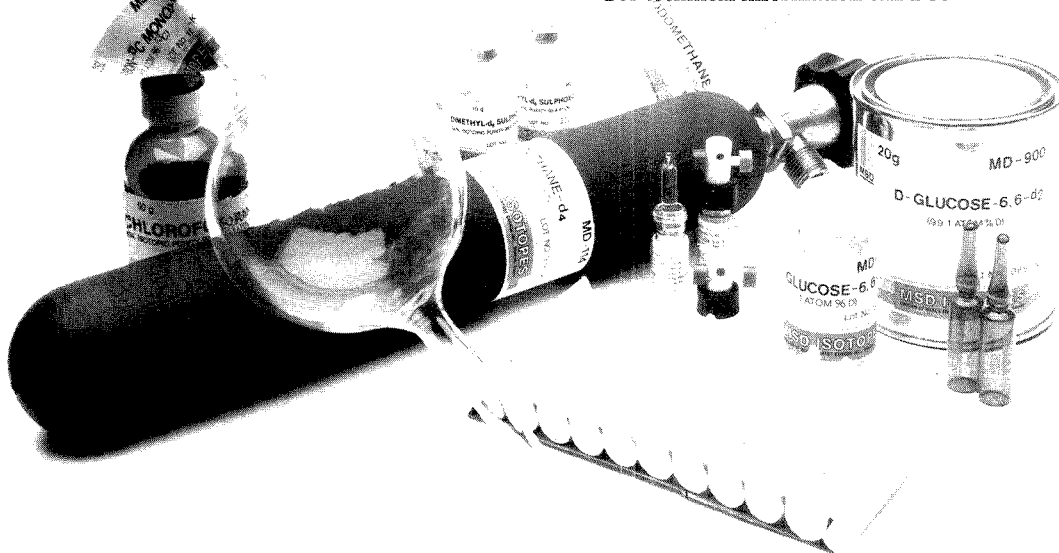
MSD Isotopes – research products that work, bringing results to researchers in biology, chemistry, physics, medicine and related fields.

Did you know that we now offer thousands of compounds labeled with deuterium, carbon-13, nitrogen-15 and other stable isotopes too? And did you know

that even if you require a compound which is not available from us immediately 'off-the shelf', we have the world's best facilities to custom synthesize it for you?

Just call or write to us for more information on what we have in stock and can make for you.

For technical information call 1-800-361-0460.



WEST COAST
 P.O. Box 2951
 Terminal Annex
 Los Angeles, CA 90051
 Los Angeles Area: (213) 723-9521
 Outside State of CA: (800) 423-4977
 State of CA: (800) 372-6454

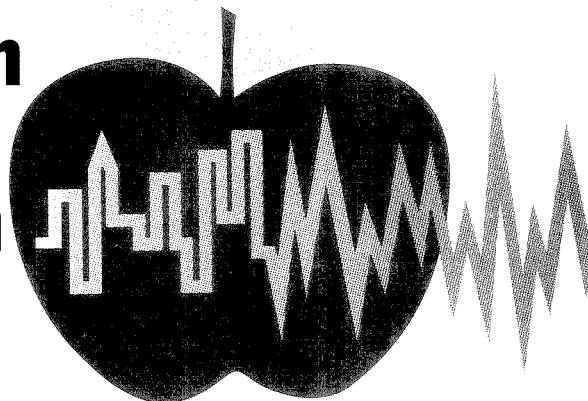
EAST COAST & CENTRAL
 4545 Oleatha Avenue
 St. Louis, MO 63116
 Outside state of MO: (800) 325-9034
 State of Missouri: (314) 353-7000

CANADA
 P.O. Box 899
 Pointe Claire/Dorval, Quebec
 Canada H9R 4P7
 Telephone: (514) 697-2823

CIRCLE 98 ON READER SERVICE CARD

41st Pittsburgh Conference and Exposition

New York City, March 5-9, 1990



The 41st Pittsburgh Conference and Exposition on Analytical Chemistry and Applied Spectroscopy will be held at the Jacob Javits Convention Center in New York City, March 5-9, 1990. This year 12,500 hotel rooms have been reserved for conference week. The technical program will feature 23 symposia and more than 1200 contributed papers. The Exposition of Modern Laboratory Equipment, showing the latest instruments and related chemicals, equipment, and publications, will include 800 different companies in more than 3000 booths.

The following symposia are scheduled to be presented as part of the technical program:

Advances in Raman Spectroscopy
Arranged by S. A. Asher, University of Pittsburgh

Application of Microdialysis in Biological Systems
Arranged by B. G. Hoebel, Princeton University

Biosensors et al.—Analysis Outside the Laboratory
Arranged by S. G. Weber, University of Pittsburgh

Characterization and Analysis of Chiral Compounds
Arranged by J. A. Feldman, Duquesne University

Characterization of High-Temperature Superconducting Oxides
Arranged by A. Pebler, Westinghouse Science & Technology Center

Chromatography and Mass Spec-

trometry in Studies on Human Diseases
Arranged by E. Jellum, University of Oslo

Data Tools for Solving Analytical Chemistry Problems
Arranged by S. R. Heller, U.S. Department of Agriculture

Frontiers of Analytical Toxicology and Substance Abuse Testing
Arranged by S.H.Y. Wong, University of Connecticut School of Medicine

Information Technology: Integrating the Laboratory into the Corporation
Arranged by R. Mahaffey, Tennessee Eastman

International Regulatory Issues on Chiral Drugs
Arranged by A. F. Fell, University of Bradford

Laboratory Accreditation and Standardization: Perspectives on Europe in 1992 (EC '92)
Arranged by H. Hertz, National Institute of Standards and Technology

Laboratory Management—An International Perspective on Excellence
Arranged by J. H. Taylor, Jr., Analytical Technologies

Multidimensional Analysis Systems
Arranged by J.F.K. Huber, University of Vienna

New Horizons in Planar Chromatography
Arranged by J. C. Touchstone, University of Pennsylvania

Polymer Characterization in Food Packaging Applications
Arranged by J. P. Auses, Aluminum Company of America

Quality and Productivity with Chromatographic Methods
Arranged by J. Q. Walker, IBM

Recent Advances in High-Molecular-Weight Mass Spectrometry
Arranged by A. G. Sharkey, University of Pittsburgh

Role of Array Detectors in Spectrochemical Analysis
Arranged by M. B. Denton, University of Arizona

Selective Detectors for Gas Chromatography—Practical Aspects
Arranged by G. D. Dupre, Exxon Research & Engineering

Selectivity in Capillary Electrophoresis
Arranged by D. Rose, Hewlett-Packard

James L. Waters First Annual Symposium on Development of Analytical Instrumentation
Arranged by J. F. Coetzee, University of Pittsburgh

Women in Science: A Blueprint for Progress
Arranged by R. L. Garrell, University of Pittsburgh

ASTM E-42: Recent Advances in Surface Analysis
Arranged by S. Bryan, BP Research

A number of award presentations will be made during the conference.

William Klemperer of Harvard



William Klemperer
*Bomem-Michelson
Award*



Milos Novotny
*Keene P. Dimick
Award*



Robert L. Grob
Dal Nogare Award



Jean-Michel Saveant
*Charles N. Reilley
Award*



George H. Morrison
*Pittsburgh Analytical
Chemistry Award*



Charles B. Harris
*Pittsburgh
Spectroscopy Award*



John F. Rabolt
*Williams-Wright
Award*

University will receive the *Bomem-Michelson Award* from the Coblenz Society. Klemperer's research is in the areas of molecular structure, energy transfer, and intermolecular forces.

Milos Novotny of Indiana University will be presented with the *Keene P. Dimick Award* by the Society for Analytical Chemists of Pittsburgh. The award, sponsored by Keene P. Dimick, is being given to Novotny in recognition of his work on separation techniques.

Robert L. Grob of Villanova University will receive the *Dal Nogare Award* from the Chromatography Forum of the Delaware Valley. Grob is being recognized for his achievements in the field of chromatography, particularly for his work on theory, instrumentation, and applications of GC and LC to environmental analysis.

Jean-Michel Saveant of the Université de Paris VII is this year's recipient of the *Charles N. Reilley Award* from the Society for Electroanalytical Chemistry and Bioanalytical Systems (West Lafayette, IN). Saveant's research has involved the study of the rates and mechanisms of chemical reactions that are triggered by electron transfer at electrodes.

George H. Morrison of Cornell University will receive the *Pittsburgh Analytical Chemistry Award* from the Society for Analytical Chemists of Pittsburgh. Morrison, editor of *ANALYTICAL CHEMISTRY*, has made significant contributions in the fields of trace element chemistry and materials characterization, and has been a leader in the development of a number of analytical techniques, including ion microscropy and neutron activation analysis.

Charles B. Harris of the University of California, Berkeley, will be presented with the *Pittsburgh Spectroscopy Award* by the Spectroscopy Society of Pittsburgh. Harris is being recognized for his contributions in the field of spectroscopy, particularly in the areas of optically detected magnetic resonance, energy transfer in solids, vibrational relaxation, picosecond spectroscopy, and chemical dynamics in liquids.

John F. Rabolt of IBM's Almaden Research Laboratory will receive the *Williams-Wright Award* from the Coblenz Society for his contributions in the field of vibrational spectroscopy. Rabolt's research has involved the development and use of Fourier transform Raman spectroscopy to study molecular assemblies on surfaces.

The following courses are being offered as part of the continuing education program: Using Computer Spreadsheets To Solve Ionic Equilibria; Basic Statistics for the Analytical Chemist; Introduction to Quality Assurance; On-Line Analysis; Understanding and Meeting Quality Standards; Searching and Using Chemical Information; Professional Analytical Chemists in Industry; Application of Supercritical Fluid Extraction to Environmental Analysis; Liquid and Gas Chromatography for Technicians; Near-IR Spectroscopy; Laboratory PC Applications—Combining the Power of Spreadsheet and Data Management Programs; LIMS for Laboratory Managers—Strategic Issues; Principles and Practice of Spectroscopic Calibration; Basic Introduction to Chirality and its Impact on Industrial Analytical Separations; Safety in Academic Laboratories; Precontrol as an Effective Method of Statistical Process Control; Supercritical Fluid Chromatography; and Analytical Laboratory Services—Solving the Mysteries. Registration information will be available in the preliminary program.

Advance registration is urged. Forms for preregistration should be postmarked no later than Feb. 1, 1990.

Registration fees are \$40 for advance and \$70 on site, \$10 for students, \$35 for advance and \$50 for on-site registration of spouses, and \$20 for advance or on-site registration for the exposition only. Registration forms will be provided in the preliminary program. Further information about registration can be obtained from Mary Louise Theodore at the Pittsburgh Conference address given below. Housing and travel information will also be available in the preliminary program. For information about the spouses program, contact Patrick J. Byrne at the Pittsburgh Conference address.

An employment clearinghouse will operate during the conference. Preregistration forms will be provided in the preliminary program. For further information, contact Hyman Schultz at the Pittsburgh Conference address.

The technical program will appear in the Feb. 1 issue of ANALYTICAL CHEMISTRY, along with further details about the conference.

For additional information about any aspect of the conference or exposition, contact the Pittsburgh Conference, 300 Penn Center Blvd., Suite 332, Pittsburgh, PA 15235 (800-825-3221).

Conferences

■ **OE/LASE '90: Optics, Electro-Optics, and Laser Applications in Science and Engineering.** Jan. 14-19. Los Angeles, CA. Contact: SPIE, P.O. Box 10, Bellingham, WA 98227 (206-676-3290)

■ **2nd International Conference on Environmental Analytical Chemistry.** Jan. 17-19. Honolulu, HI. Contact: Charles Fay, Center for Environmental Research, Cornell University, 467 Hollister Hall, Ithaca, NY 14853 (607-255-7535) or Colleen Martin, Center for Environmental Research, Cornell University, 345 Corson Hall, Ithaca, NY 14853 (607-255-4617)

■ **2nd Annual National Forum on Laboratory Accreditation.** April 30-May 1. Baltimore, MD. Contact: Robin Gilderleeve, CEEM, P.O. Box 200, Fairfax Station, VA 22039 (703-250-5900)

Short Courses and Workshops

■ **Short Course on Membranes and Ultrafiltration.** Dec. 13-14. New Brunswick, NJ. Contact: Joe Robles, Cook College, Office of Continuing Professional Education, P.O. Box 231, New Brunswick, NJ 08903

1990

■ **Introduction to Laboratory Techniques: Biochemical Separations.** Jan. 17-18. New Brunswick, NJ. Contact: Joe Robles, Cook College, Office of Continuing Professional Education, P.O. Box 231, New Brunswick, NJ 08903 (201-932-9271)

■ **Design and Operation of Clean Rooms.** March 12-13. San Francisco, CA; March 15-16. Los Angeles, CA; March 20-21. Dallas, TX; March 22-23. Orlando, FL; April 2-3. Boston, MA; April 4-5. Newark, NJ; April 9-10. Chicago, IL. Contact: Contamination Control Seminars, 11844 Brookfield Ave., Livonia, MI 48150 (313-427-8450)

■ **Workshop on Molecular Microspectroscopy.** June 17-20. Oxford, OH. Contact: Molecular Microspectroscopy Laboratory, Miami University, Oxford, OH 45056 (513-529-2873)

ACS Courses

■ **The Computer-Integrated Laboratory: A Hands-On Experience in Lab Automation.** Dec. 10-15, 1989, and April 22-27, 1990. Blacksburg, VA. Raymond E. Dessy

■ **Gas Chromatography: Packed and Capillary Columns.** Feb. 12-16, 1990. Blacksburg, VA. Harold McNair

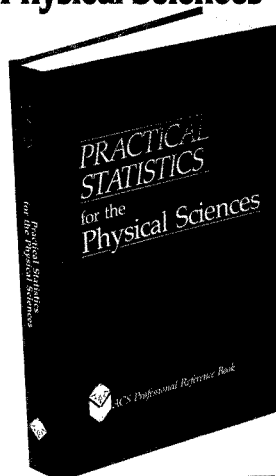
For information on these and other ACS courses, contact the Department of Continuing Education, American Chemical Society, 1155 16th St., N.W., Washington, DC 20036 (202-872-4508).

Call for Papers

■ **Symposium on Chemometrics with Environmental Applications.** Las Vegas, NV. Oct. 30-Nov. 1, 1990. Topics will include quality assurance/quality control, expert systems/artificial intelligence, modeling and experimental design, and hypothesis testing and data analysis. Prospective authors should submit papers by May 1, 1990, to M. Stapanian, Lockheed Engineering & Sciences Co., 1050 E. Flamingo Rd., Las Vegas, NV 89119 (702-734-3208).

These events are newly listed in the JOURNAL. See back issues for other events of interest.

Practical Statistics for the Physical Sciences



Statistical procedures can make an important contribution to evaluating scientific research. Now you can get a better understanding of how to use and apply these procedures to obtain the maximum amount of information from your data. With this dynamic new "how-to" book, you'll learn the concepts underlying the use of statistics through understandable, easy-to-follow steps. You'll cover the basic principles and assumptions required for using statistical analyses. Then you'll learn how to select and apply statistical techniques—and to properly interpret your results.

A comprehensive reference, this book includes worked-out examples illustrating each procedure. Plus, commonly used formulas have been printed on the inside covers and a separate colored section of statistical tables has been included for easy reference.

Practical Statistics for the Physical Sciences offers a useful and practical approach to working with and understanding statistical procedures. No prior knowledge of statistics is necessary, and only a basic knowledge of mathematics and algebra is required.

Larry L. Havlicek, *University of Kansas*
Ronald D. Crain, *MicroAge Computer Store*
ACS Professional Reference Book
512 pages (1988) Clothbound
ISBN 0-8412-1453-0 LC 88-10573
US & Canada \$59.95 Export \$71.95

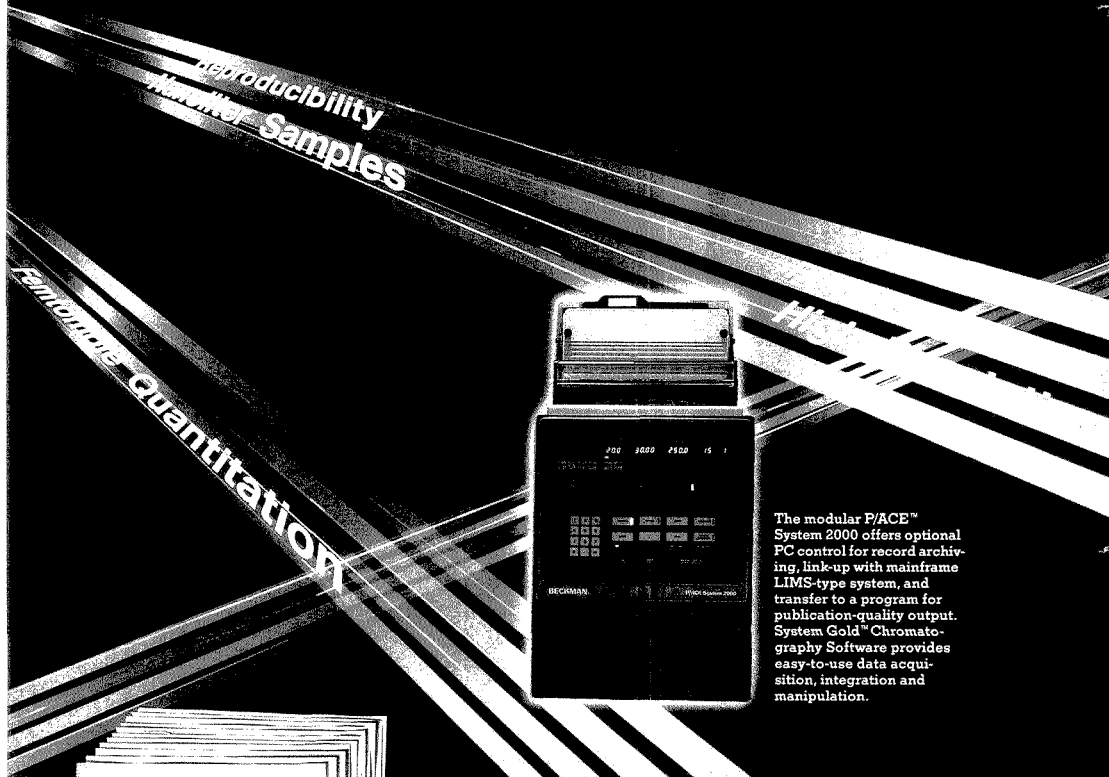
Order from: American Chemical Society
Distribution Office Dept. 99
1155 Sixteenth St., N.W.
Washington, DC 20036

or CALL TOLL FREE

800-227-5558

and use your credit card!

Beckman Sets the P/ACE for Automated Electrophoretic Separations...



The modular P/ACE™ System 2000 offers optional PC control for record archiving, link-up with mainframe LIMS-type system, and transfer to a program for publication-quality output. System Gold™ Chromatography Software provides easy-to-use data acquisition, integration and manipulation.

The P/ACE™ System 2000 from Beckman is designed for today and tomorrow. A modular system, P/ACE leads the evolution of capillary electrophoresis.

A removable detector allows multiple future detection options. Interchangeable cartridges let you change capillaries in minutes. Temperature control provides unmatched reproducibility. And sealed vials minimize sample evaporation. All unique to P/ACE. Unique too—the surprisingly affordable price.

Keep P/ACE with the latest in electrophoretic separation techniques! And achieve rapid success separating proteins, peptides, synthetic oligonucleotides, DNA fragments, and more. Call 800/742-2345, or write to Beckman Instruments, Inc., Spinco Division, Customer Service Department, 1050 Page Mill Rd., Palo Alto, CA 94304. Offices in major cities worldwide.

BECKMAN

A SMITHKLINE BECKMAN COMPANY

Shows 11 injections in 90 min from a total sample of 5 μ L, accomplished with P/ACE™ Migration time CV less than .25%.

Chromatography, MS/MS, NMR, and Natural Products

Size Exclusion Chromatography. B. J. Hunt and S. R. Holding, Eds. x + 286 pp. Chapman & Hall, 29 West 35th St., New York, NY 10001. 1989. \$125

Reviewed by Howard G. Barth, Central Research and Development Department, E. I. du Pont de Nemours and Company, Experimental Station, Wilmington, DE 19880-0228

Although size exclusion chromatography (SEC) is by far the most popular technique for determining molecular weight distributions of polymers, it is surprising that only several general SEC textbooks have been published during the past decade. The present book, written by a number of contributors, is a useful reference but falls short of being a textbook.

The book is divided into three parts: Fundamentals, Applications, and Special Techniques. The Fundamentals part, written by the editors, consists of three short chapters dealing with theory, instrumentation, and calibration and data analysis. Although well written, this part of the book covers elementary aspects of SEC and will be of value only to beginners with no background in either SEC or high-performance liquid chromatography (HPLC). It is essentially an overview of the field. For example, the chapter on calibration and data analysis is a nonmathematical treatment of the topic, which was rather disappointing. There was essentially no meaningful discussion of band broadening except for a statement that band-broadening corrections are not necessary if the column is operated at maximum efficiency.

Part 2, Applications, consists of these chapters: "High Temperature SEC" (M. R. Haddon and J. N. Hay), "Copolymer Analysis" (S. Mori), "SEC of Small Molecules" (D. E. Hillman and C. Heathcote), and "Aqueous SEC" (Y. Kato). The high-temperature SEC chapter is very informative and

useful. Coverage includes SEC of polyolefins, poly(ethylene terephthalate), nylon, polyether ketone, and poly(phenylene sulfide). The chapter on copolymer analysis is thorough and comprehensive. It contains a detailed discussion on calibration approaches for copolymers and the use of multidetectors for determining copolymer chemical heterogeneity. Briefly reviewed are orthogonal chromatography, liquid adsorption chromatography, and TLC of copolymers.

With the high resolution, selectivity, and peak capacity obtained from HPLC, the use of SEC to separate small molecules (< 1000 g/mol) has fallen into relative disuse. However, as

ation (FFF) chapter deals mainly with the comparison of thermal FFF to SEC and covers theory, instrumentation, and applications. Since thermal FFF separates on the basis of both molecular size and chemical composition, it offers a number of potential advantages over SEC. The treatment of this subject is thorough and also includes excellent discussions on other FFF subtechniques.

The chapter on supercritical fluid chromatography (SFC) is a comprehensive survey of the theory, practice, and application of this technique to the separation of macromolecules of less than 10⁶ g/mol. The authors stress both the advantages and limitations of SFC

“The chapter on . . . SFC is a comprehensive survey of the theory, practice, and application of this technique to the separation of macromolecules . . .”

discussed in the chapter on SEC of small molecules, SEC has a number of unique advantages. This chapter also covers column selection, and a number of application areas are reviewed. The aqueous SEC chapter is a brief overview of the field, and most key references are not cited. What is more disturbing, however, is that the only aqueous SEC packings mentioned by the author are those produced by his company. Nevertheless, this chapter does provide the reader with some useful guidelines for mobile-phase selection.

Part 3, Special Techniques, contains these chapters: "Field Flow Fractionation" (J. C. Giddings), "Supercritical Fluid Chromatography" (K. D. Bartle, I. L. Davies, and M. W. Raynor), and "Hydrodynamic Chromatography" (A. J. McHugh). The field-flow fraction-

over other liquid chromatographic methods. The hydrodynamic chromatography (HDC) chapter provides a rather brief review; however, since the technique has a number of serious limitations and is not widely used, a separate chapter on HDC of particles seems out of place in a book on SEC.

Overall, this is a well-edited and well-written book. For the most part, chapters are not in-depth reviews, but overviews. Literature coverage, which includes references up to 1986, is not comprehensive. Many of the chapters stress practice rather than theory and fundamentals, which may prove useful to those seeking a qualitative description of SEC. Experienced chromatographers would benefit most from the chapters on high-temperature SEC, copolymer analysis, FFF, and SFC.

Mass Spectrometry/Mass Spectrometry: Techniques and Applications of Tandem Mass Spectrometry. Kenneth L. Busch, Gary L. Glish, and Scott A. McLuckey. 333 pp. VCH Publishers, Suite 909, 220 East 23rd St., New York, NY 10010-4606. 1989. \$39

Reviewed by Kenneth B. Tomer, NIEHS, P.O. Box 12233, Research Triangle Park, NC 27709

This book is written by three authors who are very active and well versed in tandem mass spectrometry (MS/MS). Their areas of interest include both fundamental studies and applications. The authors state that their goals in writing this text are twofold: to offer a text that is useful to the novice by providing a solid foundation in MS/MS and to stimulate new experimental ideas for current practitioners of the technique.

The authors have attained their goals with this text, which is extremely detailed and encompasses a large amount of material. In fact, the authors have exceeded their goals and have written a book that also provides a solid foundation in the basics of mass spectrometry.

The first three chapters cover the fundamental aspects of MS/MS. After a brief history and overview in Chapter 1, instrumentation used to obtain MS/MS data is detailed in Chapter 2. The authors provide brief, lucid discussions of the variety of mass analyzers available. This section can serve as a good foundation in the basics of MS instrumentation. The approaches that can be taken to obtain MS/MS data by each instrument type are then addressed. Included are comparisons of reaction modes, resolution, and energy regimes accessible.

In Chapter 3, reactions in MS/MS are discussed. To provide a solid foundation for this topic, MS theory in general (the quasi-equilibrium and RRKM theories) is described. The authors detail various means of ion activation with emphasis on energy deposition, variation, and distribution. The discussion of the different processes that might be involved in high- and low-energy collisions is especially useful.

The remaining chapters turn to MS/MS applications, beginning with fundamental studies of ion structures, reaction mechanisms, and thermochemistry. The discussion of analytical applications begins with a section covering sampling considerations, choice of ionization methods, and interpretation of MS/MS data.

Chapter 6, by far the longest chapter, covers analytical applications. The au-

thors have admirably assembled a large body of knowledge in a useful and accessible manner. The power of MS/MS as an analytical tool for a wide variety of applications from petroleum chemistry through environmental analysis to biological problems is well documented.

The lead time between writing and publication is such that few of the 899 references are from 1988, and coverage of 1987 is incomplete. This is especially unfortunate in the rapidly advancing area of analytical applications. The small typeface, although permitting incorporation of a great deal of information into the text, makes reading somewhat difficult. A number of the figures, especially in the fundamentals chapters, could have used more detailed labeling and legends.

The authors provide an excellent, detailed description of MS/MS instrumentation, techniques, and applications, which is backed up by a thorough index and table of contents. The latter two permit easy access to sections covering specific areas. This book, however, is not designed to cater to an individual interested exclusively in learning about a specific instrument. Such a reader is, per force, led to a much fuller understanding of MS/MS.

In summary, the authors have written a book that should be useful for both individuals entering the field of MS/MS and for current practitioners.

High-Performance Liquid Chromatography: Advances and Perspectives, Vol. 5. Csaba Horváth, Ed. ix + 331 pp. Academic Press, Inc., 1250 Sixth Ave., San Diego, CA 92101. 1988. \$75

Reviewed by Willie L. Hinze, Department of Chemistry, Wake Forest University, P.O. Box 7486, Winston-Salem, NC 27109

High-Performance Liquid Chromatography: Advances and Perspectives is a series of small volumes dedicated to providing state-of-the-art accounts of various current hot topics in HPLC. Volume 5 of this series continues the tradition of providing high-quality reviews that are timely, informative, thorough, and important to the separation scientist. In this volume there are three chapters, each prepared by two or more experts who have made significant contributions to the subject considered in the review. Overall, the chapters represent a wealth of practical (and even some theoretical) information on the specifics of the topics surveyed.

In Chapter 1, Unger, Janzen, Gilje,

Lork, and Anspach review "Bonded Silica Phases for the Separation of Biopolymers by Means of Column Liquid Chromatography." This chapter provides valuable information on the preparation, characterization, and applications of such bonded silica stationary phases in biopolymeric liquid chromatographic separations. Of particular interest is an exhaustive survey of available commercial packing materials. This 93-page review contains 14 tables and 14 figures, and cites over 260 references.

Chapter 2, by Bergold, Muller, Hanggi, and Carr, provides an overview of "High-Performance Affinity Chromatography," HPAc. Topics covered include fundamental aspects of and detection schemes in HPAc, preparation and characteristics of various affinity supports, and a brief survey of the literature detailing the development of HPAc. This review contains 16 tables and 19 figures, cites over 290 references, and is 114 pages in length.

The last chapter, by Frenz and Horváth, is entitled "High-Performance Displacement Chromatography," HPDC. The review traces the development of HPDC, discusses both the theoretical and experimental aspects of the technique, describes the instrumentation, and provides some representative selected applications of preparative displacement chromatography. This chapter contains three tables and 65 figures, lists 189 references, and is 103 pages in length.

This volume is well written, edited, and produced. Each chapter has a useful table of contents that is judiciously divided into a number of subsections, and there is a good composite subject index at the end of the book. There is no difficulty in locating a particular topic. All chapters are well organized and documented. The literature coverage generally extends into early 1987. Although there are some citations for 1988, many are listed as "to be published" or "in press." Due to the usual publishing lag time, an addendum preceding the subject index that lists the pertinent papers published pursuant to the publication of the monograph should be considered for future volumes. The book is generally free from factual and typographical errors.

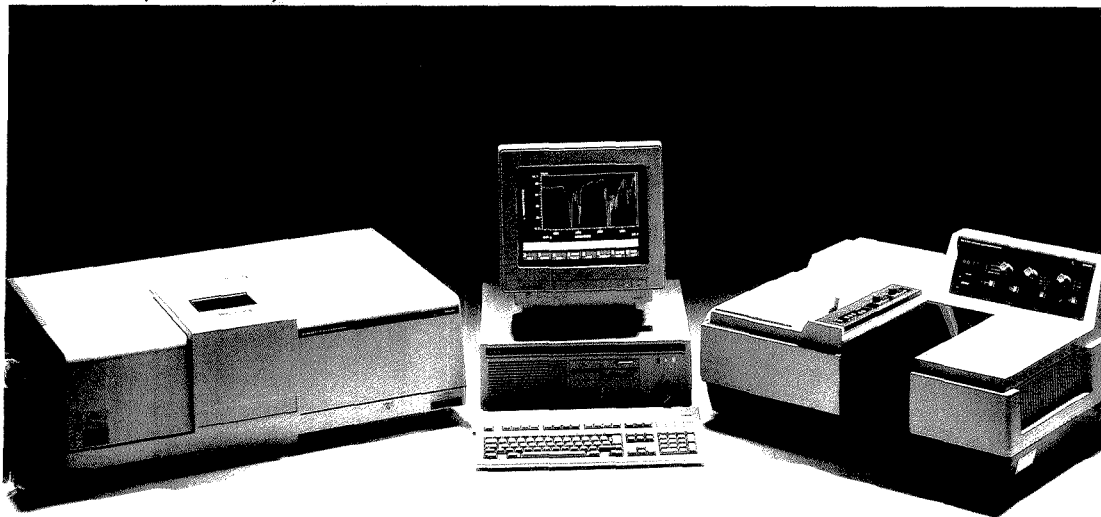
This monograph provides an excellent overview of the three topics. The level and content of the presentation are such that both newcomers and more experienced practitioners involved with high-performance affinity or displacement chromatography or biopolymeric separations on bonded silica phases will find this monograph to be very useful. In addition, as was



PHILIPS

Two IR systems – one concept

Philips Analytical



More performance for less money

The application determines the choice

PU9800 – high performance FTIR spectrometer with EAGLE-IR software

- Easy-to-use, menu-operated facilities
- Flexible programming
- Library search
- Multi-component, quantitative software

PU9700 Series – IR spectrophotometers offering tremendous value for money

- Ideal for routine applications
- Easy-to-use
- Available with IRIS-software systems for
 - High performance data station package
 - IBM PC environment
 - Rapid data acquisition
 - Push-button simplicity of operation

Whichever system you choose, you can be sure of more performance and better value. For more information contact us today



PHILIPS ANALYTICAL - BIGGER IDEAS FOR BETTER ANALYSIS

For more information about the Philips Analytical IR spectrometer contact:

Philips Scientific Analytical Division York Street, Cambridge Great Britain CB1 2PX Tel: 0223 358866 Telex: 817331 Fax: 0223 312764
or telephone direct **Austria:** (0222) 60101 – 1792 **Belgium:** (02) 525 62 75 **Denmark:** (01) 57 22 22 **Finland:** (09) 502 63 56 **France:** (1) 49 42 91 62
Germany: (0561) 501 384 **Italy:** (02) 64 49 12 **Netherlands:** (040) 783 901 **Norway:** (02) 68 02 00 **Spain:** (1) 404 22 00 **Sweden:** (08) 782 1591
Switzerland: (01) 488 22 11.

CIRCLE 125 ON READER SERVICE CARD

IR 10

THE AMERICAN CHEMICAL SOCIETY PRESENTS . . .

24 Unique Sources of Archival-Quality Chemistry Research and News

ACCOUNTS OF CHEMICAL RESEARCH

Editor, Fred W. McLafferty
Cornell University
12 issues a year. ISSN 0001-4842
Member \$24 Nonmember \$110

ANALYTICAL CHEMISTRY

Editor, George H. Morrison
Cornell University
24 issues a year. ISSN 0003-2700
Member \$27 Nonmember \$49

BIOCHEMISTRY

Editor, Hans Neurath
University of Washington
26 issues a year. ISSN 0006-2960
Member \$80 Nonmember \$549

BIOCONJUGATE CHEMISTRY

Editor, Claude F. Meares
University of California, Davis
The unifying medium of conjugation
chemistry. BIOCONJUGATE CHEMISTRY
will emphasize the joining of two
different molecular functions by chemical
or biological means.
6 issues a year. ISSN 1043-1802
Member \$29 Nonmember \$249

New in 1990!

CHEMICAL & ENGINEERING NEWS

Editor, Michael Heylin
51 issues a year. ISSN 0009-2347
Nonmember \$55

CHEMICAL RESEARCH IN TOXICOLOGY

Editor, Lawrence J. Marnett
Vanderbilt University
For the latest original findings, in primary
research, on the toxicological effects of
chemical agents.
6 issues a year. ISSN 0893-228X
Member \$46 Nonmember \$269

CHEMICAL REVIEWS

Editor, Josef Michl
University of Texas, Austin
8 issues a year. ISSN 0009-2665
Member \$26 Nonmember \$161

CHEMISTRY OF MATERIALS

Editor, Leonard V. Interrante
Rensselaer Polytechnic Institute
This new, international journal provides
a molecular-level perspective at the
interface of chemistry, chemical
engineering, and materials science.
6 issues a year. ISSN 0897-4756
Member \$49 Nonmember \$299

Just Published!

CHEMTECH

Editor, Benjamin J. Luberoff
12 issues a year. ISSN 0009-2703
Member \$37 Nonmember (Pers.) \$65
Nonmember (Inst.) \$282

ENERGY & FUELS

Editor, John W. Larsen
Lehigh University
A practitioner's guide to the chemistry of
fossil fuels—from formation to methods
of utilization.
6 issues a year. ISSN 0887-0624
Member \$48 Nonmember \$289

ENVIRONMENTAL SCIENCE & TECHNOLOGY

Editor, William H. Glaze
University of North Carolina,
Chapel Hill
12 issues a year. ISSN 0013-936X
Member \$33 Nonmember (Pers.) \$61
Nonmember (Inst.) \$212

INDUSTRIAL & ENGINEERING CHEMISTRY RESEARCH

Editor, Donald R. Paul
University of Texas, Austin
12 issues a year. ISSN 0888-5885
Member \$55 Nonmember \$321

INORGANIC CHEMISTRY

Editor, M. Frederick Hawthorne
University of California, Los Angeles
26 issues a year. ISSN 0020-1669
Member \$82 Nonmember \$499

JOURNAL OF AGRICULTURAL AND FOOD CHEMISTRY

Editor, Irvin E. Liener
University of Minnesota
6 issues a year. ISSN 0021-8361
Member \$25 Nonmember \$138

JOURNAL OF THE AMERICAN CHEMICAL SOCIETY

Editor, Allen J. Bard
University of Texas, Austin
26 issues a year. ISSN 0002-7863
Member \$75 Nonmember \$499

JOURNAL OF CHEMICAL AND ENGINEERING DATA

Editor, Bruno J. Zwolinski
Texas A&M University
4 issues a year. ISSN 0021-9568
Member \$30 Nonmember \$184

JOURNAL OF CHEMICAL INFORMATION AND COMPUTER SCIENCES

Editor, George W.A. Milne, N.I.H.
4 issues a year. ISSN 0095-2338
Member \$18 Nonmember \$97

JOURNAL OF MEDICINAL CHEMISTRY

Editor, Philip S. Portoghesi
University of Minnesota
12 issues a year. ISSN 0022-2623
Member \$42 Nonmember \$257

THE JOURNAL OF ORGANIC CHEMISTRY

Editor, Clayton H. Heathcock
University of California, Berkeley
26 issues a year. ISSN 0022-3263
Member \$56 Nonmember \$340

JOURNAL OF PHYSICAL AND CHEMICAL REFERENCE DATA

Editor, David R. Lide, Jr.
National Institute of Standards &
Technology
4 issues a year. ISSN 0047-2689
Member \$65 Nonmember \$290

THE JOURNAL OF PHYSICAL CHEMISTRY

Editor, Mostafa A. El-Sayed
University of California, Los Angeles
26 issues a year. ISSN 0022-3654
Member \$70 Nonmember \$540

LANGMUIR

Editor, Arthur W. Adamson
University of Southern California
6 issues a year. ISSN 0743-7463
Member \$58 Nonmember \$376

MACROMOLECULES

Editor, Field H. Winslow
AT&T Bell Laboratories
12 issues a year. ISSN 0024-9297
Member \$57 Nonmember \$428

ORGANOMETALLICS

Editor, Dietmar Seyferth
Massachusetts Institute of Technology
12 issues a year. ISSN 0276-7335
Member \$59 Nonmember \$432

For subscription information write:

American Chemical Society
Marketing Communications Dept.
1155 Sixteenth Street, N.W.
Washington, D.C. 20036 U.S.A.

Or call toll free 1-800-227-5558.
In Washington, D.C. and outside the U.S.
call 202-872-4363.

Telex: 440159 ACSP UI or 89 2582
ACSPUBS. FAX: 202-872-4615.

For nonmember rates in Japan
contact: Maruzen Co., Ltd.



Rates are valid through December 31, 1989.

concluded in another review (*J. Chromatogr.* 1989, 472, 344), this monograph "is a must for everyone who is doing preparative chromatography, especially in biotechnology" and related areas.

Natural Products Isolation: Separation Methods for Antimicrobials, Antivirals, and Enzyme Inhibitors. Gerald H. Wagman and Raymond Cooper, Eds. xiii + 619 pp. Elsevier Science Publishers, 52 Vanderbilt Ave., New York, NY 10017. 1989. \$139

Reviewed by Stig Allenmark, *Laboratory of Microbiological Chemistry, University of Göteborg, Guldhedsgatan 10A, S-41346 Göteborg, Sweden*

This latest volume of the *Journal of Chromatography* Library Series consists of 14 contributions from selected experts in the field and is intended to cover the most important techniques used today for the isolation of natural products of medical and related importance. An earlier volume in the series (No. 15) addressed the same field but was limited to antibiotics. Although the book focuses on preparative separation methods, it also deals with structure elucidation, physical and chemical properties, and biological activities of the isolated compounds.

The first three chapters aim at presenting in some detail the important techniques used in natural products isolation and are devoted mainly to countercurrent chromatographic methods, HPLC (including the use of photodiode array detectors), and affinity chromatography. The remainder of the volume (except for the last chapter) deals with specific classes of compounds and the routes used for their isolation and characterization. These chapters are organized in a rather similar fashion; they describe producing organisms, physical and chemical properties, biological activities, isolation and purification methods, and structure determination. Most of the contributions present a summary of an enormous amount of work carried out to elucidate the structures and properties of the isolated compounds, which often possess very complicated structures. The chapters are generally well written and readable, even for the nonspecialist. As in most multiauthored publications, however, one finds a certain inhomogeneity and overlap of facts, but on the whole the editors have been successful. An excellent chapter on marine natural products gives a nice exposure to exploitation of the sea as a source of exciting new bioactive compounds. Re-

cent literature, up to 1988, is well covered by the references given in each chapter.

The book illustrates well the difficulties in isolating a particular compound from a complex mixture and the increasing importance of liquid chromatographic techniques in the isolation procedures. Many of the isolation schemes presented, developed by industrial scientists, start with several hundred liters of fermentation broths or biological extracts and often involve a large number of extraction and chromatographic steps. Although these procedures obviously serve their purpose, rationales for their use, in terms of the discussion of a purification strategy, are often lacking. In the reviewer's opinion, an introductory chapter in which extraction, concentration and chromatographic separation steps, and their role in an isolation scheme are discussed from a more general point of view would have been valuable.

A nice example of the use of high-resolution preparative reversed-phase LC in the isolation of structurally very closely related natural products, such as stereoisomers, is given in the last chapter by the successful separation of the three diastereomeric pairs of dehydrodiconiferyl alcohol β -D-glucosides.

Very few errors or typos were found, and the text is supported by many illustrative figures and chemical formulas. The book should be a most valuable source of information, particularly for anyone working with or interested in natural product chemistry and related areas.

Nuclear Magnetic Resonance, Vol. 17. G. A. Webb, Ed. 484 pp. Royal Society of Chemistry, Distribution Centre, Blackhorse Rd., Letchworth, Herts SG6 1HN, England. 1988. \$220

Reviewed by F. A. Bovey, *Bell Telephone Labs, Murray Hill, NJ 07974*

This volume reviews the published literature on nuclear magnetic resonance from June 1986 to May 1987. It was published in 1988 and reached this reviewer's hands in August 1989. Thus the developments reported are approximately two years old, and readers wishing to be entirely current must keep this in mind.

The following subjects are covered: Chapter 1, "Theoretical and Physical Aspects of Nuclear Shielding" by Cynthia J. Jameson; Chapter 2, "Applications of Nuclear Shielding" by Mark J. Foster; Chapter 3, "Theoretical Aspects of Spin-Spin Couplings" by Jens Oddershede; Chapter 4, "Nuclear Spin

**There are
224 reasons
why...**

**most
chemists
in the U.S.
belong to the
American
Chemical
Society.**

The fact is, there are more than 137,000 chemists in this vital, career-enhancing society — *the largest scientific organization in the world dedicated to chemistry-related sciences!*

To learn those reasons,
CALL TOLL FREE
1-800-ACS-5558 or mail
this coupon to:

American Chemical Society
Membership Division
1155 Sixteenth St., NW
Washington, DC 20036

Yes!

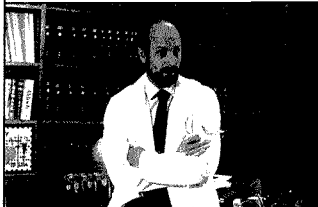
I would like to know 224 reasons to join the American Chemical Society. Please send free brochures to:

Name _____

Address _____

City, State, ZIP _____

Me? Enroll in the ACS Employment Service?



I'm head of a major research department!

Even for the successful chemist or scientist in an allied field, sometimes the best way to get ahead is to make a change.

The ACS Employment Service offers the opportunity to investigate the possibilities discreetly—and at very low cost. Our Employment Service is free to all ACS members. If you request confidentiality from current employers or other designated organizations there is a nominal charge.

For more information write,
use coupon, or
CALL TOLL FREE
800-227-5558

Employment Services Office,
American Chemical Society
1155 Sixteenth Street, NW,
Washington, DC 20036

Yes, I am a member of ACS and I
would like to learn how the ACS
Employment Service can help me
advance my career.

Name (please print) _____
Membership # _____
Address _____
City _____
State _____ ZIP _____

BOOKS

Relaxation in Liquids" by H. Weingärtner; Chapter 5, "Solid State NMR" by R. Dupree; Chapter 6, "Multiple Pulse NMR" by D. L. Turner; Chapter 7, "Natural Macromolecules" by D. B. Davies; Chapter 8, "Synthetic Macromolecules" by A. Bunn; Chapter 9, "Conformational Analysis" by A. Gryff-Keller and P. Szczecinski; Chapter 10, "Nuclear Magnetic Resonance of Living Systems" by P. G. Morris; Chapter 11, "Oriented Molecules" by C. L. Kheterepal, B. S. Arun Kumar, and S. Raghobhama; and Chapter 12, "Heterogeneous Systems" by T. K. Halstead.

The reviews of the cited literature are necessarily brief because of the vastness of the field. Even at that, these volumes have increased steadily in size, from 343 pages for Vol. 1 to 484 pages for the present volume—a reflection of the growth of the literature. The reviews are almost entirely noncritical; the quality and significance of the reported work usually do not come through, although of course all readers know that such variability does exist. Some of the chapters are mainly unadorned catalogues of the literature while others (clearly preferable) provide some background and indication of trends and discrepancies.

This volume and its predecessors provide an extremely useful service to workers in this field and can save many hours of library work. In the immediate area of the researcher's interest, however, and especially in regard to the most recent developments, this is not a royal road. One must do the searching oneself, although with modern computer methods this process is not as onerous as it once was.

The excessive price of this book will limit its purchase to libraries rather than individuals.

Advances in Chromatography, Vol. 28.
J. Calvin Giddings, Eli Grushka, and
Phyllis Brown, Eds. xviii + 371 pp.
Marcel Dekker, 270 Madison Ave.,
New York, NY 10016. 1989. \$100

Reviewed by Merle Evenson, *University of Wisconsin-Madison, 1300 University Ave., Madison, WI 53706*

This volume continues the long tradition of this series as a well-respected compendium of literature devoted to chromatography. Most of the volumes contain five to eight chapters. The chapters usually may be classified as brief reviews, as theoretical aspects of chromatography, or as established applications of chromatography. Volume 28 is so organized.

Chapters that might be considered applied in this volume are entitled "HPLC of Penicillin Antibiotics" and "Gas Chromatographic Analysis of Plasma Lipids." Chapters that could be classified as reviews are entitled "The Use of Dynamically Modified Silica in HPLC as an Alternate to Chemically Bonded Materials," "Column Switching in Gas Chromatography," "The Use of Mixed Stationary Phases in Gas Chromatography," and "Online Small Bore Chromatography for Neurochemical Analysis in the Brain." The theoretical chapter in this volume is "Theoretical Aspects of Quantitative Affinity Chromatography: An Overview."

I examined the timeliness of the references by using a five-year cutoff. In two of the chapters about 50% of the references cited were less than five years old. In another two chapters 40% of the references were less than five years old, and in two other chapters 30% of the references were less than five years old. In one chapter 20% of the citations were less than five years old, and in another chapter only 10% of the references were less than five years old. The review-type articles are those that have mostly older literature citations. However, none of the chapters suffer from being out of date even though the percentage of references older than five years is high in many of the chapters.

In the applied chapters, my preference is to include much more information and detail on the sample preparations prior to chromatographic analysis. I prefer chapters that put more emphasis on accuracy and precision of the analyses (including sample preparation) so readers can make quantitative decisions about the various chromatographic methods.

There are more typographical and editing errors than usual in a book of this type. I found three journal article references where the date of publication was missing. In the contents to other volumes, I found five misspelled words in 10 pages. There are several places in the book where an author's surname is misspelled at the end of a chapter. However, these errors do not significantly detract from the quality of the book.

I believe this book's greatest value is in the summaries it presents on the seven different subjects. The chapters are written for the serious and experienced chromatographer. Libraries should have several copies of this volume, and researchers working directly in one of these chromatography fields may want to purchase a personal copy so that they may refer to the literature cited in each area.

Thermal Analysis: Techniques and Applications. Michael E. Brown. ix + 211 pp. Routledge, Chapman & Hall, 29 West 35th St., New York, NY 10001. 1988. \$40

Reviewed by David Dollimore, Department of Chemistry, University of Toledo, Toledo, OH 43606

This book fills a gap in the literature. There are many erudite volumes available on thermal analysis. There are specialist editions dealing with individual techniques, but no text dealing with the subject as a whole that could serve as the basis for teaching a course. Well, here at last is such a book, written as the author suggests: to help someone with little or no knowledge of the topic, indicating what the subject is all about and giving an adequate description of the more common techniques. What's it all about? In large bold letters, the author sets this out at the very beginning: "THERMAL ANALYSIS is the measurement of changes in physical properties of a substance as a function of temperature whilst the substance is subjected to a controlled temperature program."

The book is divided into various

chapters dealing with the different techniques available. However, these chapters are preceded by two chapters entitled "Introduction" and "Thermal Effects." The Introduction gives a historical perspective and sets out the main techniques, and the second chapter categorizes the various thermal events that can occur in a system. Thus, starting with a solid material, it is apparent that these techniques can be used to follow transitions, oxidation, tarnishing, combustion, volatilization, heterogenous catalysis, addition reactions, and double decomposition reactions.

As noted, subsequent chapters deal with thermogravimetry (TG), differential thermal analysis (DTA), differential scanning calorimetry (DSC), thermopometry, thermodilatometry (TD), thermomechanical analysis (TMA), and dynamic mechanical analysis (DMA). There is a chapter dealing with the increasing practice of combining these techniques and a further chapter on evolved gas analysis (EGA). The less common techniques are not neglected, and a single chapter deals with emanation thermal analysis (ETA), thermomagnetometry (TM), thermoelectrometry, thermosonimetry, and ther-

moacoustimetry. The author devotes a chapter to the use of microcomputers in thermal analysis but points out that events are moving so rapidly in this field that a report on the subject is soon out of date. The calculation of reaction kinetics from thermal analysis data rates a complete chapter that is a selective but pertinent account of the topic. There is a chapter concerning purity determination using DSC. The penultimate chapter on the literature and nomenclature of thermal analysis is very useful. One appendix deals with a selection of experiments showing the scope of thermal analysis; a second appendix discusses thermal analysis software. Various programs are given. One deals with data capture and storage; others deal with display of data, baseline corrections, smoothing and scaling of data, and numerical differentiation; and a final program deals with peak integration. The last appendix explains the symbols used in the text. Each chapter has a good bibliography.

This is a book that many people will use and about which the author has a right to be proud. I have already started using it in teaching undergraduate and graduate courses and in planning laboratory experiments.

When Buying TitraLab™ be Sure to Check your Tennis Racket

TitraLab™ Titration Systems ensure you more time away from tedious routine tasks.

TitraLab automatically switches between electrodes and titrant/reagent burettes according to your methods. Time is saved and errors are eliminated.

Live titration curves on the screen make method development faster, and errors during routine operation can be seen immediately.

Time for instrument set-up is kept to a minimum by guided dialogue in plain English, German or French.

Check with your Radiometer product specialist to determine which TitraLab system will suit your needs, and find out about Radiometer's application support.

If you need precision and reliability in titration, be sure to contact your local Radiometer office and experience the convenience of TitraLab yourself.

...when you need to be sure...

RADIOMETER ANALYTICAL A/S
KROGSHØJVEJ 49 · DK-2880 BAGSVAERD · DENMARK

CIRCLE 138 ON READER SERVICE CARD

SPEND \$15 AND MAKE YOUR ENVIRONMENTAL ANALYSES "A DAY AT THE BEACH"

FREE J&W SUNGLASSES WITH EVERY ORDER!



J&W's new DB-5.625 column, designed for the analysis of base-neutral/acid (BNA) extractable compounds, makes your environmental analyses as easy as "a day at the beach"! For only \$15 more than you would pay for our standard column, you get extensive documented testing that guarantees the performance of each DB-5.625 column.

DB-5.625 IS THE MOST THOROUGHLY TESTED ENVIRONMENTAL COLUMN IN THE INDUSTRY.

After a rigorous "Grob" test, **EVERY** DB-5.625 column must then pass additional tests that satisfy U.S. EPA criteria. A three point linearity plot and relative response factors are obtained for Pentachlorophenol, 2,4-Dinitrophenol, N-Nitrosodiphenylamine and Carbazole. Results are included with each column.

DB-5.625 COLUMNS COME IN THE WIDEST SELECTION OF DIAMETERS AND FILM THICKNESSES AVAILABLE IN THE INDUSTRY.

Columns are 30 meters in length with 0.25 or 0.32 mm internal diameter and film thickness of 0.25, 0.50 or 1.00 micron.

WE HAVE HUNDREDS OF DB-5.625 COLUMNS IN STOCK - READY FOR IMMEDIATE DELIVERY.

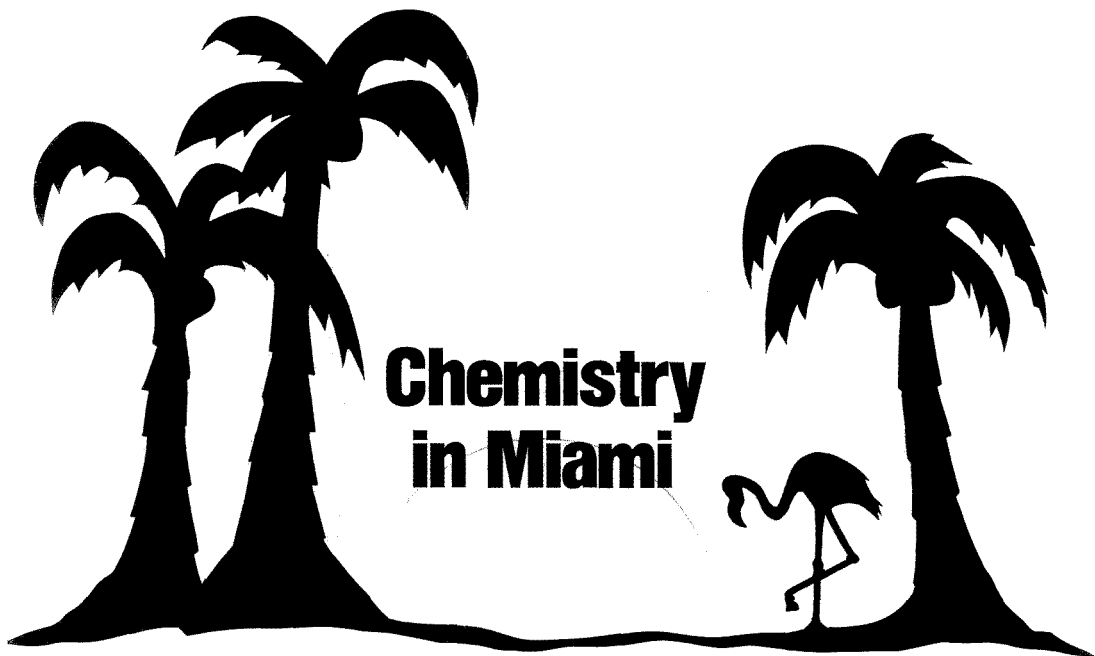
We're so sure our DB-5.625 column will make your environmental analyses as easy as "a day at the beach" that with every order we'll send you a pair of J&W neon sunglasses free! Hurry! Offer Expires 1/31/90.

To order call:
(800) 553-5837 In CA
(800) 223-3424 Outside CA
(916) 985-1101 FAX

Or call your local J&W distributor

For more information call Angela for a free J&W Environmental Catalog today!

J&W SCIENTIFIC
SPECIALIZING IN HIGH RESOLUTION CHROMATOGRAPHY **FISONS**
91 BLUE RAVINE ROAD, FOLSOM, CA 95630-4714
(916) 985-7888



Chemistry in Miami

Typical hot, humid Florida weather greeted chemists arriving in Miami Beach for the fall national ACS meeting. Luckily, rain and wind from Hurricane Hugo held off until everyone had gone home following an enjoyable week of technical sessions, social events, and visits to the ACS Exposition and the multimedia event "Molecules and Society."

The Division of Analytical Chemistry program featured presentation of the four Division awards along with symposia and sessions on electrochemistry, applications of capillary chromatography, ultrasensitive and ultrasensitive detectors in chromatography, two-dimensional NMR, analytical measurements based on piezoelectric crystal response, expert systems, solid-state luminescence, supercritical fluid extraction and chromatography, and general topics.

The Division of Analytical Chemistry Award in Electrochemistry was presented to Ralph Adams, professor of chemistry at the University of Kansas. Although Adams's early research centered on the mechanisms of organic electrode reactions, his interest shifted to problems in neuroscience in 1969. Both aspects of his career were represented at a three-session award symposium organized by J. Q. Chambers of the University of Tennessee. The first session, on Monday afternoon, featured talks by S. W. Feldberg (Brookhaven National Laboratory) on simulation of electrochemical phenomena,

M. D. Hawley (Kansas State University) on electrochemical oxidative decarboxylation of 3,4-dihydroxymandelic acid, R. A. Osteryoung (SUNY—Buffalo) on interaction of protons and dimethylaniline in ambient-temperature chloroaluminate ionic liquids, Z. Galus (University of Warsaw) on mixed-solvent effects in electrode kinetics, R. L. McCreery (Ohio State University) on surface structure and electron transfer activity of carbon electrodes, and R. P. Buck (University of North Carolina) on Nernst-Donnan Fermi distribution potentials.

FOCUS

The symposium continued on Tuesday morning with presentations focusing on applications of electrochemistry to neurological problems, including presentations by R. M. Wightman (University of North Carolina), J. B. Justice (Emory University), A. G. Ewing (Penn State University), and I. N. Mefford (National Institute of Mental Health). Adams's award address centered on the various methods for electrical pretreatment of carbon fibers for in vivo voltammetry. "There are probably as many pretreatments in the literature as there are kinds of fibers," said Adams. All produce a surface modification that is assumed to involve some form of hydrous oxide surface state. Al-

though this surface normally enhances sensitivity to catecholamine-like species and provides some selectivity among species, it also introduces unwanted side effects (e.g., increased time constants for chronoamperometric responses, adsorption). Careful control of pretreatment parameters, said Adams, can minimize these side effects while allowing sensitive and selective detection of the target compounds.

The final electrochemistry award session on Tuesday afternoon featured various applications of electrochemical studies to electroactive biological molecules by J. O. Schenk (Washington State University), G. A. Gerhardt (University of Colorado Health Sciences Center), B. A. Feinberg (University of Wisconsin—Milwaukee), C. L. Blank (University of Oklahoma), Chambers, and P. J. Kulesza (University of Warsaw). Those who attended the award symposium came away with a clear idea of the ways in which electrochemistry is helping neurochemists understand brain function.

The Division's Award in Chemical Instrumentation was presented to M. Bonner Denton, professor of chemistry at the University of Arizona. Denton, known for his application of technological advances in electronics, physics, optics, astronomy, acoustics, mechanical engineering, and computer science to the development of chemical instrumentation, was honored Monday afternoon and Tuesday morning at a symposium organized by R. B. Bilhorn of

Eastman Kodak.

The Monday session featured talks by Alexander Scheeline (University of Illinois) on data arrays from transient analytical discharges, Andrew Zander (Varian Research Center) on the role of analytical chemists in instrument development, Bilhorn on atomic and molecular spectroscopy with a slow-scan charge transfer device, and K. J. Leiper (Glaxo) on the use of spectroscopy in process control.

Denton's award address discussed some of the past successes and future goals of spectrochemical analysis. Today's demands for high sample throughput, increased sensitivity, enhanced selectivity, and improved accuracy, said Denton, provide strong incentives for continued development of both molecular and atomic spectroscopy. He pointed out that improvement in any specific case can best be achieved using a systems approach in which optimal results are obtained through integration of the best state-of-the-art technologies. Improved sample handling, optical sources, detectors, and data reduction algorithms can be combined to yield improved system performance. For example, new multichannel charge transfer device detectors (see Denton's INSTRUMENTATION articles in the February 15, 1988, and March 1, 1988, issues of ANALYTICAL CHEMISTRY) along with modern computer technology can be used to provide improved detectability, system diagnostics, and precision.

On Tuesday morning the symposium concluded with talks by Gary Horlick (University of Alberta) on photodiode array systems for ICP-AES, Gary Hieftje (Indiana University) on electronic imaging systems in analytical spectrometry, J. D. Winefordner (University of Florida) on detection at low light levels, and Jonathan Svedler (Stanford University) on spatial interference.

Atomic and molecular spectrochemical analysis was also the topic of the three-session symposium honoring Gary Hieftje as the 1989 winner of the Division's Award in Spectrochemical Analysis. The symposium was organized by John Olesik of the University of North Carolina and J. E. Freeman of the Upjohn Company. Hieftje led off the symposium by addressing the question "Analytical Atomic Spectrometry—Is the End Near?" Analytical atomic spectrometry is inherently simple, said Hieftje, and in its ultimate embodiment would involve decomposing a target sample into its constituent atoms, separating the atoms according to kind, and counting the separated atoms. Ultimately, this procedure would

provide single-atom detection limits, perfect selectivity, and a complete absence of matrix interferences; current reality, of course, is substantially more complicated. No method has yet been found by which samples can be quantitatively atomized; techniques intended for distinguishing atoms of different elements have been limited in resolution; and detection efficiency for isolated atoms has been lower than desired. "Naysayers have for years been projecting the decline or demise of the field," said Hieftje, "but on roughly 10-year intervals, important new techniques have proven them wrong." Prospects for future developments indicate there is no reason to believe that the end is near for atomic spectrometry.

Hieftje's conviction that new developments are still taking place in atomic spectrometry was confirmed by the speakers following him on the program. Several new spectroscopic techniques were described: E. L. Wehry (University of Tennessee) described molecular photofragmentation fluorescence spectrometry, L. R. Layman (Los Alamos National Laboratory) discussed determination of trace elements in uranium using an ICP coupled to a high-resolution Fourier transform spectrometer, R. M. Miller (Unilever Research) described spectroscopic imaging, and G. J. Bastiaans (Integrated Chemical Sensors) talked about acoustic waveguide sensors.

In addition, methods for obtaining improved detection limits were discussed by J. M. Ramsey (Oak Ridge National Laboratory), Charles Boss (North Carolina State University), S. W. Downey (AT&T Bell Labs), and C. A. Monnig (University of North Carolina), while processes occurring in the ICP were described by M. W. Blades (University of British Columbia), Olesik, Mao Huang (Indiana University), and G. D. Rayson (New Mexico State University). E. S. Yeung (Iowa State University) spoke about improved diagnostics for laser-produced sample plumes.

The spectrochemical analysis award symposium wound up with talks featuring applications of state-of-the-art spectroscopic techniques. R. E. Russo (Lawrence Berkeley Laboratory) discussed the use of pulsed-laser deposition for fabrication of thin-film high-temperature semiconductors. A. G. Childers (Glaxo) discussed evaluation of pharmaceutical metered-dose inhalers, and Frank Bright (SUNY—Buffalo) talked about the use of time-resolved fluorescence spectroscopy for elucidation of supercritical fluid solvodynamics. Finally, Charles Boss delivered a "roast" of Hieftje in the spirit of

Bill Fateley, who was unexpectedly unable to attend.

The final Division award, the Award for Excellence in Teaching, was presented to Theodore Williams, professor of chemistry at the College of Wooster and the first recipient of this award from an undergraduate liberal arts institution, at an award symposium organized by Margaret Merritt of Wellesley College. Henry Blount (National Science Foundation) led off the symposium, noting that despite opportunities for analytical chemistry to have an impact on a broad array of problems, from biotechnology to materials synthesis and processing, we are producing far fewer analytical chemists than necessary to meet the growing demands in both academia and industry. Blount stressed that excellence and innovation in the teaching of analytical chemistry are key factors in attracting students to careers in the chemical sciences, which is essential to maintaining U.S. technological competitiveness.

The rest of the symposium speakers reflected Williams's interest in bioanalytical chemistry. Isiah Warner (Emory University) described studies of cyclodextrin complexes in the presence of nonionic surfactants, Lee Limbird (Vanderbilt University) discussed receptor signaling, John Stults (Genentech) described advances in sequencing peptides and proteins using tandem mass spectrometry, and Margaret Merritt discussed nitrogen-15 labels of arginine and aspartic acid in cyanophycin granule polypeptide by GC/MS. Williams's award address described his research on the changes in chemical composition that occur when lenses of the human eye form cataracts. Differential scanning calorimetry, NMR imaging, and thermal gravimetric analysis have been used to determine the nature of both diseased and normal eye tissues.

The meeting was not devoted totally to technical topics, however. Those who attended the French exhibit "Molecules and Society" praised it as both educational and entertaining. The exhibit, obtained by the ACS with generous support from Rhône-Poulenc from the French museum Cité des Sciences et de l'Industrie, tours the past 200 years of chemistry with lasers, music, and light. The triumphs of chemistry, from the early days of alchemy to the use of science in space, demonstrate the extent to which chemistry has changed our society. The exhibit will be touring North America for the next year. If you missed it at the meeting, be sure to watch for it in your area.

Mary Warner



People who make the news, read the News.

When you're managing a chemical company these days, you need to get to the bottom of the news that affects your business. That's why executives throughout the industry read **CHEMICAL & ENGINEERING NEWS** each week.

It's the only weekly chemical magazine that covers the news from all three angles, business . . . science . . . technology. And with a full-time Washington bureau, C&EN covers the White House, Capitol Hill, the Supreme Court, and the federal regulatory agencies that affect science policy.

Read the weekly the newsmakers read.

Read **CHEMICAL & ENGINEERING NEWS**.

American Chemical Society, 1155 Sixteenth Street, NW, Washington, DC 20036, 800-227-5558

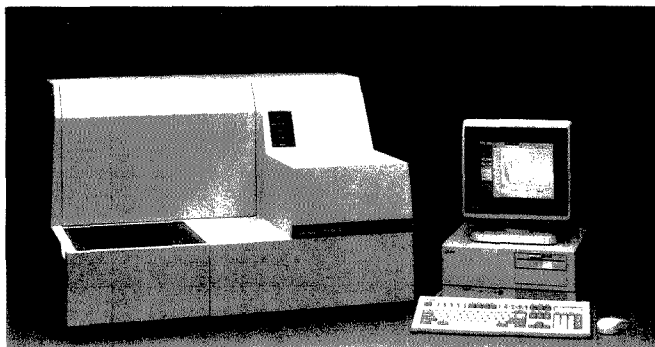
Telex: 440159 ACSP UI or 89 2582 ACSPUBS

Telecopier: 202-872-4615



*BUSINESS
SCIENCE
TECHNOLOGY*

NEW PRODUCTS



REMEDI, designed for rapid emergency drug identification, identifies unknown drugs in a 500- μ L sample of serum, plasma, or urine. The system includes a computerized library of more than 300 prescription, OTC, and illicit drugs. Bio-Rad Laboratories 401

Ozone. TG-800-KA portable ozone detector contains a dedicated electrochemical sensor that is unaffected by interfering gases. The detector operates for 30 h on battery power and features user-adjustable audio and visual alarms. CEA Instruments 406

XRF. Courier 10-Exp is an explosion-proof, on-line X-ray fluorescence analyzer that simultaneously measures up to seven elements from Si to U in a single process stream. Solutions, slurries, and powders can be analyzed. Princeton Gamma-Tech 408

Calorimeter. Quantitative reaction calorimeter, designed for analysis of thermal processes during chemical reactions, consists of a calorimeter, three syringe reagent delivery pumps, a refrigeration/heating unit, and a real-time control/data acquisition system. Columbia Scientific Industries 410

Centrifuges. L and XL Optima series ultracentrifuges feature Freon-free thermoelectric heating/cooling systems that provide operating temperatures from 0 to 40 °C. Tubes can be checked visually for balancing rotor loads. Beckman Instruments 411

Preconcentration. Trace-Con is an automated preconcentration system that interfaces to all commercial atomic and plasma spectrometers. The sys-

tem is supplied with pumps, valves, PC-compatible software, and an optional autosampler/fraction collector. Questron 412

X-ray. MPD1880/HR high-resolution X-ray diffractometer, designed for use in semiconductor applications, features five-crystal diffraction capability and a choice of goniometer configurations and sample cradles. The system's control software runs under MS-DOS. Philips Electronic Instruments 413

Spectrophotometer. Model LPS-521 spectrophotometer system allows detailed studies of the optical and electronic properties of ceramics, superconductors, semiconductors, and optical materials at temperatures from 15 to 1500 K. Features include a laser-produced plasma, laser sample heating, and cryogenic sample cooling. Acton Research Corp. 404

Software

IR. Quick IR data analysis software runs on IBM PS/2, PC/AT, and compatible computers. Data manipulation and plotting functions include quantitative analysis, library search, Kramers-Kronig transformation, and Fourier self-deconvolution. Spectra-Tech 415

Waveform editing. WavEdit is a program for reviewing and editing experimental data stored in Apple Macintosh files. The software allows users to cut, copy, and paste regions of interest to new files for display and analysis. World Precision Instruments 416

Graphs. Techni-Curve, a software package for producing publication-quality plots, includes statistics, block functions, and data transform routines. Up to six curves can be overlaid on one graph. Labtronics 417

Manufacturers' Literature

Chromatography. Brochure discusses chromatography systems and products for analysis of food and agricultural samples. A variety of applications are described. 24 pp. Waters Chromatography Division of Millipore 418

SFE. Literature describes the 3000 series analytical supercritical fluid extractors, which can be directly coupled to existing GC and SFC instruments or operated as free-standing extraction and accumulation devices. Computer Chemical Systems 419

Amino acids. Technical note lists more than 100 literature references for the analysis of PTH-amino acids by HPLC. An index to key experimental variables also is included. HPLC Technology 421

Newsletter. *Biotext*, Vol. II, No. 2, features articles on separation of very basic compounds, purification of biomolecules by affinity chromatography, and HPLC determination of penicillins. 12 pp. Supelco 422

LIMS. "CALs Connections" are technical information sheets that describe the use of CALs LIMS with various instruments in quality control and research and development laboratories. Beckman Instruments 423

For more information on listed items, circle the appropriate numbers on one of our Readers' Service Cards

Environmental analysis. Series of application notes includes information on new trends in environmental analysis, application of ICP/MS to the EPA contract lab program, and instrumentation for organic and inorganic determinations. Perkin-Elmer 420

Newsletter. *The Leeman Letter*, No. 14, includes articles on oil analysis by ICP and on assessment of routine laboratory performance in the EPA contract laboratory program. 16 pp. Leeman Labs 424

NMR. Brochure discusses the MSL multipurpose solids and liquids NMR spectrometer. Applications include high-resolution solid-state NMR, wide-line FT-NMR, high-resolution solution-state NMR, and experiments that do not require an external field. Bruker Instruments 430

Catalogs

Liquid handling. Catalog includes Eppendorf pipets, dispensers, digital burets, and microcentrifuges and related accessories. 12 pp. Brinkmann Instruments 428

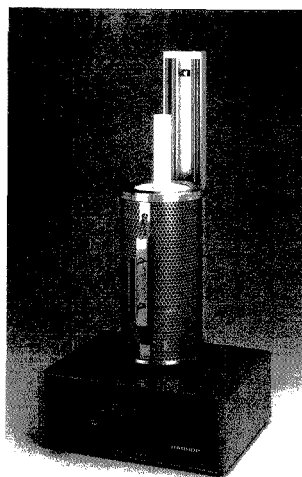
Nucleic acids. Catalog features reagents, probes, instruments, and accessories for nucleic acid analysis. Included are hybridization systems and products for parentage/forensic analysis. Oncor 425

Chromatography. Affinity chromatography catalog contains matrices and ligands for use in the isolation and purification of biologically active compounds. Sigma Chemical Co. 426

Sample management. Catalog features products for sample preparation, handling, measurement, and storage. Plasticware, cabinets, calculators, pH meters, timers, and centrifuges are included. Whatman LabSales 427

Electrophoresis. Catalog contains BDH purified reagents for electrophoresis, including gel media and components, buffer systems, dyes and stains, and calibration standards. 22 pp. Gallard-Schlesinger Industries 431

Biochemistry. Catalog includes products for sequencing nucleic acids, detection/purification and labeling systems, modifying enzymes, and nucleic acids/markers. Promega 429

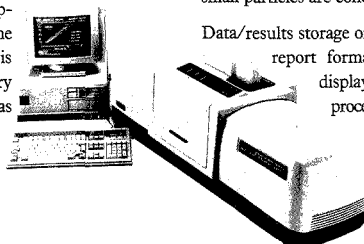


Model ST-732 Totalab thermal analysis module provides simultaneous differential thermal analysis and thermogravimetric analysis. Temperatures as high as 1200 °C can be attained. Harpor Industries 402

NO ONE UNDERSTANDS PARTICLE SIZING BETTER THAN MALVERN.

MasterSizer is the result of over 12 years' experience in laser diffraction particle sizing at Malvern.

Its wide size range, 0.1 to 600 microns, and fully automatic sample handling facilities make it ideal for on-line or laboratory applications. The Small Volume Sample Presentation Unit is a particularly useful accessory for organic media as well as for aqueous samples.



Automatic alignment and Malvern's acclaimed software make MasterSizer easy to use. And yet, whether you select the standard analysis or choose to enter the specific optical data for your sample, you get full Mie theory analysis - vital where small particles are concerned.

Data/results storage on disk and a wide range of report formats are standard. Colour display, colour plotter and 32-bit processor are among the options.

MALVERN

Malvern Instruments, Inc.,

10 Southville Road, Southborough, MA 01772.

Telephone: (508) 480 0200 Telex: 311397 Fax: (508) 460 9692

U.K. Malvern Instruments Ltd., Spring Lane South, Malvern, Worcestershire WR14 1AQ.
Telephone: (0684) 892456 Telex: 339679 MALINS G Fax: (0684) 892789

W. Germany Mutek GmbH, Arzbergerstrasse 10, D-8036 Herrsching.
Telephone: 08152 2046 Telex: 5270249 Fax: 08152 4374

CIRCLE 94 ON READER SERVICE CARD

ANALYTICAL CHEMISTRY, VOL. 61, NO. 22, NOVEMBER 15, 1989 • 1295 A

LABORATORY SERVICE CENTER

4-Acetamidobenzaldehyde • Ammonium Purpurate • Benzalacetophenone
 Benzylisothiurea HCl • Bromoethylamine HBr • 2, 3-Butanediol • Cellobiose
 N, N-Dihydroxyethylglycine & Sodium Salt • Disodium Malonate • Esculin
 Ethanesulfonic Acid • Ethyl Lactate • N-(p-Hydroxyphenyl) glycine
 Malonic Acid • Melibiose • Methyl-n-Amyl Ketone • Methyl Butyrate
 p-Naphtholbenzein • 1-Nitroso-2-Naphthol • Phenylthiourea • Phenylurea
 Rhamnose • Succinic Acid • Tetrahydrofurfuryl Acetate • Thioacetamide
 Thiobarbituric Acid • Trimethylene Glycol • Veratraldehyde • Xylose

Write for our Products List of over 3,000 chemicals

Tel: 516-273-0900 • TOLL FREE: 800-645-5566 Telefax: 516-273-0858 • Telex: 497-4275

EASTERN CHEMICAL

A Division of UNITED-GUARDIAN, INC.

P. O. Box 2500

DEPT. AC

SMITHTOWN, N. Y. 11787

Laboratory Service Center (Equipment, Materials, Services, Instruments for Leasing), Maximum space — 4 inches per advertisement. Column width, 2-3/16"; two column width, 4-9/16". Artwork accepted. No combination of directory rates with ROP advertising. Rates based on number of inches used within 12 months from first date of first insertion. Per inch: 1" — \$155; 12" — \$153; 24" — \$150; 36" — \$145; 48" — \$140.

CALL OR WRITE JANE GATENBY

ANALYTICAL CHEMISTRY

500 Post Road East

P.O. Box 231

Westport, CT 06880

203-226-7131/FAX: 203-454-9939

NMR ANALYSIS

MULTINUCLEAR LIQUID or
 MULTIFIELD SOLID STATE
 SPECTRAL DATA SERVICES, INC.
 818 Pioneer
 Champaign, IL 61820
 (217) 352-7084

HELP WANTED ADS

ROP display at ROP rates. Rate based on number of insertions within contract year. Cannot be combined for frequency.

Unit	1-TI	6-TI	12-TI
1" (25 mm)	\$180	\$180	\$150
	24-TI	48-TI	72-TI
	\$140	\$130	\$125

CALL OR WRITE JANE GATENBY

ANALYTICAL CHEMISTRY

500 Post Road East

P.O. Box 231

Westport, CT 06880

203-226-7131

FAX: 203-454-9939

Must reading for any professional in any major chemistry field...

JOURNAL OF THE AMERICAN CHEMICAL SOCIETY

The most frequently cited chemical publication throughout the world, this biweekly journal delivers:

- original research articles that cover every key area in the field of chemistry
- up-to-the-minute communications
- authoritative information with direct application to your own work
- a subscription value unmatched by "competitive" journals!

EDITOR: Allen J. Bard, University of Texas

1989 Rates	ACS Members**		Nonmember 1 Year
	1 Year	2 Years	
US	\$75	\$135	\$499
Canada & Mexico	\$123	\$231	\$547
Europe*	\$179	\$343	\$603
All other countries*	\$249	\$483	\$673

*Air service included

**Member rates are for personal use only

Order your own subscription to the number one chemical journal today!

Call Toll Free 1-800-227-5558

Telex: 440159 ACSPUI or 892582 ACSPUB

Cable Address: JEICHEM

For more information or to subscribe:

American Chemical Society

Marketing Communications Department

1155 Sixteenth Street N.W.

Washington D.C. 20036

INDEX TO ADVERTISERS IN THIS ISSUE

CIRCLE INQUIRY NO.	ADVERTISERS	PAGE NO.	CIRCLE INQUIRY NO.	ADVERTISERS	PAGE NO.
2	*A&D Engineering, Inc.	1256A	156	*Thermo Jarrell Ash Corporation Noon, Inc.	1245A
18	*Beckman Instruments, Inc.	1284A	170	*Varian Lang Associates	1254A
28, 29	*Conostan Division/Conoco Specialty Products Robert Lamons & Associates	1261A, 1269A	<i>Directory section, see page 1296A.</i>		
26	Corporation Scientifique Classe, Inc.	1274A	<i>* See ad in ACS Laboratory Guide.</i>		
32	Delal/Nermag Instruments	1246A	<i>** Company so marked has advertisement in Foreign Regional edition only.</i>		
60	*Galileo Electro-Optics Corp. Legasse Associates Advertising, Inc.	1276A	<i>Advertising Management for the American Chemical Society Publications</i>		
58	Geiman Sciences	1251A	CENTCOM, LTD		
65, 66	*Hewlett-Packard Company Brooks Communications	1267A, OBC	<i>President</i>		
63	*Hitachi Instruments, Inc.	1265A	Thomas N. J. Koerwer		
70-76	*Instruments SA, Inc./J-Y Division Kathy Wyatt & Associates	1249A	<i>Executive Vice President Senior Vice President</i>		
80	J & W Scientific	1290A	James A. Byrne Benjamin W. Jones		
94	*Malvern Instruments, Inc.	1295A	<i>Clay S. Holden, Vice President</i>		
100-107	*Matheson Gas Products Kenyon Hoag Associates	1253A	Robert L. Voepel, Vice President		
98	*Merck Sharp & Dohme Isotopes BGH Advertising Associates, Inc.	1280A	Joseph P. Stenza, Production Director		
96	*Metrohm Ltd. Ecknauer + Schoch Werbeagentur ASW	1270A	500 Post Road East P.O. Box 231 Westport, Connecticut 06880 (Area Code 203) 226-7131 Telex No.643310 FAX: 203-454-9939		
120	*Ovonc Synthetic Materials Company, Inc. Ross & Associates	1283A	ADVERTISING SALES MANAGER		
125	*Phillips Scientific/Analytical Division Connors Publicity Ltd.	1286B	Bruce E. Poorman		
127	Precision Scientific Winterkorn Lillis, Inc.	IFC	ADVERTISING PRODUCTION MANAGER		
138	Radiometer Analytical A/S	1289A	<i>Jane F. Gatenby</i>		

CENTCOM, LTD

President

Thomas N. J. Koerwer

Executive Vice President Senior Vice President

James A. Byrne Benjamin W. Jones

Clay S. Holden, Vice President

Robert L. Voepel, Vice President

Joseph P. Stenza, Production Director

500 Post Road East
P.O. Box 231
Westport, Connecticut 06880
(Area Code 203) 226-7131
Telex No.643310
FAX: 203-454-9939

ADVERTISING SALES MANAGER
Bruce E. Poorman

ADVERTISING PRODUCTION MANAGER
Jane F. Gatenby

SALES REPRESENTATIVES

Philadelphia, PA . . . Patricia O'Donnell, CENTCOM, LTD., GSB Building, Suite 405, 1 Belmont Avenue, Bala Cynwyd, Pa. 19004. Telephone: 215-667-9666, FAX: 215-667-9353

New York, NY . . . John F. Rafferty, CENTCOM, LTD., 60 East 42nd St., New York, N.Y. 10165. Telephone: 212-972-9660

Westport, CT . . . Edward M. Black, CENTCOM, LTD., 500 Post Road East, P.O. Box 231, Westport, Ct. 06880. Telephone: 203-226-7131, Telex 6433 10, FAX: 203-454-9939

Cleveland, OH . . . Bruce E. Poorman, John C. Guyot, CENTCOM, LTD., 325 Front St., Suite 2, Berea, Ohio 44017. Telephone: 216-234-1333, FAX: 216-234-3425

Chicago, IL . . . Michael J. Pak, CENTCOM, LTD., 540 Frontage Rd., Northfield, Ill. 60093. Telephone: 708-441-6383, FAX: 708-441-6382

Houston, TX . . . Michael J. Pak, CENTCOM, LTD. Telephone: 708-441-6383

San Francisco, CA . . . Paul M. Butts, CENTCOM, LTD., Suite 1070, 2672 Bayshore Frontage Road, Mountain View, CA 94043. Telephone: 415-969-4604

Los Angeles, CA . . . Clay S. Holden, CENTCOM, LTD., Newton Pacific Center, 3142 Pacific Coast Highway, Suite 200, Torrance, CA 90505. Telephone: 213-325-1903

Boston, MA . . . Edward M. Black, CENTCOM, LTD. Telephone: 203-226-7131

Atlanta, GA . . . John F. Rafferty, CENTCOM, LTD. Telephone: 212-972-9660

Denver, CO . . . Paul M. Butts, CENTCOM, LTD. Telephone: 415-969-4604

United Kingdom

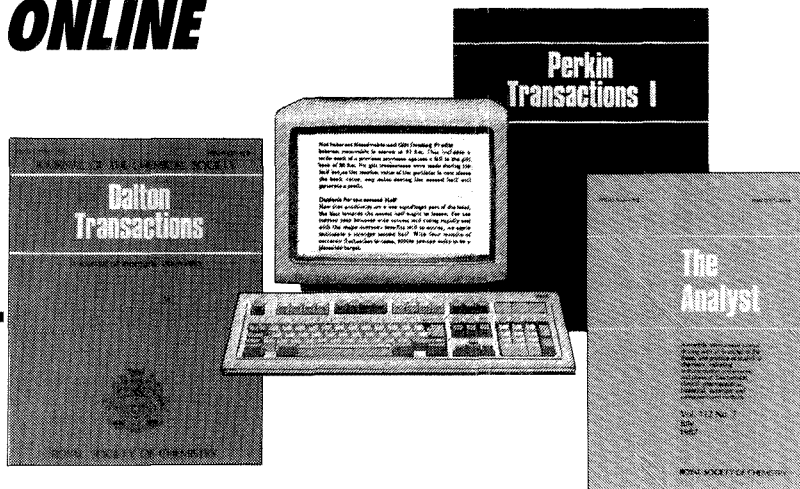
Reading, England . . . Malcolm Thiele, Technomedia Ltd., Wood Cottage, Shurlock Row, Reading RG10 0QE, Berkshire, England. Telephone: 073-434-3302, Telex #848800, FAX: 073-434-3848

Lancashire, England . . . Technomedia Ltd., c/o Meconomics Ltd., Meconomics House, 31 Old Street, Ashton Under Lyne, Lancashire, England. Telephone: 061-308-3025

Continental Europe . . . Andre Jamar, International Communications, Inc., Rue Maltat 1, 4800 Verviers, Belgium. Telephone: (087) 22-53-85, FAX: (087) 23-03-29

Tokyo, Japan . . . Sumio Oka, International Media Representatives Ltd., 2-29 Toranomon, 1-Chome Minato-ku Tokyo 105 Japan. Telephone: 502-0656, Telex #22633, FAX: 591-2530

NOW YOU CAN SEARCH RSC JOURNALS ONLINE



The main primary journals published by the Royal Society of Chemistry (RSC) are now searchable online via **CHEMICAL JOURNALS ONLINE (CJO)** – a family of new online files produced by the American Chemical Society and available through STN International.

The RSC journals file (**CJRSC**) includes Chemical Communications, Dalton Transactions, Faraday Transactions (**I*** & **II**), Perkin Transactions (**I** & **II**), The Analyst, Journal of Chemical Research,* Journal of Analytical Atomic Spectrometry, Faraday Discussions.

*Available from 1988

CJRSC may be searched alone or in conjunction with other components of the **CJO** database which includes ACS journals and polymer journals published by Wiley.

The unique Crossover facility from STN enables you to perform the same search on **CJRSC** and **CAS ONLINE** thereby combining the breadth of coverage of Chemical Abstracts with the depth of coverage of RSC journals.

Online access to the RSC journals provides you with a convenient, rapid and economical means of keeping up with the latest significant research in the chemical sciences.

For more information, call (614) 421-3600, or return the form below to: STN International, c/o Chemical Abstracts Service, 2540 Olentangy River Road, P.O. Box 02228, Columbus, OH 43210.

Please send me more information on **CJRSC** and the Chemical Journals Online data base.

Name

Address

.....

.....

**CHEMICAL JOURNALS
ONLINE**

EDITOR: GEORGE H. MORRISON

ASSOCIATE EDITORS: Klaus Biemann,
Georges Gulochon, Walter C. Herlihy,
Robert A. Osteryoung, Edward S. Yeung

Editorial Headquarters

1155 Sixteenth St., N.W.
Washington, DC 20036
Phone: 202-872-4570
Telefax: 202-872-6325

Managing Editor: Sharon G. Boots

Associate Editors: Louise Voress,
Mary Warner

Assistant Editors: Grace K. Lee,
Alan R. Newman

Editorial Assistant: Felicia Wach

Director, Operational Support: C. Michael
Phillippe

Production Manager: Leroy L. Corcoran

Art Director: Alan Kahan

Designer: Amy Meyer Phifer

Production Editor: Elizabeth E. Wood

Circulation: Claud Robinson

Editorial Assistant, LabGuide: Joanne Mullican

Journals Dept., Columbus, Ohio

Associate Head: Marianne Brogan

Journals Editing Manager: Joseph E. Yurvati

Associate Editor: Rodney L. Temos

Staff Editor: Sharon K. Hatfield

Advisory Board: Bernard J. Bulkin, Michael S.
Epstein, Renaat Gijbels, Peter R. Griffiths,
Thomas L. Isenhour, Nobuhiko Ishibashi,
James W. Jorgenson, Peter C. Jurs, Mary A.
Kaiser, David L. Nelson, Lawrence A. Pachla,
Ralph E. Sturgeon, George S. Wilson, Mary J.
Wirth, Andrew T. Zander, Richard N. Zare
Ex Officio: Sam P. Perone

Instrumentation Advisory Panel: James B.
Callis, Bruce Chase, R. Graham Cooks, L. J.
Cline Love, Sanford P. Markey, Ronald E. Ma-
jors, Linda B. McGown, Gary W. Small, R. Mark
Wightman

Published by the
AMERICAN CHEMICAL SOCIETY
1155 16th Street, N.W.
Washington, DC 20036

Publications Division

Director: Robert H. Marks

Journals: Charles R. Bertsch

Special Publications: Randall E. Wedin

Manuscript requirements are published in the
January 1, 1989 issue, page 91. Manuscripts
for publication (4 copies) should be submitted
to ANALYTICAL CHEMISTRY at the ACS Washing-
ton address.

The American Chemical Society and its editors
assume no responsibility for the statements
and opinions advanced by contributors. Views
expressed in the editorials are those of the
editors and do not necessarily represent the
official position of the American Chemical
Society.

Amankwa, L., 2562

Bialkowski, S. E., 2479, 2483
Bindra, D. S., 2566

Cantwell, F. F., 2562
Capar, S. G., 2589
Castles, M. A., 2534
Castro, M. E., 2528
Clifford, R. H., 2589
Cody, R. B., 2511
Crouch, S. R., 2475

Danielson, N. D., 2585
Deterding, L. J., 2504
Dill, K. A., 2540
Dorsey, J. G., 2540
Dose, E. V., 2571

Fales, H. M., 2500
Fitzpatrick, C. P., 2551

Grimsrud, E. P., 2523
Guiochon, G., 2571

Hanson, C. D., 2528
Hercules, D. M., 2516

Ishii, I., 2589

Jackson, W. A., 2466
Johnson, D. C., 2466
Jorgenson, J. W., 2504
Jurs, P. C., 2489

Kerley, E. L., 2528
Kim, H., 2475
Kubis, A. J., 2516

LaCourse, W. R., 2466
Lacy, M. J., 2584

Maciel, G. E., 2579

Markey, S. P., 2582
Mason, R. T., 2500
Matsunaga, T., 2471
Montaser, A., 2589
Moore, B. L., 2534
Moseley, M. A., 2504

Nakamura, N., 2471

Pang, H.-m., 2546
Pannell, L. K., 2500
Pardue, H. L., 2551
Pu, Q.-L., 2500

Ranc, M. L., 2489
Robbins, G. A., 2584
Roe, V. D., 2584
Russell, D. H., 2528

Sears, L. J., 2523
Sharkey, A. G., 2516
Shigematsu, A., 2471
Shih, M.-c., 2582
Sinex, S. A., 2589
Slaby, J., 2496
Somayajula, K. V., 2516
Stephenson, J. L., 2500
Stuart, J. D., 2584

Targove, M. A., 2585
Tomer, K. B., 2504

Wang, T.-C. L., 2582
Wangsa, J., 2585
Ward, S. R., 2534
Wilson, G. S., 2566

Yeung, E. S., 2546, 2557
Ying, P. T., 2540

Zabik, M. J., 2475
Zhang, M., 2579
Zhu, J., 2557

Pulsed Amperometric Detection of Alkanolamines following Ion Pair Chromatography

William R. LaCourse,* Warren A. Jackson, and Dennis C. Johnson

Department of Chemistry, Iowa State University, Ames, Iowa 50011

The quantitative determination of alkanolamines is not always simple due to the lack of an inherent chromophore or fluorophore. In addition, separation by gas chromatography or liquid chromatography is difficult due to the high polarity of these compounds. Ion pair chromatography was demonstrated for the separation of mono-, di-, and trialkanolamines using a C-18 reversed-phase column with a mobile phase consisting of an aqueous/acetonitrile/dodecanesulfonate salt mixture. On-line pulsed amperometric detection (PAD) of the alkanolamines at a Au electrode followed postcolumn addition of an alkaline buffer to the column effluent. PAD utilized a three-step potential waveform that combined amperometric detection with alternating anodic and cathodic polarizations to maintain electrode activity.

INTRODUCTION

With the present and ever-increasing concern related to the levels and fates of environmental pollutants, electrochemical detection with liquid chromatography has gained prominence as a useful analytical technique (1). This popularity can be attributed to the efficient separations achieved by contemporary chromatography and the tunable selectivity and low detection limits of electrochemical determinations.

A major shortcoming of amperometric detection at noble metal electrodes for a constant (direct current (dc)) applied potential has been the loss of activity during anodic detections of organic compounds resulting from adsorption of carbonaceous products of the ensuing reactions (e.g., radicals). Pulsed amperometric detection (PAD) based on a multistep waveform ($E-t$) overcomes the problem of lost activity on noble metal electrodes by alternating amperometric detection with anodic and cathodic polarizations to clean and reactivate the electrode surface. PAD efficiently exploits the catalytic activity of the clean electrode surface oxide to oxidize aliphatic molecules, which typically do not have strong chromophores. Liquid chromatography with PAD has been shown to be a simple, selective, and sensitive method for the determination of alcohols, polyalcohols, carbohydrates (2), amino acids (3), and many inorganic and organic sulfur-containing compounds (4).

The determination of alkanolamines is currently of great interest, as these compounds are used widely in chemical and pharmaceutical industries. Alkanolamines are needed for the production of emulsifying agents, corrosion inhibitors, laundry materials, dyes, medicines and for purifying gases (5). In addition, environmental concerns, raw material shortages, and rising energy costs are behind the push to remove hydrocarbon-based solvents from coating systems. Water is now becoming the major solvent of choice; and in the switch from organic solvents to water, alkanolamines are making valuable contributions.

The quantitative determination of alkanolamines is not always simple due to the lack of an inherent chromophore, fluorophore, or dc-active electrophore. Furthermore, chromatographic separations are difficult due to the high polarity of these compounds (6). In liquid chromatography, the effect of the amine functionality on silica-based reversed-phase columns can manifest itself in significant tailing of the

chromatographic peak. Derivatization with nitroaromatic moieties is often used to improve both the chromatographic behavior and detection properties of alkanolamines (7). Ion pair chromatography followed by postcolumn addition of alkaline buffer with pulsed amperometric detection is ideally suited to the efficient separation and detection of alkanolamines. Determinations of alkanolamines in "real-world" sample matrices are simple, direct, and sensitive.

Described here are the development, optimization, and application of LC with PAD for the determination of alkanolamines. The mechanism of detection is discussed to emphasize the basic tenets of PAD. Also, the compatibility of ion pair chromatography with PAD is stressed.

EXPERIMENTAL SECTION

Apparatus and Procedures. Voltammetric data were obtained at a Au rotated disk electrode (RDE) (Pine Instrument Co., Grove City, PA) with a computer-aided electroanalysis system (Cypress Systems, Lawrence, KS) or a Model RDE4 potentiostat (Pine).

Liquid chromatographic work employed an isocratic/gradient chromatography system (Dionex Corp., Sunnyvale, CA). Alkaline buffer, pumped by a Rabbit-HP solvent delivery pump (Rainin Instrument Co., Woburn, MA), was added to the column effluent through a tee connector followed by a woven Teflon mixing coil. Separations were performed with a C-18 μ Bondapak column (Waters Chromatography Division, Millipore Corp., Milford, MA) or a Hamilton PRP-1 column (Phenomenex, Rancho Verdes, CA). Mobile phases were filtered through a 0.45- μ m Nylon 66 filter (Rainin) with the use of a solvent filtration kit (Waters).

PAD was performed with either a Model UEM or a Model PAD-2 detector (Dionex). Two electrochemical cell configurations were used interchangeably. A homemade cell consisted of a Au-wire working electrode, a Pt counter electrode, and a saturated calomel reference electrode (SCE). A thin-layer electrochemical cell (Dionex) consisted of a planar Au working electrode, a glassy carbon counter electrode, and a SCE.

Reagents. All solutions were prepared from reagent grade chemicals as received. Mobile phase solvents were from Fisher Scientific Co. Water was purified in a Millipore Milli-Q system or a Barnstead Nanopure II system, followed by filtration (0.2 μ m).

RESULTS AND DISCUSSION

Voltammetry. The current-potential ($I-E$) response is shown in Figure 1 for a Au RDE in 10% acetonitrile/90% water, containing 0.1 M NaOH with 1 mM sodium dodecanesulfonate, with (—) and without (---) ethanolamine. The residual response for the supporting electrolyte (---) exhibits anodic waves on the positive potential scan in the regions +0.2 to +0.9 V (A) for oxide formation and $E > 0.8$ V (B) for O_2 evolution, and a cathodic peak on the negative scan in the region +0.2 to -0.2 V (C) for dissolution of the oxide formed on the positive scan. Cathodic reduction of dissolved O_2 is observed in the region -0.2 to -1.0 V (D) for both the positive and negative scans. For the presence of ethanolamine (—), an anodic wave is observed on the positive scan in the region of ca. -0.2 to +0.3 V (E), where alcohols are observed to be oxidized, and in the region ca. +0.3 to +0.7 V (F) for oxidation of adsorbed amine simultaneously with the formation of surface oxide on the Au electrode (A). The absence of any anodic signal on the negative scan in the region +1.0 to +0.2

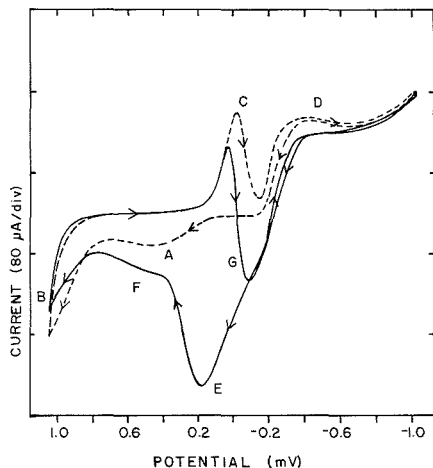


Figure 1. Voltammetric response (I - E) for ethanolamine at a Au rotating disk electrode. Conditions: 10% acetonitrile/0.1 M NaOH/1 mM sodium dodecanesulfonate, nondegassed, 1000 revolutions min^{-1} rotation speed, 100 mV s^{-1} scan rate. Sample concentration: (---) 0 mM ethanolamine, (—) 16 mM ethanolamine.

It is clear evidence of the absence of any reactivity of the oxide-covered surface for ethanolamine oxidation. When the oxide is cathodically dissolved on the negative scan to produce peak C, the surface reactivity for ethanolamine oxidation is immediately returned and an anodic peak G is observed for the alcohol functionality of ethanolamine. Anodic waves E, F, and G all were observed to be increased in height with increases in the ethanolamine concentration.

The net anodic current in wave E for detection of the alcohol functionality of ethanolamine increased markedly with increases in electrode rotation speed, yet exhibited negligible change with variations in the potential scan rate. These observations are consistent with the conclusion that the mechanism producing wave E for the adsorbed amine functionality of the ethanolamine is under mass-transport control. In contrast, wave F increased with increases in the potential scan rate, yet showed very little change as a result of variations in electrode rotation speed. These observations are consistent with the conclusion that the anodic reaction for wave F is under the control of an electrode surface process. This is consistent with the proposed mechanism of an oxide-catalyzed oxidation of the adsorbed amine. The rates of the various anodic processes producing waves E, F, and G all increased with increasing pH, and pH > ca. 11 was concluded to be optimum for analytical applications.

Figure 2 shows the voltammetric responses for the pure mobile phase (---) as well as for separate solutions of mobile phase containing ethanol (---), ethylamine (...), and ethanolamine (—). Waves E, F, and G for ethanolamine (—) are the same as discussed for Figure 1. Ethanol present in the mobile phase (---) does not exhibit an anodic response in this media, even though alcohols are known to be detected anodically in the region of wave E in pure 0.1 M NaOH. This observation is concluded to be the result of an interference by acetonitrile (ACN) with the detection mechanism for the alcohol. ACN is strongly adsorbed at Au electrodes, and the adsorbed ACN is concluded to block surface sites required for a preadsorption step in the anodic detection of the alcohol. In comparison, the amine functionality of ethylamine (...) is strongly adsorbed at the Au surface and exhibits an oxide-catalyzed wave on the positive scan in the region corresponding to wave F for eth-

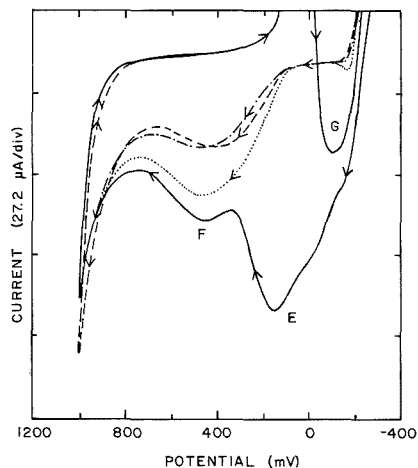


Figure 2. Voltammetric response (I - E) for ethanol, ethylamine, and ethanolamine at a Au rotating disk electrode. Conditions: 10% acetonitrile/0.1 M NaOH/1 mM sodium dodecanesulfonate, nondegassed, 1000 revolutions min^{-1} rotation speed, 100 mV s^{-1} scan rate. Solutions: (---) supporting electrolyte only, (---) 16 mM ethanol, (...) 16 mM ethylamine, (—) 16 mM ethanolamine.

anolamine (—). At extremely high concentrations of ethanol (i.e., > ca. 1 M), anodic waves were observed in the potential region corresponding to waves E and G of ethanolamine, confirming the conclusion that these waves for ethanolamine are the result of oxidative detection of the alcohol functionality.

The presence of an anodic response for the alcohol functionality of ethanolamine (wave E), whereas no response was observed for ethanol, is concluded to be a beneficial consequence of the adsorption of the amine functionality of the ethanolamine, which occurs even in the presence of ACN on the oxide-free Au surface (i.e., $E < \text{ca. } 0.0 \text{ V}$). The fact that wave E for ethanolamine is under virtual mass-transport rather than surface control is consistent with the conclusion that the adsorption of amine groups is reversible, and following oxidation of the n -alcohol group to a carboxylate, rapid desorption of the ionic aminocarboxylate occurs. Since surface oxide is not formed on the positive scan in the region of wave E, unreacted ethanolamine is adsorbed following desorption of the carboxylate product to support the continuous flow of anodic current.

The oxidation of adsorbed amine requires the simultaneous formation of electrocatalytic surface oxide, and therefore, the anodic process (wave F) exhibits the characteristics of a surface-controlled reaction. The maximum anodic response for wave F for a given ethanolamine concentration is expected to be limited by the adsorption isotherm, *vide infra*, for the particular alkanolamine being detected. The fully developed oxide-covered surface exhibits insignificant catalytic reactivity, and detection of the amine group of ethanolamine at Au electrodes is only possible via a transient electrocatalytic mechanism achieved within a pulsed potential waveform. All other alkanolamines display voltammetric behavior similar to that of ethanolamine. At $E > \text{ca. } +0.7 \text{ V}$ on the positive scan, the anodic response of the amine is rapidly attenuated due to the unreactivity of the fully developed surface oxide. On the subsequent negative scan, the formation of surface oxide ceases with the result of a zero value of electrode current. The surface oxide is cathodically dissolved in the region ca. $+0.2$ to -0.2 V (wave C in Figure 1) with the result that fresh

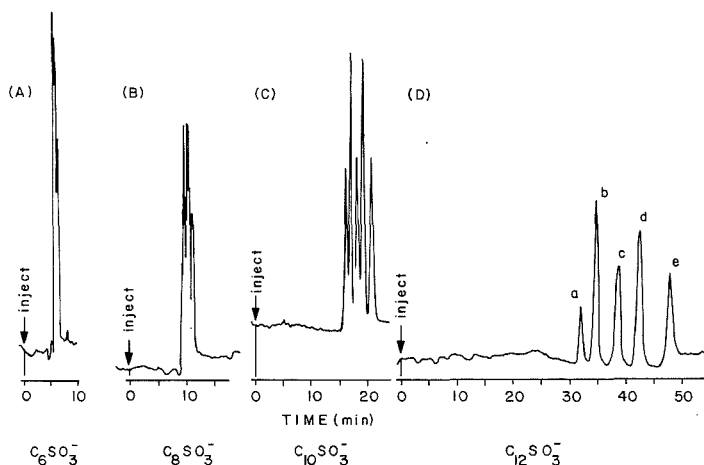


Figure 3. Effect of ion pair alkyl chain length on alkanolamine separation. Mobile phase: 20% acetonitrile/2 mM paired ion reagent at 0.75 mL/min. Paired ion reagent: (A) sodium hexanesulfonate, (B) sodium octanesulfonate, (C) sodium decanesulfonate, (D) sodium dodecenesulfonate. Other conditions: postcolumn reagent, 0.2 M NaOH at 0.25 mL/min; column, Waters 10- μ m, C-18 μ Bondapak; waveform, Table I; injection volume, 200 μ L. Samples (10 ppm): (a) 2-amino-1-ethanol, (b) 4-amino-1-butanol, (c) 5-amino-1-pentanol, (d) 2-amino-1-butanol, (e) 6-amino-1-hexanol.

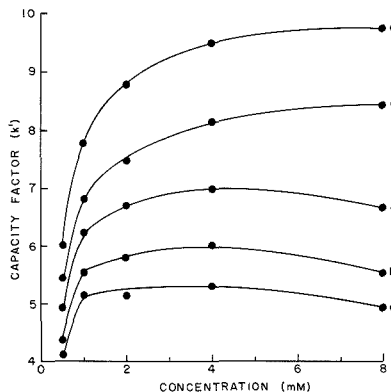


Figure 4. Effect of paired ion reagent concentration on k' . Conditions were the same as in Figure 3, except that the mobile phase was 20% acetonitrile/2 mM sodium dodecenesulfonate.

ethanolamine is adsorbed with concurrent oxidation of the alcohol functionality. The oxidation products of the *n*-alcohol and amine groups are tentatively concluded to be the corresponding carboxylate (8) and hydroxylamine (9); however, proof must await further research.

Liquid Chromatography. Alkanolamines are ideal candidates for ion pair separation on reversed-phase columns. Alkanesulfonate salts are effective ion pairing reagents, are PAD inactive, and can be obtained easily with variable alkyl chain lengths. Figure 3 illustrates the effect of changing the carbon number of the ion pairing reagent on the separation of five alkanolamines. Base-line resolution was achieved with dodecenesulfonate anion as the ion pairing reagent. The optimum ion pairing reagent concentration was found to be ca. 2 mM from the plots of capacity factor versus reagent concentration shown in Figure 4. At this concentration, resolution was achieved without excessive retention times. As expected, the capacity factor (k') was determined to decrease as the concentration of organic modifier (ACN) in the mobile phase was increased. Retention of the alkanolamines also

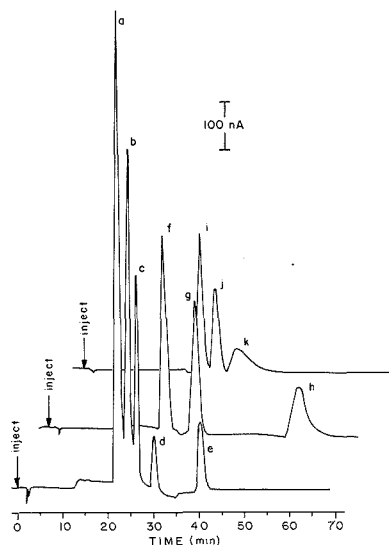


Figure 5. Results of the separation of several alkanolamines with pulsed amperometric detection (PAD). Conditions were the same as Figure 3, except that the mobile phase was 20% acetonitrile/2 mM sodium dodecenesulfonate. Samples (25 ppm): (a) 2-amino-1-ethanol, (b) 3-amino-1-propanol, (c) 4-amino-1-butanol, (d) 5-amino-1-pentanol, (e) 6-amino-1-hexanol, (f) 2-amino-1-propanol, (g) 2-amino-1-butanol, (h) 2-amino-1-pentanol, (i) 1-amino-2-propanol, (j) 2-amino-2-methyl-1-propanol, (k) 2-amino-1-phenylethanol.

decreased with an increase in pH >5, due to deprotonation of the amine functionality, which results in less ion pair formation, and the effect of an additional ionic strength of the mobile phase. At higher pH values, equilibration time of the chromatographic column appeared to be increased. The separation of five alkanolamines was achieved with a mobile phase of 20% acetonitrile/2 mM sodium dodecenesulfonate.

The LC-PAD separation of linear, branched, and complex alkanolamines is shown in Figure 5 to illustrate the range and

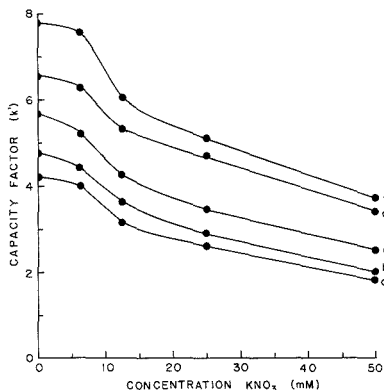


Figure 6. Effect of NaNO_3 concentration on k' . Conditions: mobile phase, 20% acetonitrile/2 mM paired ion reagent/ NaNO_3 at 0.75 mL/min flow rate; waveform, Table I; injection volume, 200 μL . Sample (ca. 10 ppm): (a) 2-amino-1-ethanol, (b) 4-amino-1-butanol, (c) 5-amino-1-pentanol, (d) 2-amino-1-butanol, (e) 6-amino-1-hexanol.

applicability of ion pairing chromatography with pulsed amperometric detection of alkanolamines. Monoethanolamine and triethanolamine were well resolved with capacity factors of ca. 14 and 15, respectively. Diethanolamine coeluted with ethanolamine under these experimental conditions. No further attempt was made to optimize the resolution of the substituted alkanolamines.

The optimized chromatographic conditions were developed for the $\mu\text{Bondapak C-18}$ column. In general, the PRP-1 column required less ion pairing reagent and less organic modifier to achieve comparable peak resolutions, in comparison to the silica-based C-18 column. The ion pairing technique was compatible with both silica and polymeric supported C-18 stationary phases.

As we observed for the organic modifier, the capacity factor (k') decreased as the concentration of electrolyte (KNO_3 or NaNO_3) was increased in the mobile phase, as is shown in Figure 6. From Figure 6, it is noted that the early-eluting compounds were affected less than the late-eluting compounds by the added electrolyte. Gradient elution by addition of NaNO_3 was performed on the Hamilton PRP-1 column. The k' values for the late-eluting compounds were reduced significantly, e.g., from ca. 50 to 20 for 2-amino-1-pentanol, whereas the resolution between all compounds was maintained, as shown in Figure 7.

To obtain reproducible results when NaNO_3 gradient elution was employed, it was found necessary to equilibrate the column with the weak solvent for at least 1 h between injections. The capacity factor (k') for each of the alkanolamines was within $\pm 2\%$ relative standard deviation (RSD ($n = 3$)) under the proposed conditions.

Sodium hydroxide (0.2 M) was added postcolumn at a ratio of 1:3 (i.e., 0.25 mL/min/0.75 mL/min). The NaOH provided the appropriate pH >11 and necessary ionic strength for efficient electrochemical detection. The necessity of high pH is attributed to the need to deprotonate the amine functionality to accommodate its adsorption on the electrode surface.

Liquid Chromatography with Pulsed Amperometric Detection. Table I describes the optimized triple-step waveform for the pulsed amperometric detection of ethanolamine. Upon stepping to the detection potential (E_1), the anodic signal was integrated for 16.7 ms after a delay of 280 ms. Since the electrode activity is diminished due to inhibition by the fully developing surface oxide and by fouling of the surface by adsorbed oxidation products, electrode activity was

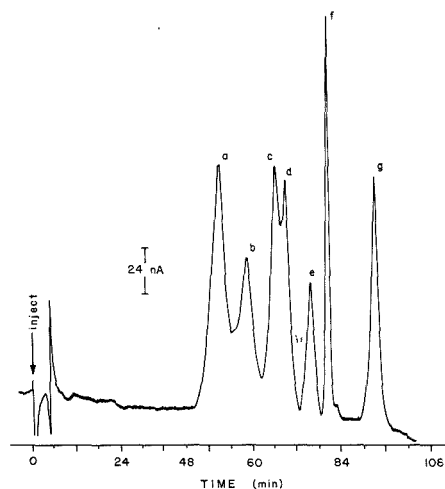
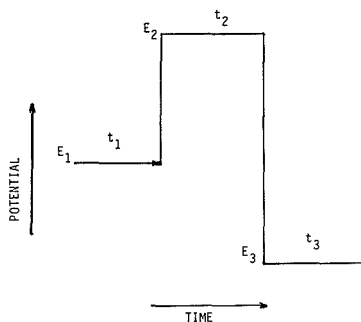


Figure 7. Gradient separation of several alkanolamines. Mobile phase: solvent 1, 0.75 mM dodecane sulfonate/15% ACN; solvent 2, 0.75 mM dodecane sulfonate/15% ACN/10 mM NaNO_3 . Program: 0–50 min, 100% solvent 1 and 0% solvent 2; 50–70 min, ramp to 10% of solvent 2; 70–71 min, ramp to 100% of solvent 2 and hold. Other conditions: flow rate, 0.5 mL/min; postcolumn, 0.3 M NaOH at 0.5 mL/min; column, PRP-1 C-18; waveform, Table I. Injection volume, 200 μL . Sample: (a) 2-amino-1-ethanol, 3 ppm; (b) 4-amino-1-butanol, 4 ppm; (c) 5-amino-1-pentanol, 4 ppm; (d) 2-amino-1-butanol, 3 ppm; (e) 6-amino-1-hexanol, 2 ppm; (f) 2-amino-1-pentanol, 2 ppm; (g) 2-amino-1-hexanol, 4 ppm.

Table I. Waveform Specifications for Pulsed Amperometric Detection



potential, mV vs SCE	time, ms	function
E_1 , 200	t_1 , 300	detection
	t_2 , 280	delay
	t_3 , 16.7	current sampling
E_2 , 1000	t_2 , 400	oxidative cleaning
E_3 , -400	t_3 , 350	reductive reactivation and adsorption of analyte

renewed by subsequent positive and negative potential steps to achieve anodic (E_2) and cathodic (E_3) polarizations, respectively. During the application of E_3 , adsorption of analyte can occur on the oxide-free surface prior to the next detection step. Figure 8 shows the anodic response of ethanolamine as a function of the duration of the third step (t_3) in the waveform, while the other parameters of the waveform are kept the same as given in Table I. Clearly, the response increased

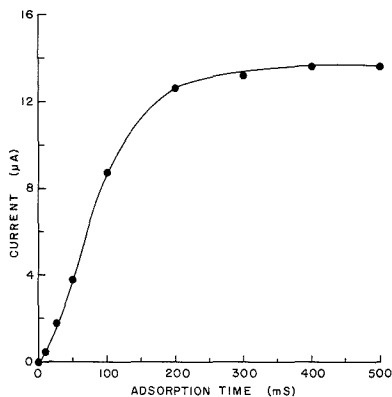


Figure 8. Response for pulsed amperometric detection of ethanolamine at a Au electrode with variation of adsorption time (t_3) in the PAD waveform. Conditions were the same as in Figure 5, except that t_3 in Table I was varied from 0 to 500 ms.

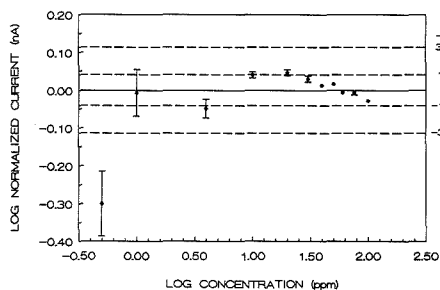


Figure 9. Normalized calibration curve for ethanolamine. Each dot represents the average of six determinations. Dots without error bars have average deviations less than the size of the dot. Δ represents percent deviation from linear fit of data determined by linear regression analysis (17).

for increased time allowed for analyte adsorption and became constant for $t_3 > \text{ca. } 200 \text{ ms}$. In a separate experiment, the $i-t$ curve was recorded, and it was determined that complete reduction (>90%) of the surface oxide at $E_3 = -0.4 \text{ V}$ required approximately 180 ms. Hence, the data in Figure 8 are concluded to indicate for this concentration of ethanolamine (22 ppm) that the rate of analyte adsorption was controlled by the rate of oxide dissolution rather than analyte flux. Furthermore, the value 200 ms is recommended as the lower limit for t_3 . These results are also consistent with the conclusion that preadsorption of the ethanolamine on the oxide-free surface is required for detection of the alcohol functionality in the presence of ACN.

Statistical analysis of calibration data was based on a modified regression analysis which assumed that variance in the signal is proportional to concentration (10). PAD response was concluded to be linear for 1–100 ppm, as is indicated in Figure 9. This style of presentation of calibration data has been presented previously (11). The limit of detection was determined to be 40 ppb (200 μL , 8 ng) for a signal-to-noise ratio of 3. Peak skew and repeatability were $1.1 \pm 9.4\%$ RSD ($n = 3$) and $\pm 3.2\%$ RSD ($n = 6$, 0.083 mM ethanolamine), respectively. Synthetic water samples spiked with ethanolamine were assayed in a single-blind study in order to further validate the LC-PAD methodology. The recovery of spiked ethanolamine was found to be 93–102% for concentrations of 0.16–7.92 ppm (Table II). As the limit of quantitation was

Table II. Results of a Single-Blind Study of Water Samples Spiked with Ethanolamine

actual, ppm	found, ppm	percent of actual	n^a
7.76	7.92 ± 0.18	102 ± 2.3	4
4.34	4.40 ± 0.03	101 ± 0.7	3
1.92	1.94 ± 0.07	101 ± 3.5	3
0.20	0.19 ± 0.03	94 ± 13	3
0.17	0.16 ± 0.03	93 ± 19	3
	overall	98 ± 4.3	16

^aNumber of determinations.

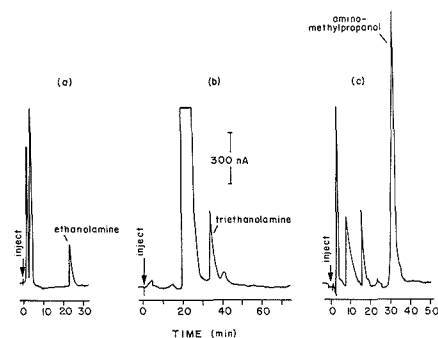


Figure 10. Detection of alkanolamines in various samples by LC with PAD. Conditions were the same as in Figure 5. Samples: (a) generic cold tablet, (b) hand lotion, (c) hairspray.

approached, the standard deviation increased, as expected. The overall percent of spiked ethanolamine was found to be $98.2 \pm 4.3\%$.

The response factors for mono-, di-, and triethanolamine were 2.7, 4.0, and 2.7 $\text{nA}/\mu\text{mol}$, respectively. Since the detection potential was fixed to monitor oxidative detection of the alcohol functionality, the increase in response of the diethanolamine as compared to that of monoethanolamine is concluded to be the result of the presence of two alcohol groups versus one. However, triethanolamine, expected to have a response factor greater than that for the diethanolamine, was approximately equivalent in response to ethanolamine. This low sensitivity is tentatively concluded to be a consequence of steric hindrance from the three alkyl arms as well as desorption of the carboxylate product of the oxidation of only one alcohol group.

The assay for alkanolamines was applied to several matrices to illustrate the analytical utility of the assay. The high selectivity and sensitivity of LC-PAD contributed to decreased time for sample preparation and simplified chromatograms. Figure 10a–c shows chromatograms for the detection of ethanolamine, triethanolamine, and aminomethylpropanol in a cold tablet, hand lotion, and hairspray formulation, respectively. The samples were all prepared by diluting a weighed portion of sample, dilution to the proper level with mobile phase, and filtering.

CONCLUSIONS

The determination of underivatized alkanolamines by ion pair chromatography with pulsed amperometric detection is direct, selective, sensitive, and simple. Ion pair chromatography is compatible with PAD with no evidence of electrode fouling even at high concentrations of the ion pairing reagent for extended run times.

ACKNOWLEDGMENT

We gratefully acknowledge the assistance and support of Lawrence Welch.

LITERATURE CITED

- (1) Kissinger, P. T. *J. Chem. Educ.* **1983**, *60*, 308.
- (2) Johnson, D. C. *Nature* **1986**, *321*, 451.
- (3) Welch, L. E.; LaCourse, W. R.; Mead, D. A., Jr.; Hu, T.; Johnson, D. C. *Anal. Chem.* **1989**, *61*, 555.
- (4) Johnson, D. C.; Polta, T. Z. *Chromatogr. Forum* **1986**, *1*, 37.
- (5) *The Merck Index*, 10th ed.; Merck: Rahway, NJ, 1983; p 541.
- (6) Heberer, H.; Bittarsohi, G. Z. *Chem.* **1980**, *20*, 361.
- (7) Chang, M.-Y.; Chen, L.-R.; Dong, X.-D.; Selavka, C. M.; Krull, I. S. *J. Chromatogr. Sci.* **1987**, *25*, 460.
- (8) Larew, L. A.; Johnson, D. C. *J. Electroanal. Chem. Interfacial Electrochem.* **1989**, *262*, 167.
- (9) Jackson, W. A.; Johnson, D. C., work in progress.
- (10) Naturella, M. *Experimental Statistics*; National Bureau of Standards Handbook 91; NBS: Washington, DC, 1963; pp 6-19.
- (11) Johnson, D. C. *Anal. Chim. Acta* **1988**, *209*, 1.

RECEIVED for review July 1, 1989. Accepted August 30, 1989. The majority of this work was supported by a grant from Dionex Corp., Sunnyvale, CA. The National Science Foundation contributed a portion of the funding through Contract CHE-8312032.

Detection of Rat Basophilic Leukemia by Cyclic Voltammetry for Monitoring Allergic Reaction

Tadashi Matsunaga,* Akinori Shigematsu, and Noriyuki Nakamura

Department of Biotechnology, Tokyo University of Agriculture & Technology, Koganei, Tokyo 184, Japan

Electrochemical detection of the rat basophilic leukemia (RBL-1) cells has been carried out by applying cyclic voltammetry. The detection system consists of a basal plane pyrolytic graphite electrode and a porous nitrocellulose membrane filter to trap RBL-1 cells. When the potential of the graphite electrode was run in the range of 0-1.0 V vs SCE, RBL-1 cells gave peak currents at 0.34 V vs SCE as well as 0.65 V vs SCE. There is a linear relationship between the peak current at 0.34 V vs SCE and the cell numbers of RBL-1 in the range of $(0.4-2.0) \times 10^5$ cells. The peak current of RBL-1 cells was attributed to serotonin. When dinitrophenylated bovine serum albumin (DNP-BSA) as a model allergen was added to RBL-1 cells sensitized with anti-DNP IgE, the peak current decreased because of the degranulation of RBL-1 cells leading to serotonin release. On the other hand, RBL-1 cells sensitized with anti-DNP IgE did not respond to egg white, pollens, house dust, and milk.

INTRODUCTION

Detection of viable cells is important in a clinical field. Various electrochemical methods have been developed for determining viable cell numbers. For example, impedance measurements of culture media have been used to determine cell numbers, although the cell numbers are measured indirectly from cell metabolite, and therefore, the results obtained sometimes do not correlated with true cell numbers. Recently, a novel method for detecting microbial cells has been developed, based on cyclic voltammetry at a basal plane pyrolytic graphite electrode (1, 2). Electron transfer between microbial cells and the graphite electrode is mediated by coenzyme A existing in the cell. Both enumeration and classification of microbial cells were possible from cyclic voltammograms by using an electrode system composed of a graphite electrode and a membrane filter retaining microbial cells. However, cyclic voltammetry of animal cells has not been reported. Therefore, cyclic voltammetry using a graphite electrode was applied to animal cells such as rat basophilic leukemia (RBL-1) and mouse lymphocytes.

The radioimmunosorbent test (RIST) (3-5), radioallergosorbent test (RAST) (6), and skin test (4, 7) have been used

for sensing immediate allergic reactions. However, RIST and RAST are time-consuming and demand complicated procedures giving results independent of clinical symptoms. The skin test is dangerous because it may produce anaphylaxis in man by means of serum antibodies. A simple and safe method is still required for the detection of the immediate allergic reactions. RBL-1 cells, like normal basophils and mast cells, have an immunoglobulin E (IgE) receptor on their surface. RBL-1 cells are passively sensitized by incubating homogeneously cells with IgE. Addition of the appropriate allergen to the stimulated RBL-1 cells causes degranulation, thereby releasing histamine and serotonin (8). Therefore, RBL-1 cells can be used for the detection of immediate allergic reactions. In this paper, the allergic reaction was also monitored with the electrode system using RBL-1 cells.

EXPERIMENTAL SECTION

Materials. Sodium 2,4-dinitrobenzenesulfonate was purchased from Tokyo Chemical Industry Co., Ltd. (Tokyo, Japan). Bovine serum albumin (BSA), 5-hydroxytryptamine hydrochloride (serotonin), and compound 48/80, condensation product of *N*-methyl-*p*-methoxyphenethylamine with formaldehyde were obtained from Sigma Chemical Co. (St. Louis, MO). Monoclonal mouse anti-DNP IgE (9), purified from the ascitic fluid of BALB/c \times C₅₇BL-F₁ mice bearing the SPE-7 hybridoma, was purchased from Seikagaku Kogyo Co., Ltd. (Osaka, Japan). Other reagents were commercially available analytical reagents or laboratory grade materials and were used as received. Distilled-deionized water was used in all procedures.

Preparation of Dinitrophenylated Bovine Serum Albumin (DNP-BSA). A DNP-BSA conjugate (13.8 mol of DNP/mol of BSA) was prepared by using sodium dinitrobenzenesulfonate and BSA as previously described by Eisen et al. (10). The DNP-BSA was employed as a model allergen.

Preparation of Allergen Extracts. Immediate allergic reaction was performed with allergens (egg white, yolk, common ragweed pollen, evening primrose pollen, house dust, cow's milk, and DNP-BSA) and mouse anti-DNP IgE. These allergens except DNP-BSA were sonicated in the phosphate buffered saline (PBS, 1.5 mM KH₂PO₄, 7.3 mM Na₂HPO₄, 137 mM NaCl, 2.7 mM KCl, pH 7.4) for 45 min and incubated at 4 °C for 12 h. Then allergens were centrifuged at 4 °C and 3000g for 30 min and the supernatants were obtained. Then, these extracts were passed through the sterilized membrane filter (pore size, 0.45 μm) and dialyzed for 3 days against 5 L of PBS. The protein concentration of allergen extracts was determined by the Lowry method (11).

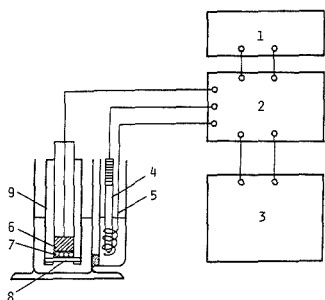


Figure 1. Schematic diagram of the electrode system for the detection of the allergic reaction: 1, function generator; 2, potentiostat; 3, X-Y recorder; 4, reference electrode (saturated calomel electrode); 5, counter electrode (platinum wire); 6, working electrode (basal plane pyrolytic graphite); 7, RBL-1 cell; 8, membrane filter; 9, holder.

Preparation of RBL-1 Cells. RBL-1 cells were cultured in Eagle's minimum essential medium with Earle's balanced salt solution supplemented with 10% fetal bovine serum and antibiotics in the atmosphere of 5% CO₂ at 37 °C. Cell viabilities were determined by using the trypan blue exclusion method. Cells were used for the experiments when viabilities exceeded 90%.

Apparatus. The electrode system for the detection of the allergic reaction is depicted in Figure 1. The electrode system consisted of a basal plane pyrolytic graphite electrode (surface area, 0.19 cm²; Union Carbide Corp., New York), a counter electrode (platinum wire), and a membrane filter for retaining RBL-1 cells. The reference electrode was the saturated calomel electrode (SCE). Cyclic voltammograms were obtained by using a potentiostat (Model HA301, Hokuto Denko, Tokyo, Japan), a function generator (Model HB104, Hokuto Denko, Tokyo, Japan), and an X-Y recorder (Model F35, Riken Denshi, Tokyo, Japan). After each run, the graphite electrode was polished with emery paper.

Procedure for the Detection of Immediate Allergic Reaction. The cultured RBL-1 cells were centrifuged at 100g for 1 min and washed twice with cold (4 °C) Tris-A buffer (25 mM Tris-base, 120 mM NaCl, 5 mM KCl, and 0.3 mg·mL⁻¹ BSA, pH 7.6). The cells were suspended to a density of 1.0×10^6 cells·mL⁻¹ in 1 mL Tris-ACM buffer (Tris-A buffer containing 0.6 mM CaCl₂ and 1.0 mM MgCl₂). Then monoclonal mouse anti-DNP IgE and allergen extracts were added to the RBL-1 cell suspension for a final concentration of 3 μg·mL⁻¹ and 5 μg of protein·mL⁻¹, respectively. After the cells were incubated for 2 h at 37 °C in 5% CO₂, 0.1–0.2 mL of cell suspension was dropped on the membrane filter (pore size, 0.45 μm). Immediately, the cells were fixed on the membrane filter by filtration using an aspirator. The cells on the membrane filter were attached to the basal plane pyrolytic graphite. Cyclic voltammetry was run in the range of 0–1.0 V vs SCE in 10 mL of PBS (pH 7.0). The degranulation of cells was confirmed by microscopy (12).

Sonication of RBL-1 Cells. RBL-1 cells (1.0×10^6 cells) were suspended in 1 mL of PBS (pH 7.0) and then disrupted by the ultrasonic disrupter (Model UR-200P, TOMY Seiko Co., Ltd., Tokyo, Japan) operated for 5 min at 0 °C over 5 times. The sonicated cells were centrifuged at 4 °C and 100g, and the exudate of sonicated cells was obtained. Collected cells were resuspended in 1 mL of PBS and cell suspension (0.1 mL) was dropped on the membrane filter and used for measurement as described above.

Preparation of Basic Granule. RBL-1 cells (1.0×10^6 cells) were washed with 0.32 M sucrose solution containing 40 μM EDTA-2Na and 1 mM Tris-HCl buffer (pH 7.4) and sonicated in sucrose solution. The sonicated solution was centrifuged at 600g for 10 min and the supernatant containing the exudate from the cells was collected. The supernatant was centrifuged at 7000g for 10 min, and basic granules were obtained as precipitate (13).

RESULTS AND DISCUSSION

Cyclic Voltammetry of RBL-1 Cells. Figure 2 shows the cyclic voltammograms of RBL-1 cells and mouse lymphocytes.

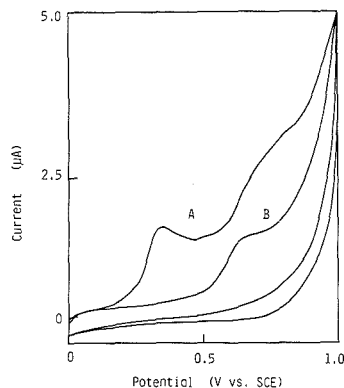


Figure 2. Cyclic voltammograms of (A) RBL-1 cells (1.2×10^5 cells) and (B) mouse lymphocytes (8.0×10^5 cells) on the membrane filter. Scan rate was 10 mV·s⁻¹. The measurements were performed in 10 mL of PBS (pH 7.0).

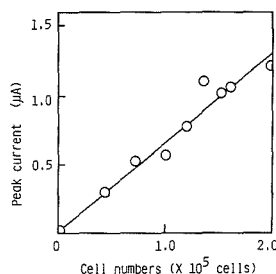


Figure 3. Relationship between peak current at 0.34 V vs SCE and RBL-1 cell numbers. Scan rate was 10 mV·s⁻¹. The measurements were performed in 10 mL of PBS (pH 7.0).

Anodic waves appeared at 0.34 and 0.68 V vs SCE for RBL-1 cells and 0.65 V vs SCE for mouse lymphocytes. The peak current at 0.34 V vs SCE was 0.76 μA for 1.2×10^5 RBL-1 cells. Upon scan reversal, no corresponding reduction peak was obtained. This shows that the electrode reactions of RBL-1 cells and lymphocytes were irreversible. The differential-pulse voltammograms of RBL-1 cells have also been obtained. The differential-pulse voltammograms were obtained by using a polarograph (Fuso Seisakusho, Model 312) and an X-Y recorder. The peak current appeared at the same potential as that of the cyclic voltammograms. The sensitivity was not improved by the differential-pulse voltammograms. Figure 3 shows the relationship between the peak currents at 0.34 V vs SCE and the cells numbers of RBL-1 on the membrane filter. The peak current increased linearly with increasing the cell numbers up to 2.0×10^6 cells. The minimum detectable cell numbers were 0.4×10^5 cells. These results show that cell numbers of RBL-1 in the range of $(0.4\text{--}2.0) \times 10^5$ cells can be determined from the peak current of cyclic voltammetry.

Mechanism of Electrochemical Reaction in RBL-1 Cells. Recently, it was found that an electron transfer between cells and the graphite electrode is mediated by coenzyme A (CoA) present in the cell wall for various microorganisms. The peak currents of the cyclic voltammograms of yeasts, Gram-positive bacteria, and Gram-negative bacteria were observed at 0.65–0.74 V vs SCE which were attributed to the oxidation of CoA present in the cells (1, 2, 14). The peak currents of lymphocyte, macrophage, ascites tumor, and erythrocyte were obtained around 0.65 V vs SCE (unpublished

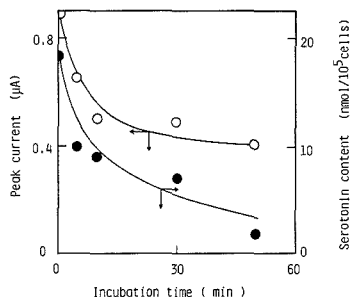


Figure 4. Time-course of (O) peak current and (●) serotonin content in RBL-1 cells when RBL-1 cells (1.4×10^5 cells) were degranulated with compound 48/80 in 10 mL of Tris-ACM buffer (pH 7.0). Scan rate was $10 \text{ mV}\cdot\text{s}^{-1}$.

data, Matsunaga et al.). As described above, RBL-1 cells showed the peak currents at 0.34 V and 0.65 V vs SCE. These results suggest that the peak current of animal cells including RBL-1 cells obtained around 0.65 V vs SCE results from the electrochemical oxidation of CoA. However, the peak current at 0.34 V vs SCE obtained from RBL-1 cells seems to be related with other compounds. RBL-1 cells have cytoplasmic granules containing mediators of anaphylaxis such as histamine, serotonin, eosinophil chemotactic factor, and neutrophil chemotactic factor. The peak current of serotonin was obtained at 0.33 V vs SCE at pH 7.0 when BPG electrode was employed. Previous papers have reported that the peak potential appeared at 0.29–0.34 V vs SCE around pH 7.0 at pyrolytic graphite electrodes (15) and carbon fiber microelectrodes (16). The peak potential of the RBL-1 cell was similar to those of serotonin in our experiment and the previous papers. On the other hand, the peak current was not obtained from other mediators of anaphylaxis such as histamine. Moreover, no corresponding reduction peak was obtained in serotonin, too. The electrode reaction of serotonin was also irreversible. The oxidation peak currents of RBL-1 cells and serotonin increased linearly with the square root of the scan rate as expected for a totally irreversible reaction. The slope of peak potentials vs pH line was 50–55 mV in the range of pH 6.0–8.0 for RBL-1 cells and serotonin. These experimental results support that the generation of peak current results from electrochemical oxidation of serotonin. Then, serotonin was eluted by sonicating RBL-1 cells in the buffer solution. As a result, the peak current from RBL-1 cells decreased to almost zero after 30 min of sonication. The amount of serotonin in the exudate of sonicated cells after elution was consistent with that of the RBL-1 cells before elution. Therefore, the serotonin concentration in the exudate solution of sonicated cells was determined by high-performance liquid chromatography (HPLC, Shimadzu Co. Model LC-6A system) on Shim-pack CLC-ODS (150 mm \times 6.0 mm diameter). As a result, $0.90 \mu\text{M}$ of serotonin was detected in the exudate of sonicated cells (1 mL).

Next, granules in the RBL-1 cells were expelled by degranulation. As a result, the serotonin content of RBL-1 cells decreased. Figure 4 shows the time-course of the peak current and the serotonin content of RBL-1 cells when RBL-1 cells were degranulated with compound 48/80. It is employed as the inducer of degranulation. After degranulation, cells were washed and centrifuged for electrochemical measurement. Then, the serotonin content of cells and the amount of serotonin released were determined by high-performance liquid chromatography (HPLC). The serotonin content of degranulated RBL-1 cells decreased gradually because serotonin eluted. The peak current at 0.34 V vs SCE also decreased with

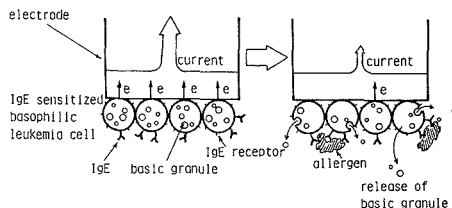


Figure 5. Schematic diagram for the detection of immediate allergic reaction.

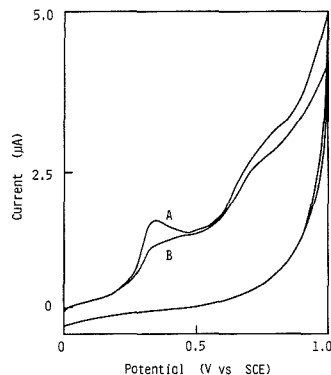


Figure 6. Cyclic voltammograms of (A) sensitized RBL-1 cells (2.0×10^5 cells) and (B) degranulated RBL-1 cells (2.0×10^5 cells). Scan rate was $10 \text{ mV}\cdot\text{s}^{-1}$. The measurements were performed in 10 mL of PBS (pH 7.0).

decreasing the serotonin content of the cells. Decrease of the serotonin content of RBL-1 cells agreed with the amount of serotonin released.

Detection of Immediate Allergic Reaction by Using Cyclic Voltammetry of RBL-1 Cells. Allergic reactions are included in immunological responses. IgE antibodies, which are secreted by activated B lymphocytes, are responsible for allergic reactions. The Fc region of IgE molecules binds to specific receptor proteins on the surface of mast cells in tissues and basophilic leucocytes in the blood. The bound IgE molecules in turn serve as receptors for allergens. Allergens cross-link those membrane-bound IgE antibodies with complementary allergen-binding sites, thereby triggering the cells to secrete histamine and serotonin. Histamine and serotonin cause dilation and increased permeability of blood vessels and are largely responsible for the clinical manifestations of such allergic reactions as pollenosis, asthma, and hives. RBL-1 cells, like mast cells and basophilic leucocytes, have IgE receptor on their surface and show the same response to allergens (17). Figure 5 shows the principle for the detection of immediate allergic reaction. When allergen was reacted with RBL-1 cells sensitized with anti-allergen IgE, RBL-1 cells were degranulated to release serotonin (8, 12). As a result, the serotonin content of the cell decreased, leading to the decrease of the peak current of cyclic voltammograms. RBL-1 cells were reacted with mouse anti-DNP IgE. Then, when allergen, DNP-BSA was added to RBL-1 cells sensitized with anti-DNP IgE, RBL-1 cells were degranulated. Figure 6 shows the cyclic voltammograms of passively sensitized RBL-1 cells with IgE and degranulated RBL-1 cells. Anodic waves of the sensitized RBL-1 cells appeared at the same potential as that of the normal RBL-1 cells. The peak current was also similar to that of the normal RBL-1 cells. However, the peak current decreased when the sensitized RBL-1 cells were degranulated

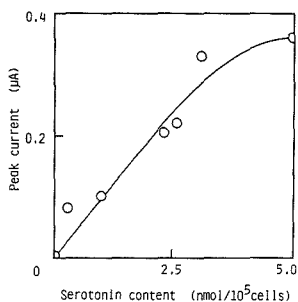


Figure 7. Relationship between peak current at 0.34 V vs SCE and serotonin content in RBL-1 cells. Scan rate was 10 mV·s⁻¹. The measurements were performed in PBS (pH 7.0).

Table I. Peak Currents of RBL-1 Cells When Anti-DNP IgE and DNP Derivatives as a Model Allergen Were Added^a

addition	peak current, μA
none	1.26
DNP-BSA ($3 \mu\text{g}\cdot\text{mL}^{-1}$)	1.20
IgE ($5 \mu\text{g}\cdot\text{mL}^{-1}$)	1.34
IgE ($5 \mu\text{g}\cdot\text{mL}^{-1}$) + DNP ($1 \mu\text{g}\cdot\text{mL}^{-1}$)	1.30
IgE ($5 \mu\text{g}\cdot\text{mL}^{-1}$) + DNP-BSA ($3 \mu\text{g}\cdot\text{mL}^{-1}$)	0.96

^aRBL-1 cells were incubated in Tris-ACM solution for 2 h and 2.0×10^6 cells of RBL-1 were employed for experiments.

with DNP-BSA. Addition of DNP-BSA to sensitized RBL-1 cells with IgE brought about degranulation of cells. Figure 7 shows the relationship between the peak current and the serotonin content of the degranulated RBL-1 cells when RBL-1 cells sensitized with anti-DNP IgE were degranulated with DNP-BSA by IgE-mediated reaction. The peak current obtained from the degranulated cells decreased with decreasing the serotonin content of the cells. This indicates that the peak current decrease was attributed to decrease of serotonin present in the RBL-1 cells after degranulation. Serotonin release by immediate allergic reaction can be detected by measuring the peak current of cyclic voltammograms.

Then, the relationship between the degranulation of RBL-1 cells and the peak current was examined. RBL-1 cells were incubated with mouse anti-DNP IgE and DNP-BSA for 2 h. After the incubation, the peak current decreased from $0.63 \mu\text{A}/10^6$ cells to $0.48 \mu\text{A}/10^6$ cells. On the other hand, the peak current did not decrease when DNP-BSA, IgE, or DNP and IgE were added to RBL-1 cells (Table I). These results suggested that cross-linking of receptor-bound IgE molecules by DNP-BSA decreased the peak current, while the binding of IgE with the receptor or the binding of DNP with receptor-bound IgE molecule did not decrease the peak current. Degranulation of RBL-1 cells occurred by cross-linking of sensitized cells with DNP-BSA. Table II shows the peak currents of RBL-1 cells when they were stimulated with various allergen extracts and mouse anti-DNP IgE. Various allergen extracts and mouse anti-DNP IgE did not show a peak current when cyclic voltammograms were directly obtained from these samples. Stimulation of RBL-1 cells by egg white, pollens (evening primrose and common ragweed), house dust, and cow's milk did not show the decrease of peak current. Only DNP-BSA and yolk decreased the peak current. How-

Table II. Peak Currents of RBL-1 Cells When Various Allergens Were Added with Anti-DNP IgE^a

extract of allergen ($3 \mu\text{g}\cdot\text{mL}^{-1}$)	peak current, μA
none	1.00
egg white	1.02
yolk ^b	0.72
pollen	
evening primrose	0.94
common ragweed	0.96
house dust	0.90
milk	1.00
DNP-BSA	0.70

^aRBL-1 cells were incubated in Tris-ACM solution for 2 h and 1.6×10^5 cells of RBL-1 were employed for experiments. ^bThe yolk was similarly decreased peak currents of RBL-1 cells without IgE.

ever, stimulation by yolk decreased the peak current of RBL-1 cells without IgE. Therefore, no specific current decrease by yolk was discriminated from a specific current decrease by DNP-BSA using RBL-1 cells not sensitized with IgE as a reference. The peak currents were reproducible with a relative error of 5% when RBL-1 cells prepared at the same time were used for the experiments. These results suggested that IgE-specific degranulation of immediate allergic reaction can be detected from the peak current of cyclic voltammetry.

The novel concept described here for detecting intermediate allergic reaction lays the groundwork for the development of methods detecting specific allergens for a person. Further developmental studies in our laboratory are now directed toward detection of allergic reaction using human IgE in the serum.

LITERATURE CITED

- (1) Matsunaga, T.; Namba, Y. *Anal. Chem.* **1984**, *56*, 798-801.
- (2) Matsunaga, T.; Namba, Y. *Anal. Chim. Acta* **1984**, *159*, 87-94.
- (3) Merrett, J.; Merrett, T. G. *Clin. Allergy* **1987**, *17*, 409-416.
- (4) Green-Graif, Y.; Ewan, P. W. *Clin. Allergy* **1987**, *17*, 431-438.
- (5) Walsh, B. J.; Elliott, C.; Baker, R. S.; Barnett, D.; Burley, R. W.; Hill, D. J.; Howden, M. E. H. *Int. Arch. Allergy Appl. Immunol.* **1987**, *84*, 228-232.
- (6) Kelly, K. A.; Lang, G. M.; Bundeson, P. G.; Holford-Strevens, V.; Bottcher, I.; Sehon, A. H. *J. Immunol. Methods* **1980**, *39*, 317-333.
- (7) Derborg, S.; Einarsson, R.; Longbottom, J. L. *Handbook of Experimental Immunology*; Weir, D. M., Ed.; Blackwell Scientific Publications: London, 1973; Chapter 10.
- (8) Ishizaka, T.; Ishizaka, K. *Prog. Allergy* **1984**, *34*, 188-235.
- (9) Eshhar, Z.; Otarim, M.; Waks, T. *J. Immunol.* **1980**, *124*, 775-780.
- (10) Little, J. R.; Eisen, H. N. *Methods in Immunology and Immunochimistry*, Vol. 7; Williams, C. A., Chase, M. W., Eds.; Academic Press: New York, 1967; pp 128-133.
- (11) Lowry, O. H.; Rosebrough, N. J.; Farr, A. L.; Randall, R. J. *J. Biol. Chem.* **1951**, *193*, 265-275.
- (12) Well, B. J.; Renoux, M. L. *Cell Immunol.* **1982**, *68*, 220-233.
- (13) Saeki, K.; Endo, E.; Yamasaki, H. *Jpn. J. Pharmacol.* **1972**, *22*, 27-32.
- (14) Matsunaga, T.; Nakajima, T. *Appl. Environ. Microbiol.* **1985**, *50*, 238-242.
- (15) Ponchon, J. L.; Cespuoglio, R.; Gonon, F.; Jouvet, M.; Pujol, J. F. *Anal. Chem.* **1979**, *51*, 1465-1466.
- (16) Wrona, M. Z.; Dryhurst, G. J. *Org. Chem.* **1987**, *52*, 2817-2825.
- (17) *Molecular Biology of the Cell*; Albert, B., Bray, D., Lewis, J., Raff, M., Roberts, K., Watson, J. D., Eds.; Garland Publishing, Inc.: New York, 1983; pp 967-969.

RECEIVED for review May 31, 1988. Revised manuscript received June 6, 1989. Accepted August 18, 1989. This work was partially supported by Grant-in-Aid for Special Project Research No. 63108002 from the Ministry of Education, Science and Culture.

Room-Temperature Phosphorescence of Compounds in Mixed Organized Media: Synthetic Enzyme Model-Surfactant System

Haidong Kim¹ and Stanley R. Crouch*

Department of Chemistry, Michigan State University, East Lansing, Michigan 48824

Matthew J. Zabik*

Pesticide Research Center, Michigan State University, East Lansing, Michigan 48824

A new kind of host molecule, the synthetic enzyme model, is compared to cyclodextrin in a mixed organized medium by a room-temperature phosphorescence study. Lumiphors included inside the synthetic enzyme model compound in the presence of heavy atoms did not show any phosphorescence at room temperature, but showed phosphorescence when premicellar concentrations of surfactant were added. The synthetic enzyme model compound employed in this system shows more selectivity and sensitivity than cyclodextrin due to the achievement of a more favorable microenvironment. The interactions of lumiphors with host molecules, heavy atoms, and surfactant molecules are discussed in detail with room-temperature phosphorescence and phosphorescence decay lifetime data.

INTRODUCTION

Room-temperature phosphorimetry (RTP) is quite different from the classic low-temperature phosphorescence technique, which is typically performed in glass matrices at liquid nitrogen temperature (1). Since the discovery of RTP, numerous techniques have been developed to induce RTP from various molecules. These include solid-state RTP (2), micellar stabilized RTP (3), sensitized RTP (4), cyclodextrin enhanced RTP (5), and colloidal or microcrystalline RTP (6). The probability for observing RTP (especially in solutions) is enhanced in a rigid molecular environment due to a reduced quenching effect by oxygen or other impurities and, in the presence of a heavy atom, due to an increase in the rate of intersystem crossing.

Photophysical and photochemical properties of organic molecules included in the cavity of cyclodextrins (CDs) have been of considerable interest in the past decade (7). Cyclodextrins form complexes with hydrophobic organic and organometallic molecules in aqueous solution. Although there is no direct proof for a fixation of the guest molecules within the void space of the cyclodextrin, the complexes are usually regarded as inclusion compounds, host-guest compounds in which hydrogen bonding, van der Waals forces, and hydrophobic interactions are the main binding forces (8). When lumiphores are included inside the cyclodextrin molecules, the resulting RTP shows enhanced intensity and lifetime because the cyclodextrins protect the lumiphores from quenchers (9).

The synthetic macrocyclic enzyme model compounds, azaparcyclophanes (APCs) can act as inclusion hosts capable of molecular organization by forming complexes with a variety of hydrophobic molecules (10). Water-soluble azaparcyclophane, *N,N,N',N',N'',N''',N''''*-octamethyl-

2,11,20,29-tetraaza[3.3.3.3]paracyclophanetetraammonium tetrafluoroborate (methyl-APC), is an excellent inclusion host toward certain organic substrates. A unique substrate specificity was observed due to its cavity size and functionality (11). The macrocyclic cavity is surrounded by the wall, which is formed by four benzene rings and four quaternary ammonium residues around the macrocyclic ring.

In this paper, we report preliminary RTP results of 6-(*p*-toluidinyl)naphthalene-2-sulfonate (TNS) and 2-bromonaphthalene obtained with methyl-APC and cyclodextrin in premicellar surfactant solutions. The binding ability and selectivity of methyl-APC in complex formation with anionic and neutral polyaromatic hydrocarbon compounds are compared with those of cyclodextrin. The effects of surfactant and heavy atom in a mixed organized medium, methyl-APC-surfactant, are also discussed.

EXPERIMENTAL SECTION

Reagents. Sodium sulfite (J. T. Baker) was recrystallized from warm water. Thallium(I) nitrate (99.999%, Aldrich), sodium bromide (99.9%, J. T. Baker), sodium dodecyl sulfate, SDS (99%, Sigma), 2-bromonaphthalene (97%, Aldrich), 6-(*p*-toluidino)-2-naphthalenesulfonic acid potassium salt, TNS (Aldrich), 1-anilino-8-naphthalenesulfonic acid ammonium salt, ANS (Aldrich), and β -cyclodextrin (Sigma) were used as received. Methanol (GR grade, EM Science) was used without further purification. Distilled and deionized water was used for RTP sample preparation.

α,α' -Dibromo-*p*-xylene (98%, Aldrich), terephthaloyl chloride (97%, Aldrich), trimethylxonium tetrafluoroborate (Aldrich), and methylamine (40% in water, Matheson Coleman & Bell) were used to synthesize the methyl-APC as discussed below.

Apparatus. All spectra were obtained with a Perkin-Elmer LS-5B spectrometer. The chart recorder output (1 V maximum) of the spectrometer was amplified 10 times and digitized by an IBM-PC data acquisition board installed on an IBM-XT compatible computer (12). Laboratory-written software was used for luminescence data acquisition and data manipulation. The range of delay and gate times for RTP measurements was 0.03-0.05 and 1-2 ms, respectively.

Sample Preparation and General Procedure. The macrocyclic compound, methyl-APC, was synthesized in highly dilute conditions according to the reported procedure by Tabushi et al. (11). The sample solutions for RTP were deoxygenated by adding sodium sulfite solutions (0.01-0.04 M) to the sample solution as reported by Garcia et al. (13). To a 10-mL volumetric flask, appropriate aliquots of lumiphor, sodium sulfite, heavy atom, and surfactant solutions were added and diluted to a 10-mL final volume with distilled and deionized water. After thorough mixing, the solution was transferred to a cuvette with a Teflon stopper, and the RTP intensity was monitored at the emission maximum with the appropriate excitation wavelength on the spectrometer. Spectra were obtained after the RTP intensity reached steady state and remained the same for at least 5 min. All the luminescence spectra shown here are uncorrected spectra.

RESULTS AND DISCUSSION

The interesting characteristics of enzymes have stimulated chemists to design and synthesize various kinds of enzyme

* Authors to whom correspondence should be addressed.

¹ Present address: 204 Pesticide Research Center, Michigan State University, East Lansing, MI 48824.

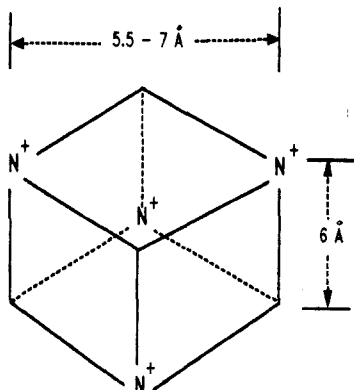


Figure 1. Simplified structural representation of the synthetic enzyme model, methylazaparacyclophane (methyl-APC) molecule.

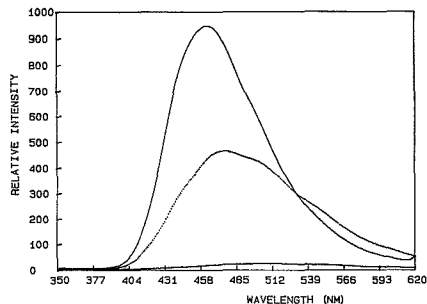


Figure 2. Fluorescence spectrum of TNS (5×10^{-5} M) in water only (bottom), in 1×10^{-4} M β -cyclodextrin (middle), and in 1×10^{-4} M methyl-APC (upper). The excitation wavelength was 337 nm.

molecules that can show enzyme-like behavior (14). Substances capable of functioning as enzyme models or receptors should have binding sites or molecular cavities and functionalities so as to be able to form inclusion complexes. The substrate specificity of enzymes is controlled largely by the specific reaction pathway, the geometry of the substrate, and the shape and size of the substrate.

The methyl-APC molecules used in this study have a cavity surrounded by four positively charged active sites. The unique molecular shape of methyl-APC resembles a "square box" (Figure 1), and the cavity size is 5.5–7 Å wide and 6 Å deep (15). The boxlike opening of the methyl-APC can vary in size, due to the single-bond character of the four quaternary nitrogen atoms and adjacent hydrocarbon chains, to include guest molecules of various sizes by "induced-fit binding" (16).

Fluorescence Enhancement of Lumiphors by APC. The compound 6-(*p*-toluidinyl)naphthalene-2-sulfonate (TNS) is one of the most widely used fluorescence probes due to the highly sensitive nature of hydrophobic binding. This probe molecule normally shows very weak fluorescence in aqueous solutions, but is highly fluorescent when bound to bovine serum albumin or to several proteins (17). The binding ability of the methyl-APC molecule was tested with TNS in aqueous solution. Figure 2 shows the change in the fluorescence spectrum of TNS on addition of host molecules. The fluorescence intensity of TNS in water was negligible (bottom), but it increased by a factor of 20 on addition of β -cyclodextrin (1×10^{-4} M) with an emission maximum at 470 nm. Upon addition of methyl-APC (1×10^{-4} M), the fluorescence in-

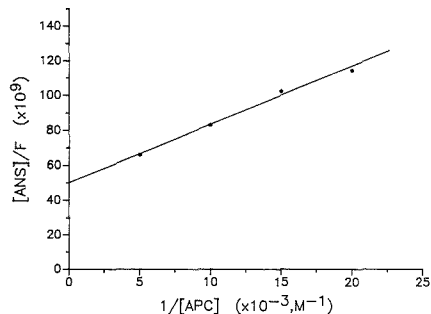


Figure 3. Double reciprocal plot of fluorescence of ANS and the concentration of methyl-APC. The concentration of ANS was 5×10^{-5} M, and the excitation wavelength was 375 nm.

tensity of TNS increased to more than twice that with β -cyclodextrin (β -CD), and the peak maximum shifted to 460 nm. Also, with methyl-APC, the fluorescence peak became narrower than that with β -CD. The same trend was observed when 1-anilino-8-naphthalenesulfonate (ANS) was used instead of TNS. Upon addition of β -CD (1×10^{-4} M) to the ANS solution, the fluorescence intensity of ANS increased by a factor of 2, but when the same concentration of methyl-APC was added, the fluorescence intensity increased by a factor of 5. The fluorescence peak blue-shifted 8 nm with β -CD and 25 nm with methyl-APC when compared to the emission maximum of ANS alone.

Although TNS has been reported to form 1:1 and 2:1 complexes with cyclodextrin (18), we have not yet confirmed the details of the complexes formed in this system. However, preliminary results on the association constant of the methyl-APC-ANS complex indicate that methyl-APC provides a much stronger binding site than β -CD for ANS through hydrophobic and electrostatic interactions. The association constant of ANS was calculated from a double reciprocal plot (18) and was found to be 1.6×10^4 /mol. The double reciprocal plot of ANS showed a linear relationship in the host concentration range employed, as shown in Figure 3. This association constant was much greater than the previous value of 110/mol with β -CD reported by Catena et al. (18).

The spectral changes observed are due to changes in the microenvironment of the ANS or TNS molecules. In both cases, methyl-APC showed a larger blue shift and a greater fluorescence enhancement than did β -CD. These data suggest that methyl-APC molecules provide stronger and more hydrophobic binding sites for TNS and ANS molecules than β -CD does.

RTP Enhancement of Lumiphors by Host. If the host molecules can provide an environment to protect excited triplet-state molecules from quenching, it is expected that the resulting phosphorescence will increase.

Sample solutions were made for the observation of RTP with various amounts of methyl-APC or β -CD. The TNS solutions (2.5×10^{-5} M) for RTP were deoxygenated with sodium sulfite (0.04 M), and thallium nitrate (0.02 M) was used as an external heavy-atom source. Under the above conditions, we could not observe any RTP of TNS. However, RTP of TNS began to show up when premicellar concentrations of SDS were added to the solution mixture, as shown in Figure 4. The RTP intensity of TNS increased by a factor of 2 when methyl-APC (0.1 mM) was added, but it decreased slightly when the same concentration of β -CD was added to the solution. There were not noticeable spectral changes of the resulting phosphorescence when either host was added.

In the case of 2-bromonaphthalene under similar experimental conditions, except for the heavy atom (NaBr was used

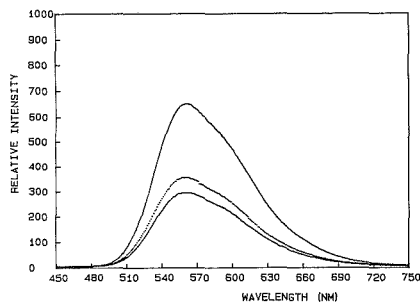


Figure 4. RTP spectrum of TNS (2.5×10^{-5} M) in 5 mM SDS: middle spectrum, no host; lower spectrum, upon addition of 0.1 mM β -CD; upper spectrum, upon addition of 0.1 mM methyl-APC. The excitation wavelength was 337 nm.

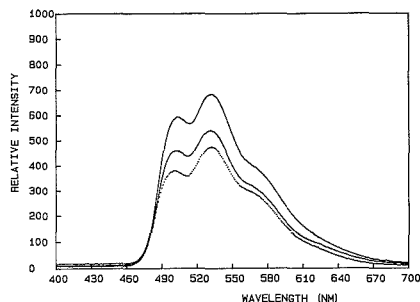


Figure 5. RTP spectrum of 2-bromonaphthalene in 5 mM SDS: lower spectrum, no host; middle spectrum, upon addition of 0.3 mM β -CD; upper spectrum, upon addition of 0.3 mM methyl-APC. The excitation wavelength was 293 nm.

instead of TlNO_3), the RTP intensity of 2-bromonaphthalene also increased upon addition of the host molecules. But again, the methyl-APC showed better RTP enhancement, as shown in Figure 5. The RTP of 2-bromonaphthalene could be observed without an external heavy atom by careful sample purification and solution deoxygenation, but the RTP intensity in that case was much weaker than that with additional external heavy atoms. Although the fluorescence of ANS was enhanced by the addition of methyl-APC, we could not observe any RTP from ANS under similar experimental conditions.

The critical micelle concentration (cmc) for SDS is reported to be 8×10^{-3} M (19). Also, the cmc of SDS was found to increase upon addition of β -CD in aqueous solution due to the association of the SDS molecules with β -CD. This results in a decrease in the amount of available surfactant monomers for micelle formation (20). The concentration of SDS employed was 5 mM, so we expect some premicellar aggregates of SDS in solution without any host. However, we should not expect any micelles in the above solutions containing host molecules. Although methyl-APC was not the only substance responsible for the observation of RTP, it appears that methyl-APC enhances RTP by efficient organization of lumiphors and SDS. The RTP of TNS at SDS concentrations above the cmc still showed enhanced intensity with methyl-APC.

The enhancement of RTP intensity upon addition of methyl-APC strongly indicates that SDS molecules aggregate around the TNS-APC complex through electrostatic and hydrophobic interaction. This provides a favorable micro-environment that stabilizes the triplet state of the TNS

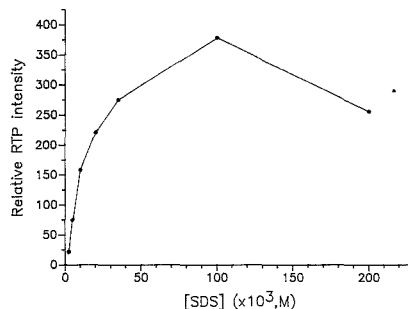


Figure 6. Effect of SDS on the RTP of TNS: [methyl-APC] = 0.1 mM; [TNS] = 2.5×10^{-5} M; $[\text{Na}_2\text{SO}_3]$ = 0.04 M; $[\text{TlNO}_3]$ = 0.02 M; excitation, 337 nm; emission, 562 nm.

molecules. It is believed that the decrease in phosphorescence intensity of TNS upon addition of β -CD is due to a preference for the aqueous bulk phase over the cyclodextrin by TNS molecules. Also, the number of available surfactant monomers for TNS in the bulk phase is expected to decrease due to the aggregation of surfactant molecules around the β -CD.

Effect of Host, Heavy Atom, and SDS on RTP. The effect of host concentration on RTP was studied at fixed concentrations of SDS, lumiphor, heavy atom, and sodium sulfite. The concentration of methyl-APC was varied from 0 to 0.6 mM, and the concentration of SDS was maintained at 5 mM. The RTP intensity of TNS steadily increased up to 0.3 mM and decreased thereafter. The same trend was observed with 2-bromonaphthalene. An increase in the SDS concentration with fixed amounts of heavy atom and sodium sulfite enhanced the RTP intensity of lumiphors up to an SDS concentration of 0.1 M. Beyond this the RTP intensity began to decrease, as shown in Figure 6. This type of change in RTP intensity was also observed in micellar stabilized RTP. But, the inflection point of SDS concentration at which the RTP intensity starts to decrease normally lies in the 0.04–0.05 M range, which is much lower than that of the methyl-APC-SDS mixed organized system.

The exact mechanism of these RTP changes is not clear at this time, but it seems that the aggregation of SDS around the methyl-APC plays a major role. Adsorption of surfactant monomers on a hydrophilic solid surface such as silica has been observed by studying the fluorescence decay of pyrene dissolved in surfactant-silica media (21). The proposed models on the basis of the adsorption data admit the existence of condensed (or organized) molecular assemblies on the surface, either in the form of micellar-like aggregates (hemimicelles) or in the form of a more extended lamellar phase (22).

The effects of heavy atoms on the RTP were quite interesting. No RTP of TNS was observed from anionic TNS with bromide ions as an external heavy-atom source. In the case of nonionic 2-bromonaphthalene, both Br^- and Tl^+ enhanced RTP, but the bromide ions enhanced the RTP intensity more than twice that of thallium ions, as shown in Figure 7. These data indicate that the effective enhancement of RTP by heavy atoms through intersystem crossing requires a closer approach of heavy atoms to the lumiphors. It is expected that thallium ions cannot approach close to the methyl-APC due to the electrostatic repulsion between the positively charged sites of methyl-APC and thallium ions. However, bromide ions can closely approach the methyl-APC due to attractive forces between them. It is worth noting in Figure 7 that the RTP development of 2-bromonaphthalene by bromide ions took more time than with thallium ions due to the electrostatic interactions of bromide ions with anionic SDS molecules around the methyl-APC.

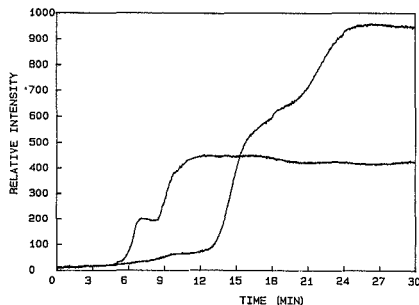


Figure 7. RTP development of 2-bromonaphthalene (5×10^{-6} M) with 0.02 M sodium bromide (upper left) and 0.02 M thallium nitrate (lower left); $[\text{Na}_2\text{SO}_3] = 0.04$ M; $[\text{SDS}] = 5$ mM; $[\text{methyl-APC}] = 0.1$ mM; excitation, 293 nm; emission, 525 nm.

Table I. Effect of Host on the RTP Lifetimes of Selected Aromatic Hydrocarbons

host	RTP lifetimes, ^a μs	
	TNS	2-bromonaphthalene
no host	124 ± 22	412 ± 11
β -cyclodextrin	117 ± 22	455 ± 12
methyl-APC	406 ± 2	529 ± 36

^aThe concentrations of lumiphors (TNS, 2-bromonaphthalene) and heavy atom (TlNO₃ or NaBr) were 5×10^{-6} and 0.02 M, respectively; $[\text{host}] = 0.2$ mM, $[\text{SDS}] = 5$ mM, $[\text{Na}_2\text{SO}_3] = 0.02$ M. Correlation coefficients of the above lifetimes were all above 0.998.

The RTP development with time directly indicates the oxygen consumption process in the sample solution. It appears to be a two-step process in both the bromide and the thallium systems. These can be observed also in a highly concentrated micellar solution. The oxygen consumption by sulfite ions should be a diffusion-controlled process. Also, the diffusion of oxygen in the bulk phase and inside the SDS-APC-lumiphor complex will be different. These data suggest that the solution is composed of two different environments for lumiphors.

RTP Decay of Lumiphors. Since the RTP lifetime is extremely sensitive to a molecule's microenvironment, information about the molecular interaction of the lumiphors in the APC-surfactant mixed media can be obtained from the RTP decay lifetimes.

RTP lifetimes of TNS and 2-bromonaphthalene were measured in aqueous solutions containing a heavy atom and 5 mM SDS. RTP lifetimes were calculated with the linear least-squares method. Table I shows the effect of host on RTP decay lifetimes of TNS and 2-bromonaphthalene. The RTP lifetime of TNS in SDS solution without any host was 124 ± 22 μs with a correlation coefficient of 0.999. In the 0.2 mM β -CD solution, the RTP lifetime of TNS was decreased slightly to 117 ± 22 μs as expected from the decreased RTP intensity upon addition of β -CD. But, when 0.2 mM methyl-APC was added to the TNS solution, the RTP lifetime of TNS increased to 406 ± 2 μs with a correlation coefficient of 0.999. The RTP decay of 2-bromonaphthalene under similar ex-

perimental conditions, except for the heavy atom (Br^- instead of Tl^+), showed increased lifetime upon addition of host. The RTP lifetime of 2-bromonaphthalene increased from 412 ± 11 to 455 ± 12 μs upon addition of 0.1 mM β -CD and increased further to 529 ± 36 μs with 0.1 mM methyl-APC.

Differences in decay lifetimes can generally be attributed to changes in the deactivation pathways of the excited state or changes in the interaction of the excited state with the surroundings (23). The increase of RTP lifetime of lumiphors upon the addition of methyl-APC indicates that the microenvironment of lumiphors in the methyl-APC-surfactant mixed organized media stabilizes the excited triplet state of the molecules.

CONCLUSIONS

This comparative RTP study of anionic and neutral lumiphors in a mixed organized media, surfactant-host, has demonstrated that synthetic enzyme model molecules can provide a favorable microenvironment for lumiphors through electrostatic and hydrophobic interactions. Since the host enzyme model molecules are synthetic in nature, a highly selective microenvironment can be obtained by designing host molecules for specific purposes. Consequently, the synthetic enzyme model molecules could open a new avenue for chemical analysis due to their inherent potential of controlled specific host-guest interaction. In the future, such synthetic enzyme model molecules may find applications in luminescence, chromatography, biological immunoassay, flow injection analysis, and many other research areas.

ACKNOWLEDGMENT

The authors are grateful to Dr. Nelson Herron and Dr. Paul Kraus for their helpful discussions and suggestions.

LITERATURE CITED

- Hurtubise, R. J. *Anal. Chem.* **1983**, *55*, 669A.
- Ward, J. L.; Walden, G. L.; Winefordner, J. D. *Talanta* **1981**, *28*, 201.
- Cline Love, L. J.; Skrliec, M.; Habarta, J. G. *Anal. Chem.* **1980**, *52*, 754.
- Donkerbroek, J. J.; Elzas, J. J.; Gooijer, C.; Frei, R. W.; Velthorst, N. *Talanta* **1981**, *28*, 717.
- Scypinski, S.; Cline Love, L. J. *Anal. Chem.* **1984**, *56*, 322.
- Weinberger, R.; Cline Love, L. J. *Appl. Spectrosc.* **1985**, *39*, 516.
- Ramamurthy, V.; Eaton, D. F. *Acc. Chem. Res.* **1988**, *21*, 300.
- Cramer, F.; Mackensen, G. *Angew. Chem., Int. Ed. Engl.* **1966**, *5*, 601.
- Turro, N. J.; Bolt, J. D.; Kuroda, Y.; Tabushi, I. *Photochem. Photobiol.* **1982**, *35*, 69.
- Tabushi, I.; Kuroda, Y.; Kimura, Y. *Tetrahedron Lett.* **1976**, *37*, 3327.
- Tabushi, I.; Kimura, Y.; Yamamura, K. *J. Am. Chem. Soc.* **1981**, *103*, 6486.
- Kim, Haidong; Zabik, M. J.; Crouch, S. R. *Appl. Spectrosc.* **1989**, *43*, 608.
- Diaz Garcia, M. E.; Sanz-Medel, A. *Anal. Chem.* **1986**, *58*, 1436.
- Tabushi, I. *Tetrahedron* **1984**, *40*(2), 269.
- Tabushi, I.; Yamamura, K.; Nonoguchi, H.; Hirotsu, K.; Higuchi, T. *J. Am. Chem. Soc.* **1984**, *106*, 2621.
- Murakami, Y.; Nakano, A.; Akiyoshi, K.; Fukuya, K. *J. Chem. Soc., Perkin Trans. 1* **1981**, 2600.
- Brand, L.; Gohlke, J. R. *Annu. Rev. Biochem.* **1972**, *41*, 843.
- Catena, G. C.; Bright, F. V. *Anal. Chem.* **1989**, *61*, 905.
- Cline Love, L. J.; Habarta, J. G.; Dorsey, J. G. *Anal. Chem.* **1984**, *56*, 1132A.
- Georges, J.; Desmettre, S. J. *Colloid Interface Sci.* **1987**, *118*, 192.
- Levitz, P.; Van Damme, H. J. *Phys. Chem.* **1986**, *90*, 1302.
- Cases, J. M. *Bull. Mineral* **1979**, *102*, 684.
- Nelson, G.; Patonay, G.; Warner, I. M. *Appl. Spectrosc.* **1987**, *41*, 1235.

RECEIVED for review July 10, 1989. Accepted August 21, 1989.

Data Analysis in the Shot Noise Limit. 1. Single Parameter Estimation with Poisson and Normal Probability Density Functions

Stephen E. Bialkowski

Department of Chemistry and Biochemistry, Utah State University, Logan, Utah 84322-0300

This paper describes some of the basic statistics required to analyze data that has random variables distributed according to shot, or more appropriately quantum, noise statistics. This type of noise is described by the Poisson and normal distributions with parameters related to the parent binomial distribution. Both the Poisson and the normal distribution functions are analyzed in terms of the estimation results for analysis of replicate data from a single process. Analytical solutions for the parameter that best describes data obtained by replicate measurements are determined from joint distribution functions by the maximum likelihood method. Parameter estimation results are different for these two distributions. Maximum likelihood parameter estimation using the Poisson distribution yields results that are equivalent to the measurement mean obtained based on a normal distribution with constant variance. The normal distribution results in a quadratic equation for the single parameter that describes both the variance and the average. The maximum likelihood method with the joint Poisson distribution is also used to determine the parameter that best describes the mean of a random variable distributed according to an independent parameter.

INTRODUCTION

Shot noise is common in many instrumental methods of analysis (1). It is the limiting noise in all optical spectroscopy, mass spectrometry, and particle counting based methods of chemical analysis. It is particularly important in emission spectroscopy, absorption spectroscopy of optically dense samples, and light scattering with low background (2). Shot noise is characterized by a variance which is proportional to the mean value of the measurement. In the absence of background signal and electronic noise, shot noise is more technically called quantum noise, to reflect the fact that the source of this noise is the discrete nature of matter (2). In the small signal limit, the quantum noise is distributed according to the Poisson probability density function (PDF). The Poisson PDF is quite different than the normal distribution and procedures of data reduction based on normally distributed random variables do not in general yield statistically correct results for quantum noise limited data.

Unfortunately, there is not the variety of data reduction and signal processing schemes that there is for normally distributed data with constant variance. For example, a literature search of the complete Chemical Abstracts Service online database using "shot" with "noise" or "Poisson" with "statistics" keyword identifiers recently resulted in a total of only 92 citations, the majority of which have little to do with the methods for data analysis. By comparison, the key word "regression" resulted in 2652 citations. There is a need for data processing schemes that are valid for use on these limited data. But the statistics governing Poisson distributed data do not allow for easy solutions in L_2 -norm, i.e. square error based mathematics (3). The difficulty of the solutions, coupled

with what has been perceived to be a reluctance on the part of the analytical community to address the problems of statistics (4), has no doubt resulted in the lack of available schemes for reduction of quantum noise limited data.

Analysis of quantum noise limited data is not necessarily any more difficult than data with normally distributed random variables. In cases where only a single parameter is to be estimated, the most probable value of the sample average can be obtained by maximizing the probability of the Poisson distribution. More difficult problems arise when the data are a function of more than one parameter, for example, in data smoothing or multiple component estimation of spectra through regression. But even this is not necessarily a problem. If the analytical signal causing a variation in the count rate is much less than the sum of background and dark signals, e.g. transmission spectroscopy of optically thin samples, then the noise variance is practically constant, and conventional regression techniques based on L_2 -norm solutions are valid. However, in the absence of large background signals, e.g. emission spectroscopy, the variance is proportional to only the analytical signal, and conventional regression disregarding the variation in variance will not result in statistically valid parameter determinations.

In this paper, the basis for analysis of data with Poisson distributed random variables is shown. In the theory section, the basic mathematical statistics for treating quantum noise are reviewed along with some useful results for Poisson distributions. Subsequent analysis is applied to the determination of the sample average and simple functions.

THEORY

What is commonly referred to as noise is a fluctuation in a measurement value that ultimately arises as a consequence of the discrete nature of matter. Measurements based on the number of photons, ions, electrons, or other discrete species, will exhibit a variance or fluctuation from the mean of the measurements. When a parent population is sampled, the mean number of particles in each sampled element is sought. It is easy to see that if the parent mean is noninteger, then there must be fluctuations in the number of particles in the individual samples since the expectation value estimate must be based on the integer valued samples. In fact, the equation that describes the result of sampling populations of discrete items is the binomial PDF

$$P_n(k) = \binom{n}{k} p^k (1-p)^{n-k} \quad (1)$$

In this equation, $P_n(k)$ is the sum normalized function that gives the probability that a particle will be observed k times in n independent trials or measurements, and p , $0 < p < 1$, is the probability that the event will occur. Although the binomial PDF describes the outcomes of discrete events, that is integral number of measurements and particle counts, it is a function of a real continuous parameter, p . This parameter is the average over the parent population that one tries to estimate by several samples.

Although the binomial distribution is exact in describing particle counting statistics, it is a difficult equation to work

with. Approximations can be used in several cases of practical importance. One such approximation is given by the Poisson theorem. The Poisson theorem states that for the limiting cases where $p \rightarrow 0$ and $n \rightarrow \infty$, $np \rightarrow a$, and the binomial PDF is approximated by (5)

$$P(k|a) = e^{-a} a^k / k! \quad (2)$$

In the Poisson PDF, $P(k|a)$ is the normalized distribution giving the probability that an event will occur k times, k being an integer, from a distribution described by the parameter a . The number of measurements, n , and the probability, p , have been recast in terms of the parent population parameter a , where $a = np$. In this definition, a is a positive real number and so can be used to account for accumulation times in particle and photon counting measurements. The rate is often sought in the analytical measurement. Sampling of a continuous rate or Poisson process for a certain amount of time is usually accounted for by assigning parameter a to the product, λt , where λ is the rate of particle emission or photon flux, and t is the sample time (2, 5). Although the Poisson PDF is a function of one parameter, the rate can be obtained by dividing the total measurement in counts by the sample accumulation time. The Poisson PDF is correct for describing the statistics in quantum noise limited experiments since $n \rightarrow \infty$ for a continuously running event counter and a low particle count rate. The difference between the Poisson and the binomial PDF is insignificant in this limit (3, 6).

The binomial PDF may also be approximated by the normal distribution in the limit of $np(1-p) \gg 1$. Thus the normal distribution is valid in the limit where the number of particle counts is high. The parameters of the normal distribution, often given by the Gaussian (5)

$$P(y|a, \sigma) = 1/(\sigma\sqrt{2\pi})^{1/2} \exp[-(y-a)^2/2\sigma^2] \quad (3)$$

where y is used here to indicate a continuous value measurement and a and σ^2 are the mean and variance values of the parent population, respectively, are both related to the number of independent measurements or sample time and the parent probability or count rate. In this case the most probable value is $a = np$ and the variance is $\sigma^2 = np(1-p)$. In this limit, the measurement y can be thought of as continuous, and the PDF is normalized through integration over the continuous range of measurement values. When the binomial probability parameter is small such that $(1-p) \approx 1$, and for large n , then the normal PDF can be approximated as a function of only one parameter

$$P(y|a) = 1/(2\pi a)^{1/2} \exp[-(y-a)^2/2a] \quad (4)$$

As with the Poisson PDF, the parameters for the normal PDF can be related to the rate of event occurrence and the sample time. Assuming again a small p , both a and σ^2 are equal to λt . Finally, although both the Poisson and the normal PDF, as derived from the binomial distribution, are valid in their respective limits, the Poisson PDF is more general in that low and high count measurements are accurately described.

There are two situations where joint statistics are important in deriving useful expressions based on a PDF. The first is where replicate measurements of a given set of processes are taken and the second is used to describe the case where there are several independent process giving rise to the measurement data. Joint statistics for measurements of independent processes are obtained by taking the product of the individual PDF's. The total probability, P_{tot} , of obtaining a particular set of measurements is the product

$$P_{\text{tot}} = \prod_i P(k_i|a_i) \quad (5)$$

where each measurement has a probability of $P(k_i|a_i)$. When the processes are concurrent, then the PDF products must

be summed in a manner as to weight all of the ways that a given measurement can occur. Thus the total probability of obtaining a count of k from two Poisson processes with constant parameters a_1 and a_2 is the sum over all products such that $k = k_1 + k_2$

$$P(k|a_1 + a_2) = \sum_n P(k-n|a_1)P(n|a_2) \quad (6)$$

where n is the summation variable, yielding

$$P(k|a_1 + a_2) = \exp[-(a_1 + a_2)](a_1 + a_2)^k / k! \quad (7)$$

Equation 7 shows that the sum of two or more independent processes is described by a single Poisson PDF. This important result allows for the statistical analysis not only of experiments where there are several simultaneous Poisson processes but also of independent replicate measurements of a single process (5). The latter case occurs when two or more nonoverlapping time intervals are sampled and summed in order to estimate a single rate process. The difference between two or more processes does not result in a simple expression. The total probability for the difference of two Poisson processes such that $k = k_1 - k_2$ is

$$P(k|a_1 - a_2) = \exp[-(a_1 + a_2)] \sum_n a_1^{k+n} a_2^n / [(n+k)!n!] \quad (8)$$

This equation cannot be reduced to a form identical with the Poisson PDF since negative difference values are possible. Such an event cannot occur by physical processes since negative events are not possible in the physical realm. However, this joint PDF describes the data obtained when subtraction is used in data processing.

The PDF of the sum and differences of independent normal random variables is well-known (6). In this instance the sum or difference of two processes will result in a normal PDF. In particular, for $y = y_1 \pm y_2$

$$P(y|a_1 \pm a_2) = \exp[-(y - (a_1 \pm a_2))^2 / 2(a_1 + a_2)] / [2\pi(a_1 + a_2)]^{1/2} \quad (9)$$

Because of the relative simplicity of this PDF versus eq 8, describing the data by the normal distribution may be useful when difference data reduction procedures, such as background subtraction, are required.

The characteristics of quantum noise can be obtained from the Poisson PDF by determining the mean and variance of distribution (7). These values can also be obtained from the normal PDF approximation given in the limiting expression in eq 4. The mean and variance obtained from the Poisson PDF over the range of valid outcomes are equivalent. The mean, $\langle y \rangle$ or $\langle k \rangle$, and the variance, σ^2 , are both equal to a .

The fact that the signal variance is equal to the same parameter as the expectation value is a feature characteristic of not only quantum noise but shot noise in general (2). This variance is the same as that of the normal distribution approximation of the binomial PDF with $p = 0$. A final feature associated with shot noise is the white noise power spectrum. This is accounted for by the nature of a discrete event since the Fourier transform of a single event, or a delta function, is a constant independent of frequency (8).

EXPERIMENTAL SECTION

A standard pseudo-random-number generator with an uniform distribution between 0 and 1 was used to obtain the synthetic data. This pseudorandom generator required a "seed" integer to operate. Different seed values were used to generate independent samples. Since the pseudo-random-number generator had an isotropic distribution of returned values, the data were generated based on the binomial distribution. Binomial p and n parameters were used which would result in an a parameter in the normal and Poisson distributions. The p parameters were

0.01 or less and the a parameters ranged from 0.5 to 50. Each datum was generated in a routine that calls the pseudo-random-number generator n times. Within this routine, the data count was incremented for each returned value that was less than or equal to p . Data sets were obtained by calling this routine with different seed values. The data were found to be Poisson distributed. This was verified by generating several hundred data and comparing the subsequent data distribution to that of the Poisson PDF. Both first and second moments of the difference were tested by using a χ^2 test.

RESULTS AND DISCUSSION

The results obtained for the Poisson and normal distribution approximations to the binomial PDF are significantly different, especially in the limit of low counts. First, the Poisson PDF is not a continuous distribution in that it only predicts the probability of discrete, positive valued events, not fractional events. In contrast the normal PDF places a probability of measuring any real continuous value of y , positive or negative. Second, the Poisson PDF is a function of only one parameter, not two as in the normal PDF. The latter results in the difficult expression for the PDF of the difference of Poisson processes. And third, the Poisson probability distribution is not symmetrical about the most probable value, that being the mean of the parent population. In fact, because it is a discrete PDF of a real parameter, the most probable value may not be directly measurable.

The maximum likelihood method for parameter estimation based on the Poisson and normal PDF approximations of the binomial PDF is equivalent to that commonly used for normally distributed data with independent mean and variance. The difference here is that the variance in the normal distribution approximation, or the effective variance of the Poisson PDF approximation, are not independent of the parent population mean. Since distribution parameter, a , is continuous, the maximum likelihood value of this parameter which results in a particular data set can be obtained by maximization of the probability function with respect to this parameter. If N measurements, k_i , of a scalar parameter are obtained, then the total probability that the measurements were taken from a parent distribution with a given scalar distribution parameter is given by

$$P_{\text{tot}} = \prod_i P(k_i|a) \quad (10)$$

where each measurement probability is $P(k_i|a)$. The maximum likelihood estimate is obtained by maximizing the total probability with respect to a , or

$$dP_{\text{tot}}/da = 0 \quad (11)$$

For the Poisson PDF

$$dP_{\text{tot}}/da = -P_{\text{tot}} \sum_{i=1}^N (k_i/a_{\text{ml}} - 1) \quad (12a)$$

$$a_{\text{ml}} = \sum_{i=1}^N k_i / N \quad (12b)$$

where the subscript, ml, is used to indicate that maximum likelihood value. Since the PDF is itself a function of only one parameter, the results of eq 12b indicate not only the maximum likelihood rate-time product of the process but also the maximum likelihood variance of this process. This variance should not be confused with the certainty in the estimate of a_{ml} . It is interesting that the result obtained by using the Poisson PDF is equivalent to that of the minimization of a constant variance normal distribution in that the mean is the maximum likelihood value. This may not have been expected since the Poisson PDF is not symmetrical about the most probable value.

Performing the same steps on the normal distribution results in expressions that are slightly more complicated. It is

Table I. Comparison of Parameter Estimates Obtained by Assuming Poisson and Normal Distribution Functions for 100 Samples^a

Binomial Parameters; ^b $n = 500, p = 0.001$					
$a = 0.5$	set 1	set 2	set 3	set 4	set 5
Poisson estimate ^c	0.5041	0.5020	0.5016	0.5055	0.4961
RMS Poisson error ^d	0.06967	0.06737	0.06456	0.08215	0.06128
normal estimate ^e	0.5006	0.4958	0.5015	0.4990	0.4921
RMS normal error	0.08268	0.07605	0.07435	0.08039	0.07097
Binomial Parameters; $n = 500, p = 0.01$					
$a = 5$	set 1	set 2	set 3	set 4	set 5
Poisson estimate	5.021	4.986	5.004	4.984	5.014
RMS Poisson error	0.2181	0.2246	0.2239	0.2449	0.2501
normal estimate	5.015	4.986	4.992	4.969	4.999
RMS normal error	0.2329	0.2419	0.2353	0.2553	0.2581
Binomial Parameters; $n = 5000, p = 0.01$					
$a = 50$	set 1	set 2	set 3	set 4	set 5
Poisson estimate	49.91	49.84	49.98	49.82	49.88
RMS Poisson error	0.6399	0.6713	0.6794	0.6841	0.6753
normal estimate	49.88	49.83	49.97	49.80	49.89
RMS normal error	0.6516	0.6681	0.6859	0.6972	0.6790

^aEach data set used a different random number generator "seed" value. ^bThe data generated should follow the binomial distribution, eq 1. The corresponding distribution parameter is given as a . ^cUsing Equation 18b. ^dRMS errors are calculated from the sum of squared absolute errors. ^eUsing equation 20b.

easy to show that for the total probability given by the normal PDF

$$P_{\text{tot}} = (2\pi a)^{-N/2} \exp\left[-\sum_{i=1}^N (y_i - a)^2 / 2a\right] \quad (13)$$

maximization results in the quadratic equation

$$a_{\text{ml}}^2 + a_{\text{ml}} - \sum_{i=1}^N y_i^2 / N = 0 \quad (14a)$$

for which

$$a_{\text{ml}} = -(1/2) + [(1/4) + \sum_{i=1}^N y_i^2 / N]^{1/2} \quad (14b)$$

Thus contrary to what one might predict, maximization of the total probability of the normal PDF of eq 4 does not result in the mean being the maximum likelihood value. It is interesting to note that for large y_i , eq 14 may be approximated by

$$a_{\text{ml}} \approx (\sum_{i=1}^N y_i^2)^{1/2} / N \quad (15)$$

Minimization of only the exponential part of the normal PDF, typical of maximum likelihood methods, also results in eq 15. However, exponential minimization is not valid in this case since the variance is equal to the parent mean. The reason of the discrepancy between eq 12 and 15 is not clear since they are both derived from the same parent distribution and have the same mean and variance.

A comparison of the two estimation equations based on the Poisson and normal PDF's is given in Table I. These data were generated using a pseudo-random-number generator and binomial p and n parameters as described in the Experimental Section. The a parameters are obtained from the product $a = pn$. The same data sets were used to calculate the normal and Poisson parameter estimates. Most striking is that the two different estimation equations give different, and ap-

parently independent, estimates of the a parameter. The independence is apparent since there is no trend for the Poisson estimate to be low if the normal estimate is low, or vice versa. However, maximum likelihood equations for both distributions seem to give accurate estimates of the a parameter. The root mean square (RMS) noise was calculated as the square root of the average squared absolute error since the a parameters were known. Each data set consisted of 100 independent synthetic measurements. The RMS error does in fact decrease as the inverse square root of the number of independent measurements, *vide infra*.

Another interesting case is for data that are dependent on another variable, for example, in the case of an emission spectrum. When the data are a function of an independent variable, x , such that the measurement k is described as the product of a magnitude, a , and an invariant function, $f(x)$, then

$$P(k_i|a) = [(af(x_i))^{k_i} e^{-af(x_i)}] / k_i! \quad (16)$$

The maximum likelihood parameter is again obtained by maximizing the total probability

$$dP_{\text{tot}}/da = -P_{\text{tot}} \sum_{i=1}^N (k_i/a - f(x_i)) \quad (17a)$$

$$a_{\text{ml}} = \sum_{i=1}^N k_i / \sum_{i=1}^N f(x_i) \quad (17b)$$

This expression shows that the most likely parameter is directly proportional to the sum of the individual k_i distributed according to the independent parameter. The sum over x_i is a constant. This somewhat curious result has previously been shown by Poston and Harris (9) starting with results of a weighted least-squares solution of a normal PDF then using propagation of errors and also by Bialkowski (10) using weighted optimal correlation filtering (11). An intuitive explanation for this result is straightforward. Since there is only one process giving rise to the distributed data, the best estimate of the process occurs when all possible data are collected. A practical example of this would be in the case of an emission spectrum where only one element is given rise to the spectrum. Clearly, the best possible data collection would be one where every photon is collected, independent of the particular state giving rise to the emission (10).

The fact that the weighted least-squares (9) and optimal correlation filter (10, 11) methods both yield the results which are equivalent to those obtained by starting with Poisson PDF is worth examination. In both cases, the variance of the normal distribution was assumed to be constant in terms of the differentiation required for probability maximization yet proportional to the parameter thereby estimated. That is, the maximum likelihood parameter was determined by assuming an independent variance, then the variance was equated to the maximized parameter for purposes of obtaining a weighted average. With respect to Equation 4, this is not a valid assumption. The reason why this method works can be seen from the results of maximum likelihood parameter estimation based on the Poisson PDF. Starting with eq 3, that for a general normal distribution, and maximizing with respect to the constant parameter, a , for a measurement dependent variance, the usual weighted least-squares equation can be obtained

$$dP_{\text{tot}}/da = -P_{\text{tot}} \sum_{i=1}^N (y_i - a) / \sigma_i^2 \quad (18a)$$

$$\sum_{i=1}^N y_i / \sigma_i^2 = a \sum_{i=1}^N 1 / \sigma_i^2 \quad (18b)$$

The comparison of eq 12a to 18a shows that they are equivalent if $\sigma_i^2 = a$, which is in fact the result obtained for the variance. In effect, it turns out that this method works only

because it is equivalent to the result obtained from the Poisson PDF, not because it is valid to assume the variance independence until after the maximization step! And although not shown here (12), this equivalence will result in solutions to Poisson probability distribution parameter maximization even for more complex models. Simply stated, *inverse function weighted least-squares solutions are valid for data with Poisson distributed data in the quantum noise limit.*

To conclude the discussion on function magnitude estimation and as a final comparison of the two different probability distributions, consider again the case where the data set has the functional relationship, $y = af(x)$. The total probability for the normal distribution is

$$P_{\text{tot}} = (2\pi a)^{-N/2} \exp\{-\sum_{i=1}^N [y_i - af(x_i)]^2 / 2af(x_i)\} \prod_{i=1}^N [1 / (f(x_i))]^{1/2} \quad (19)$$

In this case, maximizing the total probability with respect to the parameter does not result in the correct equation. The reader may wish to prove this by setting the derivative of the total probability to zero and solving the resulting equations. However, a_{ml} may also be found by minimizing the exponent part of eq 19. This results in the equation for the square estimated parameter

$$a_{\text{ml}}^2 = \sum_{i=1}^N y_i^2 / f(x_i) / \sum_{i=1}^N f(x_i) \quad (20)$$

In this instance it is easier to compare the Poisson to the normal PDF solutions. The similarity between the latter and eq 17b is apparent when one considers that by definition, $y_i/f(x_i) \approx a$. However, eq 20 is much less stable in that zeros in $f(x_i)$ will result in a singularity in the upper sum.

Finally, the standard deviation in the estimate of a_{ml} may be obtained from the usual Student t equation relating the estimate to the number of independent measurements and the variance (7). The standard deviation of the estimate will decrease as $N^{1/2}$. This can also be seen from the joint statistics. For N measurements, k_i , obtained such that $k = \sum k_i$, the total probability that the measurements result in k were taken from a parent population with a scalar value, a , is given by the convolution of the N individual PDF. Extending eq 5 and 6 to the case of N nonoverlapping measurements

$$P(k|Na) = P(k_1|a) * P(k_2|a) * P(k_3|a) \dots P(k_N|a) \quad (21a)$$

$$P(k|Na) = \exp[-Na] (Na)^k / k! \quad (21b)$$

where the individual measurement probabilities are the $P(k_i|a)$ and * is the discrete convolution given in eq 5. The maximum likelihood parameter is again obtained by maximizing the total probability with respect to a

$$a_{\text{ml}} = k / N \quad (22)$$

Thus the relative standard deviation defined as the ratio of the standard deviation to the estimate will decrease as $1/N^{1/2}$. This result is equivalent to that which would be obtained with a larger sample or longer sampling time. The relative standard deviation is in fact inversely proportional to the square root of the total number of events, independent of whether the data are obtained as one sample or in several replicate measurements. This inverse root relationship is apparent in the data given in Table I. Since each set was comprised of 100 dependent data, there should be an improvement to the parameter estimation precision of 10. So that the RMS error should be approximately equal to $0.1a^{1/2}$. Inspection of the calculated error values in Table I will confirm this feature of the shot noise data.

In summary, the equations in this paper have illustrated the procedures for parameter estimation by using the Poisson

and normal PDF's for quantum noise limited data. It was shown that the maximum likelihood method yields the mean as being the most likely parameter for single valued data for the Poisson distribution but a quadratic function when starting with the normal PDF. The certainty of the parameter estimate increases in the same fashion as does the signal to noise ratio for quantum noise data. That is, the greater the number of independent measurements or the longer the signal averaging time, the greater will be the signal to noise ratio of the result. Assuming that the binomial random variable converges to a standard normal distribution results in estimates which are not equivalent to those assuming the Poisson distribution limit. Subsequently, great care must be taken in using the normal equations to ensure that the results obtained are valid in the equivalent Poisson distribution.

ACKNOWLEDGMENT

The author is indebted to the unknown reviewer who through criticisms, constructive comments, and careful proofreading has no doubt increased the quality and readability of the paper.

LITERATURE CITED

- (1) Skoog, D. A. *Principles of Instrumental Analysis*, 3rd ed.; Saunders College Publishing: New York, 1985.
- (2) Ingle, J. D.; Crouch, S. R. *Spectrochemical Analysis*; Prentice-Hall: Englewood Cliffs, NJ, 1988; Chapter 5.
- (3) Luenberger, D. G. *Optimization by Vector Space Methods*; John Wiley & Sons: New York, 1969; Chapters 2 & 5.
- (4) Workman, J.; Mark, H. *Spectroscopy* 1988, 3, 41-43.
- (5) Papoulis, A. *Probability, Random Variables, and Stochastic Processes*, 2nd ed.; McGraw-Hill: New York, 1984; Chapter 3.
- (6) Foster, J.; Kouris, K.; Matthews, I. P.; Spyrou, N. M. *Nuclear Instrum. Methods* 1983, 212, 301-305.
- (7) Papoulis, A. *Probability, Random Variables, and Stochastic Processes*, 2nd ed.; McGraw-Hill: New York, 1984; Chapter 7.
- (8) Papoulis, A. *Probability, Random Variables, and Stochastic Processes*, 2nd ed.; McGraw-Hill: New York, 1984; Chapter 12-3.
- (9) Poston, P. E.; Harris, J. M. *Anal. Chem.* 1987, 59, 1620-1626.
- (10) Bialkowski, S. E. *Appl. Spectrosc.* 1988, 42, 807-811.
- (11) Bialkowski, S. E. *Rev. Sci. Instrum.* 1987, 58, 687-695.
- (12) Bialkowski, S. E. *Anal. Chem.*, following paper in this issue.

RECEIVED for review December 1, 1988. Revised manuscript received May 3, 1989. Accepted August 24, 1989. Support for this work by CHE-8520050 awarded by the National Science Foundation is gratefully acknowledged.

Data Analysis in the Shot Noise Limit. 2. Methods for Data Regression

Stephen E. Bialkowski

Department of Chemistry and Biochemistry, Utah State University, Logan, Utah 84322-0300

The equations for multiple parameter estimation are found by applying the method of maximum likelihood to Bayes' theorem probability distribution for data obtained in the shot noise limit. Bayes' theorem limits the estimates by the a priori probability restricting the Poisson distribution parameters to be positive. Bayes' theorem is applied prior to formulation of the total probability. Subsequent application of the maximum likelihood method results in nonlinear equations describing the coefficients for the independent processes. The main innovation of these equations over the usual minimum covariance ones is that there is an additional term which can take on real values such that the solution is obtained within the bounds prescribed by the Bayes probability. It is reasoned that by the presence of this term, the simultaneous equations for the maximum likelihood estimates will be independent of regressors which would yield negative parameters by their inclusion in the basis set. Three methods for coefficient estimation based on these nonlinear equations using conventional matrix methods are tested on synthetic data. It is found that the row-weighted least-squares equations do not perform as well as does a direct interpolation solution of the governing equations.

INTRODUCTION

Shot or quantum noise limited data is quite common in many instrumental methods (1, 2). Analysis of data obtained in this limit requires methods that are quite different than those used to treat "white" noise limited data. White noise limited data are characterized by constant, normally distributed errors. Since the data have constant errors, mathematical treatments can be greatly simplified. On the other hand, shot

noise limited data have errors that are related to the magnitude of the measurement and so cannot be neglected. The shot noise limited measurement is precisely described by the binomial probability density function (PDF). However, for describing the statistics of a "rate of particle emission", or more simply, Poisson processes, it is more convenient to use either a Poisson PDF or a normal PDF where the mean and variance of the parent population are equal (3, 4). The Poisson PDF is valid when the particle emission rate is low while the normal PDF is valid in the limit of high total counts. The differences between the binomial and the approximate PDF's are insignificant in their respective limits. And although the two approximate distributions are different in their mathematical form, both are functions of a single parent population parameter and both have the same expectation and variance values (3, 4). This single parameter is equal to the product of the sample time with the emission rate.

In another paper, the procedure for single parameter estimation based on the maximum likelihood (ML) method for shot noise limited data was examined (4). The first step in this procedure was to find the joint or total probability for replicate measurements of a single Poisson process. Starting with either the Poisson or the normal PDF, it was shown that summing the replicate measurements results in a total probability that is itself either Poisson or normally distributed with only one parameter. The next procedural step was to find the ML parent population parameter. In this step, different results for the ML estimate of the parent population parameter were found for the Poisson and normal PDF's. Interestingly enough, both estimates were accurate though apparently independent.

Since the mean and variance are equivalent in shot noise limited data, it is often assumed that least-squares error (LS) data reduction can be accomplished by inverse weighting by

the data itself (5). However, by inspection of the equations leading to the ML estimate, it was shown that the ML estimate obtained from the Poisson PDF was equivalent to the row-weighted LS (WLS) solution were the inverse weights are equal to the estimate itself (4-6). Thus the minimum-covariance, linear unbiased estimate, herein called general least square (GLS), is in fact valid for shot noise limited data (7). But it can be used only if an a priori error distribution is known. Implicit in using WLS and GLS is that the mean and nonstationary variance of a normal PDF are independent. This assumption is not strictly valid for shot noise. A single parameter describes the effective mean and variance in a Poisson processes. In this light, it is almost ironic that the ML result for Poisson distributed data is equivalent to an LS solution derived by using normal statistics, with independent mean and variance assumptions. Moreover, it was shown that ML parameter estimation for the normal PDF representation of the shot noise limited data results in equations which bear no relationship to conventional LS, and that could fail to yield feasible results (4).

In this paper, methods for obtaining parameter estimates from shot noise limited data obtained from data that are a sum of simultaneous Poisson processes are examined. This is a much more difficult task than single parameter estimation in that simultaneous, nonlinear equations must be solved. Another complication is that in an attempt to regress the data by a linear combination of functions (5-7), zero probability solutions can often occur. These zero probability solutions are indicated by negative coefficients in the linear combinations. This complication is addressed by using Bayes' theorem (3) probability with an a priori probability density function for the coefficients which restricts them to being positive valued. The individual measurement PDF's are restricted through the use of Bayes' theorem prior to formulation of the total probability. Rather than using the Bayes estimate, which would require finding the maximum of the total Bayes' probability, the ML method is applied to the total probability obtained as the product of the individual Bayes' PDF's.

As was the case for the single parameter estimates, this method results in equations that are related to the normal equations derived in LS analysis. The results obtained by using the Poisson PDF imply that a LS solution, where the weights are iteratively updated according to previous parameter estimates, could converge to the correct solution. Three related solutions to this regression problem are explored (5-7). The first is the conventional WLS with iterative improvement to the row weight matrix (5, 6). The second method is based on the GLS estimation technique of Paige (8, 9). Again, this method utilizes iterative improvement to the row weight matrix based on the current estimate of the variance. However, row weight singularity problems are avoided by using total orthogonal basis set expansion. The last method is based on direct calculation of the ML parameter estimates obtained directly from the PDF's. The parameters are determined by using a method similar to the method of steepest descent used for nonlinear parameter estimation in LS problems (5).

THEORY

Consider data that is described by a linear combination of three functions of an independent variable, x , such that $y = a_1f_1(x) + a_2f_2(x) + a_3f_3(x)$. Since the sum of Poisson processes is itself a Poisson process (3, 4), this functional representation of the data could represent three independent Poisson processes or one process that is itself a function of three parameters. In either case the PDF is

$$P(y_i|a_1, a_2, a_3) = [F(x_i)]^{y_i} e^{-F(x_i)} / y_i! \quad (1)$$

where the index i ranges over the N individual (x_i, y_i) measurements and $F(x_i) = a_1f_1(x_i) + a_2f_2(x_i) + a_3f_3(x_i)$ has been

substituted for brevity. Restricting the derivations to the case of a sum of three distinct processes, the range of the coefficients, a_j , must also be restricted to that which is valid for the Poisson distribution, that being $a_j \geq 0$ for each j . This restriction constitutes a "prior knowledge" of the coefficients and is easily treated by Bayes' theorem (3, 7). The Bayes' theorem result is

$$P(a_1, a_2, a_3 | y_i) = P(y_i | a_1, a_2, a_3) P(a_1, a_2, a_3) / P(y_i) \quad (2)$$

where $P(a_1, a_2, a_3)$ is the prior probability of the coefficients and $P(y_i)$ is the probability that the y_i is obtained. The $P(y_i)$ is essentially a normalization factor that does not influence the ML results since it is independent of the coefficients. For the present case, the total probability is first obtained from the individual ones in eq 1

$$P_{\text{tot}}(y|a_1, a_2, a_3) = \prod_{i=1}^N P(y_i | a_1, a_2, a_3) \quad (3)$$

and Bayes' theorem probability is subsequently formulated from the measurement set. Thus

$$P_{\text{tot}}(a_1, a_2, a_3 | y) = P_{\text{tot}}(y | a_1, a_2, a_3) U(a_1) U(a_2) U(a_3) / P(y) \quad (3)$$

where the $U(a_j)$ is the unit step function. The latter limits the range of possible a_j . The total probability for the set of measurements is the product of the N individual PDF's.

The derivative of the total probability with respect to the individual parameters results in the equations

$$dP_{\text{tot}}(a_1, a_2, a_3 | y) / da_1 = P_{\text{tot}}(a_1, a_2, a_3 | y) \left\{ \sum_{i=1}^N f_1(x_i) [y_i / F(x_i) - 1] + \delta(a_1) / U(a_1) \right\} \quad (5a)$$

$$dP_{\text{tot}}(a_1, a_2, a_3 | y) / da_2 = P_{\text{tot}}(a_1, a_2, a_3 | y) \left\{ \sum_{i=1}^N f_2(x_i) [y_i / F(x_i) - 1] + \delta(a_2) / U(a_2) \right\} \quad (5b)$$

$$dP_{\text{tot}}(a_1, a_2, a_3 | y) / da_3 = P_{\text{tot}}(a_1, a_2, a_3 | y) \left\{ \sum_{i=1}^N f_3(x_i) [y_i / F(x_i) - 1] + \delta(a_3) / U(a_3) \right\} \quad (5c)$$

where the $\delta(a_j)$ are delta functions. These yield the ML estimates when the results are zero since the PDF has a zero slope at the most probable value. When put into a form similar to the normal equations used in LS

$$\sum_{i=1}^N \{f_1(x_i) [y_i - F(x_i)] / F(x_i)\} + \delta(a_1) / U(a_1) = 0 \quad (6a)$$

$$\sum_{i=1}^N \{f_2(x_i) [y_i - F(x_i)] / F(x_i)\} + \delta(a_2) / U(a_2) = 0 \quad (6b)$$

$$\sum_{i=1}^N \{f_3(x_i) [y_i - F(x_i)] / F(x_i)\} + \delta(a_3) / U(a_3) = 0 \quad (6c)$$

Clearly, the simplicity of the previous equations for single parameter estimation is lost in this higher order functional form of the data (4). But the feature of an inverse function weighting of residuals is common to both single and multiple parameter equations. These equations do not allow for a direct solution since they are not linear in the coefficients and they contain a sequential division of vectors.

Equation 6 is further complicated by the ill-defined functions. The delta function is zero everywhere but at zero, where it takes an infinite, definite value (10). The unit step function is unity for all positive values of the argument, is not defined at zero, and is zero for negative values. For a_j coefficient values greater than zero, the ratios on the left-hand side of eq 6 are zero, and the equations reduce to those of weighted LS. The

problem then occurs at the most critical point, that being as a coefficient approaches zero. Examination of the behavior of this ill-defined function ratio in the limit as the argument approaches zero may be performed by using Fourier transform methods (10). However, this is not necessary in this case. It is easy to see that the ratio serves to restrict the a_j coefficient to a positive or zero value and that the value of the ratio will take on some real positive value as the argument approaches zero. Thus the components to eq 6 may be summarized by two conditions

$$\sum_{i=1}^N \{f_j(x_i)[y_i - F(x_i)]/F(x_i)\} = 0 \quad a_j > 0 \quad (7a)$$

$$\sum_{i=1}^N \{f_j(x_i)[y_i - F(x_i)]/F(x_i)\} + \rho = 0 \quad a_j = 0 \quad (7b)$$

where ρ is that positive real number that satisfies eq 7b.

The above is more of a statement than it is an algebraic equation. Although the numerical value for ρ can be found, it may not be necessary to do so in practice. If an a_j has a tendency to be negative, and so eq 7b is solved, the resulting a_j is always zero. Consequently, the equations for the nonzero coefficients become independent of the zero a_j since $F(x_i)$ is a linear combination. Thus a solution to eq 6 may be found simply by first assuming that eq 7a is satisfied. If it is not, that is, if an a_j is less than zero, then the associated basis function is removed from the basis set, and a new solution is found for the reduced basis. This two-step procedure has been tested and appears to be equivalent to finding the solution of eq 6 with the implication of eq 7 for small basis sets. For large basis set calculations, it may in fact be easier to solve eq 6 for reasons discussed below.

To show the connection to the WLS solution, Equation 6 is cast in matrix notation. Defining y_i as the data vector, \mathbf{y} , the a_j coefficients as the vector, \mathbf{a} , and the column matrix of basis regressors as $\mathbf{F} = [f_1(x_i), f_2(x_i), f_3(x_i), \dots]$, eq 6 and 7 can be rewritten in a generalized form as

$$\mathbf{F}^T \mathbf{W}^{-1} \mathbf{y} = \mathbf{F}^T \mathbf{W}^{-1} \mathbf{F} (\mathbf{a} + \mathbf{r}) \quad (8)$$

where superscript T is the transpose and \mathbf{W} is the row weight matrix defined below. The latter is a common equation in row-weighted LS with the exception of the additional vector, \mathbf{r} , which is equal to $(\mathbf{F}^T \mathbf{W}^{-1} \mathbf{F})^{-1} \rho$ in eq 7. Incorporating ρ in this fashion makes it easy to see how one would determine that value which makes the coefficient positive. The r_j are zero if the corresponding a_j is positive. If the solution to eq 8 is such that $a_j + r_j$ is negative, then the r_j is equal to that solution, and the a_j is zero. The row weight matrix is defined by

$$\mathbf{W} = \text{diag}\{\mathbf{F}\mathbf{a}\} \quad (9)$$

where $\text{diag}\{\}$ indicates that a diagonal matrix is formed from the vector argument. The nature of the problem is now apparent. The inverse \mathbf{W} matrix is a function of the parameters to be estimated. But it is not a linear function in the sense that there is no simple vector-matrix operation that can be used to express \mathbf{W} . Subsequently, the parameters cannot be estimated directly.

Equation 8 is equivalent to that obtained for the conventional row-weighted LS problem (6). This may be stated as

$$\text{minimize} \|\mathbf{B}^{-1}(\mathbf{F}(\mathbf{a} + \mathbf{r}) - \mathbf{y})\|_2 \quad (10a)$$

where

$$\mathbf{W} = \mathbf{B}^T \mathbf{B} \quad (10b)$$

defines \mathbf{B} . The variance matrix, \mathbf{W} , must be positive definite in order to obtain \mathbf{B} . This too is ensured by incorporating \mathbf{r} . One solution to eq 10 is to set $\mathbf{F}' = \mathbf{B}^{-1} \mathbf{F}$ and $\mathbf{y}' = \mathbf{B}^{-1} \mathbf{y}$, and solve for the p2-norm minimum

$$\text{minimize} \|\mathbf{F}'(\mathbf{a} + \mathbf{r}) - \mathbf{y}'\|_2 \quad (11)$$

which results in the linear equation

$$\mathbf{a} + \mathbf{r} = (\mathbf{F}'^T \mathbf{F}')^{-1} \mathbf{y}' \quad (12)$$

Since the \mathbf{F}' and \mathbf{y}' are dependent on \mathbf{a} , the final solution must be found through iterative methods. One such method is to iteratively update \mathbf{F}' and \mathbf{y}' based on the previous solution for \mathbf{a} from eq 12, until \mathbf{a} , and therefore \mathbf{B} , no longer changes. The first solution to this iterative method is the LS solution.

A more numerically stable method is to use the GLS solution prescribed by Paige (8, 9) and Golub and Van Loan (6). The solution to the problem in eq 10 is recast to minimize $\mathbf{v}^T \mathbf{v}$, subject to $\mathbf{y} = \mathbf{F}(\mathbf{a} + \mathbf{r}) + \mathbf{B}\mathbf{v}$, where the errors are given by the vector, \mathbf{v} . Assuming that the a_j have been shown to be positive

$$\mathbf{a} = \mathbf{a}_{LS} - \mathbf{R}^{-1} \mathbf{Q}_1^T \mathbf{B} \mathbf{P} \mathbf{S}^{-1} \mathbf{Q}_2^T \mathbf{y} \quad (13)$$

where \mathbf{a}_{LS} is the normal LS solution, \mathbf{Q} and \mathbf{R} are the full orthogonal factorization of \mathbf{F} such that $\text{rank}\{\mathbf{Q}_1\} = \text{rank}\{\mathbf{F}\}$, and \mathbf{Q}_2 is the extended basis. Matrices \mathbf{P} and \mathbf{S} are defined such that

$$\mathbf{Q}_2^T \mathbf{B} \mathbf{P} = [0, \mathbf{S}] \quad \mathbf{P} = [\mathbf{P}_1, \mathbf{P}_2] \quad (14)$$

where $\text{rank}\{\mathbf{P}_2\}$ and $\text{rank}\{\mathbf{S}\}$ are equal to $\text{rank}\{\mathbf{Q}_2\}$. Again, the solution must be iteratively updated based on the previous solution. But here, the inverse of \mathbf{B} does not have to be taken, thus avoiding problems with zero's in the variance matrix \mathbf{W} . The disadvantage is that full rank \mathbf{Q} and \mathbf{P} matrices must be calculated. Subsequently, this method is practical only for small data sets. And since \mathbf{B} , \mathbf{P} , and \mathbf{S} must all be updated with each iteration, the time required to obtain the final solution could be prohibitively long.

The steepest descent approach may be formulated based on the errors generated from the current estimates using the equation which is to be solved. Again assuming that all coefficients are positive, the error for the coefficients in eq 6 is

$$\epsilon_1 = \sum [f_1(x_i) y_i / F(x_i)] - \sum f_1(x_i) \quad (15a)$$

$$\epsilon_2 = \sum [f_2(x_i) y_i / F(x_i)] - \sum f_2(x_i) \quad (15b)$$

$$\epsilon_3 = \sum [f_3(x_i) y_i / F(x_i)] - \sum f_3(x_i) \quad (15c)$$

From this system of equations an error variation matrix can be derived such that

$$\epsilon' = \begin{bmatrix} d\epsilon_1/da_1 & d\epsilon_1/da_2 & d\epsilon_1/da_3 \\ d\epsilon_2/da_1 & d\epsilon_2/da_2 & d\epsilon_2/da_3 \\ d\epsilon_3/da_1 & d\epsilon_3/da_2 & d\epsilon_3/da_3 \end{bmatrix} \quad (16)$$

The update to the most recent set of parameters is calculated from the inverse and the error

$$\mathbf{a}' = -(\epsilon')^{-1} \epsilon \quad (17)$$

and a new vector is calculated from the past vector as the update $\mathbf{a} + \mathbf{a}'$. In practice, some fraction of the update vector may be added on each iteration as in the Marquardt algorithm (7). While this slows down convergence, it results in more stable calculations. In the event that a coefficient is negative, then the function corresponding to negative coefficient must be removed from the basis in order to avoid error matrix inversion problems. This approach has been verified by subsequently calculating the positive real value of eq 7b and using this value in a modified error similar to eq 15.

EXPERIMENTAL SECTION

The computer codes for the three methods of parameter estimation, WLS, GLS, and direct, were written in Borland's Turbo C version 1.1. The WLS program was based on the QR decom-

position method (6). The GLS and direct programs were coded as shown in the theory section. All calculations were performed in double precision using a 20-MHz clock speed 80386/80387 "AT" type computer. A library of software functions for matrix and vector mathematics was written and linked into the compiled main routine prior to run time in order to facilitate program development and to ensure that all three methods used similar code. Performance was evaluated by the estimation accuracy, the ability to converge to the solution predicted by the PDF, and time or iterations required to obtain a solution to within a given calculation precision limit. The calculation limit was based on the errors given in eq 15. For this purpose, the individual function-parameter errors were summed as absolute values. The convergence limit was set to 0.0001% of the LS solution error for all cases reported here.

Performance parameters were normally evaluated based on 100 synthetic data sets. The same data sets were used to test each method. Accuracy for each data set was calculated as the difference between parameters input to the Poisson distribution generating routine described below and the parameters estimated by the particular method. The accuracy over several data sets was accumulated as the squared error and reported as the root mean square (RMS) value. Several rules were used to indicate an inability of a particular to converge. The main rule was that the calculations had to converge in under 100 iterations for GLS and WLS. For the direct method, the calculations had to converge in under 100 with the current error correction update factor. Starting with an update factor of 1, the latter factor was decreased by 50% each time a calculation did not converge in 100 iterations. Other rules for failure conditions were dependent on the particular method. For example, not being able to take a matrix inverse or a convergence "stalled" at a given error. Parameter estimation convergence times were determined by C function calls to the operating system (MS-DOS). The minimum time that could be distinguished was 0.054 s but averages over several data sets allow more precise comparison.

Test data were generated based on linear combinations of normalized power series functions and synthetic spectra. Spectra were calculated based on tables of atomic emission lines. The same functions were used as both the basis set and the test data. The test data were synthesized by using the pseudo-random-number generator based binomial distribution function described in the previous paper (4). The linear combinations were used as a probability, scaled to have a maximum probability of less than 0.01. The binomial PDF generator was called multiple times in order to obtain data accurately described by the Poisson PDF. Two random numbers were generated for each subsample. One random number was used to locate the position along the x coordinate while the second was tested against the probability level of the linear combination of functions/spectra. If the random number was less than the probability level, then a "count" was added to that channel. Thus the synthetic data emulated an energy dispersive particle counting, multichannel averaging experiment. The counting operation was terminated after a specified number of subsamples were taken.

Evaluations tests were performed on data sets generated with the same linear combination of vectors but with different random number generator "seed" values. Different seed values resulted in the calculation of independent data sets based on the same parent population parameters. For purposes of calculating accuracies, the parent population parameters were determined based on the combination weights, the maximum probability, and the total number of subsamples per data set.

RESULTS AND DISCUSSION

A comparison of the three methods for shot noise limited data processing discussed in the theory section are compared to conventional LS in Tables I-III. The basis for these data was a normalized power series

$$F(x_i) = a_1/50 + a_2x_i/1125 + a_3x_i^2/40425 \quad (18)$$

where the constant in the denominator of each term is the normalization. The length of x was 50, with a range from 0 to 49. Thus each data set consisted of 50 separate "channels". Each entry in the table represents 100 trials where each trial

Table I. Comparison of Conventional Least Squares and Three Methods of Regression of High Magnitude Data^a with Poisson Distributed Errors in Terms of Execution Times and Results for Using a Three-Parameter Power Series Model^b

	time ^c	a_1	a_2	a_3
LS ^d	0.019	1009 (102) ^e	989 (321)	1001 (234)
WLS(4)	0.208	1009 (101)	990 (303)	1001 (220)
GLS(4)	49.34	1009 (101)	990 (303)	1001 (220)
Direct(2)	0.144	1009 (101)	990 (303)	1001 (219)

^aTotal count number was 3000 for each of 100 data sets. ^bEach data set was 50 data (x, y) pairs. The normalized power series, $y = a_1/50 + a_2x/1125 + a_3x^2/40425$, was used. Convergence was to 0.0001% of the LS error. ^cExecution times are the average per trial given in seconds and averaged over the 100 trials. ^dMethods are as follows: LS, conventional least squares; WLS, weighted least squares; GLS, general least squares; Direct, direct interpolation by steepest descent. ^eResults are averages over 100 trials. The RMS errors are in parentheses.

Table II. Comparison of Conventional Least Squares and Three Methods of Regression of Low Magnitude Data^a

	time	failures ^b	a_1	a_2	a_3
LS	0.019		34.7 (18.2) ^c	27.8 (58.8)	36.6 (44.8)
WLS ^d (13)	0.514	2	33.1 (12.6)	32.1 (30.1)	34.0 (24.1)
GLS(12)	136.0	0	33.1 (12.4)	32.0 (29.9)	34.0 (24.1)
Direct(5)	0.227	0	32.5 (13.7)	33.3 (32.0)	33.3 (24.5)

^aTotal count was 100 for each data set. Theoretical coefficients were all 33.3. ^bFailure to converge with correct weights to an error of 0.0001% of error of the LS calculation. ^cResults are averages over 100 trials. The RMS errors are in parentheses. ^dResults include failures.

Table III. Comparison of Least-Squares and Poisson Regression for Low Magnitude Data with a Low Constant^a

	time	failures ^b	a_1	a_2	a_3
LS	0.019		9.5 (36.4) ^c	231.5 (143.4)	258.1 (115.3)
WLS ^d (26)	0.862	63	6.8 (12.6)	241.6 (67.6)	250.7 (65.7)
GLS(23)	199.0	18	6.3 (12.5)	244.4 (69.1)	248.6 (66.8)
Direct(7)	0.323	0	5.8 (12.3)	244.9 (67.3)	248.4 (65.6)

^aTotal count was 500 for each data set. Theoretical coefficients for the power series were $a_1 = 2.5$, $a_2 = 248.75$, and $a_3 = 248.75$. ^bFailure to converge with correct weights to an error of 0.0001% of the LS error. ^cResults are averages over 100 trials. The RMS errors are in parentheses. Results include those which failed. ^dOf the total of 63 failures, only 18 were due to convergence failure. The balance were indicated as errors due to the addition of a small offset to avoid division by zero.

was for a different data set generated from the same basis, but with a different random number sequence. The average number of event counts is listed at the bottom of each table. For example, the average event counts for the data of Table I was 3000. And so each of the coefficients is, on the average, equal to 1000. The average coefficients determined by the particular methods are listed along with their respective errors. Using the average to represent the coefficient is correct in Poisson statistics (4). The errors were calculated as the RMS value of the theoretical less that value determined by the method.

For the high count data summarized in Table I, there is little difference between the LS and Poisson statistical methods. The average coefficient values are nearly the same for all four methods and, in particular, are exactly the same for the three Poisson statistical methods. However, the RMS errors for the Poisson statistical methods are significantly

lower than those of LS. With all methods, the RMS errors reflect the factor of 10 signal to noise ratio improvement obtained in averaging over the 100 trials. The most significant difference between the three Poisson statistical methods is in the average time required for the regression to converge. The factor of 30 or so in time for the GLS routine is no doubt due to orthogonalization and basis set expansion calculations that must be performed iteratively.

WLS is perhaps the easiest method to adapt to numerical processing of shot noise limited data (5, 6). In this method, both the regressor and measurement data are weighted inverse to the second moment of the Poisson PDF prior to performing LS regression. But while the row weight methods may be appealing in that common regression procedures can be utilized, there are some problems that can arise. In particular, there is always a computational problem when there are zeros in the estimated function describing the data. If a zero occurs in this estimation, then the weight matrix, being the square root of the inverse, cannot be calculated, and the WLS calculation fails.

This zero inverse weight matrix failure problem is apparent in the data summarized in Table II. These data are similar to those of Table I, but with only 100 counts per data set. For these low count data, the WLS method failed because the estimated data vector contained zeros. Since the basis set was essentially a quadratic equation restricted to positive coefficients, this zero inverse weight condition occurs when the a_1 coefficient is zero. Removal of the constant $f_1(x)$ from the basis could not help since the range of x was 0 to 49. If the iterative calculation was terminated whenever a zero occurred in the measurement estimate vector, the failure rate would be much higher than that indicated in Table II. In these trials, the iterative calculation was performed by adding a small constant (10^{-6} count) to the estimate prior to calculating the current weight matrix. Clearly, the coefficients obtained with the addition of this constant in the last iteration were nearly identical with that obtained with the GLS method, which does not calculate the inverse of the weight matrix. Nonetheless, the calculation was indicated as a failure since convergence with the proper weighting could not be performed.

A more subtle problem in iterative updating of the row weight matrix is that it does not guarantee that the parameter estimates will converge to the correct result. In fact, there may be oscillations in the parameter estimates. These oscillations are difficult to detect and there is no apparent remedy. Parameter oscillation was found to be a source of failure for the data summarized in Table III. Here, the first coefficient was purposefully chosen to be less than the predicted variance due to the other two coefficients. In this instance both the WLS and the GLS methods failed due to oscillations in the updated parameters. The failure rate was 18%. The problem with this type of failure is that there are no adjustable parameters to stop the oscillation. Oscillations may also occur in the direct method. But with this method, the rate of convergence can be adjusted by changing the fraction of the error correction added to the previous estimate. The algorithm used in these calculations did in fact decrease this fraction if the calculations failed to converge in a set number of iterations.

In light of the three test cases summarized in Tables I-III, it can be seen that in all cases the methods which take into account the error statistics are more accurate than the conventional LS method. This is apparent in both the average value for the 100 trials and the RMS accuracies. The three methods for regression of data with Poisson distributed yielded nearly equivalent results in cases where the calculation did not fail. Moreover, the zero inverse weight matrix failure results were nearly correct as Table II illustrates. However,

Table IV. Comparison of Least Squares and Steepest Descent Poisson Regression for Low Magnitude Spectra^a

	a_{Mo}^b	$a_{Ar(I)}$	$a_{Ar(II)}$
LS	164.0 (23.7)	168.9 (19.9)	165.5 (18.3)
Direct	164.6 (14.5)	166.6 (14.2)	165.9 (14.7)

^aTotal count was 500 for each data set. Theoretical coefficients for normalized spectra illustrated in Figure 1 are $a_{Mo} = 166.7$, $a_{Ar(I)} = 166.7$, $a_{Ar(II)} = 166.7$. The data summarize 100 trials. ^bAverage coefficients for component spectra. Numbers in parentheses are RMS errors.

Table V. Comparison of Least Squares and Steepest Descent Poisson Regression for Low Magnitude Spectra with a Low Mo Content^a

	a_{Mo}^b	$a_{Ar(I)}$	$a_{Ar(II)}$
LS	-0.4 (29.6)	988.9 (41.2)	9.3 (7.6)
Direct	0.4 (2.0)	988.1 (30.6)	9.9 (5.0)

^aTotal count was 1000 for each data set. Theoretical coefficients for normalized spectra illustrated in Figure 1 are $a_{Mo} = 0.99$, $a_{Ar(I)} = 898.1$, $a_{Ar(II)} = 9.89$. The data summarize 100 trials. ^bAverage coefficients for component spectra. Numbers in parentheses are RMS errors.

given the fact that the GLS and WLS methods failed due to nonconvergence while the direct method did not, the direct method does appear to be superior, always yielding an answer. Another benefit of the direct method appears to be in the time required to find the solution. The direct method was slightly faster than WLS and orders of magnitude faster than GLS.

As a final example we consider the determination of coefficients for more complex data. Shown in Figure 1 are the three-component spectra used to simulate shot noise limited experimental data. These components were chosen to emulate those which could be obtained from an ICP atomic emission spectrometer. These synthetic spectra each have 512 resolution elements. The full width at half maximum for each Gaussian shaped line is 0.25 nm and the relative intensities are for a temperature of 6000 K. The latter temperature was used in the calculation of the level population densities. The simulated spectra are used as the $f_j(x)$ in eq 8. Figure 2 illustrates a simulated shot noise limited data set as points and the spectrum estimated by the steepest descent program, shown as a solid line. A relatively high total count was used to generate the data illustrated in this figure. Qualitatively speaking, the fit is good.

It is perhaps more interesting to quantitatively examine what happens when the total number of counts of the data is low and when the analyte level is low relative to the interferences. Tables IV and V summarize the results of using the steepest descent program versus conventional LS under these more adverse conditions. On the basis of the RMS errors, the method using the proper statistics clearly performs better than LS in both cases. The implication here is that using the correct statistics in the regression of shot noise limited spectra should result in better estimates of the concentrations of the components making up the analyte.

CONCLUSIONS

The equations describing the ML coefficients for data arising from multiple Poisson processes were examined in the theory section. These equations are different than the Markov, minimum covariance estimates by virtue of the use of Bayes' theorem to restrict the range of the coefficients. Admittedly, there is more work to be done in order to fully understand the implication of eq 6 and 7 to more general, nonlinear problems which must be solved by the steepest descent method. But although the equation was complicated

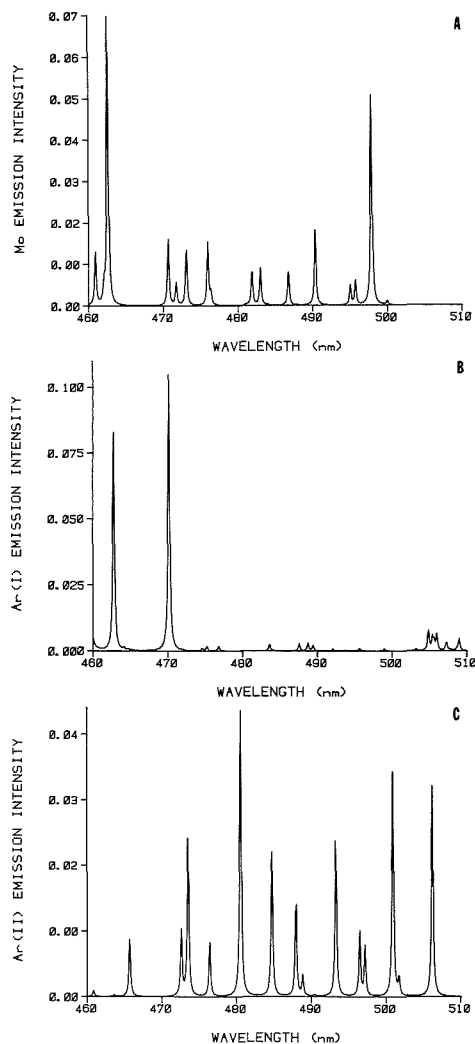


Figure 1. Three normalized component spectra used to test the programs. These spectra were simulated based on persistent atomic emission lines. The simulations assumed a temperature of 6000 K. The three components are (A) Mo, (B) Ar(I), and (C) the Ar(II) ion.

by an ill-defined function, a solution was apparent based on the way this ill-conditioned function changed the coefficient dependence of the simultaneous equations. In effect, the regressor function describing the process which would result in a zero-probability solution can be removed from the basis set. The effective removal of a basis function is inherent in the WLS method described in eq 10–12. But the removal must actually be performed in the GLS and steepest descent methods.

Alternatively, the real value of the ill-defined function which results in a finite probability solution can be determined upon each iteration of the GLS and direct solution estimates. In fact, this method may be necessary for cases in which there are many basis functions. In the present study, the regressor functions were eliminated from the basis set one at a time

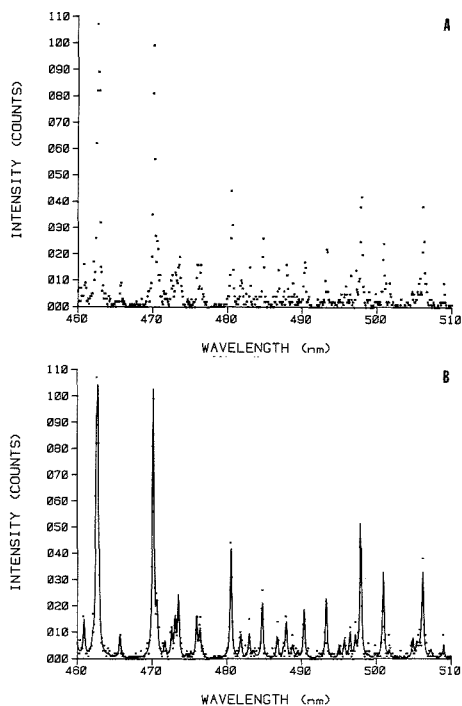


Figure 2. Simulated shot noise limited spectrum in part A was synthesized using equal parts of the spectrum components in Figure 1. The total count for these data were 3000 and the theoretical coefficients for each component were thus 1000. The estimated spectrum shown as the solid line in part B was obtained by using the direct, steepest descent program. The coefficients determined in this case were 1003 for Mo, 965 for Ar(I), and 951 for Ar(II).

when negative coefficients occurred in a given solution. This procedure allowed for the possibility that the elimination one of basis function may cause a sign change in another. As a practical matter, the choice of which of two, or perhaps more, basis functions to eliminate first is not straightforward. A conservative approach would be to eliminate both functions, one at a time, and choose that solution which resulted in the lesser error. It would seem that rather than testing several basis function elimination permutations of a multiple negative coefficient solution, an easier approach should no doubt be to determine the real values which result in nonnegative coefficients iteratively while allowing for these values to return to zero as the solution algorithm progresses.

The ML estimate based on Bayes' probability is not limited to cases where the coefficients are to be greater than or equal to zero. It can also be used whenever the Poisson PDF has a priori probability distributions. In the present case we restricted only the coefficients to be positive. Another important case for the analysis of shot noise limited data is where the regressor functions describing the measurement data are not known. This is the case of estimation where the coefficients can be negative, but where the estimated data are everywhere nonnegative. Following the procedures of ML parameter estimation based on Bayes' probability PDF as outlined in the theory section, one finds that the matrix equation describing estimation for data with Poisson distributed errors is

$$\mathbf{F}^T \mathbf{W}^{-1} \mathbf{y} = \mathbf{F}^T \mathbf{W}^{-1} (\mathbf{I} - \mathbf{R}) \mathbf{F} \mathbf{a} \quad (19)$$

where \mathbf{R} is a diagonal matrix of real positive values or zeros. The utility of $(\mathbf{I} - \mathbf{R})$ is to "preweight" \mathbf{F}_a in such a fashion as a disallow occurrences of $(\mathbf{F}_a)_i < 0$. For example, eq 19 could be used for smoothing data known to have Poisson distributed errors or for determining coefficients of nonlinear functions, such as in first-order lifetime determinations common in fluorescence and nuclear decay analysis. Iterative updating of \mathbf{R} is probably the best method here.

LITERATURE CITED

- (1) Skoog, D. A. *Principles of Instrumental Analysis*, 3rd ed.; Saunders College Publishing: New York, 1985.
- (2) Ingle, J. D.; Crouch, S. R. *Spectrochemical Analysis*; Prentice-Hall: Englewood Cliffs, NJ, 1988; Chapter 5.
- (3) Papoulis, A. *Probability, Random Variables, and Stochastic Processes*, 2nd ed.; McGraw-Hill: New York, 1984; Chapter 3.

- (4) Bialkowski, S. E. *Anal. Chem.* **1989**, *61*, 2479-2483.
- (5) Bevington, P. R. *Data Reduction and Error Analysis for the Physical Sciences*; McGraw-Hill: New York, 1969.
- (6) Golub, G. H.; Van Loan, C. F. *Matrix Computations*; Johns Hopkins University Press: Baltimore, MD, 1983; Chapter 6.
- (7) Norton, J. P. *An Introduction to Identification*; Academic Press: New York, 1986.
- (8) Paige, C. C. *Mathematics Comp.* **1979**, *33*, 171-183.
- (9) Kourouklis, S.; Paige, C. C. *J. Am. Stat. Assoc.* **1981**, *76*, 620-625.
- (10) Poularikas, A. D.; Seely, S. *Signals and Systems*; PWS Publishers: Boston, MA, 1985; Chapter 3.

RECEIVED for review December 1, 1988. Revised manuscript received May 3, 1989. Accepted August 24, 1989. Support for this work by CHE-8520050 awarded by the National Science Foundation is gratefully acknowledged.

Simulation of Carbon-13 Nuclear Magnetic Resonance Spectra of Piperidines

Martha L. Ranc and Peter C. Jurs*

Department of Chemistry, The Pennsylvania State University, 152 Davey Laboratory, University Park, Pennsylvania 16802

The carbon-13 nuclear magnetic resonance spectra for a series of methyl-substituted piperidines have been simulated by using computer-aided methodology. Numerical descriptors were calculated to encode structural features about each carbon center. Multiple linear regression techniques were used to generate models relating these descriptors to the observed chemical shifts, from the conformationally averaged (room temperature) spectra. These models were then used to simulate the complete observed spectra. The resulting spectra were accurate enough to separate conformationally averaged spectra from low-temperature spectra and to distinguish between cis/trans isomers in library searches. Simulated spectra for an external prediction set were generated and evaluated. In addition, these models were used to predict the chemical shifts for low-temperature ^{13}C NMR spectra. The spectra for the minor low-temperature conformations were not as accurate as those for the major conformations; however, the simulated spectra were accurate enough to differentiate between the two low-temperature conformations. Also investigated were the effects of the N-H conformation, that is, the placement of the hydrogen axial versus equatorial.

INTRODUCTION

Carbon-13 nuclear magnetic resonance spectroscopy (^{13}C NMR) is a valuable analytical technique, especially for the structure elucidation of organic compounds. However, such spectra are often complex and difficult to interpret. One method used to aid in interpretation is the comparison of the unknown (experimental) spectrum with standard reference spectra from a library. Library searching is useful provided suitable reference spectra exist; however, if such spectra are not available, then other methods must be employed to interpret a complex spectrum. One such method, spectrum simulation, allows the chemist to approximate the observed ^{13}C NMR spectra of organic compounds.

One approach to spectrum simulation involves the development of linear equations, or models, based on structural

parameters which describe the structural environments of carbon atoms. Such models have the form

$$S = b_0 + b_1X_1 + b_2X_2 + \dots + b_dX_d$$

where S is the predicted chemical shift for the carbon center of interest, the X_i are numerical descriptors which encode its chemical environment, the b_i are coefficients determined by multiple linear regression analysis, and d denotes the number of descriptors used in the model.

This approach was first used with linear and branched alkanes (1, 2) and then extended to compounds with heteroatoms and unsaturations (3, 4). Similar work has been done with rigid alkanes, cycloalcohols, and cycloketones (5, 6). An interactive, computer-based system (ADAPT) has been developed which allows complex descriptors to be easily calculated and managed. This system also aids in model development and evaluation and provides spectral prediction capabilities (7, 8). Spectra have been successfully simulated for a variety of compound classes including cyclohexanols and decalols (9), steroids (10), cyclopentanes and cyclopentanols (11), carbohydrates (12, 13), norboranols (14), cyclohexanones and decalones (15), and polychlorinated biphenyls (16).

This study represents the extension of this methodology to compounds containing nitrogen atoms. Additional aspects addressed in this study include geometric isomers, orientation of the hydrogen attached to the nitrogen, and low-temperature spectra. Specifically, can models be generated which are accurate enough to distinguish between cis/trans isomers? What differences or problems arise when the hydrogen attached to the nitrogen is axial as opposed to equatorial? Also, can models generated by using chemical shifts from conformationally averaged spectra be used to simulate the low-temperature spectra of similar compounds? And if these spectra can be simulated, are they accurate enough to differentiate low-temperature conformers? Also investigated is the simulation of ^{13}C NMR spectra for pyrrolidines using models developed from piperidines.

EXPERIMENTAL SECTION

Figure 1 shows the compounds used in this study. The 35 piperidines and their associated ^{13}C NMR spectra were taken from

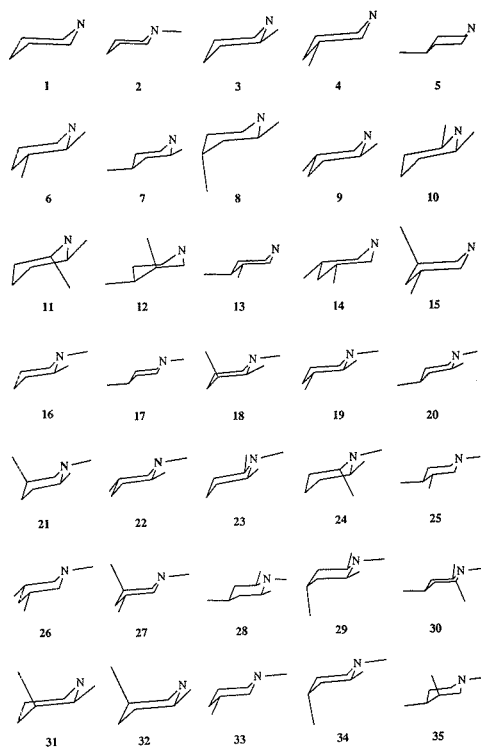


Figure 1. Compounds used in this study. Compounds 1–30 comprise the training set and compounds 31–35 the prediction set.

work presented by Eliel and co-workers (17). In the first part of this study, the spectra were obtained at room temperature by using a Varian XL-100 pulsed Fourier transform spectrometer in FT mode. The shifts were reported relative to tetramethylsilane (Me_4Si). In the second part of this study, low-temperature (-80 to -95 °C) spectra of compounds 8, 12, 18, 21, and 31–35 were used. The N -methyl spectra were recorded in a 1:1 mixture of CHCl_3 and CD_2COCD_3 while the NH spectra were recorded in CD_2Cl_2 . Again, the shifts were reported relative to Me_4Si . For each compound in the second part of the study two ^{13}C NMR spectra—the major and minor conformations of each compound—were recorded. These conformations are shown in Figure 2. For the major conformation the hydrogen attached to the nitrogen is equatorial, while it is axial in the minor conformation. The major conformation is the thermodynamically favored conformation.

To begin the study the chemical structures and their associated ^{13}C NMR chemical shifts were entered into the computer files by using the ADAPT software system (18–20). Approximate three-dimensional atomic coordinates were obtained by using an interactive molecular modeling program (21) and Allinger's MM2 program (22, 23).

The computer programs used in this study are written in FORTRAN and implemented on a PRIME 750 operating in the Department of Chemistry at The Pennsylvania State University and on a Sun 4/110 workstation. Graphics capabilities are provided by Tektronix PLOT-10 software.

RESULTS AND DISCUSSION

Definition of Study. This study involves piperidines 1–35. The training set consists of 30 piperidines, 1–30, while the five remaining compounds, 31–35, comprise the prediction set. The prediction set was used in the final stage of the study to analyze the external predictive ability of the models generated

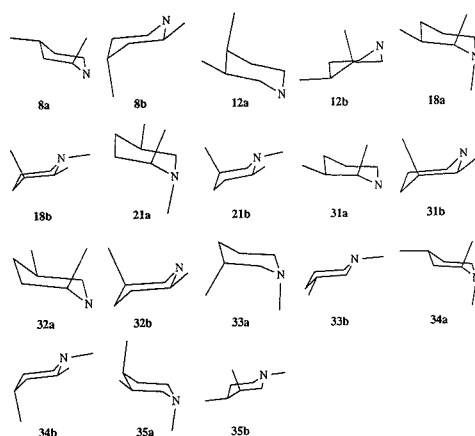


Figure 2. Conformations used in the low-temperature study. The number identifies the compound. Those structures labeled "a" are the minor conformations and those labeled "b" are the major conformations.

from the training set. The prediction set members are five of the nine conformationally mobile compounds in the data set (17).

The 30 training set compounds contain a total of 220 carbons. Duplicate carbons were removed in order to prevent skewing or biasing the regression models, leaving a total of 182 unique carbon centers. In order to simplify the problem of chemical shift prediction, these carbons were divided into subsets. In the past subsetting based on atom connectivity has proven useful and this was the scheme adopted here. The 60 primary carbons are in subset 1 and the 78 secondary carbons are in subset 2. Subset 3 contains 44 tertiary carbons. There are no quaternary carbons in the data set.

Descriptor Generation and Model Formation. After approximate three-dimensional atomic coordinates were obtained for each compound, a series of numerical descriptors encoding the surrounding environment were calculated for each carbon center. These descriptors were of three general types: topological, depending solely on atom type and connections; electronic; and geometric, which depend on the three-dimensional atomic coordinates. Topological descriptors include atom counts and connectivity indexes. The electronic descriptors currently calculated are topological in nature and encode various sigma charge parameters. Geometric descriptors tend to be the most complex and, because of their dependence on three-dimensional atomic coordinates, are sensitive to the molecular modeling process. Geometric descriptors include measures of throughspace distance, shell counts, and van der Waals energies. Several new geometric descriptors were tested in this study, including van der Waals energy descriptors involving the nitrogen and measures of throughspace distance to the nitrogen atom. These descriptors, adapted from those developed by McIntyre and Small (12), are discussed in greater detail below.

For each of these subsets, the descriptors were screened by using statistical procedures described previously (8, 9) so that information-poor descriptors and those with high information overlap (highly correlated descriptors) were eliminated from consideration. Descriptors that are considered information-poor are those with less than 50% nonzero values or those with greater than 90% identical values.

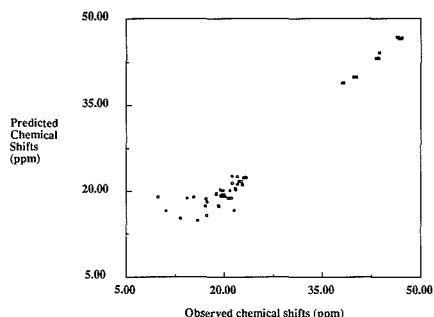
For each atom subset numerous models were constructed by submitting statistically significant descriptors to stepwise multiple linear regression analysis procedures. The resulting

Table I. Chemical Shift Models for Connectivity Subsetting

<i>p</i>	desc ^a	mean	SD ^b	coefficient	mean effect, ppm
Model 1: Primary Carbons (Subset 1)					
1	MNCG 1	-0.0600	0.00905	-125 ± 7	7.50 ± 0.42
2	NTCG 2	-0.149	0.137	-25.0 ± 3.5	3.73 ± 0.52
3	CHVD 1	0.476	0.259	8.53 ± 1.6	4.06 ± 0.76
4	intercept			10.4	
Model 2: Secondary Carbons (Subset 2)					
1	HXVD 1	0.298	0.307	9.790 ± 0.90	2.92 ± 0.27
2	CNET 1	0.977	1.035	-7.61 ± 0.13	-7.43 ± 0.13
3	NNCA 3	1.59	0.80	16.8 ± 0.5	26.7 ± 0.8
4	ARD2 3	0.177	0.050	-201 ± 7	-35.6 ± 1.2
5	HHVD 1	0.536	0.268	-6.09 ± 0.77	-3.26 ± 0.41
6	HSHL 4	2.92	1.14	0.914 ± 0.270	2.67 ± 0.79
7	HSHL 3	3.36	1.48	1.27 ± 0.25	4.27 ± 0.84
8	ASHL 2	0.846	0.646	-1.55 ± 0.35	-1.31 ± 0.30
9	intercept			51.1	
Model 3: Tertiary Carbons (Subset 3)					
1	NNCA 1	2.57	0.50	-20.4 ± 0.4	-52.4 ± 1.0
2	HX13 1	0.114	0.033	336 ± 16	38.3 ± 1.8
3	HXT3 2	0.156	0.038	-189 ± 12	-29.5 ± 1.87
4	ICON 3	1.34	0.39	4.84 ± 0.60	6.49 ± 0.80
5	NNCA 2	2.23	0.08	-1.05 ± 0.31	-2.34 ± 0.69
6	intercept			81.8	

^aDescriptor definition ("heavy atoms" denotes all non-hydrogen atoms). Simple topological: NNCA 1, number of carbons one bond from the carbon center; NNCA 2, number of carbons two bonds from the carbon center; NNCA 3, number of carbons three bonds from the carbon center; ICON 3, the molecular connectivity index computed over bonds three bonds from the carbon center. Topological electronic: MNCG 1, most negative σ charge among atoms one bond from the carbon center; NTCG 2, sum of the σ charges for atoms two bonds from the carbon center. Geometrical: CHVD 1, the van der Waals energy due to interactions between the carbon center and hydrogen atoms in the molecule; HXVD 1, the van der Waals energy due to interactions between hydrogen atoms attached to the carbon center and heavy atoms; HHVD 1, the van der Waals energy due to interactions between the hydrogen atoms attached to the carbon center and other hydrogens in the molecule; CNET 1, the van der Waals energy due to interactions between the carbon center and all nitrogens two or more bonds away; ARD2 3, sum of the inverse squared throughspace distance from the carbon center to all heavy atoms three bonds away; ASHL 2, the number of heavy atoms contained in a spherical shell 3.4–4.1 Å from the carbon center; HSHL 3, the number of hydrogens contained in a spherical shell 2.4–3.2 Å from the carbon center; HSHL 4, the number of hydrogens contained in a spherical shell 3.2–3.6 Å from the carbon center; HX13 1, the average of the sum of the inverse cubed throughspace distances from hydrogens attached to the carbon center to heavy atoms three bonds away; HXT3 2, the average of the sum of the inverse cubed throughspace distances from hydrogens attached to the carbon center to all heavy atoms three to four bonds away. ^bSD, standard deviation.

models were evaluated based on several statistical criteria including standard error (*s*), correlation coefficient (*R*), outlier detection, and internal validation (24–27). In the selection of superior models the models' performance as a unit in predicting complete simulated spectra was also considered.

**Figure 3.** Predicted vs observed chemical shifts for primary carbons.

The best model for each subset is shown in Table I. The descriptor labels are defined and the mean, the standard deviation, the regression coefficient, and the mean effect on the predicted chemical shift are presented for each descriptor in each model. The mean effect is a measure of the shielding or deshielding effects of each descriptor.

Model Evaluation. A summary of some important statistics for each atom subset and their corresponding regression models is given in Table II. The low, high, mean, and standard deviation of the chemical shifts for each subset and the number of carbons in each group are presented. For all three models the correlation coefficients are quite good, as are the standard errors for models 2 and 3 which are less than 1 ppm. The standard error for model 1 is somewhat higher which may be due to the fact that although the range of chemical shifts is comparable to those of the other atom subsets, in reality there are two distinct groups of carbons. This is illustrated in Figure 3, a plot of the predicted vs observed chemical shifts for the primary carbons in compounds 1–30, displaying two separate clusters of chemical shift values. The cluster in the upper right of this plot represents the chemical shifts of the primary carbons attached to nitrogen while the chemical shifts of the primary carbons attached to carbon are clustered in the lower left. An attempt to improve these results by further subdividing the primary carbons into those attached to the nitrogen atom and those attached to carbon, as suggested by Figure 3, did not yield superior models. The *F* value of each model is well above the statistical cutoff.

The major goal of this work is to accurately simulate observed spectra. In order to evaluate how well the generated models work, the chemical shifts predicted by each model were combined to form a complete spectrum for each compound and the residual mean square (rms) error between the predicted and observed spectra was calculated. For the 30 piperidines the mean rms spectral error was 1.10 ppm with a low of 0.42 ppm and a high of 3.82 ppm. Figure 4 shows the predicted and observed spectra of *N*,2-dimethylpiperidine, an example typical of such spectra for this data set. As can be seen, the observed and predicted spectra are visually similar

Table II. Summary of Chemical Shift Data and Model Statistics for Connectivity Subsets

model ^a	observed chemical shifts					model statistics				
	low	high	mean	SD ^b	<i>n</i> ^c	<i>d</i> ^d	<i>R</i>	<i>R</i> (adj) ^e	<i>F</i> ^f	<i>s</i> ^g
1	9.71	47.00	25.69	1.09	60	3	0.984	0.984	575	1.99
2	19.30	65.36	39.98	1.19	78	8	0.998	0.997	1726	0.89
3	25.28	66.16	42.29	1.24	44	5	0.998	0.997	1516	0.93

^aModel 1, primary carbons; model 2, secondary carbons; model 3, tertiary carbons. ^bSD, standard deviation. ^c*n*, number of carbons in the subset. ^d*d*, number of descriptors in the model. ^e*R* (adj), multiple correlation coefficient, adjusted for degrees of freedom. ^f*F*, *F* value for statistical significance of the model. ^g*s*, standard error of estimate, in ppm.

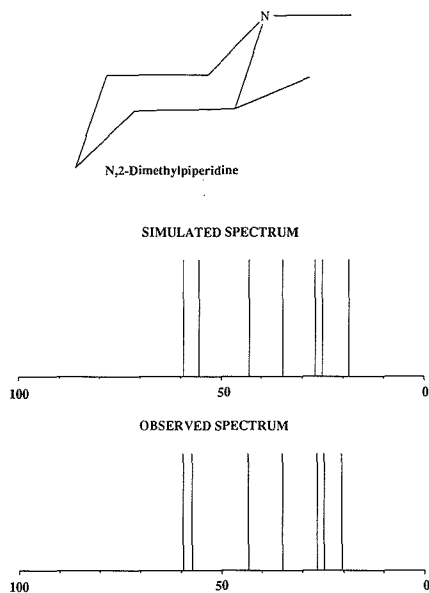


Figure 4. Predicted and observed ^{13}C NMR spectra for *N*,2-dimethylpiperidine. The spectral standard error, s , is 1.07 ppm and the correlation coefficient, R , is 0.998. The axis is in parts per million.

and have a spectral standard error of 1.07 ppm.

To further evaluate how well the simulated spectra approximate the observed spectra, a computer-aided library search procedure was used. This procedure uses the Euclidean distance metric as the measure of similarity between two spectra and reports the top five matches to each simulated spectrum. Two libraries were searched by using this method. The first consisted of the conformationally averaged (room-temperature) spectra of all 35 piperidines. The second, expanded, library contained 18 low-temperature (piperidine) and 5 pyrrolidine spectra in addition to the 35 spectra found in the first library.

When the first library was searched, the top match to each simulated spectrum was the corresponding observed spectrum in all 30 cases. One important question posed at the beginning of this study was whether the simulated spectra would be accurate enough to differentiate the spectra of *cis/trans* isomers. The previous results indicate that this is the case. The first library contained the spectra of 12 *cis/trans* pairs, compounds 6–15, 18–27, 31, 32, 34, and 35. Twenty compounds in the training set have a *cis/trans* isomer, for 19 of these the spectrum of the isomer was included among the top five matches. These results indicate that spectra have successfully been simulated for the 30 piperidines in the training set with sufficient accuracy to differentiate between *cis/trans* isomers.

In order to verify the preceding results, the second library was searched. For 29 of the 30 simulated spectra, the top match was the corresponding observed spectrum. For the remaining compound the actual spectrum was chosen as the second match while its low-temperature spectrum was chosen as the top match. For four compounds 8, 12, 18, and 21, corresponding low-temperature spectra were present in the library, and in each case that low-temperature spectrum was chosen among the top five matches. Fifteen of the 20 piperidines that have a *cis/trans* isomer present in the library had that isomer's spectrum chosen among the top five matches. In addition, the low-temperature spectra of a

Table III. Carbon Atom Distribution among Subsets

connectivity	location			total
	1 bond	2 bonds	3+ bonds	
primary	16	19	25	60
secondary	27	32	19	78
tertiary	19	14	11	44
total	62	65	55	182

cis/trans isomer was present in the library for eight compounds. For five of these compounds the spectrum of the isomer's major conformation was chosen among the top five matches.

The simulated spectra for the training set compounds have a mean spectral rms error of 1.10 ppm. The two library searches show that these simulated spectra are accurate enough to distinguish between *cis/trans* isomers and also to differentiate low-temperature spectra from their corresponding room-temperature spectra. It is interesting to note that the low-temperature counterparts to the observed spectra are chosen prior to the spectra of the geometric isomers, further confirming the ability to differentiate *cis/trans* isomers.

Simulation of Prediction Set Spectra. To test the external predictive ability of these three models, the ^{13}C NMR spectra of the five piperidines (31–35), not used in generating the regression models, were simulated. The spectra were generated by using the coefficients of the regression models discussed above with descriptor values calculated for these prediction compounds. The mean rms spectral error was 1.38 ppm with a range of 0.77–1.89 ppm. When the first library was searched, the top match to each simulated spectrum was the observed spectrum for that compound, and the spectrum of the *cis/trans* isomer was also reported among the top five matches for the four compounds having such an isomer. When the expanded library was searched, the observed spectrum was chosen as the first or second match in every case. For every compound the spectrum of the major low-temperature conformation was also chosen as either the first or second match. In addition, for four of the five compounds the spectrum of the minor low-temperature conformation was identified as one of the top five matches. For three of the four compounds having a *cis/trans* isomer, the corresponding conformationally averaged spectrum of that isomer was included among the top five matches.

External predictive ability is one of the main objectives of this research. The results obtained from these library searches show that ^{13}C NMR spectra for nitrogen-containing compounds have been successfully simulated and that the models developed allow for a high degree of external predictive ability.

Alternate Atom Subsetting. Since the model developed for primary carbons was not as good as the other models (based on standard error), it was decided to investigate an alternate atom subsetting scheme. This new approach was based on a carbon's location relative to the nitrogen atom. Three new subsets resulted: subset 4 containing 62 carbons located one bond from the nitrogen, subset 5 with 65 carbons two bonds removed from the nitrogen, and subset 6 with 55 carbons located three or more bonds from the nitrogen. Further division into groups three bonds and four bonds from the nitrogen atom was not productive due to the small size of the resulting subsets. These subsets differ from the connectivity groups, as can be seen in Table III, which shows the distribution of members for each subset.

Models were generated and evaluated in the same manner as discussed above. The best model for each subset is shown in Table IV and the statistics for each subset and model are given in Table V. The correlation coefficient and the standard error for model 4 are good; however, the statistics for models

Table IV. Chemical Shift Models for Location Subsetting

<i>p</i>	desc ^a	mean	SD ^b	coefficient	mean effect, ppm
Model 4: Carbons One Bond from Nitrogen (Subset 4)					
1	HHI3 2	0.183	0.0820	39.0 ± 5.4	7.14 ± 0.99
2	HXVD 1	0.537	0.323	4.98 ± 1.05	2.67 ± 0.56
3	AVC1 3	0.855	0.721	5.16 ± 0.41	4.41 ± 0.35
4	HX13 2	0.0433	0.0218	-186 ± 15	-8.05 ± 0.65
5	HHT3 2	0.324	0.145	19.9 ± 2.4	6.45 ± 0.78
6	ASHL 2	1.10	0.78	-1.74 ± 0.27	-1.91 ± 0.30
7	HHVD 1	0.515	0.222	-3.23 ± 0.87	-1.66 ± 0.45
8	intercept			42.4	
Model 5: Carbons Two Bonds from Nitrogen (Subset 5)					
1	HHI3 2	0.127	0.071	115 ± 4	14.6 ± 0.5
2	AVC2 1	0.846	0.795	3.72 ± 0.68	3.15 ± 0.58
3	HHI3 1	0.171	0.109	16.8 ± 4.7	4.56 ± 0.80
4	AVC1 3	0.815	0.659	1.14 ± 0.41	0.93 ± 0.27
5	intercept			8.09	
Model 6: Carbons Three or More Bonds from Nitrogen (Subset 6)					
1	HXVD 1	0.0922	0.154	34.7 ± 2.5	3.20 ± 0.23
2	HHVD 1	0.402	0.043	8.90 ± 1.28	3.58 ± 0.51
3	HHI3 2	0.0476	0.0428	-17.9 ± 7.8	-0.85 ± 0.37
4	TOCG 2	0.111	0.068	86.8 ± 12.1	9.63 ± 1.34
5	AVC3 1	0.782	0.567	-8.61 ± 1.51	-6.73 ± 1.18
6	intercept			16.7	

^a Descriptor definition ("heavy atoms" denotes all non-hydrogen atoms). Simple topological: AVC1 3, number of primary heavy atoms three bonds from the carbon center; AVC2 1, number of secondary heavy atoms one bond from the carbon center; AVC3 1, number of tertiary heavy atoms one bond from the carbon center. Topological electronic: TOCG 2, sum of the absolute values of σ charges for atoms two bonds from the carbon center. Geometrical: HXVD 1, the van der Waals energy due to interactions between hydrogen atoms attached to the carbon center and heavy atoms; HHVD 1, the van der Waals energy due to interactions between the hydrogen attached to the carbon center and other hydrogens in the molecule; HHI3 1, sum of the inverse cubed throughspace distance from α hydrogens to all hydrogens three bonds away; HHI3 2, sum of the inverse cubed throughspace distance from α hydrogens to all hydrogens four bonds away; HHI3 3, sum of the inverse cubed throughspace distance from α hydrogens to all hydrogens five bonds away; HHT3 2, sum of the inverse cubed throughspace distance from α hydrogens to all hydrogens from three to four bonds away; HX13 2, sum of the inverse cubed throughspace distance from α hydrogens to all heavy atoms four bonds away; ASHL 2, the number of heavy atoms contained in a spherical shell 3.4–4.1 Å from the carbon center. ^bSD, standard deviation.

5 and 6 show that the fit to the observed chemical shift values was not as good. For all three models the *F* value is well above the statistical cutoff.

A significant test of the models is how well they work as a unit to simulate observed spectra. In the case of the location-based subsets, the mean rms spectral error was 1.46 ppm with a range of 0.38–3.82 ppm for the training set. The mean rms error is 0.36 ppm higher than that for the connectivity-based subsets and the range of errors is slightly larger. For the prediction set, the mean rms spectral error was 1.69 ppm

with a range of 0.82–2.54 ppm. As with the training set, the mean rms error is higher, by 0.31 ppm, and the range of errors is also larger. Library search results are essentially identical whether the spectra are simulated by using the connectivity-based models or the location-based models.

These results indicate that either method of subsetting, connectivity based or location based, produces simulated spectra with sufficient accuracy to identify an unknown piperidine and to distinguish between *cis/trans* isomers. There is a slight preference toward the connectivity-based models due to the lower mean rms spectral error for both the training and the prediction sets.

Assessment of New Descriptors. A total of 14 new descriptors were tested in this study, 4 van der Waals energy descriptors and 10 throughspace distance descriptors. A summary of these descriptors and their fate is shown in Table VI. Most of the new descriptors were removed from consideration in the early stages of descriptor analysis for each atom subset. These descriptors were considered information poor and not worth retaining as, individually, they had 50% or fewer nonzero values. In other cases, descriptors were eliminated due to a high information overlap; that is, the descriptor in question was highly correlated to another descriptor. In 12 cases the descriptors were never chosen in the model formation process; however, in four cases a descriptor was chosen in this process. In one of these four cases, the descriptor in question survived the model evaluation phase and is found in the model for the secondary carbons (subset 2).

It appears that with this particular set of compounds the throughspace distance descriptors are not useful. This is because few of the carbons in any subset are located a sufficient distance (number of bonds) from the nitrogen atom; that is, a given descriptor for a given subset contains a small percentage of nonzero values. This is especially true in the location-based subsets, which already take into account distance to the nitrogen. Several of the van der Waals energy descriptors show promise with this data set, and they will be further evaluated when additional nitrogen-containing data sets are investigated.

Assessment of N–H Orientation. In the compounds used to calculate the previous models hydrogens attached to the nitrogen atom were equatorial (compounds 1, 3–17) as were the hydrogens in two of the prediction set members, compounds 31 and 32. Anet and Yavari (28) report the equatorial position to be favored (ΔG° value of 0.36 kcal/mol for the N–H equilibrium); however, the molecular mechanics modeling processes that were used placed the hydrogen in the axial position and the lone pair electrons equatorial. As mentioned previously, the predictive models developed were based on compounds in a single, locked conformation; however, in reality there exists an equilibrium between the two conformations discussed here and also the ring-flipped conformation. The equilibrium between the two conformations (NH equatorial and NH axial) arises due to nitrogen inversion. Thus it was decided to investigate the conformational isomers where

Table V. Summary of Chemical Shift Data and Model Statistics for Location Subsetting

model ^a	observed chemical shifts				<i>n</i> ^c	\bar{d} ^d	<i>R</i>	model statistics		
	low	high	mean	SD ^b				<i>R</i> (adj) ^e	<i>F</i> ^f	<i>s</i> ^g
4	37.88	66.16	51.46	7.36	62	7	0.994	0.993	597	0.88
5	9.71	43.98	29.65	8.21	65	4	0.971	0.969	245	2.04
6	13.08	42.90	25.51	7.41	55	5	0.971	0.970	182	1.76

^aModel 4, carbons one bond from nitrogen; model 5, carbons two bonds from nitrogen; model 6, carbons three or more bonds from nitrogen. ^bSD, standard deviation. ^c*n*, number of carbons in the subset. ^d \bar{d} , number of descriptors in the model. ^e*R*(adj), multiple correlation coefficient, adjusted for degrees of freedom. ^f*F*, *F* value for statistical significance of the model. ^g*s*, standard error of estimate, in ppm.

Table VI. Evaluation of New Descriptors

descriptor ^a	set 1	set 2	set 3	set 4	set 5	set 6
CND3 1	NZ ^b	NZ	NZ	NC ^c	NZ	NZ
CND3 2	NZ	NZ	NZ	NZ	NC	NZ
CND3 3	NZ	NZ	NZ	NZ	NZ	NC
CND3 4	NZ	NZ	NZ	NZ	NZ	NZ
CND3 5	NZ	NZ	NC	NZ	NZ	NZ
HND3 1	NZ	NZ	NZ	CORR ^d	NZ	NZ
HND3 2	NZ	NZ	NZ	NZ	CORR	NZ
HND3 3	NZ	NZ	NZ	NZ	NZ	NC
HND3 4	NZ	NZ	NZ	NZ	NZ	NZ
HND3 5	NZ	NZ	NC	NZ	NZ	NZ
CNEL 1	NZ	NZ	NZ	NZ	NZ	NC
HNEL 1	NC	MODL ^e	NC	NZ	NC	MODL
CNET 1	MODL	MODL	NC	NZ	CORR	CORR
HNET 1	CORR	CORR	CORR	NC	CORR	CORR

^aDescriptor definition. CND3 *n*, the sum of the inverse cubed throughspace distance from the carbon center to nitrogens *n* (1–5) bonds away. HND3 *n*, the sum of the inverse cubed throughspace distance from α hydrogen(s) to nitrogens *n* (1–5) bonds away. CNE1 1, the van der Waals energy between the carbon center and all nitrogens three or more bonds away. HNEL 1, the van der Waals energy between α hydrogen(s) and all nitrogens three or more bonds away. CNET 1, the van der Waals energy between the carbon center and all nitrogens two or more bonds away. HNET 1, the van der Waals energy between α hydrogen(s) and all nitrogens two or more bonds away. ^bNZ, eliminated due to 50% or less nonzero values. ^cNC, not chosen among the top models during regression analysis. ^dCORR, eliminated because of correlation with another descriptor. ^eMODL, chosen among the top models during regression analysis.

the hydrogen in question is axial instead of equatorial to determine what affect this would have on the connectivity-based models and the spectrum simulation.

Descriptors were calculated for the new conformations of compounds 1 and 3–17 plus the original configurations of 2 and 18–35. The correlation between the original and the new descriptor values was determined. As expected, since they depend only on atom types and connections, there were no differences in the topological or the topological electronic descriptors. Of the 16 descriptors used in the calculated models, six fall into one of these two categories. Although the remaining 10 descriptors are geometrical, six of these also show a correlation of 1.00 while three of the remaining six correlate at 0.96 or higher. Only one of the descriptors falls below a correlation of 0.90—it has a correlation of 0.88.

By use of the previously generated models and the new descriptors, the spectra of the 30 piperidines in the training set were simulated. The mean rms spectral error increased by 0.08 ppm, from 1.10 to 1.18 ppm using the alternate conformations. The range of the error was 0.36–3.82 ppm. The low end of the range has been decreased but the upper end of the range of rms errors has remained constant. When the original library, consisting of 35 piperidines, was searched, each of the simulated spectra was correctly matched to the observed spectrum. For each of the 20 compounds with a cis/trans isomer, the isomer's spectrum was also identified among the top five matches. Results almost identical with those obtained with the original conformations were found when searching the expanded library.

These results indicate that the models would not have been greatly degraded had the NH axial conformation been used to generate the equations. These results also show that even though an equilibrium exists between the two conformations, excellent models can be generated from a fixed conformation. If these new descriptors are used to generate new coefficients for the regression models, the mean rms spectral error and the library search results are even closer to those of the original models, supporting the conclusions drawn here.

Simulation of Low-Temperature Spectra. This part of the study involves two conformations each of nine piperidines, which are the conformationally mobile compounds in the data

Table VII. Low-Temperature Spectral Statistics

conformation	std error, ppm			correlation coefficient		
	high	low	mean	high	low	mean
major	2.58	0.70	1.51	0.999	0.989	0.996
minor	5.64	2.65	3.72	0.993	0.948	0.974
combined	5.64	0.70	2.62	0.999	0.948	0.985

set. These 18 conformations, illustrated in Figure 2, are treated as 18 distinct compounds since the chemical shifts of the conformers differ, giving rise to distinct ¹³C NMR spectra.

These compounds have a total of 134 carbons, all of which are unique. Subsets similar to the original subsets were used, consisting of primary, secondary, and tertiary carbons. There were no quaternary carbons in this set.

The necessary descriptors were calculated for each subset. The connectivity-based models, generated in the first part of this study (Table I), were used to predict the chemical shifts of the 134 carbons in the low-temperature data set, using the entire set as a prediction set. The mean rms spectral error was 2.62 ppm with the largest errors occurring for the minor conformations, a mean error of 3.72 ppm, and the smallest errors for the major conformations, a mean of 1.51 ppm. These and other statistics are presented in Table VII. It is not unexpected that the major conformations are modeled better than the minor conformations. The models generated earlier in the study, though using conformationally averaged chemical shifts, are based on descriptors from a single, locked conformation. The conformation that was determined as the lowest-energy conformation is identical with the major low-temperature conformation. In addition, the low-temperature spectra for the minor conformations reported by Eliel et al. (17) were missing chemical shift data for four carbons. Values were estimated for these shifts based on the reported ratio of the major to the minor conformation at low temperatures (17) and the chemical shift for each carbon in the conformationally averaged spectrum and in the low-temperature spectrum of the major conformation. However, the values estimated by the regression models differ from those previously estimated. This causes an increase in the rms spectral error for the three conformations containing these estimated shifts, thus increasing the mean rms error for the minor conformations. For these reasons it was expected the major conformations would have a lower mean rms spectral error than the minor conformations.

To further evaluate how well the actual spectra are simulated, two library searches were performed. These were similar to the searches described above. The first library searched consisted of the 18 low-temperature spectra. In all cases the observed spectrum of the low-temperature conformer was among the top five matches and in 12 cases the observed spectrum was the top match. For 17 of the 18 conformers the spectrum of the corresponding low-temperature conformational isomer was also among the top five matches. When the expanded library previously described was searched, 17 of the conformers had their observed low-temperature spectrum chosen as one of the five matches. In addition, 12 of the 18 conformers found as a match the low-temperature spectrum of their conformational isomer while the conformationally averaged spectrum of the piperidine was included among the top five matches for 17 of the conformers. Of the nine compounds in the low-temperature study, eight (8, 12, 18, 21, 31, 32, 34, 35) had cis/trans isomers among the conformationally averaged, that is the original, data set. In 8 of the possible 16 cases the spectrum of the corresponding cis/trans isomer was among the top five matches. In the best case a given simulated, low-temperature spectrum would be matched with two low-temperature spectra (the conformer and the con-

formational isomer) and two conformationally averaged spectra (the compound and a *cis/trans* isomer). This happened in 6 of the 18 cases and in one additional case there was no corresponding *cis/trans* isomer. The worst case that occurred involved the minor conformation of compound 33 in which the observed low-temperature spectrum was chosen as the second match but neither the spectrum of the conformational isomer nor the conformationally averaged spectrum was among the top five matches. Compound 33 has no *cis/trans* isomer. For six of the remaining ten conformers the top five matches included three of the four possible spectra, while the remaining four included only two of the four possible "correct" spectra among the top five matches.

This work has shown that models generated from conformationally averaged spectra can be used to simulate low-temperature spectra. The simulated spectra are accurate enough to distinguish between different piperidines and also between *cis/trans* isomers. In addition, in most cases the simulated spectra were accurate enough to differentiate low-temperature conformational isomers. However, the conformationally averaged spectrum was more similar to the simulated spectrum than the observed spectrum was for most of the minor conformations and slightly more than half the major conformations.

Simulation of Pyrrolidine Spectra. In the past, regression models have been developed for each class of compounds being investigated. An attempt was made to simulate the spectra of a set of pyrrolidines using the connectivity-based models developed from the piperidines. This seemed feasible since all 16 descriptors involved in the models encoded structural features at a distance less than that which exists in the pyrrolidines.

The set of pyrrolidines contained five compounds: pyrrolidine, *N*-methylpyrrolidine, *N*,3-dimethylpyrrolidine, *cis*-*N*,3,4-trimethylpyrrolidine, and *trans*-*N*,3,4-trimethylpyrrolidine. The spectra for these compounds were reported by Hawthorne and co-workers (29). The ¹³C NMR spectra were obtained at room temperature on a Varian CFT20 spectrometer in approximately 20% solutions in CDCl₃. The chemical shifts are reported relative to tetramethylsilane (Me₄Si).

The structures were submitted to a molecular mechanics modeling program and the necessary descriptors (see Table I) were calculated. The mean rms spectral error at 5.21 ppm is higher than that normally accepted; however, it is acceptable for preliminary results since this type of spectral simulation has not been previously attempted. Even more encouraging is the fact that when searching the expanded library each of the pyrrolidines was correctly identified as the top match.

In order to verify that this is not due to the fact that these compounds are five-membered rings as opposed to the six-membered rings of most of the compounds, the library was searched taking into account the possibility that the simulated spectra may be missing peaks (11, 15). Three additional searches were performed with the following criteria: (1) the reference spectrum may have one peak more than the simulated spectrum, (2) the reference spectrum may have up to two peaks more than the simulated spectrum, and (3) the reference spectrum may have as many as three peaks more than the simulated spectrum. In all three cases, each simulated pyrrolidine spectrum was correctly matched to the corresponding reference spectrum.

These results should be considered as preliminary only, due both to the high mean rms error and to the low number of compounds used in this portion of the study. The results are promising and suggest that the use of regression models developed from one class of compounds can be successfully used to simulate the spectra of a different, but similar, class of

compounds. The results would be more conclusive if a larger prediction set of pyrrolidines were utilized.

CONCLUSIONS

We have succeeded in showing that this simulation methodology can be extended to include nitrogen-containing compounds. The simulated conformationally averaged spectra are accurate enough (in library searching) to distinguish *cis/trans* isomers, even when corresponding low-temperature spectra are present in the library. This is true whether the subsets used to generate the models are based on connectivity or on location relative to the nitrogen atom. Library search results for the two sets of models are essentially identical; however, the connectivity-based models have a lower mean rms spectral error, 1.10 ppm, than the location-based models, 1.46 ppm, and are thus favored.

Piperidines that have a hydrogen attached to the nitrogen exhibit two conformations, one with the hydrogen equatorial (the favored conformation) and one with the hydrogen axial, due to nitrogen inversion. The models used were generated on a single, locked conformation; however, the results indicate that spectra can be accurately simulated from such conformations and still be representative of the observed conformationally averaged spectra.

The models that have been developed can also be used to simulate low-temperature spectra of compounds similar to those used in generating the models. It was found that the simulated spectra for the major conformations are more accurate than those for the minor conformations. In both cases the spectra were accurate enough to distinguish various piperidines, as well as to differentiate *cis/trans* isomers; however they were not as successful in differentiating conformationally averaged spectra and low-temperature spectra. The models were also able to provide estimates for chemical shift values that were not reported in the literature.

An attempt was also made to utilize the models generated from methyl-substituted piperidines to simulate the spectra of several pyrrolidines. Preliminary results indicate some promise for this task. The library search results are promising, as the pyrrolidines are consistently correctly identified, but the mean rms spectral error is higher than hoped.

Use of models to simulate low-temperature spectra and also to simulate spectra of a class of compounds not used in generating the models shows some promise, and additional work in these areas should be pursued.

ACKNOWLEDGMENT

This opportunity is taken to thank Debra S. Egoif for her help with this project and for adapting the descriptors developed by Gary Small. Also, G. Paul Sutton is gratefully acknowledged for his help in the various stages of this project and for many useful discussions.

LITERATURE CITED

- (1) Grant, D. M.; Paul, E. G. *J. Am. Chem. Soc.* **1964**, *86*, 2984-2989.
- (2) Lindeman, L. P.; Adams, J. Q. *Anal. Chem.* **1971**, *43*, 1245-1252.
- (3) Echart, A. *Org. Magn. Reson.* **1980**, *13*, 368-371.
- (4) Echart, A. *Org. Magn. Reson.* **1981**, *15*, 22-24.
- (5) Bernassau, J. M.; Fetizon, M.; Maia, E. R. *J. Phys. Chem.* **1986**, *90*, 6129-6134.
- (6) Bastard, J.; Bernassau, J. M.; Maia, E. R. *Magn. Reson. Chem.* **1988**, *26*, 992-1002.
- (7) Smith, D. H.; Jurs, P. C. *J. Am. Chem. Soc.* **1978**, *100*, 3316-3321.
- (8) Small, G. W.; Jurs, P. C. *Anal. Chem.* **1983**, *55*, 1121-1127.
- (9) Small, G. W.; Jurs, P. C. *Anal. Chem.* **1983**, *55*, 1128-1134.
- (10) Small, G. W.; Jurs, P. C. *Anal. Chem.* **1984**, *56*, 2307-2314.
- (11) Egoif, D. S.; Jurs, P. C. *Anal. Chem.* **1987**, *59*, 1586-1593.
- (12) McIntyre, M. K.; Small, G. W. *Anal. Chem.* **1987**, *59*, 1805-1811.
- (13) Small, G. W.; McIntyre, M. K. *Anal. Chem.* **1989**, *61*, 666-674.
- (14) Egoif, D. S.; Brockett, E. B.; Jurs, P. C. *Anal. Chem.* **1988**, *60*, 2700-2706.
- (15) Sutton, G. P.; Jurs, P. C. *Anal. Chem.* **1989**, *60*, 863-871.
- (16) Egoif, D. S.; Jurs, P. C., unpublished work.
- (17) Eilal, E. L.; Kandasamy, D.; Yen, C.; Hargrave, K. D. *J. Am. Chem. Soc.* **1980**, *102*, 3698-3707.
- (18) Brugger, W. E.; Jurs, P. C. *Anal. Chem.* **1975**, *47*, 781-783.

- (19) Stuper, A. J.; Jurs, P. C. *J. Chem. Inf. Comput. Sci.* **1976**, *16*, 99-105.
- (20) Rohrbaugh, R. H.; Jurs, P. C. "UDRAW", Quantum Chemistry Exchange, Program 300, 1988.
- (21) Stuper, A. J.; Brugger, W. E.; Jurs, P. C. *Computer-Assisted Studies of Chemical Structure and Biological Function*; Wiley-Interscience: New York, 1979; pp 83-90.
- (22) Burkert, U.; Allinger, N. L. *Molecular Mechanics*; ACS Monograph 177; American Chemical Society; Washington, DC, 1982.
- (23) Clark, T. A. *Handbook of Computational Chemistry: A Practical Guide to Chemical Structure and Energy Calculations*; Wiley: New York, 1985.
- (24) Draper, N. R.; Smith, H. *Applied Regression Analysis*, 2nd ed.; Wiley-Interscience: New York, 1981.
- (25) Belsley, D. A.; Kuh, E.; Welsch, R. E. *Regression Diagnostics: Identifying Influential Data and Sources of Collinearity*; Wiley-Interscience: New York, 1980.
- (26) Allen, D. M. Technical Report 23, Department of Statistics, University of Kentucky; Lexington, KY, 1971.
- (27) Snee, R. D. *Technometrics* **1977**, *19*, 415-427.
- (28) Anet, F. A. L.; Yavari, I. *J. Am. Chem. Soc.* **1977**, *99*, 2794-2795.
- (29) Hawthorne, D. G.; Johns, S. R.; Willing, R. I. *Aust. J. Chem.* **1976**, *29*, 315-326.

RECEIVED for review July 24, 1989. Accepted August 31, 1989. This work was supported by the National Science Foundation under Grant CHE-8815785. The PRIME 750 computer and the Sun 4/110 workstation were purchased with partial financial support of the National Science Foundation. Portions of this paper were presented at the 197th National American Chemical Society Meeting, Dallas, TX, April 1989.

Background Illumination Filtering in Thermal Lens Spectroscopy

Jerzy Slaby

Institute of Experimental Physics, Warsaw University, Hoza 69, 00-681 Warsaw, Poland

A thermal lens spectrometer with spatial filtering of a probe beam has been analyzed. A circular opaque mask placed in the probe beam significantly reduces the constant, signal-independent detector response, whereas useful thermal lens signal is much less affected. In this modified configuration, in comparison to the classical arrangement, 5-fold enhancement of signal to constant background ratio has been experimentally verified. Theory is presented where diffraction at the blocking filter is calculated and improvement of thermal lens signal to constant background is discussed. Assuming the typical configuration, with a detector in the center of the probing beam, we have obtained expressions applicable for both single and dual-beam arrangement. Experimental data are well reproduced by theoretical curves.

1. INTRODUCTION

The first observation of a thermal lens (TL) inside a laser cavity (1) led to the new technique of thermal lens spectroscopy. The extracavity single-beam thermal lens spectrometer was developed by Chenming Hu and Whinnery (2), and thermal lens spectroscopy (TLS) was vastly improved when a dual-beam version of the method was developed by Swofford and Morell (3). Now the TLS technique can be used in many various fields including molecular and solid-state spectroscopy, material testing, combustion studies, plasma diagnostics, research on heat diffusion, transport phenomena, and phase transitions studies. Sensitive, laser-based absorbance measurements have proved to be an invaluable analytical tool particularly for molecular systems, where strongly absorbing molecules are much more common than strongly fluorescent ones.

The general scheme of the TLS (4) is usually modified in various ways to enhance specific features of the instrument's performance. A very interesting, although perhaps the simplest, arrangement of the TL spectrometer ever constructed was presented by Inasaka et al. (5), where optical fibers are applied for both introducing light into the sample and monitoring the outgoing light beam. In such a system no additional optical elements are necessary and a more simple experimental setup is hardly imaginable. Another configuration, one of the most important arrangements of the TL spectrometer, is a

crossed-beam instrument (6, 7) designed and particularly well suited for studying extremely small volume samples. A very elegant approach for improving classical thermal lens spectroscopy was suggested by Janssen and Harris (8), where optical processing is used to directly determine the probe beam spot size. A radially symmetric mask, with a parabolic transmission profile, ensures greater immunity to spatial noise and also results in more precise measurements, compared to the usual beam-center detection. The present paper considers a similar category of TL spectrometer, with optical processing applied to obtain better performance characteristic of the instrument.

In order to detect a thermal lens, a laser-heated sample is placed some distance, typically about $3^{1/2}$ confocal parameters, either after or before the waist of a probe beam. In a thermal lens method, however, there is constant nonzero detector response, even when no absorption occurs and no thermal lens is generated. This may be a serious problem since the presence of a background masks the signal of interest. Moreover, strong background requires a large dynamic range of the detector to precisely recover the weak useful signal. Reducing signal-independent detector illumination is thus of practical interest. We have presented this sort of thermal lens detecting arrangement in ref 9, where we report preliminary experimental data on partial separation of useful signal beam from the unperturbed probe beam, and we discuss its implications to signal/noise ratio. This approach is particularly advantageous if probe beam fluctuations are the limiting noise source. In the case when beam wander is more important, reduction of the pointing noise and improvement of detection limit by means of spatial filtering were reported by Long and Bialkowski (10) for a pulsed-laser operated TL spectrometer.

The present paper gives new experimental evidence of filtering out the undesired background signal, with a 5-fold gain in signal to background over the usual scheme of a thermal lens instrument. Rigorous diffraction calculations have been performed to supplement the propagation model (9) with some considerations that are necessary to give a proper quantitative description of filtered detection of thermal lens. This new model gives a simple and satisfactory explanation of filtered system operation. Moreover, as we show in application to experimental data, the model can be used to predict exactly the signal to background improvement expected in a filtered measurement configuration.

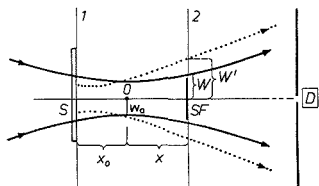


Figure 1. Optical configuration for filtered probe beam system of thermal lensing detection: S, sample; SF, spatial filter; D, photodetector; 0, position of the waist of probing laser beam.

2. THEORY

2.1. Probe Beam Propagation in a Filtered System.

The basic concepts fundamental to the thermal lens effect are very straightforward, but a complete quantitative description of this technique is quite elusive. This is so because rough simplifications are made on both stages of the theory necessary to describe the effect: first, in solving the heat diffusion equation, therefore in what the refractive distribution in a sample illuminated by a heating beam is, and second, in the calculation of probing beam propagation in a medium with gradient index of refraction. Carter and Harris (11) made an interesting comparison of various models describing the thermal lens effect. The authors have demonstrated that quite different parameters describing physical properties of a sample can be deduced from experimental data. It is a rather confusing situation, but even such an important feature as the time constant of thermal lens evolution turns out to be dependent on the model used in the calculations. In recent years significant effort has been made to reach a better understanding of thermal lens detection. In ref 12 and 13, contrary to previous studies, a more rigorous diffraction approach is used and true phase shift, different from the ideal parabolic model, is assumed. The excellent results of these two papers, however, cannot be so easily applied for the description of a TLS system containing a spatial filter. These papers discuss the light amplitude only in the very center of a probe beam. Precise knowledge of light field amplitude in the whole filter plane is necessary to determine the signal value expected in the system considered in the present paper. One possible way to solve this problem is to use the model of a thermal lens presented in ref 14. If there is only small absorption and consequently a low rate of heat release in a sample, then for times shortly following the illumination onset one can assume that the temperature rise in the sample is proportional to the amount of energy deposited and is a Gaussian function of coordinates. For that reason a Gaussian probe behind a thermal lens can be decomposed into the sum of two Gaussian beams, with different confocal parameters and waist locations. One of the beams has its amplitude proportional to thermal lens strength, whereas the other is just the original unperturbed probe. This model quite naturally suggests a detection scheme with a high-pass spatial filter in the path of a probing beam.

The scheme of the detection system considered in the present paper is shown in Figure 1. A thermal lens is generated in a sample S placed in input plane 1 of the system, in the converging part of the probing Gaussian beam. A probing beam, after passing through the sample, travels to the second reference plane 2, containing a circular mask SF. This is the filter plane of the system. The filter plane can be located at any distance x from the waist plane of the probe beam. It is noted that at $x = 0$, filtering is performed in the spatial Fourier spectrum of the probe beam. For generality, however, arbitrary nonzero x is allowed in the present analysis. The sample is a distant x_0 from the waist of the probe. Finally, far from the filter plane 2 is the detection plane of the system,

with a detector D and a pinhole in front of it, centered on the optical axis. Propagation of the probing beam from the first reference plane to the detector plane can be described as a two-stage process. The first stage is Gaussian beam propagation in free space, and for any position along the system axis, one can easily determine the beam size, its radius of curvature, and its amplitude (15). The second stage is the propagation of a wave diffracted at the mask, which is placed in the filter plane. The amplitude of this wave can be found by means of the diffraction integral.

Light field amplitude a_i of the probe beam incident onto the sample can be written as

$$a_i(r, X = -x_0) = w_0/w \exp[i\Phi - r^2(1/w^2 - ik/2R)] \quad (1)$$

It is simply the amplitude of a Gaussian beam with a radius of curvature R and beam diameter $2w$. Beam size at the waist plane is w_0 and Φ denotes the initial phase shift and can be set to zero at the waist plane $X = 0$. If the sample is thin, then the light field amplitude a_b behind the thermal lens, as stated before, can be decomposed into the sum

$$a_b(r, X = -x_0) = a_i(r) + a_S(r)$$

The second component, $a_S(r)$, is another Gaussian beam (14), the magnitude of its amplitude being proportional to the power absorbed in the sample. This wave is thus the useful signal wave and, according to the assumption of small perturbation, $|a_S(r)| \ll |a_i(r)|$. In the first plane, and on the system axis, the amplitude of the signal wave is equal to $a_S(r = 0) = a_i(r = 0)[ikW_H^2/4F]$. F is the focal length of the thermal lens that is obtained in the model of the parabolic phase shift, and W_H is the radius of the laser beam heating the sample.

In the filter plane 2 the amplitude of the unperturbed probing beam can be expressed by (1), but with another beam radius denoted by W . We assume that distance x measured along the system axis X is given in dimensionless units, where actual distance is normalized by the confocal parameter of the probing beam. For the unperturbed probing wave, one has thus in the filter plane (at $X = x$) beam parameters

$$W^2 = w_0^2(1 + x^2), R = kw_0^2(1 + x^2)/2x, \Phi = \arctan(x) \quad (2)$$

Signal beam diameter $2W'$ can be written as (9)

$$W' = w_0'[1 + x'^2(w_0/w_0')^4]^{1/2}$$

where

$$x' = x_0 + x - x_0', x_0' = x_0/G, G = \frac{1 + 2(w_0/W_H)^2(1 + x_0^2)}{1 + 2(w_0/W_H)^2(1 + x_0^2)}$$

and

$$(w_0')^2 = w_0^2(1 + x_0^2)/(G + x_0^2/G)$$

In the above set of equations w_0' is the signal beam diameter at its waist plane, and x_0' is the distance from this plane to the sample. With these parameters known, the radius of curvature R' in filter plane and the phase Φ' , relative to that of the unperturbed probing beam, can be calculated. After simple algebraic manipulations one obtains

$$R' = (w_0'/w_0) kW'^2/2x'$$

and

$$\Phi' = \pi/2 + \arctan[x_0'(w_0/w_0')^2] + \arctan[x'(w_0/w_0')^2] - \arctan(x_0) - \arctan(x) \quad (3)$$

The first three terms in (3) give the change of the phase of the signal beam between the first and the second reference plane, the last two refer to the unperturbed part of the probing beam. Propagation phase factor $\exp[ik(x_0 + x)]$ is simply omitted, as it is the same for both beams. Although the ratio

of the power carried on by the signal beam to that of unperturbed probe beam does not depend on X , the ratio W'/W does not remain constant as X is changed. Thus for any position between the first reference plane and the filter plane, the ratio of signal to unperturbed probe beam amplitudes is slightly different. Nevertheless, in this paper only the relative increase of the thermal lens signal is the point of interest. Therefore it can be assumed that in the filter plane, the signal beam amplitude is K ($K \ll 1$), and the amplitude of unperturbed probing beam is equal to unity. With these assumptions, using expressions (1-3) for beam parameters, we can discuss the second stage of filtered system operation. In order to find an expression for the light field amplitude a_d in the detection plane, the diffraction integral can be applied. Assuming radial symmetry of the problem, one can write for the far field diffraction

$$a_d(\rho_d) = \frac{\exp(ikX_0)}{i\lambda X_0} \exp\left(\frac{ik}{2X}\rho_d^2\right) \int_D a_r(\rho_r) \times \exp\left(\frac{ik}{2X}\rho_r^2\right) \rho_r J_0\left(\frac{k\rho_d\rho_r}{X_0}\right) d\rho_r \quad (4)$$

In the above equation ρ_d and ρ_r are radial distances from the system axis, in detection and filter plane, respectively. Distance between these two planes is denoted as X_0 . Spatial filter diameter is $2D$. Finally, J_0 is the Bessel function of the first kind and zero order, and a_r is the light field amplitude in the filter plane. The latter can be written as

$$a_r(\rho_r) = \exp[-\eta\rho_r^2] + K \exp(i\Phi') \exp[-\eta'\rho_r^2] \quad (5)$$

In (5) the parameters η and η' are defined to be

$$\eta = 1/W^2 + ik/2R; \eta' = 1/W'^2 + ik/2R' \quad (6)$$

To compute (4) one has to perform the integration from D to infinity. This can be calculated as the difference of two integrals. The first one is from zero to infinity, and its result can be obtained by using formula 6.631.4 from ref 16. Then the integral from 0 to D has to be subtracted. The result of the second integral is used in the theory of diffraction on tapered lenses and can be found, for example, in ref 17. With (5) and (6) substituted to (4), assuming $1/X \rightarrow 0$ and omitting constant factors, one can write the following expression for the light field amplitude a_d in the detector plane:

$$a_d(\rho_d) = A_i(\rho_d) + A_S(\rho_d) \quad (7)$$

where

$$A_i(\rho_d) = \exp(-\eta D^2) / \eta \sum_{r=0}^{\infty} (-k\rho_d/2X_0 D)^r J_r(kD\rho_d/X_0) \quad (8)$$

A_i describes that part of light beam amplitude in the detection plane that originates from the unperturbed probing beam. A_S is light field amplitude resulting from the signal wave diffracted at the mask and is expressed in the same way as A_i , except that η is replaced by η' . In (8) the term $\exp(ik\rho_d^2/2X_0)$ is neglected as it describes a uniform spherical wave front that is the same for the unperturbed probe and for the signal beam and hence does not influence intensity measurements.

2.2. Filtering Efficiency. It can be assumed that the strength of the thermal lens is monitored by means of a small diameter detector placed in the center of the probing beam at $\rho_d = 0$. It is worth noting that eq 8 is applicable also to a more general geometry and one can obtain a complete map of detection sensitivity, as a function of the detector's displacement ρ_d from the axis of the detecting system. The choice of $\rho_d = 0$ results from the requirement to retain utmost ease of setting and adjusting the TL spectrometer. The formula (8) for $\rho_d = 0$ is just

$$A_i(\rho_d = 0) = \exp(-\eta D^2) / \eta \quad (9)$$

It can be noted that in (8), in the limit $D \rightarrow 0$ and for any ρ_d , the whole sum reduces to only one term with $r = 0$ and this term equals unity. The same is obtained, at $D \rightarrow 0$, from eq 9.

For the signal beam one can write

$$A_S(\rho_d = 0) = K \exp(i\Phi') \exp(-\eta' D^2) / \eta' \quad (10)$$

If there is no heating of a sample, then the detector's signal is proportional to $|A_i|^2$, and with thermal lensing the signal is proportional to $|a_d|^2$. The useful signal s , that results from the presence of the TL, is defined as the relative change in the detector's response measured in those two cases, i.e. with and without a thermal lens. Therefore we have

$$s = (|A_i|^2 - |a_d|^2) / |A_i|^2$$

Let this useful TLS signal be denoted as s_0 without the spatial filter, and with the mask inserted as s_t . The ratio s_t/s_0 determines the efficiency of filtering the background illumination $|A_i|^2$. From the above and using eq 7-10, the final expression can be found, which describes the signal due to thermal lensing and observed in the detection arrangement with spatial filtering

$$s_t(D) = |1 + K \exp(i\Phi') \exp[(\eta - \eta')D^2] \eta / \eta'|^2 - 1$$

For small thermal lens signals ($K \ll 1$), the above can be written as

$$s_t = 2\text{Re}\{K \exp(i\Phi') \exp[(\eta - \eta')D^2] \eta / \eta'\} \quad (11)$$

Re denotes the real part of a complex number, and Φ' , η , and η' can be found by using eq 2, 3, and 6.

3. EXPERIMENTAL SECTION

We have performed the experiment with a sample of methylene blue dissolved in methyl alcohol. The absorbance of a 1 mm thick sample at $\lambda = 633$ nm was equal to 0.045. We used a dual-beam TL spectrometer, with small modifications and details of the optical system listed below. The heating beam, and the approximately 20 times less intensive probing beam, were derived from the same He-Ne laser. In order to prevent formation of light-induced thermal diffraction gratings, one of the beams was passing an optical delay line, which was about 50 cm long. To ensure a spatial separation between two beams in the detection plane, the probe and the heating beam intersected at the sample at a small angle (approximately 0.03 rad). The confocal parameter of the probing beam was equal to 40 cm, this figure being equivalent to the probe beam size $2w_0 = 0.57$ mm at its waist plane. The sample was located in the converging part of the probe beam, two confocal distances before the waist plane. The ratio of the heating beam size to the size of the probe beam, measured in the same plane, was equal to 0.88.

The experimental procedure consisted of two steps. First, the ratio s_0 of thermal lensing signal to the total signal from the detector was determined. The thermal lensing signal was measured as a time-dependent component of the detector response, resulting from small changes in its irradiation caused by the TL effect generated by the heating beam. The value of s_0 was used as a reference during the next steps of the experiment. Afterward, a circular opaque mask was inserted in the path of the probe beam and then moved along the axis of the probing beam. For any chosen position of the mask, the ratio s_t of TL signal to total signal was measured, but this time with constant illumination of the detector significantly reduced. The experiment was repeated twice with the ratio of the mask diameter to the probing beam size D/w_0 equal to 0.88 and 1.32, respectively.

4. RESULTS AND DISCUSSION

The increase in TL signal-to-background ratio is of particular interest when probing-beam intensity fluctuations are the main source of noise, limiting sensitivity of the experimental system. In Figure 2 both experimental data s_t/s_0 are

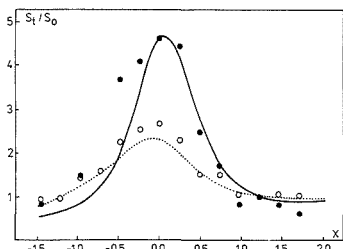


Figure 2. Signal/background improvement s_1/s_0 in a spatially filtered thermal lens spectrometer; experimental points for $x_0 = -2$ and two blocking masks, $D/w = 0.88$ (O) and 1.32 (●); dotted and solid lines, theoretical curves.

shown, as well as the curves resulting from theoretical considerations and calculated from eq 11. As has been expected, the ratio of TL signal to constant background is better in the system with a spatial filter. In the experiment reported, the ratio is up to about 5 times higher when the $D/w_0 = 1.32$ filter is placed close to the waist of the probe beam. It can be easily observed that, within the limits of experimental error (about 10%), good similarity between theoretical and experimental data is obtained. In particular there is quite satisfactory agreement in location of the blocking mask giving maximum increase of signal to background. A simple model evaluating efficiency of filtering and presented in ref 9 gives a discrepancy between the best theoretical and actual position of about one-half confocal parameter.

There are two independent variables describing the construction of a filtered TL spectrometer, the position x of the mask and the ratio of the mask radius to the probe beam size. We have performed a numerical experiment, using eq 11 and calculating filtering efficiency s_1/s_0 , in order to gain insight into how filtering of background TL signal works. At first sight it could be expected that under any circumstance, the most effective filtering should be obtained with the filter placed exactly in the waist of the probing beam. This is expected because as the mask is moved from that position, the ratio of filter radius to beam size D/W decreases. Therefore a smaller part of probing beam is filtered out and, as a consequence, filtering efficiency decreases. On the other hand, this consideration may be oversimplified and misleading. Even if the same portion of the probe beam would be blocked for any distance x , the difference between the radii of curvature of the unperturbed beam and the signal beam would give rise to a different diffraction of both beams. In order to clarify the matter, we have done calculations of s_1/s_0 for various positions x of the mask, whereas we kept the ratio D/W constant. These calculations give a better understanding of filtered TLS operation than the simple intuitive considerations presented above.

In Figure 3 the results of calculating s_1/s_0 are shown, as a function of the position of the blocking mask, for D/W equal to 1.2 and for three different locations of a sample, $-x_0 = 1$,

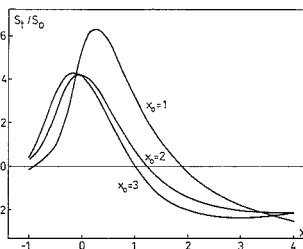


Figure 3. Dependence of thermal lens signal, in a single-beam detection system with spatial filter, on the position of a blocking mask, at any distance x always the same portion $D/W = 1.2$ of probe beam is blocked.

2, and 3. A single beam version of the TL spectrometer has been assumed in the calculations. It can be noticed that the sign of the thermal lens signal is reversed when a mask is moved away from the probe's waist. Thus some care should be taken in designing a filtered thermal lens spectrometer, in order to avoid unexpected results. The curves plotted in Figure 3 indicate that diffraction at the mask is much more important to explain filtered system operation than pure energy consideration of light beam power flowing out the edge of a mask. However, for a system arrangement with a mask placed close to the waist of probe beam, simple theory considering only energetic efficiency of filtering would give satisfactory results, that is the proper sign of the effect, as well as its approximate magnitude.

ACKNOWLEDGMENT

This work was supported by INTIBS, Polish Academy of Sciences, under Grant CPBP 01.12.

LITERATURE CITED

- Gordon, J. P.; Leite, R. C. C.; Moore, R. S.; Porto, S. P.; Whinnery, J. R. *J. Appl. Phys.* **1965**, *36*, 3.
- Chenming Hu; Whinnery, J. R. *J. Appl. Opt.* **1973**, *12*, 72.
- Swofford, R. L.; Morrell, J. A. *J. Appl. Phys.* **1978**, *49*, 3667.
- Harris, J. M. Thermal Lens Effect; In *Chemical Analysis*; Vol. 87, Analytical Applications of Lasers; Piepmeyer, E. H., Ed.; Wiley-Interscience: New York 1986; Chapter 13, pp 451-476.
- Imasaka, T.; Nakanishi, K.; Ishibashi, N. *Anal. Chem.* **1987**, *59*, 1554.
- Dovichi, N. J.; Nolan, T. G.; Weimer, W. A. *Anal. Chem.* **1984**, *56*, 1700.
- Nolan, T. G.; Weimer, W. A.; Dovichi, N. J. *Anal. Chem.* **1984**, *56*, 1704.
- Janssen, K. L.; Harris, J. M. *Anal. Chem.* **1985**, *57*, 1698.
- Slaby, J. *Opt. Commun.* **1987**, *64*, 89.
- Long, G. R.; Bialkowski, S. E. *Anal. Chem.* **1986**, *58*, 80.
- Carter, C. A.; Harris, J. A. *J. Appl. Opt.* **1984**, *23*, 476.
- Sheldon, S. J.; Knight, L. V.; Thorne, J. M. *J. Appl. Opt.* **1982**, *21*, 1663.
- Bialkowski, S. E. *J. Appl. Opt.* **1985**, *24*, 2792.
- Slaby, J. *Opt. Commun.* **1986**, *60*, 133.
- Yariv, A. *Quantum Electronics*; Wiley: New York, 1975.
- Gradshteyn, I. S.; Ryzhik, I. M. *Tables of Integrals, Series, and Products*; Academic Press: Orlando, FL, 1980; eq 8.631.4, p 717.
- Northover, F. H. *Applied Diffraction Theory*; American Elsevier: New York, 1971; pp 282-284.

RECEIVED for review May 8, 1989. Accepted August 28, 1989.

Intermolecular Processes in the Ion Trap Mass Spectrometer

L. K. Pannell and Q.-L. Pu

Laboratory of Bioorganic Chemistry, National Institute of Diabetes, Digestive and Kidney Diseases, National Institutes of Health, Bethesda, Maryland 20892

H. M. Fales* and R. T. Mason

Laboratory of Chemistry, National Heart, Lung, and Blood Institute, National Institutes of Health, Bethesda, Maryland 20892

J. L. Stephenson

Finnigan MAT, Frederick, Maryland 21701

Abnormal (M + 1)/M ratios in the ion trap mass spectrometer were examined to resolve questions about their source. Compounds showing minimal fragmentation provide normal (M + 1)/M ratios except under conditions of space charging (high ion concentration). Substances providing abundant alkyl ions form (M + H)⁺ ions through proton transfer to neutrals. Concentrations causing this effect in the ion trap mass spectrometer and the sources of the proton in the case of methyl decanoate are discussed.

Formation of (M + 1)⁺ ions is commonly observed in electron impact mass spectrometry as sample pressure is raised (1). Onset of the ion-molecule reaction is usually earlier with compounds that can both readily supply and accept a proton. The process is particularly favored with aliphatic molecules containing oxygen or nitrogen (1) since the alkyl fragment ions of such species have relatively high gas-phase acidities (2). Aliphatic alcohols, amines, ketones, and esters are typical examples. In mass spectrometers depending on ion storage, such as ion traps and ion cyclotron resonance spectrometers, the problem is magnified since long residence times result in collisions even at low sample pressure.

In recent publications, mostly in this journal, several authors have addressed this problem and come to somewhat different conclusions. Ghaderi et al. first described (2) the process in a Fourier transform ion cyclotron resonance (FTICR) spectrometer and used the term "self-CI (chemical ionization)" in application to ion storage devices. When methyl stearate was used as an example, (M + H)⁺ was the most abundant ion detected at 20-ms residence time with a sample pressure of 10⁻⁷ Torr. When the ions were confined for 200 ms, the (2M + H)⁺ ion was the most abundant ion. Olson and Diehl (3) extended the term "self-CI" to explain the enhanced (M + 1)/M ratio in spectra produced on a gas chromatograph/Fourier transform infrared/ion trap detector (GC/FTIR/ITD) combination instrument. Self-CI was seen to be a minor process with naphthalene but significant with dicyclohexylamine and short-chain esters. Somewhat surprisingly, they found the effect not even noticeable with certain compounds of high proton affinity including phenol, aniline, alcohols, and nonanal. Concentration dependence was easily observed as the substances eluted in a gas chromatograph peak. Although no exact sample sizes are mentioned, it is important to note that much of the sample was split off prior to transfer to the ITD. About the same time, Ratnayake et al. (4), examining the use of the ITD for certain lipids including fatty esters, isopropylidene derivatives, and phenolic acetates, remarked on increased (M + 1)/M ratios as well as other differences in the spectra. Since the magnitude of the (M + H)⁺ ions was

found to be concentration dependent, these authors also considered them due to self-CI, although they did not use the term.

Eichelberger and Budde (5), surveying the use of the ITD for environmental analysis, noted excessive (M + 1)/M and (M/2) + 1 ratios using >50 ng of polycyclic aromatic hydrocarbons. With pyrene, analysis of the peak profiles revealed saturation of the data system with consequent peak broadening as well as a shift of the peak area toward higher mass. Since the ITD normally measures abundance at 1 mass unit intervals rather than analyzing the shape of each peak, this area would be incorrectly assigned to the next higher mass. The peak shift was attributed to space charging by C. Campbell of the Finnigan Corporation (personal communication in ref 5). Consequent limitation of the dynamic range available to the ITD was regarded by these authors as a limitation of the instrument. They also noted that the manufacturer was about to modify the software to automatically adjust the ionization time appropriate to sample size (automatic gain control (AGC), Finnigan MAT).

Shortly thereafter, noting the paper by Olson and Diehl (3), these authors pursued the matter further (6) using both anthracene-*d*-10 and hexachlorobenzene, i.e., compounds incapable of forming (M + 1)⁺ ions. Since peaks continued to be observed at M + 1, they concluded that all of the abundance at this mass was caused by space charging rather than self-CI. Space charging was considered to reduce the effective radio frequency (rf) potential experienced by an ion, shifting it to higher mass. In fact, Armitage et al. (7), in agreement with Fisher (8), have shown that the effect of space charging is the same as adding a direct current (dc) potential to the ring electrodes of the ion trap. The resulting region of ion stability is both theoretically and experimentally skewed to higher masses. A further effect is that ions at lower mass fall outside the stability region and are lost. Though this conclusion was not specifically stated, the communication by Eichelberger et al. (6) could be read to imply that space charging is also the explanation for the abundant M + 1 ions observed by Olson and Diehl (3) using dicyclohexylamine and short-chain esters.

Meanwhile, we had acquired versions of Finnigan ion traps equipped with the AGC software modification. Even with this modification, we found the (M + 1)/M ratios excessive, and we suggested once again that the phenomenon was due to self-CI (ASMS Conference, June 5-10, 1988) (9). As proof, we pointed out that these excessive ratios were obtained only on the molecular ions, even when considerably more abundant fragment ions were present. Further experiments involving peak shape analysis and deuterated samples confirmed this point. These experiments are now discussed in detail below with further information on the sources of the proton.

More recently, a communication by McLuckey et al. (10) outlined thoroughly the conditions necessary for self-CI in the ion trap. Using methane, these authors obtained a rate constant for its self-reaction consistent with that obtained with other mass spectrometers. In the case of ethyl formate, they showed, both by peak profile analysis and MS/MS, that the $M + 1$ ion was a true $(M + H)^+$ ion. Furthermore, sources of the proton were found to include the molecular ion (m/z 74) and the fragment ion (31) rather than water or other substances. A high $(M + 1)/M$ ratio was obtained even under regular electron impact (EI) conditions in the trap, i.e., without using long ion storage times. These authors concluded that a 50-ng sample of any substance capable of reacting with itself (or its fragment ions) with a rate constant of ca. 3×10^{-9} cm³/molecule s is expected to show about 5% excess $(M + H)^+$ as it elutes from a typical gas chromatograph. These authors made the important point that automatic gain control, while preventing space charging, should cause no change in the $(M + 1)/M$ ratio because, for a fixed number of ions, the percentage of self-CI depends only on the amount of neutrals present. Experiments presented below suggest that their theoretical estimate of the quantity of sample necessary for self-CI may be low.

EXPERIMENTAL SECTION

Chemicals used in this work were of the highest quality available from commercial sources and were used without purification. Both the Model 700 ITD and the ITMS were purchased from the Finnigan Corp., Sunnyvale, CA. The latter was used in the supplied configuration with an open split between the Hewlett-Packard Model 5880 gas chromatograph, while the former was adapted with a short, direct inlet from a Hitachi gas chromatograph. Versions 3 and 4 of the software were used in both instruments. Transfer lines were maintained at 250 °C, while the ITD was fixed at 225 °C and the ITMS at 100 °C. Samples were run isothermally on the GC at temperatures such that the sample eluted in 3–4 min. The mass range was scanned at the default setting of 5555 amu/s.

RESULTS AND DISCUSSION

A 70-ng sample of naphthalene-*d*₈ was first investigated to replicate closely the experiments of Olson and Diehl (3) with ordinary naphthalene. As Figure 1a shows, without AGC a normal $(M + 1)/M$ ratio was obtained with an ionization time of 1 ms. At 12 ms (Figure 1b) the $(M + 1)/M$ ratio is clearly excessive, and by 25 ms (Figure 1c), $M + 1$, rather than $M + 2$, i.e., $(M + D)^+$ expected from self-CI, dominates the spectrum. Examination of the peak profiles (inset, Figure 1c) as the compound elutes from the GC shows, in agreement with a similar study on pyrene by Eichelberger and Budde (5), that the effect is due to peak distortion from space charging. When the sample size is tripled (Figure 1d), still with a 25-ms ionization time, the peak is broadened so that the data system indicates the presence of many ions beyond M^{++} . Furthermore, peaks at lower mass are diminished in abundance, as predicted by the perturbed stability diagram shown by Armitage et al. (7). Under these conditions the molecular ion appears to shift back to its correct position in spite of the excessive broadening. The reason for this is not entirely clear, but at this point the peak is so distorted that estimation of its centroid is difficult.

Using ordinary naphthalene, Olson and Diehl (3) had found the $(M + 1)/M$ ratio to be about 17% high. It appears that their results are best explained by the space charging phenomenon. Under normal conditions, there is no evidence for self-CI in naphthalene before space charging occurs.

To determine whether self-CI might occur under more extreme conditions with naphthalene, the sample was studied by using other modes available with the ITMS. Ions other than the candidate ion were first ejected from the trap by using a combination of rf and dc on the ring electrode. The selected

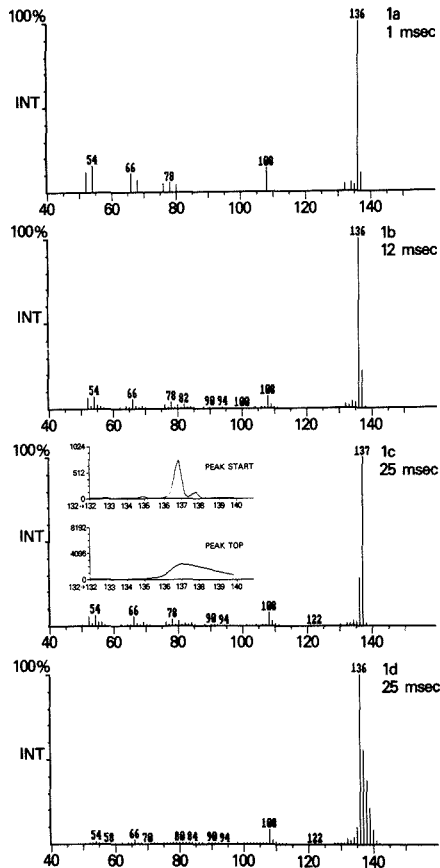


Figure 1. Mass spectra of naphthalene-*d*₈ at varying ionization times with 70 ng (a, b, c) and 210 ng (d) of sample entering the ion trap.

ion was then retained in the trap for varying times to allow accumulation of product ions from reaction with neutral naphthalene-*d*₈. In this fashion, by isolation of m/z 136 (M^{++}) and retention in the trap for up to 50 ms, no increase was seen in $M + 2$; the only effect noted was the appearance of about 0.2% of the dimer $(2M)^{++}$ at m/z 272 and 5% of $(2M - D)^+$ at m/z 270. Similarly, isolation of the odd-electron ion representing loss of acetylene (C_2D_2) at m/z 108 resulted only in the production of 52% of the molecular ion by charge exchange, even when it was held for 50 ms. On the other hand, the even-electron ion (C_2D_2)⁺ at m/z 54 whose conjugate base has a low proton affinity was completely lost after 50 ms, as it formed a mixture of ions of m/z 108 (33%), 122 (1%), 136 (54%), and of $M + D$ (11%) (self-CI) at m/z 138.

Compounds such as aliphatic acid methyl esters show the self-CI effect much more readily (2, 10). For example, Tulloch found it necessary to resort to trimethylsilyl rather than methyl esters in order to analyze the deuterium content of a series of specifically deuterated decanoic acids (11). When the chain length of the acid was increased to C16 (palmitic acid), self-CI of the methyl esters diminished considerably. We have examined both methyl decanoate and methyl palmitate using an ordinary magnetic sector spectrometer (LK-B-9000), and Figure 2A confirms Tulloch's observations re-

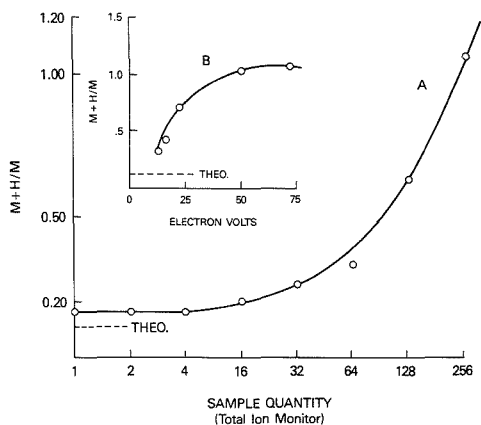
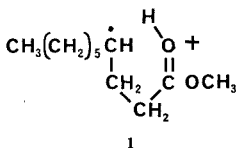


Figure 2. Variation in (M + H)/M ratios with sample pressure (A) and ionizing voltage (B) obtained with the LKB-9000 spectrometer.

garding the increase in the (M + 1)/M ratio of methyl decanoate with sample pressure. Interestingly, even at the lowest pressures the (M + 1)/M ratio was about 0.18 instead of the theoretical value of 0.12, and it appeared to plateau at this value, suggesting the existence of a second, pressure-independent, proton-transfer process.

In a later report (12), Tulloch and Hogge used deuterium labeling to show that the (M + H)⁺ protons derived mostly from protons attached to C-4, C-5, and C-6 (37, 15, and 9%, respectively) of the ester. They suggested that the reaction involved combination of rearranged forms of the molecular ion such as 1 with neutral ester. The failure of methyl pal-



mitate to show the same effect was ascribed to protection afforded by its longer alkyl chain as it wrapped around the protonated ester group, shielding it from further reaction. These authors also pointed out that their data did not rule out the possibility that rearrangement ions such as *m/z* 74 and 87 might be alternative sources of the proton since these species are deuterated in accord with the neutral ester. On the other hand, Ghaderi et al. (2) ascribed the source of the protons to the many fragment ions occurring in these ester spectra whose conjugate bases have low proton affinity. In fact, this is the only conclusion possible from the appearance of their spectrum of methyl stearate confined for 20 ms where (M + H)⁺ was by far the most abundant ion.

Before further examination of this process using the ITMS, it was necessary to prove unequivocally that self-CI rather than space charging was responsible for the excess abundance at M + 1. By use of 6 ng of perdeuterated methyl palmitate, with AGC on, a correct (M + 1)/M ratio is obtained (Figure 3a), but at 24 ng M + 2, i.e., (M + D)⁺ at *m/z* 306, exceeds the molecular ion in intensity (Figure 3b). The peak profiles retain their symmetry (inset, Figure 3b) showing that under these conditions the AGC is correctly performing its function of preventing space charging. We therefore confirm Ghaderi's observation that self-CI does occur with long-chain methyl esters, at least under ITMS conditions. As with naphthalene-*d*₈, increasing the number of ions in the trap by a factor

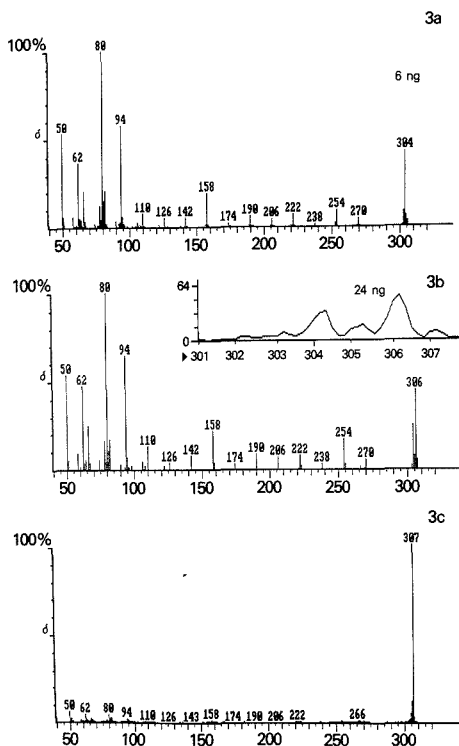


Figure 3. Spectra of methyl palmitate-*d*₃₄ in "AGC on" mode: (a) 6 ng with 1-ms ionization time; (b) 24 ng with 1-ms ionization time; (c) 24 ng with 20-ms ionization time.

of 20 by increasing the ionization time again shifts (M + D)⁺ 1 mass unit higher (Figure 3c), distorting the appearance of the isotope cluster. Again, intensity at lower masses is lost under these extreme conditions of space charging.

Under operating conditions defined above where self-CI but not space charging occurs, major ions in the spectrum of methyl decanoate were examined to determine the extent to which they participate in the self-CI process. In this experiment, the ionization times were adjusted for each candidate ion in relation to its normal abundance to ensure the same initial number of ions in the trap. Examining first the rearrangement ion at *m/z* 74 (Figure 4a), one can see that no protons are transferred to neutral ester even after 50 ms. The only process observed is charge exchange to form about an equal number of ester molecular ions at *m/z* 186. In contrast, even-electron alkyl ions such as *m/z* 101 do indeed supply protons, forming even-electron (M + H)⁺ ions at *m/z* 187 (Figure 4b). The abundance of these ions diminishes smoothly with mass of the reacting ion as shown in Figure 5, reaching zero at M - C₂H₅. Lower mass ions such as *m/z* 41, whose conjugate bases have very low proton affinity, cause subsequent fragmentation of the (M + H)⁺ ion as shown in Figure 4c. Losses of H₂, methanol, or both appear to be major pathways. We have also noted interesting differences in the nature of the fragmentation depending on the structure of these reactant ions. This will be discussed in a forthcoming publication.

These studies fail to provide any evidence for the process involving 1 as suggested by Tulloch and Hogge (12). Even when *m/z* 186 was confined for 50 ms, far longer than allowed

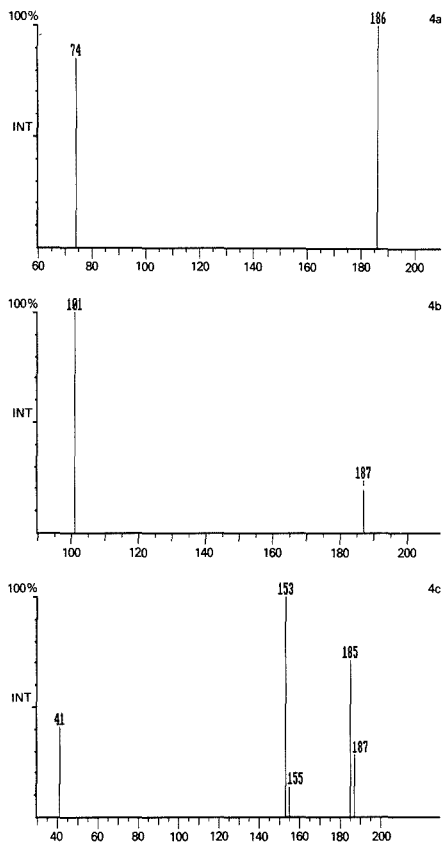


Figure 4. Spectra obtained by reaction of low-mass ions with neutral methyl decanoate: (a) m/z 74 reactant ion; (b) m/z 101 reactant ion; (c) m/z 41 reactant ion.

Methyl Decanoate 50ng Injected on DB-1

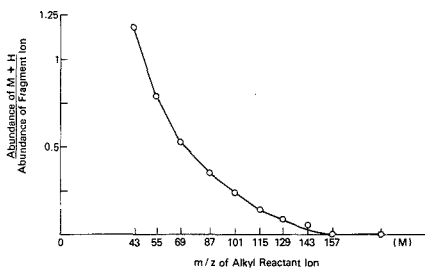


Figure 5. Tendency of fragment ions from methyl decanoate to donate proton to neutral ester. A 50-ng sample of methyl decanoate was injected on DB-1.

under normal EI conditions with magnetic mass spectrometers, the only reaction observed was $\approx 3\%$ dimerization to form $2M^{++}$. Essentially identical results were obtained when all the above experiments were repeated using methyl palmitate.

If the fragment ions are the sources of the proton causing self-CI, the ratio of $(M + 1)/M$ should decrease as the ionizing

energy is lowered and the fragmentation diminishes. Unfortunately, it is not possible to study this process in the ITMS where all ions are necessarily produced at >100 eV. Using a magnetic spectrometer (LKB-9000) (Figure 2, curve B) shows that this is correct, although again, the theoretical value of ≈ 0.11 was not reached at the lowest voltage where ions are detectable.

CONCLUSIONS

Under suitable conditions virtually all compounds are capable of self-CI. If the process is not one of simple proton transfer, then either dimerization to form $2M^{++}$ (or $(2M + H)^+$) or transfer of some other fragment may be expected. The proton-transfer process is important when alkyl fragments whose conjugate bases have low proton affinity are present in profusion. When the spectrum is dominated by a molecular ion, as in the case of naphthalene, peak distortion due to space charging can be expected with the ITMS and ITD long before self-CI occurs. This is likely the reason that Olson and Diehl (3) failed to observe self-CI with aniline and phenol although their results with alcohols and nonanal are not so easily explained.

In general our results are in accord with the principle that odd-electron ions react with neutral compounds by forming odd-electron ions through charge exchange, while even-electron ions form even-electron products through proton or alkyl group transfer. These are all the products of bimolecular reactions, and it is perhaps not surprising that electron parity is maintained. Although the transferring proton can arise from interaction between molecular ions and neutrals as in, for example, methane and methyl formate, with larger molecules the source of protons is more likely to be the fragment ions whose conjugate bases have low proton affinity.

Finally, the point made by McLuckey et al. (10) is worth reiterating: The automatic gain control feature of the ITMS and ITD will not affect the magnitude of self-CI observed in these spectrometers. Other measures must be taken to ensure that the sample load entering the trap is appropriate for the sample structure since this feature alone determines the magnitude of its tendency to exhibit self-CI. It is obvious that a good ratio can be realized even under these excessive conditions if scans are examined near the base of chromatographic peaks. One can even envision a program that would continuously examine the $(M + 1)/M$ ratio over a gas chromatographic peak and alert the analyst to the presence of either phenomenon.

Registry No. d₂, 7782-39-0; naphthalene, 91-20-3; methyl palmitate, 112-39-0; methyl decanoate, 110-42-9.

LITERATURE CITED

- Beyon, J. H. *Mass Spectrometry and Its Applications to Organic Chemistry*; Elsevier Publishing Co.: New York, 1960; pp 275-282.
- Ghaderi, S.; Kulkarni, P. S.; Ledford, E. B., Jr.; Wilkins, C. W.; Gross, M. L. *Anal. Chem.* **1981**, *53*, 428-437.
- Olson, E. S.; Diehl, J. W. *Anal. Chem.* **1987**, *59*, 443-448.
- Ratnayake, W. M. N.; Timmins, A.; Ohshima, T.; Ackman, R. G. *Lipids* **1986**, *21*, 518-524.
- Eichelberger, J. W.; Budde, W. L. *Biomed. Environ. Mass Spectrom.* **1987**, *14*, 357-362.
- Eichelberger, J. W.; Budde, W. L.; Silvon, L. E. *Anal. Chem.* **1987**, *59*, 2732-2734.
- Armitage, M. A.; Fulford, J. E.; Hughes, R. J.; March, R. E.; Mather, R. E.; Waldron, R. M.; Todd, J. F. *Adv. Mass. Spectrom.* **1980**, *88*, 1754-1763.
- Fischer, E. Z. *Phys.* **1959**, *156*, 1-26.
- Pannell, L. K.; Pu, Q.-L.; Fales, H. M.; Mason, R. T.; Stephenson, J. L. Presented at the 36th ASMS Conference on Mass Spectrometry and Allied Topics, San Francisco, CA, June 5-10, 1988, 725-726.
- McLuckey, S. A.; Glish, G. L.; Asano, K. G.; Van Berkel, G. J. *Anal. Chem.* **1988**, *60*, 2312-2314.
- Tulloch, A. P. *Chem. Phys. Lipids* **1987**, *37*, 197-213.
- Tulloch, A. P.; Hogge, L. R. *Chem. Phys. Lipids* **1985**, *37*, 271-281.

RECEIVED for review May 22, 1989. Accepted August 21, 1989.

Coaxial Continuous Flow Fast Atom Bombardment in Conjunction with Tandem Mass Spectrometry for the Analysis of Biomolecules

Leesa J. Deterding, M. Arthur Moseley,¹ and Kenneth B. Tomer*

Laboratory of Molecular Biophysics, National Institute of Environmental Health Sciences, Research Triangle Park, North Carolina 27709

James W. Jorgenson*

Department of Chemistry, University of North Carolina at Chapel Hill, Chapel Hill, North Carolina 27514

The capability of interfacing coaxial continuous flow fast atom bombardment (CF-FAB) with tandem mass spectrometry (MS/MS) is demonstrated. The goal of this research is to demonstrate the ability of obtaining on-the-fly (i.e. chromatographic real time) MS/MS spectra of biomolecules and to demonstrate the feasibility of using open tubular CF-FAB as a means of introducing and maintaining a constant flux of analyte into the mass spectrometer over long periods of time. On-the-fly MS/MS spectra of a tripeptide, Met-Leu-Phe, were obtained on a 220-pg injection and a 22-pg injection. With a total acquisition time of 2 s, fragment ions resulting from common backbone cleavages were observed. With a 50 μ m i.d. packed microcapillary column, the separation of a mixture was obtained and the MS/MS spectra were acquired as the analytes were eluting from the column. Through the use of the coaxial CF-FAB interface to deliver a constant flow of analyte, MS/MS spectra of a variety of compounds, including peptides, sugars, fatty acids, phospholipids, and steroids, were obtained as well as an MS/MS/MS spectrum of a tetrapeptide.

Since the development of fast atom bombardment mass spectrometry (FAB/MS) (1), FAB/MS has become a widely used desorption technique for the analysis of biomolecules. There are several disadvantages, however, associated with FAB/MS: (1) Due to the high concentration of matrix on the probe tip, mass spectra can be complicated by the high level of chemical background noise; (2) often, few structurally informative fragment ions are produced, and those that are produced may be obscured by matrix ions; (3) the sample ion beam can be short-lived, since only small amounts of analyte can be used; (4) a "suppression" effect due to the hydrophobicity/hydrophilicity index of the compounds being analyzed may occur, which results in one or more of the analytes preferentially occupying the surface of the sample droplet, thus suppressing the analysis of the other compounds (2); and (5) quantification can be difficult and time-consuming because the FAB probe must be removed for each analysis. Recently, two techniques, tandem mass spectrometry (MS/MS) and continuous flow FAB (CF-FAB), have been developed to alleviate some of these problems associated with FAB.

The first technique to achieve widespread attention was FAB used in conjunction with MS/MS. In MS/MS the ion of interest is selected in MS-I and allowed or forced by col-

lisional activation to fragment. The fragmentations are subsequently analyzed by MS-II. Thus, ions due to the matrix are eliminated, and parent ion-daughter ion relationships in mixtures can be determined. Also, collisional activation decomposition (CAD) of FAB-desorbed ions often yields structurally informative fragment ions that aid in the substance identification.

The second technique developed to overcome some of the disadvantages of FAB was frit-FAB (3) and continuous flow fast atom bombardment (CF-FAB) (4). The continuous flow of aqueous solutions containing small amounts of matrix to the probe tip results in a significant decrease in the chemical noise. Therefore, higher sensitivities are observed due to improved signal-to-noise (S/N) ratios (5). In addition, the continuous introduction of analyte into the mass spectrometer leads to the production of a steady ion beam over long periods of time. Also, it has been observed that the use of CF-FAB significantly reduces the suppression effect because there is a constant flow of analytes to the probe tip (6). Another advantage of CF-FAB is increased reproducibility and sample throughput because removal of the probe from the mass spectrometer after each analysis is not necessary.

We are currently involved in an ongoing research project in which the goal is to couple open tubular liquid chromatography (OTLC) with mass spectrometry. Our initial efforts were successful at interfacing OTLC with MS under electron impact (EI) and chemical ionization (CI) conditions (7), but the interface was unsuitable for peptides and other complex biomolecules. To analyze more polar and less volatile compounds, we have utilized CF-FAB/MS. The CF-FAB/MS interfaces developed thus far employ a single fused silica capillary column to transport the analytes to the FAB probe tip in the mass spectrometer. Addition of the matrix is accomplished either by adding the matrix to the analyte solutions or by postcolumn addition (3, 4, 8). However, precolumn addition of the matrix into the LC mobile phase can compromise the chromatography due to changes in the polarity and viscosity of the mobile phase. Postcolumn addition of the matrix sometimes leads to chromatographic peak broadening. These problems are significantly enhanced in OTLC due to the lower flow rates involved (<1 nL/s).

To avoid these problems, we have recently developed a coaxial CF-FAB interface in which the analytes and the matrix are delivered separately to the probe tip (9, 10). Briefly, the coaxial CF-FAB interface consists of a fused silica capillary column that is surrounded by a second fused silica column in which the matrix is introduced. As a result, there is no mixing of the matrix with the analytes until both have reached the FAB probe tip. This coaxial continuous flow design is advantageous since the chromatography is not affected by the matrix. In addition, the ability to independently control both

* Authors to whom correspondence should be addressed.

¹ Also at the Department of Chemistry, University of North Carolina at Chapel Hill, Chapel Hill, NC 27514.

the OTLC flow rate and the matrix flow rate and composition is desirable.

This coaxial continuous flow system is chromatographically advantageous since the OTLC columns being employed offer a greater separation efficiency than that of conventional columns (i.e., over 1×10^6 theoretical plates can be obtained with these OTLC columns (11)). Compared to conventional columns (4 mm i.d.) and microbore columns (1 mm i.d.), these OTLC columns (10 μm i.d.) and microcapillary columns (50 μm i.d. packed with 10- μm particles) have a much smaller internal diameter. This system is more compatible with mass spectrometry because the smaller internal diameters allow a much lower flow rate.

In our previous work using this coaxial CF-FAB interface (10), we have demonstrated the ability to obtain on-the-fly (i.e. chromatographic real time of 5–10 s) full scan mass spectra for a variety of compounds, including peptides, sugars, steroids, and phospholipids. Detection limits of 1.8 fmol in the scanning acquisition mode and 500 amol in the multichannel analysis (MCA) acquisition mode for the tripeptide Met-Leu-Phe were obtained. Parallel to our interest in OTLC/MS, we have been exploring the application of MS/MS to biomolecules such as modified oligonucleotides and glutathione conjugates (12, 13). To tie together our activities in MS/MS and OTLC CF-FAB/MS, we have explored the compatibility of OTLC CF-FAB/MS and tandem mass spectrometry.

The goal of this research project has been twofold: (1) to demonstrate the ability of obtaining MS/MS spectra of biomolecules eluting on the OTLC time scale (i.e. 5–10 s wide peaks) and, thus, its compatibility with OTLC columns currently under development; and (2) to demonstrate the feasibility of using open tubular continuous flow FAB as a technique to introduce and maintain a constant flux of analyte over long time periods. We report our results here.

EXPERIMENTAL SECTION

Chemicals. Substance P, bradykinin, Met-Leu-Phe, *N*-acetyl angiotensin I, maltotetraose, dihydrostreptomycin, dipalmitoylphosphatidylcholine, palmitoleic acid, corticosterone, taurothiocholic acid-3-sulfate, and Phe-Gly-Leu-Met-NH₂ were purchased from Sigma Chemical Co. (St. Louis, MO).

Sample Injection. Samples were injected by using a capillary liquid chromatography system that was developed in this laboratory for use with open tubular liquid chromatography (6). A Valco injection valve is used to make injections. The injection valve is connected with stainless steel tubing to a sample tee, which holds the OTLC column. The other side of the sample tee is connected to a waste valve. To make an injection onto the OTLC column, the injection valve and the waste valve are opened to the sample tee. Approximately 200 μL of analyte solution is needed to fill the tubing and the sample tee. The waste valve is then closed, and the injection valve is opened to the pressurized mobile-phase reservoir, which starts the flow of the sample solution into the column. Opening the waste valve flushes the sample solution out of the sample tee and replaces it with mobile phase. Closing the waste valve repressurizes the system and flow recommences. In this manner, short injections (i.e. seconds) or long continuous injections (i.e. hours) can be made onto the OTLC column. Therefore, injections of approximately 10 μL to 10 nL of analyte solution can be made without any evidence of the chromatographic peak broadening that can sometimes occur with traditional loop-type LC injection systems. Therefore, this injection system offers the capability of doing on-the-fly or constant flux tandem mass spectrometry. Water was used as the mobile phase except for the analysis of bradykinin, where the mobile phase was 0.1% trifluoroacetic acid (TFA) in water.

It should be noted that this injection method is only one of four different methods that we have used with our microcolumns. While it requires 200 μL of sample, greater than 99.99% of the sample is recovered in a vial from the "waste" line from our 5-s (4.4 nL) injection. This method is routinely used because it is the most facile. The second method requires the removal of the

in-line filter from the injector, allowing the analytical capillary to be positioned within a few centimeters of the injection valve. This permits analysis from as little as 10 μL of sample (4.4 nL of sample used with 9.996 μL recovered). Careful filtering of all sample solutions and mobile phases permits the use of this type of injection without plugging the OTLC column. The third injection method uses a stainless steel pressure "bomb" which is of sufficient size to contain a microvial of sample solution. The analytical column is inserted into the filtered sample solution, and a pressure seal around the column is made with a $1/16$ -in. fitting and a vespel ferrule. The bomb is pressurized to 1000 psi for the time interval required to inject the desired volume of sample onto the column. After injection, the analytical column is reconnected to the LC pumps for analysis. This method obviates the need for a sample syringe, and >99.9% of the sample remains in the sample vial, precluding any sample loss due to adsorption on metal surfaces. The most efficient injection method used with microcolumns in our laboratories utilizes a pneumatic microinjector in conjunction with a microscope and micromanipulators for direct on-column injection of nanoliter volumes (14–16). The utility of this system has been exploited for the analysis of individual neurons by OTLC (14, 16) and has demonstrated a relative standard deviation of 2.7% in volume delivered for 10-nL injections onto an OTLC column (15).

Coaxial Continuous Flow FAB Interface. The coaxial continuous flow FAB interface used in this work has been previously described (9). A fused silica capillary column is inserted into a sheath capillary column. The analytes flow through the inner column (typically 10 μm i.d., 150 μm o.d.) while the matrix simultaneously flows through the outer column (typically 200 μm i.d., 350 μm o.d.). No mixing of the matrix with the analytes occurs until both have reached the FAB probe tip. A microliter syringe pump (Isco, Inc., Lincoln, NE) was used to regulate the flow of the matrix through the sheath column.

Packed Microcapillary Column. A packed microcapillary column was used to obtain the separation that is demonstrated. The column, 2.2 m \times 50 μm i.d., was packed with 10- μm ODS2 Spherisorb (Alltech, Inc.) particles. A gradient from 30% acetonitrile/water to 90% acetonitrile/water over 15 min at a flow rate of approximately 85 nL/min was used as the capillary mobile phase.

Mass Spectrometry. All mass spectra were acquired on a VG ZAB-4F mass spectrometer (17). This instrument is of B₁E₁-E₂B₂ design and is operated at 8 kV. An Ion Tech atom gun and a standard VG continuous flow FAB source heated at 40–60 °C were used. The samples were bombarded with 8-keV xenon atoms. The MS/MS experiments were carried out by focusing the parent ion through MS-I. Daughter ion spectra were obtained by collisional activation at 8 keV. The parent ions were activated by colliding them with helium gas (at approximately 50% beam reduction) in the collision cell located in the third field-free region. Collisionally activated decomposition (CAD) spectra of the resulting daughter ions were obtained by a linear E₂B₂ linked scan of MS-II, which was typically operated at unit mass resolution.

In the MS/MS/MS experiment, the parent ion is focused through B₁ and collisionally activated in the second field-free region. The resulting daughter ion is then focused through E₁ into the third field-free region. This daughter ion is collisionally activated, and the resulting MS³ spectrum is acquired by an E₂B₂ linked scan. The data acquisition system used was a VG Analytical 11-250 data system.

RESULTS AND DISCUSSION

We have shown that this coaxial continuous flow FAB interface allows for increased sensitivity over that of other continuous flow FAB interfaces (10). This is due to the ability of the capillary LC system to deliver a high concentration of analyte in a short period of time. This advantage as well as the ability to easily introduce a low and constant flux of analyte for an extended period of time makes this coaxial CF-FAB interface very useful for the acquisition of MS/MS data.

MS/MS in Chromatographic Real Time. Our primary goal in this study was to ascertain the compatibility of OTLC elution times with MS/MS data acquisition on the VG

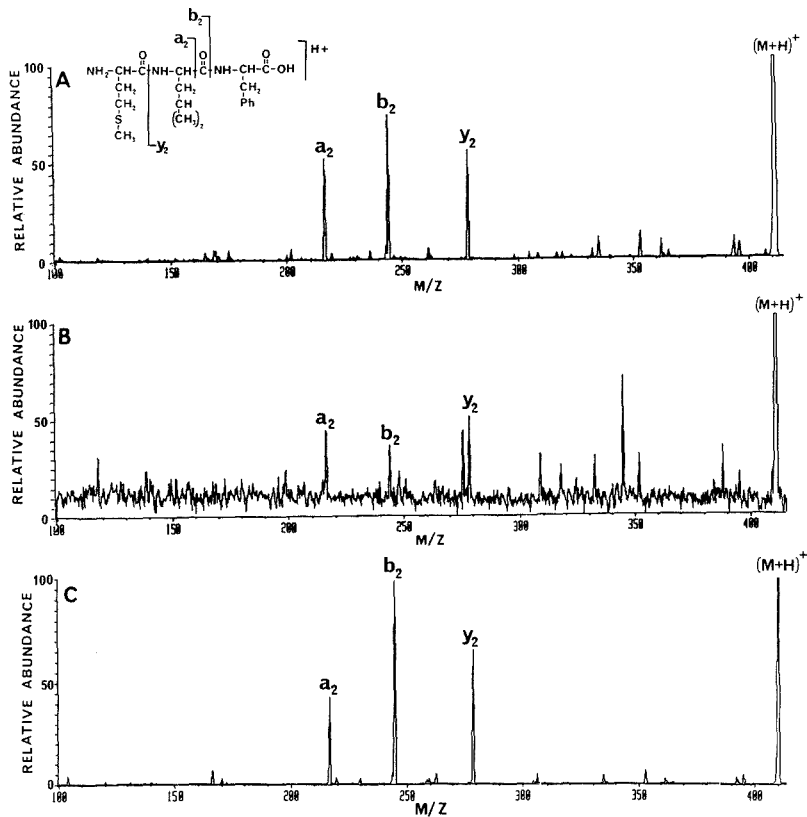


Figure 1. MS/MS spectra of (A) 220 and (B) 22 pg of the $(M + H)^+$ ion of Met-Leu-Phe acquired on-the-fly by using the OTLC column. (C) Static FAB MS/MS spectrum of the $(M + H)^+$ ion of Met-Leu-Phe.

four-sector instrument. Thus, our initial efforts centered on experiments designed to test MS/MS acquisitions under the limits imposed by OTLC (i.e. sensitivity and elution times). Although relatively concentrated solutions (i.e. 1 mg/mL) can be injected onto the OTLC columns, these columns can easily be overloaded. Overloading of typical OTLC columns occurs with analyte amounts on the order of 5–50 ng (a 5-s injection of a 5 mg/mL solution at a flow rate of 1 nL/s places 25 ng of analyte on the column). MS/MS spectra on low-nanogram levels of FAB-desorbed analytes have been reported for magnetic sector MS/MS instruments (18–20), but these amounts have been the exception rather than the rule. Thus, there was a real question as to whether MS/MS spectra could be acquired routinely from low-picogram amounts of analyte. A second limiting factor for OTLC is the elution time. In contrast to the wide peaks observed in microbore LC (i.e. minutes), OTLC peaks are on the order of 5–20 s wide at half-height. Thus the scan rate of MS-II becomes critical. The combination of fast scan speeds and low analyte amounts, therefore, imposes stringent performance criteria on the equipment.

Our experiments designed to ascertain the compatibility of MS/MS and OTLC in real time (on-the-fly) were performed with the tripeptide Met-Leu-Phe (MW = 409). From our initial experiments involving full scan spectra, a detection limit of 500 amol was obtained (10). We felt, therefore, that the coaxial CF-FAB interface would provide sufficient sensitivity

for the acquisition of on-the-fly CAD data. MS/MS spectra of the $(M + H)^+$ ion of Met-Leu-Phe were acquired on-the-fly from a 220-pg and 22-pg injection (Figure 1A and Figure 1B, respectively) of the peptide. The mass spectrometer was scanned from 420 to 100 amu at 3 s/decade resulting in a total acquisition time of 2 s. Since the peak width at half-height for the 22-pg injections is 6 s, the MS/MS spectrum in Figure 1B is thus representative of <10 pg of material. The MS/MS spectrum of the 220-pg injection compared well with that obtained from 1 μ g on the direct insertion FAB probe (Figure 1C). The $(M + H)^+$ ion of m/z 410 fragments into the common backbone cleavages of a_2 , b_2 , and y_2 as shown. Nomenclature for the peptide cleavages is that of Roepstorff (21) as modified by Biemann (22). Although the 22 pg level spectrum is not clean enough to identify an unknown, it is of sufficient quality to confirm the identity of the compound. Thus, MS/MS spectral acquisition is compatible with both the elution times and upper concentration limits imposed by the capillary system using the coaxial CF-FAB interface.

As the assignment of daughter ion masses in the MS/MS spectra is based on a linear interpolation rather than a calibrated scan, it is of interest to note the accuracy of the mass assignment. The mass assigned to the three major daughter ions of Met-Leu-Phe and one daughter of bradykinin as a function of scan rate is shown in Table I. These data, acquired at a resolution of approximately 500 for Met-Leu-Phe and 1000 for bradykinin, indicate for the instrument used that

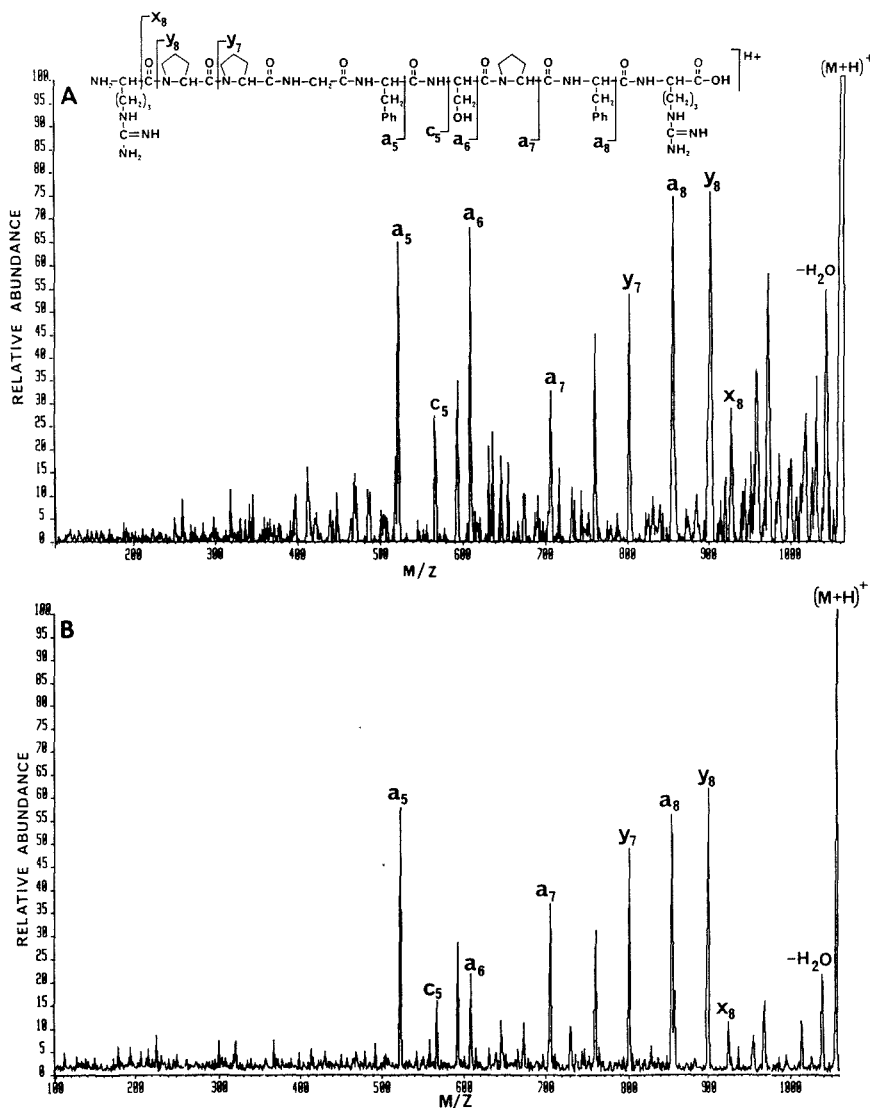


Figure 2. MS/MS spectrum of the $(M + H)^+$ ion of bradykinin acquired (A) by constant flux of analyte and (B) from the static FAB probe tip.

the mass assignment does not degrade significantly until scan rates of 2 s/decade are reached. It should also be noted that this may vary when different mass ranges are analyzed and that this is also instrument dependent.

Constant Flux MS/MS. One problem often encountered in the acquisition of MS/MS data is that the level of analyte can decrease significantly during analysis, and data acquisition often has to be interrupted for reloading of the sample. Using a continuous flow interface permits maintenance of a continuous flux of analyte, if the analyte can be continuously injected. The OTLC CF-FAB injection system is designed such that a continuous amount of analyte solution can be introduced into the mass spectrometer over extended periods of time (i.e., hours) as well as over short time periods (i.e.,

seconds). In fact, at the typical OTLC flow rates of <1 nL/s, an injection volume of 200 μ L can deliver a constant amount of analyte for several days. Even at high analyte concentrations (1 mg/mL), an hour-long acquisition would consume only 60 ng of analyte. With the sensitivity observed from our on-the-fly experiments, the combination of continuous flow injections with the coaxial CF-FAB interface should be able to provide good-quality MS/MS spectra from a continuous flux of analyte.

We have obtained MS/MS spectra from a variety of compounds, including peptides, sugars, phospholipids, fatty acids, and steroids, using the coaxial CF-FAB interface to deliver a constant flux of analyte. The compounds for which we have obtained MS/MS data are listed in Table II. Data acquisition

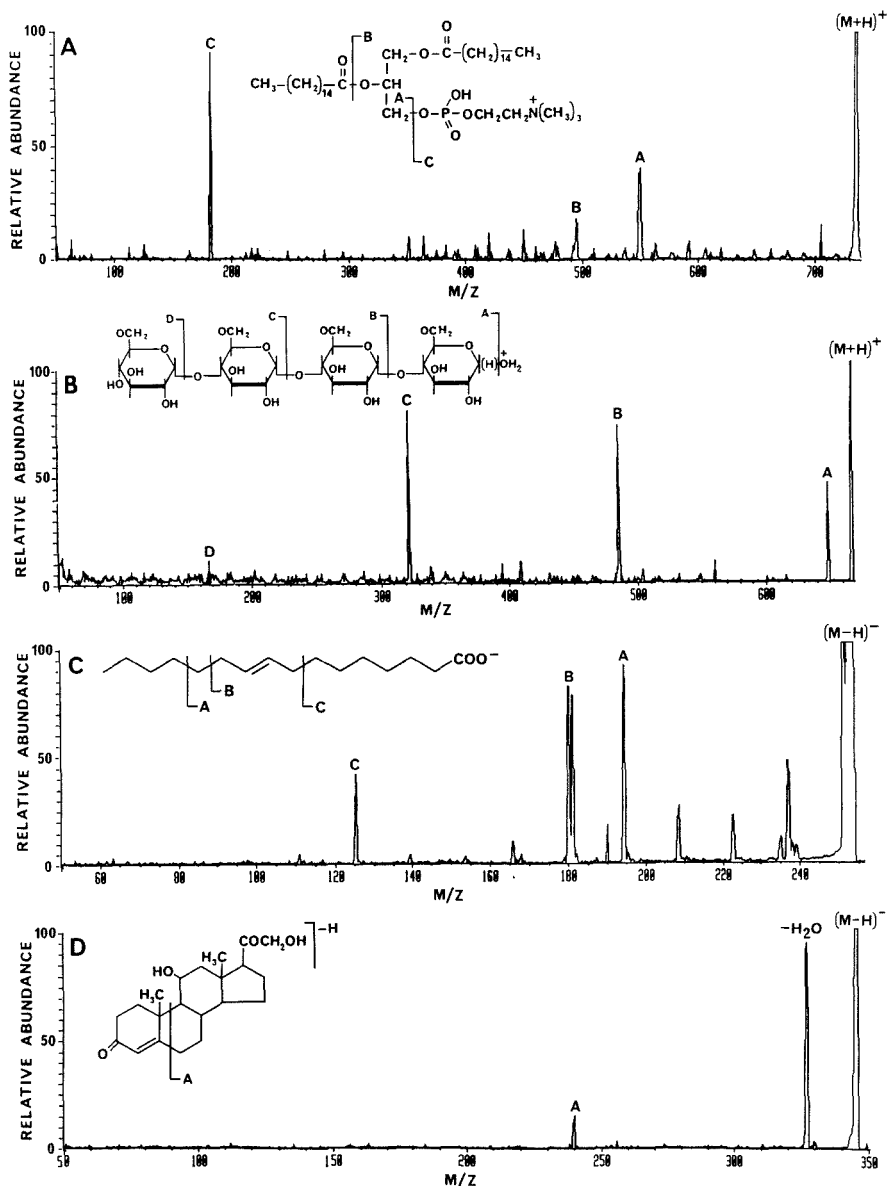


Figure 3. MS/MS spectrum (A) of the $(M+H)^+$ ion of dipalmitoylphosphatidylcholine, (B) of the $(M+H)^+$ ion of maltotetraose, (C) of the $(M-H)^-$ ion of palmitoleic acid, (D) of the $(M-H)^-$ ion of corticosterone.

times varied from 3 s to 68 min with the total amount of analyte consumed varying from 10 ng to 3.6 μ g. It should be noted that this study was not designed to test the limits of detection. Reasonable data can be acquired on significantly lower amounts (i.e., lower by 1–2 orders of magnitude).

The MS/MS spectrum of 35 ng of bradykinin acquired over 43 s is representative of the peptide data (Figure 2A). No interpretable MS/MS spectrum could be obtained from this level loaded on the direct insertion FAB probe. As a comparison the MS/MS spectrum of 1 μ g of bradykinin acquired

from the direct probe is shown in Figure 2B. These spectra are similar to other published CAD spectra of bradykinin (23). Typical examples of other MS/MS spectra acquired are presented in Figure 3. These data show that the open tubular CF-FAB/MS interface can be used to introduce a sufficiently high flux of analyte over the time period necessary to obtain good-quality MS/MS data.

The capability of acquiring MS/MS spectra over long periods of time is demonstrated in Figure 4. The MS/MS spectrum of the $(M+H)^+$ ion of *N*-acetyl angiotensin I was

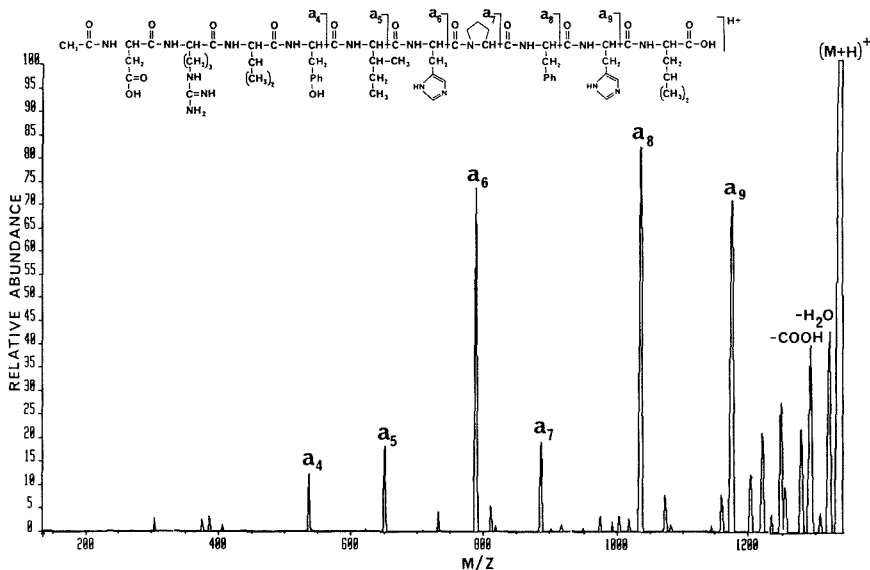


Figure 4. MS/MS spectrum of the $(M + H)^+$ ion of *N*-acetyl angiotensin I acquired over 68 min.

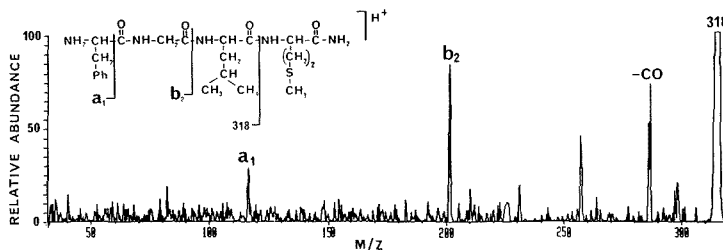


Figure 5. MS/MS/MS spectrum of m/z 318 originating from the reaction sequence m/z 466 \rightarrow m/z 318 from Phe-Gly-Leu-Met-NH₂.

Table I. Mass Assignment of the Daughter Ions of m/z 217, 245, and 279 of Met-Leu-Phe and for the Daughter Ion of m/z 527 of Bradykinin at Varying Scan Speeds

scan rate, s/decade	m/z 217	m/z 245	m/z 279	m/z 527
100 ^a	217.0	244.7	278.7	526.6
10 ^b	217.0	244.8	278.8	526.7
5 ^c	217.0	244.9	278.9	527.0
3 ^d	217.4	245.3	279.3	527.5
2 ^e	217.7	245.7	279.7	530.2

^a Average of five single scans for m/z 217, 245, and 279; measured from signal averaged data of six scans for m/z 527. ^b Average of 11 single scans for m/z 217, 245, and 279; measured from signal averaged data of 12 scans for m/z 527. ^c Average of 22 single scans for m/z 217, 245, and 279; measured from signal averaged data of 23 scans for m/z 527. ^d Average of 25 single scans for m/z 217, 245, and 279; measured from signal averaged data of 25 scans for m/z 527. ^e Average of 22 single scans for m/z 217, 245, and 279; measured from signal averaged data of 22 scans for m/z 527.

Table II. Compounds for Which MS/MS Spectra Have Been Acquired by Using Coaxial Continuous Flow FAB in Conjunction with Tandem Mass Spectrometry

compound	pos ion		neg ion	
	time, s	amt	time, s	amt
Met-Leu-Phe	2	22 pg	335	1.8 μ g
dihydrostreptomycin	3	33 ng		
bradykinin (acidified)	43	38 ng		
maltotetrose	10	110 ng		
corticosterone	42	231 ng	246	2.7 μ g
taurothiocholic acid-3-sulfate	45	495 ng	156	1.7 μ g
dipalmitoylphosphatidylcholine	27	2.3 μ g		
palmitoleic acid			230	2.5 μ g
<i>N</i> -acetyl angiotensin I	4070	3.6 μ g		

MS/MS/MS Acquisition. In addition to its capability for obtaining MS/MS spectra of biomolecules, the potential of this coaxial CF-FAB interface for the acquisition of MS/MS/MS data has also been studied. We have shown previously that MSⁿ experiments are feasible using the VG ZAB-4F mass spectrometer (11). By following the fragmentation pattern, one can verify the sequence of building blocks within a biomolecule. These experiments, however, can be cumbersome if the daughter ions are of relatively low abun-

acquired over 68 min and is representative of 3.6 μ g of material. This demonstrates that the coaxial CF-FAB interface is useful in obtaining MS/MS data over long as well as short acquisition time periods.

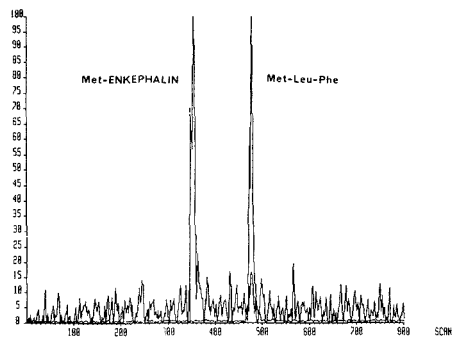


Figure 6. Overlaid mass chromatograms of the $(M + H)^+$ ions of Met-enkephalin (2 pmol) and Met-Leu-Phe (3 pmol) acquired from a separation using a packed microcapillary column.

dance. Much time can be involved due to the need to replenish the FAB probe tip with fresh sample. Therefore, the constant flow of analyte to the probe tip via a continuous flow FAB probe makes this interface ideal for such experiments.

The sequencing of the tetrapeptide Phe-Gly-Leu-Met-NH₂ is shown in Figure 5. Upon collisional activation, the $(M + H)^+$ ion of m/z 466 fragments to give the ion of m/z 318, which corresponds to the loss of HMetNH₂. In the MS/MS/MS experiment (Figure 5), the $(M + H - \text{HMetNH}_2)^+$ ion fragments to give the loss of CO and the Leu residue (fragment b_2). The daughter ion of m/z 120 (fragment a_1) corresponds to the loss of CO from the Phe residue. The mass spectrom-

eter was scanned at 50 s/decade for a period of approximately 6 min. The analyte concentration was 5 mg/mL, and the flow rate was 50 nL/min. Therefore, approximately 500 ng of material was used for the acquisition of the MS/MS/MS spectrum.

MS/MS from Column Separation. Using the packed microcapillary column, a separation of a mixture of Met-enkephalin and Met-Leu-Phe was obtained and is shown in Figure 6. The peaks represent 2 pmol of Met-enkephalin and 3 pmol of Met-Leu-Phe, and peak widths at one-half peak height are on the average of 40 s. The MS/MS spectra of the analytes (Figure 7) were obtained while the mass spectrometer was scanned at 5 s/decade. Fragmentations resulting from typical backbone cleavages were observed for both of the analytes studied.

CONCLUSIONS

Coaxial continuous flow FAB has proven to be very useful for combining liquid chromatography with tandem mass spectrometry. The ability to obtain on-the-fly MS/MS data makes this coaxial CF-FAB interface compatible with time restraints encountered in chromatography. With the use of packed microcapillary columns, the MS/MS spectra can be obtained on the analytes of a mixture as they are separated and elute from the column. In addition, the MS/MS spectra of a variety of compounds, such as peptides, sugars, fatty acids, phospholipids, and steroids, have been acquired by delivering a constant flow of analyte into the mass spectrometer. This constant flux of analyte can be advantageous for the acquisition of CAD spectra that are otherwise cumbersome (e.g., MS/MS/MS spectra).

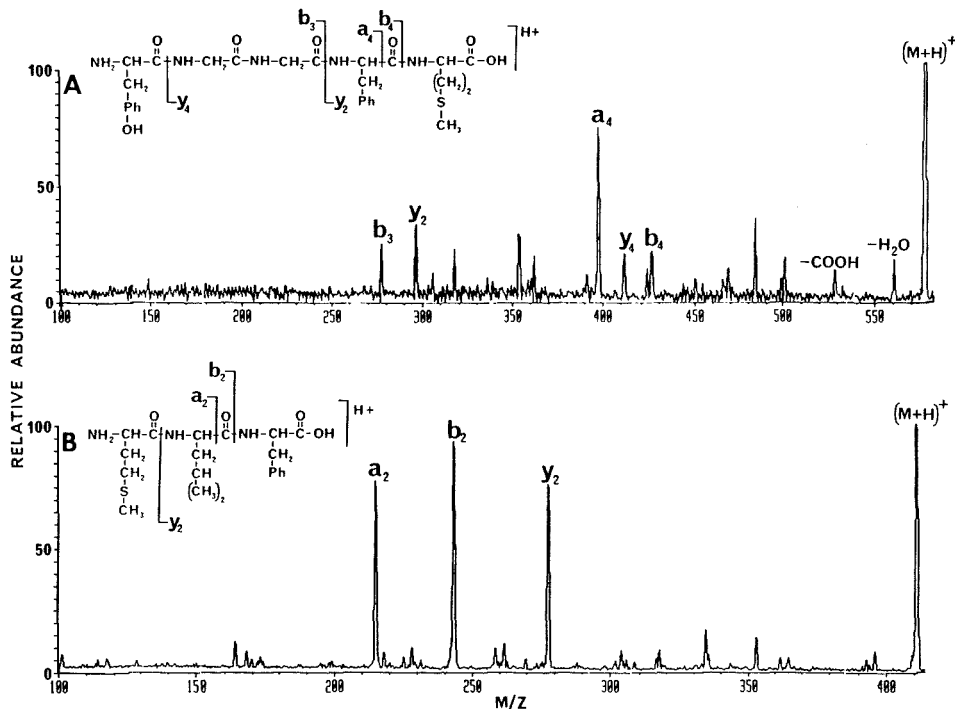


Figure 7. MS/MS spectra of the $(M + H)^+$ ion of (A) Met-enkephalin (single scan) and (B) Met-Leu-Phe (summation of five scans) acquired from the separation of the mixture using the coaxial CF-FAB interface with a packed microcapillary column.

ACKNOWLEDGMENT

The packed microcapillary column was made by Ms. Nancy Bragg at the University of North Carolina—Chapel Hill under the direction of Professor James W. Jorgenson.

LITERATURE CITED

- (1) Barber, M.; Bordoli, R. S.; Sedwick, R. D.; Tyler, A. N. *J. Chem. Soc., Chem. Commun.* **1981**, 325-327.
- (2) Naylor, S.; Findeis, F.; Gibson, B. W.; Williams, D. H. *J. Am. Chem. Soc.* **1986**, *108*, 6359-6363.
- (3) Ito, Y.; Takeuchi, T.; Ishii, D.; Goto, M. *J. Chromatogr.* **1985**, *346*, 161-166.
- (4) Caprioli, R. M.; Fan, T.; Cottrell, J. S. *Anal. Chem.* **1986**, *58*, 2949-2954.
- (5) Caprioli, R. M.; Fan, T. *Biochem. Biophys. Res. Commun.* **1986**, *141*, 1058-1065.
- (6) Caprioli, R. M.; Moore, W. T.; Fan, T. *Rapid Commun. Mass Spectrom.* **1987**, *1*, 15-18.
- (7) de Wit, J. S. M.; Parker, C. E.; Tomer, K. B.; Jorgenson, J. W. *Anal. Chem.* **1987**, *59*, 2400-2404.
- (8) Games, D. E.; Pleasance, S.; Ramsey, E. D.; McDowell, M. A. *Biomed. Environ. Mass Spectrom.* **1988**, *15*, 179-182.
- (9) de Wit, J. S. M.; Deterding, L. J.; Moseley, M. A.; Tomer, K. B.; Jorgenson, J. W. *Rapid Commun. Mass Spectrom.* **1988**, *2*, 100-104.
- (10) Moseley, M. A.; Deterding, L. J.; de Wit, J. S. M.; Tomer, K. B.; Kennedy, R. T.; Bragg, N.; Jorgenson, J. W. *Anal. Chem.* **1989**, *62*, 1577-1584.
- (11) Jorgenson, J. W.; Guthrie, E. J. *J. Chromatogr.* **1983**, *255*, 335-348.
- (12) Tomer, K. B.; Guenat, C. R.; Deterding, L. J. *Anal. Chem.* **1988**, *60*, 2232-2236.
- (13) Deterding, L. J.; Srinivas, P.; Mahmood, N. A.; Burka, L. T.; Tomer, K. B. *Anal. Biochem.*, in press.
- (14) Kennedy, R. T.; St. Claire, R. L., III; White, J. G.; Jorgenson, J. W. *Mikrochim. Acta* **1987**, *II*, 37-45.
- (15) Kennedy, R. T.; Jorgenson, J. W. *Anal. Chem.* **1988**, *60*, 1521-1524.
- (16) Kennedy, R. T.; Jorgenson, J. W. *Anal. Chem.* **1989**, *61*, 436-441.
- (17) Hass, J. R.; Green, B. N.; Bateman, R. H.; Bott, P. A. *Proceedings of the 32nd Annual Conference on Mass Spectrometry and Allied Topics*; **1984**, p 380.
- (18) Jensen, N. J.; Tomer, K. B.; Gross, M. L. *Anal. Chem.* **1985**, *57*, 2018-2021.
- (19) Deterding, L. J.; Gross, M. L. *Anal. Chim. Acta* **1987**, *200*, 431-445.
- (20) Adams, J.; Gross, M. L. *Anal. Chem.* **1987**, *59*, 1576-1582.
- (21) Roepstorff, P.; Fohlman, J. *Biomed. Environ. Mass Spectrom.* **1984**, *11*, 601.
- (22) Biemann, K. *Biomed. Environ. Mass Spectrom.* **1988**, *16*, 99-111.
- (23) Neumann, G. M.; Derrick, P. J. *Aust. J. Chem.* **1984**, *37*, 2261-2277.

RECEIVED for review March 21, 1989. Accepted August 21, 1989.

Separation of the Reagent Ions from the Reagent Gas in Ammonia Chemical Ionization Mass Spectrometry

Robert B. Cody

Nicolet Analytical Instruments, 6416 Schroeder Road, Madison, Wisconsin 53711

Competitive reactions can occur between neutral ammonia and the $[M + H]^+$ and $[M + NH_4]^+$ species produced in ammonia chemical ionization mass spectrometry. For some compounds, these competitive reactions can result in the loss of the $[M + H]^+$ and $[M + NH_4]^+$ species; however, these undesirable reactions can be avoided by using a Fourier transform mass spectrometer with a dual trapped-ion cell to separate the reagent ions from the reagent gas. Aqueous ammonia ("ammonium hydroxide") is shown to be a convenient and inexpensive substitute for anhydrous ammonia as a reagent for low-pressure chemical ionization mass spectrometry.

INTRODUCTION

Anhydrous ammonia is widely used as a reagent gas for chemical ionization mass spectrometry (CIMS) (1-7). For analytes that have a proton affinity greater than the proton affinity of ammonia (204 kcal/mol) (8), ammonia chemical ionization occurs by proton transfer to produce the $[M + H]^+$ species. For analytes that have polar functional groups, chemical ionization occurs by $[NH_4]^+$ attachment to produce the $[M + NH_4]^+$ species. Under high-pressure chemical ionization conditions (0.5 Torr), ammonia chemical ionization may occur by complex mechanisms involving reactions of $[NH_4]^+$ and solvated ammonium ions of the type $[(NH_3)_n \cdot H]^+$ (6, 7).

Low-pressure chemical ionization mass spectrometry (LPCIMS) (9-12) is performed with trapped-ion mass spectrometers at pressures in the 10^{-6} - 10^{-4} Torr range and reaction periods ranging from a few milliseconds to several seconds. Under these conditions, ionization of the analyte occurs by simple bimolecular ion/molecule reactions such as proton

transfer, charge exchange, or condensation and elimination of a neutral product. Low-pressure chemical ionization mass spectrometry is particularly useful for ionizing compounds that have low vapor pressures.

Anhydrous ammonia has been used as a reagent for LPCIMS in several studies (10-12). In all of these reports, the reactions involved proton transfer between $[NH_4]^+$ and an analyte with a high proton affinity. Reactions involving the attachment of an ammonium cation to a polar functional group were not reported. Such cation attachment reactions are not expected to occur at low pressures because the adduct ions usually require stabilizing collisions to remove the excess energy released by bond formation (9, 11, 12).

A few reports of bimolecular attachment reactions have appeared in the literature. Complexes between $[SiH_3]^+$ and ethylene were studied by using an ion-beam scattering apparatus (13-15). Bimolecular attachment reactions of the trimethylsilyl cation with acetone and methanol were studied by using ion cyclotron resonance (16-20). Adducts are formed under low-pressure conditions by reactions of aromatic compounds or protonated ester compounds with neutral ammonia; these adducts were studied by using Fourier transform mass spectrometry (FTMS) and by using a quadrupole mass spectrometer and a hybrid sector mass spectrometer (21).

In this report, we show that the ammonium ion undergoes bimolecular attachment to compounds that have polar functional groups. Competitive reactions between analyte ions and ammonia will be identified, and we show that these competitive reactions can be avoided by a Fourier transform mass spectrometer with a dual trapped-ion cell (22, 23) to separate the reagent ions from the reagent gas. In addition, we show that aqueous ammonia is a convenient and inexpensive substitute for anhydrous ammonia as a reagent for low-pressure chemical ionization mass spectrometry.

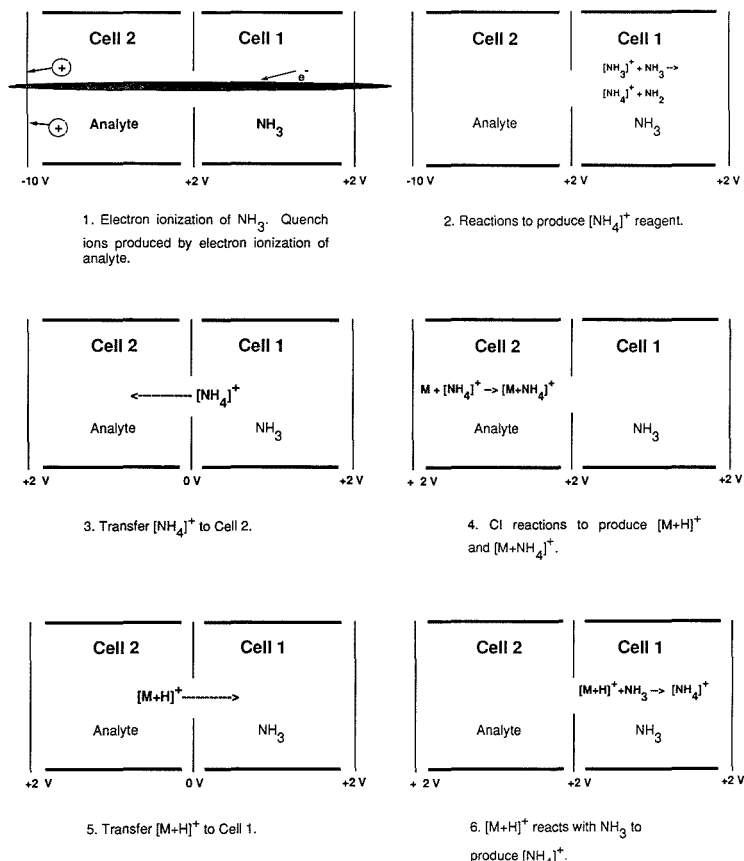


Figure 1. Schematic representation of the dual trapped-ion cell chemical ionization experiment.

EXPERIMENTAL SECTION

Experiments were performed by using a Nicolet FTMS-2000 dual-cell Fourier transform mass spectrometer. For the single trapped-ion cell experiments, reagent gases were introduced through a batch inlet system to provide a pressure of 2×10^{-6} Torr in the mass spectrometer vacuum chamber. The compounds studied were introduced via the septum inlet or the automatic direct insertion probe; the partial pressure of each sample was less than 1×10^{-7} Torr. Low-pressure chemical ionization was accomplished by confining the reagent gas, the analyte molecules, and the reagent ions in the trapped-ion cell for a reaction period of 300 ms. The same conditions (300 ms reaction time and an analyte pressure of 1×10^{-7} Torr) were used for the "self-CI" (11) experiments, except that no reagent gas was added; reagent ions were formed by electron ionization of the analyte.

For the dual trapped-ion cell experiments, the aqueous ammonia reagent gas was introduced through a leak valve into one of the trapped-ion cells (cell 1, normally referred to as the "analyzer" cell) at a pressure of 1.0×10^{-6} Torr. The analyte was introduced into the other trapped-ion cell (cell 2, normally referred to as the "source" cell). During the ionization event, the partition between the two cells (the conductance limit), trapping plates, and the trapping plate for cell 1 were kept at a positive trapping potential, while cell 2 was switched to a negative trapping potential. In this way, ions formed by electron ionization of the reagent gas were trapped in cell 1, while ions formed by electron ionization of the analyte were removed ("quenched") from cell 2. Following a reaction period, the trapping plate in cell 2 was

restored to the trapping potential and the $[\text{NH}_4]^+$ reagent species produced in cell 1 were transferred into cell 2 by grounding the conductance limit. Chemical ionization of the analyte occurred in cell 2 by reactions of the reagent ions with the neutral analyte molecules. In order to study the reactions of the protonated ions with neutral ammonia, the protonated analyte ions were transferred to cell 1 by grounding the conductance limit a second time. A schematic representation of the experiment is shown in Figure 1.

All compounds and reagents were obtained from commercial sources, and they were used without additional purification. Reagent grade aqueous ammonia (NH_3 content 28–30%) was used as the reagent for aqueous ammonia chemical ionization. After two freeze-pump-thaw cycles, the ammonia-rich vapor in the headspace above the liquid aqueous ammonia was introduced into the inlet system of the mass spectrometer by rapidly opening and closing the isolation valve between the sample container and the inlet system expansion volume.

RESULTS AND DISCUSSION

Chemical Ionization with a Single Trapped-Ion Cell.

Because molecular ions are not formed from tertiary alcohols under electron ionization conditions, these compounds are often analyzed by CIMS. Therefore, *tert*-pentyl alcohol was chosen for a comparison of reagent gases for low-pressure chemical ionization. The results are shown in Figure 2. Self-CI (Figure 2a) results in the formation of a small amount of $[\text{M} + \text{H}]^+$, but fragment ions from electron ionization

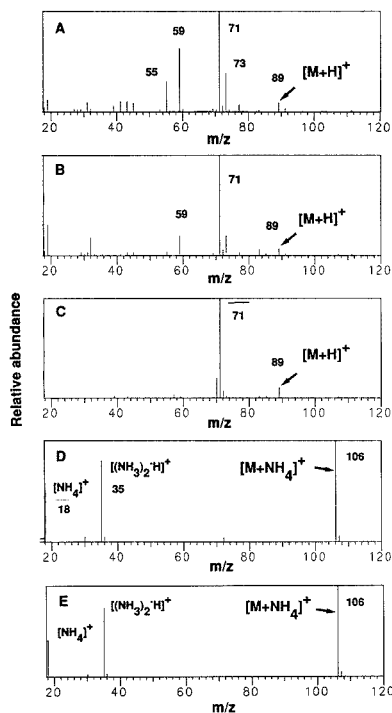


Figure 2. (a) "Self-CI" mass spectrum of *tert*-pentyl alcohol. (b) Methane chemical ionization spectrum of *tert*-pentyl alcohol. (c) Pentane chemical ionization mass spectrum of *tert*-pentyl alcohol. (d) Aqueous ammonia chemical ionization mass spectrum of *tert*-pentyl alcohol. (e) Anhydrous ammonia chemical ionization mass spectrum of *tert*-pentyl alcohol.

dominate the spectrum. Chemical ionization with methane reagent gas (Figure 2b) also results in the formation of $[M + H]^+$, but the dominant species are $[C_5H_{11}]^+$. The $[M + H]^+$ species are slightly more abundant when pentane is used as the reagent gas (Figure 2c), but the spectrum is still dominated by $[C_5H_{11}]^+$.

If anhydrous ammonia is used as the reagent gas (Figure 2d), the most abundant species are $[M + NH_4]^+$; the other significant ions are $[NH_4]^+$ and $[(NH_3)_2H]^+$. The absolute abundance of the $[M + NH_4]^+$ species produced by ammonia chemical ionization is a factor of 4.5 greater than that of the $[M + H]^+$ species produced by pentane chemical ionization, and it is 35 times greater than the absolute abundance of the $[M + H]^+$ species produced by self-CI or methane CI. If aqueous ammonia is substituted for anhydrous ammonia as the reagent gas, the results are virtually identical (Figure 2e).

A high-resolution mass spectrum (resolving power = 27 000) obtained with aqueous ammonia present in the mass spectrometer vacuum chamber at a pressure of 2×10^{-6} Torr verified that the reactive species in aqueous ammonia chemical ionization are predominantly $[NH_3]^+$ and $[NH_4]^+$. Water vapor is present to a lesser extent; the abundances of $[H_2O]^+$ and $[H_3O]^+$ are less than 10% of the abundance of the $[NH_4]^+$ species. If the reaction time (i.e., the ion-trapping time) is increased to 300 ms, the only significant ionic species remaining in the trapped-ion cell are $[NH_4]^+$. It is significant that the proton-bound dimer of ammonia $[(NH_3)_2H]^+$ is not formed under these conditions although it is present in a

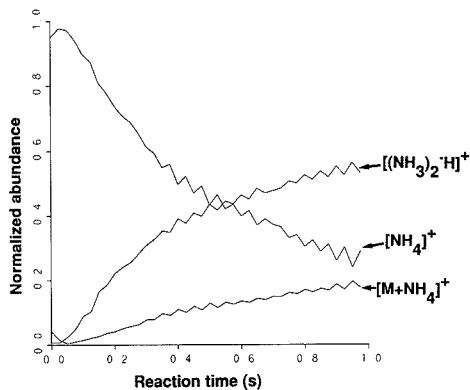


Figure 3. Variation in $[NH_4]^+$, $[(NH_3)_2H]^+$, and $[M + NH_4]^+$ abundance with reaction time for aqueous ammonia chemical ionization of *tert*-pentyl alcohol.

significant amount in the ammonia and aqueous ammonia chemical ionization mass spectra of *tert*-pentyl alcohol.

The presence of the proton-bound dimer of ammonia in the ammonia and aqueous ammonia chemical ionization spectra of *tert*-pentyl alcohol may be explained by reactions of $[M + NH_4]^+$ with neutral ammonia, as proposed by Rudewicz and Munson (6, 7)

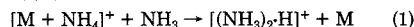
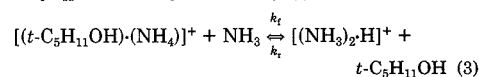
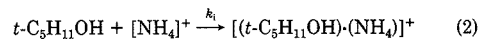


Figure 3 shows the variation of the $[NH_4]^+$, $[(NH_3)_2H]^+$, and $[M + NH_4]^+$ abundances with reaction time for aqueous ammonia chemical ionization of *tert*-pentyl alcohol at a total pressure of 1×10^{-6} Torr. The abundances of the $[(NH_3)_2H]^+$ and $[M + NH_4]^+$ species increase at the same rate, while the $[NH_4]^+$ abundance decreases.

Ion ejection experiments (also known as "double resonance" experiments) may be used to elucidate ion/molecule reaction pathways (24). In order to determine the mechanism for ammonia and aqueous ammonia chemical ionization, each selected reactant ion was ejected during the reaction period by continuous excitation at its cyclotron frequency. Product ions were identified by subtracting the mass spectrum obtained with reactant ion ejection from a mass spectrum obtained without reactant ion ejection. The resulting "reaction product spectrum" shows only those ions that decrease or disappear when the reactant ion is ejected. It should be recognized that the reactant ion will appear in its reaction product spectrum along with any product ions that are formed (either directly or indirectly) as result of ion/molecule reactions of the reactant ion.

The $[(NH_3)_2H]^+$ and the $[M + NH_4]^+$ species are both observed in the reaction product spectrum for reactions of $[NH_4]^+$. This indicates that the proton-bound dimer of ammonia and the $[M + NH_4]^+$ are produced by reactions of $[NH_4]^+$; this observation is supported by the variation of ion abundance with reaction time (Figure 3). The adduct species are the only products observed in the reaction product spectrum for reactions of $[(NH_3)_2H]^+$, while the $[(NH_3)_2H]^+$ species are the only products observed in the reaction product spectrum of $[M + NH_4]^+$. These results suggest the following reaction scheme:



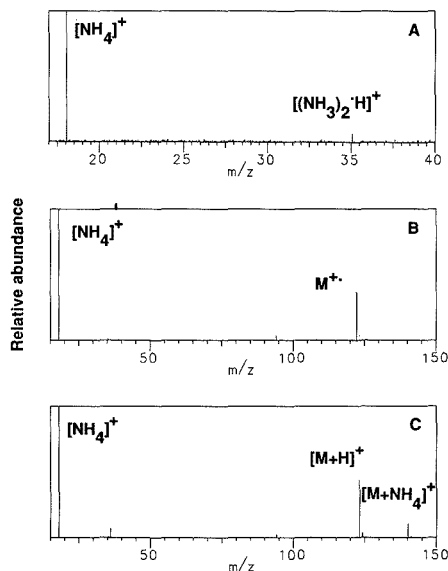


Figure 4. (a) Reaction product spectrum for examples of the $[M + \text{NH}_4]^+$ species in the single trapped-ion cell aqueous ammonia chemical ionization of phenetole. This spectrum was obtained by continuous ejection at the cyclotron frequency for the $[M + \text{NH}_4]^+$ species. (b) Single trapped-ion cell aqueous ammonia chemical ionization mass spectrum for phenetole. (c) Dual trapped-ion cell aqueous ammonia chemical ionization mass spectrum for phenetole.

where the rate constant k_f for the forward reaction is approximately equal to the rate constant k_r for the reverse reaction. Depending on the amount of water vapor present, a small amount of $[(\text{NH}_3)_2 \cdot (\text{H}_2\text{O})\text{H}]^+$ may be observed in the aqueous ammonia chemical ionization spectra. However, reactions of this species are not significant in aqueous ammonia chemical ionization.

Reactions of the analyte ions with ammonia can result in a significant loss of sensitivity for ammonia or aqueous ammonia chemical ionization of some compounds. The $[M + \text{NH}_4]^+$ species was previously observed by Munson and Rudewicz for high-pressure ammonia chemical ionization of anisole and phenetole (6). However, in our FTMS studies, no $[M + \text{NH}_4]^+$ is directly observed for low-pressure ammonia chemical ionization mass spectra for these compounds when the reactions are carried out in a single trapped-ion cell.

Although the $[M + \text{NH}_4]^+$ species were not observed for ammonia or aqueous ammonia chemical ionization of phenetole with a single trapped-ion cell, indirect evidence for their existence was obtained by an ion ejection experiment. The $[M + \text{NH}_4]^+$ was ejected by applying a continuous excitation at its resonant frequency. By subtraction of a background spectrum obtained without continuous ejection, the resulting reaction product spectrum (Figure 4a) shows that the phenetole $[M + \text{NH}_4]^+$ species lose $[\text{NH}_4]^+$ or react to product $[(\text{NH}_3)_2 \cdot \text{H}]^+$.

Chemical Ionization with the Dual Trapped-Ion Cell. In order to avoid the problem of the $[M + \text{NH}_4]^+$ species undergoing a reaction with neutral ammonia, the dual trapped-ion cell can be used to separate the reagent ions from the reagent gas. The key feature of these experiments is that $[\text{NH}_4]^+$ is isolated and allowed to react with the analyte in the absence of neutral ammonia. The $[M + \text{NH}_4]^+$ species formed during chemical ionization of the analyte are stable, because no neutral ammonia is present. Significant differences

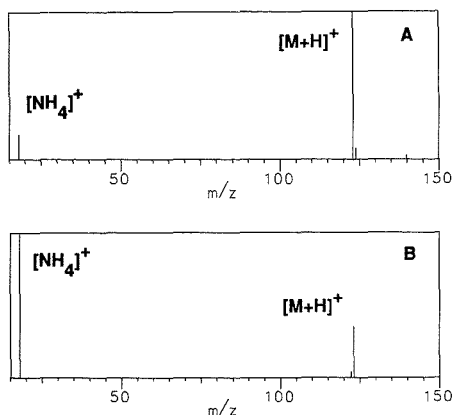
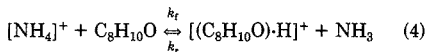


Figure 5. (a) Mass spectrum showing the species present in cell 1 immediately following transfer of the phenetole $[M + \text{H}]^+$ species from cell 2 to cell 1. (b) Mass spectrum showing the species present in cell 1 at 300 ms after the phenetole $[M + \text{H}]^+$ was transferred from cell 2 to cell 1. The $[M + \text{H}]^+$ species has reacted with neutral ammonia to produce the $[\text{NH}_4]^+$ species.

are evident in a comparison of the aqueous ammonia chemical ionization mass spectrum of phenetole obtained in this manner (Figure 4c) with the mass spectrum obtained when both ammonia and phenetole are present in the cell simultaneously (Figure 4b). The major analyte species in the dual-cell chemical ionization mass spectrum are $[M + \text{NH}_4]^+$ and $[M + \text{H}]^+$. The predominant analyte species in the single-cell chemical ionization mass spectrum is the molecular ion; a small amount of $[(\text{NH}_3)_2 \cdot \text{H}]^+$ is also observed.

The striking differences between these two spectra may be explained as follows. In the single-cell experiment, the $[M + \text{NH}_4]^+$ is not observed because it undergoes a fast reaction with neutral ammonia to produce the $[(\text{NH}_3)_2 \cdot \text{H}]^+$ species. Because the ionization potential of $[\text{NH}_3]^+$ is 10.18 eV and the ionization potential of $\text{C}_8\text{H}_{10}\text{O}^+$ is 8.42 eV (25), the molecular ion, M^+ , is produced by charge exchange between $[\text{NH}_3]^+$ and phenetole. This was confirmed by obtaining a reaction product spectrum for $[\text{NH}_3]^+$. The $[M + \text{H}]^+$ species are not observed in the single-cell experiment because it can undergo a reaction with neutral ammonia to produce $[\text{NH}_4]^+$



This reaction can be demonstrated (Figure 5) by grounding the conductance limit a second time so that the $[M + \text{H}]^+$ species produced in cell 2 are transferred to cell 1, where they undergo a reaction with neutral ammonia to produce $[\text{NH}_4]^+$.

Analytical Utility. The results for low-pressure aqueous ammonia chemical ionization of 20 polar or basic compounds are summarized in Table I. The $[M + \text{H}]^+$ species are observed for compounds that have proton affinities that are larger than 204 kcal/mol. Although the proton affinities for isophorone and methylsalicylate are not known, these results indicate that the two compounds must have proton affinities that are greater than 204 kcal/mol. The fact that the $[M + \text{H}]^+$ species can be observed for ammonia chemical ionization of anisole suggests that the literature value for the proton affinities of this compound may be low.

Provided that the dual trapped-ion cell conditions are used, the $[M + \text{NH}_4]^+$ species are observed for all but two compounds; the two remaining compounds (aniline and ethylpropylamine) have high proton affinities and only produce $[M + \text{H}]^+$. For the analysis of compounds such as alcohols by

Table I. Molecular-Like Species Produced by Aqueous Ammonia Chemical Ionization of Various Compounds^a

compound	proton affinity	M ⁺⁺	[M + H] ⁺	[M + NH ₄] ⁺
acetophenone	205.4		×	×
amyl acetate	198			×
aniline	209.5		×	
anisole	200.3	×	*	*
benzotrile	195.9			×
cyclohexanone	201.4			×
<i>n</i> -decyl alcohol				×
ethylpropylamine	227.4		×	
<i>n</i> -heptaldehyde				×
isophorone			×	×
methyl alcohol	181.9			*
methyl benzoate	203.7		×	×
methyl salicylate			×	×
methyl stearate				×
<i>tert</i> -pentyl alcohol				×
phenetole		×	*	*
isopropyl alcohol	191.2			*
<i>n</i> -propyl nitrate				*(weak)
sucrose				×
triolein				×

^a Proton affinities were obtained from ref 8. The proton affinity for amyl acetate was obtained from ref 26. An asterisk indicates that the [M + NH₄]⁺ species is only observed if the reagent gas is separated from the analyte by using the dual ion-trapping cells. Electron-impact fragment ions can also be observed in the ammonium hydroxide chemical ionization mass spectra for many of these compounds if single trapped-ion cell conditions are used.

low-pressure chemical ionization, the *tert*-pentyl alcohol results show that ammonia or aqueous ammonia chemical ionization is more efficient than many other common reagent gases for producing molecular-like species. Therefore, ammonia or aqueous ammonia chemical ionization can provide increased sensitivity for analysis of these compounds.

The results for anisole and phenetole are a special case. The spectra obtained with single trapped-ion cell and dual trapped-ion cell conditions are markedly different. In the single trapped-ion cell experiment, the primary analyte species produced by chemical ionization are M⁺⁺; this is produced by charge exchange from NH₃⁺⁺. However, in the dual trapped-ion cell experiment, the primary analyte species are [M + H]⁺ and [M + NH₄]⁺. In the latter experiment, the [NH₄]⁺ reagent is separated from the reagent gas and also from other reagent ions (i.e., [NH₃]⁺⁺). For ammonia or aqueous ammonia chemical ionization, the [NH₄]⁺ species can be easily isolated by choosing a long reaction time before the reagent ions are transferred to cell 2. For other reagent gases, where a variety of reactive species might exist in cell 1, a variety of methods are available to provide additional reagent ion selectivity. With the dual trapped-ion cell geometry, reagent ion selection may be easily accomplished by combining the mass-selective ion partition method proposed by Russell and co-workers (27) with the "timed-ion-transfer" method described by Giancaspro and Verdun (28). Stored-waveform inverse Fourier transform (SWIFT) excitation (29-32) can also be used or combined with these methods to provide a high degree of selectivity for one or more reagent ions.

The value of "selected reagent ion chemical ionization" has been discussed by Brodbelt and co-workers (12) and also by Glish and co-workers (31). The dual trapped-ion cell FTMS experiments show that it is also important to control the identity of neutral species present during chemical ionization. Similar experiments can be performed by using pulsed-valves to introduce the reagent gas. However, in a pulsed-valve experiment, the partial pressure of the reagent gas varies with time, and it cannot easily be measured. In addition, it is more

difficult to control the reactive species in a pulsed-valve experiment because ions are initially formed by electron ionization of both the reagent gas and the analyte. The dual trapped-ion cell approach provides a convenient solution to both of these problems.

The data in Table I show that aqueous ammonia is an effective reagent for low-pressure chemical ionization of polar or basic compounds. Because it is a liquid at room temperature, aqueous ammonia is safer and more convenient to handle than anhydrous ammonia, which is a gas at room temperature. Aqueous ammonia is also less expensive than anhydrous ammonia, and it does not require the hardware necessary for handling gases. Therefore, aqueous ammonia is a desirable substitute for anhydrous ammonia for most applications that require low-pressure chemical ionization.

Registry No. NH₃, 7664-41-7; NH₄OH, 1336-21-6.

LITERATURE CITED

- (1) Munson, M. S. B.; Field, F. H. *J. Am. Chem. Soc.* **1966**, *88*, 2621-2630.
- (2) Harrison, A. G. *Chemical Ionization Mass Spectrometry*; CRC Press: Boca Raton, FL, 1983.
- (3) Dzidic, I.; McCloskey, J. A. *Org. Mass Spectrom.* **1972**, *6*, 939.
- (4) Hunt, D. F. *Adv. Mass Spectrom.* **1974**, *6*, 517.
- (5) Rudewicz, P.; Munson, B. *Anal. Chem.* **1986**, *58*, 358-361.
- (6) Rudewicz, P.; Munson, B. Presented at the 32nd Conference on Mass Spectrometry and Allied Topics, San Antonio, TX, May 27-June 1, 1984.
- (7) Rudewicz, P.; Munson, B. Presented at the 33rd Annual Conference on Mass Spectrometry and Allied Topics, San Diego, CA, May 26-31, 1985.
- (8) Lias, S. G.; Liebman, J. F.; Levin, R. D. *J. Phys. Chem. Ref. Data* **1984**, *13*, 695-808.
- (9) Mather, R. E.; Todd, J. F. *J. Int. J. Mass Spectrom. Ion Processes* **1979**, *30*, 1-37.
- (10) Hunter, R. L.; McIver, R. T., Jr. *J. Anal. Chem.* **1979**, *51*, 699-704.
- (11) Ghaderi, S.; Kulkarni, P. S.; Ledford, E. B., Jr.; Wilkins, C. L.; Gross, M. L. *Anal. Chem.* **1981**, *53*, 428-437.
- (12) Brodbelt, J. S.; Louris, J. N.; Cooks, R. G. *J. Anal. Chem.* **1987**, *59*, 1278-1285.
- (13) Allen, W. N.; Lampe, F. W. *J. Am. Chem. Soc.* **1977**, *99*, 6816.
- (14) Abernathy, R. N.; Lampe, F. W. *J. Am. Chem. Soc.* **1981**, *103*, 2573.
- (15) Abernathy, R. N.; Lampe, F. W. *Int. J. Mass Spectrom. Ion Processes* **1983**, *57*, 3.
- (16) Hendewerk, M. L.; Weil, D. A.; Stone, T. L.; Ellenberger, M. R.; Farneth, W. E.; Dixon, D. A. *J. Am. Chem. Soc.* **1982**, *104*, 1794-1799.
- (17) Ellenberger, M. R.; Hendewerk, M. L.; Weil, D. A.; Farneth, W. E.; Dixon, D. A. *Anal. Chem.* **1982**, *54*, 1309-1313.
- (18) Hendewerk, M. L.; Frey, R.; Dixon, D. A. *J. Phys. Chem.* **1983**, *87*, 2026-2032.
- (19) Weil, D. A. Ph.D. Thesis, University of Minnesota, 1984.
- (20) Oriando, R.; Munson, B., Department of Chemistry, University of Delaware, private communication, 1988.
- (21) Schmitt, J. P.; Beaudet, S.; Porter, C. Presented at the 33rd Annual Conference on Mass Spectrometry and Allied Topics, San Diego, CA, May 26-31, 1985.
- (22) Cody, R. B.; Kinsinger, J. A.; Ghaderi, S.; Amster, I. J.; McLafferty, F. W.; Brown, C. E. *Anal. Chim. Acta* **1985**, *178*, 43-66.
- (23) Cody, R. B.; Kinsinger, J. A. In *Fourier Transform Mass Spectrometry: Evolution, Innovation, and Applications*; Buchanan, M. V., Ed.; American Chemical Society Symposium Series Number 359; American Chemical Society: Washington, DC, 1987.
- (24) Comisarow, M. R.; Grassi, V.; Parisod, G. *Chem. Phys. Lett.* **1978**, *57*, 413-416.
- (25) Levin, R. D.; Lias, S. G. Ionization Potential and Appearance Potential Measurements, *Natl. Stand. Ref. Data Ser., Natl. Bur. Stand. (U.S.)* **1982**, 71.
- (26) Weiskam, R. J.; Toren, P. C. Presented at the 31st Annual Conference on Mass Spectrometry and Allied Topics, Boston, MA, May 8-13, 1983.
- (27) Hanson, C. D.; Kerley, E. L.; Russell, D. H. *Anal. Chem.* **1989**, *61*, 83-85.
- (28) Giancaspro, C.; Verdun, F. R. *Anal. Chem.* **1986**, *58*, 2097-2099.
- (29) Marshall, A. G.; Wang, T.-C. L.; Ricca, T. L. *J. Am. Chem. Soc.* **1985**, *107*, 7983-7987.
- (30) Chen, L.; Wang, T.-C. L.; Ricca, T. L.; Marshall, A. G. *Anal. Chem.* **1987**, *59*, 449-454.
- (31) Cody, R. B.; Hein, R. E.; Goodman, S. D. *Rapid Commun. Mass Spectrom.* **1987**, *1*, 99-102.
- (32) Cody, R. B. *Analysis* **1988**, *16*, 30-36.
- (33) Glish, G. L.; Van Berkel, G. J.; Asano, K. G.; McLuckey, S. A. "MS" Experiments with an Ion Trap Mass Spectrometer"; Proceedings of the 36th ASMS Conference on Mass Spectrometry and Allied Topics, San Francisco, CA, June 5-10, 1988.

RECEIVED FOR REVIEW May 1, 1989. Accepted July 28, 1989.

Laser Mass Spectrometric Analysis of Compounds Separated by Thin-Layer Chromatography

Alan J. Kubis, Kasi V. Somayajula, Andrew G. Sharkey, and David M. Hercules*

Department of Chemistry, University of Pittsburgh, Pittsburgh, Pennsylvania 15260

The combination of thin-layer chromatography (TLC) and laser mass spectrometry (LMS) is established as a potentially powerful analytical technique. LMS is used to detect the separated compounds directly from the polyamide TLC plate. One can analyze directly from polyamide because it does not alter compound identification, and polyamide does not interfere with the mass spectrum owing to its low mass fragment ions ($m/z < 150$). The spatial resolution of the laser ionization is only limited by the diameter of the laser beam ($\approx 5 \mu\text{m}$). The application of TLC-LMS to the separation of aromatic hydrocarbons and purine bases is demonstrated. R_f values can be measured accurately with TLC-LMS. The technique can determine if broad TLC spots are due simply to tailing or to overlapping spots from two compounds.

INTRODUCTION

The combination of mass spectrometry with chromatography has been particularly powerful for the analysis of complex mixtures. The ability of mass spectrometry to yield structural and molecular weight information makes it ideally suited to characterizing materials that are eluted from chromatographs.

Gas chromatography-mass spectrometry (GC-MS) was the first such hyphenated technique to be demonstrated. Its use has become commonplace in many areas of science and technology (1). Liquid chromatography is an even better separations method for coupling to mass spectrometry because of the greater number of compounds it can potentially handle (2). Interfacing liquid chromatography to mass spectrometry (LC-MS) has been more difficult, but LC-MS has become more widely adopted as the interfacing problems have been solved (3). The combination of supercritical fluid chromatography and mass spectrometry shows considerable potential (4).

Thin-layer chromatography (TLC) is probably the most widely used separations technique (5). Of course there has been much interest in interfacing TLC with mass spectrometry. However, the problems involved in such coupling are more difficult than for GC and LC. In the latter two the component of interest is eluted from a column, whereas in TLC the analyte is not eluted from the stationary phase. Therefore, compounds separated by TLC cannot be introduced into a mass spectrometer by using continuous flow. The most widely used technique has been to locate the desired spot on a TLC plate, extract it, and then introduce the extract (or its residue) into the mass spectrometer (6-8). However, this procedure suffers from a number of faults, such as possible contamination during transfer and loss of material.

Coupling TLC with mass spectrometry is best accomplished by using one of the solid-state mass spectrometric methods developed over the last decade. Indeed, several authors have reported coupling fast atom bombardment (FAB) and secondary ion mass spectrometry (SIMS) with TLC (9-12). One technique was to visualize spots on the plate, remove a spot for analysis from the TLC plate by adhesive tape, add glycerol,

and do FAB analysis (13). Busch et al. have been particularly active in adapting SIMS for analysis of TLC plates (14, 15).

Laser mass spectrometry is ideally suited to coupling with TLC. The laser can be focused to a small spot size ($\sim 5 \mu\text{m}$), and large (7 cm diameter) samples can be handled by modern microprobes (LAMMA-1000) and positioned accurately (1 μm). Thus, laser mass spectrometry can be used to analyze TLC plates directly with good spatial resolution (16). It is also possible to map samples for organic fragments (17), a capability ideally suited to characterization of TLC plates by laser mass spectrometry.

In this communication we report a detailed study of the coupling of TLC with laser mass spectrometry using the laser microprobe, which we will call TLC-LMS. We present a study of a variety of organic functionalities obtained directly from TLC plates and show that the relevant ions for compound identification are the same as those obtained from metal foils. We also present several examples of measurements on TLC plates in which a separation has been carried out by conventional, one-dimensional development. We show that the laser microprobe can be used to determine if the "tail" of a TLC peak is simply due to broadening of the spot of a single compound or is caused by the overlap of two components.

EXPERIMENTAL SECTION

Laser mass spectra were obtained by using a LAMMA-1000 laser microprobe mass spectrometer. The basic instrument has been described in detail elsewhere (18). The ionization source consists of a Q-switched and pulsed (pulse width 15 ns), frequency quadrupled ($\lambda = 265 \text{ nm}$) Nd:YAG laser in the $45^\circ/90^\circ$ configuration. The laser irradiance can be varied continuously by a pair of twisted polarizers. The beam diameter at its focal point is elliptically shaped; the long axis is typically $5 \mu\text{m}$. The ions are accelerated by using 4-kV potential into a time-of-flight (TOF) mass analyzer (1.8 m), which is equipped with a second-order energy focusing ion reflector to compensate for the initial spread of ion kinetic energies. The resolution of the instrument is 800 at m/z 350. The ions are postaccelerated at a potential of 15 kV and detected by a Cu-Be secondary electron multiplier (Thorn-EMI 9643/4A). The signal is preamplified (LeCroy 100 BTB) in two stages providing 1 \times , 10 \times , or 100 \times amplification. The preamplified signal is fed to a Biomart 8100 transient recorder (100 MHz, 8 bit, 2 kbyte). The digitized data are transferred and processed by a Hewlett-Packard 1000-E series minicomputer. The sample plate is mounted on an x, y, z micromanipulator having a maximum scanning range of $50 \text{ mm} \times 50 \text{ mm} \times 70 \text{ mm}$, respectively; because of sample holder geometry, 31 mm is the practical limit of the scan range in the y direction.

All compounds studied were obtained from Aldrich Chemical Co. (Milwaukee, WI) except for the polyaromatic hydrocarbons (PAHs), which were obtained from Chemical Services, Inc. (West Chester, PA), and the amino acids and alkaloids, which were obtained from Sigma Chemical Co. (St. Louis, MO). All compounds were used as received without further purification. The TLC plates used were Polyamide A-1700 backed with aluminum obtained from Schleicher and Schuell, Inc. (Keene, NH). The plates were preirradiated with methanol to remove contamination. These TLC plates were chosen because they gave more intense molecular ions for most compounds studied than did other thicker plates (0.1-0.2 mm), such as silica and cellulose. Approximately 0.02 g of each compound was dissolved individually in 20 mL of

chloroform; the PAHs were dissolved in benzene. One drop of each solution was deposited on zinc foil or the polyamide TLC plate to obtain a reference mass spectrum for each medium. The laser irradiance was increased until ions appeared (threshold). Laser power and focusing conditions were optimized to obtain strong molecular or quasimolecular ion peaks and to minimize fragmentation. When spectra were obtained from zinc, low to moderate energy (2.0–4.0 μJ) was usually needed, and the sample was moved 50 μm away from the laser focal plane. To obtain comparison spectra of the compounds from TLC plates, the optimum conditions required higher energy (15–18 μJ) with the TLC plate surface in focus. Usually laser mass spectra are reported as averages of several spectra to minimize variations in peak height. Because the tracing of TLC plates is of interest, all spectra shown here are single-shot spectra.

Separation procedures for PAHs and nitrogen-containing compounds using TLC have been described (19–21). Separations were performed on mixtures prepared from equal volumes of the individual solutions; 0.2 μL of a mixture was spotted onto the plate so that ~ 50 pg of each compound was deposited. Four purine derivatives, adenine, guanine, methyladenine, and purine, were separated by using methylene chloride as the mobile phase (22). The separation took approximately 15 min and reached 3.5 cm from the starting position when development was concluded. The spots were visualized by using iodine vapor for comparison with LMS results. Three PAHs, coronene, methylanthracene, and rubrene, were separated by using methylene chloride/methanol (60:40 v/v) as the mobile phase (23). The separation was concluded when the solvent reached 3.5 cm, and the compounds were visualized with UV fluorescence. In both cases the literature cited was used as a general guide, and conditions were optimized for the individual separations.

When one is mapping for the presence of the ions after the separation of a mixture, the sample area is viewed by a light microscope at a magnification of 250 \times , and the TLC plate is positioned manually on the sample stage so that the laser is initially focused where the sample was first spotted ($R_f = 0$). The laser is then fired and a complete spectrum taken and stored along with the position on the TLC plate. The TLC plate is then moved a fixed distance along the separation path and another spectrum taken. This procedure is repeated until the path length of the TLC plate is traced. Care needs to be taken that the step size is small enough that compounds are not missed and that enough data points are obtained for each compound to give well-defined positions for all components. Initially, total ion current (TIC), the sum of the areas of all peaks in each spectrum, can be plotted versus position on the TLC plate. The compounds separated are detected as increases in TIC above background, and a chromatogram is generated. This procedure permits location of the compounds. The spectra corresponding to these peaks can then be analyzed and characteristic masses assigned. This procedure uses very little material, and if needed, the TLC plate can be repositioned so that more spectra can be obtained and conditions changed to induce fragmentation so structural information can be obtained. Once peaks characteristic of a given compound are identified, the intensity of a characteristic peak is plotted versus position on the plate and the R_f values are calculated. To maximize the reproducibility of the step size, the stage movement is performed by using stepper motors (Superior Electric Corp.) controlled by a Daedel, Inc., Model PC410 controller. For these experiments, spectra were taken at intervals of 250 and 500 μm . Steps of intervals of 1.25 μm are possible. This procedure can be performed manually or under computer control. Computer control of sample manipulation, spectra acquisition, and data display has been demonstrated previously (24) for the LAM-MA-1000. Initial and final analysis positions on the TLC plate, along with distance between analysis points, are given as input to the computer, and no other operator assistance is needed. The computer controls laser firing and sample manipulation so spectra are obtained at the positions selected. The data can then be searched and displayed as required by the operator.

RESULTS AND DISCUSSION

Organic compounds having different functionalities were surveyed to determine the general applicability of TLC-LMS. The compounds studied are listed in Table I, along with their

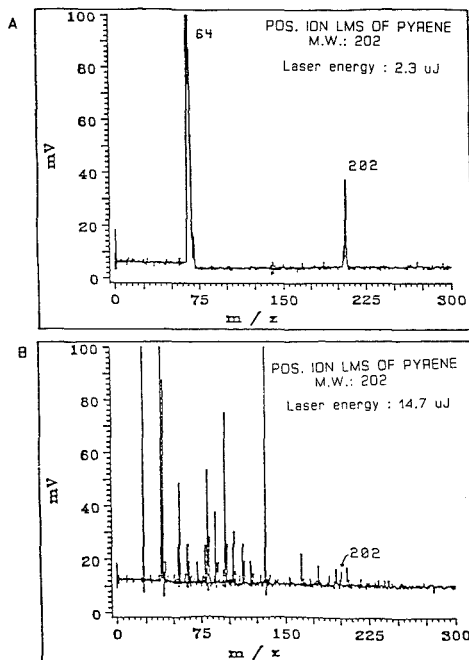


Figure 1. Positive ion spectra of pyrene on zinc, defocused (laser focal plane 50 μm behind sample). Laser energy: (a) 2.3 and (b) 14.7 μJ .

molecular weights and the ions observed in their laser mass spectra (LMS). To obtain reference spectra, compounds were first studied on zinc foil and were subsequently studied on TLC plates to compare the spectra and to optimize experimental conditions. Two larger groups of compounds were investigated to demonstrate mapping of TLC plates to locate organic compounds on developed plates and to identify them. The compounds separated by TLC were polyaromatic hydrocarbons and purine derivatives.

Survey of Compounds Desorbed from Zinc Foils. Alcohols, aldehydes, amino acids, amines, ethers, ketones, and phenols show protonated molecular ions ($M + H$) $^+$ in their positive ion spectra, along with carbon clusters at low masses. The peaks observed are summarized in Table I. Two exceptions are norcamphor and cresol, which also give molecular ions M^+ . The carboxylic acids show only carbon clusters at all laser irradiances in their positive ion spectra. Brucine shows both a protonated molecular ion and an ($M - 15$) $^+$ peak due to loss of a methyl group. Erythromycin gives a base peak at ($M + 23$) $^+$ due to sodium cationization, along with a weaker ($M + H$) $^+$ peak at m/z 736. Strychnine gives only the ($M + H$) $^+$ peak in its positive ion spectra. The sugars all give base peaks at ($M + 23$) $^+$ in their positive ion spectra.

Alcohols, aldehydes, amino acids, amines, ethers, ketones, and phenols show only deprotonated molecular ions ($M - H$) $^-$ in their negative ion spectra. The negative ion spectra of the acids show both ($M - H$) $^-$ and ($M - \text{CO}_2\text{H}$) $^-$ peaks. Brucine and strychnine show ($M - H$) $^-$ ions; only carbon clusters are seen for erythromycin and the sugars in the negative ion mode.

Figure 1A shows the LMS of pyrene on zinc at threshold irradiance with the sample defocused 50 μm away from the laser focus. When the laser irradiance is increased to 7 times threshold, carbon clusters dominate the spectra, as seen in Figure 1B. The cluster of peaks at m/z 64 is due to zinc ions.

Table I. Compilation of Compounds Studied and Ions Observed from both Zinc and Polyamide TLC Plates

	MW	peak mass			
		pos ion (M + H) ⁺	neg ion (M - H) ⁻		
acids					
benzoic acid	122		121	(M - CO ₂ H) ⁻ (77)	
<i>trans</i> -cinnamic acid	148		147	(M - CO ₂ H) ⁻ (103)	
phthalic acid	166		165	(M - CO ₂ H) ⁻ (121)	
succinic acid	118		117	(M - CO ₂ H) ⁻ (74)	
alcohols					
cinnamyl alcohol	134	135	133		
3(4-hydroxyphenyl)-1-propanol	152	153	151		
hydroquinone	110	111	109		
alkaloids					
brucine	430	431	429	(M - CH ₃) ⁺ (415)	
erythromycin	735	736		(M + Na) ⁺ (757)	
strychnine	334	335	333		
aldehydes					
<i>p</i> -hydroxybenzaldehyde	122	123	121		
benzaldehyde	106	107	105		
amino acids					
histidine	155	156	154		
isoleucine	131	132	130		
phenylalanine	165	166	164		
tyrosine	181	182	180		
amines					
aminophenol	109	110	108		
3-hydroxypyridine	95	96	94		
phthalimide	147	148	146		
esters					
ethyl hydroxybenzoate	166	167	165		
methyl hydroxybenzoate	152	153	151		
methyl anisate	152	153	151		
ethers					
1,3-dithiane	120	121	120		
benzoin ethyl ether	240	263	239		
ketones					
4-aminobenzophenone	197	198	196		
1,3-cyclohexadione	112	113	111		
cyclooctanone	126	127	125		
norcamphor	110	111	109	M ⁺ (110)	
phenols					
cresol	108	109	107	M ⁺ (108)	
naphthol	144	145	143		
nitrophenol	139	140	138		
resorcinol	110	111	109		
peak mass for pos ion					
	MW	M ⁺	other		
polyaromatic hydrocarbons					
anthracene	178	178			
2,3-benzofluorene	216	216			
benzo[<i>a</i>]pyrene	252	252			
coronene	300	300			
decacyclene	450	450			
9,10-diphenylanthracene	332	332		(M - C ₆ H ₅) ⁺ (255)	
2-methylanthracene	192	192		(M - CH ₃) ⁺ (177)	
9-methylanthracene	192	192			
3-methylcholanthrene	268	268		(M - CH ₃) ⁺ (253)	
9-phenylanthracene	254	254			
pyrene	202	202			
rubrene	532	532		(M - C ₆ H ₅) ⁺ (455)	
				(M - C ₆ H ₅) ⁺ (378)	
tritycene	254	254			
peak mass					
	MW	pos ion		neg ion	
		(M + H) ⁺	other	(M - H) ⁻	other
purines					
adenine	135	136	(M - NH ₂) ⁺ (119)	134	
2-aminopurine	135	136		134	
2-amino-6-purinethiol	167	168		166	
caffeine	194	195		193	
6-cyanopurine hydrate	145	146		144	(M - CN) ⁻ (119)
cytosine	111	112		110	
guanine	151	152	(M - NH ₂) ⁺ (135)	150	

Table I (Continued)

	MW	peak mass			
		pos ion		neg ion	
		(M + H) ⁺	other	(M - H) ⁻	other
3-methyladenine	149	150		148	(M - CH ₃) ⁻ (134)
6-methylpurine	134	135		133	(M - CH ₃) ⁻ (119)
purine	120	121		119	
uracil	112	113		111	
uric acid	168	169		167	(M - CNO) ⁻ (126)
sugars					
galactose	180		(M + Na) ⁺ (203)		
glucose	180		(M + Na) ⁺ (203)		
mannose	180		(M + Na) ⁺ (203)		

Table II. Background Ions from Polyamide TLC Plates and Their Relative Intensities

positive ion spectra		negative ion spectra	
<i>m/z</i>	rel int	<i>m/z</i>	rel int
27 Al ⁺	11	24 C ₂ ⁻	14
40 Ca ⁺	6	26 (CN) ⁻	100
		42 (CNO) ⁻	18
Titanium Isotopes			
46	22	58 (C ₂ H ₄ NO) ⁻	8
47	22	64 (C ₅ H ₂ N) ⁻	11
48	100	117	19
49	44	132	9
50	28		
56 (CaO) ⁺	3		
Titanium Oxide			
62	11		
63	11		
64	100		
65	20		
66	22		

These spectra are shown to emphasize the importance of operating near the threshold condition when one is obtaining LMS of organic compounds to gain molecular weight and structural information. This applies equally well to spectra obtained from metal foils or from TLC plates.

The positive ion spectra of the PAHs all show molecular ions, and several show loss of substituent groups. For example, 9,10-diphenylanthracene shows a loss of one of its phenyl groups at *m/z* 255, and 2-methylanthracene and 3-methylcholanthrene show loss of methyl groups. Rubrene gives peaks for loss of one and two of its phenyl groups at *m/z* 455 and 378. The polyaromatic hydrocarbons gave no negative ions other than carbon clusters at any laser irradiance.

Purine and pyrimidine derivatives gave protonated molecular ions (M + H)⁺ in their positive ion spectra; adenine and guanine give (M - NH₂)⁺ peaks also. In the negative ion spectra all compounds showed a deprotonated molecular ion (M - H)⁻. Uric acid gave a peak corresponding to (M - NCO)⁻, and 6-cyanopurine shows an (M - CN)⁻ peak in its negative ion spectrum.

Spectra of Compounds Desorbed from TLC Plates. Laser mass spectra of all compounds were obtained individually from TLC plates. The spectra obtained from TLC plates were compared to spectra obtained from zinc to see if there were any significant differences in fragmentation and to compare experimental conditions used to obtain spectra. The spectra obtained from TLC plates were also used to identify major peaks for subsequent tracing of TLC separations. When spectra were obtained from TLC plates, the conditions used were significantly different than when the same compounds were desorbed from zinc, as discussed above. At laser power densities comparable to those used to obtain spectra from zinc (2.0–4.0 μJ), laser mass spectra could not be observed from

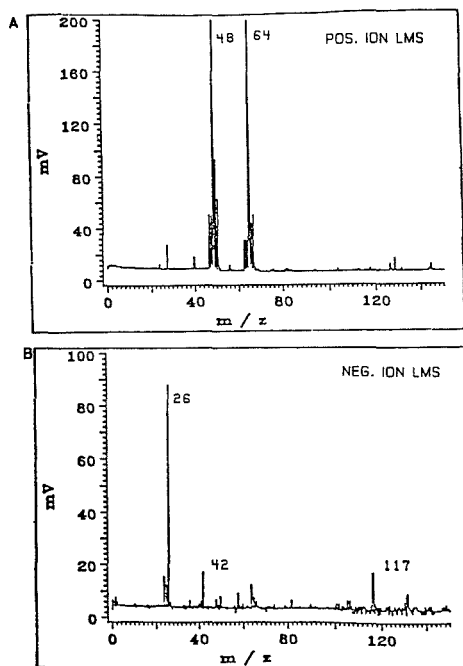


Figure 2. Background spectra from polyamide TLC plates: (a) positive ion spectrum, focused laser energy 16.4 μJ; (b) negative ion spectrum, focused laser energy 13.8 μJ.

TLC plates. In all cases the laser irradiance needed to be higher (15–18 μJ) to produce spectra from TLC plates. This may be due to a combination of scattering and absorption by the TLC plate. Many functional groups could interact with the polyamide stationary phase, making desorption of the compounds more difficult. Also, it was necessary to focus the laser on the TLC plate, as opposed to defocusing 50 μm behind the Zn foil.

The background spectra (both positive and negative) observed for TLC plates are shown in Figure 2. The peaks that are seen consistently are listed in Table II, along with their approximate relative intensities. In the positive and negative background spectra, peaks are not seen above *m/z* 150 and so do not interfere with any of the molecular ion species observed in this study. Since high irradiance and focused conditions are needed for all compounds, minimal optimization of conditions is required to obtain spectra from TLC plates. This is an advantage when one is recording a series of spectra

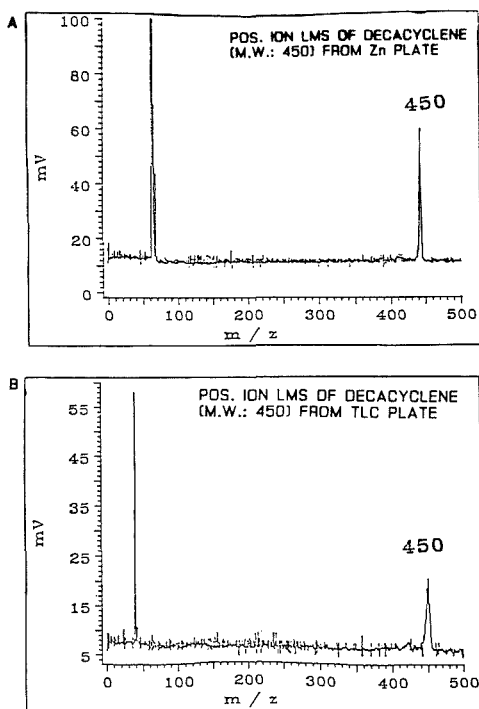


Figure 3. Positive ion spectra of decacyclene: (a) from zinc, defocused (laser focal plane 50 μm behind sample), laser energy 3.2 μJ ; (b) from TLC plate, focused at sample, laser energy 18.1 μJ .

from a TLC plate. Experimental conditions can be held constant while the spectra of a series of compounds are obtained; as a result minimal operator assistance is needed.

Characteristic peaks in the laser mass spectra obtained from TLC plates and from zinc foils were the same for all compounds studied. Several sets of both positive and negative ion spectra will be presented here (for widely differing compound types) to illustrate this point. In total, spectra were obtained for a group of 55 compounds; this set is tabulated as an appendix to the M.S. thesis of Kubis (25). Anyone desiring a set of those spectra should contact one of the authors.

The positive ion spectra of 2-amino-6-purinethiol were obtained from zinc and TLC plates. This compound gives an $(M + H)^+$ peak at m/z 168; background peaks were observed below m/z 100, but no interferences occur near the protonated molecular ion. A cluster at m/z 64 resulted from zinc.

The positive ion spectrum of ethyl hydroxybenzoate shows more interferences on the Zn foil than on the TLC plate. The $(M + H)^+$ peak at m/z 167 was easily seen. In both cases, the peak is about the same absolute intensity for Zn foil and TLC. Figure 3 shows the spectrum for decacyclene; the M^+ peak is clearly visible at m/z 450. In this case, the absolute intensity for the TLC plate is lower than for the Zn foil (15 vs 50 mV).

In the negative ion spectra of 2-amino-6-purinethiol from both Zn foil and the TLC plate, an $(M - H)^-$ ion is seen at m/z 166. Figure 4 shows similar spectra for histidine; the peak at m/z 154 is due to $(M - H)^-$. It can be seen that the negative ion spectra show no significant interference with peaks from the organic compounds at $m/z > 100$.

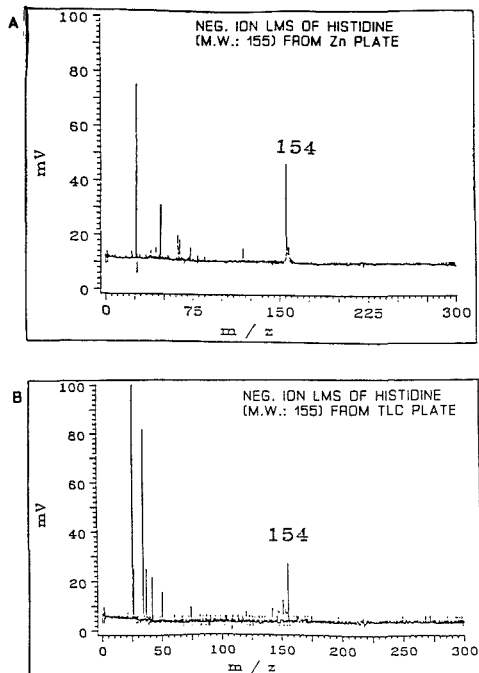


Figure 4. Negative ion spectra from histidine: (a) from zinc, defocused (laser focal plane 50 μm behind sample), laser energy 2.8 μJ ; (b) from TLC plate, focused at sample, laser energy 12.8 μJ .

Typically the intensity of the molecular ion species from TLC plates is the same or less than that for spectra obtained from a zinc surface. Exceptions to this seem to be purine derivatives; several gave more intense molecular ion species from TLC plates than from zinc. In general, matrix effects caused large changes in both relative and absolute intensities of ions formed in LMS (26). The absolute intensities of the analyte peaks varied less when obtained from a TLC plate than from a zinc substrate. This may be due to the fact that the analyte is more homogeneously dispersed in the TLC matrix than on zinc, giving more reproducible conditions from shot to shot.

Combined TLC-LMS Experiments. *Polynuclear Aromatic Hydrocarbons.* Several PAHs were separated on polyamide TLC plates to demonstrate interfacing of TLC with LMS. In all cases the molecular ion was the most intense peak and could be used to determine the positions of compounds on the TLC plate. Figure 5 shows a plot of the absolute intensity of the molecular ions versus distance along the path of development for three PAHs: coronene, 2-methylanthracene, and rubrene. Although there is a certain amount of scatter in the molecular ion intensities, the peaks of all three components could be clearly seen. Using a step size of 250 μm gives enough data points that R_f values of 0.27, 0.52, and 0.79 can easily be calculated for coronene, 2-methylanthracene, and rubrene, respectively. The values are the same as those obtained by using UV fluorescence, except for coronene, which gave an R_f value of 0.23 with fluorescence. Coronene shows tailing in this separation, which made defining its shape and calculating an R_f value difficult when UV fluorescence was used. In Figure 5 the plot of intensity of the molecular ion versus position for coronene clearly shows the tailing, and an accurate R_f value can be calculated, even though visually no

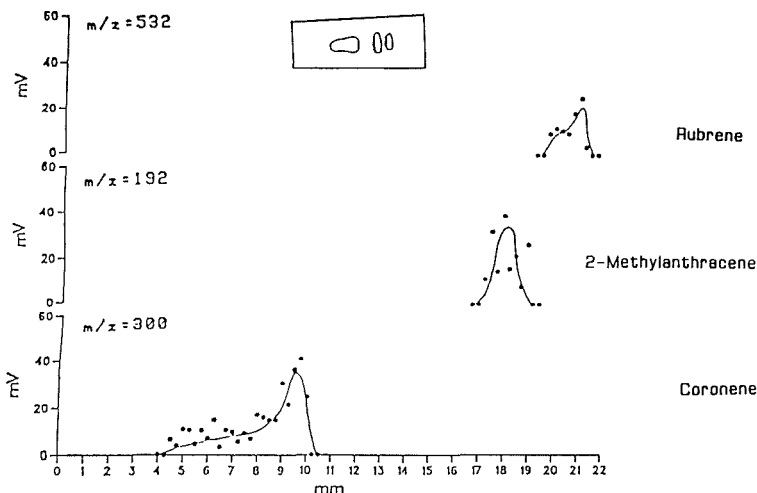


Figure 5. Positive ion TLC-LMS of polynuclear aromatic hydrocarbons: rubrene $m/z = 532$, 2-methylanthracene MW = 192, coronene MW = 300. Plot shows molecular ion intensity vs distance along the TLC plate. Spectra were taken at $250\text{-}\mu\text{m}$ intervals.

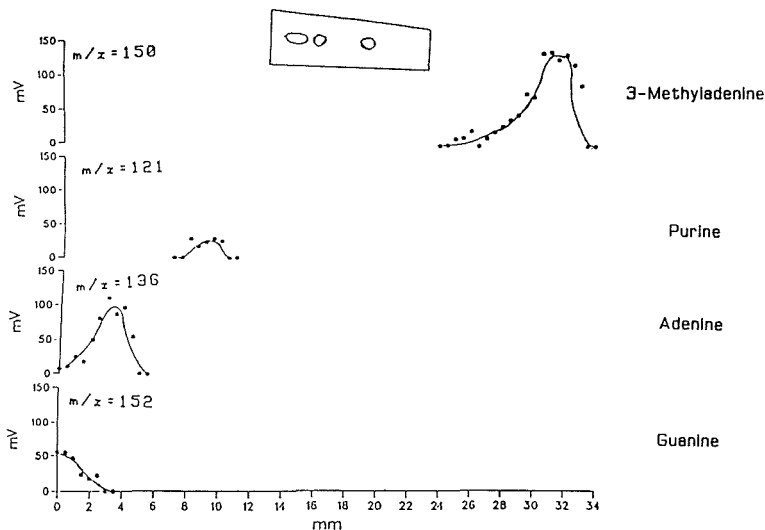


Figure 6. Positive ion TLC-LMS of four purine derivatives: 3-methyladenine $m/z = 150$, purine $m/z = 121$, adenine $m/z = 136$, guanine $m/z = 152$. Plot shows intensity of the protonated molecular ion versus distance along the TLC plate. Spectra were taken every $500\ \mu\text{m}$.

clear peak is defined by UV fluorescence. LMS has the advantage of being able to distinguish between tailing of a single compound and overlapping of two or more compounds to produce a broad TLC peak. Hence, mutually interfering compounds can be distinguished from poor transfer of a single compound along the plate, minimizing confusion in identifying different components of a mixture. In the case of coronene, no peaks other than the M^+ at $m/z = 300$ could be observed between 4.0 and 10.5 mm along the TLC plate, clearly indicating that the broad peak was due to tailing.

Purine Derivatives. Figure 6 shows a plot of peak intensity versus distance along the separation path of four purine derivatives: guanine, adenine, purine, and 3-methyladenine. R_f values of 0.00, 0.11, 0.29, and 0.90 can be calculated for the

four compounds, respectively. A step size of $500\ \mu\text{m}$ was needed to fully define the peaks. To trace the separation shown in Figure 6, the TLC plate was offset 2 cm during analysis because the sample stage used has a range of only 3.1 cm, and the separation took 3.5 cm to complete. The R_f values for purine and 3-methyladenine are the same as those measured when iodine vapor is used to visualize the spots, within experimental error. No R_f values could be obtained by iodine for adenine and guanine due to overlap.

Adenine and guanine can be resolved by using their $(M + H)^+$ ions, and their R_f values can be calculated. Figure 7 shows eight spectra taken from 0 to 3.5 mm at 0.5-mm intervals along the TLC plate. The protonated molecular ion for guanine at $m/z = 151$ decreases in intensity as the protonated molecular

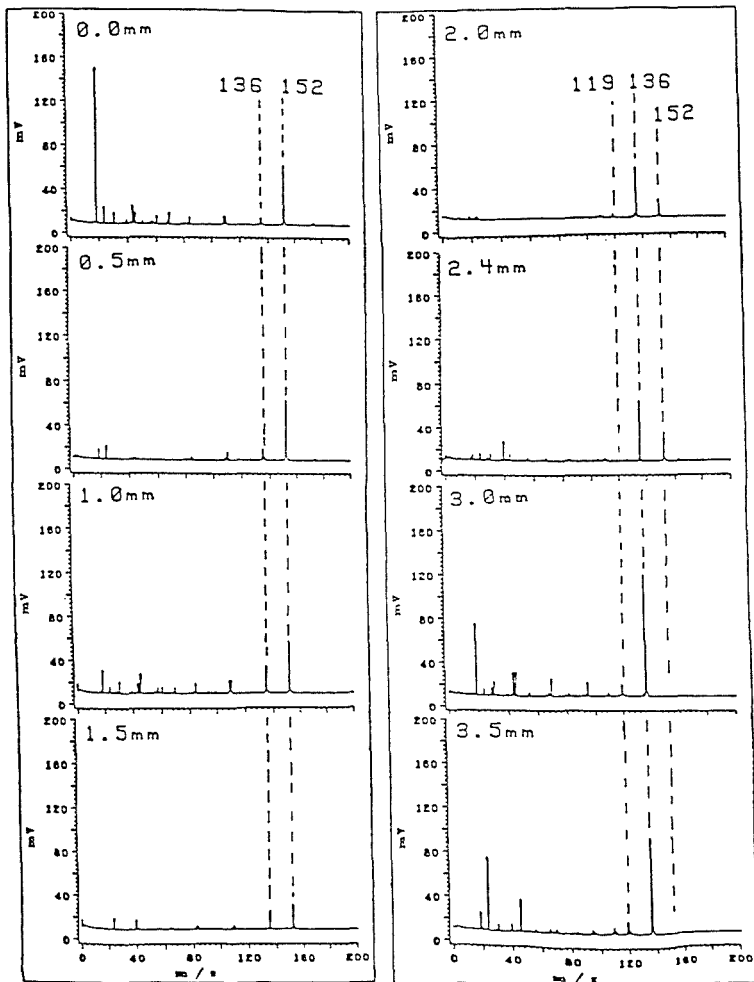


Figure 7. Positive ion LMS of guanine (MW = 151) and adenine (MW = 135) obtained from a TLC plate. Spectra were taken every 0.5 mm for 0–3.5 mm.

ion for adenine at m/z 135 increases. When one is analyzing a section of the TLC plate having only one component. This region could then be further analyzed to induce fragmentation in the mass spectra and gain structural information to aid in compound identification. The intensities of fragment ions and molecular ion species for a single compound will increase and decrease together. For example, in Figure 7 the peak seen at m/z 119 is a fragment ion of adenine because the relative intensity change follows that of the protonated molecular ion. Therefore, one can clearly establish that the elongated spot on the TLC plate arises from two components, and their spectra can be obtained independently of each other. Also, it is clear that the peak at m/z 119 is a fragment of the ion at m/z 136.

It has been demonstrated that interfacing laser mass spectrometry with thin-layer chromatography is a useful technique for obtaining both molecular weight and structural information about compounds on a TLC plate. R_f values

measured by TLC-LMS are the same as those measured by other means. No special sample preparation is needed for TLC-LMS, avoiding the loss of material and introduction of contaminants that are possible with other TLC-MS combinations. The limit of detection of TLC-LMS is at the picogram level or below. Because TLC-LMS is a microprobe technique, it has the ability to perform mapping of the TLC plate to obtain spatial information about compound distribution. This is especially important when separation is not complete, as demonstrated for adenine and guanine. The microprobe capability of LMS can be used to determine if tailing is real or due to a mixed spot.

The examples shown demonstrate that TLC-LMS has a wide variety of potential applications. A large number of organic molecules can be desorbed from a TLC plate by LMS, and by use of appropriate separation conditions, difficult mixtures can be analyzed. This information can augment retention information from the separation itself, helping to identify unknown compounds. These advantages make

TLC-LMS a potentially very useful analytical technique.

LITERATURE CITED

- (1) McFadden, W. *Techniques of Combined Gas Chromatography/Mass Spectroscopy: Applications in Organic Analysis*; Wiley: New York, 1973.
- (2) *Modern Practices of Liquid Chromatography*; Kirkland, J. J., Ed.; Wiley: New York, 1971.
- (3) Arpino, P. J.; Guiochon, G. *Anal. Chem.* **1981**, *51*(7), 682A-701A.
- (4) Covey, T. R.; Lee, E. D.; Bruins, A. P.; Henion, J. D. *Anal. Chem.* **1986**, *58*, 1451-1461A.
- (5) *Journal of Chromatography—HPTLC High Performance Thin Layer Chromatography*; Zelikis, A., Kalsner, R. E., Eds.; Elsevier Scientific: Amsterdam, 1977; Vol. 9.
- (6) Kalsner, R. *Chem. Brit.* **1969**, *5*, 54-61.
- (7) Jacob, J. J. *Chromatog. Sci.* **1975**, *13*, 415-422.
- (8) Durden, D. A.; Juorio, A. V.; Davis, B. A. *Anal. Chem.* **1980**, *52*, 1815-1820.
- (9) Scheifers, S. M.; Verma, S.; Cooks, R. G. *Anal. Chem.* **1983**, *55*, 2260-2266.
- (10) Warner, M. *Anal. Chem.* **1987**, *59*, 47-48A.
- (11) Unger, S. E.; Vincze, A.; Cooks, R. G. *Anal. Chem.* **1981**, *53*, 976-981.
- (12) DiDonato, G. C.; Busch, K. L. *Anal. Chem.* **1986**, *58*, 3231-3232.
- (13) Chang, T. T.; Lay, J. O., Jr.; Francol, R. J. *Anal. Chem.* **1984**, *56*, 109-111.
- (14) Stanley, M. S.; Busch, K. L. *Anal. Chim. Acta* **1987**, *194*, 199-209.
- (15) Fiola, J. W.; DiDonato, G. C.; Busch, K. L. *Rev. Sci. Instrum.* **1986**, *57*(9), 2294-2302.
- (16) Novak, F. P.; Wilk, Z. A.; Hercules, D. M. *J. Trace Microprobe Tech.* **1985**, *3*(3), 149-163.
- (17) Novak, F. P.; Hercules, D. M. *Anal. Lett.* **1985**, *18*(A4), 503-518.
- (18) Heinen, H. J.; Meier, S.; Vogt, H.; Wechsung, R. *Int. J. Mass Spectrom. Ion Phys.* **1983**, *47*, 19-22.
- (19) Kraft, R.; Buttner, D.; Franke, P.; Etlzold, G. *Biomed. Environ. Mass Spectrom.* **1987**, *14*, 5-7.
- (20) Kraft, R.; Otto, A.; Zopff, H. J.; Etlzold, G. *Biomed. Environ. Mass Spectrom.* **1987**, *14*, 1-4.
- (21) Chang, W. C.; Lee, M. L.; Chou, C. K.; Lee, S. C. *Anal. Biochem.* **1983**, *132*, 342-344.
- (22) Jost, W.; Hauck, H. E. *Anal. Biochem.* **1983**, *135*, 120-127.
- (23) Armstrong, D. W.; McNeely, M. *Anal. Lett.* **1979**, *12*(A12), 1285-1291.
- (24) Hercules, D. M.; Novak, F. P.; Viswanadham, S. K.; Wilk, Z. A. *Anal. Chim. Acta* **1987**, *195*, 61-71.
- (25) Kubis, A. J. M.S. Thesis, University of Pittsburgh, 1988.
- (26) Karas, M.; Bachman, D.; Bahr, U.; Hillenkamp, F. *Int. J. Mass Spectrom. Ion Processes* **1987**, *76*, 53-68.

RECEIVED for review June 26, 1989. Accepted July 14, 1989.
This work was supported, in part, by the National Science Foundation under Grant CHE-84-11835.

Elimination of Unexpected Ions in Electron Capture Mass Spectrometry Using Carbon Dioxide Buffer Gas

L. J. Sears and E. P. Grimsrud*

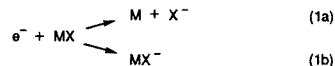
Department of Chemistry, Montana State University, Bozeman, Montana 59717

The high-pressure electron capture (HPEC) mass spectra of tetracyanoethylene (TCNE), tetracyanoquinodimethane (TCNQ), perfluoro-*p*-benzoquinone (fluoranil), perchloro-*p*-benzoquinone (chloranil), and perchloro-5,5-bis(cyclopentadiene) (pentac) are shown to be greatly simplified when carbon dioxide, rather than methane, is used as the buffer gas. These compounds have previously been shown to be particularly susceptible to reaction with gas-phase or surface-bound radical species, which are prevalent in an ion source containing methane. Through these secondary processes and subsequent electron capture (EC) reactions, unexpected ions of major intensity are observed with the use of CH₄ buffer gas. With CO₂ buffer gas these unusual ions are eliminated, and only ions that can be explained in terms of simple resonance and dissociative EC processes are observed. The high level of sensitivity normally expected of HPEC mass spectrometry is also maintained with CO₂ buffer gas. Other non-hydrocarbon buffer gases, including helium, argon, xenon, and nitrogen, are found to yield greatly diminished sensitivity relative to that observed with CH₄ and CO₂.

INTRODUCTION

The high-pressure electron capture (HPEC) ion source has demonstrated extraordinarily high chemical specificity and sensitivity in the mass spectrometric (MS) analysis of numerous molecules of environmental and biomedical importance (1-3). In HPECMS negative ions are generally formed in thermal electron capture (EC) reactions by either the dissociative or resonance EC mechanisms (4,5), shown in re-

actions 1a and 1b, respectively. A considerable body of



knowledge exists concerning these two EC mechanisms, and HPEC mass spectra can be readily interpreted or predicted for a given molecule when these reactions, alone, are operative. An inspection of the literature reveals, however, that HPEC spectra are often not explainable in terms of the simple dissociative and resonance EC reactions alone (6-11). In order to account for the HPECMS spectra reported in several studies, it has been necessary to suggest the occurrence of various secondary processes often involving the participation of gas-phase (6) or surface-bound (10) free radicals. These reactive species originate from the e-beam irradiation of the buffer gas and are thought to react with the analyte molecule prior to electron capture. The terminal negative ions thereby formed often include all or part of the reactive free radicals along with all or part of the analyte molecule. These secondary reactions invariably complicate the spectra of molecules that undergo these reactions and can greatly confuse their identification by HPECMS.

In this paper we report recent attempts in our laboratory to eliminate secondary reactions of free radicals in a high-pressure ion source while maintaining the high level of sensitivity normally achieved by HPECMS. Since previous studies have indicated the participation of hydrocarbon-derived free radicals in secondary ion source processes (6-10), we will focus here on the use of several non-hydrocarbon buffer gases—helium, argon, xenon, nitrogen, and carbon dioxide; and we will compare the results obtained with those observed

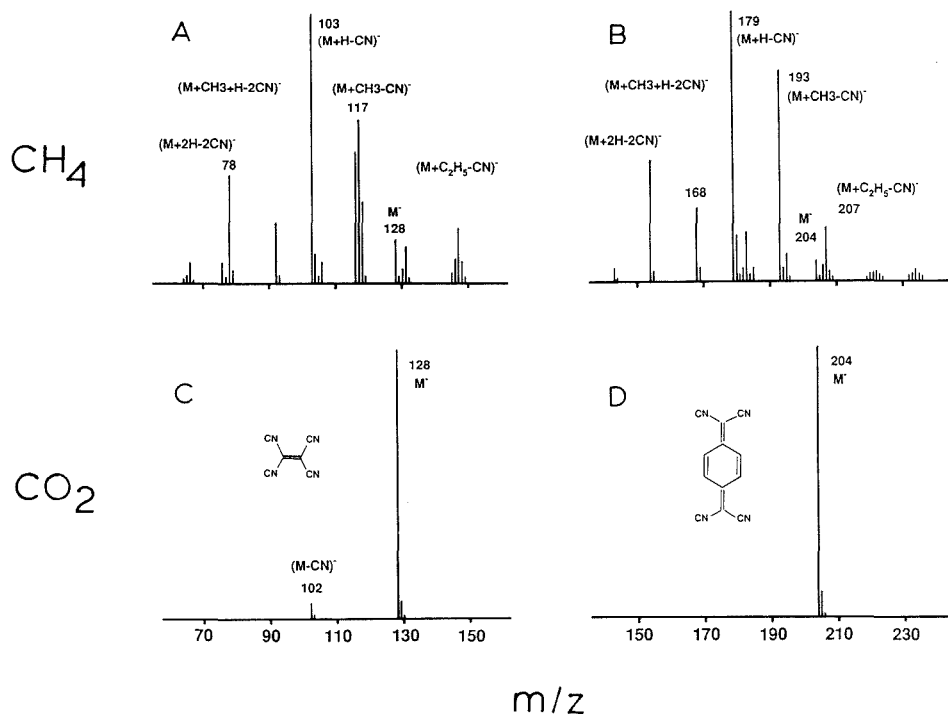


Figure 1. HPECMS spectra of tetracyanoethylene (A and C) and tetracyanoquinodimethane (B and D) obtained by using methane (A and B) and carbon dioxide (C and D) buffer gases. The ion source pressure was 0.5 Torr, and its temperature was 150 °C.

in methane. In view of several previous studies in which carbon dioxide has been reported to be particularly effective for thermalizing low-energy electrons (12–16), special consideration will be given to the use of this buffer gas.

The EC-active molecules selected for study here have been previously shown to be particularly sensitive to prior reactions of gas-phase and surface-bound free radicals in a HPECMS ion source. These include tetracyanoethylene (TCNE) and tetracyanoquinodimethane (TCNE), which McEwen and Rudat (6) have shown to react rapidly with many gas-phase hydrocarbon-derived free radicals prior to EC; and perfluoro-*p*-benzoquinone (fluoranil), perchloro-*p*-benzoquinone (chloranil), and perchloro-5,5'-bis(cyclopentadiene) (pentac), which Sears et al. (10) have shown to react rapidly with surface-bound hydrogen atoms, but not gas-phase radicals, prior to EC. The relatively well-documented behavior of these selected molecules in a HPECMS ion source undoubtedly also accounts for unusual and unexpected ions observed in the HPEC spectra of numerous other molecules; many such examples can be noted by careful inspection of the recent compilation of 361 HPEC mass spectra determined in methane buffer gas by Stemmler and Hites (17).

EXPERIMENTAL SECTION

All spectra reported here were obtained by using a double-focusing, medium-resolution mass spectrometer (VG Model 7070 E-HF). The pressure within the ion source was measured with a capacitance manometer and was maintained at 0.5 Torr. The temperature of the ion source was 150 °C. The filament emission current was 200 μA, and the electron energy was 150 eV. Fluoranil, chloranil, and pentac (about 1 ng of each per analysis) were introduced to the ion source by a capillary gas chromatographic column, which was threaded through the GC/MS interface and

into the ion source block. The flow rate of helium carrier gas was 1–2 atm cm³ min⁻¹, and the flow rate of the buffer gas was about 10 times greater. Tetracyanoethylene and tetracyanoquinodimethane (about 50 ng of each per analysis) were introduced to the ion source by a temperature-programmed direct insertion probe. All assignments of ion identity were verified by accurate mass measurements to within 1.0 millimass unit.

The buffer gases used in this study were obtained as follows: CO₂ (99.99%), CH₄ (99.97%), and Xe (99.9%) from Matheson; N₂ (Prepurified Grade), Ar (Prepurified Grade), and He (High Purity Grade) from Linde Specialty Gases. Nitrogen, argon, and helium were passed through an oxygen-removing trap (Alltech Associates) and molecular sieve filter (Alltech) prior to their introduction to the ion source. Methane was passed through an oxygen-removing trap, only, and xenon and carbon dioxide were used as received.

In addition to the experiments to be reported here, each was also performed by using an ion source block in which a layer of gold had been electroplated on all interior surfaces. The mass spectral results obtained with this ion source using methane buffer gas, as well as the non-hydrocarbon gases, were essentially identical with those obtained with the normal stainless steel ion source.

RESULTS AND DISCUSSION

Of the five non-hydrocarbon gases examined here for their potential use as buffer gases in HPECMS, only carbon dioxide was found to provide detection sensitivities comparable to those obtained in methane. The results obtained with carbon dioxide will be presented first, followed by a discussion of results and problems associated with use of the other non-hydrocarbon gases.

Carbon Dioxide as Buffer Gas. The HPEC mass spectra of tetracyanoethylene (TCNE) and tetracyanoquinodimethane (TCNQ) obtained with methane buffer gas are shown in Figure

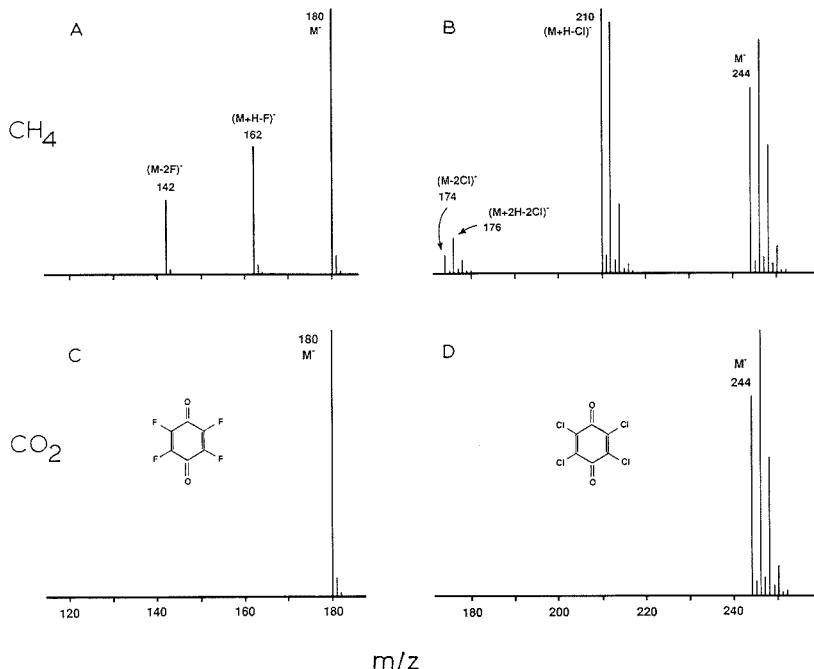
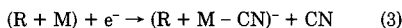


Figure 2. HPECMS spectra of fluoranil (A and C) and chloranil (B and D) obtained by using methane (A and B) and carbon dioxide (C and D) buffer gases.

1A,B. McEwen and Rudat (6) have shown that in hydrocarbon buffer gases these two molecules react rapidly with gas-phase free radicals prior to electron capture, as shown in generalized form in reactions 2 and 3 where M is TCNE or

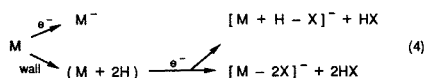


TCNQ, R^* is one of several free radicals formed by the continuous e-beam irradiation of the buffer gas, and $(R + M - CN)^-$ is a negative ion that contains R^* and a major fragment of TCNE (or TCNQ). In spectra A and B of Figure 1, the occurrence of reactions 2 and 3 is evident, where the radical species involved are primarily H^* , CH_3^* , and $C_2H_5^*$, all of which are expected in the irradiation of methane gas (6). Ions that indicate the attachment of two radical species to TCNE and TCNQ and the loss of two CN groups are also observed in spectra A and B. The precise sequence of the multiple reactions that lead to these ions is not known. The abundance of the molecular negative ions for TCNE and TCNQ in methane buffer gas is relatively low in both cases. As we have previously shown (10), this reflects a relatively low EC rate coefficient for the TCNE and TCNQ parent molecules, while the radical adducts of these molecules, $(R + M)$, undergo electron attachment much more rapidly.

The HPEC mass spectra for TCNE and TCNQ obtained by using CO_2 buffer gas are shown in Figure 1C,D. In striking contrast to the spectra obtained in CH_4 , both of these CO_2 HPEC spectra are very simple, consisting of a dominant molecular negative ion for both compounds and a low-abundance fragment ion for TCNE. These spectra clearly indicate that with carbon dioxide, only resonance and dissociative EC leads to negative ions of significant relative abundance for

these two compounds. One would expect that some reactive neutral species, particularly atomic oxygen, would also be formed in the e-beam irradiation of CO_2 , and that atomic oxygen might also have led to unusual ions by reactions 2 and 3 for TCNE and TCNQ. The fact that processes of this type are not observed in spectra 1C and 1D may be due to a rapid removal of atomic oxygen by their reaction with CO_2 to form CO_3 . This suggestion is supported by the continuous observation of a low-abundance background ion at m/z 60, which may result from electron attachment to CO_3 by virtue of its large electron affinity (18).

In Figure 2 the HPECMS spectra of fluoranil and chloranil are shown. In spectra A and B, obtained by using CH_4 as a buffer gas, several unexpected ions of significant relative abundance are observed, in addition to the parent molecular negative ions. In contrast to the mass spectra shown in Figure 1, the unusual ions in these spectra indicate the incorporation of H atoms, only, and no hydrocarbon radicals into the fragment ions. We have shown (10) that these unusual ions of fluoranil and chloranil are formed by a mechanism involving a prior wall reaction in which two hydrogen atoms are added to a double bond of the molecule as shown in reaction sequence 4, where X is either an F or Cl atom. As this reaction sequence



indicates, even the $[M - 2X]^-$ species observed for these molecules is not due to simple dissociative EC of the parent molecule, but it is formed along with the $[M + H - X]^-$ species through the prior wall reaction. The $[M + 2H - 2Cl]^-$ species observed for chloranil in spectra 2B was shown to occur by

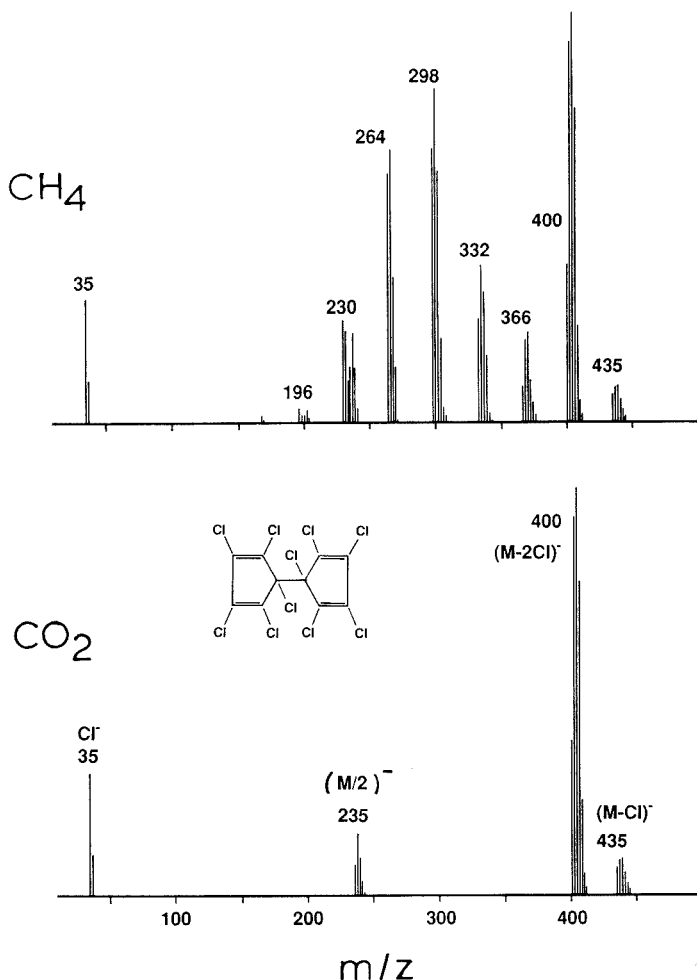
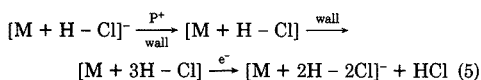


Figure 3. HPECMS spectra of pentac obtained by using methane and carbon dioxide buffer gases.

a repetition of sequence 4 following neutralization of the dominant ion in that sequence, as follows:



It was shown in our previous study (10) of HPECMS dynamics that these wall processes can be much faster than the gas-phase radical reactions discussed above for the cases of TCNE and TCNQ and can lead to unexpected ions of significant abundance even when the direct EC by the parent molecule is extremely fast.

The HPEC spectra for fluoranil and chloranil obtained by using CO_2 as buffer gas are shown in Figure 2C,D. Again, a remarkable simplification of the spectra is noted; the only ions detected are those due to resonance EC to form the parent molecular negative ions. The secondary processes described by sequences 4 and 5 are clearly not operative in CO_2 buffer gas.

Stemmler and Hites (9) have shown that the methane

HPEC spectra of numerous highly chlorinated, unsaturated hydrocarbons exhibit unusual ions that cannot be explained by simple EC processes. In Figure 3 the HPEC spectra of one compound included in their study group, pentac, is shown. With use of methane as the buffer gas, a large number of ions are observed. Particularly surprising are the group of ions from m/z 196 to 366, which differ by 34 mass units ($+H - Cl$) from the next larger isotope cluster of ions in the sequence. We have suggested (10) a mechanism for the HPEC methane spectrum of pentac in which the ions at m/z 35, 235, 400, and 435 were thought to result from a branched dissociative EC process in which all of these ions are simultaneously formed upon EC by pentac. We suggested (see Figure 12 of ref 10 and accompanying discussion) that the group of ions from m/z 196 to 366 were formed by a repeated sequence of wall-related reactions similar to that shown above in sequences 4 and 5 for the case of chloranil. The CO_2 HPEC spectrum of pentac in Figure 3 indicates absolutely no formation of the unusual ion series between m/z 196 and 366. The only ions observed in carbon dioxide buffer gas are those which were previously suggested (10) to result from the branched, dissociative EC

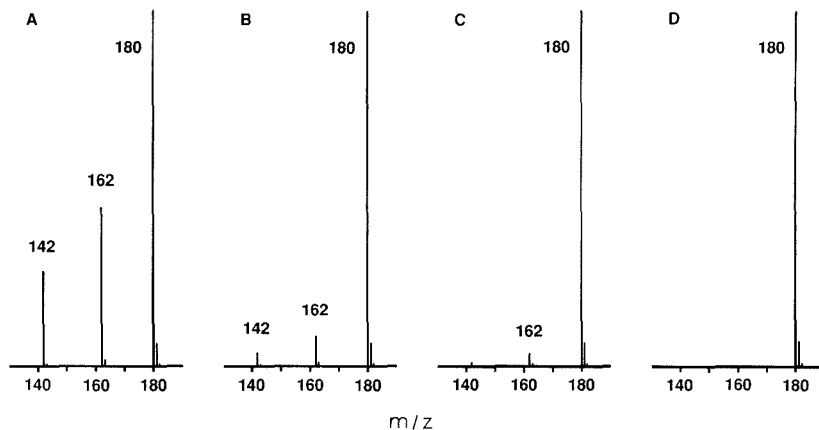


Figure 4. HPECMS spectra of fluoranil obtained by using methane buffer gas (A) and at various times, 0.5 min (B), 1.2 min (C), and 5.0 min (D), after switching from methane to carbon dioxide buffer gas.

Table I. Relative HPECMS Sensitivities^a of Fluoranil and Nitrobenzene Derivatives Obtained with Various Buffer Gases^b

compd	buffer gas					
	He	Ar	Xe	N ₂	CH ₄	CO ₂
fluoranil	0.011	0.04	0.0004	0.12	0.90	1.00
nitrobenzene (NB)	0.005	0.01	0.0006	0.03	1.00	0.86
<i>p</i> -fluoro NB	0.005	0.02	0.0012	0.03	0.98	1.00
<i>p</i> -bromo NB	0.007	0.05	0.0003	0.04	1.00	0.82
<i>p</i> -nitro NB	0.012	0.04	-	0.02	0.52	1.00
<i>m</i> -CF ₃ NB	0.007	0.03	0.0013	0.04	0.86	1.00
<i>m</i> -chloro NB	0.009	0.07	0.0010	0.04	0.93	1.00

^aBased on the detection of the molecular negative ion, which was the most abundant ion observed for all compounds listed.

^bThe ion source pressure was 0.5 Torr, and the temperature was 150 °C.

reaction of the parent molecule. We have also measured the HPEC spectra of other highly chlorinated hydrocarbons included in the study group of Stemmler and Hites (9). These include hexachlorocyclopentadiene and several of its derivatives: mirex, dieldrin, endrin, heptachlor, and heptachlor epoxide. The HPEC spectra of these compounds were similarly simplified when carbon dioxide, rather than methane, was used as the buffer gas.

We have shown (10) that the walls of a high-pressure ion source will retain hydrogen atoms after e-beam irradiation of methane buffer gas even if the ion source is allowed to rest under high-vacuum conditions at 150 °C for many hours. In Figure 4A, the HPECMS spectrum of fluoranil obtained by using methane buffer gas is shown, and Figure 4B-D shows spectra obtained at several time intervals after switching to carbon dioxide buffer gas. The unexpected ions at *m/z* 142 and 162 disappear quite rapidly after switching to CO₂; after 5 min, no wall reactions of fluoranil are observable in spectra 4D. From this result, we conclude that CO₂ has the desirable effect of rapidly removing hydrogen atoms from the walls of an ion source in which methane buffer gas has recently been used.

Other Non-Hydrocarbon Buffer Gases. Other non-hydrocarbon buffer gases, including helium, argon, xenon, and nitrogen, were also tested for use in HPECMS. While some simplifications of EC spectra were noted with some of these gases, the level of sensitivity achieved with them was consistently very much lower than that achieved with either CH₄

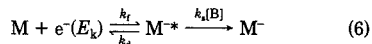
Table II. Electron Thermalization Rates and Number of Collisions Required for Vibrational Quenching in Various Buffer Gases

gas	<i>K_e</i> , cm ³ s ^{-1a}	<i>Z^b</i>	gas	<i>K_e</i> , cm ³ s ^{-1a}	<i>Z^b</i>
Ar	1.3 × 10 ⁻¹³	77	N ₂	2.2 × 10 ⁻¹¹	70
Ne	2.5 × 10 ⁻¹³	100	CH ₄	8.6 × 10 ⁻¹⁰	40
He	6.4 × 10 ⁻¹²	150	CO ₂	5.8 × 10 ⁻⁹	18

^aElectron thermalization rates taken from ref 12. ^bNumber of collisions required for quenching of photoexcited bromobenzene positive ions, taken from ref 20.

or CO₂. Comparisons of HPECMS sensitivities achieved with the various buffer gases are provided in Table I. The compounds listed in Table I are known to undergo EC rapidly by the resonance mechanism to form the molecular negative ion. It is seen that the magnitude of responses observed in CO₂ was consistently competitive with that observed in CH₄. Detection sensitivities in N₂, He, Ar, and Xe, however, were at least 1 and up to 3 orders of magnitude lower than those observed with CO₂ and CH₄ for all compounds studied here.

The high sensitivity obtained by CO₂ HPECMS for all of the compounds listed in Table I can be understood in terms of reaction sequence 6 in which the formation of a stable



negative ion, M⁻, proceeds through an excited intermediate, M^{*}. The rate constant, *k_f*, for the initial formation of this intermediate ion will depend strongly on the kinetic energy, *E_e*, of the electron and will be greatest for the high-electron-affinity compounds studied here if *E_e* has been reduced to near-thermal energy by collisions with the buffer gas molecules (19). In Table II, the second-order rate constants of Warman and Sauer (12) for the thermalization of low-energy electrons in various gases are listed. These thermalization coefficients, obtained with CCl₄ as a probe of electron energy, indicate that the rate of electron thermalization is particularly great for CO₂; it exceeds that of methane by almost 1 order of magnitude, that of nitrogen by more than 2 orders of magnitude, and those of the three noble gases by 3-4 orders of magnitude. In addition, several other investigations have also shown CO₂ to be particularly effective relative to other simple gases for the thermalization of electrons. These studies have involved a range of experimental methods including electron swarms (13), ion cyclotron resonance mass spec-

trometry (14, 15), and high-pressure negative ion mass spectrometry (16). It is expected, therefore, that CO₂ will most effectively thermalize the electrons formed in a HPECMS ion source and that k_1 will be greatest with this buffer gas.

A second factor that may affect the relative formation rates of stable molecular anions in a HPECMS ion source is k_2 , the second-order rate constant for collisional stabilization of the excited intermediate in reaction 6. Ideally, the pseudo-first-order rate for this process, $k_2[B]$, should be fast with respect to the autodetachment rate constant, k_4 . In order to gain a qualitative assessment of this factor for the various gases used here, a quantity called collision number, Z , is also listed for each buffer gas in Table II. This quantity is the number of collisions, reported by Ahmed and Dunbar (20), required to quench a population of vibrationally photoexcited bromobenzene positive ions contained within an ion cyclotron resonance cavity. Of the gases included in Table II, CO₂ was found to most effectively remove excess internal energy from the excited ion. It seems reasonable to suggest, therefore, that CO₂ might also be relatively effective as a buffer gas in HPECMS for removing excess internal energy from excited polyatomic negative ions, as shown in the second step of sequence 6.

SUMMARY

With respect to use of CO₂ as a buffer gas for HPECMS, the following conclusions can be drawn: (1) Simple EC spectra reflecting resonance and dissociative EC processes, alone, can be observed for compounds that are susceptible to secondary ion source reactions that involve gas-phase and surface-bound free radicals. (2) The high level of sensitivity normally expected of HPECMS is maintained. (3) The walls of the ion

source will be rapidly cleansed of hydrogen atoms that are deposited by prior use of hydrocarbon buffer gases.

LITERATURE CITED

- Hunt, D. F.; Crow, F. W. *Anal. Chem.* **1978**, *50*, 1781.
- Martin, J. T.; Barchas, J. D.; Faull, K. F. *Anal. Chem.* **1982**, *54*, 1806.
- Dougherty, R. C. *Anal. Chem.* **1981**, *53*, 625A.
- Wentworth, W. E.; Chen, E. C. M. *Electron Capture, Theory and Practice in Chromatography*; Zlatkis, A., Poole, C. F., Eds.; Elsevier Scientific Publishing Company: New York, 1981; pp 27-68.
- Harrison, A. G. *Chemical Ionization Mass Spectrometry*; CRC Press: Boca Raton, FL, 1983.
- McEwen, C. N.; Rudat, M. A. *J. Am. Chem. Soc.* **1981**, *103*, 4343.
- Stockl, D.; Budzikiewicz, H. *Org. Mass Spectrom.* **1982**, *17*, 376.
- Hilbert, L. R.; Byrd, G. D.; Vogt, C. R. *Anal. Chem.* **1984**, *56*, 1842.
- Stemmler, E. A.; Hites, R. A. *Anal. Chem.* **1985**, *57*, 684.
- Sears, L. J.; Campbell, J. A.; Grimsrud, E. P. *Biomed. Environ. Mass Spectrom.* **1987**, *14*, 401.
- Kassel, D. B.; Kaysanich, K. A.; Watson, J. T.; Allison, J. *Anal. Chem.* **1988**, *60*, 911.
- Warman, J. M.; Sauer, M. C. *J. Chem. Phys.* **1975**, *62*, 1971.
- Christophorou, L. G.; Grant, K. S.; Baird, J. K. *Chem. Phys. Lett.* **1975**, *30*, 104.
- Woodin, R. L.; Foster, M. S.; Beauchamp, J. L. *J. Chem. Phys.* **1980**, *72*, 4223.
- George, P. M.; Beauchamp, J. L. *J. Chem. Phys.* **1982**, *76*, 2959.
- Gregor, I. K.; Guilhaus, M. *Int. J. Mass Spectrom. Ion Processes* **1984**, *56*, 167-176.
- Stemmler, E. A.; Hites, R. A. *Electron Capture Negative Ion Mass Spectra of Environmental Contaminants and Related Compounds*; VCH Publisher, Inc.: New York, 1988.
- Hong, S. P.; Woo, S. B.; Helmy, E. M. *Phys. Rev. A* **1977**, *15*, 1563.
- Christophorou, L. G.; Grant, M. W. *Advances in Chemical Physics*; Prigogine, I., Rice, S., Eds.; John Wiley and Sons: New York, 1977; pp 413-519.
- Ahmed, M. S.; Dunbar, R. C. *J. Am. Chem. Soc.* **1987**, *109*, 3215.

RECEIVED for review June 6, 1989. Accepted August 28, 1989. This work was supported by the Chemical Analysis Division of the National Science Foundation under Grant No. CHE-8711618.

Axial Magnetic Inhomogeneities and Low Energy Ion Injection in Fourier Transform Ion Cyclotron Resonance Spectrometry

Eric L. Kerley, Curtiss D. Hanson, Mauro E. Castro, and David H. Russell*

Department of Chemistry, Texas A&M University, College Station, Texas 77843

Material choice in cell/lens construction is crucial for systems that must be used in strong magnetic fields. Magnetic inhomogeneities generated by stray fields present near paramagnetic lenses can dramatically alter the trajectories of low momentum ions. In this paper, low energy ion injection into a Fourier transform ion cyclotron resonance spectrometry cell is studied by using empirical and theoretical data for a two-section cell constructed of paramagnetic and diamagnetic materials.

INTRODUCTION

To achieve maximum performance in Fourier transform ion cyclotron resonance (FT-ICR) mass spectrometry, ion detection must occur in the absence of ion-neutral collisions. Because the duration of observation of the time domain ICR signal directly determines sensitivity and resolution, ICR detection is most effective at pressures of 10⁻⁸ Torr or less. The pressure limitations of FT-ICR detection can be circumvented by separating sample introduction and mass analysis.

Separation of these steps can be achieved either temporally (e.g. by the use of pulsed valves (1, 2)) or spatially (e.g. by the use of external ion sources (3-6) and the two-section cell (7)). In each of these approaches, the desired result is coupling of a high-pressure (10⁻⁷ Torr or greater) experimental step (e.g., ionization, ion-molecule reaction, or collision-induced dissociation) with ion detection at low pressure (10⁻⁸ Torr). Remote source techniques require that ions move from the source into the detection region; however, movement of ions from one region to another requires that the ions be accelerated toward the detection cell. That is, ions that have relatively low translational energy along the axis between source and cell (Z axis) are accelerated. Thus the process of Z-axis excitation changes the conditions under which ion detection is performed.

Ideally, ions trapped in the ICR cell have very low translational energies (thermal in the X-Y plane, a few electronvolts maximum along the Z axis). The Z-axis energy is higher because ions must be trapped in an electrostatic trapping well such that their Z-axis motion is restricted. In order to trap sufficient numbers of ions for detection, trapping potentials that trap translationally suprathermal ions are employed. Ions

entering the FT-ICR cell from a remote source (either an external source or another cell) can have up to 10 eV of translational energy along the *Z* (magnetic) axis. Another factor to consider is the effects of *Z*-axis energy on motion of the ions in the *X*-*Y* plane. If during the ion injection process *Z*-axis energy is transferred into the *X*-*Y* plane, then the injected ion ensemble is trapped with significant spatial and energetic distribution resulting in loss of signal (8). Although collisional relaxation of injected ions is effective in reducing ion translational energy (9), collisional relaxation does not eliminate problems arising from spatial distribution. Ions encountering magnetically inhomogeneous regions during *Z*-axis ion injection can be deflected into the *X*-*Y* plane.

In this paper, we attempt to describe the effects of axial magnetic inhomogeneities on ion partitioning and subsequent trapping of the ions in a two-section cell FT-ICR mass spectrometer. Axial inhomogeneities arise because of the weakly ferromagnetic or strongly paramagnetic properties of the materials used for construction of ICR cells. The effects of axial inhomogeneities on the FT-ICR signal have been studied previously and were found to have little effect on resolution or signal broadening (10). Factors influencing ion partitioning in two-section cells have also been considered (e.g. pressure or ion mass) but without considering the effects of magnetic inhomogeneities (11-13). Axial magnetic inhomogeneities localized in the conductance limit aperture of a two-section cell constructed of high magnetic susceptibility material cause significant redirection and spatial distribution of low-energy ions entering the ion cell. Therefore, a semi-quantitative description of trapped ion distributions due to low-energy injection through an axially inhomogeneous magnetic region is useful for considering the design requirements for external ion source FT-ICR instruments. For example, some type of ion guide (either rf only quadrupoles or electrostatic lens elements) is required for external ion source instruments. The effect of a given means of injection on ion detection must be considered. Ions that are injected into the ion cell must have relatively low *Z*-axis kinetic energies. Thus, at some point along the ion path (source to ion cell) low-energy ions must pass through a potentially inhomogeneous magnetic field resulting in ill-defined ion trapping conditions and reduced instrument performance.

EXPERIMENTAL SECTION

Fourier Transform Ion Cyclotron Resonance Spectrometer. All experiments reported here were performed on a prototype Fourier transform ion cyclotron resonance mass spectrometer constructed at TAMU. The system is centered around a Nicolet 1280 computer system and is equipped with an Oxford 3-T large bore superconducting magnet described previously (14). The vacuum system and electronics have been modified to accommodate a two-section cell. The two-section cell consists of two cubic cells ($3.8 \times 3.8 \times 3.8$ cm) mounted collinearly along the central axis of the magnetic field. The two cells share a common trap plate that also serves as a conductance limit for the differential pumping system. No modifications to cell geometry were made to the cell with the exception of the thickness and aperture configuration in the conductance limit as specified below. The vacuum is maintained by two 200 L s⁻¹ oil diffusion pumps. Background pressures for both sections of the vacuum system were 1×10^{-8} Torr or less. Ionization was performed by electron impact (50-eV electrons). The electron gun consisted of a resistively heated rhenium ribbon (1 mm) mounted approximately 5 mm from the source region trap plate. An extractor having a 2-mm aperture was placed between the filament and the trap plate and was maintained at ground potential. Trapping potentials were maintained between 0.5 and 10 V. Excitation of the ions in either the source or the analyzer region of the cell was performed by electronically switching the rf excite pulses between the cell regions.

Ion Partitioning Studies. Ion partitioning was performed by pulsing the conductance limit trap plate from the normal ion

trapping potential to some potential less than the trapping potential for 60 μ s to 1 s. In most cases, the conductance limit was pulsed to ground. Ions formed in the analyzer region were removed by rf sweeps. The condition of an ion-free analyzer region was verified by detecting in the analyzer region with a partitioning pulse duration of zero. Benzene and argon were the neutral reagents in all studies with the molecular ion being the ion of interest for benzene. The emission current was maintained at less than 100 nA for all studies in order to avoid ion partitioning as a result of space-charge explosion along the *Z* axis. In addition, at sample pressures of 1×10^{-7} Torr and emission currents of 100 nA, the number of ions formed (ca. 10^8) is small and ion trapping and detection are not complicated by space charge effects.

The quantitative signal-to-noise study was performed by estimating the noise level as the arithmetic mean of the magnitude of the signal at 10 points of the base line near the peak of interest. The mean noise level was then compared to the peak height of interest. It was assumed that for a constant number of scans that the signal is directly related to the number of ions (15).

Magnetic Field Calculations. Magnetic field topologies for various two-section cell materials were calculated by using the Poisson/Superfish codes. (POISSON/SUPERFISH was developed by R. F. Holsinger and K. Halbach. The codes are distributed R. K. Cooper, Accelerator Theory and Simulation Group, AT-6, Los Alamos National Laboratory, Los Alamos, NM 87545.) The Poisson representation of the magnetic field was solved numerically by implementing a nonuniform triangular mesh (16). Input for the program consists of defining the parent magnetic field strength (*H*), the geometry of the two-section cell, and the magnetic permeability ($1 + \chi_m$) of the cell material. Magnetic susceptibilities (χ_m) were measured by the Gouy method (17). Calculations were performed on a VAX 11/780 computer.

Ion Trajectories. Ion trajectories were calculated and displayed by using the trajectory calculation program SIMON (V4.0) (SIMION PC/PS V4.0 was developed by D. C. McGilvery and modified by D. A. Dahl. The program is distributed by D. A. Dahl, MS 2208, EG&G Idaho, Inc., Idaho National Engineering Laboratory, P.O. Box 1625, Idaho Falls, ID 83415.) on a math coprocessor equipped PC/AT type IBM compatible computer. SIMION allows placement of electrodes in a user-defined array as well as allowing magnetic fields to be defined along any axis within the array. The array used for all calculations was 90×25 points (*X*, *Y* in SIMION; *Z*, *Y* in FT-ICR conventions). The spacing between grid points corresponds to 1 mm in the actual system. The array was defined for positive values of the ordinate; the remainder of the cell was generated by rotation. Maximum deviation in the refinement of the array was set to 0.0001 V. Magnetic fields were vectorially added by coordinate as estimated from the Poisson plots.

RESULTS AND DISCUSSION

The original two-section ICR cell configuration used by this group for the study of ion partitioning was constructed entirely of 2.54 mm thick 304 stainless steel plate. The conductance limit aperture was 4 mm in diameter and tapered from both sides at approximately 30°. No benzene positive ion partitioning into an ion-free analyzer region was observed for benzene ions formed by electron impact at an emission current of 100 nA, ionization periods of up to 10 ms, and trap potentials ranging from 0.5 to 10 V. On the basis of signal-to-noise (*S/N*) measurements, most of the ions initially located in the source region were lost when the conductance limit was pulsed to ground.

The original cell configuration was modified for the following experiment by enlarging the conductance limit and placing a 70% transmittance gold grid across the enlarged aperture (grid diameter = 23 mm). This cell yielded inefficient ion partitioning at trapping potentials of 7-8 V. No partitioning was observed for lower or higher trapping potentials. The two-section cell was tilted approximately 5° in all directions with respect to the *Z* axis with no significant effect on ion partitioning efficiency. By comparison of signal-to-noise ratio measurements for ions detected in the source region (prior to partitioning) and in the analyzer region (after par-

tioning), it appeared that approximately 90% of the ions initially located in the source region were lost when the conductance limit was pulsed, but the remaining ions (ca. 10%) were partitioned almost evenly between the source and analyzer regions. Significant ion losses can be attributed to the transmissive properties of the gold grid because approximately 30% of the ions will be lost on each pass through the grid.

In the subsequent attempt to efficiently partition ions, the stainless steel analyzer and source region trap plates were replaced with oxygen-free high conductivity copper plates. This cell has a square-edge conductance limit aperture of 6 mm diameter. On the basis of comparative S/N ratio measurements, we estimate that at least 80% of the Ar⁺ ions formed in source region partition to the analyzer region. Ion partitioning was observed for this cell at trap potentials of 1–4 V. The effects of higher trapping potential on ion partitioning were not studied.

We performed an experiment to qualitatively investigate the effects of space charge on Ar⁺ partitioning at 2×10^{-7} Torr source pressure. The trap voltage was set to 4 V, the ionization event lasted 5 ms, and the partitioning pulse duration was set to zero. The emission current was varied in subsequent experiments between 35, 60, and 110 nA. No Ar⁺ partitioned to the analyzer region at an emission current of 35 nA, but at 110 nA of emission current, the signal for ion partitioning of Ar⁺ was intense. The analyzer cell was quenched during the ionization event; hence this signal was not due to Ar⁺ formation in the analyzer cell. This result implies that partitioning experiments performed with emission currents in the high nanoamperes to the microamperes range must be performed carefully to avoid space-charge ion partitioning. While partitioning by Coulombic repulsion could be of some utility in analytical studies, it is undesirable for controlled probes of ion chemistry. Overall, space charge partitioning would result in poor control ion location and is avoided in all experiments reported here.

Magnetic Materials. All materials possess magnetic properties that alter the shape and local intensity of a magnetic field into which the material is placed. The induced magnetic flux density (magnetic induction, \mathbf{B} ($\text{kg A}^{-1} \text{s}^{-2}$, the tesla)) *inside* a material placed within a homogeneous magnetic field is given by eq 1 where \mathbf{H} (A m^{-1}) is the magnetic force within the material, \mathbf{I} (A m^{-1}) is the intensity of magnetization within the material, and μ_0 ($4\pi \times 10^{-7} \text{ N A}^{-2}$) is the magnetic permeability of a vacuum. \mathbf{H} is due to the prevailing field into which the object has been placed. The material composing the object interacts with the magnetic force in order to increase or decrease the magnetic induction within the body. This effect can be quantified as the magnetic susceptibility, χ_m , defined in eq 2. χ_m is, of course, unitless as formulated here.

$$\mathbf{B} = \mu_0(\mathbf{H} + \mathbf{I}) \quad (1)$$

$$\chi_m = \mathbf{I}/\mathbf{H} \quad (2)$$

Materials fall into one of several categories. If the magnetic susceptibility of a substance is positive, the substance is termed paramagnetic. If χ_m is negative, the material is diamagnetic. Ferromagnetic materials have very large positive susceptibilities resulting from cooperative coupling among the electron spins of such materials. The origin and dependence of para- and ferromagnetism are different; consequently, ferromagnetism is not simply a special case of paramagnetism. Ferromagnetic materials become paramagnetic above the Curie temperature. The materials considered in this paper are diamagnetic (copper) or paramagnetic (304 stainless steel) only. It must be noted that 304 (or 18-8) stainless steel has a Curie point that is below 0 °C if the amount of cold work performed in machining the parts has not been excessive (18).

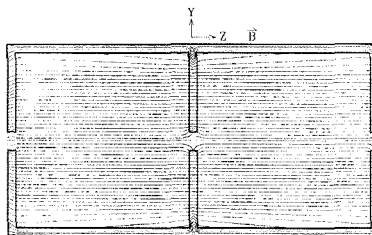


Figure 1. Poisson plot of two-section cell constructed of paramagnetic material ($\chi_m = 0.16$) bathed in a 3-T magnetic field. The magnetic Z axis is the abscissa; the Y axis is the ordinate.

Both diamagnetic and paramagnetic susceptibilities are roughly constant for increasing \mathbf{H} , whereas ferromagnetic susceptibilities decrease significantly as \mathbf{H} increases. At the saturation point, $\mathbf{B} - \mathbf{H}$ and \mathbf{I} level off and a break in \mathbf{B} occurs. As \mathbf{H} is increased past the saturation point, \mathbf{B} increases slowly and indefinitely (18).

Values for the magnetic susceptibility of 304 stainless steel vary widely depending upon the exact composition and history of the sample. To obtain a reasonable estimate of the magnitude of χ_m for the stainless steel used for the construction of our ICR cells, the magnetic susceptibility of a sample of raw cell material was measured by using the Gouy method (see Experimental Section); a magnetic susceptibility of 0.16 was obtained. This compares favorably with the lower end of literature values which range from 119 (indicating a ferromagnetic component) to 0.4 (18). Consequently, the conclusions drawn in this study could represent a lower limit of the effects observed. As a control, the susceptibility of the oxygen-free high conductivity copper stock used in cell construction was also measured; a value of 0.00 was obtained.

Mapping Inhomogeneities. Equations 1 and 2 describe the magnetic induction on the *interior* of a substance placed in a magnetic field. These fields are directly related to the fringing fields of interest generated *outside* of the ICR cell plates. Calculations of magnetic fields outside of materials submerged in parent fields are not simple because the geometry of an object placed in the field plays a significant role in the perturbed form of the field. In most cases, the equations describing these stray fields cannot be solved explicitly. The Poisson/Superfish codes allow the calculation of the topology of a magnetic system given values for the susceptibility of the material of choice, the geometry of the system of interest, and the parent field magnitude and direction.

Figure 1 contains the result of Poisson computations for a 304 stainless steel cell of the geometry employed for these partitioning studies. The value of χ_m used for the calculation was 0.16; the value measured by the Gouy method. The highest intensity of magnetization is found wherever the length of the material along the parent field (Z) axis is larger than the width (X or Y dimension) of the object. For example, the excite-receive plates in Figure 1 show significantly increased magnetic induction, whereas the trap plates have increased induction only near the edges in the X–Y plane. An explanation for this increased induction (and, hence, axial inhomogeneity) near the trap plate apertures can be rationalized by considering the region of the plates immediately surrounding the apertures as thin cylinders with lengths greater than their widths. The inhomogeneity for the center aperture is somewhat more intense than those for the outer trap plates; a result of two effects. The field topology calculation takes into account magnetic homogeneity of the field due to the superconducting magnet. This field is somewhat weaker at the outer trap plates than at the center of the cell resulting in reduced aberration. Secondly, the field interacting with

the outer trap plates is less affected by the excite-receive plates than is the center trap plate. It is imperative to realize that the cell geometry synergistically contributes to local magnetic topologies. Local, axial inhomogeneities as those depicted in Figure 1 would have little effect on the single cell FT-ICR experiment because ion interaction with these regions would be minimal in this case. Such inhomogeneities are destructive, however, to experiments requiring ions to pass through the inhomogeneous regions near the trap plate apertures (e.g., an ion partitioning experiment). A Poisson plot of the two-section cell system with oxygen-free high conductivity copper (not shown) used for cell construction ($\chi_m = 0.00$) demonstrates that the cell is effectively transparent with respect to the parent magnetic field giving rise to no significant magnetic inhomogeneities throughout the cell.

Trajectory Calculations. SIMION was used to model ion trajectories during partitioning in a two-section cell with a 304 stainless steel conductance limit trap plate. This version of SIMION can be used to "paint" magnetic fields along any axis and with any reasonable magnitude. For the trajectory calculations, a homogeneous parent magnetic flux density of 3 T was defined throughout the entire cell along the Z axis. The magnetic field inhomogeneities in the region of the conductance limit aperture were estimated from Figure 1 and added to the parent field.

It is important to understand that there is little benefit in trying to rigorously mimic the axial magnetic inhomogeneities near the conductance limit aperture of the *actual* two-section cell used here for two reasons. First, the magnetic susceptibility of the stainless steel composing a given part can be known only approximately. This is due to the fact that machining of parts may lead to precipitation of magnetic phases within the material. Also, slight variances in alloy composition lead to large changes in χ_m . It is probably not possible to know the magnetic susceptibility of a given part (assuming that it is homogeneous in composition) to better than a factor of 3. Thus, two identical items machined from the same stock could have significantly different magnetic properties. Secondly, as mentioned above, the magnitude of fields generated outside of materials bathed in magnetic fields are strongly geometry dependent such that in describing one real case explicitly, the principles of interest would be obscured. Furthermore, varying operating parameters (trapping potential, for example) for a given system significantly changes the effect of magnetic inhomogeneities. In this paper, the *thrust will be to represent the form of the inhomogeneity near the aperture with intensities that are considered to be reasonable.*

With SIMION, several specific examples of the interaction of ions with the magnetic inhomogeneity of the aperture region depicted in Figure 1 are considered below. These examples are based on ion partitioning in a two-section cell. In all cases considered, the cell consisted of two 3.8-cm³ cells joined by a conductance limit. The conductance limit was 3 mm thick and had a 4 mm diameter squared-edge aperture. The symmetry of the system was considered to be cylindrical along the Z axis. The outer trap plates were set to a potential of 4 V while the conductance limit was maintained at ground. Four volts was chosen as the trapping potential because this is the maximum potential used for ion partitioning for two-section cell studies performed on this instrument. Ions placed near the Z axis of one cell travel toward the aperture where they encounter the magnetically inhomogeneous region defined above. SIMION provides views of the resulting trajectories in all three planes.

The perturbation of the trajectories of the ionizing electrons will not be considered here. The momentum of the electrons piercing the defined magnetic inhomogeneities is about 1% of the lowest momentum ion considered below. Intuitively,

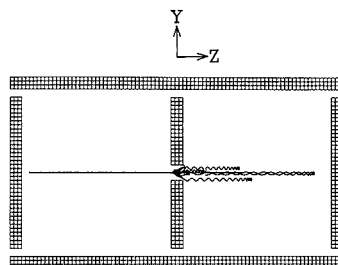


Figure 2. $Y-Z$ plane projection of the trajectories of ten m/z 100 ions with E_z varying from 0.19 to 3.48 eV as they partition through an axial inhomogeneity as described in the text.

Table I. Effects on Ion Partitioning Through a Stainless Steel Conductance Limit Trap Plate^a

ion	E_z , eV	fate	trapped?	S_p , mm	$(\bar{E}_z)^{-1/2}$, eV ^{-1/2}	ΔE_{sp} , eV	Δ_c , mm
1	3.485	XP ^b	yes	0.9	0.56	0.70	0.8
2	2.763	QP ^c	no				
3	2.125	QP	no				
4	1.593	QP	no				
5	1.171	XP	yes	2.9	1.1	0.63	2.4
6	0.848	XP	yes	2.8	1.3	0.47	1.6
7	0.604	XP ^d	no	4.1	1.8	0.56	1.9
8	0.478	XP	yes	3.7	1.4	0	1.2
9	0.290	RQ ^e	no				
10	0.190	QP	no				

^a See text for a description of the parameters: S_p , $(\bar{E}_z)^{-1/2}$, ΔE_{sp} , and Δ_c . ^b XP = ion center-of-motion shift upon successful partitioning. ^c QP = ion quench during partitioning through aperture. ^d Ion 7 successfully partitioned with a center-of-orbit shift, but collided with the conductance limit in < 60 μ s. ^e RQ = reflect then quench.

it would seem that lower momentum would result in increased charged particle deflection and preliminary SIMION trajectories performed in this lab indicate this to be the case. As one referee has pointed out, such deflection of the electron beam could result in the formation of ions that are spatially disallowed from partitioning to the analyzer region of the two-section cell.

Energy, Partitioning, and Inhomogeneity. In order to study the effect of Z -axis energy on low-energy ion partitioning, SIMION calculations were performed on ten m/z 100 ions initially placed uniformly across the Z axis of the cell. The initial placement of ions in the gradient electric trapping field determines the ion's Z -axis energy on reaching the conductance limit (0.01 eV in the $X-Y$ plane). Ions beginning closer to the outer trap plate have up to 4 eV of Z -axis translational energy when they reach the conductance limit. Ions placed near the conductance limit have near zero translational energy in the Z axis when they reach the aperture. The ions were placed such that their cyclotron orbit guiding centers coincided with the Z axis. Figure 2 shows a trajectory plot of 10 ions ranging from 0.19 to 3.48 eV as they are allowed to undergo partitioning through the axial inhomogeneity defined above. Figure 2 qualitatively portrays the spatial and energetic distribution of ions arising from low-energy interaction with a magnetic inhomogeneity. Table I quantitatively summarizes the conditions and fate of the 10 ions in this study. The trajectories were terminated at 60 μ s if collision with an electrode had not occurred. This time limit represents the minimum period for an event on the Nicolet FTMS-1000 and, therefore, the shortest partitioning pulse. The plot corresponds to a projection of the trajectories at $X = 0$ (Z is the horizontal coordinate; Y is the vertical coordinate). It is apparent that the aperture inhomogeneity dra-

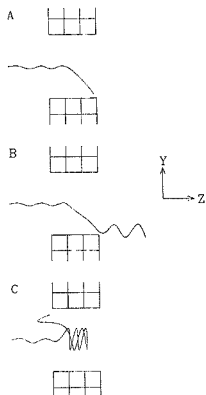


Figure 3. Enlarged view of the conductance limit trap plate aperture during ion partitioning: (A) ion collision on partitioning (for example, ion 2 in Table I), (B) ion guiding center shift and gain of energy in the X - Y coordinate on partitioning (for example, ion 1 in Table I), (C) the ion reflects off the axial inhomogeneity and returns to the first cell region (ion 9 in Table I).

matically affects ion partitioning trajectories. It is noteworthy that no deflection of the ion paths is observed for the same calculations performed on an oxygen free high conductivity copper cell (not shown). Three basic trajectories (or combination of these) are observed for the stainless steel cell: (i) (Figure 3A) the ion collides with the conductance limit during the first pass, (ii) (Figure 3B) the ion partitions but gains energy in the X - Y plane usually followed by collision with the conductance limit, or (iii) (Figure 3C) the ion undergoes reflection and subsequent collision with the conductance limit. In the first case, ions can normally be trapped in the second cell region by proper timing of the conductance limit grounding pulse. Guiding center shifts occur for all ions entering the inhomogeneity within the aperture.

Figure 4 shows the projection of the trajectories for the ions that partition in Figure 2 onto the X - Y plane. It should be clear from the figure that the axial inhomogeneity due to the stainless steel conductance limit induces significant complexity on ion partitioning trajectories at low translational energy. In addition, one observes that ions formed with little spatial distribution and equal energy in the cyclotron orbit (X - Y plane energy) are distributed spatially and can gain significant energy in the X - Y plane upon partitioning through the axial inhomogeneity. The mechanism for cyclotron orbit energy gain is deflection into the X - Y plane due to the X - Y component of the magnetic field in the conductance limit aperture. These latter effects are summarized in Table I (Δ_c is the center-of-orbit shift upon partitioning, ΔE_w is the energy gained in the X - Y plane). From the figures and Table I, one sees that only four of the ten ions partition such that the ions are trapped in the second cell region. Ion no. 7 partitions but collides with an electrode before 60 μ s. These five ions have an appreciable energy spread (0.7 eV) with respect to the defined energy spread of zero before partitioning. On extrapolation of this result to the observable experiment, it appears that much of the ion signal would be lost on partitioning ions in the cell for this example. In addition, ions that are partitioned to the second cell region are not as detectable as before partitioning due to the large resultant energy and spatial distributions of the ions (8).

The dependence of ion trajectories on Z -axis energy can be determined upon examination of the trajectories of the five ions that partition to the second cell region in the 10-ion study above (Figures 3 and 5 and Table I). Figure 5 shows pro-

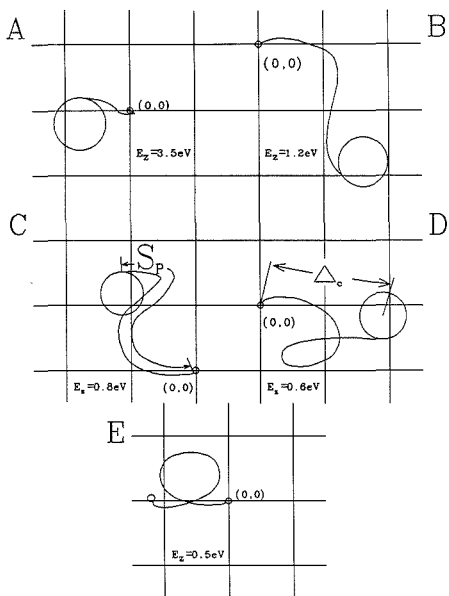


Figure 4. X - Y plane projection of the ions that partition in the ion energy study. Ions a-e correspond to ions 1, and 5-8 in Table I, respectively.

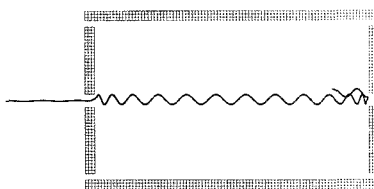


Figure 5. SIMION plot of the Y - Z plane projection of an ion injected into an ICR cell. The ion begins with 8 eV in the Z direction, the left trap plate is maintained at 5.0 V, and the right trap plate is at 5.4 V. The ion reflects off magnetic inhomogeneities in the trap plate apertures.

jections of the ion trajectories onto the X - Y plane for these five ions as well as the physical definitions of some of the parameters in Table I (S_p , ΔE_w , and Δ_c).

Physically, S_p is a measure of how well the ion cyclotron guiding center follows a given flux line in the axially inhomogeneous region. S_p is defined as the path length of the X - Y plane projection of the trajectory from the cessation of stable cyclotron oscillation in the source region to the resumption of a stable orbit in the analyzer region. Upon examination, one observes that the ion orbit guiding center generally follows a magnetic flux line on entering and leaving the inhomogeneity but tends to cross field lines in the central region of the inhomogeneity where the field lines are parallel to the parent field. Therefore, S_p is a measure of the perpendicular component of ion motion with respect to the portion of the magnetic inhomogeneity that is parallel to the parent field (see Figure 1). In two cases discussed below, the ion guiding center crosses field lines in the entry region of the inhomogeneity (where the flux lines are approximately oriented 45° off the Z axis) and the projection of the ion trajectory into the X - Z plane must be considered.

ΔE_w is the energy transferred from the Z -axis component to the X - Y plane during partitioning through the aperture

Table II. Effects of Mass on Ion Partitioning through a Stainless Steel Conductance Limit Trap Plate^a

mass	fate	trapped?	S_p , mm	ΔE_w , eV	Δ_c , mm	$(ME_z)^{-1/2}$ (amu·eV) ^{-1/2}
100	XP	yes	3.3 ^b	0.63	1.6	0.15
200	QP	no				
300	QP	no				
400	QP	no				
500	XP	yes	1.6	0.32	1.8	0.058
600	XP	yes	2.3	0.46	2.7	0.056
700	XP	yes	1.7	0.21	1.9	0.047
800	XP	yes	1.7	0.34	1.8	0.046
900	XP	yes	1.2	0.05	1.4	0.039
1000	QP	yes	1.6 ^b	0.05	0.2	0.037

^aLegend is as for Table I. ^bAdjusted for X-Z plane component, see text.

axial inhomogeneity. In addition, the arithmetic mean of the z-axis energy on entering and leaving the axial inhomogeneity, \bar{E}_z , is defined by eq 3. Δ_c is the shift of ion cyclotron guiding

$$\bar{E}_z = (2E_z - \Delta E_w) / 2 \quad (3)$$

centers in the x-y plane on partitioning from the source region to the analyzer region. Two trends are observed for the partitioning of five m/z 100 ions through the inhomogeneity: (i) the x-y plane projection of the path through the inhomogeneous region becomes less linear with increasing energy, and (ii) S_p correlates well with $(\bar{E}_z)^{-1/2}$. If the magnetically inhomogeneous region is considered to be a crude magnetic analyzer and \bar{E}_z to be a reasonable estimate of the actual mean z-axis energy within the inhomogeneity, then S_p can be expressed as a function of the reciprocal of ion momentum. Because mass is constant in this study, S_p can be expressed as a function of $(\bar{E}_z)^{-1/2}$. A plot of S_p versus $(\bar{E}_z)^{-1/2}$ is reasonably linear ($r = 0.980$), and the first-order regression of the plot very nearly passes through 0,0 ($b = -0.12$ mm) as would be expected. A higher order of correlation between S_p and Z-axis energy could only be approached through more rigorous treatment of the form of the inhomogeneous magnetic field within the aperture and the magnitude of E_z with respect to position in the aperture region.

Mass, Partitioning, and Inhomogeneity. In a study precisely analogous to the energy study above, the mass dependence on ion partitioning was examined. Ions of m/z 100–1000 were “partitioned” through the paramagnetic conductance limit using SIMION calculations with the same array definitions as before. All ions were placed 21 mm from the outer trap so that the energy upon reaching the magnetically inhomogeneous aperture region would be 0.758 eV. Ions were given 0.01 eV of energy in the X-Y plane and placed such that the guiding center of each ion’s orbit before partitioning coincided with the Z axis ($X = Y = 0$) of the cell. The results of this study are summarized in Table II. As mentioned earlier, S_p represents the component of the ion’s path (while within the inhomogeneous region) that is perpendicular to the local magnetic field. Analysis of the trajectories of the m/z 100 and the m/z 1000 ions in this study indicate that a large fraction of this perpendicular component is in the X-Z plane. In this case, the X-Y plane projection of an ion’s trajectory gives poor S_p values. Table II reflects adjusted values for these ions which consider the X-Z plane components. Again, two trends emerge: (i) trajectories are more linear for higher momentum ions, and (ii) S_p correlates with momentum. For this study, S_p varies linearly with respect to $(ME_z)^{-1/2}$, where M is the ion’s mass in amu. \bar{E}_z must be included in this correlation because it is related to both the ion’s initial and final energy. A plot of S_p versus $(ME_z)^{-1/2}$ is roughly linear ($r = 0.915$) with a y intercept of 0.60 mm.

Magnetic Trapping. Magnetic inhomogeneities in the entry aperture of a cell can give rise to ion trapping effects for ions injected from external sources. This trapping arises from the ability of magnetic inhomogeneities to redirect the energy component distribution along other axes. For example, Figure 5 is the Y-Z plane projection of an ion being injected into a rectangular ICR cell at 8.0 eV along the Z axis and 0.01 eV in the X-Y plane. The left trap plate is biased to 5.0 V while the right plate is held at a potential of 5.4 V. A magnetic field of 3.0 T was placed over the entire potential array oriented along the Z axis (horizontal). The inhomogeneity used for the two-section cell studies above was doubled in magnitude and placed in both apertures. The form of the inhomogeneity was not altered. It is important to note that doubling the inhomogeneity intensity still results in a very weak aberration with respect to that possible for 304 stainless steel (see Magnetic Materials, above).

The ion enters the cell at about 3.0 eV along the Z axis and approximately 2.6 eV of this energy is transferred into the X-Y plane resulting in a significant gain in cyclotron orbit radius. The ion guiding center is also shifted as the ion is deflected into the X-Y plane. The ion falls into the cell trapping well accelerating to roughly the cell’s center (as evidenced by the projection of an expanding helix). As the ion approaches the right trap plate, it decelerates along the Z axis, encounters the inhomogeneity in the aperture region, and is reflected back along the Z direction. Upon reflection, the ion guiding center shifts in the X-Y plane and the ion loses approximately 1 eV of energy from the X-Y plane into Z-axis motion. It is obvious in this example that the ion is not actually trapped in the cell and would most likely collide with the left trap plate, but it remains equally obvious that the inhomogeneities of this cell would assist in ion trapping. Stronger inhomogeneities or geometrically optimized inhomogeneities would result in efficient trapping.

CONCLUSIONS

Several conclusions emerge on considering the partitioning of ions in a two-section FT-ICR cell with an axial magnetic inhomogeneity in the region of the conductance limit aperture. First, ion deflection in the X-Y plane (measured as S_p or Δ_c) increases with increasing ion momentum. Δ_c only roughly correlates with momentum and is highly path sensitive. ΔE_w roughly decreases with increasing ion momentum and is also highly path sensitive. Whether energy was varied with a set m/z ratio or m/z was varied for a given injection energy, it is apparent that significant energy gain and ion deflection results under the low-momentum conditions defined above. The resulting ion packets trapped after such ill-defined injection will have poor spatial (5–10 mm diameter) and significant energy (0.7eV) distributions.

The implications of this work are far-reaching throughout FT-ICR. In the two-section cell experiment, one must choose to optimize geometry or use low susceptibility materials in order to build cells that perform well under the conditions of the experiment. Optimizing geometry largely centers around the use of plates that are thin in the Z direction. This increases the demagnetizing effect which causes the induced magnetization, I , to approach the field due to the parent magnetic force, $\mu_0 H$. This group has opted to use oxygen-free high conductivity copper for cell construction. The two-section cell in use here has worked well with good partitioning efficiency for approximately 2 years.

The implications of ion dispersion due to axial magnetic inhomogeneities are important for external ion source FT-ICR. For the same number of ions, the detectable signal is degraded as the spatial and energetic definition of an ion packet becomes less defined. This effect could be particularly dramatic for cells using fine grids of high magnetic permeability materials

where the wire thickness approaches the mesh size. In this case, ions that partition *must* be intimate with axial inhomogeneities. This effect is offset somewhat by the fact that the grids are normally thin along the Z axis. However, if the wire's thickness along the Z and X (or Y) axes is comparable, local inhomogeneities could be quite strong.

Finally, the performance degradation of stainless steel single cell instruments (19) could largely be due to the effects discussed above. The signal would degrade due to the cell's decreasing ability to trap ions properly (small energetic and spatial distribution), as the permeability of the material increases with time.

LITERATURE CITED

- (1) Sack, T. M.; Gross, M. L. *Proc. Annu. Conf. Mass Spectrom. Allied Top.*, 31st 1983, 396.
- (2) Carlin, T. J.; Freiser, B. S. *Anal. Chem.* 1983, 55, 571-574.
- (3) Kotel, P.; Alleman, M.; Kellerhals, Hp.; Wanczek, K.-P. *Int. J. Mass Spectrom. Ion Processes* 1985, 65, 97-103.
- (4) McIver, R. T.; Hunter, R. L.; Bowers, W. D. *Int. J. Mass Spectrom. Ion Processes* 1985, 64, 67-77.
- (5) Alford, J. M.; Williams, P. E.; Trevor, D. J.; Smalley, R. E. *Int. J. Mass Spectrom. Ion Processes* 1986, 72, 33-51.
- (6) Hanson, C. D.; Castro, M. E.; Russell, D. H.; Hunt, D. F.; Shabanowitz, J. *ACS Symp. Ser.* 1987, No. 359, 100-115.

- (7) Ghaderi, S.; Littlejohn, D. *Proc. Annu. Conf. Mass Spectrom. Allied Top.*, 33rd 1985, 727-728.
- (8) Hanson, C. D.; Kerley, E. L.; Russell, D. H. *Treatise Anal. Chem.* (2nd Ed.) 1989, 11, 117-187.
- (9) Elkind, J. L.; Alford, J. M.; Weiss, F. D.; Laaksonen, R. T.; Smalley, R. E. *J. Chem. Phys.* 1987, 15, 2397-2399.
- (10) Laukien, F. H. *Int. J. Mass Spectrom. Ion Processes* 1986, 73, 81-107.
- (11) Giancaspro, C.; Verdun, F. R.; Muller, J.-F. *Int. J. Mass Spectrom. Ion Processes* 1986, 72, 63-71.
- (12) Verdun, F. R.; Giancaspro, C. *Anal. Chem.* 1986, 58, 2097-2099.
- (13) Honovich, J. P.; Markey, S. P.; Wang, T.-C. L.; Shih, M.-C. *Proc. ASMS Conf. Mass Spectrom. Allied Top.*, 35th 1987; 1112-1113.
- (14) Kerley, E. L.; Russell, D. H. *Anal. Chem.* 1989, 61, 53-57.
- (15) Comisarow, M. B. *J. Chem. Phys.* 1978, 69, 4097-4104.
- (16) Winslow, A. M. *J. Comp. Phys.* 1967, 2, 149-172.
- (17) Selwood, P. W. *Magnetochemistry*; Interscience: New York, 1943; p 2.
- (18) Bozorth, R. M. *Ferromagnetism*; D. Van Nostrand, Inc.; New York, 1951, Chapters 1, 2, and 5.
- (19) Dunbar, R. C., personal communication.

RECEIVED for review May 9, 1989. Accepted August 4, 1989. This work was supported by the National Science Foundation (CHE-8821780). We gratefully acknowledge the Texas Agricultural Experiment Station for providing a portion of the funds for purchase of the Nicolet FTMS-1000 mass spectrometer.

Measurement of Linear Alkylbenzenesulfonates in Aqueous Environmental Matrices by Liquid Chromatography with Fluorescence Detection

Mark A. Castles,¹ Billy L. Moore,* and Susan R. Ward

The Procter and Gamble Company, Ivorydale Technical Center, Cincinnati, Ohio 45217

A high-performance liquid chromatography method for the determination of linear alkylbenzenesulfonate (LAS) in complex environmental matrices has been developed. The method takes advantage of the inherent sensitivity of fluorescence detection, as compared to that obtained with conventional UV detection or the popular desulfonation-gas chromatography method for determining LAS in complex matrices. The chromatography has been designed to combine all of the isomers of each homologue into single peaks representing the respective C₁₀-C₁₄ LAS constituents. This serves to enhance the detection levels, as well as the overall accuracy and precision of the measurement. Solid-phase extraction procedures have been employed to isolate the LAS from such matrices as sewage treatment plant influent, final effluent, and the subsequent receiving river water. The average recovery of LAS from influents and effluents and river waters was found to be 95%, 85%, and 81%, respectively. The precision of the method, in terms of the relative standard deviation for influent, effluent, and river water was determined to be 1.4%, 4.6%, and 13.5%, respectively. The limit of detection ($S/N \geq 3$) was found to be 1.5 ng per component injected onto the column or 2 ppb of total LAS concentrated from a 200-mL sample volume. Therefore, the limit of quantitation ($S/N \geq 10$) was found to be 7-10 ppb. A discussion of the analytical method and the results from the analysis of various samples is presented.

* Author to whom correspondence should be addressed.

¹ Current address: Degussa Corp., Mobile, AL.

Linear alkylbenzenesulfonates (LAS), shown in Figure 1, are water-soluble materials used extensively in detergent formulations as surface-active agents. Ionic surfactants are unique in the sense they possess both hydrophobic and hydrophilic characteristics, due to the ionic and long chain alkyl portions of the molecule. This property promotes considerable concentrations of the surfactant at interfaces, thus dissolving hydrophobic materials into the aqueous phase. These properties account for the widespread use of LAS as an active cleaning agent in detergent formulations.

Commercial LAS materials consist of a mixture of homologues and isomers. Individual LAS homologues and isomers are identified by the length of the hydrophobic alkyl substituent and by the position of attachment of the alkyl chain to the benzene ring. The predominant formulation consists of alkyl chain lengths from C₁₀ to C₁₄, with the average distribution being approximately C₁₂. Isomer configurations range from the 2-phenyl position to the 7-phenyl position, depending on alkyl chain length.

Due to the nature of anionic surfactant product usage, the majority of LAS is disposed to sewage treatment facilities. LAS is highly removed (e.g. >95% for activated sludge processes) during the sewage treatment process as result of biodegradation processes (1) and adsorption to solids (2). Due to the high removability of LAS, only very small quantities (i.e. low parts per billion levels) are discharged from wastewater treatment plants into the receiving waters. Analytical methodology to quantitate low parts per billion levels in environmental matrices is required to validate mathematical models designed to predict environmental concentrations of

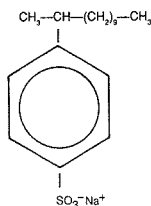


Figure 1. Structure of the 2- C_{12} linear alkylbenzenesulfonate (C_{12} LAS) homologue. Commercial mixtures range from C_{10} to C_{14} in alkyl chain length.

target materials (3), as well as detect and quantify target materials in their natural environment in support of a wide range of biodegradation and ecotoxicological studies.

Various analytical methods are available for the measurement of LAS. These include simple colorimetric methods, gas and liquid chromatography, as well as mass spectrometry. Colorimetric methods are one of the oldest methods used for the measurement of anionic surfactants in aqueous samples (4). In general, colorimetric methods are based on the formation of an ion pair between the anionic surfactant and a cationic dye. The complex is extractable into a nonpolar solvent, whereas both the free surfactant and dye remain in the aqueous phase. Methylene blue cationic dye is generally the colorimetric dye of choice, due to its surfactant complexing ability and the intense blue color that develops upon extraction of the complex into the organic phase. Obviously, any substance that can form an extractable complex with the dye yields a positive bias to the quantitation of anionic surfactants, in particular LAS.

In addition, the presence of various cationic compounds (e.g. quaternary amines) will compete with the methylene blue dye for the ion pairing of anionic materials present. Depending upon both the strength of the ion pair formed and the concentration of the competing ions, LAS may be extracted into the nonpolar phase as the ion pair of an interfering cationic compound rather than that of the methylene blue dye. As a result, a color enhancement would not result and a negative bias in the quantitation of LAS would be present.

Colorimetric methods are not specific to any particular anionic surfactant (1), thus colorimetric results are expressed as concentrations of methylene blue active substances (MBAS) per unit volume. As a result, MBAS results contain only minimal useful information regarding the concentration of a specific anionic material in an aqueous sample. This is particularly true for complex mixtures, such as sewage influents, effluents, and river water samples.

Various modifications have been implemented to improve the specificity of colorimetric methods. Among these modifications are the implementation of hydrolysis steps and cation exchange resins prior to the MBAS measurement (5). The hydrolysis step is used to remove organic sulfates and the cation exchange resins are used to eliminate interfering quaternary amines. These implementations do enhance the selectivity of the MBAS method; however, the results should still be considered as an approximation of the levels of anionic surfactant present and not an absolute measurement of LAS concentration.

Gas chromatography techniques have been used for the specific determination of LAS in environmental matrices. LAS is not sufficiently volatile to permit direct measurement by GC. As a result, LAS must be either derivatized to form a volatile compound or desulfonated to form the respective linear alkylbenzenes (LAB). The desulfonation technique has generally been regarded as the technique of choice for measuring LAS. As early as 1963, Setzkorn and Carel (6)

described a microdesulfonation procedure for generating the volatile LAB. The alkylbenzenes were generated by heating the LAS in concentrated phosphoric acid. Modifications of this technique have been used by Swisher (7) for the examination of wastewater samples. Waters and Garrigan (8) have described a desulfonation-GC procedure for the determination of LAS in a river water matrix. Detection levels of 25–50 ppb were reported from an initial sample volume of approximately 2 L. Osburn (5) extended the methodology to include solid matrices, such as, digester sludge and stream sediments. A Soxhlet extraction procedure, using acidic methanol, was used to extract the LAS from the particles.

Various other methods, using gas chromatography with mass spectral detection, have been carried out (9). In addition to the desulfonation procedure, the surfactant molecules may be transformed into a volatile product through conversions to the respective sulfonyl chloride (10) or sulfonate ester (11) derivatives.

High-performance liquid chromatography (HPLC) has been widely applied to the measurement of LAS. Various applications of HPLC have appeared in the literature. The main advantage of HPLC over other analytical techniques is its simplicity. LAS can be separated and detected without prior derivatization or desulfonation. Various chromatographic approaches to the separation of LAS into the homologues and respective isomers have been reported.

One of the initial accounts on the use of reverse-phase chromatography, with fluorescence detection, to quantitate LAS in aqueous environmental samples was by Nakae et al. (12, 13). He was able to quantitate the levels of LAS in river waters without prior preconcentration or sample cleanup. In this approach, a C_{18} column was employed with a methanol/water mobile phase containing 0.1 M sodium perchlorate ion-pair phase modifier. The method yielded a partial isomer separation per respective homologue constituent but was unable to yield resolutions comparable to various GC methods. In addition, this method was somewhat limited to relatively clean aqueous samples with >100 ppb of LAS, since there was no attempt to implement any type of cleanup/preconcentration steps prior to the HPLC analysis.

Linder and Allen (14) used HPLC with fluorescence detection to follow the progress of LAS biodegradation in a simulated river die away study. Using tetrahydrofuran and water with a C_{18} column, they were able to monitor the disappearance of the parent LAS and the appearance of the sulfophenyl carboxylates intermediates.

Matthijs and De Henau (15), as well as Kikuchi (16), have reported on an HPLC method based on the chromatographic procedure of Nakae et al. (12, 13), but they modified the method to make use of gradient elution with acetonitrile and water with a sodium perchlorate modifier and UV detection. In addition, a solid-phase extraction cleanup procedure was employed prior to the chromatographic analysis in order to extend the methodology to the measurement of LAS in both aqueous and solid environmental matrices.

Marcomini et al. (17) recently reported on an HPLC method for simultaneous quantitation of LAS and alkylphenol ethoxylates in solid environmental compartments (e.g. sewage sludge, river sediments, soils, etc.). Soxhlet extraction procedures were used to extract the LAS and ethoxylates from the solid particles, as well as from detergent powders.

This paper presents a modified chromatographic and solid-phase extraction (i.e. sample cleanup) approach to the determination of LAS in aqueous environmental samples. The methodology offers a simple, specific, and sensitive procedure for quantitatively measuring the aromatic surfactant at trace levels (low parts per billion) within complex environmental matrices.

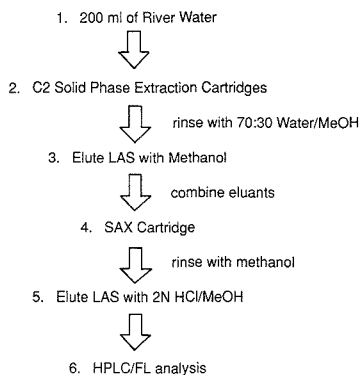


Figure 2. Flow diagram of the LAS isolation and preconcentration procedure.

EXPERIMENTAL SECTION

Reagents and Materials. The C_2 and SAX solid-phase extraction cartridges were purchased from Analytichem International. Both resins consisted of 40 μ m based silica particles and contained 500 mg of the bonded phase material. Both cartridges were first preconditioned with 5 mL of methanol followed by 10 mL of Milli-Q water. HPLC grade sodium perchlorate and tetrahydrofuran were obtained from Aldrich Chemical and Fisher Scientific, respectively. The LAS standards (both commercial and ^{14}C labeled material) and the C_9 and C_{15} LAS internal standards were synthesized and purified at the Miami Valley Laboratories, Procter & Gamble Co. Scintillation cocktail was prepared with equal parts of Reagent Grade ethanol from Fisher Scientific and ACS Scintanalyzed Fisher Scientific toluene to which was added 214 g/L PPO-dimethyl-POPOP from Research Products International Corp.

Samples. The influent, effluent, and river water samples were 24-h composites taken over a 3–5-day period. The samples were taken from different sewage treatment facilities and receiving waters across the U.S. All samples were immediately preserved with 1% formalin (37% formaldehyde) to prevent further microbial degradation of the LAS present in the sample.

Isolation and Concentration Procedures. Prior to extraction, each sample was shaken to ensure adequate mixing and suspension of particulate material. Depending on the nature of the sample, the appropriate volume of sample was removed from the container, acidified to a pH of 3–4 with glacial acetic acid, and spiked with the C_9 LAS internal standard. The acidification of the sample aided in the retention of the C_9 LAS on the C_2 resin.

In general, river waters, sewage treatment plant effluent, and primary influent samples required the preconcentration of 200 mL, 150 mL, and 10 mL, respectively. However, the volume of sample used is directly dependent on LAS concentration and can be adjusted accordingly. The LAS concentration in the sample can only be estimated; thus a knowledge of the sampling site characteristics and sewage treatment facility removal efficiency would be helpful when making this estimate for the volume of original sample to be used.

The concentration of internal standard spiked into the sample was approximately 5-fold less than the estimated concentration of the total LAS in the sample. The 5-fold decrease was deemed necessary to ensure that the internal standard peak area was similar in magnitude to that of the separate LAS homologues. Thus, yielding a linear molar correlation between the concentration of the internal standard and the LAS homologues being measured. The sample was then allowed to equilibrate overnight, although significantly different extraction efficiencies were not encountered after an equilibration time of 3 h (2).

The procedure used to preferentially isolate and preconcentrate the LAS from the environmental matrices is shown in the flow diagram in Figure 2. The first step in the extraction scheme was the preconditioning of the solid-phase extraction resins to ensure uniform wetting of the hydrophobic bonded phases. This was

accomplished by passing a minimum of 5 mL of methanol through each C_2 cartridge and each strong anion exchange (SAX) cartridge. The methanol rinse was followed by 10 mL of Milli-Q water.

Following preconditioning, a maximum of 50-mL aliquots of the sample were passed through a single C_2 cartridge and the eluant was discarded. Each cartridge was then rinsed with 5 mL of a 70:30 water to methanol solution to rid the resin of loosely bound material. The retained LAS was then eluted from each C_2 cartridge with 10 mL of methanol. The methanol eluates were combined and passed through a single preconditioned SAX cartridge. The SAX resin was then rinsed with 5 mL of a 2% acetic acid in methanol solution, followed by 5 mL of methanol. The LAS was eluted with 15 mL of a 1:1 2 N HCl (in high-purity water) and methanol. At this point, an additional standard, C_{15} LAS, was added into the SAX eluate. It is important to note that the addition of C_{15} LAS prior to this point in the extraction procedure yields unpredictable results due to the low solubility of the C_{15} LAS homologue in water.

The eluate was evaporated to dryness on a steam bath and reconstituted in a solution of 50:50 methanol and water and 0.025 M sodium dodecyl sulfate (SDS). The SDS was used to aid in the resolubilization of the LAS after evaporation of the solvent. The reconstitution volume was 5 mL but may be varied in order to increase or decrease the concentration of the LAS in the extract.

Spike and Recovery Procedures. The overall efficiency of the isolation procedure was determined with both radiolabeled and nonradiolabeled LAS. The radiolabeled LAS was used in the initial experiments. A 0.15- μ Ci quantity of radiolabeled LAS was added to the sample and the mixture was allowed to equilibrate overnight. The sample was then treated as described in the isolation and concentration section. The final eluate was redissolved in scintillation cocktail and quantitatively measured with a Beckman Model LS 7800 liquid scintillation counter.

The efficiency of the isolation procedure was also determined with nonradiolabeled LAS. The procedure was the same as described for the radiolabeled material, but instead, the chromatographic system was used for the quantitation. The recovery of the spiked material was determined by direct comparison to an internal standard of known concentration.

Chromatographic Analysis. The method development work was performed on a Waters 840 system, which consisted of dual Model 510 pumps and the WISP Model 710 autosampler. The data were collected and manipulated with a DEC Pro 380 computer, containing the Waters, Version 5.1 Expert Chromatography Software. Fluorescence detection was performed by a Hitachi Model F1000 dual grating fluorescence spectrophotometer. The detector was operated at an excitation wavelength of 225 nm and an emission wavelength of 290 nm, with a spectral band-pass of 10 nm. The volume of the flow cell was 12 μ L.

The chromatographic separation was performed in the reverse-phase mode with a 5- μ m, C_1 Spherisorb analytical column (25 cm \times 4 mm i.d.) from Alltech Associates. The analytical column was preceded by a cyano guard column (3 cm \times 4 mm i.d.) from Brownlee Laboratories. A binary solvent system was employed by using tetrahydrofuran (THF) and water and 0.1 M sodium perchlorate as a phase modifier. The separation was carried out in the isocratic mode using 45% THF and 55% water and a flow rate of 1 mL/min. To prevent crystallization of the inorganic phase modifier, the chromatographic system was rinsed thoroughly with water at the end of the day. This preventative measure extended the life of the chromatographic system, including the autosampler and the flow cell in the fluorescence detector. In the event the system was going to be idle for more than 3 days, it was stored in 50/50 methanol–water to prevent microbial growth within the system.

Quantitation. C_9 LAS and C_{15} LAS internal standards were used to accurately determine the concentration of LAS in the environmental samples. Each of the LAS homologues with an alkyl chain greater than six carbons possesses the same molar absorptivities, as well as the same fluorescence quantum efficiencies (16, 18). Thus, peak area ratios are directly proportional to the molar ratios of the various homologues. Each of the peak areas was corrected for differences in the molecular weight between the individual homologues and the internal standard. The molecular weight correction factor was simply derived by taking the ratio of the molecular weight (in the sodium salt form) of the

individual homologues (C_{10} – C_{14}) to that of the internal standard and multiplying the peak area of each homologue by the respective correction factor. This correction yields a mole to mole relationship between the individual homologues and the internal standard.

The peak areas associated with the C_{10} through C_{14} homologues were summed and the ratio of the total area was compared with that of the two internal standards. This ratio was then multiplied by the known concentration of the internal standard to yield the concentration of total LAS in the sample. The relative homologue distribution was obtained by simply ratioing the peak area of each individual homologue with that of the total peak area (excluding the internal standard).

RESULTS AND DISCUSSION

Solid-Phase Extraction. Solid-phase extraction (SPE) procedures are becoming increasingly popular for the extraction and isolation of a target compound from a complex matrix. SPE has proven to be quite versatile in terms of the range of resin polarities and functionalities available. Various investigators have used SPE procedures to isolate and preconcentrate surfactant-type compounds. In general, hydrophobic and ion exchange resins are used due to the hydrophobic and ionic nature inherent to many surfactants. The isolation and preconcentration schemes were divided into two distinct sections. The first step constitutes isolation based on hydrophobic character and the second based on the ionic nature of anionic surfactants.

The three hydrophobic resins examined were the C_{18} , C_8 , and C_2 stationary phases. Initial isolation experiments were conducted with radiolabeled (^{14}C) LAS. The use of radiolabeled tracers make initial isolation experiments very efficient and straightforward. With the quantity of ^{14}C LAS placed in the original sample known, the amount of LAS that resides in each step of the extraction procedure can be quantitatively measured. Thus, one can readily track the pathway of the analyte through the isolation scheme.

Although radiolabeled tracers provide a rapid and convenient means of developing an isolation scheme, it should be noted that confirmation of the efficiency of the procedure must also be demonstrated with nonlabeled analyte for each analytical method being developed. In the case of LAS, each of the hydrophobic resins showed a high level of analyte retention and subsequent recovery. However, upon analysis of the extract by HPLC with fluorescence detection, it was immediately recognized that both the C_{18} and C_8 resins had retained a high quantity of fluorescing interferences. These interferences eluted at the beginning of the chromatogram and in many cases overwhelmed the fluorescence signal originating from the desired LAS. Therefore, it is difficult to determine the quantity of interferences present by using radiolabeled tracers only.

Of the hydrophobic resins examined, the C_2 functional group yielded the best results in terms of specific isolation of LAS. Although the C_{18} and C_8 resins quantitatively retained the LAS in the sample, they also retained many of the hydrophobic materials (e.g. humic materials, alkylphenol ethoxylates, natural surfactants, etc.). These materials gave rise to a strongly fluorescing background signal, which interfered with the accurate measurement of low levels of LAS. The C_2 resin offered sufficient hydrophobic character to quantitatively retain the LAS, but allowed the more polar materials to pass through the resin. The result was an eluate that contained significantly lower levels of the interfering components, as compared to that obtained for the C_8 and C_{18} resins.

Strong anion exchange was used for the final clean up portion of the LAS isolation scheme. The ion exchange step was included in order to rid the C_2 eluate of various nonionic fluorescers which may have coeluted with LAS. Of these nonionic materials, alkylphenol ethoxylates have the highest

potential of interfering with the quantitation of LAS. This is due to the fact that alkylphenol ethoxylates exhibit similar spectral characteristics and, therefore, could potentially bias the quantitation of LAS high. A quaternary amine functional group was used for the ion exchange portion of the LAS isolation scheme. Matthijs et al. (15) used the SAX resin as the initial step in the cleanup procedure, followed by a hydrophobic resin for final isolation of the analyte. However, it was observed that upon using the SAX initially, many of the fluorescing interferences remained, even after repeated rinsings of the resin with solvents ranging from methanol to tetrahydrofuran to 2% acetic acid in methanol.

The conclusion drawn from this observation was that the interferences present in the environmental samples were ionic in nature and were strongly retained on the SAX resin. In addition, an induced hydrophobic retention mechanism resulting from the interaction of the hydrophobic portion of the interfering molecules with the alkyl chain of the ionically bound LAS may have contributed to the retention of the interferences. However, this type of retention mechanism was not considered to be the controlling factor, since nonpolar solvents, such as tetrahydrofuran, did not remove significant quantities of the interferences from the SAX resin.

On the basis of the retention mechanisms previously described, one would predict a similar end product, regardless of the order in which the SAX and C_2 resin are used. This, however, was not observed to be the case. The procedure which called for the C_2 resin to be placed first in the isolation scheme yielded a more interference-free chromatogram than did the reverse situation. This observation is not thoroughly understood; however, one could speculate that the high concentration of interfering compounds in the SAX eluate resulted in an overall change in hydrophobic character. The components providing interferences were likely converted from salts to acids by the highly acidic eluate and therefore were more hydrophobic and retained by the C_2 SPE resin. Apparently acidification of the original sample solution to a pH of 3–4 with glacial acetic acid was not acidic enough to provide this effect and therefore the interferences were not adsorbed on the C_2 SPE resin when the described sample preparation scheme was followed. The potential agglomeration or micellar formation of these naturally occurring materials, such as humic acids and lignin sulfonates, may have also resulted in a significantly more hydrophobic character. This, in effect, would hinder the elution of these materials off of the C_2 resin.

Chromatography. The most common procedure (12–17) for separating the homologous components of LAS by HPLC consists of using a C_{18} column and acetonitrile (or tetrahydrofuran) and water, with approximately 0.1 M of a counterion salt as the phase modifier. Both isocratic and gradient elution are used; the choice of which is dependent upon the pertinent experimental constraints. Shown in Figure 3A is a chromatogram of a C_{18} LAS standard obtained with a C_{18} (5 μm) column and acetonitrile and water. Each of the LAS homologues is partially separated into the respective isomer distribution. The major drawback of this approach is that only partial isomer separation is achievable with liquid chromatography, contrary to the total isomer separation attainable after desulfonation and capillary GC analysis. As a result, the chromatography was modified such that each of the isomer constituents, per homologue component, would elute as a single peak representing each LAS homologue. For example, the 1–5 phenyl isomers of C_{10} LAS will be represented as a single peak, etc. These conditions are contrary to the partial isomer separation achieved with the C_{18} column.

Shown in Figure 3B is a chromatogram of the LAS reference material obtained by using the C_1 column and isocratic elution with tetrahydrofuran and water (45:55) and a 0.05 M sodium

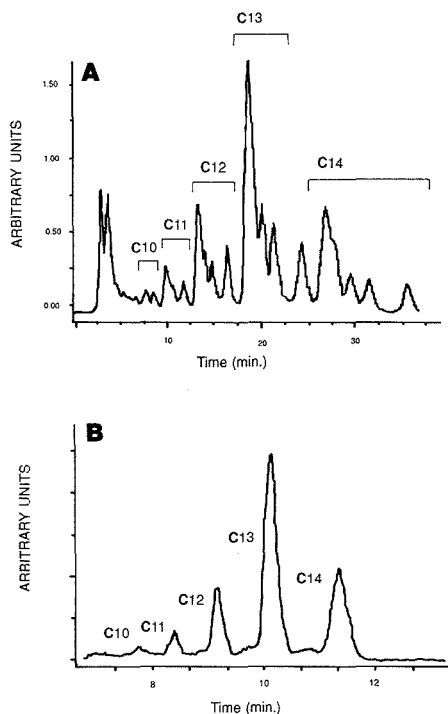


Figure 3. HPLC chromatograms of a standard mixture of LAS homologues. The average chain length is C_{13} : (A) gradient elution of LAS using a C_{18} (5 μ m), 25 cm column, with acetonitrile and water (gradient elution). (B) isocratic separation of LAS using a C_1 (5 μ m), 25 cm column, with tetrahydrofuran and water. Both were monitored with a fluorescence detector.

perchlorate modifier. The main advantages of coeluting all of the isomers into a single peak that represents a respective LAS homologue are 2-fold. The first is an improvement in detection limits. With the isomers of each homologue lumped into a single peak, the peak representing that homologue increases proportionally in intensity, thus increasing sensitivity of the method and providing a means of measuring lower concentrations of LAS. This is especially appreciated at the low concentrations that are encountered in environmental matrices.

The second advantage is one of simple interpretation and quantitation. By designing the chromatography such that each homologue of the LAS mixture is represented by a single peak, quantitation and interpretation of the chromatograms are greatly simplified. It was assumed that all of the isomers per homologue had the same fluorescent quantum yield. Samples of the individual isomers were not available to conduct a relative sensitivity study.

Quantitation and Detection. The quantity of LAS present in the various environmental samples was measured through use of internal standards. The two standards used were C_9 LAS and C_{15} LAS. These were chosen since they do not exist as components of environmental samples. Since LAS with alkyl chain lengths of greater than or equal to six carbons have the same molar absorptivities and fluorescence quantum efficiencies (16, 18), the peak area ratios of the measured LAS to that of the internal standards are directly proportional to the molar ratios of the LAS components. Thus, the average molecular weight and concentration of the LAS present in the

Table I. Accuracy of the Overall Isolation and Chromatographic Procedures for the Determination of LAS in Aqueous Environmental Matrices

sample	av background level, mg/L	spike levels, mg/L	no. of samples	av % recovery ^a
sewage influent	6.2	5.0/8.0	5	95 \pm 5
final effluent	0.066	0.15/0.60	5	85 \pm 6
water	0.025	0.02/0.050/0.20	9	81 \pm 10

^a Arithmetic mean \pm one standard deviation.

Table II. Precision of the Overall Isolation and Chromatographic Procedures for the Determination of LAS in Aqueous Environmental Matrices

sample	replicates	rel std deviation, ^a %
sewage influent	6	1.4
final effluent	6	4.6
river water	6	13.5

sample can be easily determined.

The detection level (LOD), based on a signal-to-noise ratio of 3 is approximately 1.5 ng per component injected on the column. This correlated with a detection limit of 2 ppb of the total LAS, derived from an initial sample volume of 200 mL, concentrated to 5 mL, of which 100 μ L is injected onto the column. Therefore, the limit of quantitation (LOQ), based on a signal-to-noise ratio of 10, was found to be 7–10 ppb.

The stated detection and quantitation levels are very much dependent on the level of interferences present in the original sample. Although the previously described cleanup procedures are effective in preferentially isolating LAS from environmental matrices, unknown components may still be present at levels that would interfere with the quantitation of LAS. In such case, the detection levels may increase. For very clean samples (e.g. groundwater) the detection levels may decrease to 1 ppb or less. Therefore, the 7–10 ppb level stated above is basically an average concentration which may vary depending on the level of interferences present in the sample.

Accuracy and Precision. The spike recoveries of the overall isolation and chromatographic procedures are listed in Table I. Nonlabeled LAS was added at the indicated concentrations to the individual samples of each matrix and analyzed, as described above, to determine the accuracy of the method. The average recovery for influents, effluents, and river waters was determined to be 95%, 85%, and 81%, respectively. The precision of the method is shown in Table II. Replicate analyses were performed on the same sample of each matrix to determine the precision of the method. The average relative standard deviation ($n = 6$) for influents, effluents, and river waters was found to be 1.4%, 4.6%, and 13.5%, respectively.

Application to Environmental Samples. The HPLC method described in this paper has been used to quantify the levels of LAS in various types of environmental samples, including sewage influent, final sewage treatment plant effluent, and the receiving river water. Shown in Figure 4 are typical chromatograms resulting from the isolation of LAS from sewage influent, effluent, and river water. The LAS contained in each sample, which was calculated from the C_9 LAS and C_{15} LAS internal standards, was determined to be 4.5, 0.08, and 0.01 pm, respectively. The average LAS chain length for the influent was 12.1 carbon units. The chain length for the effluent and river water shown in Figure 4 was determined to be 12.0 and 11.7 carbon units, respectively. Both

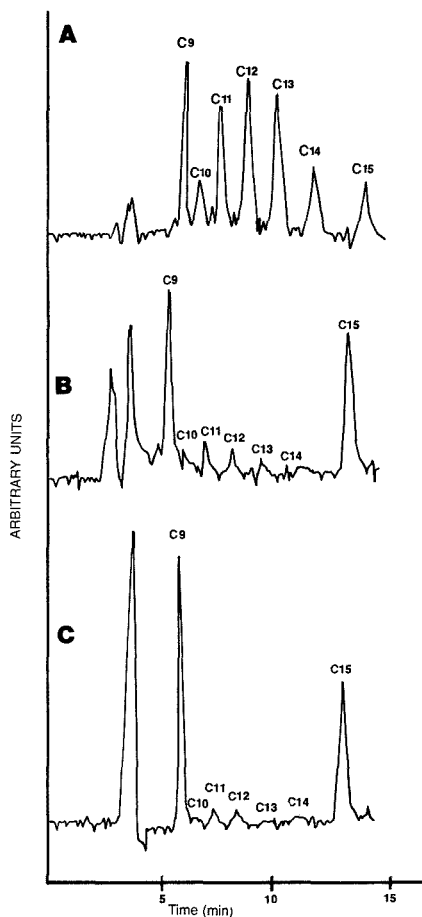


Figure 4. HPLC chromatograms of LAS isolated from various environmental matrices: (A) sewage influent, (B) final effluent, (C) receiving river water.

the measured and predicted levels of LAS found in these samples were consistent with the values previously reported for anionic surfactants (1, 3), in environmental matrices. The identification of LAS was based on the measured retention times and the homologue distribution pattern of LAS.

The LAS homologue distribution varies markedly between influents, effluents, and river waters due to both the sorption of LAS to particulate matter and biodegradation of LAS during sewage treatment and in the receiving river waters. The homologue distribution is considered a very important parameter in the study of the ecotoxicological effects of LAS on various aquatic species, due to the relationship between increased toxicity and increasing alkyl chain length (19). As a result, the accurate determination of the alkyl chain length of LAS in each of the environmental matrices was an absolute requirement of the HPLC method. Both spikes and replicates were run on a routine basis to ensure the accuracy and precision of the analysis were within the limits shown in Table I and Table II.

The major problem encountered with the measurement of LAS in environmental matrices was strongly fluorescing in-

terferences that coeluted with the C_9 LAS internal standard. The sewage treatment effluent samples were the most prone to these type of interferences, even though they are generally several times higher in LAS content than the river water samples. In cases where the interferences rendered the C_9 LAS internal standard useless, the quantitation was based on the C_{15} LAS internal standard. Since the C_{15} homologue is more hydrophobic in nature than the C_9 homologue, it elutes last within the homologous series and is free from the early eluting interferences. Therefore, in cases where interferences are present, quantitation based on the C_{15} LAS standard yields the more accurate result.

CONCLUSIONS

The analytical method that has been described has proven to be particularly useful for the measurement of the anionic surfactant LAS in a variety of aqueous environmental matrices. The reproducibility of the overall isolation and chromatographic procedures, expressed in terms of the relative standard deviation, was found to be 1.4% for sewage influents, 4.6% for sewage effluents, and 13.5% for river water samples taken below the outfall of a wastewater treatment facility. The average recovery of LAS from influents, effluents, and river waters was 95%, 85%, and 81%, respectively. The detection limits based on a signal-to-noise ratio of 3:1 is 1.5 ng per homologue injected on the column. This correlates with an average detection limit of approximately 2 ppb and a limit of quantitation of 7–10 ppb of total LAS concentrated from a 200-mL sample. Since the detection level is dependent on the quantity of interferences present, the 7–10 ppb level will vary depending on the nature of the sample.

The method offers several distinct advantages over other reported methods. First is the coelution of the isomers of each homologue in a single chromatographic peak. This not only simplifies the interpretation and quantitation of the chromatographic peaks but also enhances the sensitivity of the measurement by increasing the total quantity of analyte present in the detector flow cell in a specified elution volume. This attribute is of special significance at the low parts per billion concentration levels that are routinely encountered in environmental matrices.

The second enhancement over previously described methods is the isolation and preconcentration scheme. By use of the C_2 resin as the first step in the isolation procedure, preferential retention of LAS is obtained while the more polar constituents pass through the resin unretained. Although this procedure works well for the majority of environmental samples, there are certain samples, such as final effluents, that contain interfering components that are not removed by the C_2 resin. In such cases, the later eluting C_{15} LAS standard is used for quantitation purposes.

Although the only applications reported in this communication have been aqueous matrices, the general principles are directly applicable to the measurement of LAS extracted from such solid matrices as sludge, sediment, soil, etc. Several accounts of successful extraction procedures (e.g. Soxhlet, acid hydrolysis/ethyl ether liquid extraction, etc.) have been reported in the literature (5, 14–16). Thus, direct implementation of the described procedures would be relatively straightforward.

ACKNOWLEDGMENT

The authors acknowledge William A. Rorie of Industrial Testing Laboratories for his valuable input and constructive criticisms during the initial stages of the project.

Registry No. Water, 7732-18-5.

LITERATURE CITED

- (1) Swisher, R. D. *Surfactant Biodegradation*. 2nd ed.; Marcel Dekker: New York, 1987.

- (2) Hand, V. C.; Williams, G. K. *Environ. Sci. Technol.* **1987**, *21*, 370.
- (3) Rapaport, R. A. *Environ. Sci. Technol.* **1988**, *7*, 107.
- (4) Greenberg, A. E.; Conners, J. J.; Jenkins, D. *Standard Methods for the Examination of Water and Wastewater*, 16th ed.; American Public Health Association: Washington, DC, 1985; Section 512A.
- (5) Osburn, G. W. *J. Am. Oil Chem. Soc.* **1986**, *63*, 257.
- (6) Setzkn, E. A.; Carel, A. B. *J. Am. Oil Chem. Soc.* **1963**, *40*, 57.
- (7) Swisher, R. D. *J. Am. Oil Chem. Soc.* **1966**, *43*, 137.
- (8) Water, J.; Garrigan, J. T. *Water Res.* **1983**, *17*, 1549.
- (9) Lienado, R. A.; Neubecker, T. A. *Anal. Chem.* **1983**, *55*, 93R.
- (10) Non-nami, H.; Hamia, T. J. *J. Chromatogr.* **1978**, *161*, 205.
- (11) Kirkland, J. J. *Anal. Chem.* **1960**, *32*, 1389.
- (12) Nakae, A.; Tsuji, K.; Yamaunaka, M. *Anal. Chem.* **1980**, *52*, 2275.
- (13) Nakae, A.; Tsuji, K.; Yamaunaka, M. *Anal. Chem.* **1981**, *53*, 1818.
- (14) Linder, D. E.; Allen, M. C. *J. Am. Oil Chem. Soc.* **1982**, *59*, 152.
- (15) Matthijs, E.; De Henau, H. *Tenside Surfactants, Deterg.* **1987**, *24*(4), 193.
- (16) Kikuchi, M.; Tokai, A.; Yoshida, T. *Water Res.* **1986**, *20*(5), 643.
- (17) Marcomini, A.; Giger, W. *Anal. Chem.* **1987**, *59*, 1709.
- (18) Weber, W. J.; Morris, J. C.; Stumm, W. *Anal. Chem.* **1962**, *34*, 1844.
- (19) Kimmerle, R. A.; Swisher, R. D. *Water Res.* **1977**, *2*, 31.

RECEIVED for review February 9, 1989. Accepted August 8, 1989.

Retention Mechanisms of Reversed-Phase Liquid Chromatography: Determination of Solute-Solvent Interaction Free Energies

Peter T. Ying¹ and John G. Dorsey^{2*}

Department of Chemistry, University of Florida, Gainesville, Florida 32611

Ken A. Dill*

Departments of Pharmaceutical Chemistry and Pharmacy, University of California, San Francisco, California 94143

Mean-field statistical thermodynamics theory has recently been developed to account for the partitioning of solutes from aqueous mobile phases into reversed-phase liquid chromatography stationary phases. Several predictions are tested here against an extensive data base of nearly 350 sets of experiments. In agreement with theory, we find that (i) the dependence of retention on mobile phase composition can often be suitably linearized through use of a type of composition plot recently suggested by Dill, (ii) retention measurements can be used to determine the binary interaction constants of solutes with solvents, and (iii) ET-30 solvent probe experiments appear to provide a direct measure of the binary interaction constants. This work suggests that the simple random-mixing approximation for solutes with solvents is often useful even for complex chromatographic solutions.

INTRODUCTION

An important goal in separation science is to develop a quantitative understanding of the molecular mechanism of retention in reversed-phase liquid chromatography. This would not only permit prediction of retention and separation behavior from molecular structures, but also permit the development of chromatographic methods for the purpose of exact physicochemical measurements of properties of solutions and for the purpose of better understanding of interphases of chain molecules, including Langmuir-Blodgett films, micelles, and bilayer membranes.

Two different lattice statistical thermodynamic theories have recently been developed to account for retention and selectivity of solutes in reversed-phase liquid chromatography

(1, 2). It emerges from these theories that two driving forces dominate the retention process: (i) the difference in the chemistry of the contacts of the solute with its surrounding molecular neighbors in the stationary and mobile phase solvents, these contact forces are the same as those which drive the oil/water partitioning process, and (ii) the partial ordering of the grafted chains which leads to an entropic expulsion of solute relative to that which would be expected in a simpler amorphous oil phase/water partitioning process. Contribution ii appears only if the chains are grafted at sufficiently high surface densities. The more recent theory (2) provides a more satisfactory treatment of ii, but both approaches are similar in their accounting for i, the solution contact interactions. Here, we present a compilation of data from the literature to assess the adequacy of these treatments of i. Limitations of our data base prevent us from testing the effects of organization of the stationary phase ii. We assume that we can neglect ii for present purposes, since the two contributions are approximately independent, thus the free energy of ii is assumed simply additive to that of i. An experimental assessment of the treatment of ii is reported elsewhere (3). We conclude that these simple solution theories work well for a wide range of systems, but we also note the few weaknesses. In addition, we show that an experimental method developed earlier, using a solvatochromic dye molecule referred to as ET-30 (4), provides a measure of the fundamental binary interaction constants.

THEORY

The details of the theories have been presented elsewhere (1, 2, 5, 6). Here we present a summary of the lattice theories pertinent to the role of the contact interactions and the role of cavities in the mobile and stationary phases. The solute transfer process, from water to oil or from a mobile phase to a stationary phase is characterized by a change in the environment of the solute. In the mobile phase the solute, S, at infinite dilution is surrounded by neighboring molecules of water, solvent A, plus molecules of any organic modifier

¹ Present address: Wesley-Jessen, 400 West Superior St., Chicago, IL 60610.

² Present address: Department of Chemistry, University of Cincinnati, Cincinnati, OH 45221.

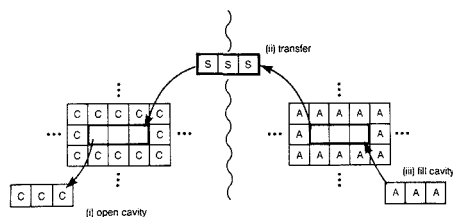


Figure 1. Partitioning process when solute molecule S is larger than solvents A and C.

present, solvent B. In the stationary phase, neglecting for the moment any penetrant solvent molecules, the solute, at high dilution, is surrounded by neighboring molecules of the grafted chain phase C. The difference in these contact interactions in the two different solvent environments is responsible for the oil/water partitioning driving force. These driving forces are described in terms of binary interaction constants, χ_{XY} (5-9). We briefly describe their meaning here.

The reversible work, w_{XY} , required to bring a spherical molecule X to within an average equilibrium separation r^* of spherical molecule Y in the gas phase, from an infinite separation, is the pair potential, $w_{XY} = u_{XY}(r^*)$. Of course, the oil/water partitioning process is not a gas-phase process characterized only by a pair potential; it occurs in the liquid state, where there are other neighboring molecules (see Figure 1). This process is comprised of three steps: (1) the opening of a cavity in solvent C, (2) the transfer from solvent A to solvent C, and (3) the closing of the cavity in solvent A. Each of these steps involves several pair interactions of the type described above. For many years, lattices have provided a simple tool for counting the average number of relevant contacts (7-9). The coordination number, z , is the number of neighbors of each molecule or of each lattice site ($z = 6$ for the simple cubic lattice, for example). Thus, when the solute is inserted into the cavity in C in the transfer step 2, it contributes zw_{SC} to the free energy. The cavity opening process leaves z sides, or $z/2$ contacts (pair of sides), without contact. Thus this contributes $(-z/2)w_{CC}$ to the free energy. The same reasoning shows that $(z/2)w_{AA}$ is contributed to the free energy from the closing of the cavity in A, step 3. Thus the total free energy change due to the contact interactions of the solute with solvents A and C is

$$\Delta F^\circ_{\text{transfer}} = z \left(w_{SC} - w_{SA} + \frac{w_{AA}}{2} - \frac{w_{CC}}{2} \right) \quad (1)$$

It is generally more convenient to express this free energy in terms of the binary interaction parameters, χ_{SC} and χ_{SA}

$$\Delta F^\circ_{\text{transfer}}/kT = \chi_{SC} - \chi_{SA} \quad (2)$$

where kT is Boltzmann's constant multiplied by the absolute temperature and

$$\chi_{XY} = \frac{z}{KT} \left(w_{XY} - \frac{w_{XX} + w_{YY}}{2} \right) \quad (3)$$

This treatment is premised on the assumption that the various solutions are randomly mixed: (i) that the solute, S, is randomly dispersed in solvent C, and (ii) that the solute and the mobile phase solvent molecules, A and B, are randomly distributed in the mobile phase solution. There are solute/mobile phase combinations for which the random-mixing approximation does not appear to hold (10, 11). In such cases, better approximations requiring additional parameters, such as the UNIFAC method (12), may be useful. Because of the assumption of rotational symmetry of the

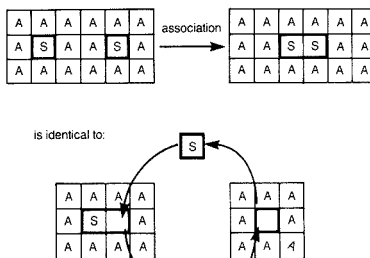


Figure 2. "Solvophobic" theory (10, 11) is based on an association rather than a partitioning process.

molecules and the neglect of the orientation dependence of hydrogen-bond interactions, this simple solution theory, if applied to water, methanol, and acetonitrile, the solvents of chromatographic interest, describes only effective and averaged interactions among those molecules. For that reason, additional considerations than those presented here would be required to account for temperature dependences of partitioning, for example.

A further approximation can be introduced, although we do not do so here. It is common to treat solution properties through use of the regular solution theory, and with the solubility parameters of Hildebrand (9). In this case, the binary interaction constant is further approximated as the geometric mean product of two unitary interaction constants, the solubility parameters

$$\chi_{xy} = \text{constant} (\delta_x - \delta_y)^2 \quad (4)$$

which are often derived from enthalpies of vaporization of the pure materials. Although the solubility parameter approach offers the advantage of requiring a smaller data base of constants, the predictions are often not particularly good unless interactions are principally due to dispersion forces (13). Nevertheless, solubility parameters have been widely used in various models of chromatographic retention (13-17).

It will be shown below that the chromatographic experiment can be used to obtain the binary interaction parameters. Inasmuch as these binary interaction constants should better characterize binary solutions than solubility parameters since they are not subject to the geometric mean approximation, we do not resort to this approximation here.

These binary interaction constants are useful by virtue of their widespread utility describing basic thermodynamic processes of solution. Thus, the oil/water partitioning process is given in terms of the equilibrium constant

$$\ln K_{C/A} = \frac{-\Delta F^\circ_{\text{transfer}}}{kT} = \chi_{SA} - \chi_{SC} = \frac{\mu^\circ_{SA} - \mu^\circ_{SC}}{kT} \quad (5)$$

Hence the basic thermodynamic process involved in chromatographic retention is (i) the creation of a cavity in the stationary phase, (ii) the transfer of solute into that cavity from the mobile phase, and (iii) the closing of the cavity in the mobile phase left behind by the solute. Martire and Jaroniec have shown that this lattice approach provides the microscopic underpinnings for the thermodynamic theory of Oscik (18).

A popular model for the chromatographic partitioning process has been that of the "solvophobic theory" (19, 20), which was modeled after the binary association process of two solute molecules in a single solvent, originally described by Sinanoglu (21, 22); see Figure 2. This association process involves (i) the creation of a cavity adjacent to a solute

molecule, (ii) the insertion of a second solute molecule next to the first, and then (iii) the closing of the cavity left behind by the associating solute molecule. The driving force for solute association in a single solvent is given by

$$\ln K_{\text{assoc}} = \ln \left(\frac{\chi_{\text{SS}}}{\chi_{\text{S}}^2} \right) = \left(\frac{2w_{\text{AS}} - w_{\text{SS}} - w_{\text{AA}}}{kT} \right) \quad (6)$$

The solute association process can be described partly in terms of the surface tension of the mobile phase

$$\gamma_{\text{A}} = -w_{\text{AA}}/2a \quad (7)$$

where a is the area per lattice contact.

Inasmuch as the formation of a cavity in the mobile phase is common to both solute association and partitioning processes, then the quantity w_{AA} , which can be characterized by the solvent surface tension, γ_{A} , will often correlate with certain properties of each process. Hence correlations between retention and solvent surface tension are readily observed (19, 20, 23, 24). Nevertheless, the surface tension of the solvent only characterizes the solvent cavity and does not provide a complete description of the partitioning process.

The solute association process is thus not an appropriate model for the partitioning process. The solute association process, eq 6, involves only the changing of the cavity size in a single solvent, whereas the transfer process, eq 5, involves the creation of a cavity in one solvent and the closing of a cavity in another. Hence the solvophobic theory considers the free energy costs of size changes of solute cavities in the mobile phase only and neglects effects of the stationary phase cavity, which are of fundamental importance for any partitioning process.

When the mobile phase is a mixed solvent of components A and B, distributed randomly with respect to each other, then the equilibrium constant is given as a simple quadratic function of the mobile phase composition (see for example eq 13a, ref 2)

$$\ln K_{\text{C/AB}} = (\chi_{\text{SA}} - \chi_{\text{SC}}) + \phi_{\text{B}}(\chi_{\text{SB}} - \chi_{\text{SA}} - \chi_{\text{AB}}) + \phi_{\text{B}}^2\chi_{\text{AB}} \quad (8)$$

where $0 \leq \phi_{\text{B}} \leq 1$ is the fraction of the mobile phase sites occupied by B molecules. It is clear that the quadratic term in this expression is due to interactions of the two mobile phase solvents, A (water) with B (organic modifier). This quadratic dependence has previously been shown by Schoenmakers and his colleagues using solubility parameter theory (13, 14, 16). Quadratic dependences may also be observed when solution behavior is dominated by long-range electrostatic interactions (25, 26). Also curvature in plots of $\ln k'$ vs ϕ_{B} may derive from insufficient end-capping of silanols, leaving substantial exposure (27, 28). This can result in a mixed adsorption/partition process for some solutes.

The quadratic form of eq 8 has previously suggested a useful form for plotting chromatographic data, which should linearize retention measurements as a function of mobile phase composition (2)

$$\left(\frac{1}{\phi_{\text{B}}} \right) \ln \left(\frac{k'}{k'_0} \right) = (\chi_{\text{SB}} - \chi_{\text{SA}} - \chi_{\text{AB}}) + \phi_{\text{B}}\chi_{\text{AB}} \quad (9)$$

where $k'_0 = k'(\phi_{\text{B}} \rightarrow 0)$.

This equation indicates that when the two mobile phase solvents are compatible with each other (χ_{AB} small), as for methanol and water, a plot of $\ln k'$ vs ϕ_{B} should be linear, or $(1/\phi_{\text{B}}) \ln(k'/k'_0)$ vs ϕ_{B} should be constant. When the mobile phases are less compatible with each other (χ_{AB} large), then $\ln k'$ will be a quadratic function of ϕ_{B} and $(1/\phi_{\text{B}}) \ln(k'/k'_0)$ will depend linearly on ϕ_{B} . Linear and quadratic dependences of $\ln k'$ on ϕ_{B} for methanol/water and acetonitrile/water

mixtures have been observed (2, 12, 16, 29, 30).

It is clear from Figure 1 that if the solute molecules are larger than molecules of solvents A and C, a case not considered in the earlier theory (2), then the transfer process would now be described approximately by

$$\left(\frac{1}{\phi_{\text{B}}} \right) \ln \left(\frac{k'}{k'_0} \right) = (\chi_{\text{SB}} - \chi_{\text{SA}} - \chi_{\text{AB}}) + n\phi_{\text{B}}\chi_{\text{AB}} \quad (10)$$

(with z replaced with $z - 2$ in eq 3 and neglecting small end effects). Here n is the ratio of the size of a solute molecule to the size of a molecule of either solvent, A or B, presumed to be of equal size. For typical solvent mixtures, of water with methanol or acetonitrile, this equal-size approximation is probably the best assumption currently possible consistent with the simplicity of the lattice treatment and the requirement of a minimum number of adjustable parameters. Of course, if the two solvents were of considerably different size, then Flory-Huggins treatment is more appropriate. However, for the typical chromatographic cosolvents of interest here, which differ by a factor of only 2 or 3, then Flory-Huggins offers no improvement, and merely introduces extra parameters (the ratio of solvent sizes and a lattice-dependent rotational partition function) which are of questionable value for size disparities this small. On other grounds as well, the distinction between equal-volume and Flory-Huggins assumptions for the mobile phase solvents in unwarranted, since differences between these assumptions are considerably smaller than more important inherent errors in both lattice methods, due to the neglect of solvent orientation, the mean-field and random mixing approximations, and effects of solvent association, for example. Hence for the problem at hand for which mean-field lattice theories are currently used, the equal-volume approximation made here is as good as any other. Also

$$\ln k'_0 = \ln \Phi \langle q \rangle + n(\chi_{\text{SA}} - \chi_{\text{SC}}) \quad (11)$$

where Φ is the volume phase ratio (stationary/mobile) and $\langle q \rangle$ accounts for the change in conformational entropy of the constrained chains upon uptake of the solute (2, 5). This expression follows since the number of contacts of solute with solvents, and the sizes of the cavities all scale directly in proportion to the size of the solute molecule. Hence, for a plot of

$$\left(\frac{1}{\phi_{\text{B}}} \right) \ln \left(\frac{k'}{k'_0} \right)$$

vs ϕ_{B} , we have

$$\text{slope} = n\chi_{\text{AB}} \quad (11a)$$

$$\text{intercept at } (\phi_{\text{B}} = 1) = n(\chi_{\text{SB}} - \chi_{\text{SA}}) \quad (11b)$$

$$\text{intercept at } (\phi_{\text{B}} = 0) = n(\chi_{\text{SB}} - \chi_{\text{SA}} - \chi_{\text{AB}}) \quad (11c)$$

For a plot of $\ln k'$ vs ϕ_{B} the intercept at $\phi_{\text{B}} = 0$

$$\text{should equal } \ln \Phi \langle q \rangle + n(\chi_{\text{SA}} - \chi_{\text{SC}}) \quad (11d)$$

In agreement with these predictions, a linear dependence of $\ln k'$ on surface area or van der Waals volume of the solute molecule, and hence on the size of the cavity, has been widely observed (19, 20, 23, 24, 31-34). It is these eq 10 and 11 which we further test here against experimental data bases.

The factor k'_0 in eq 9-11 contains the entire stationary phase contribution to retention. This follows from (i) the separability of the free energy contributions due to the contact and chain ordering interactions, which is a central assumption of the lattice theories, and (ii) the simplest implementation of the lattice theory here, according to which penetration of either solvent, A or B, into the stationary phase is assumed

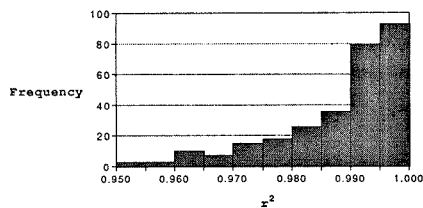


Figure 3. Histogram of coefficient of determination, r^2 , for the plots of $1/\phi_B \ln(k'/k'_0)$ vs ϕ_B for all the data sets.

to be a second-order contribution to partitioning (2). Such effects do exist (11, 35), and can be readily taken into account in the lattice theories. The principal result of solvent penetration would be effectively concentration dependent χ 's, leading to nonlinear composition plots. In contrast, since we generally observe linear composition plots (see below), then it is justified to assume these effects are small. Moreover, there is good reason that they should be small. The magnitude of any errors are limited by thermodynamic driving forces. Cosolvent B can only become increasingly concentrated in the stationary phase as it increases its compatibility with the stationary phase, but this immediately implies that the stationary-phase environment for the solute becomes increasingly similar to the pure stationary phase with changes in the chemistry of B. In other words, consider two cases: (i) If the mobile phase modifier is chemically very different than the stationary phase, then it will not partition and will not much affect the chemical potential of the solute probe in the stationary phase. On the other hand (ii) if the mobile phase modifier is chemically very similar to the stationary phase, then it will partition, but it will be so similar to the stationary phase that it will also not much affect the chemical potential of the solute probe in the stationary phase. Thus over the full range of possible mobile phase cosolvents, the chemical potential of the solute in the stationary phase should be affected to only a relatively small degree by the cosolvent. Evidence presented elsewhere (2) shows that the free energies obtained chromatographically according to eq 8-11 are in close agreement with data taken independently from partitioning experiments.

EXPERIMENTAL DATA BASE

Here we test these predictions with a large data base we have previously used for correlations of solvatochromic solvent polarity measurements with reversed phase retention (4). The data base is used here in its entirety, with the omission of six data sets which had retention values at only three mobile phase compositions. Additional data sets generated in this laboratory (36) with ethanol-water and propanol-water mobile phases are also included.

Linear regression calculations were performed by using the program CURVE FITTER (Interactive Microwave, State College, PA) on an Apple II Plus 48K microcomputer. The program was used to calculate the coefficient of correlation of the data and was modified to allow calculation of confidence intervals for the slope and intercept values. This program was also used to extrapolate k' to the composition of pure water, denoted k'_0 herein. This value is seldom reported in the literature as it is not easily experimentally determined. We extrapolated plots of $\log k'$ vs $E_T(30)$ polarity to the polarity value of 100% water to obtain the values used here. This method has been shown to give accurate k'_0 values, as the value calculated for a given solute is self-consistent among methanol-water, ethanol-water, and acetonitrile-water mobile phases (37). F values were obtained from the program STATWORKS (Heydon & Sons, Inc., Philadelphia, PA) on an Apple Macintosh SE computer.

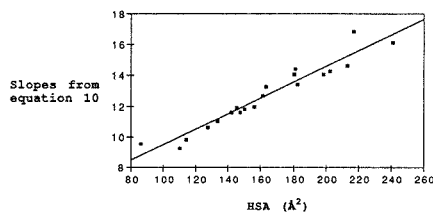


Figure 4. Plot of slopes from eq 10 vs hydrocarbonaceous surface area (HSA) for the Separylite C-18 column with acetonitrile as modifier (see eq 12 and 13).

RESULTS AND DISCUSSION

The extensive data base presented here permits certain tests of the cavity contributions to the retention theory described above. Figure 3 shows a histogram of the coefficient of determination, r^2 , for the plots of $(1/\phi_B) \ln k'/k'_0$ vs ϕ_B for the 346 data sets tested here. From the figure, it is clear that this plot provides a linear representation of the experimental data. More than 80% of the data sets are found to have r^2 values of 0.9 or higher and almost 50% with r^2 of 0.99 and higher. An F value, which is used to compare the significance level of fitting the data to a quadratic model, is calculated and expressed as α in Table I for all data sets. The quadratic model fit the data significantly better (at the 90% confidence level) in 148 out of 346 sets. Table I (available as supplementary material) presents an extensive compilation of the results of plotting data in this form, for a wide range of solutes and stationary phases, for principally acetonitrile/water and methanol/water mixtures. From the correlation coefficients shown, it is clear that, with a small number of exceptions, the degree of linearity of this type of plot is extremely good. The principal exception is the Separylite C2 column, with methanol as mobile-phase modifier, for which r^2 varies from 0.4660 to 0.9162, with an average value of 0.7287. These poor correlations may be because for these short-chain phases, adsorption is expected to be the dominant retention mechanism rather than partitioning, treated above. Another possibility is that non-end-capped silanols may contribute more significantly for these short-chain phases than for longer chains. Where linearity is found to be good, it implies that the random-mixing approximation is valid. This linearity is expected to be limited to the intermediate compositions explored here; the random-mixing approximation is not expected to be generally viable in the limits of extreme composition (16), less than a few percent of either mobile phase component. In those cases, solutes or the minor component of the mobile phase may associate to form nonrandom mixtures. It is also important to note that if the range of compositions measured involves less than a 10-fold change in concentrations, as is generally the case here, then small amounts of curvature can readily go undetected within the experimental errors of these plots.

According to eq 10, the slope of the line of this composition plot equals the binary interaction constant characterizing the pair interaction between molecules of the A and B solvents, multiplied by the size of the cavity occupied by the solute. Tests of this prediction of the cavity-size dependence are shown in Figure 4. The slopes of the composition plots are found to be linear with increasing cavity size. That is

$$\text{slope of } \left(\frac{1}{\phi_B} \ln \frac{k'}{k'_0} \right) \text{ vs } \phi_B = n\chi_{AB} \quad (12)$$

$$\partial \text{slope} / \partial n = \chi_{AB} \quad (13)$$

It is the derivative in eq 13 that is represented in Tables II and III, i.e., χ_{AB} . Because the range of solute sizes is limited, this linearity is observed when cavity "size" is either the cavity

Table II. Linear Regression Results of Slope from Equation 10 vs van der Waals Volume (V_w)

column	modifier	slope ($\times 10^3$)	r^2
Sepralyte C-2	acetonitrile	16.51	0.9561
Sepralyte C-4	acetonitrile	16.61	0.9263
Sepralyte C-8	acetonitrile	7.817	0.7897
Sepralyte C-18	acetonitrile	9.582	0.9164
Sepralyte C-4	methanol	7.286	0.9189
Sepralyte C-8	methanol	6.228	0.9305
Hypersil ODS	acetonitrile	12.78	0.5499
Unisil Q C-18	acetonitrile	8.640	0.4106
Ultrasphere ODS	methanol	10.33	0.9977
Ultrasphere ODS	ethanol	5.948	0.2490
Ultrasphere ODS	1-propanol	4.662	0.0495
Ultrasphere ODS	acetonitrile	18.57	0.8091
Silasorb C-8	methanol	3.051	0.2339
Silasorb C-8	acetonitrile	2.595	0.2083

Table III. Linear Regression Results of Slope from Equation 10 vs Hydrocarbonaceous Surface Area (HSA)

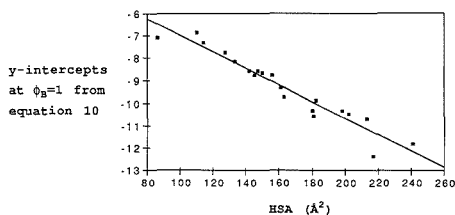
column	modifier	slope ($\times 10^2$)	r^2
Sepralyte C-2	acetonitrile	8.511	0.9642
Sepralyte C-4	acetonitrile	8.785	0.9465
Sepralyte C-8	acetonitrile	4.115	0.8226
Sepralyte C-18	acetonitrile	5.099	0.9280
Sepralyte C-4	methanol	3.817	0.9068
Sepralyte C-8	methanol	3.358	0.9520

volume (slopes in Table II) or cavity area, as measured by the accessible surface area of the solute molecule (Figure 4; slopes in Table III). (Note that the χ values will have different units depending on whether cavity size is taken to be that of volume or area). This linearity is found to be generally good; with the r^2 values for many of these plots found to be better than 0.9. This linearity implies that the slopes of the composition plot are proportional to the size of the cavity occupied by the solute. The slope of Figure 4 represents the contact-free energy of the solvent A with B per unit area of the cavity. For the Sepralyte C18 column, shown in Figure 4 and Table III, the quantity χ_{AB} is found to equal

$$(5.099 \times 10^{-2})kT = (5.099 \times 10^{-2})(592 \text{ cal/mol}) = 30.2 \text{ cal/(mol } \text{Å}^2) \quad (14)$$

for these data taken at ca. 25 °C.

Several column/mobile phase combinations gave poor correlations for the slope of eq 9 vs van der Waals volume. For the Hypersil/acetonitrile case, most of the solutes were nitrogenous compounds such as aniline, pyridine, and amino-substituted PAH's. Their retention is most likely a mixed partition/adsorption process, and would not be expected to fit the theory tested here. The Unisil Q C-18 data include many isomers of substituted benzene. The van der Waals volumes for geometric isomers are identical, yet they give different slopes for eq 9. The failure of the correlations shown in Table II is likely a manifestation of this calculational anomaly for the van der Waals volume, rather than a breakdown of the retention theory. It has been previously shown that isomeric alkylbenzenes give relatively poor correlation with van der Waals volume (43, 44). The poor correlations for the ethanol and propanol data on the Ultrasphere ODS column may be due to the changing stationary phase environment as these more hydrophobic modifiers are used in the mobile phase. Theory has yet to account for the uptake of solvent by the stationary phase chains. We have recently shown that propanol appears to saturate the stationary phase at a very low mobile phase percentage of propanol (37). We cannot yet account for the poor correlations with the Silasorb data.

**Figure 5.** Plot of y intercepts at $\phi_B = 1$ from eq 10 vs hydrocarbonaceous surface area (HSA) for the Sepralyte C-18 column with acetonitrile as modifier (see eq 15 and 16).**Table IV. Linear Regression Results of y Intercept at $\phi_B = 1$ from Equation 10 vs van der Waals Volume (V_w)**

column	modifier	slope ($\times 10^2$)	r^2
Sepralyte C-2	acetonitrile	-8.523	0.9542
Sepralyte C-4	acetonitrile	-7.484	0.9344
Sepralyte C-8	acetonitrile	-9.793	0.9112
Sepralyte C-18	acetonitrile	-6.936	0.9178
Sepralyte C-4	methanol	-12.73	0.9489
Sepralyte C-8	methanol	-12.17	0.9136
Hypersil ODS	acetonitrile	-377.2	0.7089
Unisil Q C-18	acetonitrile	-109.0	0.5035
Ultrasphere ODS	methanol	-22.23	0.9993
Ultrasphere ODS	ethanol	10.96	0.2696
Ultrasphere ODS	1-propanol	95.35	0.1945
Ultrasphere ODS	acetonitrile	-345.8	0.5705
Silasorb C-8	methanol	721.2	0.2434
Silasorb C-8	acetonitrile	629.9	0.2139

Table V. Linear Regression Results of y Intercept at $\phi_B = 1$ from Equation 10 vs Hydrocarbonaceous Surface Area (HSA)

column	modifier	slope ($\times 10^2$)	r^2
Sepralyte C-2	acetonitrile	-4.383	0.9658
Sepralyte C-4	acetonitrile	-3.957	0.9389
Sepralyte C-8	acetonitrile	-5.118	0.9052
Sepralyte C-18	acetonitrile	-3.689	0.9282
Sepralyte C-4	methanol	-6.752	0.9460
Sepralyte C-8	methanol	-6.378	0.9489

The theory predicts that the intercepts (at $\phi_B = 1$) of these composition plots equal the free energy of transfer of the solute between pure A and B solvents, multiplied by the cavity size, i.e.

$$\text{intercept of } \left\{ \frac{1}{\phi_B} \ln \frac{k'}{k'_0} \right\} \text{ vs } \phi_B \text{ at } (\phi_B = 1) = n(\chi_{SB} - \chi_{SA}) \quad (15)$$

We have determined these intercepts as a function of cavity volume and cavity area (Figure 5). Figure 5 shows a typical case, the Sepralyte C18 column, with acetonitrile as the organic modifier (B) of the water solvent (A). These intercepts of the composition plots are found to increase linearly with cavity size (either volume or area), as expected from the theory; the correlation coefficients are generally greater than 0.9 (see Tables IV and V) with the exceptions noted above. The value of

$$\partial \text{intercept} / \partial n = \chi_{SB} - \chi_{SA} \quad (16)$$

is obtained from Figure 5 (and Table V) as

$$\chi_{SB} - \chi_{SA} = -(3.689 \times 10^{-2})(592 \text{ cal/mol}) = -21.8 \text{ cal/(mol } \text{Å}^2) \quad (17)$$

and is approximately constant. This test confirms the pre-

Table VI. Linear Regression Results of $\log k'_0$ vs Number of Methylene Units of the Alkylbenzene Homologue

column	modifier	slope	r^2
Sepralyte C-2	acetonitrile	0.5598	0.9996
Sepralyte C-4	acetonitrile	0.6719	0.9923
Sepralyte C-8	acetonitrile	0.6404	0.9725
Sepralyte C-18	acetonitrile	0.5493	0.9999
Sepralyte C-2	methanol	0.6419	0.9936
Sepralyte C-4	methanol	0.8205	0.9912
Sepralyte C-8	methanol	0.7348	0.9992

Table VII. Linear Regression Results of $\log k'_0$ vs Number of Phenyl Units of the Homologue Benzene, Naphthalene, and Anthracene

column	modifier	slope	r^2
Sepralyte C-2	acetonitrile	1.175	0.9999
Sepralyte C-4	acetonitrile	1.120	0.9997
Sepralyte C-8	acetonitrile	1.300	0.9794
Sepralyte C-18	acetonitrile	1.044	0.9997
Sepralyte C-2	methanol	1.307	0.9998
Sepralyte C-4	methanol	1.415	0.9963

dicted dependence on cavity size and suggests that this is a convenient way to experimentally determine binary interaction constants.

Two other principal tests of these composition plots are shown through comparison of different parts of Table I. First, the slope of the composition plot (eq 12) divided by n (see eq 13) should equal χ_{AB} and be independent of the nature of both the solute and the stationary phase and dependent on the nature of the organic modifier in the mobile phase.

In agreement with this prediction, we observe that the slopes are independent of solute and dependent on the organic modifier. However, the slopes differ by about a factor of 2 for short-chain stationary phases in comparison with long-chain stationary phases. This variation may be due to two factors: (i) surface silanols may be more exposed in the short-chain phases; their interactions with the solutes are not taken into account here, and/or (ii) the retention mechanism for short-chain phases should be dominated by adsorption, rather than partitioning (2); this factor is also neglected here. These factors can be readily taken into account in the lattice partitioning theories (2). It should be noted that this observed difference could not be accounted for if the retention mechanism were based on an association process, such as that envisioned in the solvophobic theory.

Second, the intercepts of the composition plot (at $\phi_B = 1$) (see eq 15) divided by n (eq 16) should be dependent on solute and organic modifier and independent of the stationary phase. This is confirmed by the data summarized in Table IV. The large differences in column 3 of that table are seen to be principally due to differences in solutes rather than differences in stationary phases.

The intercept (at $\phi_B = 0$) of $\ln k'$ equals $\ln k'_0$ given by eq 11, which represents the free energy of transfer of solute between pure A solvent (water) and the stationary phase, multiplied by the cavity size, added to a term which includes the phase ratio and multiplied by a factor due to the chain organization, (q). The chain conformational factor (q) will also depend on n , but detailed theory for this dependence is not yet available. In accord with the theory, this intercept is observed to be linearly dependent upon the number of methylene groups in a series of alkylbenzenes. Different cases of this linearity are given in Table VI for different stationary phases and organic modifiers. This linearity also holds for a homologous series of molecules of different numbers of phenyl units; see Table VII.

Table VIII. Linear Regression Results of Slopes from Equation 10 vs Slopes from $E_T(30)$ Plots

column	modifier	slope ($\times 10^2$)	r^2
Sepralyte C-2	acetonitrile	3.238	0.9996
Sepralyte C-4	acetonitrile	2.699	0.9909
Sepralyte C-8	acetonitrile	5.396	0.8796
Sepralyte C-18	acetonitrile	4.047	0.9997
Sepralyte C-2	methanol	14.67	0.9966
Sepralyte C-4	methanol	9.315	0.9820
Sepralyte C-8	methanol	11.03	0.9955
Silasorb C-8	methanol	7.342	0.8369
Silasorb C-8	acetonitrile	5.137	0.9987
Unisil Q C-18	acetonitrile	4.913	0.9303
Hypersil ODS	acetonitrile	3.671	0.9187
Ultrasphere ODS	methanol	8.055	0.9997
Ultrasphere ODS	ethanol	6.166	0.8827
Ultrasphere ODS	1-propanol	2.467	0.2630
Ultrasphere ODS	acetonitrile	4.066	0.8702

As the solute surface area approaches zero, Figures 4 and 5 show that the transfer-free energy does not equal zero. These should not be expected to equal zero, however, because solution processes cannot be meaningfully extrapolated to zero cavity size. Minimum sizes of cavities are dictated by the packing problems of molecules. This is reflected in nonzero intercepts generally observed for partition coefficients of homologous series' of solutes.

We have previously shown that a solvatochromic dye molecule, referred to as ET-30, can be used to probe the chemical nature of the mobile phase and measure its strength (4). Plots of $\ln k'$ vs $E_T(30)$ polarity are generally found to be better descriptors of retention than commonly used plots of $\ln k'$ vs percent organic modifier (4). The reason for the utility of this dye is that for water and the organic modifiers studied here it appears to provide a direct measure of the free energy of transfer of the solute between solvents A and B. The visible spectral shift of the dye is linearly proportional to the binary interaction parameter, χ_{AB} .

For the Sepralyte C18 column with acetonitrile as organic modifier, this slope is observed to be $(4.047 \times 10^{-2}) \times (592) = 23.96$ units/(cal mol). We observe the same linearity on other stationary phases and with other organic modifiers; see Table VIII. While perhaps only a convenient covariance, this may represent a simple, direct way to measure binary interaction parameters.

Extensive as it is, our data base is nevertheless limited to the middle solvent composition ranges and therefore cannot provide a full test of the theory at the extremes. Severe practical experimental limitations prohibit a given experiment from covering a much wider range than those we report here, of 30–50% variation in solvent composition. Moreover, these mid-ranges are of much greater experimental interest for practical chromatography, for whatever reasons, and this undoubtedly accounts for the abundance of data in that range. In any case, the data for testing these extremes are simply largely unavailable. It clearly would be desirable to have more experimental data in these extremes of solvent compositions in order to better explore the limitations of theory and the random-mixing approximation.

Since most of the intrinsic weaknesses of the theory should be reflected in nonlinearities in the composition plot, we find it surprising that linearity holds as often as it does. When nonlinearity is observed in the composition plot, it is a sign that the theoretical premises have failed. When linearity is observed, then the various slopes and intercepts described here of these composition plots will reflect, at least approximately, the free energies of binary interactions of solutes and solvents.

Supplementary Material Available: Linear regression results of eq 9 and results of slopes and intercepts (17 pages).

Photocopies of the supplementary material from this paper or microfiche (105 × 148 mm, 24× reduction, negatives) may be obtained from Microforms & Back Issues Office, American Chemical Society, 1155 16th Street, NW, Washington, DC 20036. Orders must state whether for photocopy or microfiche and give complete title of article, names of authors, journal issue date, and page numbers. Prepayment, check or money order for \$31.00 for photocopy (\$33.00 foreign) or \$10.00 for microfiche (\$11.00 foreign), is required and prices are subject to change.

LITERATURE CITED

- (1) Martire, D. E.; Boehm, R. E. *J. Phys. Chem.* **1983**, *87*, 1045.
- (2) Dill, K. A. *J. Phys. Chem.* **1987**, *91*, 1980.
- (3) Santell, K. B.; Dorsey, J. G. *Anal. Chem.* **1989**, *61*, 930.
- (4) Johnson, B. P.; Khaledi, M. G.; Dorsey, J. G. *Anal. Chem.* **1986**, *58*, 2354.
- (5) Marqusee, J. A.; Dill, K. A. *J. Chem. Phys.* **1986**, *85*, 434.
- (6) Dorsey, J. G.; Dill, K. A. *Chem. Rev.* **1989**, *89*, 331.
- (7) Hill, T. L. *Introduction to Statistical Thermodynamics*; Addison-Wesley: Reading, MA, 1960.
- (8) Flory, P. J. *Principles of Polymer Chemistry*; Cornell University: Ithaca, NY, 1953.
- (9) Hildebrand, J. H.; Scott, R. L. *The Solubility of Nonelectrolytes*; Reinhold: New York, 1950.
- (10) Lochmuller, C. H.; Hamzavi-Abedi, M. A.; Ou, C.-X. *J. Chromatogr.* **1987**, *387*, 105.
- (11) Gilpin, R. K.; Gangoda, M. E. *J. Chromatogr. Sci.* **1983**, *21*, 352.
- (12) Petrovic, S. M.; Lomic, S.; Sefer, I. *J. Chromatogr.* **1985**, *348*, 49.
- (13) Schoenmakers, P. J.; Billiet, H. A. H.; Tijssen, R.; de Galan, L. *J. Chromatogr.* **1978**, *149*, 519.
- (14) Schoenmakers, P. J.; Billiet, H. A. H.; de Galan, L. *Chromatographia* **1982**, *15*, 205.
- (15) Tijssen, R.; Billiet, H. A. H.; Schoenmakers, P. J. *J. Chromatogr.* **1976**, *122*, 185.
- (16) Schoenmakers, P. J.; Billiet, H. A. H.; de Galan, L. *J. Chromatogr.* **1983**, *282*, 107.
- (17) Karger, B. L.; Snyder, L. R.; Eon, C. *Anal. Chem.* **1978**, *50*, 2126.
- (18) Martire, D. E.; Jaroniec, M. *J. Liq. Chromatogr.* **1985**, *8*, 1363.
- (19) Horvath, C.; Melander, W.; Molnar, I. *J. Chromatogr.* **1976**, *125*, 129.
- (20) Melander, W. R.; Horvath, C. In *High Performance Liquid Chromatography: Advances and Perspectives*; Horvath, C., Ed.; Academic Press: New York, 1980; Vol. 2.
- (21) Sinanoglu, O. In *Advances in Chemical Physics*; Hirschfelder, J. O., Ed.; Wiley: New York, 1967; Vol. 12, p 283.
- (22) Sinanoglu, O. In *Molecular Associations in Biology*; Pullman, B., Ed.; Academic Press: New York, 1968; p 427.
- (23) Kaliszan, R. *J. Chromatogr. Sci.* **1984**, *22*, 362.
- (24) Hammers, W. E.; Meurs, G. J.; DeLigny, C. L. *J. Chromatogr.* **1982**, *246*, 169.
- (25) El Tayar, N.; Van de Waterbeemd, H.; Testa, B. *J. Chromatogr.* **1985**, *320*, 293.
- (26) Borowko, M.; Jaroniec, M.; Piotrowska, J. *J. Liq. Chromatogr.* **1987**, *10*, 2033.
- (27) Nahum, A.; Horvath, C. *J. Chromatogr.* **1981**, *203*, 53.
- (28) Bij, K. E.; Horvath, C.; Melander, W. R.; Nahum, A. *J. Chromatogr.* **1981**, *203*, 65.
- (29) Raymond, D.; Chung, G. N.; Mayer, J. M.; Testa, B. *J. Chromatogr.* **1987**, *391*, 97.
- (30) Pekic, B.; Petrovic, S. M.; Slavica, B. *J. Chromatogr.* **1983**, *268*, 237.
- (31) Funasaki, N.; Hada, S.; Neya, S. *J. Chromatogr.* **1986**, *361*, 33.
- (32) Arai, Y.; Hirukawa, M.; Hanai, T. *J. Chromatogr.* **1987**, *384*, 279.
- (33) Kaliszan, R. *CRC Crit. Rev. Anal. Chem.* **1986**, *16*, 323.
- (34) Mockel, H. J.; Welter, G.; Meizer, H. *J. Chromatogr.* **1987**, *388*, 255.
- (35) McCormick, R. M.; Karger, B. L. *Anal. Chem.* **1980**, *52*, 2249.
- (36) Michels, J. J.; Dorsey, J. G., unpublished work.
- (37) Michels, J. J.; Dorsey, J. G. *J. Chromatogr.* **1988**, *457*, 85-98.
- (38) Woodburn, K. B. Doctoral Thesis, University of Florida, 1985.
- (39) Jandera, P. *Chromatographia* **1985**, *19*, 101.
- (40) Hanai, T.; Hubert, J. *HRC CC, J. High Resolut. Chromatogr. Commun.* **1983**, *6*, 20.
- (41) Johnson, B. P. Doctoral Thesis, University of Florida, 1986.
- (42) Lipford, L. C. M.S. Thesis, University of Florida, 1985.
- (43) Smith, R. M. *J. Chromatogr.* **1987**, *209*, 1.
- (44) Jinno, K.; Kawasaki, K. *Chromatographia* **1983**, *17*, 337.

RECEIVED for review March 20, 1989. Revised manuscript received August 29, 1989. Accepted August 29, 1989. The authors are grateful for support of this work by NIH GM-33382. K.A.D. is also grateful to the PEW Scholars Foundation for support.

Laser-Enhanced Ionization as a Diagnostic Tool in Laser-Generated Plumes

Ho-ming Pang and Edward S. Yeung*

Ames Laboratory—USDOE and Department of Chemistry, Iowa State University, Ames, Iowa 50011

Laser-enhanced ionization can be used to generate ions in the laser microprobe when the vaporization wavelength is tuned in resonance with the analyte absorption band. A 70-fold enhancement of the ion intensity has been observed. Abnormal spectral band broadening and absorption peak shift are found. In order to correct for pulse-to-pulse variations in the formation of the laser plasma, the acoustic wave generated from the laser plume in He was used as the internal standard to monitor the total amount of material vaporized during each pulse. Linear correlation between the acoustic wave and the ion signal at different laser energies and focusing conditions has been obtained.

INTRODUCTION

The laser microprobe technique is an important solid sample introduction method in atomic spectroscopy (1-3) and mass spectrometry (4-6). With the use of different power and wavelength conditions, neutral particles (such as atoms, clusters, and molecules) and ions can be generated in the laser plasma. However, laser microprobe analysis still remains a

qualitative or semiquantitative method (3, 7) due to the uncertainties arising from the laser power fluctuations, matrix effects, surface conditions, and focusing conditions. Since the amount of material produced by the laser vaporization process depends on the pulse-to-pulse laser power stability (most modern pulsed lasers provide <5% fluctuation), a large error can still be obtained by normalizing the amount of material evaporated to the laser power (8, 9). The matrix effects (7, 10-12) caused by the different physical and chemical properties provide different environments for the vaporization process in which different temperatures and excitation processes can occur. In addition, the local power density resulting from different focusing conditions and incidence angles is difficult to control and measure. Although there are several methods to improve the precision of laser microprobe analysis, such as signal averaging (3), crater size measurement (13), standard materials calibrations (14), etc., each one has its own limitations.

One of the natural phenomena of the laser-generated plume is the plasma expansion process. When this plasma is generated in an inert gas environment, collisions between the evaporated particles and the inert gas molecules will create acoustic waves. Since this acoustic signal is correlated to the

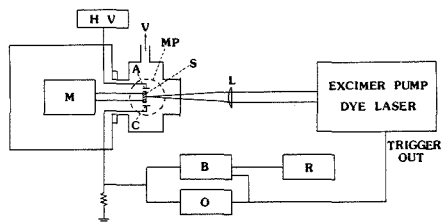


Figure 1. Schematic of experimental setup: HV, bias power supply; A, anode; C, cathode; S, sample; M, motor; MP, microphone; L, lens; B, boxcar averager; O, oscilloscope; R, recorder.

total amount of material vaporized, one can use this signal as an internal calibration to monitor the vaporization process. It has been demonstrated that the acoustic wave measurement can normalize the atomic emission signal generated from the laser plume so that the influence from laser power fluctuations and matrix effects is minimized (15).

Another characteristic feature of the laser plasma is that ions can be formed through either thermal ionization (16, 17) or laser-induced ionization processes (18–22). The thermal ionization process under these experimental conditions only induces very small amounts of atomic ions. According to the Saha-Eyert equation, n^+/n value will be on the order of less than 10^{-5} . However, if the excitation laser wavelength is tuned in resonance with the absorption band of the analyte, the ionization process is enhanced significantly. The atoms or the molecules can be excited by absorbing one or more photons. These highly excited atoms or molecules can be ionized subsequently by collisions or by absorbing more photons to reach the ionization continuum. The first process has been referred to as laser-enhanced ionization (LEI) (18–20). LEI combined with an analytical flame, which serves as an atom reservoir, has been used for trace elemental analysis. The second process, multiphoton ionization (MPI), has been used in mass spectrometric analysis (21, 22). The advantages of using LEI or MPI are the high sensitivity and selectivity. Since the ionization efficiency is relatively high within the laser probe zone (18, 23) and all ions can be collected and measured efficiently, high sensitivity can be obtained. In addition, since both ionization methods are based on the resonant transitions of the analytes, a relatively high degree of selectivity is obtained. In conjunction with mass spectrometry, Muller et al. (24) have demonstrated that one laser can be used for both vaporization and resonant two-photon ionization using UV radiation. However, in most laser vaporization–laser resonant ionization experiments (25–27), two lasers are used to separate the vaporization and the ionization process.

In this report, the possibility of using LEI to directly probe the dense plasma formed by laser vaporization (without mass spectrometry) is examined. Only one visible-tunable dye laser is used for both vaporization and ionization. In addition, the correlation of the ion signal and the acoustic signal are investigated under different focusing conditions and different laser energies. The results provide insight into the processes that occur at the early stages of the formation of the plume.

EXPERIMENTAL SECTION

Figure 1 shows the schematic diagram of the experimental setup. A pulsed excimer laser (Lumonics, Ottawa, Canada, Model Hyper EX460) running at the 308-nm XeCl transition with 10-Hz repetition rate and 25-ns pulse duration is used to pump a tunable dye laser (Lambda Physik, Fl 3001). The dyes used in these experiments are Rhodamine 6G and Coumarin 102. A 32 cm focal length lens is used to focus the visible laser into a spot with <0.1 mm in diameter upon the sample surface. This lens is mounted on a translation stage with a movement of $1/64$ mm resolution so that the focusing conditions can be finely adjusted. The pulsed

dye laser energy output is regulated by varying the operating voltage on the excimer laser. The laser beam energy levels are measured with an energy ratiometer (Laser Precision, Utica, NY, Model Rj-7200) with an energy probe (Laser Precision, Utica, NY, Model RjP734) just before the objectives. Typical laser energies used are between 10 and 900 μJ /pulse.

The samples, Na_2O_3 and Cu, are cut to 6 mm \times 6 mm \times 1.5 mm disks and then mounted to a stainless rod which is attached to a motor so that the sample can be rotated during the spectroscopic experiments. All samples are polished with the use of #600 gritpaper and carefully cleaned with methanol to avoid imbedded grit. A +300 V potential is applied to a copper electrode to serve as an ion repeller. The positive potential used here is low enough to prevent any perturbation of the atomic transition or arcing caused by the high local plasma density but high enough to repel the ion efficiently. Another copper electrode is grounded through a load resistor to serve as an ion collector. The electrodes are square plates 1 cm \times 1 cm and are separated by 1 cm. In order to measure the ion intensity formed from the laser plume, the voltage across the resistor is measured. A 1-M Ω resistor is used in order to measure the small amount of current formed from the ion collection, even though the use of 1-M Ω load resistor increases the time of the detection of ions, which are eventually integrated. The optical excitation process, naturally, occurs only during the laser pulse. The electronic signal thus reflects what happened during the laser pulse. A 0.5 in. diameter condenser microphone (Knowles, Franklin Park, IL, Model BT-1759) is mounted to a Pyrex cell for measuring the acoustic signal. A quartz window is glued to this cell to allow the laser light to irradiate the sample. This Pyrex cell is then attached to a copper chamber which contains the motor so that the entire system is enclosed and the sample chamber can be changed from vacuum to an inert gas environment. A two-stage glass diffusion pump backed by a mechanical pump is used to maintain the low pressure (10^{-4} Torr) for the spectroscopic experiments.

For the wavelength-dependence studies, the ion signal is monitored with a boxcar averager and gated integrator (EG&G Model 162 boxcar averager and Model 164 gated integrator) as a function of the dye laser wavelength. An effective time constant of 4 s is used to achieve reasonable signal to noise (S/N) ratio and scan time. The averaged output from the boxcar averager is plotted on a strip-chart recorder.

In order to measure the acoustic signal, 50 Torr of He gas is filled into the cell to transfer the acoustic wave. It has been demonstrated (15) that at this pressure range, a linear correlation between the acoustic signal and the amount of the evaporated material can be obtained. The same sample surface is irradiated with different laser energies and focusing conditions to obtain the ion and acoustic signals for the correlation studies. The signal outputs from the cathode and the microphone are sent to a two-channel waveform preamplifier (Data Precision, Danvers, MA, Model D1000). Then a waveform analyzer with a 9-bit amplitude resolution and a sampling rate of 18 MHz for each channel (Data Precision, Danvers, MA, Model D6000 with Model 630) is used to process the signals. The peak area of the ion current and the height of the acoustic signal are measured by the mathematical functions built into the waveform analyzer. A 1-ms time gate is used to determine the peak area that represents the total ion signal. An IBM PC/AT computer is used to perform the linear regression.

RESULTS AND DISCUSSION

Figure 2 shows the laser vaporization–laser-enhanced ionization spectrum of Na at the D line region. When the dye laser wavelength is tuned to 589 nm, the ion signal is enhanced substantially. Compared with the nonresonant transition regions, the resonant excitation provides over a factor of 70 enhancement of sensitivity (larger signal). In spite of the use of low laser energies (<10 μJ), thermal processes are still sufficient to vaporize the neutral atoms or molecules into the gas phase. These superheated atoms then can absorb one or more photons in the same laser pulse for the ionization process. However, for Na, a three-photon (589 nm, $h\nu = 2.11$ eV) absorption is required to provide enough energy to excite into the ionization continuum (ionization potential (IP) = 5.1 eV).

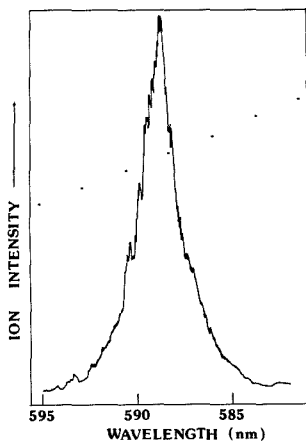


Figure 2. Laser vaporization-laser-enhanced ionization spectrum of Na obtained by using a laser energy of $\sim 10 \mu\text{J}/\text{pulse}$ in vacuum. Dots represent the dye laser gain curve.

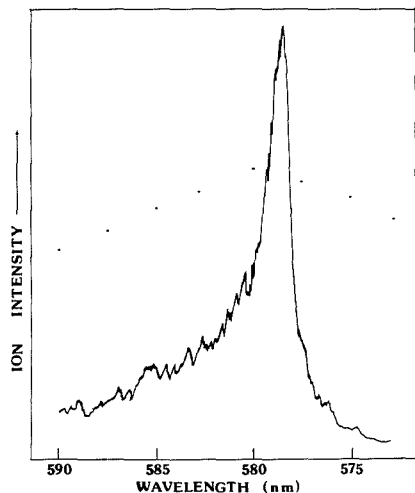


Figure 3. Laser vaporization-laser-enhanced ionization spectrum of Cu obtained by using a laser energy of $\sim 10 \mu\text{J}/\text{pulse}$ in vacuum. Dots represent the dye laser gain curve.

This process is unlikely because of the use of low laser energies and the small cross section for three-photon absorption even when the first photon is in resonance. Also, a log-log plot of ion intensity vs laser energy reveals a linear dependence. From the acoustic wave measurements, *vide infra*, we found that the amount of material produced per laser shot is linearly dependent on the laser energy in this range. This implies a zeroth-order dependence on the laser energy for the ionization process. So, the resonant absorption transition is saturated at these power levels, which are at least 1000 times larger than the critical power of 22 W cm^{-2} (28). Therefore, collisional ionization is needed to ionize these excited Na atoms. This is also true for the Cu transition at 578 nm as shown in Figure 3. Copper has a 7.7-eV ionization potential; a sum of three photon (578 nm) energies ($h\nu = 2.15 \text{ eV}$) is required to reach the ionization continuum from this state. This three-photon absorption process will be unfavorable compared to the

Table I. Maximum Ionization Signal for Sodium Dimer at Different Focusing Conditions

distance, mm	ionization maximum, nm	distance, mm	ionization maximum, nm
0	476	1.5	484
0.5	478	2.0	484
1.0	479		

one-photon event. In addition, the log-log plot of ion intensity vs laser energy for Cu also indicates a linear dependence over 2 orders of magnitude. Therefore, multiphoton ionization is not the main mechanism for these two elements. Since the laser plasma has a relatively high density, thermal collisions occur much more frequently between the excited atoms with other atoms than in analytical flames (18). There are certainly enough collisions to provide enough energy for the ionization of the excited atoms.

In Figures 2 and 3, an unusual broadening (a full width at half maximum (fwhm) of 2.2 and 1.4 nm for Na and Cu, respectively) is observed. The sodium D lines cannot be resolved. Spectral broadening has also been observed by Muller (24) in the UV region for Cd- and Cu-doped epoxy resin samples. However, the line widths here are about 10-fold broader. In addition, the transition bandwidth is found to increase with the use of higher laser powers or higher buffer gas pressures. Line widths as broad as 6 and 7 nm for Na and Cu, respectively, have been observed in 1 atm He gas. This broadening is too large to be due to the Doppler effect. Other researchers have used similar laser powers in flames and observed narrow spectral features (18). This rules out contributions of this magnitude (several nanometers) from power broadening. A collisional broadening effect can explain this phenomenon (29). The plasma density can be increased either by evaporating more material under higher laser power or by confining the plasma under higher pressure conditions. Therefore, large broadening effects are observed. The laser-generated plasma could be so dense that it may attain a liquid-like density. The collisions of excited atoms with other atoms (not the inert gas, which is at a much lower density) result in a serious broadening. The Lorentzian line width for Na at 1 atm is around 0.003 nm for 2500 K (30). Since liquids are roughly 1000 times denser than atmospheric pressure gases (Na metal has a density 1000 times that of Na gas at 1 atm at 273 K), widths of several nanometers are reasonable here. This larger broadening phenomenon indicates that the initial moments of the laser plume formation are being monitored. Because of the use of short laser pulses ($\sim 25 \text{ ns}$), only in this time period can the neutral atoms absorb the photons to induce ionization. At longer times, after the plasma expands, the density as well as the collision frequency decreases significantly. Less broadening effect should then be obtained.

Figure 4 shows the vaporization-ionization spectrum of $\text{Na}_{0.7}\text{WO}_3$ in the 470–500-nm region. This represents the $\text{B}(1) \ ^1\pi_u \leftarrow \text{X}(1) \ ^1\Sigma_g^+$ transition region (31) of the sodium dimer. Since the sum of energies of two photons is larger than the ionization potential of Na_2 (IP = 4.9 eV), resonant two-photon ionization or collision-induced ionization can occur. Sodium atoms do not absorb in this region; therefore, the ions formed at this laser wavelength should be mainly due to the ionization of sodium dimer. A linear correlation between the ion signal and the laser energy is observed. A very broad spectral feature with fwhm = 10 nm is observed in this study. This is caused by the overlap among the many rovibronic transitions in this wavelength region. Another interesting result was observed in which the Na dimer absorption maximum shifts when the relative distance between the laser focal point and the sample surface changes. When the distance increases, a red shift occurs, as listed in Table I. One explanation of this abnormal

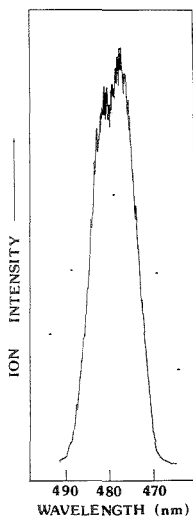


Figure 4. Laser vaporization-laser-enhanced ionization spectrum of Na dimer obtained by using a laser energy of $\sim 10 \mu\text{J}/\text{pulse}$ in vacuum. Dots represent the dye laser gain curve.

shift is collisions which will change the vibrational amplitudes and cause the absorption band to shift. When the focusing condition changes, the density of the laser plume will also vary. As a result, the molecular interactions are altered too. Since this perturbation depends on the collision frequency or the density of the plasma, the magnitude of the shift is difficult to estimate. This shift cannot be observed for the Na D line transition or for the Cu transition at 578 nm. This is due to the presence of rovibronic transitions in Na dimers, while for Na and Cu only a single transition is allowed.

Another possible explanation for this abnormal shift is plasma absorption (prefilter effect). If the maximum absorption occurs for the O-O transition at 492 nm under low density conditions (32), a large amount of excitation intensity at this wavelength will be lost due to the highly absorbing outer layer of the plasma. Therefore, less of the dimers inside the plasma are irradiated by the laser. Although the absorption coefficient at 478 nm is smaller, the blue light can penetrate the plasma more easily and induce more ionization. Therefore, the maximum ionization signal shifts to the blue wavelength in a higher density plasma when the laser focal point is moved closer to the surface. However, further experiments will be necessary to confirm this explanation.

To further understand the ionization process, the acoustic wave associated with each plume is recorded. Although the ion intensity will decrease and pressure broadening will become much more serious in the presence of 50 Torr He (which is required for the acoustic wave measurement), the enhanced ionization efficiency by the resonant transition process can easily compensate for this loss and provide a reasonable signal-to-noise ratio for the measurements. The detection limit for both ion and acoustic signals (at the minimum laser energy) is the background noise. The former is associated with the plasma and the latter is due to vibrations. The maximum measurable signal has not been explored because of the limited energies provided by our pulsed dye laser ($< 1 \text{ mJ}/\text{pulse}$). No saturation of either signal was observed at these power levels.

Figure 5a shows a typical screen display on the waveform analyzer. The upper trace is the Na ion signal while the lower trace shows several early acoustic waves with the laser op-

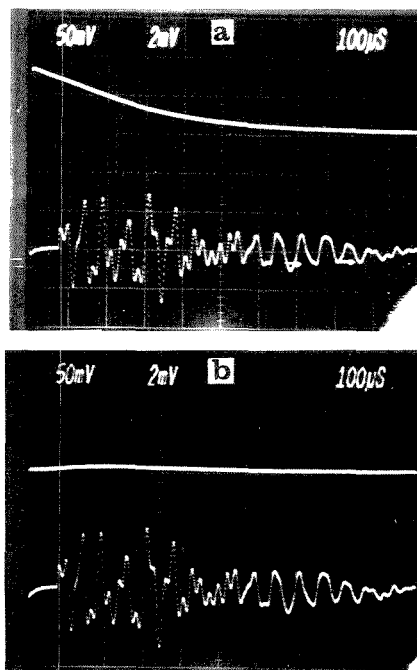


Figure 5. Waveform analyzer screen display obtained from vaporization of $\text{Na}_{0.7}\text{WO}_3$ at 50 Torr He buffer gas: (upper trace) Na ion signal; (lower trace) acoustic wave; (a) 589 nm, (b) 580 nm.

erated at 589 nm. Figure 5b shows the same traces but the dye laser is tuned to 580 nm. It is clear from the acoustic signals that the same amount of material is generated at these two wavelengths but much larger ion formation is obtained when the dye laser is tuned to the Na resonant line. This result also indicates that the vaporization and ionization processes are separated events; otherwise, the acoustic signal obtained at 580 nm should be much smaller than that at 589 nm. In addition, if these two processes occurred simultaneously, a much broader spectral band would be obtained to reflect the absorption characteristics of the solid phase, which is essentially flat in this region.

Among the acoustic peaks, the first several peaks are found to have a good linear correlation with the ion peak area. This is consistent with earlier studies on atomic emission (15). Although the first peak originates for the first impulse without complications from wave reflection and mixing that follow, the largest peak provides a very good correlation with the ion signal and, more importantly, a better sensitivity. So, the maximum acoustic peak height is used throughout the entire investigation.

Figure 6 shows the correlation between the laser-enhanced ionization signal and the acoustic signal for Na at 589 nm for a series of plumes produced at different laser energies on the same $\text{Na}_{0.7}\text{WO}_3$ crystal surface. A good linear correlation at the lower energy range with $r^2 = 0.993$ is obtained. At higher laser energies, a significant negative deviation occurs. One may suspect that the condenser microphone is saturated. However, a good linear correlation between the ion signal (0-4600 μV s) and the acoustic signal (0-250 mV) with $r^2 = 0.996$ (21 data points) is obtained for Cu at 578 nm. This indicates that another process must be responsible for the

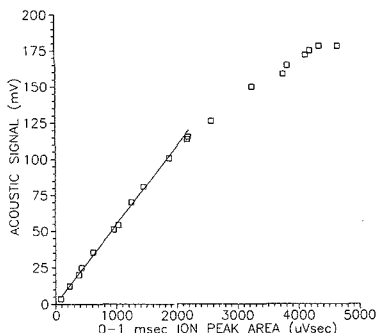


Figure 6. Ion peak area vs acoustic peak height at different laser energies on the same sample surface spot: sample, $\text{Na}_{0.7}\text{WO}_3$; laser, 589 nm, 1 Hz, 0.9–0.04 mJ/pulse, focal point 2 mm above the surface; 50 Torr He buffer gas.

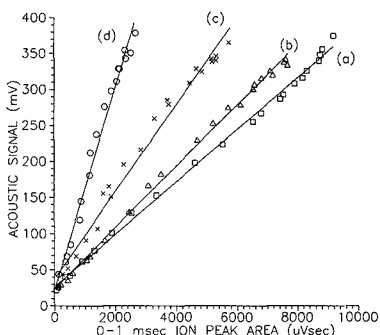


Figure 7. Ion peak area vs acoustic peak height at different laser energies on the same sample surface spot: sample, $\text{Na}_{0.7}\text{WO}_3$; laser, 480 nm, 1 Hz, 0.6–0.04 mJ/pulse; 50 Torr He buffer gas; focal point position, (a) 0 mm, (b) 1 mm, (c) 2 mm, (d) 3 mm.

deviation at high energies for Na. This may be explained by the fact that at a high laser energy, more Na atoms are generated. As the density of this plasma increases, larger numbers of collisions will be experienced by the Na atoms following laser excitation. Collision-induced ionization will be enhanced. This process therefore creates a larger ion signal for the same amount of material vaporized (same acoustic signal). For Cu, even more collisions are needed to bring about a similar effect, since the IP is much higher. So, a negative deviation is not observed in these experiments.

Neutral Na dimers can be formed as a result of condensation or through a sputtering process in which the dimers are formed directly from the violent vaporization event. These dimers can then absorb laser photons to produce ions. If the Na dimer is formed from condensation, the yield of Na_2^+ will be expected to have a quadratic dependence on the atomic vapor density ($\text{Na} + \text{Na} \rightarrow \text{Na}_2$). However, as shown in Figure 7, a linear correlation is found throughout the entire range between the acoustic signal and the ion peak area produced by different laser powers at 480 nm. This result indicates that the dimer is formed directly during vaporization. A similar mechanism for dimer formation has also been observed previously by using a spatial mapping technique (33).

Different focusing conditions have been used to study the spatial dependence of the ionization process. A very good linear correlation between the Na_2^+ ion signal and the acoustic signal with $r^2 = 0.997$ is obtained (as shown in Figure 7) when the laser focal point is adjusted right on the surface or 1 mm above the sample surface. However, when the focal point is

moved further away from the surface, the correlation degrades but a fairly linear relationship still remains with $r^2 = 0.983$. Na and Cu ions show a similar linear correlation with the acoustic signal regardless of the focusing conditions.

From Figure 7, one notes that for the same acoustic signal intensity, which indicates the same amount of material has been vaporized, higher Na_2^+ ion intensity can be obtained if the focal point is moved closer to the sample surface. This can be simply explained by the fact that the ionization efficiency in the laser plasma depends on the collisions. When the laser beam is focused in the high-density region, the overall ionization efficiency will be increased substantially. This is also true for Na and Cu ion formation, since collisional excitation is also involved in the overall ionization process.

CONCLUSION

Laser vaporization and laser-enhanced ionization can be easily achieved with use of one laser. Enhanced ion signals have been obtained if the laser wavelength is tuned in resonance with an analyte transition band, whether it involves a ground-state atom (Na), an excited-state atom (Cu), or a dimer (Na_2). Substantial broadenings of the transition and wavelength shift have been observed as a result of the high plasma density. A very good linear correlation (over 3 orders of magnitude) between the ion peak area and the acoustic signal has been obtained. The acoustic wave intensity can be used to monitor the amount of material evaporated to elucidate the ionization mechanism. Future work will be based on two lasers so that the ionization process can be studied as a function of time delay and height above the surface. LEI may well be one of very few techniques that can be used to probe very dense plasmas with good spatial and temporal resolution. An article on this topic (34) appeared after the present study was completed. Those authors concluded both experimentally and theoretically that LEI detection directly in a laser-produced plasma at atmospheric pressure is not feasible. That is a two-laser experiment with different vaporization and ionization beams. This is in variance with the results here and can be explained by the smaller pulse energies (3.5 μJ) of the ionization beam and the longer time delays (30 ns to 20 μs) between the two lasers used there.

Registry No. Na, 7440-23-5; Cu, 7440-50-8; $\text{Na}_{0.7}\text{WO}_3$, 111569-08-5; He, 7440-59-7; Na dimer, 25681-79-2.

LITERATURE CITED

- Manabe, R. M.; Piepmeyer, E. H. *Anal. Chem.* **1979**, *51*, 2066–2070.
- Lewis, A. L.; Beenen, G. J.; Hosch, J. W.; Piepmeyer, E. H. *Appl. Spectrosc.* **1983**, *37*, 263–269.
- Dittrich, K.; Wennrich, R. *Prog. Anal. At. Spectrosc.* **1984**, *7*, 139–198.
- Conzemius, R. J.; Svec, H. J. *Anal. Chem.* **1978**, *50*, 1854–1860.
- Conzemius, R. J.; Capellen, J. M. *Int. J. Mass Spectrom. Ion Phys.* **1980**, *34*, 197–217.
- Cotter, R. J. *Anal. Chem.* **1984**, *56*, 485A–504A.
- Van Deijk, W.; Balke, J.; Massen, F. J. M. *J. Spectrochim. Acta, Part B* **1979**, *34B*, 353–369.
- Peppers, N. A.; Scribner, E. J.; Atterton, L. E.; Hony, R. C.; Beatrice, E. S.; Harding-Barlow, I.; Rosan, R. C.; Glick, D. *Anal. Chem.* **1988**, *40*, 1178–1182.
- Saffir, A. J.; Marich, K. W.; Orenberg, J. B.; Treylt, W. J. *Appl. Spectrosc.* **1972**, *26*, 469–471.
- Karr, F. S.; Singer, J. M. *Fuel* **1968**, *47*, 235–240.
- Cerri, E.; Trucco, R. *Energy. Nucl. (Milan)* **1968**, *15*, 581–587.
- Wennrich, R.; Dittrich, K.; Bonitz, U. *Spectrochim. Acta, Part B* **1984**, *39B*, 657–666.
- Morton, K. L.; Nohe, J. D.; Madsen, B. S. *Appl. Spectrosc.* **1973**, *27*, 109–117.
- Piepmeyer, E. H. In *Analytical Applications of Lasers*; Piepmeyer, E. H., Ed.; Wiley, 1986; Chapter 19.
- Chen, G.; Yeung, E. S. *Anal. Chem.* **1988**, *60*, 2258–2263.
- Knox, B. E. In *Trace Analysis by Mass Spectrometry*; Ahearn, A. J., Ed.; Academic Press: New York, London, 1972.
- Egorov, S. E.; Letokhov, V. S.; Shibanov, A. N. In *Surface Studies with Lasers*; Ausseuneq, F. R.; Leitner, A.; Lippitsch, M. E., Eds.; Springer Series in Chemical Physics Vol. 33; Springer-Verlag: Berlin, 1973.
- Travis, J. C.; Turk, G. C.; Green, R. B. *Anal. Chem.* **1982**, *54*, 1006A–1018A.

- (19) Green, R. B. In *Analytical Applications of Lasers*; Piepmeier, E. H., Ed.; Wiley: New York, 1986, Chapter 3.
- (20) Turk, G. C.; Travis, J. C.; DeVoe, J. R.; O'Haver, T. C. *Anal. Chem.* 1979, 51, 1890-1896.
- (21) Johnson, P. M. *Acc. Chem. Res.* 1980, 13, 20-26.
- (22) Schlag, E. W.; Neusser, H. J. *Acc. Chem. Res.* 1983, 16, 355-360.
- (23) Duncan, M. A.; Dietz, T. G.; Smalley, R. E. *Chem. Phys.* 1979, 44, 415-419.
- (24) Verdun, F.; Krier, G.; Muller, J. F. *Anal. Chem.* 1987, 59, 1383-1387.
- (25) Lubman, D. M.; Tembreull, R. *Anal. Instrum.* 1987, 16, 117-131.
- (26) Boesl, U.; Grotemeyer, J.; Walter, K.; Schlag, E. W. *Anal. Instrum.* 1987, 16, 151-171.
- (27) Williams, M. W.; Beekman, D. W.; Swan, J. B.; Arakawa, E. T. *Anal. Chem.* 1984, 56, 1348-1350.
- (28) Calcar, R. A.; Ven, M. J. M.; Uilert, B. K.; Biewenga, K. J.; Hollander, T.; Alkamado, C. Th. J. *J. Quant. Spectrosc. Radiat. Transfer* 1979, 21, 11-18.
- (29) Kirkbright, G. E.; Sargent, M. In *Atomic Absorption and Fluorescence*; Academic Press: New York, 1974.
- (30) Hinnov, E.; Kohn, H. J. *Opt. Soc. Am.* 1957, 47, 156-162.
- (31) Schlejen, J.; Jalink, C. J.; Korving, J.; Woerdman, J. P.; Müller, W. J. *Phys. B* 1987, 20, 2691-2711.
- (32) Fredrickson, W. R.; Watson, W. W. *Phys. Rev.* 1927, 30, 420-437.
- (33) Huie, C. W.; Yeung, E. S. *Spectrochim. Acta, Part B* 1985, 40B, 1255-1258.
- (34) Coche, M.; Berthoud, T.; Mauchien, P.; Camus, P. *Appl. Spectrosc.* 1989, 43, 646-650.

RECEIVED for review May 9, 1989. Accepted August 22, 1989. The Ames Laboratory is operated by Iowa State University for the U.S. Department of Energy under Contract W-7405-Eng-82. This work was supported by the Director of Energy Research, Office of Basic Energy Sciences, Division of Chemical Sciences.

Characteristics of Methods for the Simultaneous Determination of Catalysts by First-Order Inhibition Kinetics

Carol P. Fitzpatrick and Harry L. Pardue*

Department of Chemistry, Purdue University, West Lafayette, Indiana 47907

Factors that affect the simultaneous kinetic determination of catalysts based on differences in rates of inhibition by a common inhibitor are investigated by computer simulation. Both derivative and integral models for the kinetic responses are studied. Nonlinear regression is used to fit data with a fixed level of noise for the combined responses due to the first-order inhibition of two catalysts. Effects of rate constants, ratios of rate constants, fitting ranges, data density, and number of replicate determinations on reliability, useful activity range, sensitivity, scatter, limits of detection, and measurement/data-processing times are considered. It is found that values for rate constants, ratios of rate constants, and fitting ranges which provide results with desired reliability are restricted. Small ratios of rate constants and short fitting ranges were observed to produce the largest useful activity ranges and shortest measurement times but also gave the worst accuracy and most dependence on initial estimates of fitting parameters. Values of the coefficients of correlation between the individual first-order responses can aid in the selection of the smallest ratio of rate constants and fitting range which will yield suitable results.

Differences in kinetic behavior have been used extensively for the simultaneous determination of two or more components in mixtures (1-3). These methods have been used to resolve mixtures of both reactants and catalysts. The resolution of reactants depends upon differences in rate constants for reaction with a common reagent; the resolution of catalysts depends on differences in rate constants for inhibition by some common reagent. Although there have been studies of optimum conditions for the simultaneous determination of reactants (4, 5), there have been no analogous studies for catalytic species quantified in this manner. Such studies are needed because there are substantive differences between the two groups of methods.

The most significant difference relates to effects of rate constants and other kinetic parameters on the maximum signal change obtainable from each type of system. Whereas the

maximum possible signal change is independent of kinetic parameters when reactants are quantified, it is very dependent on rate constants when catalysts are quantified via inhibition of their catalytic activities. For example, if the rate of inhibition of a catalyst is very fast relative to the catalytic reaction, then the signal change will be very small compared to that observed if the rate of inhibition is slow relative to the rate of the catalytic reaction. Thus performance characteristics such as sensitivity, imprecision, detection limits, and useful activity range are more dependent on kinetic parameters when catalysts are quantified than when reactants are quantified.

To date, most methods for resolution of catalysts have relied on fixed-time, single-point determinations of activity in which catalysts are differentiated by extents of inhibition rather than by inhibition rate constants. Multipoint methods, however, reduce errors due to variability in rate constants (6), produce statistics which can be used to detect model errors (7), and provide data for the determination of three or more catalysts from a single set of kinetic data (8). The last advantage is particularly significant because single-point, fixed-time methods require measurements for the same number of different conditions as there are catalysts to be resolved. Not only is this labor intensive, but also errors inherent in the individual steps are propagated to the final result (9). Several examples of multipoint methods for the simultaneous determination of two or more catalysts have been demonstrated and include first- and zero-order (10), parallel first- and zero-order (11), and simultaneous first-order kinetic models (8, 12).

This study was undertaken to better understand the effects of variables such as rate constants, ratios of rate constants, data rates and data-fitting ranges on the performance characteristics of a nonlinear regression method for the simultaneous determinations of catalysts based on different rates of inhibition. Synthetic data were used to permit better control of the variables to be studied.

MATHEMATICAL DESCRIPTION

The mathematical model is developed for two components that catalyze a common reaction to form a common product.

It is assumed that the progress of the reaction is monitored by a signal, S , that changes in proportion to changes in product concentration, that the two catalysts behave independently, so that the rates are additive, and that the rate for each catalyst is proportional to the uninhibited concentration of the catalyst. It follows that the rate of signal change can be represented by

$$dS/dt = (k_{1,0})(C_{1,0}) + (k_{2,0})(C_{2,0}) \quad (1)$$

in which $k_{1,0}$ and $k_{2,0}$ are the pseudo-zero-order rate constants for components 1 and 2 and $C_{1,t}$ and $C_{2,t}$ are the time-dependent concentrations of the two catalysts.

It is assumed that inhibitor is present in excess, that each catalyst is inhibited completely and irreversibly, and that the inhibition processes follow pseudo-first-order kinetics as follows

$$C_{i,t} = C_{i,0} \exp(-k_{i,1}t) \quad (2)$$

in which $k_{i,1}$ is the pseudo-first-order rate constant for the inhibition of the i th component. Substitution of eq 2 into eq 1 and recognizing that the product, $(k_{i,0})(C_{i,0})$, is the initial (zero-order) velocity, $V_{i,0}$, for the i th component, the resulting equation is

$$dS/dt = V_{1,0} \exp(-k_{1,1}t) + V_{2,0} \exp(-k_{2,1}t) \quad (3)$$

By fitting this model to time-dependent rate data, it is possible to compute values of initial velocities and rate constants that give the best fit of the model to the data. This is called the derivative model.

Equation 3 can be integrated to obtain

$$S_t = S_0 + (V_{1,0}/k_{1,1})[1 - \exp(-k_{1,1}t)] + (V_{2,0}/k_{2,1})[1 - \exp(-k_{2,1}t)] \quad (4)$$

By fitting eq 4 to data for signal vs time it is possible to calculate values of S_0 , $V_{1,0}$, $V_{2,0}$, $k_{1,1}$, and $k_{2,1}$ that give the best fit of the model to the data. Actually, the fitting process evaluates $V_{i,0}/k_{i,1}$; $V_{i,0}$ is computed by multiplying that quantity by $k_{i,1}$. When the inhibition processes are complete ($t = \infty$), the signal is given by

$$S_\infty = S_0 + V_{1,0}/k_{1,1} + V_{2,0}/k_{2,1} \quad (5)$$

and it is apparent that the contribution to the change in signal from the i th component is proportional to the initial velocity divided by the inhibition rate constant for that component.

EXPERIMENTAL SECTION

Nonlinear Regression. Nonlinear least-squares fits were obtained by using the gradient-expansion method developed by Marquardt (13). Implementation of the algorithm on the MASSCOMP 5500 supermicrocomputer is based on Bevington's CURFIT program (14) and has been described elsewhere (15). Signal values, S_t , were measured directly; rate data (dS/dt) were computed from signal values by using the method of Savitzky and Golay (16). Unless stated otherwise, initial estimates of initial velocities (eq 3) or ratios of initial velocities to rate constants (eq 4) were obtained by dividing the total by two (e.g. $(V_{1,0} + V_{2,0})/2$); initial estimates of rate constants were obtained by underestimating the larger rate constant by 20% and by overestimating the smaller rate constant by 20%. The initial signal, S_0 , was estimated as the signal at the first data point. In this study, the true values of all the fitting parameters were known. However, the differences between initial estimates and true values simulate guesses that might be made under real conditions when approximate values are known. The nonlinear fitting algorithm was allowed to continue for as many iterations as necessary to meet the convergence criterion of successive values of χ^2 (sum of the squared differences between observed and computed signals) within 0.01%.

Synthetic Data. Synthetic data sets were obtained by using eq 4 and parameters shown in Table I. Parameter values were determined from the ratio of rate constants and fitting range of interest for each study; the fitting range is reported as the number

Table I. Parameters Used To Generate Synthetic Data

parameter	value or computational formula
data points	200
noise (1 std dev)	0.001
replicates	3
$k_{1,2}$	0.002 s ⁻¹
$k_{1,1}$	0.002/($k_{1,2}/k_{1,1}$) s ⁻¹
ratio of catalysts ($V_{1,0}$ to $V_{2,0}$)	1 to 1, 1 to 4, 4 to 1
$V_{1,0} + V_{2,0}$	7×10^{-4} signal s ⁻¹
rate of data collection	$200(k_{1,1})/[(t/t_{1/2}) \ln 2]$ s ⁻¹

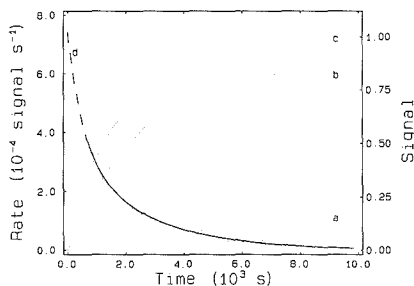


Figure 1. Simulated signal and rate responses for two-component sample: signal vs time for individual (a, b) and combined (c) reactions (right ordinate); derivatives (d) for 5- (---) and 25- (—) point smooths (left ordinate); projected response of 25-point smooth (---); rate constants (a) 0.002 s⁻¹, (b) 0.0004 s⁻¹.

of half-lives, $t/t_{1/2}$, for the component with the smaller inhibition rate constant, $k_{1,1}$. At each ratio and range, three replicates at each of three concentration ratios (1 to 1, 1 to 4, 4 to 1) were generated, thus selection of a single ratio of rate constants and fitting range led to the generation of nine data files. Kinetic data within a file were generated for a fixed data rate and Gaussian-distributed noise was added at a level of 0.001 unit of signal response. Parameters were chosen so that the minimum signal change for a single component was 0.07, well above the minimum (0.03) required to obtain a reasonable first-order fit. All data sets for which the effects of two factors were investigated included a full factorial of at least 72 different combinations of factor levels.

RESULTS AND DISCUSSION

Unless stated otherwise, imprecision in computed quantities is quoted at the level of one standard deviation and values of imprecision are included in parentheses after the numerical values of the computed quantities. All errors refer to differences between computed values of different parameters and the values of these parameters used to generate the response curves. Data ranges are expressed in multiples of the half-life of the component with the smallest inhibition rate constant.

Response Curves. Data in Figure 1 will help to illustrate some important features of methods based on inhibition of catalytic activity. Data in curves a and b are for equal concentrations of two catalysts with different rate constants for the inhibition process ($k_{a,1} = 2 \times 10^{-3}$ s⁻¹, $k_{b,1} = 4 \times 10^{-4}$ s⁻¹). Even though the data are for equal concentrations of the two catalysts, the signal change produced by component a with the larger inhibition rate constant is much smaller than the signal change for component b with the smaller rate constant. Thus, to the extent that one can vary the inhibition rate constants independently, the optimum value for the ratio of rate constants will involve a compromise between larger values of the ratio needed to give good kinetic resolution of the two components and a value of the larger rate constant that is small enough to give adequate sensitivity for that component. This is very different than the situation in which two reactants are resolved kinetically; in that case, equal concentrations of

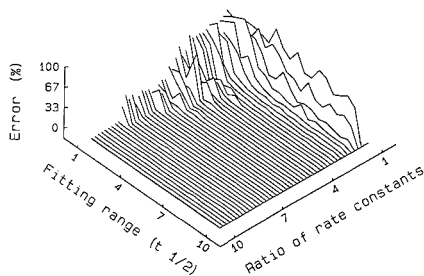


Figure 2. Effects of fitting range and ratio of rate constants on accuracy of computed catalytic velocities.

the two components would produce the same total signal change regardless of the relative magnitudes of the rate constants. This and other features that influence the quantitative resolution of two catalysts from signal vs time (curve c) or rate vs time (curve d) for simultaneous inhibition reactions are discussed in more detail below.

Factors That Affect Accuracy and Precision. *Fitting Range and Ratio of Rate Constants.* Ratios of rate constants studied ranged from 1.5 to 10.1 and fitting ranges were varied from 1 to 10 half-lives of the response due to the component with the smaller rate constant. It should be noted that most data sets involved the same number of data points and, accordingly, different data ranges involved different data densities. Initial estimates of parameters were obtained as described in the Experimental Section except for data with a ratio of rate constants of 1.5, for which initial estimates of rate constants were $\pm 15\%$ of true values. Activities were computed from the nine files at each fitting range and ratio of rate constants and the absolute values of the errors were averaged. Fits with a runs statistic (the number of times the plot of residuals vs time crosses 0) of less than 80 (40% of total points) were considered to have diverged or to have converged on a local minimum and these results are excluded from the averages. Although the value of 80 used in the decision rule is based on visual inspection of the fits and mean square errors, this choice is somewhat arbitrary.

Effects of lower limits for fitting range and ratios of rate constants on average errors are illustrated in Figure 2. Not surprisingly, errors are largest at low ratios of rate constants and fitting ranges where first-order responses are highly correlated. The largest correlation coefficient between responses (0.9990) occurred at a fitting range of one half-life and a ratio of rate constants of 1.5; the average error for this combination was 65%. Evaluation of a reduced range of ratios of rate constants (3 to 7) and fitting ranges (1 to 8 half-lives) showed that the accuracy of fits to data which had correlation coefficients of 0.87 or less was always within 2% of true values with average errors of 0.82% (0.27%). This is illustrated in Figure 3 in which a transition between errors less than 2% and greater than 10% occurs in a narrow region of correlation coefficients between 0.87 and 0.90.

The relationship between correlation of the first-order responses and accuracy suggests a method for determining lower limits for fitting range and ratio of rate constants. From Figure 2 it can be seen that the minimum fitting range required to predict catalytic activities within 2% increases in a nonlinear fashion as the ratio of rate constants decreases. For a fixed ratio of rate constants, the shortest fitting range which has a correlation coefficient of first-order responses of 0.87 or less should produce acceptable results. Conversely, if the data-collection parameters are fixed (analogous to the optimized data-collection routines suggested by Margerum (4) or Meites (17)), correlation coefficients can be used to

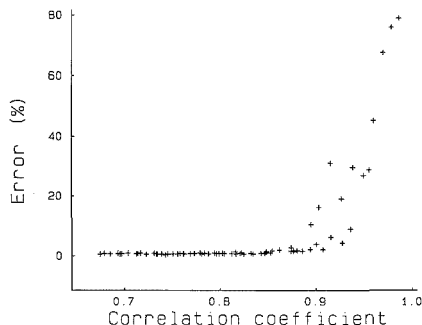


Figure 3. Relationship between accuracy of computed velocities and degree of correlation between individual first-order responses.

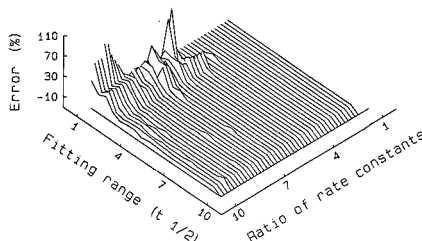


Figure 4. Effects of fitting range and ratio of rate constants on the differences in mean errors between fits of all data sets and those for which residuals changed signs at least 80 times in the fitting range.

evaluate the smallest ratio of rate constants for which catalytic activities can be determined reliably. The cutoff value of 0.87 assumes no model error, a signal-to-noise ratio of 70 or greater, and convergence of the fitting routine such that the number of runs of residuals is at least 40% of the number of data points.

Poor fits were common when fitting ranges were less than three half-lives. Plots in Figure 4 show differences between errors determined by using all fits and those using only fits that converged to reasonable estimates. The region in which differences are large (ratios of rate constants from 4 to 10 and fitting ranges of less than 3) indicates situations for which the fitting algorithm broke down either due to divergence or convergence on a local minimum, despite the fact that correlation coefficients were as small as 0.67 in some cases. It should be noted, however, that it is a relatively simple matter to screen for poor fits by using test statistics such as the mean square error (MSE) or the number of runs of residuals. Also, the fits would likely have improved if initial estimates of rate constants and signal changes had been more accurate.

Upper limits for the fitting range were found to be so large that any reasonable choice should provide reliable fits. In Figure 2, the mean error is 0.79% for a ratio of rate constants of 10.1 and fitting range of 10 half-lives despite the fact that the faster response for the component with the larger rate constant (95% completion) is represented by only eight data points. In a separate study, computed activities were determined for a 4 to 1 ($C_{1,0}$ to $C_{2,0}$) ratio of catalytic concentrations with a ratio of rate constants of 10 to 1 and fitting ranges varying from 8 to 61 half-lives. For this ratio of concentrations, the response due to $C_{2,0}$ is relatively small compared to that of $C_{1,0}$. For example, in the extreme case of 61 half-lives, the response due to $C_{2,0}$ is 2.5% of the total response and is complete in 1500 s which is only 1.4-fold the time per data point. Linear regression of the mean errors resulting from triplicate determinations against fitting range gave a 95%

Table II. Comparison of Results for Fits with Derivative and Integral Models

ratio of rate constants $k_{2,1}/k_{1,1}$	model	averaged results		
		RSD, ^a %	rel error, %	no. of iterations
5	integral	0.63	0.66	21
	derivative, 5 pt ^b	1.4	1.0	4.8
	derivative, 25 pt ^b	1.8	8.8	5.7
3	integral	1.9	1.5	10
	derivative, 5 pt ^b	5.5	4.6	6.1
	derivative, 25 pt ^b	1.2	3.7	6.1

^a Values reported are the pooled relative standard deviations calculated from triplicate determinations at each of three ratios of initial velocities; 1 to 1, 1 to 4, and 4 to 1. ^b Smoothing window (16).

confidence interval for the slope of 0.0078 to 0.086. Accordingly, there is at most a 4.6% increase in mean error from 8 to 61 half-lives.

For inhibition processes, equal catalytic activities do not produce equal signal changes (see Figure 1) and the larger the ratio of rate constants, the larger the difference. This condition places an upper limit on the ratio of rate constants which will give signal changes in a measurable range. If the signals for both components are monitored to completion, then the upper limit for the ratio of rate constants can be determined from the equation

$$(k_{2,1}/k_{1,1})_{\max} = [(V_{1,0}/V_{2,0})_{\min}] / [(\Delta S)_{\min}/(\Delta S)_{\max}] \quad (6)$$

where $(V_{1,0}/V_{2,0})_{\min}$ is the smallest ratio of catalytic velocities to be determined and ΔS_{\max} and ΔS_{\min} are the largest and smallest signal changes that can be accurately measured. For this study, the smallest catalytic ratio was 1 to 4, ΔS_{\max} was 2 signal units, and ΔS_{\min} was approximately 0.07 signal unit. These parameters suggest a maximum ratio of rate constants of 7. For the ratio of 10 investigated earlier in this study, the limit was exceeded and the total signal change was 2.9 in some cases. Although this large change in signal is satisfactory when using synthetic data, it is outside the linear range for some spectrophotometers. It is interesting to note that if ratios of initial velocities of 1 to 10 or 1 to 50 were to be determined and ΔS_{\min} is 0.02 signal unit, the maximum ratio of rate constants for this system would be 10 to 1 and 2 to 1, respectively. Determination of velocities in the ratio 1 to 50 is essentially prohibited under these conditions; however, it might be feasible to accurately determine velocities in this ratio with an instrument for which the noise, and consequently ΔS_{\min} , was very small.

Derivative vs Integral Model. The derivative and integral models (eq 3 and 4) were compared by using data sets representing ratios of rate constants of 5 and 3 with a fitting range of 6 half-lives. Results are summarized in Table II. The integral method gave the smallest errors for both groups of data as well as the smallest imprecision for the larger ratio of rate constants. The derivative model gave slightly smaller imprecision for the smaller ratio of rate constants and required fewer iterations for convergence due to the smaller number of fitting parameters (4 vs 5).

Although this latter effect is predictable, it is not clear that the integral model should yield parameter estimates with less error. For fits with the integral model, initial catalytic velocities are predicted by multiplying two of the estimated parameters $((V_{i,0}/k_{i,1})k_{i,1})$, whereas with the derivative model, catalytic activities are estimated directly. Derivatization, however, tends to increase signal noise and although large smoothing windows reduce this effect, some distortion of the rate is evident early in the reaction when 5-point and 25-point

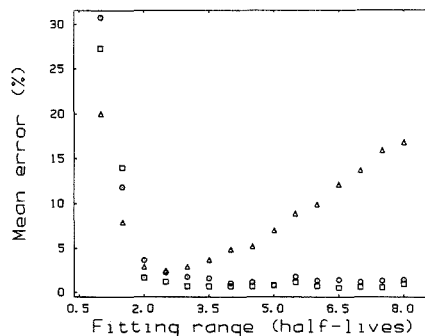


Figure 5. Effects of fitting range on accuracy for fits with the derivative and integral model: integral model (□), derivative model with 5-point (○) and 25-point (△) smooths.

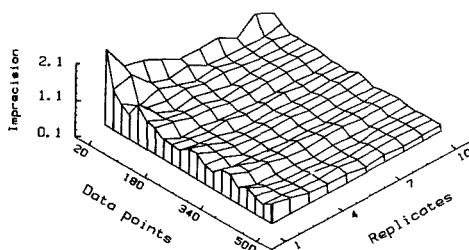


Figure 6. Effects of data density and number of replicate determinations on imprecision.

smoothing windows are compared (see curve d in Figure 1).

A comparison of the accuracy of derivative and integral fitting methods was also made for a fixed ratio of rate constants with different fitting ranges and these results are shown in Figure 5. For a ratio of rate constants of 5 and fitting ranges varying from 1 to 8 half-lives, the model that gave the best fits depended on whether the fitting range was below or above two half-lives. Below two half-lives, the 25-point derivative smooth gave the best results although all mean errors were above 7% in this range. For fits that included at least two half-lives, the integral fit was best in all cases, with errors not exceeding 2% and averaging 0.82% (0.32%). For 5-point derivative fits, errors did not exceed 4% in this same range and averaged 1.6% (0.72%). The fits to 25-point derivative data were progressively worse with increased fitting range, with the principal source of error being the computed signal change, $\Delta \hat{S}$, for the faster-reacting component. It seems probable that the increasing error is due to the facts that the first rate value is obtained late in the process (the 13th point for a 25-point smooth) and that the faster response is represented in proportionally fewer data points as the fitting range is increased with the same number of data points in each fit.

Point Density and Number of Replicates. The effect of increasing the density of data points and number of replicate determinations on imprecision, expressed in terms of average differences between observed and mean values for initial velocities, is illustrated in Figure 6. For this study the ratio of rate constants and fitting range was fixed at four and five, respectively. The number of data points ranged from 20 to 500 and the number of replicate files (each with a different sequence of random noise) varied from 1 to 10. For each data density and number of replicates, the absolute values of differences between the observed and true velocities for ten determinations were averaged. Results show that imprecision was only 2.1% for 20 data points and 1 run and decreased

exponentially with both the data density and the number of replicates. In order to determine whether imprecision decreased in proportion to $1/n^{1/2}$ as expected, simple linear regressions of mean differences vs $1/n^{1/2}$ were obtained for fixed data densities with n being the number of replicates. The average coefficient of determination (R^2) for the 27 linear fits was 0.927 (0.058) and visual inspection of the plots showed no obvious deviations from linearity. When data for a fixed number of replicates and variable numbers of data points were processed the same way, R^2 averaged 0.885 (0.035) for the 10 regressions and plots of the data were slightly curved in all cases. It appears that to a first approximation only, precision will improve as $1/n^{1/2}$ with increased data density and numbers of replicate determinations. A more accurate estimate of the improvement with data density might be obtained by the method of Meites (18).

Effects of Initial Estimates. A reduced data set of the type illustrated in Figure 2 was chosen to study the effects of initial estimates on accuracy of computed activities. Fits to data representing ratios of rate constants from 3 to 7 and fitting ranges from 1 to 8 half-lives were done by using perfect initial estimates in one case and imperfect (as described previously) initial estimates in another case. For all situations in which correlation coefficients among responses were 0.87 or less, the mean errors with both perfect and imperfect initial estimates were within 0.01%. When responses were highly correlated ($r > 0.87$), the mean error ranged from 1.5% to 18% and from 1.6% to 79% for perfect and imperfect initial estimates, respectively.

Optimal Values for Inhibition Rate Constants. For a two-component system, the optimal value of the inhibition rate constant for the faster-reacting component is determined by the minimum detectable signal and the lowest activity to be determined, $k_{1,2} = (V_{i,0})_{\min}/\Delta S_{\min}$. These values will be influenced by the turnover number, k , for the catalyst and the sensitivity factor, ϵ (e.g. molar absorptivity), between signal and detected species as follows:

$$V_{i,0} = k\epsilon C_{i,0} \quad (7)$$

where $C_{i,0}$ is the concentration of the catalyst. The optimum value for the inhibition rate constant for the slower-reacting component will be determined by the desired ratio of rate constants as discussed above.

Lower Limit of Detection for Catalytic Activities. Lower limits of detection for catalytic activity can be predicted and optimized by considering the relationship between signal changes, initial velocity, and rate constant stated previously; namely $\Delta S_i = (V_{i,0})/k_{i,1}$. The minimum initial velocity which can be determined can be predicted from the product of the rate constant and the minimum signal change which produces a good fit. The only problem is that the minimum signal changes which produces a good fit can be substantially larger than the detection limit of the signal. For this study it was observed that mean errors in activity computed from ten replicate fits to first-order data (measured though 8 half-lives, noise = 0.001 unit) were between 2% and 3% when signal changes were on the order of 0.03 unit. This is a 10-fold increase over the expected detection limit for a good spectrophotometer.

The minimum catalyst concentration that can be determined can be decreased by adjusting experimental conditions to maximize the signal change for a fixed concentration of catalyst. Often, catalytic activities and inhibition rate constants both vary with factors such as temperature, pH, ionic strength, substrate concentration, and inhibitor concentration. Levels of these factors, which increase the ratio of initial velocity to rate constant, will simultaneously increase the sensitivity ($d\Delta S/dC$) and decrease the minimum catalytic concentration that can be detected.

Useful Activity Range. The range over which two components can be quantified simultaneously is less than the useful range for either component quantified by itself. The minimum and maximum activities which can be reliably determined for a single component system can be predicted by eq 8a and 8b. The term enclosed in braces in eq 8b is a

$$(V_{i,0})_{\min} = (k_{i,1})(\Delta S_{\min}) \quad (8a)$$

$$(V_{i,0})_{\max} = (k_{i,1})\{(\Delta S_{\max})/[1 - \exp(-t/t_{1/2}) \ln 2]\} \quad (8b)$$

straightforward result of the integrated equation for first-order kinetics and represents the change in signal that would be observed for the component with the smaller rate constant if the reaction were monitored to completion.

For the simultaneous determination of two catalysts, the minimum velocity is determined by the component with the larger rate constant and the maximum velocity is determined by the component with the smaller rate constant. Equations to compute the combined activity range are obtained by substitution of the larger ($k_{1,2}$) and smaller ($k_{1,1}$) rate constants into eq 8a and 8b, respectively. It is easily shown that the range between these limits is less than for one component or the other taken alone. In order to generalize the relationships, we evaluated the ratios of the maximum and minimum velocities rather than differences because the ratios of velocities depend upon the ratios of rate constants and are therefore representative of any combination of rate constants that give the indicated ratios. The ratio of the maximum to the minimum velocity contained in the useful range for the two-component system, termed the activity ratio (AR), is as follows:

$$AR = (\Delta S_{\max}/\Delta S_{\min})(k_{1,1}/k_{2,1})[1 - \exp(-t/t_{1/2}) \ln 2]^{-1} \quad (9)$$

Equation 9 was used to evaluate the activity ratio for combinations of ratios of rate constants (1.5 to 10) and fitting ranges (1 to 10). Values for the maximum and minimum signal change used in the calculation were 2 and 0.02. These results indicate that the activity ratio is largest at the smallest values of fitting range and decreases exponentially with increased values of each parameter. For example, at the smallest ratio of rate constants and fitting range evaluated, the activity ratio is 130, whereas for less-correlated conditions such as a ratio of rate constants of 4 and fitting range of 6 half-lives, the activity ratio is 25. At conditions for which both the ratio and fitting range are equal to 10, the activity ratio is only 10. Again, these values would be increased if the noise in the data were reduced.

Comparison with Parallel First-Order Responses for Reactants. Results from the data set, which included ratios of rate constants from 3 to 7 and fitting ranges from 1 to 8 half-lives, were compared with results for simultaneous determinations of reactants based on fits of a parallel first-order model to kinetic data for the same ratios of rate constants and fitting ranges. For the noncatalytic system, the total signal change was 1.05 in each case with concentration ratios of 1 to 1, 1 to 4, and 4 to 1, analogous to the initial velocity ratios for the catalytic system. Imperfect initial estimates were used to begin the fitting procedures. The mean and standard deviations of average errors in computed concentration and component fractions were 2.4 (6.0) and 0.68 (1.7) for the noncatalytic system and 7.0 (16) and 2.4 (5.5) for the catalytic system. The smaller errors in computed concentrations for the noncatalytic system result from the fact that the total signal change is independent of kinetic parameters.

CONCLUSION

The results of these studies suggest guidelines for determining conditions that produce optimal estimates of catalytic activities. The most important of these conditions is the choice

of inhibitor and its concentration. The most significant issue in this choice is the tradeoff between a sufficiently large ratio of inhibition rate constants to distinguish between the catalysts, and a sufficiently small ratio to ensure adequate signal for the faster-reacting component relative to the slower-reacting component. The optimal choice for the ratio of rate constants is the smallest value which produces a kinetic response which can be accurately resolved. It was observed empirically that first-order responses that had correlation coefficients of 0.87 or less met this criterion and that the optimum ratio of rate constants is approximately 3, depending on the number of replicates, data density, fitting range, and noise. Larger ratios of rate constants led to smaller values of the useful activity ratio. The optimal concentration of the inhibitor will give a value for the larger rate constant for which the minimum initial velocity to be determined yields the minimum detectable signal change, ΔS_{\min} (see eq 8a). Any other value will give a suboptimal activity ratio.

Reaction conditions can also be varied in such a way as to increase the sensitivity and decrease the lower limit of detection for the catalysts. Condition that increase the ratio of initial velocity to the rate constant for a fixed amount of catalyst will improve these parameters but may cause others to deteriorate. If the signal due to a fixed amount of catalyst increases because the rate constant for inhibition decreases while the initial velocity remains constant, the detection limit is reduced at the expense of the measurement time. If, however, the initial velocities can be increased without increasing the inhibition rate constant, the minimum concentration of catalyst that can be determined will decrease without affecting the measurement time.

To optimize the measurement/data-processing time, the kinetic response for the component with the smaller rate constant need only be followed for as many half-lives as is required to produce individual responses with correlation coefficients of 0.87 or less. For the ratio of rate constants of 3 suggested earlier, fitting ranges in excess of eight half-lives of the slower component are required for optimum performance. If the fitting range is reduced to four half-lives, however, the error for a single determination is not expected to exceed 3–5%. Not only does the shorter fitting range reduce the measurement time, but it also increases the useful activity ratio.

The time required to process the data can be reduced by using the minimum number of data points necessary to obtain

the desired precision. For a ratio of rate constants of 4 and fitting range of 5 half-lives, it was observed that 20 data points and 1 run were sufficient to predict the catalytic velocities with reasonable precision. Data processing times are also shorter when the derivative model is used. This advantage is offset somewhat by the time required to derivatize the data and the decreased accuracy. Derivatization methods such as the fixed-time integrating ratemeter (19), which is said to be robust toward instrumental noise, might increase speed without degrading accuracy.

In practice, optimization may be difficult because rate constants, ratios of rate constants, and initial velocities often vary in the same ways with reaction conditions. However, results of this study should be useful in predicting the feasibility of determinations based on differences in rates of inhibition of catalytic species.

ACKNOWLEDGMENT

We thank Mark Merrick, Purdue University, for suggesting the study of the relationship between correlations of first-order responses and accuracy.

LITERATURE CITED

- (1) Mark, H. B., Jr.; Rechnitz, G. A. *Kinetics in Analytical Chemistry*; Interscience: New York, 1968.
- (2) Mottola, H. A. *Kinetic Aspects of Analytical Chemistry*; Wiley: New York, 1988.
- (3) Pardue, H. L. *Anal. Chim. Acta* **1989**, *216*, 69–107.
- (4) Ridder, G. M.; Margerum, D. W. *Anal. Chem.* **1977**, *49*, 2090–2098.
- (5) Wentzell, P. D.; Karayannis, M. I.; Crouch, S. R. *Anal. Chim. Acta*, in press.
- (6) Bacon, B. L.; Pardue, H. L. *Clin. Chem.* **1989**, *35*, 360–363.
- (7) Rutan, S. C.; Fitzpatrick, C. P.; Skoug, J. W.; Weiser, W. E.; Pardue, H. L. *Anal. Chim. Acta*, in press.
- (8) Brown, P. B.; Lewis, K. O. *Ann. Clin. Biochem.* **1980**, *17*, 192–198.
- (9) Tilyer, C. R. *Clin. Chem.* **1988**, *34*, 2490–2493.
- (10) Weiser, W. E.; Pardue, H. L. *Anal. Chem.* **1986**, *58*, 2523–2527.
- (11) Harner, R. S.; Pardue, H. L. *Anal. Chim. Acta* **1981**, *127*, 23–38.
- (12) PetitClerc, C. *Clin. Chem.* **1976**, *22*, 42–48.
- (13) Marquardt, D. W. *J. Soc. Ind. Appl. Math.* **1963**, *11*, 431–441.
- (14) Bevington, P. R. *Data Reduction and Error Analysis for the Physical Sciences*; McGraw-Hill: New York, 1969; p 237.
- (15) Mieling, G. E.; Pardue, H. L. *Anal. Chem.* **1978**, *50*, 1611–1618.
- (16) Savitzky, A.; Golay, M. L. *Anal. Chem.* **1964**, *36*, 1627–1639.
- (17) Meites, L.; Hussam, A. *Anal. Chim. Acta* **1988**, *204*, 295–309.
- (18) Meites, L.; Fanelli, N.; Papoff, P. *Anal. Chim. Acta* **1987**, *200*, 387–396.
- (19) Cordos, E. M.; Crouch, S. R.; Malmstadt, H. V. *Anal. Chem.* **1968**, *40*, 1812–1818.

RECEIVED for review June 8, 1989. Accepted September 5, 1989. This work was supported by Grant Number GM13326-21 from the National Institutes of Health.

Elemental Analysis Based on Chemiluminescence in the Laser Microprobe

Jianzhong Zhu and Edward S. Yeung*

Ames Laboratory—USDOE and Department of Chemistry, Iowa State University, Ames, Iowa 50011

Chemiluminescence produced by the reactions of Si, Ge, Al, and Cu atoms with F₂ or fluorine-containing compounds such as SF₆ and NF₃ was observed in laser-generated plumes. The emission spectra correspond to the individual monofluorides. The reaction of Si with SF₆ was examined, and the chemiluminescence intensity was found to be first order with respect to SF₆ pressure for low pressures. Chemiluminescence as an elemental detection method for laser microprobe analysis was evaluated. The limit of detection of Si was around 10 pg. The acoustic signal associated with the laser-generated plume was linearly related to the chemiluminescence intensity over 2 orders of magnitude. The acoustic signal can thus be used as an internal standard for chemiluminescence determination of elements, even though the amount of material vaporized is different for each laser pulse.

INTRODUCTION

Direct solid analysis to provide local concentrations and depth profiles of trace elements has become one of the important applications of lasers (1, 2). Because of the high irradiance, the laser microprobe is able to interrogate a variety of samples: electrically conductive or nonconductive. The ability to focus the beam to a diffraction-limited spot size allows two-dimensional profiling on the micrometer scale. Thus, the laser microprobe technique has been used for the identification of inclusions and for the analysis of elemental distributions in solid samples, such as alloys, semiconductors, wood, ores, polymers, ceramics, and glass (3-6).

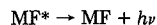
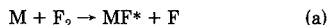
Laser microprobe analysis includes two processes: sample vaporization and signal detection. Upon irradiation, material is removed from the surface and a microplasma is formed. This contains atoms, ions, electrons, molecular fragments, and particles. Signals related to the analyte species in the plasma are then measured. Detection methods include mass spectrometry (7), atomic emission (8-10), atomic absorption (11, 12), Raman spectrometry (13), inductively coupled plasma atomic emission (14, 15), and atomic fluorescence (16), etc. Among them, direct atomic emission is probably the simplest and the most straightforward detection scheme, since analyte atoms and ions contained in the plume are excited without additional sophisticated instruments. Moreover, no sample-transfer process is involved, and thus the amount of sample vaporized can be reduced to a minimum (nanograms or even picograms) to obtain high spatial resolution.

Direct observation of the atomic emission from the plume, unfortunately, often suffers from high background due to the continuum plasma emission, and from self-absorption by the cooler vapor (ground-state atoms) at the edge of the plasma. Consequently, the sensitivity is poor (9). To improve that, cross-excitation by a spark discharge was developed, where a pair of electrodes is placed a few millimeters apart above the sample surface (8). This brings additional energy to excite the cooler wings of the plume and results in higher emission. Improvement of the signal-to-noise ratio (S/N) by a factor of 10 is achieved (9). However, some disadvantages are present, for example, contamination by the electrode im-

purities. The reproducibility was reported to be twice as bad because additional discharge fluctuation is introduced upon laser vaporization (9). The variation in the fraction of sample reaching the spark region has also contributed to the uncertainty. The mass sensitivity may also be affected by the sample-transfer efficiency (1).

A new detection method, chemiluminescence, is explored in this study for laser microprobe analysis. The chemiluminescence is produced by the reactions of the analyte atoms formed in the laser-generated plume with an ambient gas reagent. The potential advantages of this method are as follows. First, the chemiluminescence can be directly measured without additional excitation and without sample transfer. Therefore it is simple and potentially quite sensitive. Second, the emission bands are broad, so spectral selectivity is not as good as in atomic emission. However, chemical selectivity is introduced by the selection of the reagent gas. Third, the chemiluminescence may be spatially separated from the plasma emission, since the reactions most likely take place at the top periphery of the plume where the atoms encounter the gas reagents, while the plasma emission is mainly localized near the sample surface. Fourth, temporal discrimination can also be used because of the time delay of the reaction (collisions) and the longer lifetimes of the chemiluminescent species, while the plasma emission lasts only a very short time. It is hoped that one can eventually decrease the background to attain better signal-to-noise ratio by chemiluminescence detection vs atomic emission.

The spectroscopy of diatomic fluorides has been of long-standing interest due to both the fundamental reactions and the potential development of chemical lasers (17-21). The generally high reaction exothermicity frequently entails the appearance of electronically excited products and produces chemiluminescence. Numerous examples of reactions



where M is a metal atom have been studied. The emission spectra of many fluorides (AlF, CuF, GeF, SiF, etc.) were reported, where the atoms were usually generated by oven-heating or prepared in volatile forms (metal hydrides) (22-26). Therefore, it is our goal to explore fluoride chemiluminescence in a laser-generated plume. Hopefully, the study may provide further understanding of the reaction and potential use as a detection scheme in laser microprobe analysis.

Quantitation is an important consideration for surface analyses. However, many factors such as laser power, focusing, sample composition, and mechanical properties as well as sample surface conditions have contributed to the irreproducibility of the sampling process (27). Much effort has been made in recent years to improve the precision. Techniques including signal averaging, monitoring the laser power fluctuations or the size of the crater, use of standard material, and use of internal reference lines were employed (28-32). Recently, the acoustic wave generated in each laser shot has been used to correct for variations of the total amount of material evaporated (33). It was shown that variations in the intensity of atomic emission (without auxiliary electrodes) can

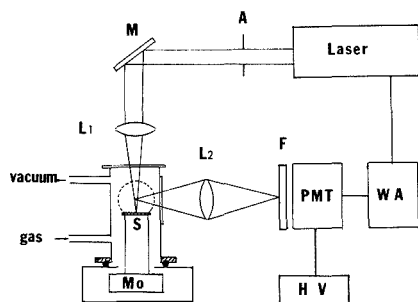


Figure 1. Experimental arrangement for chemiluminescence measurement in a laser-generated plume: A, aperture; M, mirror; L1 and L2, lens; S, sample; Mo, motor; F, filters; WA, waveform analyzer; HV, high voltage supply; PMT, photomultiplier tube. The dashed line indicates a microphone coupled from the back.

be normalized by the acoustic signals over 3 orders of magnitude, regardless of experimental conditions. So, the correlation between the chemiluminescence and the acoustic signals is also investigated here to evaluate the utility of the latter as an internal standard for quantitation.

EXPERIMENTAL SECTION

The schematic diagram of the experimental arrangement is shown in Figure 1. A pulsed excimer laser (Lumonics, Ottawa, Canada, Model Hyper EX 460) operating at the 308-nm XeCl transition was used. The size of the laser beam was confined by either a 6 or a 10 mm diameter aperture. The laser energy was directly regulated by varying the operating voltage and was measured by an energy ratiometer (Laser Precision, Utica, NY, Model Rj-7200) with an energy probe (Laser Precision, Model Rap-734) right after the aperture. The pulse duration was about 25 ns, and the pulse repetition rate was set typically at 1 Hz. The laser pulse-to-pulse fluctuation was found to be $\pm 2\%$ at an operating voltage of 20 kV. The reproducibility deteriorates to $\pm 5\%$ at the minimum operating voltage of 16 kV. The laser energies used varied from 0.5 to 5 mJ. The laser beam was focused onto the sample surface by a 5 cm diameter and 15 cm focal length UV lens, which has been mounted in a micrometer translational stage so that the focusing condition can be precisely adjusted.

The sample cell, made from a bar of 3 cm \times 3 cm \times 8 cm brass, has a 2.5 cm internal diameter \times 8 cm cylindrical chamber with three 2 cm diameter side windows. A 0.5 in. diameter condenser microphone (Knowles, Franklin Park, IL, Model BT-1759) was attached to one of the side windows to measure the acoustic signal. The top of the cell (where the laser beam is introduced) and the other two side windows, one for emission measurement and the other for visual observation, were sealed with 3 \times 3 \times 0.2 (cm) quartz plates by 5-min epoxy. The sample cell was mounted against an O-ring on the bottom to an aluminum chamber where a stepping motor (Hurst, Princeton, IN) was accommodated, so that the whole system could remain airtight. A finely adjustable needle valve was connected to a gas islet of the sample cell to control the gas pressure. The vacuum was maintained through a two-stage glass diffusion pump. The sample cut to 1 \times 1 \times 0.1 (cm) was placed on top of the axis of the motor and right in the middle of the cell. The stepping motor, driven by a motor controller (Hurst), was rotated at 0.1 deg/s to produce a new sample surface for each laser shot.

To ensure interference-free spectroscopy, several pure materials were used: silicon wafer (99.999%, SEH, Inc.), germanium wafer (99.99%, Semiconductor Processing Co.), copper (>99.5%), and aluminum (>99.5%). Three reference standard aluminum alloy samples were purchased (National Institute of Standards and Technology, SRM 1256a, SRM 1258, and SRM 1241a containing 9.2%, 0.78%, and 0.16% of Si, respectively). Samples were polished by No. 600 gritpaper and cleaned by methanol before use. F₂ (5% in Ne), SF₆ (99.999%), and NF₃ (99.9%) were examined as chemiluminescence reagents. The 5% SF₆ and 5% NF₃ were made with He as a buffer gas and stored in glass chambers.

All gases were obtained from Matheson (Seacaucus, NJ) and used as received.

The chemiluminescence emission was collected with a 1 in. diameter UV lens (focal length, 2.5 cm) to assure better collection efficiency. Only the region of the plume 10–20 mm above the sample surface was imaged on the photomultiplier tube (PMT) to achieve spatial resolution and to avoid saturation by the intense plasma emission which was confined to a few millimeters from the surface. The PMT (RCA Electron Optics, Mount Joy, PA, Model 1P28) used was more sensitive in the blue to UV region. The high-voltage power supply was normally set at 500 V. For SiF chemiluminescence detection, two 440-nm interference filters were used to collect the A²Σ–X²π band emission and to block most of the continuum background. The signal was directly sent to a waveform analyzer (Data Precision, Davers, MA, Model D6000) with a 1.4-kΩ terminator. The system capacitance is estimated to be less than 0.5 nF, providing a time constant below 0.5 μs. The peak area can be calculated in any selected time period by using the mathematical functions built into the waveform analyzer. The microphone signal was measured by an oscilloscope (Tektronix, Inc., Beaverton, OR, Model 7904 and 7A22) with a sensitive differential amplifier.

To acquire the chemiluminescence spectra, a monochromator (Heath Co., St. Joseph, MI, Model EU-700) was used to replace the filters. A 10 cm focal length borosilicate glass lens was used to match the *f*-number of the monochromator. The signal of the PMT was sent to a boxcar averager (EG&G Model 162 with Model 164 gated integrator) in which the amplifier was gated at 1–6 μs. An effective time constant of 1 s and a laser pulse rate of 20 Hz were used to obtain a reasonable signal-to-noise ratio. Plots were made on a strip chart recorder. The sample chamber and all the optical components were rigidly mounted on an optical table (Newport, Fountain Valley, CA, Model NRCSX-46).

RESULTS AND DISCUSSION

Chemiluminescence Spectra. Chemiluminescence of MX in the reaction of metal atoms with halogen or halogen-containing compounds is by no means a rare event. However, we believe this represents the first investigation in a laser-generated plume. When the sample cell was filled with 200 mTorr of reagent gas (5% SF₆ in He), a strong bluish violet emission was observed on the top periphery of the plume produced by a laser shot on a silicon wafer. As the reagent gas pressure decreased, the emission region gradually expanded to a few cubic centimeters in volume, and the emission became weaker and vanished for pressures around a few mTorr. When pure SF₆ was used, the expanded bluish violet emission could still be seen in the low-milliTorr range. As the pressure increased, the emission region was confined and became merged with the plasma emission zone, and eventually could not be distinguished from it. The use of NF₃ as the reagent gas led to no observable differences from SF₆. However, the use of F₂ (5% in Ne) showed a weaker emission, although the same color and similar pressure dependence were obtained. A reddish band was also present just above the plasma region, the intensity of which increased with increasing Ne pressure, that was identified as the Ne atomic emission (632 nm) since it also appeared in pure Ne buffer gas. Germanium sample exhibits almost the same phenomenon as described above. However, the bluish violet emission could not be observed in either aluminum or copper samples in the presence of SF₆, NF₃, or F₂. Instead, a pale yellow emission was observed for aluminum samples when the three gases were used, and the intensity was in the order of NF₃, F₂, and then SF₆. The green atomic emission was predominant in copper.

The fact that the bluish violet emission was not observed in aluminum and copper samples can exclude the reagent gases themselves as the corresponding emitters. If the chemiluminescence was produced by dissociation or excitation of the reagent gases in the laser plasma, the chemiluminescence will not depend on the solid media as long as a laser plasma was created. Since large amounts of reactive atoms are produced

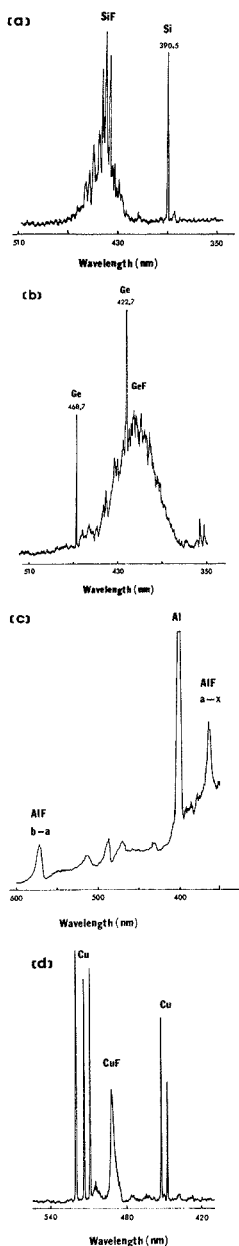


Figure 2. Chemiluminescence spectra of metal monofluorides (a) SiF, (b) GeF, (c) AlF, (d) CuF. Resolution: (a, b) 0.3, (c) 3, and (d) 0.6 nm.

in the laser plume, it is quite clear that the atoms may react with the reagent molecules to yield electronically excited products.

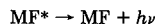
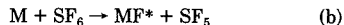
Figure 2 shows the total emission spectra (i.e. without time gating) responding to (a) Si, (b) Ge, (c) Al, and (d) Cu in the presence of SF₆. In all cases, the spectrometer was scanned

in the wavelength region of 350–600 nm, but only the regions with chemiluminescence were shown in the figures. The emission spectra appeared similar when F₂ or NF₃ was used as reagent. Since many of the metal oxides and metal fluorides possessing chemiluminescence reactions have been studied by beam-gas experiments, the emission bands can be easily identified by comparing with the literature. Their assignments are as follows: (a) SiF (A²Σ⁺–X²π), (b) GeF (A₂Σ⁺–X²π), (c) AlF (a³π–X¹Σ⁺, b³Σ⁺–a³π), and (d) CuF (C¹π–X¹Σ) (17, 19, 22, 23, 25, 26). It should be noted that all reactions produced monofluoride emission.

One of the important features of laser-generated plumes is the extremely high temperature environment where large populations of species with high kinetic energy and reactive metastables can occur. Therefore, the study of chemiluminescence in a laser-generated plume may show interesting reaction pathways and unusual high energy state transitions. In a beam-gas experiment, Rosano and Parson were not able to observe the electronic transitions of monofluoride in Si + SF₆ reaction, where the Si atoms were thermally generated (34). Instead they reported the transition of dihalides in the reactions of Si, Ge, and Sn with SF₄, SF₆, and ClF₃. It is not surprising since the formation of difluorides is highly exothermic (around 130 kcal/mol), enough to reach the ³B₁ state of MF₂ around 75 kcal/mol.

From the reported bond strengths, the reactions of Si and Ge with SF₆ are exothermic by 67 and 47 kcal/mol, and with SF₄ are exothermic only by 44 and 24 kcal/mol, respectively (35). The energies required to reach the first electronically excited A state of SiF and GeF are 65 and 66 kcal/mol. Thus, the transitions of monofluorides may not be observed.

In a laser-generated plume, however, the large kinetic energy and the existing metastable states will provide extra energy, so the reaction schemes



are energetically accessible. In fact, Verdasco et al. have studied the reaction of metastable Ca*(³P) with SF₆ and observed A²π and B²Σ⁺ excitation of CaF. There, the metastable atoms were produced by heating and then further excited by a direct current discharge (36).

In particular, it is worth noting that the spectra of SiF obtained here show vibrational structure, and the highest peak corresponds to the ν(0,0) transition. This agrees with ref 25 and 26, but is in variance with ref 17, where one finds an essentially continuous spectrum. This is because the excitation and relaxation mechanisms in the different studies are different.

Reagent Gas Pressure Dependence. If the chemiluminescence is first order relative to the reagent gas pressure, it can be described by the following equation:

$$I \approx pe^{-\alpha p} \quad (1)$$

where *I* is the integrated intensity of the emission, *p* is the reagent gas pressure, and *α* is an attenuation factor related to the total cross section for removal of atoms before entering the viewing region (17, 37, 38). The emission of SiF (440 nm) was studied as a function of SF₆ pressure over 0.5–30 mTorr (10–660 mTorr, 5% SF₆ in He). The plot of emission intensity against the pressure of SF₆ is shown in Figure 3. The solid curve represents the best fit curve of eq 1, with an *α* value of 0.1. These results indicate the reaction is first order relative to the reagent gas pressure.

The chemiluminescence temporal peak positions were also evidence supporting reaction scheme b. Figure 4 shows a set of SiF emission signal traces for pressures of 10⁻⁴ to 5 Torr (5% SF₆). As the pressure decreases, the peak maximum shifts

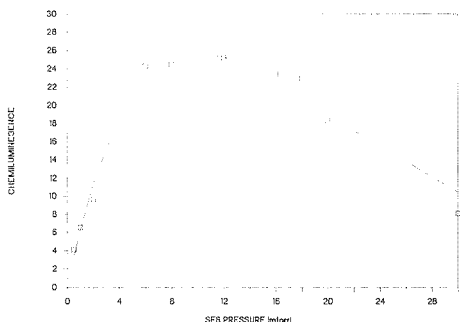


Figure 3. Chemiluminescence signal of SiF vs SF_6 pressure: (□) experimental data; (solid curve) simulation of eq 1.

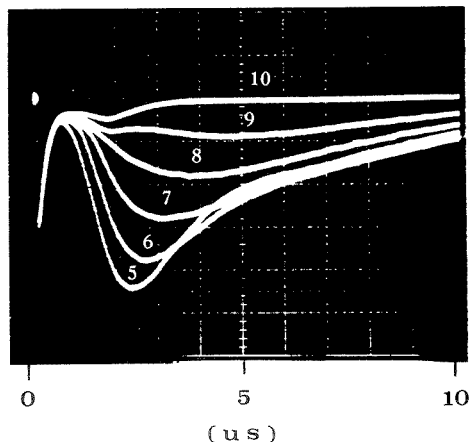
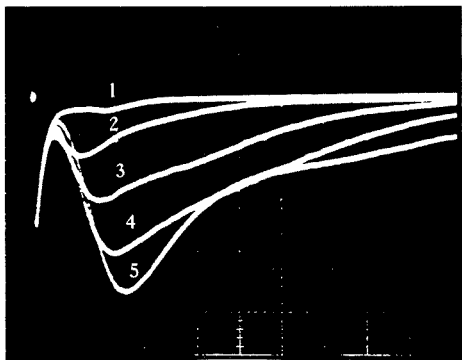


Figure 4. Peak shift of SiF chemiluminescence with pressure (SF_6 5%): trace 1, 5 Torr; trace 5, 0.1 Torr; trace 10, 10^{-4} Torr.

from 1 to 6 μs . The peak corresponds to the amount of SiF* in the 1–2-cm viewing zone above the surface. This shift is expected if reaction is directly with SF_6 . At high pressures, most of M reacted before entering and only small amounts of the luminescence species appeared in the viewing window, resulting in a small, early peak. At low pressures, many atoms

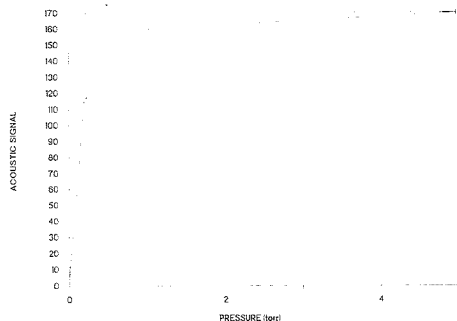
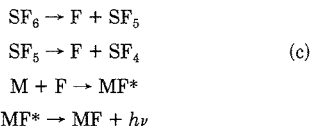


Figure 5. Dependence of acoustic signal on buffer (He) gas pressure.

passed into the window without reaction, resulting in a late, broad peak. The signal at the left edge of each trace is the plasma emission. Since that is well separated from the chemiluminescence, temporal discrimination can be implemented.

Laser Power Dependence. Since the reagent gas may dissociate in the laser plasma before the chemiluminescence reaction, the following mechanism is still possible:



If this mechanism dominates, the emission intensity should have a high-order dependence on laser power, because both the silicon and the reagent species are produced by the laser. However, if the chemiluminescence signal is directly proportional to the amount of silicon atoms, this reaction scheme must be unimportant.

In order to account for the amount of material generated at different laser powers, the acoustic signal was utilized as an internal standard. This has been demonstrated earlier for atomic emission measurements (33).

Figure 5 shows the acoustic signal dependence on buffer gas pressure. The data continues to 72 Torr with the acoustic signal staying constant at 170 units. This indicates that the gas coupling efficiency of the sound wave to the microphone has reached a plateau at around 1 Torr. Figures 3 and 5 show that the reagent gas, SF_6 , must be mixed with an inert gas to optimize both chemiluminescence and acoustic detection. Figure 6 presents the typical acoustic waveforms generated by a 3-mJ laser pulse at cell pressures of (a) 200 mTorr and (b) 50 Torr. Sound can be transmitted by gas collisions and also by the solid media. At low pressures, the solid media (sample, sample mount, and cell body) transfer should be prevalent. The nice harmonic decay is characteristic of the microphone diaphragm, slightly damped. The acoustic frequency (ringing pattern) was found to be independent of cell pressures at low pressure. In contrast, the waveform became irregular at high pressures. It can be explained on the basis of sound wave reflection, which is complicated by the irregular cell geometry. The gas coupling signal is very likely added to the solid transferred signal as the composite value observed in b. The first peak appeared at about 90 μs , which is invariant when the cell pressure is changed. This peak height was thus used in this study as the acoustic signal.

Figure 7 is a plot of the chemiluminescence intensity of SiF (440 nm) vs acoustic signal for a cell pressure of 150 mTorr, where chemiluminescence was determined by area and the acoustic signal was measured as the first peak height. Figure

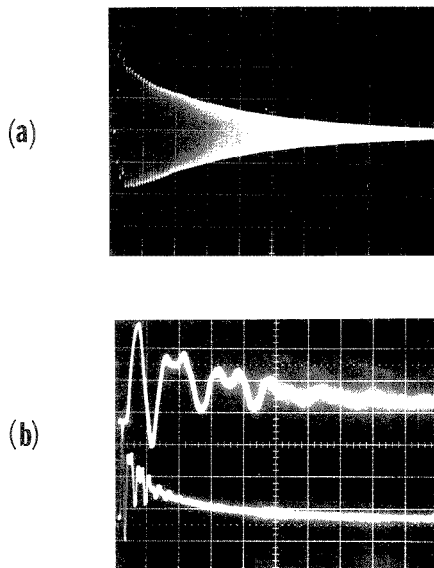


Figure 6. Acoustic wave for (a) cell pressure of 200 mTorr ($X = 1$ ms per division, $Y = 20$ mV) and (b) cell pressure of 50 Torr (top, $X = 0.5$ ms; bottom, $X = 0.1$ ms, $Y = 50$ mV).

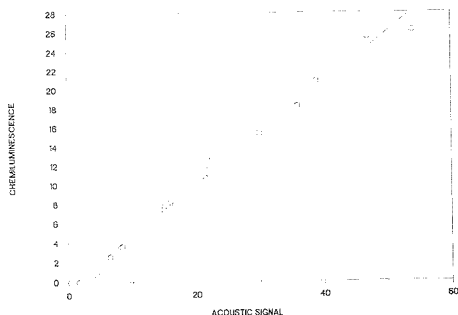


Figure 7. Chemiluminescence signal of SiF vs acoustic signal at a cell pressure of 150 mTorr.

7 manifests a linear relation over a nearly 80-fold change in chemiluminescence, except at low signal levels where uncertainties in integrating the signal become large. For 17 data points between 0.2 and 54 mV for the acoustic signal, a correlation $r^2 = 0.992$ was found. The results have two implications. First, the luminescence was produced by the reaction of atoms with reagent gas directly and not with F atoms dissociated from the fluorine-containing compounds. The data in Figure 7 was produced over a large range of laser powers, and the chemiluminescence signal only depends on the amount of Si produced. Second, the acoustic signal may be used as an internal standard in chemiluminescence detection for quantitation to improve precision.

Laser Microprobe Analysis. In comparison with atomic emission, chemiluminescence occurs after a relatively long time delay. The Si atomic emission peak occurs at about 1.2 μ s with peak width of 0.6 μ s, while chemiluminescence lasts for about 30 μ s. It was found that the area determined by integrating from 3 μ s onward showed better signal-to-noise ratio. An improvement of S/N of 6 was obtained over atomic

emission, when the Si (390.5 nm) atomic emission and SiF (440 nm) chemiluminescence were compared. The chemiluminescence background was measured with inert gas but without SF₆.

We studied the chemiluminescence determination of Si in aluminum alloys with acoustic signal as an internal standard. For the SRM samples studies, linearity was found over the range 10%–0.1% Si. Two 440-nm interference filters were used, and the cell pressure was maintained at 150 mTorr with 5% SF₆ in He. The laser pulse energy used was 2.7 mJ so that the amount of material vaporized could be kept in the low nanograms. The volume of material removed was estimated by measuring the size of the crater with an electron microscope, and the weight removal was calculated from the density of the sample. Twenty nanograms of sample is typically removed within a range of $\pm 50\%$, for laser energies of 2.7 mJ $\pm 5\%$. The mass detection limit of Si was in the 10^{-11} g range based on the 0.1% concentration limit of detection estimated from direct observation (oscilloscope trace). These results are very good in laser microprobe analysis. They are worth comparing with atomic absorption detection of Si, in which the limits of detection reported were only 1% and 10^{-7} g. Quantitation by chemiluminescence with acoustic signal normalization was quite satisfactory at approximately $\pm 5\%$, in contrast to $\pm 20\%$ – 30% without normalization.

LITERATURE CITED

- (1) Laqua, K. In *Analytical Laser Spectroscopy*; Omenetto, N., Ed.; Wiley: New York, 1979; Chapter 2.
- (2) Dittrich, K.; Wennrich, R. *Prog. Anal. At. Spectrosc.* **1984**, *7*, 139–198.
- (3) Korolev, N. V.; Faivilevich, G. A. *Zavodsk. Lab.* **1964**, *30*, 557–558.
- (4) Klein, P.; Banatz, J. *Frensenius' Z. Anal. Chem.* **1981**, *308*, 283–286.
- (5) Delouie, E.; Floy, J. F. *Chem. Geol.* **1982**, *37*, 192–202.
- (6) Ryan, J. R.; Ruh, E.; Clark, C. B. *Am. Chem. Soc. Bull.* **1966**, *45*, 260–262.
- (7) Conzemius, R. J.; Capellen, J. M. *Int. J. Mass Spectrom. Ion Phys.* **1980**, *34*, 194–271.
- (8) Hein, S. J.; Piepmeier, E. H.; *TRAC, Trends Anal. Chem. (Pers. Ed.)* **1988**, *7*, 137–142.
- (9) Dejjick, W. V.; Balke, J.; Maessen, F. J. M. *J. Spectrochim. Acta* **1979**, *34B*, 359–369.
- (10) Talmi, Y. *Anal. Chim. Acta* **1981**, *127B*, 71–85.
- (11) Quentmeier, A.; Laqua, K.; Hagenah, W. D. *Spectrochim. Acta* **1980**, *35B*, 139–154.
- (12) Mossotti, V. G.; Laqua, K.; Hagenah, W. D. *Spectrochim. Acta* **1967**, *23B*, 197–206.
- (13) Pasteris, J. D.; Kuehn, C. A.; Bodnar, R. J. *Econ. Geol.* **1986**, *81*, 915–920.
- (14) Ishizuka, T.; Uwamino, Y. *Spectrochim. Acta* **1983**, *38B*, 519–525.
- (15) Thompson, M.; Goulter, J. E.; Sleper, F. *Analyst* **1981**, *106*, 32–39.
- (16) Dreyfus, R. W.; Kelly, R.; Walkup, R. E. *Appl. Phys. Lett.* **1986**, *49*, 1478–1482.
- (17) Rosano, W. J.; Parson, J. M. *J. Chem. Phys.* **1983**, *76*, 2696–2709.
- (18) Luria, M.; Eckstrom, D. J.; Edelstein, S. A.; Perry, B. E.; Benson, S. W. *J. Chem. Phys.* **1976**, *64*, 2247–2252.
- (19) Brayman, H. C.; Fishell, D. R.; Cool, T. A. *J. Chem. Phys.* **1980**, *73*, 4247–4259.
- (20) Rosenwaks, S. *Chem. Phys. Lett.* **1979**, *64*, 352–359.
- (21) Schwenz, R. W.; Parson, J. M. *J. Chem. Phys.* **1982**, *76*, 4439–4444.
- (22) Rosenwaks, S. *J. Chem. Phys.* **1976**, *65*, 3668–3673.
- (23) Baltayan, O.; Hartmann, F.; Pebay-Peyroula, J. C.; Sadeghi, N.; *Chem. Phys.* **1984**, *120*, 123–129.
- (24) Schwenz, R. W.; Parson, J. M. *J. Chem. Phys.* **1980**, *73*, 259–267.
- (25) Armstrong, R. A.; Davis, S. J. *J. Chem. Phys.* **1979**, *71*, 2433–2444.
- (26) Conner, C. P.; Stewart, G. W.; Lindsay, D. M.; Gole, J. L.; *J. Am. Chem. Soc.* **1977**, *99*, 2540–2544.
- (27) Webb, M. S. W.; Webb, R. J. *Anal. Chim. Acta* **1971**, *55*, 67–75.
- (28) Kirchheim, R.; Nagorny, U.; Maier, K.; Tolg, G. *Anal. Chem.* **1976**, *48*, 1505–1508.
- (29) Peppers, N. A.; Scribner, E. J.; Alterton, L. E.; Honey, R. C.; Beatrice, E. S.; Harding-Barlow, I.; Rosan, R. C.; Glick, D. *Anal. Chem.* **1968**, *40*, 1178–1182.
- (30) Morton, K. L.; Nohn, J. D.; Macken, B. S. *Appl. Spectrosc.* **1973**, *27*, 109–117.
- (31) Piepmeier, E. H. In *Analytical Applications of Lasers*; Piepmeier, E. H., Ed.; Wiley: New York, 1986; Chapter 19.
- (32) Carr, J. W.; Horlick, G. *Spectrochim. Acta* **1982**, *37B*, 1–15.
- (33) Chen, G.; Yeung, E. S. *Anal. Chem.* **1988**, *60*, 2258–2263.
- (34) Rosano, W. J.; Parson, J. M. *J. Chem. Phys.* **1986**, *84*, 6250–6260.
- (35) James, E. H. *Inorganic Chemistry*, 3rd ed.; Harper & Row: New York, 1983.
- (36) Verdasco, E.; Rabanos, V. S.; Aoz, F. J.; Urena, A. G. *J. Phys. Chem.* **1987**, *91*, 2073–2075.

- (37) Dickson, C. R.; George, S. M.; Zare, R. N. *J. Chem. Phys.* 1977, 67, 1024-1030.
 (38) Ottinger, C.; Zare, R. N. *Chem. Phys. Lett.* 1970, 5, 243-248.

RECEIVED for review July 10, 1989. Accepted August 28, 1989.

The Ames Laboratory is operated by Iowa State University for the U.S. Department of Energy under Contract W-7405-Eng-82. This work was supported by the Director of Energy Research, Office of Basic Energy Sciences, Division of Chemical Sciences.

Measurement of the Rate of Oxidation of Iodide by Iron(III) Using Solvent Extraction

Lawrence Amankwa and Frederick F. Cantwell*

Department of Chemistry, University of Alberta, Edmonton, Alberta, Canada T6G 2G2

A rapid-stir cell with porous Teflon phase separator and spectrophotometric detector is used to monitor the extraction of I_2 into chloroform during the oxidation of I^- by Fe^{3+} . The observed absorbance (A) versus time (t) curve includes contributions from the chemical reaction itself, from mass transfer of iodine, and from instrument band broadening. Mathematical deconvolution of the measured A versus t curve with an impulse response function obtained by injecting I_3^- makes it possible to obtain the curve for the chemical reaction. (Pseudo)-first-order rate constants were measured as a function of $[I^-]^2$ to obtain the third-order rate constant, which agreed with literature values. (Pseudo)-first-order rate constants as high as 0.4 s^{-1} were measured, and it is estimated that reducing instrument band broadening would permit the measurement of first order rate constants as high as 2 s^{-1} (i.e. $t_{1/2} \approx 0.4 \text{ s}$).

INTRODUCTION

Solvent extraction of a colored ion-pair (1, 2) or metal-ligand complex (3) followed by a photometric measurement is an important technique in both manual and automated (4) analytical determinations. Solvent extraction is also extensively used in industry, especially in the recovery and purification of metals (5). The synthetic technique of "phase-transfer catalysis" is a third major area in which solvent extraction principles are important (6). In all of these cases a chemical reaction accompanies the transfer of solute from one phase to the other. The chemical reaction can be *homogeneous*, if it occurs in one of the bulk liquid phases, or it can be *heterogeneous*, if it occurs at the liquid-liquid interface and involves at least one interfacially adsorbed reactant (7). It is important to be able to measure the rate of the chemical reaction in all of these systems.

In a typical experiment, the concentration of product in the organic phase, C_o , is monitored as a function of time, t . The observed C_o vs t curve reflects three independent processes: the chemical reaction rate, the solute mass transfer rate, and the instrument band broadening (8, 9). Expressed in terms of variances (i.e. second statistical moments, σ^2) the variance of the observed, overall curve, σ_o^2 , is given by

$$\sigma_o^2 = \sigma_R^2 + \sigma_M^2 + \sigma_I^2 \quad (1)$$

where σ_R^2 is due to the chemical reaction, σ_M^2 is due to mass transfer, and σ_I^2 is due to instrument band broadening (9). Thus, in order to directly measure the rate of the chemical reaction, it is necessary to have σ_R^2 much greater than $\sigma_M^2 +$

σ_I^2 . If σ_R^2 is only slightly greater, equal to, or even smaller than $\sigma_M^2 + \sigma_I^2$, then it is necessary to use mathematical deconvolution in order to separate the chemical reaction contribution from the contributions of mass transfer and instrument band broadening. However, deconvolution will be successful only if σ_R^2 is not too much smaller than $\sigma_M^2 + \sigma_I^2$. Since σ_R^2 is inversely related to the rate of the chemical reaction, it is a general conclusion that in order to measure the rates of faster chemical reactions it is necessary to design the experiment so as to reduce $\sigma_M^2 + \sigma_I^2$.

The "rapid-stir" experiment in which one phase is dispersed in the other under turbulent conditions is a particularly attractive technique to measure the rates of relatively fast homogeneous chemical reactions because the mass transfer rate can be made quite high (8, 10). In fact it has been found that in a well-designed rapid-stir device with a small hold-up volume, σ_M^2 can be made an order of magnitude smaller than σ_I^2 so that instrumental band broadening, rather than mass transfer, imposes the upper limit on the chemical reaction rate that can be accurately measured.

In the present work we have used a previously described rapid stir cell with remote sample injection, porous Teflon phase separator, and low hold-up volume (9) to study the rate of the homogeneous oxidation of I^- by Fe^{3+} in the aqueous phase, by monitoring the rate of appearance of I_2 in the chloroform phase. One purpose of this study is to discover the upper limit of reaction rate that can be measured with this improved rapid-stir apparatus.

EXPERIMENTAL SECTION

Apparatus. The rapid-stir cell has previously been described and characterized (9). The phase separator consisted of two layers of 1.3 cm diameter by 0.0055 in. thick, 5-10 μm pore size porous Teflon (Zitex, No. E60-6122, Chemplast, Wayne, NJ). The cell was thermostated at $20.0 \pm 0.1 \text{ }^\circ\text{C}$. The variable wavelength photometric detector (UV 50, Varian Associates) was set at 520 nm to monitor the absorbance of the chloroform phase flowing through it. The detector signal was acquired on an IBM-XT microcomputer which was interfaced to the detector via a Lab Master ADC interface board (TM-40-PCL, Tecmar, Cleveland, OH).

Reagents and Solvents. All water was demineralized, distilled, and finally distilled over alkaline permanganate. All solvents and chemicals were reagent grade. Chloroform (Caledon Laboratories, Ltd.) was washed with distilled water prior to use. A 1.00 M potassium iodide stock solution was prepared in water that had been purged with nitrogen. Solutions of 1.00 M KNO_3 , 0.100 M $Fe(NO_3)_3$, and 0.20 M HNO_3 were prepared in water. A solution of 0.0166 M KI_3 was prepared by combining 5.00 mL of 0.100 M $Fe(NO_3)_3$, 5.00 mL of 1.00 M KI , 2.00 mL of 0.20 M HNO_3 , and 3.00 mL of water.

Table I. Data and Results for the Measurement of (Pseudo)-First-Order Rate Constant (Terms Defined in Text)

$[\Gamma^-]_{t=0}$, M	$[\Gamma^-]_{t=\infty}$, M	$[\Gamma^-]_{t=d}$, M	$\alpha_{Fe^{3+}}$	F_0^0	$A_{t=\infty}$	% reaction at $t = d$	first-order rate constant, s^{-1}
0.0200	0.019	0.0199	0.84	0.84	0.40	10	0.0057 ± 0.0002
0.0500	0.049	0.0497	0.85	0.67	0.35	26	0.0299 ± 0.0016
0.0800	0.079	0.0795	0.87	0.56	0.29	46	0.0695 ± 0.0023
0.100	0.099	0.0995	0.88	0.51	0.27	54	0.133 ± 0.001
0.150	0.149	0.1492	0.90	0.41	0.21	76	0.259 ± 0.001
0.200	0.199	0.1991	0.93	0.34	0.17	90	0.423 ± 0.037

^a $[\text{Fe(III)}]_{t=0} = 1.00 \times 10^{-3}$ M for all experiments.

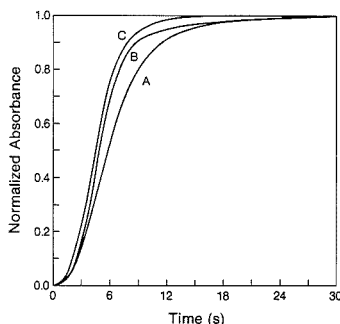


Figure 1. Absorbance in the chloroform phase vs time: (A) for injection of Fe^{3+} into 0.200 M Γ^- , (C) for injection of I_3^- into 0.200 M Γ^- , and (B) after deconvolution of curve A with the IRF from curve C. Each curve is normalized by its own $A_{t=\infty}$ value.

Procedure. The chemical reaction between Γ^- and Fe^{3+} was studied as follows: First, 100 mL of chloroform was placed in the extraction cell. Then aqueous stock solutions of KI, KNO_3 , and HNO_3 were pipetted into the cell along with water to give 99 mL of a 0.050 M HNO_3 aqueous phase that had an ionic strength of 0.300 M and contained either 0.020, 0.050, 0.080, 0.100, 0.150, or 0.200 M KI. While the solutions were stirred at 2300 rpm and the chloroform phase was pumped through the detector at 1.0 mL/min, a volume of 1.00 mL of aqueous 0.100 M $\text{Fe}(\text{NO}_3)_3$ was injected to initiate the reaction.

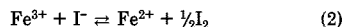
In another experiment the initial aqueous and organic phases in the extraction cell were the same as described above, but the solution injected was 1.00 mL of aqueous 0.0166 M KI_3 . Data from this experiment were used to generate the impulse response function (IRF) required for deconvolution.

Deconvolution. All observed absorbance (A) vs time (t) profiles exhibited a distorted sigmoidal shape (e.g. Figure 1). Deconvolution was performed to obtain the A vs t profile associated with only the chemical reaction between Γ^- and Fe^{3+} , free of contributions from both mass transfer of I_2 and instrument band broadening. The process was as follows: The sample A vs t profile (e.g. Figure 1A) was differentiated and smoothed to obtain a peak. Next, the A vs t profile from the injection of KI_3 (e.g. Figure 1C) was inverted as described previously (8) in order to obtain the IRF. Fast Fourier transforms (FFT's) were taken of the peak-shaped sample function and of the IRF, the former was divided by the latter and the resultant was subjected to inverse FFT to yield the peak-shaped function which was then integrated to give the desired A vs t profile (e.g. Figure 1B). Calculations were performed on an IBM-XT microcomputer using programs written in ASYST (MacMillan Software Co.).

RESULTS AND DISCUSSION

The oxidation of Γ^- by Fe^{3+} has been chosen for study for several reasons: (i) it has a complex reaction mechanism exhibiting a third-order rate law and a retardation effect but, nevertheless, can be made (pseudo) first order under suitable experimental conditions; (ii) one product (I_2) can be extracted into chloroform; (iii) the (pseudo)-first-order rate constant can be varied over a range of values.

Oxidation of Γ^- by Fe^{3+} . The thermodynamic equilibrium constant for the reaction



at zero ionic strength is 3.8×10^2 at 25 °C (11). This corresponds to a concentration equilibrium constant at ionic strength 0.3 of about 1.0×10^2 . At the excess concentrations of Γ^- used in the present work, reaction 2 can be considered to be quantitative at equilibrium so that only the forward reaction rate needs to be considered. Also, reaction 2 is followed by a very rapid reaction to form I_3^- ion



for which the second-order forward rate constant is about 10^{10} $\text{L}\cdot\text{mol}^{-1}\cdot\text{s}^{-1}$ (12). In the presence of chloroform I_2 extracts from the aqueous phase



Reactions 3 and 4 define the distribution of iodine in the zero oxidation state, I^0 , when the system has reached equilibrium. The absorbances of the chloroform phase that are observed when equilibrium has been reached ($A_{t=\infty}$) are presented in column 6 of Table I. The equilibrium constants for reactions 3 and 4 were measured as follows. It can be shown that

$$\frac{1}{A_{t=\infty}} = \frac{1 + K_{D,\text{I}_2}}{K_{D,\text{I}_2} A_{\text{MAX}}} + \frac{K_{t,\text{I}_3} [\Gamma^-]_{t=\infty}}{K_{D,\text{I}_2} A_{\text{MAX}}} \quad (5)$$

where K_{D,I_2} is the distribution coefficient for I_2 between chloroform and aqueous phase corresponding to reaction 4, K_{t,I_3} is the formation constant for I_3^- in the aqueous phase corresponding to reaction 3, and A_{MAX} is the absorbance that would be obtained if all of the I^0 formed at equilibrium were present as I_2 in the chloroform phase. Equation 5 suggests that a plot of $1/A_{t=\infty}$ vs $[\Gamma^-]_{t=\infty}$ will be linear. For the data in Table I such a plot was linear with a slope of 19.0 ± 0.9 standard deviation and an intercept of 2.0 ± 0.1 standard deviation. The ratio of the slope to the intercept of this plot is the quantity $K_{t,\text{I}_3}(1 + K_{D,\text{I}_2})^{-1}$. We independently measured the value of K_{D,I_2} to be 75 ± 2 by equilibrating a 5×10^{-4} M solution of I_2 in chloroform with a 0.050 M HNO_3 aqueous phase that had an ionic strength of 0.300 and contained no Γ^- . Combining this value of K_{D,I_2} with the value of 9.5 for the ratio of slope/intercept for the above plot yields a value of $(7.2 \pm 0.7) \times 10^2$ for K_{t,I_3} . This is in agreement with the literature value of 7.4×10^2 at 20 °C (13).

The rate of the oxidation, reaction 2, depends on ionic strength, pH, presence of complexing anions, and concentration of Fe^{2+} , as well as on concentrations of Fe^{3+} and Γ^- (11, 14–16). At $[\text{H}^+]$ above about 0.02 M the rate is independent of pH (16). The observed rate law is

$$-\frac{d[\text{Fe}^{3+}]}{dt} = \frac{k_1[\text{Fe}^{3+}][\Gamma^-]^2}{1 + k_2[\text{Fe}^{2+}]/[\text{Fe}^{3+}]} \quad (6)$$

in which k_1 is a constant and k_2 depends on the concentration

of I^- (13, 15). If the rate of reaction 2 is measured by monitoring the rate of formation of I_2 , then it can be shown, by rearranging eq 6, and employing the stoichiometric relationship in eq 2, that

$$\frac{d[I^0]}{dt} = \frac{k_1}{1 + R} [I^-]^2 ([I^0]_{t=\infty} - [I^0]) \quad (7)$$

where

$$R = k_2 [Fe^{2+}] / [Fe^{3+}] \quad (8)$$

and $[I^0]_{t=\infty}$ is the concentration of all species of iodine in the zero oxidation state formed upon complete reaction. Because k_2 is a function of $[I^-]$, R depends on $[I^-]$ as well as on $[Fe^{2+}] / [Fe^{3+}]$. Therefore, kinetic studies of this reaction are usually done by measuring its "initial rate", which is always found strictly to follow a third-order rate law because $R \ll 1$ at the beginning of the reaction.

Since reaction 3, which occurs after reaction 2, is fast, it has no effect on the overall reaction rate. Also the rate of extraction of I_2 , once formed, is what constitutes the *mass transfer rate* in this system and is not part of the chemical reaction rate.

In the experiments discussed below the initial concentration of $Fe(III)$ is always 1.00×10^{-3} M while the initial concentration of I^- is varied from 0.0200 to 0.200 M (Table I). Although the chemical reaction takes place homogeneously in the aqueous phase, its rate is measured by photometrically monitoring the concentration of I_2 in the chloroform phase. The fraction of I^0 formed which is extracted, F_{I^0} , is given by

$$F_{I^0} = \frac{K_{D,I_2}}{1 + K_{D,I_2} + K_{t,I_2}[I^-]} = \frac{75}{1 + 75 + (7.2 \times 10^2)[I^-]} \quad (9)$$

The quantity F_{I^0} varies from 0.84 to 0.34 for $[I^-]$ between 0.0200 and 0.200 M, respectively, as shown in column 5 of Table I. For purposes of measuring the rate of reaction 2 it does not matter what fraction of iodine extracts, but it is important that the fraction extracted remains constant during a given reaction. Because I^- is present in excess, this condition is met. For example, in the worst case, with the lowest initial concentration of I^- , the fraction extracted varies from the value of 0.84 by less than 1% relative, over the whole course of the reaction.

There is a further consequence of the fact that $[I^-]$ remains constant during the reaction. When $R \ll 1$, eq 7 has the form of a (pseudo)-first-order rate law with the rate constant $k_1[I^-]^2$.

Extraction Rate. If the time required for mass transfer of I_2 were zero (which it is not), then the rate of change of I_2 concentration in chloroform $d[I_2]_o/dt$ would be the same as the rate of change of I^0 in the whole system, $d[I^0]/dt$. Since I_2 is the only light-absorbing species in chloroform, the rate of change of absorbance (A) in the chloroform phase is also a measure of the rate of reaction 2 and dA/dt can be substituted for $d[I^0]/dt$. The result of deconvolution is to "remove" both the effect of the time required for mass transfer of iodine and the effect of instrument band broadening. Thus, dA/dt for the deconvolved absorbance vs time data is a measure of the rate of the chemical reaction 2. Curve B in Figure 1 shows the deconvolved A vs t profile associated with the chemical reaction carried out in the presence of 0.200 M I^- . In Figure 2, Curves A through F are the deconvolved A vs t profiles for the chemical reaction carried out in the presence of various $[I^-]$. Each curve in Figure 2 has been normalized by dividing all of its absorbance values by its equilibrium absorbance ($A_{t=\infty}$).

The upward concave shape seen during the first couple of seconds in these profiles probably arises, at least in part, as an artifact of smoothing the observed curve before taking its

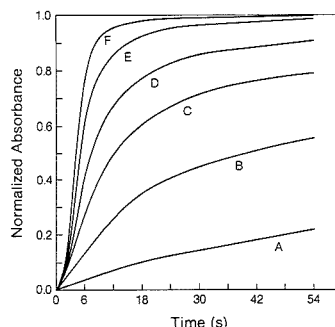


Figure 2. Absorbance in the chloroform phase vs time for the chemical reaction (after deconvolution). Concentration of I^- is (A) 0.020, (B) 0.050, (C) 0.080, (D) 0.100, (E) 0.150, and (F) 0.200 M. Each curve is normalized by its own $A_{t=\infty}$ value.

derivative and deconvolving it. Smoothing was necessary since noise has a deleterious effect on deconvolution. The upward concave curvature might also arise in part from an uncompensated lag time associated with diffusion through the Nernst diffusion layer (8, 9), as follows: The extraction is occurring in a "mixed regime" in which the extraction rate is controlled to a significant extent by both the chemical reaction rate and the mass transfer rate. When Fe^{3+} is injected it mixes rapidly by convection and coalescence/redispersion with the *bulk* liquid in the dispersed aqueous phase drops. There it begins both to react with I^- in the bulk phase and to diffuse into the stagnant Nernst film, where it also reacts with I^- . Thus I_2 is produced not only in the bulk aqueous phase but also in the Nernst film. In the presence of excess I^- the value of the (pseudo)-first-order rate constant does not depend on the local $[Fe^{3+}]$, so that the overall rate of production of I_2 in the aqueous drop is independent of how much of the reaction occurs in bulk phase and how much in the Nernst film. However, deconvolution employs an IRF corresponding to extraction of I_2 which comes from injected aqueous KI_3 . This IRF should compensate for the time required for I_2 produced in the *bulk* aqueous phase to diffuse across the Nernst film, under both steady-state and non-steady-state (i.e. lag time) conditions but might not correctly compensate for I_2 produced in the Nernst film. The net effect could be an additional uncompensated lag time. Whatever its origin, the upward concavity in the early part of the deconvolved A vs t profile precludes the use of data from the very early part of the reaction.

In Figure 3, curves A through F are plots of $\ln(A_{t=\infty}(A_{t=\infty} - A)^{-1})$ vs t for the corresponding data in Figure 2. For a first-order chemical reaction such a plot would be linear. The curves in Figure 3 are characterized by three sections. The initial upwardly concave section in the first few seconds arises for reasons discussed above in connection with Figure 2 and does not contain readily usable information. The second section, seen at longer times, is linear and corresponds to the (pseudo)-first-order rate of reaction 2 that is observed when $R \ll 1$. In column 8 of Table I are presented the values of the (pseudo)-first-order rate constant obtained at various $[I^-]$.

The third section of the curves in Figure 3 which is observed at still longer times is characterized by a downward curvature. In columns 1, 2, and 3 of Table I are presented the values of $[I^-]_{t=0}$, $[I^-]_{t=\infty}$, and $[I^-]_{t=d}$, which correspond respectively to the initial concentration, the concentration when the reaction is completed, and the concentration at time d , above which the curves in Figure 3 exhibit significant downward curvature. Comparison of the *squares* of these iodide concentrations, as required by eq 7, shows that the deviation from (pseudo)-

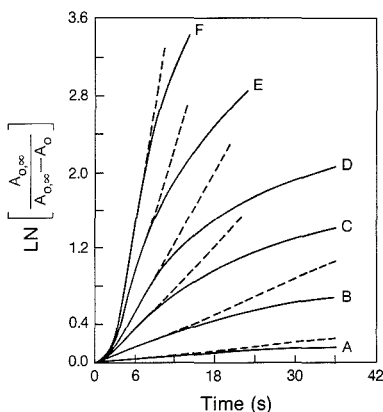


Figure 3. "First-order" kinetic plots of the data from Figure 2. Dashed lines extend the linear (pseudo)-first-order section of the curve.

first-order behavior occurs where $[I^-]_{t=d}^2$ is, at most, only 1% smaller than $[I^-]_{t=0}^2$. Thus, the deviation from linearity is not due to a decrease in $[I^-]$ in the (pseudo)-first-order rate constant, $k_1[I^-]^2$. Rather, it is due to the fact that R has increased above the point where it is much smaller than 1. This, in turn, is due to the increase in $[Fe^{2+}]/[Fe^{3+}]$ (eq 8). During the course of a reaction k_2 in eq 8 remains constant because $[I^-]$ remains essentially constant. The value of k_2 has been shown to be smaller at higher I^- concentrations (13, 15). Thus, for reactions carried out with a higher $[I^-]$ the value of R at any percent reaction is smaller so that (pseudo)-first-order conditions are expected to prevail over a greater percentage of the reaction. This is confirmed by the entries in column 7 of Table I which show that the curves in Figure 3 are linear to higher percent reaction in the presence of higher $[I^-]$.

When the (pseudo)-first-order rate constants are plotted vs $[I^-]^2$, a straight line ($r = 0.997$) with zero intercept (0.009 ± 0.008 standard deviation) results, as predicted from eq 7 when $R \ll 1$. The slope of this line ($10.6 \pm 0.4 L^2/(\text{mol}^2 \text{ s})$) is the third-order rate constant k_1 . This value of k_1 at $\mu = 0.30$ and $t = 20^\circ \text{C}$ is close to values reported in the literature. At 19–20°C Fudge and Sykes found k_1 to be 23 at $\mu = 0.07$ and to be 7 at both $\mu = 0.16$ and $\mu = 0.60$ (15).

Nitrate, which complexes Fe^{3+} , is present in all of our experiments at fixed concentrations ranging from 0.1 to 0.3 M. At ionic strength 0.3 the complex formation constant, K_{FeNO_3} , is about 0.7 (17), which means that in our experiments the fraction of $Fe(III)$ present as the Fe^{3+} species is given by the expression

$$\alpha_{Fe^{3+}} = \frac{[Fe^{3+}]}{[Fe(III)]} = \frac{1}{1 + 0.7[NO_3^-]} \quad (10)$$

Values of $\alpha_{Fe^{3+}}$ are shown in column 4 of Table I where it can be seen that between 84% and 93% of $Fe(III)$ is present as Fe^{3+} . It is not known whether only the hydrated Fe^{3+} species can act as an oxidant for I^- or whether the nitrate complex $FeNO_3^{2+}$ can also perform that role and, if so, what the relative values of the rate constant k_1 would be for these two $Fe(III)$ species (15, 16). Equation 7 implies that Fe^{3+} and $FeNO_3^{2+}$ behave, kinetically, in an identical manner. Alternatively, if it is assumed that the other extreme case is true, that is that $FeNO_3^{2+}$ is inactive as an oxidant for I^- , then eq 7 can be modified simply by multiplying the numerator term by $\alpha_{Fe^{3+}}$. This makes the (pseudo)-first-order rate constant $k_1\alpha_{Fe^{3+}}[I^-]^2$. When we plotted the (pseudo)-first-order rate constants from column 8 of Table I vs the quantity $\alpha_{Fe^{3+}}[I^-]^2$, the resulting

straight line ($r = 0.996$) had a slope of 11.2 ± 0.5 , which is the third-order rate constant, k_1 . This is close to the value of 10.6 obtained when $FeNO_3^{2+}$ is assumed to be redox-active, as discussed above. Thus, whether $FeNO_3^{2+}$ is assumed to be redox-active or not the calculated value of k_1 is little-affected and, importantly, the agreement of the k_1 that we have obtained by the solvent extraction method with literature values attests to the accuracy of this method of measuring homogeneous reaction kinetics.

Limitations. The oxidation of I^- by Fe^{3+} is an example of a homogeneous reaction in which both reactants are initially combined in the aqueous solution. The results of the study of this particular system allow one to answer the more general question, what is the maximum rate of any homogeneous (pseudo)-first-order chemical reaction that can be measured by solvent extraction? Equation 1 shows that the contribution of the chemical reaction is obtained by somehow removing the contributions of mass transfer and instrument band broadening. For the fastest rate measured in the present study, which was in 0.200 M I^- , σ_c^2 was 19.8 s^2 and $(\sigma_M^2 + \sigma_r^2)$ was 6.6 s^2 , so that σ_R^2 was 13.2 s^2 . For faster chemical reaction rates σ_R^2 gets smaller and, in practice, will eventually become lost in the uncertainty in the difference between σ_c^2 and $(\sigma_M^2 + \sigma_r^2)$. The same conclusion can be drawn by comparing curves A and C in Figure 1. For faster chemical reaction rates curve A would be closer to curve C. Eventually the difference between the two curves would be lost in the noise, and deconvolution would be impossible. It is, of course, the uncertainty, or noise, rather than the absolute magnitude of two functions that imposes the limit on taking the difference of their variances or deconvoluting them.

If the relative uncertainty in σ_r^2 is independent of the absolute magnitude of σ_r^2 , then, since $\sigma_r^2 \gg \sigma_M^2$ in this rapid stir instrument (9), reducing σ_r^2 would be the most effective way of making feasible the measurement of faster rates of chemical reaction. It was shown in previous experiments using this apparatus (9) that, for extractable compounds whose distribution ratio is very large so that they are quantitatively extracted, the value of σ_M^2 is on the order of 0.3 s^2 . If instrument band broadening could be eliminated completely then, since there should be no difficulty in accurately obtaining by deconvolution the A vs t curve associated with a chemical reaction for which the variance σ_R^2 is about equal to σ_M^2 , it should be possible to measure rates of chemical reactions for which $\sigma_R^2 \geq 0.3$. This corresponds to a (pseudo)-first-order rate constant of about 2 s^{-1} ($t_{1/2} \approx 0.4 \text{ s}$). The likelihood of reducing the magnitude of σ_M^2 by more rapid stirring is not promising both because drop diameter seems to reach a lower limit at high stirring rates and because the thickness of the Nernst diffusion film is not readily reduced below about 0.002 cm in a rapid stir system (8, 9).

Other Reactions. We have so far considered only the case in which both reactants start out in the same (i.e. aqueous) phase. However, solvent extraction is often used to measure the rate of metal-ligand reactions by combining a solution of the metal ion in water with a solution of the ligand in a water-immiscible organic solvent. What is the maximum rate of such a reaction that can be followed by solvent extraction? Two limiting cases can be imagined. In the first case, the ligand is essentially insoluble in the aqueous phase so that the metal ion reacts heterogeneously with ligand adsorbed at the liquid-liquid interface. In this case the processes giving rise to σ_R^2 and σ_M^2 can still be treated as independent of one another (7) and, when the ligand is present in large stoichiometric excess, (pseudo)-first-order reaction conditions prevail and deconvolution can be used to measure the rate of such heterogeneous reactions with rate constants as high as about 2 s^{-1} .

In the second case, the ligand starts in the organic phase but has a reasonable solubility in the metal-ion-containing aqueous phase and the metal-ligand reaction takes place in the aqueous phase. Here, the rates of the mass transfer processes and chemical reaction cannot be treated as independent of one another. σ_M^2 and σ_R^2 are not independent. A suitable impulse function for deconvolution cannot be obtained and the rate of a chemical reaction occurring in the presence of a comparably fast mass transfer cannot be obtained by deconvolution. In this mixed regime the chemical reaction rate is, in fact, difficult to measure in any way by solvent extraction alone (7).

In contrast to this variable situation regarding the role of mass transfer with various classes of chemical reaction, the contribution of *instrument band broadening* will always be independent of both mass transfer and chemical reaction so that deconvolution with a suitable IRF (8, 9) can be used to remove it, subject to the limitations of signal noise discussed above. This is fortunate since in current instrument design it is instrument band broadening, rather than mass transfer, which imposes a practical limit on the magnitude of chemical reaction rates that can be measured by rapid stir solvent extraction.

Registry No. Γ , 20461-54-5; Fe^{3+} , 20074-52-6.

LITERATURE CITED

- (1) Schill, G. In *Ion Exchange and Solvent Extraction*; Marinsky, J. A.; Marcus, Y., Eds.; Marcel Dekker: New York, 1974; Vol. 6, Chapter 1.
- (2) Cantwell, F. F.; Carmichael, M. *Anal. Chem.* **1982**, *54*, 697-702.
- (3) De, A. K.; Khopkar, S. M.; Chalmers, R. A. *Solvent Extraction of Metals*; Van Nostrand: Toronto, 1970.
- (4) Fossey, L.; Cantwell, F. F. *Anal. Chem.* **1982**, *54*, 1693-1697.
- (5) *Handbook of Solvent Extraction*; Lo, T. C.; Baird, M. H.; Hanson, C., Eds.; Wiley: New York, 1983.
- (6) Weber, W. P.; Gokel, G. W. *Phase Transfer Catalysis*; Springer-Verlag: New York, 1977.
- (7) Danesi, P. R.; Chiarizia, R. *CRC Crit. Rev. Anal. Chem.* **1980**, *10*, 1-126.
- (8) Cantwell, F. F.; Freiser, H. *Anal. Chem.* **1988**, *60*, 226-230.
- (9) Amankwa, L.; Cantwell, F. F. *Anal. Chem.* **1989**, *61*, 1036-1040.
- (10) Arahamian, E., Jr.; Cantwell, F. F.; Freiser, H. *Langmuir* **1985**, *1*, 79-82.
- (11) Hershey, A. V.; Bray, W. C. *J. Am. Chem. Soc.* **1936**, *58*, 1760-1772.
- (12) Eigen, M.; Kustin, K. *J. Am. Chem. Soc.* **1962**, *84*, 1355-1361.
- (13) "Stability Constants" *J. Chem. Soc. Spec. Publ.* **1964**, No. 17, 344.
- (14) Laurence, G. S.; Ellis, K. J. *J. Chem. Soc., Dalton Trans.* **1972**, 2229-2233.
- (15) Fudge, A. J.; Sykes, K. W. *J. Chem. Soc.* **1952**, 119-124.
- (16) Sykes, K. W. *J. Chem. Soc.* **1952**, 124-129.
- (17) Smith, R. M.; Martell, A. E. *Critical Stability Constants*; Plenum: New York, 1976; Vol. 4.

RECEIVED for review April 5, 1989. Accepted August 23, 1989. This work was supported by the Natural Sciences and Engineering Research Council of Canada and by the University of Alberta.

Pulsed Amperometric Detection of Glucose in Biological Fluids at a Surface-Modified Gold Electrode

Dilbir S. Bindra and George S. Wilson*

Department of Chemistry, University of Kansas, Lawrence, Kansas 66045

A nonenzymatic glucose sensor that utilizes permselective membranes to achieve the selectivity required for screening glucose in biological fluids has been described. Interference from endogenous oxidizable substances such as amino acids, urea, ascorbic acid, and uric acid, as well as the effect of chloride and proteins on glucose response, is studied by using flow injection analysis. A set of membranes made of Nafion perfluorinated membrane and collagen, when arranged in front of the working electrode (gold), result in significant improvement in the system selectivity. Even at physiological pH, which is far from being the optimum pH for pulsed amperometric detection of carbohydrates, the sensor shows a good limit of detection (4-5 μg of glucose injected).

INTRODUCTION

The detection of glucose in biological fluids has long been essential in bioanalysis. As a result of development of the enzyme electrode by Clark (1) and by Updike (2), glucose detection based on the highly specific glucose oxidase catalyzed reaction has been the method of choice. Despite the specificity of the enzyme reaction, sensor response is influenced by the partial pressure of oxygen (a cosubstrate) in the medium and by the presence of electroactive interferents such as ascorbic

acid and uric acid. By the use of permselective membranes it has been possible to eliminate most of these difficulties but at some cost in sensor complexity (3).

Glucose sensors based on direct oxidation of glucose at noble metal electrodes have been known for many years. Direct oxidation has been suggested as the basis for an implantable glucose sensor (4) or generally as a means for the detection of glucose in biological fluids. Glucose is not well-behaved electrochemically, and analysis based on the interpretation of current-voltage curves is complicated and time-consuming (5). Response is subject to electrode fouling by oxidation products (6) and to interference from amino acids, ascorbic acid, urea (7), and a variety of drugs such as acetaminophen. Moreover, chloride is known to have a significant inhibitory effect on glucose oxidation kinetics (5).

In spite of the numerous difficulties mentioned above, direct oxidation of glucose can be made tractable by suitable conditioning or modification of the sensing electrode. For example, the application of multistep potential waveforms to the working electrode, which incorporates cleaning and activation steps along with detection, has made possible rapid, sensitive, and reproducible measurements. This technique, known as pulsed amperometric detection, has proven useful for the measurement of a wide range of analytes separated by liquid chromatography (8). A recent study (9) has shown that a Cu-based chemically modified electrode yields a stable response over a considerable period of time without recourse to a potential pulse sequence.

* To whom correspondence should be directed.

In this paper we describe a pulsed amperometric sensor that is able to reliably measure physiological glucose levels without any prior sample separation or cleanup. The interferences are limited to a large extent by using suitable membranes that not only selectively control the diffusion of certain species, but also protect the electrode from coming in direct contact with biological fluid.

EXPERIMENTAL SECTION

Apparatus. The flow injection system consisted of a Shimadzu Model LC-6A pump and SCL-6A controller, Waters Associates Model 710B autosampler, a Princeton Applied Research Model 400 electrochemical detector, and a flow-through thin-layer electrochemical cell consisting of single gold working electrode (MP1300), Pt counter electrode, and Ag/AgCl (saturated KCl) reference electrode. The detector output was processed by a Shimadzu CR 4A integrator, the peak area being used as the basis for analysis. The PARC Model 400 is designed to apply a repeating sequence of three applied potentials to the electrochemical cell according to a specified timing sequence.

Materials. All solutions were prepared from analytical grade chemicals with water from a Barnstead Nanopure II system. All buffers were refiltered through a 0.45- μm filter after preparation. L-ascorbic acid solutions were prepared just before use, as ascorbic acid is subject to oxidative decomposition in solution. Soluble Nafion (5% by weight in 90% lower aliphatic alcohols and 10% water) was obtained from Aldrich Chemical Company, Milwaukee, WI. The collagen and cellulose acetate (MW cutoff 12000–14000) membranes were supplied by YSI, Yellow Springs, OH, and Viscase Corporation, Chicago, IL, respectively. Normal control serum was obtained from Ortho Diagnostic Systems, Inc., Raritan, NJ. Normal human serum was also used and was obtained from Lawrence Memorial Hospital, Lawrence, KS.

All measurements were performed in 0.1 M phosphate buffer (PB), pH = 7.4, unless specified otherwise. Samples for the glucose recovery experiment were prepared by adding appropriate amounts of glucose (50–500 mg/dL) to control serum or human blood serum. These samples were diluted 1:5 with 0.1 M phosphate buffered saline (PBS), pH = 7.4 (100 mequiv/L NaCl), before injecting.

Nafion Coating. A Nafion membrane was cast over the working electrode by spreading a thin layer of Nafion solution on the clean and dry surface of the Kel-F block holding the electrode. Exactly 50 μL of the Nafion solution was placed over the electrode and was spread with a brush over the whole flow channel (2.5 \times 0.8 cm) including the gold electrode surface. The electrode was then left to dry at room temperature overnight. The thickness of the Nafion film was roughly estimated as 2–3 μm by using a density of 1.58 gm/cm³ for Nafion film (10). A precast collagen (100 μm thick, dry state) or cellulose acetate (30 μm thick) membrane was used for the outer protective layer. The Teflon gasket (spacer) was replaced on top of the membranes before reassembling the cell.

The three-step potential sequence for the detection of glucose at a gold electrode has been optimized elsewhere (11, 12) and was adopted without any major modifications. In general, the choice of potentials is determined from the current-potential response curve of the analyte of interest. A sequence consisting of a detection potential (+100 mV, 0.499 s), an oxidative cleaning potential (+650 mV, 0.249 s), and a cathodic reactivation potential (–800 mV, 0.166 s) was used for all experiments. As the time period for completion of one cycle is less than 1 s, the detection is essentially continuous as in direct current (dc) amperometry.

RESULTS AND DISCUSSION

Glucose Calibration Curves. The choice of 0.1 M PB, pH = 7.4, as the mobile phase was made to be consistent with physiological pH even though the optimal condition for measurement is pH = 12–14 (11). The protective membranes are, moreover, not stable at such pH extremes. The function of these membranes is discussed in the next section.

The background current for a freshly polished gold electrode took around 3 h to reach a steady-state value after initial application of the pulse sequence. This coincides with the time it took for the sensor to produce a reproducible response

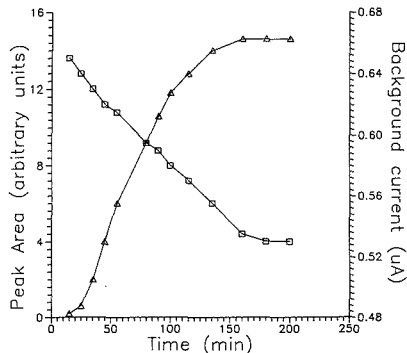


Figure 1. Stabilization of glucose response (Δ) and background current (\square) after initial application of the pulse: sample injected, 30 μL of 25 mg/dL glucose in 0.1 M PB, pH = 7.4.

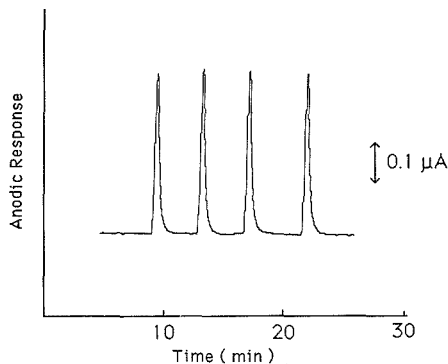


Figure 2. Multiple flow injection peaks for glucose: sample injected, 30 μL of 60 mg/dL glucose; mobile phase, 0.1 M PB, pH = 7.4 at 0.25 mL/min; working electrode, gold covered with Nafion and collagen.

to a given amount of glucose injected repeatedly (Figure 1). This phenomenon has been explained previously as being due to the continuous microscopic roughening of the electrode surface (until a constant area is obtained) by alternate formation and removal of surface oxide through electrochemical pulsing (13). However, reported times for background stabilization were only 5–10 min when 0.2 N NaOH was used as the mobile phase (13). Presumably the physiologic medium conditions do not favor formation and the subsequent reduction of the deposit formed.

The glucose response was found to be linear within the physiological range. The detection limit was approximately 25 nmol in a 30- μL sample (4.5 μg of glucose) for $S/N = 10$. The reproducibility of the sensor response was evaluated by repetitive injection of the 30- μL sample. Ten injections were used to calculate a relative standard deviation of 1%. Multiple flow injection peaks obtained with a modified electrode are shown in Figure 2. A flow rate of 0.25 mL/min was selected, as it provided a good compromise between the sensitivity and the speed of analysis. The sensor response was found to be stable for at least 1 week.

Effect of Chloride. Figure 3 shows the effect of increasing chloride concentration in a glucose sample on the oxidation current for a bare gold electrode and a Nafion-coated gold electrode. About 80% of the response was lost for the bare gold electrode at physiological concentrations of chloride. Even though the variation in chloride ion concentration within

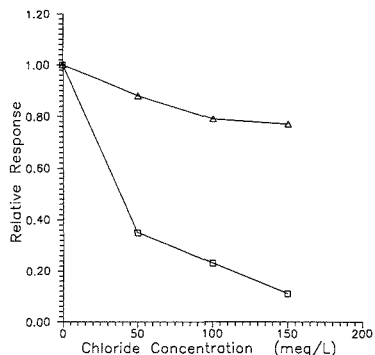


Figure 3. Effect of chloride on glucose response for bare gold electrode (□) and Nafion-coated gold electrode (Δ): glucose concentration, 100 mg/dL; sample size, 30 μ L.

Table I. Results of Glucose Recovery from Control Serum for Different Working Electrode Conditions

conditions ^a	% recovery ^b
bare gold (pH = 13)	~50
bare gold	~24
Nafion-coated gold	~60
collagen on Nafion-coated gold	95 \pm 3 (n = 4)

^a All measurements made at pH = 7.4, unless specified.

^b Samples were prepared by adding 100 mg/dL glucose to control serum. Samples were diluted 1:5 before injecting. The recovery results were calculated by comparing the signals from glucose-spiked serum samples (corrected for the serum blank) and glucose samples in 0.1 M PBS.

the normal physiological range (100–106 mequiv/L) had little effect on the glucose oxidation current, the overall loss in sensitivity was too significant to be overlooked. Nafion, in the form of a cation-exchange polymer membrane, is effective in selectively excluding anions from the electrode surface. This property of Nafion has previously been exploited for elimination of a chloride interference effect on cupric ion-selective electrodes (14) and of ascorbic acid interference in the determination of dopamine (15). Nafion also has been successfully employed as a dialysis membrane to provide a protein- and interferent-free environment near the electrode for the determination of glucose in whole blood (10). As seen in Figure 3, a Nafion-coated electrode preserves most of its response in the presence of chloride.

The effect of chloride ion was far less pronounced when 0.2 N NaOH (pH = 13) was used as the mobile phase. This was primarily due to the greatly enhanced sensitivity for glucose at high pH as the absolute magnitude of the effect is the same.

Effect of Proteins. The effect of proteins on glucose response was studied by adding bovine serum albumin (BSA) to the glucose standards. For a bare electrode the response was largely suppressed due to the surface poisoning by BSA adsorption. But unlike the case of dc amperometry, where protein adsorption tends to be irreversible, the electrode here regained its original activity within 10 min of protein injection as the pulsing slowly removed all of the surface adsorbed protein. At pH 13, though the poisoning was less severe (probably because denatured protein did not adsorb well to the electrode surface), it was still sufficient to affect the results in a glucose recovery experiment (Table I). The Nafion-coated electrode also did not offer complete protection against protein fouling, resulting in poor recovery of glucose from biological samples. It was, however, possible to put a collagen membrane in front of the Nafion to prohibit protein from

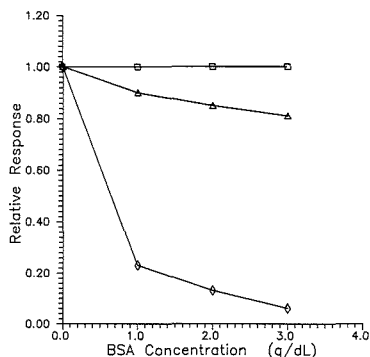


Figure 4. Effect of BSA on glucose response for bare gold electrode, pH = 7.4 (◇), (b) bare gold electrode, pH = 13 (Δ), and collagen on Nafion-coated gold electrode, pH = 7.4 (□): glucose concentration, 100 mg/dL; sample size, 30 μ L.

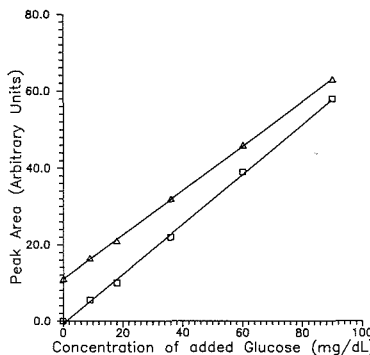


Figure 5. Glucose response curves for aqueous glucose samples (□) and glucose-spiked human blood serum samples (1:5 diluted) (Δ): sample size, 30 μ L; working electrode, gold covered with Nafion and collagen.

reaching the inner Nafion layer. This bilayer membrane structure completely eliminated the inhibitory effect resulting from the protein adsorption while maintaining the desired permselective characteristics (Figures 4 and 5). A similar bilayer coating, with a cellulose acetate film covering the Nafion layer, has been utilized previously by Wang and co-workers (16) for selective detection of cationic neurotransmitters in urine samples.

Interference Studies. All interfering compounds were studied at their physiological minimum and maximum levels with glucose concentration being kept constant at 100 mg/dL. As expected, the glucose measurement was strongly influenced by the presence of ascorbic acid, uric acid, amino acids, and acetaminophen.

Under the conditions of measurement, the bare sensor was found to be far more sensitive toward ascorbic acid and uric acid than toward glucose. Therefore, even though both ascorbic acid (0.2–2 mg/dL) and uric acid (4.0–8.5 mg/dL) are present in body fluids at concentrations that are significantly lower than that of glucose (60–110 mg/dL), the errors caused by their presence were fairly significant. For example, the response for a glucose sample (100 mg/dL) on a bare electrode was increased by 140% when ascorbic acid was added to the sample at its physiological maximum concentration (2 mg/dL). On the other hand, as both ascorbic acid and uric acid are present as anions at physiological pH, their transport to the

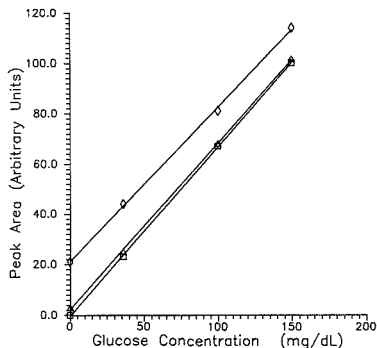


Figure 6. Effect of urea and amino acids on glucose response. Curves: glucose only (□), (b) glucose in presence of all amino acids at physiological maximum (◇), and glucose in presence of urea at physiological maximum (Δ). Sample size, 30 μ L.

electrode surface can easily be restricted by putting a Nafion coating on the electrode surface. The presence of ascorbic acid and uric acid at their physiological maximum values caused an error of less than 5% apparent glucose concentration for a Nafion-coated electrode.

As the molar concentrations of urea are comparable to that of glucose in body fluids, its presence has always created difficulties in the development of the electrocatalytic glucose sensor. This is especially true for Pt black-based sensors, where the reported errors are as high as 20% resulting from the influence of urea (7). As urea is uncharged in neutral solution and is smaller than glucose, it is not trivial to realize a membrane that will selectively discard urea while allowing glucose to pass through. Fortunately, under the measurement conditions of the present experiment, urea was almost inactive, causing an error of less than 2% (Figure 6) at its physiological maximum (26 mg/dL).

Amino acids are also potential physiological interferences, and a considerable amount of work has been done previously dealing with the elimination of their influence. A wide variety of membranes such as polysulfone (4) and Permion 1025 (7) have been employed for this purpose. In the pulsed amperometric mode, the potentials required for amino acid oxidation are much higher (+500 mV) than the one used for glucose oxidation. It is believed that the amino acid oxidation is catalyzed by the metal oxide formation (17), unlike the glucose oxidation, which is inhibited by such a process. Despite this, interference from a mixture of all amino acids (present at their physiological maximum levels) for a bare electrode was so great that the response toward glucose was almost obscured. However, the transport of these amino acids was greatly restricted by the Nafion membrane, probably because of their zwitterionic character at neutral pH. For a modified electrode with a collagen membrane over the Nafion film, an error of approximately 19% resulted in the response of a 100 mg/dL glucose solution (Figure 6) when all amino acids were added at their physiological maximum level. However, the response for all glucose concentrations fluctuated within $\pm 3\%$ when amino acid concentrations were varied from physiological average to the physiological extremes. Therefore, the error resulting from amino acid interference can be cut down to less than 3% by adding amino acids at their average physiological concentrations to the calibration standards.

A few other carbohydrates besides glucose are also found in body fluids, but at comparatively much lower concentrations. Sensor response to their presence is summarized in Table II. As one can see, only galactose causes some interference at its physiological concentration level.

Table II. Sensor Response for Various Carbohydrates

compound	response at equal concn (rel)	physiological concn, mg/dL	response at physiological max (rel)
glucose	1.0	60–110	1.0
galactose	1.7	<4.5	0.06
D-(–)-fructose	ND ^a	<7.5	0
lactose	0.54	<5	0.02

^a ND, not detected.

Table III. Effect of Membrane Properties on Electrode Sensitivity^a

conditions	rel sensitivity
bare gold	1.0
Nafion-coated gold	2.4
collagen on Nafion-coated gold	1.3

^a Conditions: sample injected, 30 μ L of 100 mg/dL glucose in 0.1 M PB, pH = 7.4; mobile phase, 0.1 M PB, pH = 7.4.

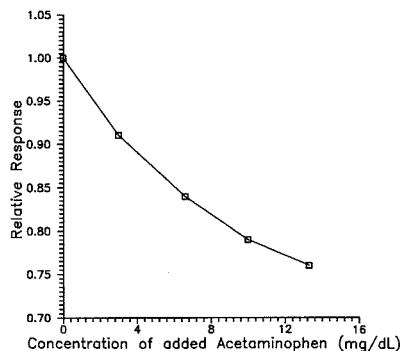


Figure 7. Effect of acetaminophen on glucose response: glucose concentration, 100 mg/dL; sample size, 30 μ L.

Recently, acetaminophen (sold as an over-the-counter drug) has generated some interest as a possible interferent (18). Under the conditions of the present experiment, acetaminophen was found to be mostly inactive, but it caused inhibition of the glucose response when injected with glucose (Figure 7). Acetaminophen may have been preferentially adsorbed, resulting in a blocked surface and decreased glucose oxidation. The normal physiological levels for acetaminophen are believed to be around 2 mg/dL. At this level, the resulting error in the response for 100 mg/dL glucose was less than 5%. Higher errors have been reported for an enzyme-based sensor under similar conditions (19).

Effect of Membrane Permeability on Glucose Sensitivity. In a recent study (20), it has been pointed out that a condition of transient alkalinity is generated in the vicinity of the working electrode surface during the cathodic reactivation step of the pulse sequence as both stripping of the oxide layer and reduction of dissolved oxygen accompany the formation of OH⁻. As a result, the determination of glucose is possible by pulsed amperometric detection in neutral and acidic media of low buffer capacity if the timing of the pulse sequence is suitably modified. Our results are consistent with this behavior. As expected, a bare gold electrode showed an increase in sensitivity with a decrease in mobile phase and sample buffer concentration (Figure 8). This effect was less pronounced when the electrode was covered with protective membranes. The glucose sensitivities for different working

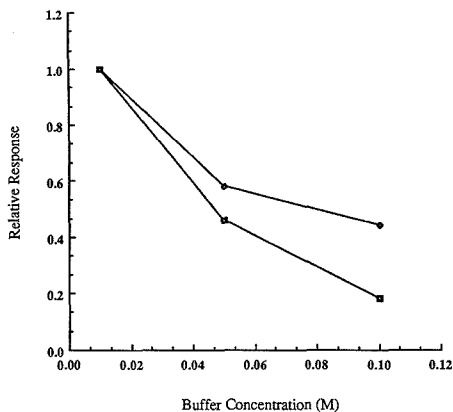


Figure 8. Effect of mobile phase buffer concentration on glucose response for bare gold electrode (□) and collagen- and Nafion-covered gold electrode (◇); sample injected, 30 μ L of 100 mg/dL glucose prepared in mobile phase buffer.

electrode membranes are summarized in Table III. As can be seen, the Nafion-coated electrode showed a higher sensitivity as compared to the bare electrode. This is probably due to the fact that Nafion, being anionic, is able to restrict the diffusion of OH^- away from the electrode, thus generating higher local pH at the electrode surface. The enhancement of the sensitivity by partitioning of glucose into Nafion also cannot be ruled out. For the Nafion/collagen system, the loss in sensitivity due to the diffusional constraints imposed by the collagen membrane was compensated by the sensitivity increase caused by the underlying Nafion layer (Table III).

CONCLUSION

This work has demonstrated that by suitable modification of the working electrode, pulse amperometric detection can be made to selectively detect glucose in biological samples. The separation steps carried out at the electrode surface help remove interferences to a large extent and avoid unnecessary sample cleanup. It has also been shown how the membrane permeabilities can be manipulated to yield increased sensi-

tivity. As mentioned earlier, a reasonable estimate of physiological glucose levels is possible provided the calibration standards are prepared with chloride and various amino acids added at their average physiological concentrations. Though the results seem satisfactory, further improvement in the system selectivity is possible through a better choice of inner permselective membrane. The work along these lines is in progress.

ACKNOWLEDGMENT

We thank Dennis C. Johnson and W. R. LaCourse for helpful discussions and for providing the preprint on this subject.

LITERATURE CITED

- Clark, L. C. Jr.; Lyons, C. *Ann. N.Y. Acad. Sci.* **1962**, *102*, 29–46.
- Updike, S. J.; Hicks, G. P. *Nature* **1971**, *214*, 986–988.
- Sternberg, R.; Barrau, M.-B.; Gangiotti, L.; Thevenot, D. R.; Bindra, D. S.; Wilson, G. S.; Velho, G.; Froguel, P.; Reach, G. *Biosensors* **1988**, *4*, 27–40.
- Lewandowski, J. J.; Sadowa, E. S.; Krzymien, J.; Nalecz, M. *Diabetes Care* **1982**, *5*(3), 238–244.
- Marincic, L.; Soeldner, J. S.; Colton, C. K.; Giner, J.; Morris, S. J. *Electrochem. Soc.* **1979**, *126* (1), 43–49.
- Lerner, H.; Giner, J.; Soeldner, J. S.; Colton, C. K. *J. Electrochem. Soc.* **1979**, *126*(2), 237–241.
- Richter, G. J.; Luft, G.; Gebhardt, U. *Diabetes Care* **1982**, *5*(3), 224–228.
- Neuburger, G. G.; Johnson, D. C. *Anal. Chem.* **1988**, *60*, 2288–2293.
- Prabhu, S. V.; Baldwin, R. P. *Anal. Chem.* **1989**, *61*, 852–856.
- Harrison, J. D.; Turner, R. F. B.; Baltas, H. P. *Anal. Chem.* **1988**, *60*, 2002–2007.
- Johnson, D. C.; Polta, J. A.; Neuburger, G. G.; Polta, T. Z.; Johnson, J.; Tang, A. P.-C.; Yeo, I.-H.; Baur, J. J. *Chem. Soc., Faraday Trans. 1* **1986**, *82*, 1081–1090.
- Neuburger, G. G.; Johnson, D. C. *Anal. Chem.* **1987**, *59*, 150–154.
- Neuburger, G. G.; Johnson, D. C. *Anal. Chem.* **1987**, *59*, 203–204.
- Hoyer, B.; Loftager, M. *Anal. Chem.* **1988**, *60*, 1237–1241.
- Nagy, G.; Gerhardt, G. A.; Oke, A. F.; Rice, M. E.; Adams, R. N.; Moore, R. B.; Szentirmay, M. N.; Martin, C. R. *J. Electroanal. Chem. Interfacial Electrochem.* **1985**, *188*, 85–94.
- Wang, J.; Tuzhi, P.; Golden, T. *Anal. Chim. Acta* **1987**, *194*, 129–138.
- Welch, L. E.; LaCourse, W. R.; Mead, D. A., Jr.; Johnson, D. C. *Anal. Chem.* **1989**, *61*, 555–559.
- Paleski, G.; Rahni, M. A. N.; Lubrano, G. J.; Ngwainbi, J. N.; Guilbault, G. G. *Anal. Biochem.* **1986**, *159*, 114–121.
- Technical notes, YSI Inc., Yellow Springs, OH, pp 23–31.
- Larew, L. A.; Johnson, D. C. *J. Electroanal. Chem. Interfacial Electrochem.* **1989**, *264*, 131–147.

RECEIVED for review June 14, 1989. Accepted September 5, 1989. The support of this work by the National Institutes of Health (DK 30718) is gratefully acknowledged.

Bias and Nonlinearity of Ultraviolet Calibration Curves Measured Using Diode-Array Detectors

Eric V. Dose and Georges Guiochon*

Department of Chemistry, University of Tennessee, Knoxville, Tennessee 37996, and Analytical Chemistry Division, Oak Ridge National Laboratory, Oak Ridge, Tennessee 37831

Models for the dependence of diode-array UV chromatographic detector response on bandpass and on the shape of the absorbing sample's spectrum are presented. The equations derived comprise terms describing two sources of non-ideal response due to the polychromatic nature of the detected radiation. The bias, or deviation at low concentrations of the measured absorbance from the ideal, zero-bandwidth value, increases roughly as the product of the spectrum's local second derivative and the square of the bandwidth. Calibration curve nonlinearity at higher concentrations, present for monochromator-based detectors and transmittance-averaging diode-array detectors, is described quantitatively. These equations confirm that the calibration curves always bend downward when the sample's absorption spectrum varies at all within the bandpass. A distinction is drawn between transmittance-averaging and absorbance-averaging diode-array detectors. Experimental results illustrate the types of bias and nonlinearity seen in each class at the high concentrations of interest to preparative-scale liquid chromatography and quality-control applications.

The ultraviolet (UV) detector's great popularity in analytical liquid chromatography (LC) is due to its generally high sensitivity, reasonable selectivity, and wide linear dynamic range over the low concentrations of usual interest to trace analysts. (In this work *detector* is used in the chromatographic sense to signify the entire absorbance-measuring instrument and *sensor* signifies the part of the detector that senses the transmitted radiation.) Detection is normally performed at or near a local maximum in the spectrum. However in quality-control and preparative-scale LC, where peak absorbance can be very high, and in separations in which there is no wavelength near which every analyte has a minimum or maximum, measured UV absorbance proportionality to concentration suffers. The physical cause of these nonidealities is the assumption of radiation monochromaticity when the radiation is in fact polychromatic, but the effects have not been quantitatively understood. Where present, nonidealities are important since analysts are not interested primarily in chromatograms but rather in the concentration profiles. The calibration curve relating the two is often quite nonlinear, and so general equations describing the forms of these curves are needed.

Theory (1) and experiment (2) show that UV absorbance sensitivity decreases as concentration increases for nonzero detection bandwidths. Carr (3) has shown in some detail that uncorrected calibration nonlinearity can greatly affect Gaussian peak area and certain other quantities calculated from higher moments of the peak shape. When detection is performed far from the spectral maximum, for example to reduce the measured absorbance in preparative-scale LC, interference from other detected components may worsen, and linear dynamic range may well decrease.

Previous investigations have generally focussed on polynomial (4, 5), Legendre polynomial (6), cubic spline (7), or piecewise linear interpolation (8) as empirical approximations

to the calibration curve. These approaches are interpolations rather than physically based models. Empirical fitting to calibration curves may account for the slight nonlinearity often seen at low concentrations, but the fits generally become useless when extended to higher concentrations. This is due either to the empirical nature of the model function or to oscillation of the approximating functions caused by the need (to assure a good fit) for too many adjustable model parameters in the model function.

A quantitative description of how measured UV absorbances depend on concentration, spectral shape, and detector bandpass would improve chromatographic detection in two important ways: (1) expected calibration curves could be computed in advance from spectral data, allowing control of the curves' shapes, and (2) experimental calibration curves could be understood in terms more physically meaningful than is possible by simply fitting to a general curve shape. Model equations resulting from such descriptions will be suitably constrained in shape and thus should require fewer adjustable parameters than would, say, a polynomial.

Stewart (9) has investigated the effect of triangular bandpass on the shapes of Gaussian and Lorentzian absorption bands and gives highly truncated power series for the resulting shapes at the limit of low absorbance. Strictly numerical approaches such as this one apply to any spectrum-bandpass combination, but cannot yield closed forms. The methods given in the present work extend to all concentrations and to all band passes within which the absorbance is nonnegative.

The diode-array bandpass is defined by the detector's optical geometry and by the selection of diodes whose responses are included in the computed absorbance (10, 11). The detection response across the bandpass is nearly rectangular since the diodes corresponding to wavelength intervals cover nearly all wavelengths in the desired range and since they are weighted equally by dividing each diode response by a reference response measured earlier by the same diode. These nearly ideal detector properties have simplified the investigations described below. Since diode-array detectors typically are noisier than monochromator-based detectors, it is tempting to increase the bandwidth (i.e., to include more diodes) to improve signal-to-noise ratio. However, greater bandwidths tend to decrease the detector's linear dynamic range to an extent that depends on the spectral shape within the bandpass. The equations derived in this work describe the effect of spectral shape, detector bandpass, and analyte concentration on calibration curve shape. Previous treatments (1, 5, 9, 10) exist but are not sufficiently accurate at high absorbances to accommodate the needs of preparative chromatography. The equations given herein allow diode-array detectors, and by extension other UV-absorbance-measuring detectors with other band-pass shapes, to be operated at wavelengths and bandwidths that give high sensitivity at low concentrations and relatively high accuracy at high concentrations even when the absorbances are well into the nonlinear range.

THEORY

The development below assumes that I_0 , the product of incident radiant power (herein "power"), optical transmission,

and sensor response, is independent of wavelength λ over the bandpass of interest and is zero outside that bandpass (rectangular bandpass); that there is no stray light; that the absorbing sample is homogeneous in absorbance; that all detected light has passed through the same sample path length; and that absorbance A is a smooth function of wavelength over the bandpass. These conditions are approximately true for diode-array detectors. If the bandpass is instead triangular (see Appendix A), the resulting expressions apply to most other UV absorbance detectors of interest to chromatographers. Finally, we assume that Beer-Lambert behavior exists at the limit of narrow bandpass; i.e. we do not consider in this work stray-light, chemical speciation, thermal, photochemical, or harmonic optical effects on absorbance (11, 12).

In a single-photomultiplier UV absorbance detector, the diode responses (transmitted power) are summed over the bandpass, in effect averaging the responses to yield a single computed absorbance. Diode-array detectors, however, first convert power at discrete and very narrow wavelength ranges into numerical responses, and these responses are combined by the detector's resident software. The most useful combining/averaging expressions are special cases of the generalized mean

$$M(d) = \left(\frac{1}{\Delta} \int_{\lambda_0 - \Delta/2}^{\lambda_0 + \Delta/2} T(\lambda)^d d\lambda \right)^{1/d} \quad (1)$$

where Δ is the bandwidth (the width of the wavelength range passed through the sample and measured at the sensor), λ_0 is the detection wavelength (the center of the wavelength range), $T(\lambda)$ is the transmittance at λ , and d is the degree of the generalized mean. Two such cases have special significance: $d = 1$, giving the arithmetic mean transmittance over the bandpass; and the limit as $d \rightarrow 0$, giving the geometric mean transmittance (13) and the arithmetic mean absorbance. These two cases, transmittance-averaging and absorbance-averaging, respectively, have fundamentally different dependencies of reported absorbance on spectral shape, detector bandwidth, and analyte concentration.

Transmittance-Averaging (Power-Summing) Detectors. Single-photomultiplier and some diode-array detectors behave as follows. Given the spectral-shape assumptions described above, measured absorbance A in the band of interest may be approximated by a Taylor expansion in λ about the band's center wavelength λ_0 . The N -order Taylor approximations for measured molar absorptivity ϵ and measured absorbance A for a spectrum with center-wavelength derivatives ϵ_i

$$\epsilon_i = \frac{\partial^i \epsilon}{\partial \lambda^i} \quad (2a)$$

which may also be written in terms of absorbance derivatives a_i

$$a_i = \frac{\partial^i A}{\partial \lambda^i} = \epsilon_i b c \quad (2b)$$

and then

$$\epsilon_{T,N} = \sum_{i=0}^N \epsilon_i (\lambda - \lambda_0)^i / i! \quad (3a)$$

and

$$A_{T,N} = A_0 + \sum_{i=1}^N a_i (\lambda - \lambda_0)^i / i! \quad (3b)$$

The fraction of light transmitted (I_0) is

$$T_{T,N} = \frac{\int I_0(\lambda) 10^{-A_{T,N}(\lambda)} d\lambda}{\int I_0(\lambda) d\lambda} \quad (4)$$

where $I_0(\lambda)$ is the product at wavelength λ of incident light I_o , optical transmission of the detector, and sensor response. Δ is the full width of the rectangular bandpass. If I_o is independent of λ (first assumption at beginning of theory section), the measured absorbance is

$$A = -\log \left(\frac{1}{\Delta} \int_{\lambda_0 - \Delta/2}^{\lambda_0 + \Delta/2} 10^{-A_{T,N}(\lambda)} d\lambda \right) \quad (5)$$

See Appendix A for results assuming triangular bandpass.

In the case of constant absorbance in the bandwidth of interest, i.e. the case $\epsilon_i = 0$, $i \geq 1$, use of 3 and 5 gives

$$A_{T,0} = A_0(\lambda) \quad (6)$$

Thus Beer-Lambert (linear) behavior is a special case of eq 5.

In the case of linear dependence of ϵ on λ , i.e., $\epsilon_i = 0$, $i \geq 2$, eq 3b can be written for $N = 1$ as

$$A_{T,1} = -\log \left(\frac{1}{\Delta} \int_{\lambda_0 - \Delta/2}^{\lambda_0 + \Delta/2} 10^{-(a_0 + a_1(\lambda - \lambda_0))} d\lambda \right) \quad (7)$$

and $A_{T,1}$ can be written in closed form as

$$A_{T,1} = A_0 - \log \left(\frac{\sinh(Ka_1\Delta/2)}{Ka_1\Delta/2} \right) \quad (8)$$

where K is the natural logarithm of 10. Thus absorbance is naturally partitioned into the Beer-Lambert absorbance and a correction term. This correction is very similar to that given by Ramsey (14) for the dependencies of measured absorbance on concentration fluctuations and on the angle between the nonparallel faces of a trapezoidal cell (sample wedging).

Where spectral curvature is included in the present model, i.e. where $\epsilon_i = 0$, $i \geq 3$

$$A_{T,2} = -\log \left(\frac{1}{\Delta} \int_{\lambda_0 - \Delta/2}^{\lambda_0 + \Delta/2} 10^{-(A_0 + 3a_1(\lambda - \lambda_0) + a_2(\lambda - \lambda_0)^2/2)} d\lambda \right) \quad (9)$$

which for $a_2 > 0$ (spectrum concave upward) is

$$A_{T,2} = A_0 - \frac{a_1^2}{2a_2} + \log \left[\Delta \left(\frac{2Ka_2}{\pi} \right)^{1/2} \right] - \log \left[\operatorname{erf} \left(\left(\frac{Ka_2}{2} \right)^{1/2} \left(\frac{a_1}{a_2} + \frac{\Delta}{2} \right) \right) - \operatorname{erf} \left(\left(\frac{Ka_2}{2} \right)^{1/2} \left(\frac{a_1}{a_2} - \frac{\Delta}{2} \right) \right) \right] \quad (10)$$

and for $a_2 < 0$ (spectrum concave downward) is

$$A_{T,2} = A_0 - \frac{a_1^2}{2a_2} + \log \left(\Delta \left(-\frac{Ka_2}{2} \right)^{1/2} \right) - \log \left[\exp \left(-\frac{Ka_2}{2} \left(\frac{a_1}{a_2} + \frac{\Delta}{2} \right)^2 \right) D \left(\left(-\frac{Ka_2}{2} \right)^{1/2} \left(\frac{a_1}{a_2} + \frac{\Delta}{2} \right) \right) - \exp \left(-\frac{Ka_2}{2} \left(\frac{a_1}{a_2} - \frac{\Delta}{2} \right)^2 \right) D \left(\left(-\frac{Ka_2}{2} \right)^{1/2} \left(\frac{a_1}{a_2} - \frac{\Delta}{2} \right) \right) \right] \quad (11)$$

where $\operatorname{erf}(x)$ is the standard error function of x , that is

$$\operatorname{erf}(x) = \frac{2}{\pi^{1/2}} \int_0^x e^{-t^2} dt \quad (12)$$

and where $D(x)$ is the Dawson integral of x , that is

$$D(x) = e^{-x^2} \int_0^x e^{t^2} dt \quad (13)$$

Again, the absorbance can be partitioned into Beer-Lambert and correction terms. Equations 10 and 11 are not equivalent forms—each is valid only in the given domain in curvature a_2 . Where $a_2 = 0$, both are undefined, and one must use eq 8, the limit of each as a_2 approaches zero.

Expressions for the absorbance under cubic and higher-order Taylor approximations to the spectrum can be reduced neither to closed form, as can be done for zero- (eq 6) and first-order (eq 8) series, nor to forms containing well-known functions, as can be done in the quadratic case (eq 10, 11). Equation 5 is thus solved numerically. Since the transmittance function and its derivatives are at least smooth as the equivalent absorbance function, we have applied adaptive quadrature algorithms (15-17). The newest such algorithms numerically approximate integrals by partitioning the integration domain into individually integrated intervals and then estimating an upper limit for the error. The partitioning is repeated in the most error-prone remaining intervals until convergence (very low estimated error) is obtained. We find that the computational speed and accuracy of adaptive quadrature nearly compensates for the unavailability of closed integral forms.

Expressions for the measured absorbance using a triangular bandpass (Appendix A) are more complicated than those for the rectangular bandpass. We could not find a closed-form solution for the case where the local spectral slope and curvature are both nonzero, and adaptive quadrature was used to obtain the computed curves in the figures in this article.

One may study some properties of eq 8, 10, and 11 (for rectangular bandpass) and the equations of Appendix A (for triangular bandpass) by expanding them as MacLaurin series (Appendix B). Like the expressions from which they are generated, the series are separable into Beer-Lambert absorbance (concentration times ϵ_0), bias, and a collection of terms describing the nonlinearity. Expanded in bandwidth Δ , there exist only even-order terms, and the rapid series convergence confirms the approximately quadratic dependence of nonlinearity and bias upon Δ . The Δ^2 term of the MacLaurin series (Appendix B) also confirms that the bias and nonlinearity are less (about half) for a triangular bandpass than for a rectangular bandpass of the same base bandwidth. Expansions in concentration (contained in the α_i terms) also converge rapidly. Since the first three Δ -containing terms in eq B2 and B4 or the first three terms in eq B1, B3, and B5 completely determine the magnitudes of the remaining terms in the series, entire calibration curves can be described with very few degrees of freedom.

Absorbance-Averaging Detectors. Diode-array detectors may average absorbances across the bandwidth in a way single-photomultiplier detectors cannot. As a result, the dependencies of reported absorbance on spectrum, bandwidth, and analyte concentration become much simpler in principle. In effect, these detectors compute the absorbance at each diode in the bandpass and report the arithmetic mean as the observed absorbance

$$A = \frac{1}{\Delta} \sum_{\Delta \text{ diodes}} A(\lambda) d\lambda = \frac{1}{\Delta} \sum_{\Delta \text{ diodes}} -\log T(\lambda) d\lambda \quad (14)$$

It may be easier computationally to obtain the average absorbance from the geometric mean of the individual transmittances as

$$A = -\frac{1}{\Delta} \log \left(\prod_{\Delta \text{ diodes}} T(\lambda) d\lambda \right) \quad (15)$$

Generally for absorbance-averaging detectors, bias is present and nonlinearity is not. The bias is the same as that for transmittance-averaging detectors since bias is defined for vanishingly small concentration and so depends only on bandpass and spectral shape. While absorbance-averaging

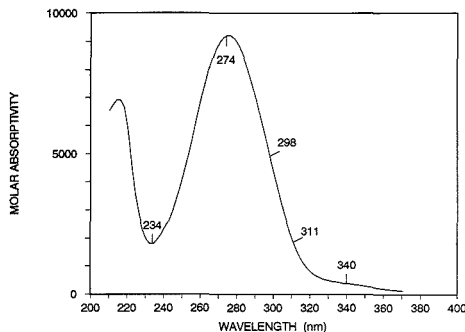


Figure 1. UV spectrum of 4-nitrotoluene measured on HP 1040A diode array detector. Data for Figures 3-7 were measured at the five wavelengths indicated.

eliminates the nonlinearity due to unequal diode responses, residual nonlinearity still exists due to the variation in detected power (which is transmittance-averaged) across the face of each diode. This persistent effect induces nonlinearity to a degree of no greater than approximately $1/n^2$ of that of the overall nonlinearity of transmittance-averaging detectors, where n is the number of diodes used to form the bandpass.

The signal-to-noise ratio of absorbance-averaging detectors is poor at high absorbances since the noise is dominated by the band-pass diode with the least incident power rather than by the diode with the greatest incident power as is the case with transmittance-averaging detectors. The price for the latter's wider useful dynamic range is much greater response nonlinearity.

EXPERIMENTAL SECTION

4-Nitrotoluene (Aldrich) was reagent grade. Acetonitrile (Burdick and Jackson) was HPLC grade, and all experiments used acetonitrile from a single manufacturer's lot to minimize spectral and base-line inconsistencies.

UV measurements were made with a Hewlett-Packard Model 1090 liquid chromatograph equipped with a Hewlett-Packard Model 1040A (HP 1040A) diode-array UV detector or a Perkin-Elmer Model LC-235 (PE LC-235) diode-array UV detector. Solutions of 4-nitrotoluene in acetonitrile were mixed with pure acetonitrile at the low-pressure pumps in frontal-analysis mode and then were passed directly into the detector. The UV spectrum of 4-nitrotoluene (Figure 1) was measured at very low concentration by using the detector's narrowest bandwidth (4 nm). This spectrum was assumed to have negligible concentration and bandwidth effects, yielding estimates of ϵ_0 . Flow rates were 1 mL/min, and all absorbances are averages over 2 min (HP 1040A) or the system was allowed to reach steady state for 3 min and then the absorbances were read to 10^{-4} absorbance unit (AU) at the longest peak width/filter setting (PE LC-235). In no case was an absorbance less than 0.01 AU (HP 1040A and PE LC-235), greater than 3.0 AU (HP 1040A), or greater than 1.5 AU (PE LC-235) used. Since the HP 1040A detector reported high-concentration absorbances to 4.0 AU, and no data above 1.5 AU were taken with the PE LC-235 detector, no stray light problems were indicated.

Mathematical expressions in the theory section and appendices were verified by use of MACSYMA software (MIT and Symbolics, Inc.). Numerical integrations were performed by using routines from the Numerical Algorithms Group or appropriate approximation formulas. Numerical computation was performed to double precision (16 decimal digits) using VAX FORTRAN on Model 8800 computers (Digital Equipment Corp.).

RESULTS AND DISCUSSION

Diode-array detector bandwidth is selected either by reporting the absorbance based on a single diode for the narrowest bandwidth or by measuring simultaneously the signals

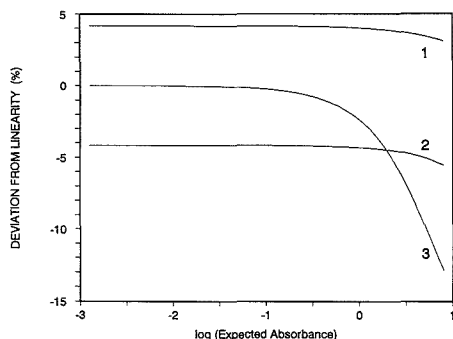


Figure 2. Effect of UV spectral slope and curvature ($\Delta = 10$ nm, $\epsilon = 1000$): curve 1, $\epsilon_1 = 0$, $\epsilon_2 = 10$ nm⁻²; curve 2, $\epsilon_1 = 0$, $\epsilon_2 = -10$ nm⁻²; curve 3, $\epsilon_1 = 50$ nm⁻¹, $\epsilon_2 = 0$.

from a number of diodes. Resident software translates the user's selected wavelength range into a range of adjacent diodes, the signals of which are combined by averaging transmittances (e.g. HP 1040A) or absorbances (e.g. PE LC-235). These two averaging methods give nearly the same results at low absorbance, say, less than 0.1–0.2 AU, but give very different behavior at higher absorbances of interest to practitioners of preparative-scale chromatography.

Transmittance-Averaging (Power-Summing) Detectors. Diode-array detectors that average raw responses *before* they compute the apparent absorbance emulate the power-summing behavior of a monochromator-based detector. The complex relationships of these reported absorbances to bandwidth, spectral slope and curvature, and analyte concentration (see Theory section, eq 8, 10, and 11) are described in the following discussion.

The predicted types of calibration-curve dependence on $\epsilon_1 = \partial\epsilon/\partial\lambda$ and $\epsilon_2 = \partial^2\epsilon/\partial\lambda^2$ for transmittance-averaging detectors are given in Figure 2. In the vertical direction of Figure 2 are given percent deviations of predicted absorbance from the Beer-Lambert absorbances. These Beer-Lambert absorbances are calculated by using the molar absorptivity ϵ_0 measurable at the limits of very low concentration and detector bandwidth. At a given concentration, the difference between the measured molar absorptivity and ϵ_0 is the sum of the *bias* and the *nonlinearity*.

This difference at very low concentrations is the bias, which is of interest if the exact molar absorptivity is needed or if the bandwidth is subject to adjustment. Strong bias may be significant for spectroscopists but is not important to chromatographers, except that it may explain differences between calibration curves obtained for the same compound with different detectors. The difference between the molar absorptivity at a given concentration and that at very low concentration is the nonlinearity, the quantity of most interest to chromatographers and others constructing calibration curves.

As is well-known, a nonzero first derivative $\epsilon_1 = \partial\epsilon/\partial\lambda$ causes marked downward bending (nonlinearity) of the log response vs log concentration curve at higher concentrations (curve 3 in Figure 2). The sign and magnitude of this effect are independent of the sign of $\partial\epsilon/\partial\lambda$ provided the other odd derivatives $\partial^i\epsilon/\partial\lambda^i$, $i = 3, 5, 7, \dots$ are zero. The magnitude of the nonlinearity depends approximately quadratically on the product of the bandwidth and the spectral slope (see Appendix B).

At a spectral maximum or minimum, the nonzero second derivative $\partial^2\epsilon/\partial\lambda^2$ causes an absorbance bias of the same sign as that of the derivative (curves 1 and 2 of Figure 2). Bias approaches a nonzero limit as the concentration and absor-

Table I. Spectral Shape Data Used To Calculate Calibration Curves: HP 1040A Detector

λ , nm	order	ϵ_0	ϵ_1	ϵ_2	ϵ_3
274	2	9337	27.8	-22.5	^b
	3	9338	29.3	-25.3	-0.167
234	2	1807	-25.2	32.5	^b
	3	1827	15.8	30.5	-4.2
298	2	5097	-275	0.612	^b
	3	5092	-283	1.11	1.00
311	2	1868	-175	12.5	^b
	3	1868	-175	12.5	0.0257
340	2	377	-9.90	0.126	^b
	3	378	-9.25	0.918	-0.0680

^a Units: ϵ_0 , cm⁻¹ mol⁻¹; ϵ_1 , cm⁻¹ mol⁻¹ nm⁻¹; ϵ_2 , cm⁻¹ mol⁻¹ nm⁻²; ϵ_3 , cm⁻¹ mol⁻¹ nm⁻³. ^b ϵ_3 nonexistent for second-order fit. ^c Path length, 6 mm.

bance decrease. While calibration curves determined near a spectral maximum are linear up to high concentrations, molar absorptivities measured at nonzero bandwidth contain more bias than low-concentration measurements near a spectral inflection point.

A nonzero second derivative of either sign also causes the calibration curve to bend downward slightly. This nonlinearity resembles that caused by spectral slope, but is smaller and occurs at higher concentrations (Figure 2). This second-order effect is significant only at absorbance greater than about 0.5. Therefore, when selecting a wavelength for UV detection, one manages a *compromise* between response *linearity* and *accuracy* of the measured absorbance. Since for chromatographic and most other analytical calibrations linearity is much more important than the exact molar absorptivity, spectral maxima are generally used.

Schwarz's inequality forbids upward curvature in a calibration curve due to spectral considerations (1). Thus while calibration curves at differing bandwidths may cross (see Figures 3–7), no UV calibration curve can have a slope more positive than that of the calibration line constructed from ϵ_0 . In single-photomultiplier detectors, this curvature may be caused by dependence of either I_0 or ϵ on λ . In diode-array detectors, the software normalizes the response at each diode, nearly eliminating the effect of I_0 dependence on λ .

Experimental results measured on 4-nitrotoluene in acetonitrile are consistent with the above predictions (Figures 2–11). 4-Nitrotoluene was chosen for its spectrum, which includes a local minimum, a local maximum, and a nearly linear region (see Figure 1). In order to emphasize bias and nonlinearity, Figures 2–7 give $100\% \times (A - A_0)/A_0$ on the ordinate, where A_0 is the Beer-Lambert absorbance at very small bandwidth, that is, the percent deviations from absorbance calculated from ϵ_0 .

To test the quadratic (eq 10 and 11) and cubic (eq 5 for $N = 3$) models at different kinds of spectral band positions, UV absorbance measurements were made on 4-nitrotoluene in acetonitrile solution using the HP 1040A detector (transmittance-averaging) at its narrowest bandwidth. In comparison of experimental and calculated absorbances five wavelengths were selected: 234 and 274 nm are near a local minimum and maximum, respectively (i.e., ϵ_1 near zero); 298 nm is near the spectral inflection point (ϵ_2 near zero, $|\epsilon_1|$ large); 311 nm has similar ϵ_0 but different derivatives from those at 234 nm; and 340 nm has very small ϵ_0 and thus might be attractive for uses like preparative-scale liquid chromatography where the most useful concentrations can be very high.

In Figures 3–7 are plotted the experimental results (points in the A vs log C plane) and theoretical results (derived from eq 5 ($N = 3$), 8, and 10. Coefficient values (Table I) were taken from fits at each band center to a second- and a third-order

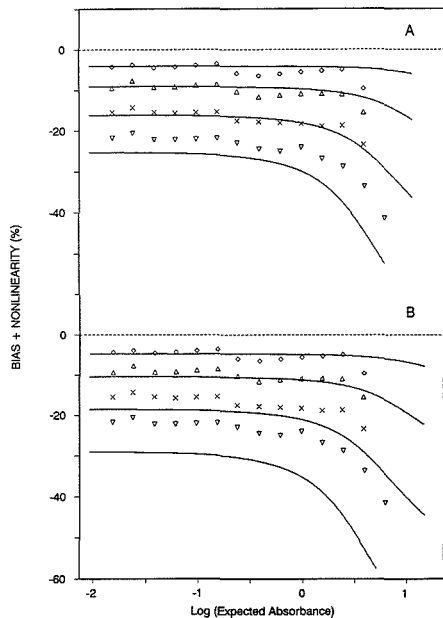


Figure 3. Bias + nonlinearity of measured absorbance relative to narrow-bandpass absorbances at 274 nm (spectral maximum): experimental points (HP 1040A) (\diamond) 20 nm bandpass, (Δ) 30 nm bandpass, (\times) 40 nm bandpass, (∇) 50 nm bandpass, all bandpasses rectangular shape; solid lines, deviations predicted for four curves in increasingly negative deviations; figure A, quadratic spectral model (eq 11); figure B, cubic spectral model (eq 5, $N = 3$).

polynomial. Since these two fits were separately performed, the resulting second-order Taylor expansion is not a truncation of the third-order estimate but instead yields a slightly better fit (relative to available spectral data) than would a truncated expansion.

At a spectral peak (274 nm) calibration curves exhibit the strong, nearly concentration-independent bias caused by a large second derivative ϵ_2 (Figure 3). The effect of negative ϵ_2 is to decrease the average molar absorptivity from that at λ_0 . The calibration curves are similar in form to curve 2 of Figure 2, indicating that a negative second derivative induces a large negative bias. This bias increases with increasing bandwidth, and the agreement of predicted and observed absorbances is excellent up to bandwidths of 30–40 nm. For bandwidths greater than 40 nm the nonlinearity prediction is very good but the bias is overestimated, probably because the spectral shape is not really quadratic or cubic far from the center but is more Gaussian and thus more positive far from the band-pass center.

Calibration curves measured at the spectral minimum (234 nm, Figure 4) are similar to those at the maximum except that ϵ_2 and thus the bias are positive. The calibration curves' downward concavity is very much like that at the spectral maximum since it results from slightly nonzero ϵ_1 and second-order ϵ_3 effects, both of which are independent of the sign of ϵ_2 . Agreement of predicted and observed absorbances is similar to that at 274 nm except that bias overestimation is caused by flattening of the spectrum at 215 nm (Figure 1). This flattening is not predicted by the quadratic or cubic forms. The bias and nonlinearity appear larger at 234 nm than at 274 nm even though the ϵ_2 values are similar since Figures 2–7 give relative deviations from A_0 .

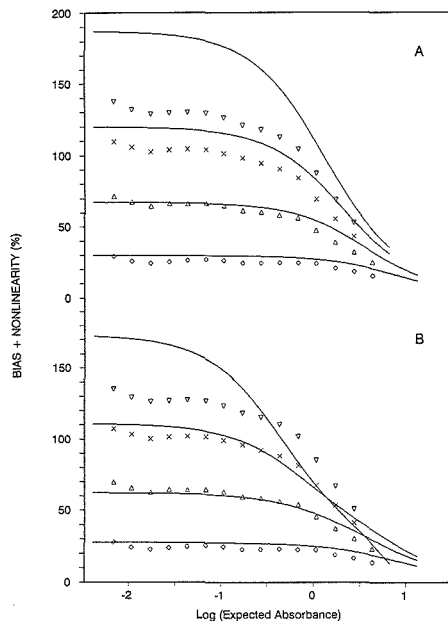


Figure 4. Bias + nonlinearity of measured absorbances relative to narrow-bandpass absorbances at 234 nm (spectral minimum): experimental points (HP 1040A) as for Figure 3; deviations predicted, 20, 30, 40, 50 nm rectangular bandpass for four curves in increasingly positive deviations; figure A, quadratic spectral model (eq 10); figure B, cubic spectral model (eq 5, $N = 3$).

Near the inflection point (298 nm, Figure 5) the lack of bias and the observed nonlinearity at moderate concentrations are consistent with the local spectrum's very small ϵ_2 value and large ϵ_1 value, respectively. Agreement between predicted and observed nonlinearity is excellent, but the bias is not predicted well. The cause of this error is not known but may be due to an inaccurate measurement of ϵ_0 . At 311 nm both bias and nonlinearity of the calibration curves are present to the degree predicted by eq 10 and 12 (Figure 6). While ϵ_0 at 311 nm is approximately equal to that at 234 nm, the calibration curves are quite different, especially at higher concentrations. Comparison of Figures 4 and 6 demonstrates that calibration curve shapes are not dependent only on the molar absorptivity.

Absorbance at long wavelengths (340 nm, Figure 7) is much less well predicted by the current methods than are those at the other wavelengths studied. It is likely that source radiant power and sensor sensitivity are not independent of wavelength as assumed and that the measured absorbance far from the absorption band center is relatively more sensitive to refractive index changes, etc., than is the shape nearer the band maximum. Since chromatographers may have no practical means of verifying such effects, it is probably better to dilute the sample or effluent or to use shorter path length absorption cells (in order to allow detection at a wavelength closer to the band maximum) than to attempt to decrease the absorbance simply by working very far from the band maximum.

Within bandwidths of 40 nm or less, UV spectra used in this work are fit very well ($R > 0.9999$) by third-order Taylor series. Even though third-order polynomials fit the experimental spectra more closely than do second-order ones, the cubic form of the present model (eq 5, $N = 3$) did not predict calibration curves shapes consistently better than did the

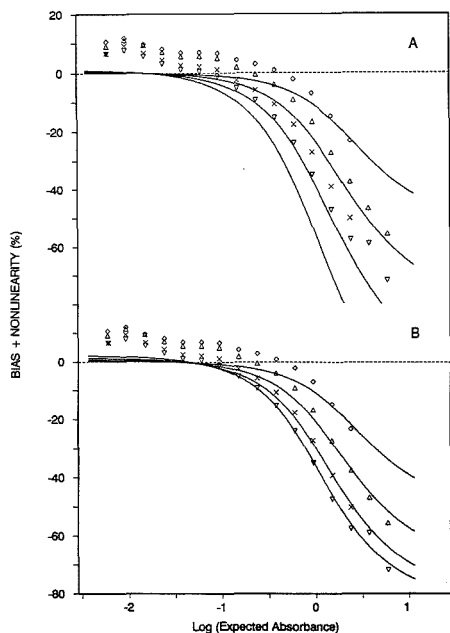


Figure 5. Bias + nonlinearity of measured absorbances relative to narrow-bandpass absorbances at 298 nm (spectral minimum): experimental points (HP 1040A) as for Figure 3; deviations predicted, 20, 30, 40, 50 nm rectangular bandpass for four curves in increasingly negative deviations; figure A, quadratic spectral model (eq 10); figure B, cubic spectral model (eq 5, $N = 3$).

Table II. Spectral Shape Data Used To Calculate Calibration Curves: PE LC-235 Detector

λ , nm	order	ϵ_0	ϵ_1	ϵ_2
275	2	9052	43.1	-20.4
300	2	5025	-250.8	0.58

^a Units: ϵ_0 , $\text{cm}^{-1} \text{mol}^{-1}$; ϵ_1 , $\text{cm}^{-1} \text{mol}^{-1} \text{nm}^{-1}$; ϵ_2 , $\text{cm}^{-1} \text{mol}^{-1} \text{nm}^{-2}$.
^b Path length, 10 mm.

quadratic forms (eq 10 and 11). In cases where the inclusion of even higher-order terms improves the agreement between observed and computed absorbance, the improvement is likely to account less for improved fit to the spectrum than to compensate for violations of the assumptions at the beginning of the theory section.

Absorbances' bias from transmittance-averaging diode-array detectors is roughly proportional to the product of the spectrum's second derivative in the bandpass and the square of the bandwidth. Figure 8 illustrates this quadratic dependence on bandwidth and the agreement in sign and magnitude of the calculated bias with that of the spectral second derivative.

Calibration curve nonlinearity at the five selected wavelengths for a 10-nm detector bandwidth are given in Figure 9. The least nonlinearity is seen for wavelengths near the spectral maximum and minimum (and at 340 nm, largely because the absorbances are low even at high concentrations). As expected from eq 8, the greatest nonlinearity by far is found near the inflection point, where the spectral slope is greatest.

Absorbance-Averaging Detectors. Comparisons of experimental absorbances and transmittance-averaged absorbances computed using the spectral data in Table II are given in Figure 10A (275 nm, close to the spectral maximum, see

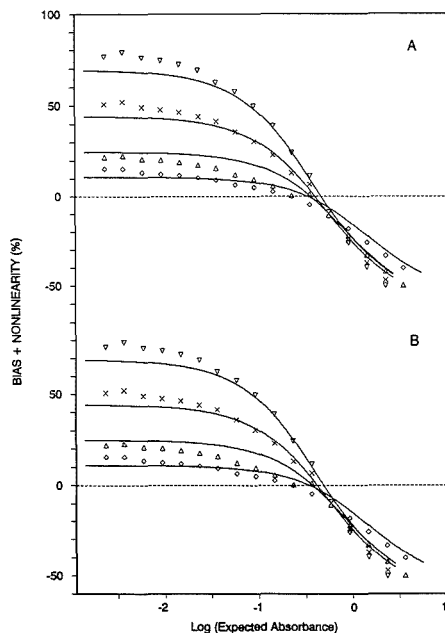


Figure 6. Bias + nonlinearity of measured absorbances relative to narrow-bandpass absorbances at 311 nm (spectral minimum): experimental points (HP 1040A) as for Figure 3; deviations predicted, 20, 30, 40, 50 nm rectangular bandpass for four curves in increasingly positive deviations at low concentrations; figure A, quadratic spectral model (eq 10); figure B, cubic spectral model (eq 5, $N = 3$).

Figure 1) and Figure 10B (300 nm, close to the inflection point). As expected, the degree of bias is accurately predicted by eq 8, 10, and 11, but the nonlinearity predicted by assuming transmittance-averaging is experimentally absent (Figure 10B). While the small experimental nonlinearity may be due to transmittance averaging within individual diodes, the nonlinearity observed is insensitive to bandwidth change, suggesting that it is may be due to nonspectroscopic cause such as refractive index effects or amplifier nonlinearity.

UV Detection Nonlinearity: Potential Advantages to Preparative Chromatographers. The chromatographic literature describes calibration curve nonlinearity in almost universally negative terms. However, nonlinearity, especially the strong downward concavity present when the spectral slope ϵ_1 is large, may be beneficial in preparative chromatography since the useful concentration range of the calibration curve may be extended upward by a factor of 5 to 10 or more without losing sensitivity or accuracy at low concentrations. The price for this extended concentration range is decreased precision and accuracy of high measured concentrations due to the decreased slope of the calibration curve. While this may seem unacceptable if high accuracy is needed, this degradation of accuracy is moot since without the nonlinear effect the higher concentrations would be entirely unmeasurable. The effect is one of data compression of the Beer-Lambert absorbances into an accessible range of measured absorbances.

Figure 11 presents the upper limit of the dynamic linear range, illustrated here as the largest 4-nitrotoluene concentration whose absorbance nonlinearity is less than or equal to 5%, at five wavelengths. As expected, linearity extends to the highest concentrations at given detector bandwidth at the wavelength (340 nm, curve 5) where the sample absorbs least. The range depends very strongly on bandwidth at the

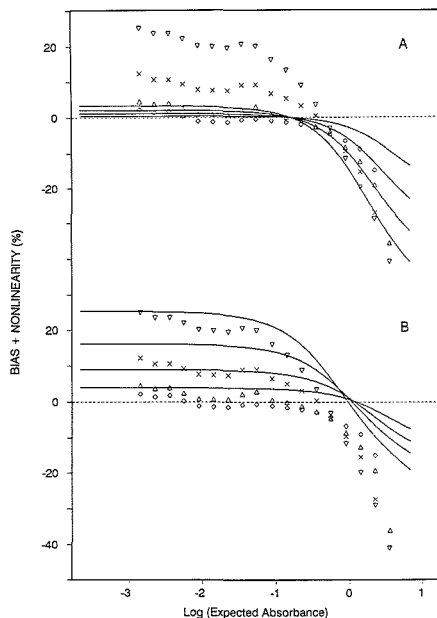


Figure 7. Bias + nonlinearity of measured absorbances relative to narrow-bandpass absorbances at 340 nm (spectral minimum): experimental points (HP 1040A) as for Figure 3; deviations predicted, 20, 30, 40, 50 nm rectangular bandpass for four curves in increasingly positive deviations at low concentrations; figure A, quadratic spectral model (eq 10); figure B, cubic spectral model (eq 5, $N = 3$).

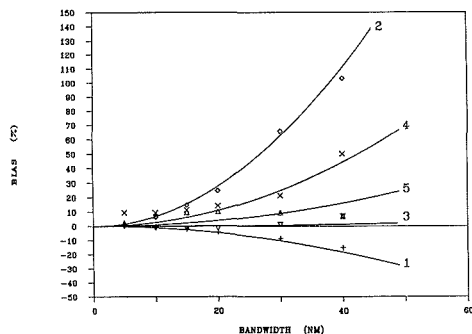


Figure 8. Bias for transmittance-averaging diode-array detector: experimental points (average over lowest four concentrations: 3) (+) 274 nm, (\diamond) 234 nm, (Δ) 298 nm, (X) 311 nm, (∇) 340 nm.

spectral minimum (234, curve 2) because the bias and nonlinearity both increase the reported absorbance as the bandwidth increases. At the spectral maximum (274 nm, curve 1), the two influences cancel to some extent to give a smaller dependence of range on bandwidth.

There is a considerable body of literature describing linear algebraic methods for determining concentration profiles of multiple components from chromatograms when the absorbances are strictly additive and linearly related to concentration. However, such linear methods are inexact in cases where the component spectral shapes differ anywhere in the bandpass. Generally, multicomponent solution absorbances measured by diode-array or other UV absorbance detectors will be greater than the sum of the measured component

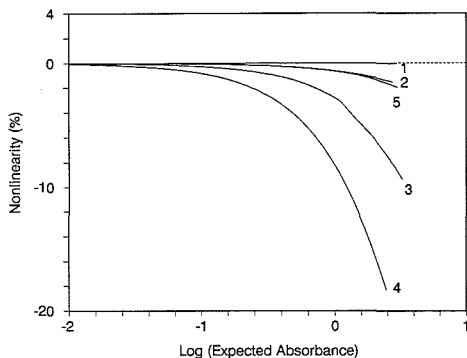


Figure 9. Calibration curve nonlinearity of a transmittance-averaging diode-array detector (HP 1040A) operated at 10 nm bandwidth and at wavelengths (1) 274 nm, (2) 234 nm, (3) 298 nm, (4) 311 nm, and (5) 340 nm.

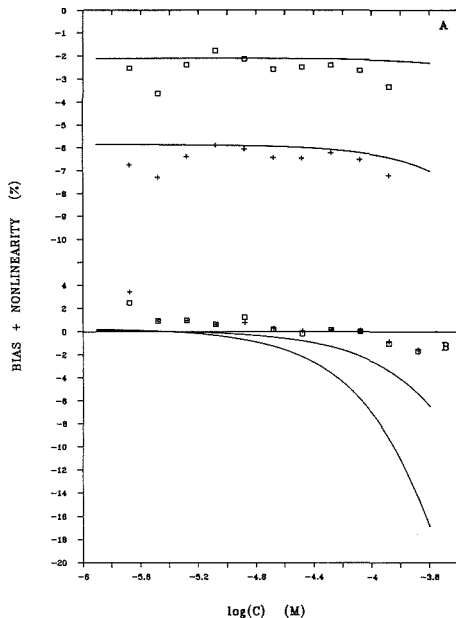


Figure 10. (A) Bias + nonlinearity of measured absorbance relative to narrow-bandwidth absorbances at 275 nm (near spectral maximum): experimental points (PR LC-235), (+) 15 nm, (\square) 25 nm, all bandpasses rectangular shape; deviations predicted (eq 11), 15 and 25 nm bandpass for two curves in increasingly negative deviations at low concentration. (b) As for 10A except 300 nm wavelength (near inflection point).

absorbances. This additional observed absorbance exists since for two components A and B , A can absorb at wavelengths where B absorbs less (and vice versa). In the special case where A and B have identical molar absorptivities and derivatives, the average absorbance is linear in concentration. Thus, for transmittance-averaging detectors the dependence of observed absorption on component concentrations must be even more complicated than the forms given in the present work. Thus extraction of concentration profiles from multicomponent chromatograms measured at nonzero bandwidth requires the solution of a system of nonlinear equations

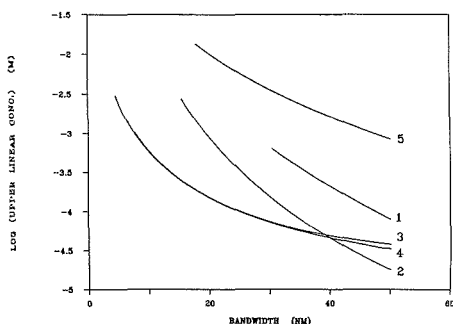


Figure 11. Dynamic linear range (highest concentration where non-linearity is 5% or less) for five wavelengths: 1, 274 nm; 2, 234 nm; 3, 298 nm; 4, 311 nm; 5, 340 nm.

which may be very complex. To our knowledge such nonlinear methods do not exist, and given the complexity of our single-component equations they are likely to be very difficult to derive and apply.

APPENDIX A. TRIANGULAR BANDPASS SHAPE

Equations 4–11 in the text assume rectangular band-pass shape as expected for diode-array detectors. Where the detector band-pass shape is isosceles triangular with width Δ , measured as the full edge-to-edge width of the radiant power window at the sensor, the equations in this appendix may be used.

If the spectrum about λ_0 may be written as

$$A(\lambda) = a_0 + a_1(\lambda - \lambda_0) + a_2(\lambda - \lambda_0)^2/2 \quad (\text{A1})$$

where $\alpha_i = K^*A_i = K^*\epsilon_i \cdot \text{concentration}$, $K = \ln(10)$, and $a_2 = 0$ and a_1 not zero

$$A = a_0 - \frac{2}{K} \log \left(\frac{\sinh(\alpha_1 \Delta/4)}{\alpha_1 \Delta/4} \right) \quad (\text{A2})$$

and for $a_1 = 0$ and a_2 not zero

$$A = a_0 + \frac{a_2 \Delta^2}{8} + \log \left(\frac{\Delta^2}{2} \right) - \log \left((2\pi\alpha_2)^{1/2} \Delta e^{\alpha_2 \Delta^2/8} \operatorname{erf} \left(\frac{(2\alpha_2)^{1/2} \Delta}{4} \right) - 4e^{\alpha_2 \Delta^2/8} + 4 \right) \quad (\text{A3})$$

APPENDIX B. MACLAURIN SERIES

The following MacLaurin series in Δ (Taylor series about $\Delta = 0$) provide simple means of obtaining very accurate approximate solutions for the expression of A , the measured absorbance, in this article. These may be taken as series in α_1 and α_2 also (and therefore in analyte concentration), where they are present. In this appendix, $\alpha_i = KA_i = K\epsilon_i(\text{concentration})$, and $K = \log(10)$.

For eq 8

$$A = A_0 + \frac{1}{K} \left(-\frac{\alpha_1^2}{2^3 3} \Delta^2 + \frac{\alpha_1^4}{2^6 3^2 5} \Delta^4 - \frac{\alpha_1^6}{2^9 3^4 5^2 7} \Delta^6 + \frac{\alpha_1^8}{2^{11} 3^3 5^2 7} \Delta^8 - \frac{\alpha_1^{10}}{2^{10} 3^5 5^2 7 11} \Delta^{10} + \frac{\alpha_1^{12}}{2^{13} 3^7 5^3 7^2 11 13} \Delta^{12} - \dots \right) \quad (\text{B1})$$

For eq 10 and 11

$$A = A_0 + \frac{1}{K} \left(\frac{\alpha_2 - \alpha_1^2}{2^3 3} \Delta^2 - \frac{2\alpha_2^2 - 4\alpha_1^2 \alpha_2 - \alpha_1^4}{2^6 3^2 5} \Delta^4 + \frac{\alpha_2^3 - 3\alpha_1^2 \alpha_2^2 - 6\alpha_1^4 \alpha_2 - \alpha_1^6}{2^9 3^4 5^2 7} \Delta^6 + \frac{2\alpha_2^4 - 8\alpha_1^2 \alpha_2^3 + 36\alpha_1^4 \alpha_2^2 + 24\alpha_1^6 \alpha_2 + 3\alpha_1^8}{2^{11} 3^4 5^2 7} \Delta^8 - \frac{\alpha_2^5 - 5\alpha_1^2 \alpha_2^4 + 7\alpha_1^4 \alpha_2^3 + 25\alpha_1^6 \alpha_2^2 + 10\alpha_1^8 \alpha_2 + \alpha_1^{10}}{2^{10} 3^5 5^2 7 11} \Delta^{10} - \{ [23\alpha_2^6 - 138\alpha_1^2 \alpha_2^5 + 7239\alpha_1^4 \alpha_2^4 - 25216\alpha_1^6 \alpha_2^3 - 29022\alpha_1^8 \alpha_2^2 - 8292\alpha_1^{10} \alpha_2 - 691\alpha_1^{12}] / 2^{13} 3^7 5^3 7^2 11 13 \} \Delta^{12} + \dots \right) \quad (\text{B2})$$

which when $\alpha_1 = 0$ (spectral maximum or minimum) reduces to

$$A = A_0 + \frac{1}{K} \left(\frac{\alpha_2}{2^3 3} \Delta^2 - \frac{\alpha_2^2}{2^6 3^2 5} \Delta^4 + \frac{\alpha_2^3}{2^9 3^4 5^2 7} \Delta^6 + \frac{\alpha_2^4}{2^{10} 3^4 5^2 7} \Delta^8 - \frac{\alpha_2^5}{2^{10} 3^5 5^2 7 11} \Delta^{10} - \frac{23\alpha_2^6}{2^{13} 3^7 5^3 7^2 11 13} \Delta^{12} + \dots \right) \quad (\text{B3})$$

The first term in parentheses above agrees with the first virial term in eq A7 or ref 5. Since the previous work (5) approximates the absorbance exponential by a polynomial early in the derivation, there are differences in later terms.

For eq A2 of Appendix A

$$A = A_0 + \frac{1}{K} \left(-\frac{\alpha_1^2}{2^4 3} \Delta^2 + \frac{\alpha_1^4}{2^9 3^2 5} \Delta^4 - \frac{\alpha_1^6}{2^{11} 3^4 5^2 7} \Delta^6 + \frac{\alpha_1^8}{2^{18} 3^3 5^2 7} \Delta^8 - \frac{\alpha_1^{10}}{2^{19} 3^5 5^2 7 11} \Delta^{10} + \frac{691\alpha_1^{12}}{2^{24} 3^7 5^3 7^2 11 13} \Delta^{12} + \dots \right) \quad (\text{B4})$$

For eq A3 of Appendix A

$$A = A_0 + \frac{1}{K} \left(\frac{\alpha_2}{2^4 3} \Delta^2 - \frac{7\alpha_2^2}{2^9 3^2 5} \Delta^4 + \frac{11\alpha_2^3}{2^{10} 3^4 5^2 7} \Delta^6 + \frac{101\alpha_2^4}{2^{18} 3^4 5^2 7} \Delta^8 - \frac{17\alpha_2^5}{2^{18} 3^5 5^2 7 11} \Delta^{10} - \frac{23\alpha_2^6}{2^{24} 3^7 5^3 7^2 11 13} \Delta^{12} + \dots \right) \quad (\text{B5})$$

LITERATURE CITED

- Finnstrom, B. *Chem. Scr.* **1978**, *13*, 155–156.
- Pfeiffer, C. D.; Larson, J. R.; Ryder, J. F. *Anal. Chem.* **1983**, *55*, 1622–1624.
- Carr, P. W. *Anal. Chem.* **1980**, *52*, 1746–1750.
- Haaland, D. M. *Computerized Quantitative Infrared Analysis*; McClure, G. L., Ed.; American Society for Testing and Materials: Philadelphia, PA, 1987; pp 78–84.
- Goldring, L. S.; Hawes, R. C.; Hare, G. H.; Beckman, A. O.; Stickney, M. E. *Anal. Chem.* **1953**, *25*, 869–878.
- Clewes, B. N. *UV Group Bull.* **1979**, *9*, 35–48.
- Wegschneider, W. *ACS Symp. Ser.* **1985**, *No. 284*, 167–181.
- Janssens, G. *Anal. Chim. Acta* **1979**, *112*, 449–453.
- Stewart, J. E. J. *Chromatogr.* **1979**, *174*, 283–290.
- Ingle, J. D., Jr.; Crouch, S. R. *Spectrochemical Analysis*; Prentice-Hall: Englewood Cliffs, NJ, 1988; pp 366, 373–376.
- Jones, D. G. *Anal. Chem.* **1985**, *57*, 1057A–1073A. Cf. Figure 4.
- Gil, M.; Escobar, D.; Iza, N.; Montero, J. L. *Appl. Spectrosc.* **1986**, *8*, 1156–1161.
- Abramowitz, M.; Stegun, I. A. *Handbook of Mathematical Functions (Ninth Printing)*; National Bureau of Standards: Washington, DC, 1970; p 10.

- (14) Ramsey, J. M. *Anal. Chem.* **1980**, *52*, 2141-2147. Cf. eq 33.
 (15) DeDoncker, E. *Signum News*, **1978**, *13*, 12-18.
 (16) Malcolm, M. A.; Simpson, R. B. *ACM Trans. Math. Software* **1976**, *1*, 129-176.
 (17) Patterson, T. N. L. *Math. Comp.* **1968**, *22*, 847-856.

RECEIVED for review May 22, 1989. Accepted September 6,

1989. This work has been supported in part by Grant DE-FG05-86ER13487 from the U.S. Department of Energy Research, and by the cooperative agreement between the University of Tennessee and Oak Ridge National Laboratory. We also acknowledge the University of Tennessee Computing Center's support of the computation effort.

Built-in Carbon-13 Intensity Reference for Solid-State Analysis by Magic-Angle-Spinning Nuclear Magnetic Resonance Spectrometry

Ming Zhang and Gary E. Maciel*

Department of Chemistry, Colorado State University, Fort Collins, Colorado 80523

The ^{13}C resonance of that portion of a large-volume magic-angle-spinning (MAS) system that is made of Delrin is examined quantitatively for its use as a "built-in" ^{13}C intensity reference for both single-pulse and cross-polarization ^{13}C MAS experiments. ^1H and ^{13}C spin-lattice relaxation measurements and variable contact time cross-polarization (CP) experiments were carried out to establish conditions in which quantitative intensity values could be obtained directly by single-pulse (SP) experiments and calibrations or, after suitable corrections and calibrations, by CP experiments. The CP and SP results, considered in terms of ratios of the aromatic or aliphatic ^{13}C signals of hexamethylbenzene to the ^{13}C signals of Delrin, yield different, yet self-consistent, empirical values of the effective number of ^{13}C spins represented by the built-in resonance of Delrin. These numbers can be used as absolute intensity standards for ^{13}C spin counting strategies aimed at examination of poorly characterized experimental systems.

INTRODUCTION

Recently we have reported on the development and characteristics of a large-volume magic-angle-spinning (MAS) system capable of spinning samples that are about 2.5 cm^3 in volume at speeds up to about 4.5 kHz (*1*). In its normal configuration, this MAS system employs Delrin as the material from which a large portion of the spinner is constructed. This configuration presented us the possibility of using the ^{13}C signal of Delrin, which occurs as a relatively sharp peak at about 88.8 ppm (relative to TMS, tetramethylsilane), as a "built-in" intensity standard for spin counting or absolute intensity measurements in ^{13}C MAS experiments.

A priori, one can think of various reasons why the Delrin ^{13}C signal might not be suitable as an intensity reference. For one thing, for some samples the Delrin signal might constitute a serious overlap or interference problem. This might be the case, for example, in studies of carbohydrate samples. However, the 88.8 ppm chemical shift for the $-\text{OCH}_2\text{O}-$ moiety of Delrin, $(-\text{CH}_2-\text{O})_n$, is in a relatively sparsely populated region of the ^{13}C NMR spectrum for most types of samples. Another class of potential problems is associated with the fact that the Delrin and the sample do not occupy exactly the same region of the coil/spinner assembly. That is, the Delrin is not

confined to the usual sample/coil region of the spinner; and hence one might expect the ability to quantitate the Delrin signal to be compromised by a distribution of coupling efficiencies between the radio frequency coil and the ^{13}C spins in the Delrin. A priori, it would seem that an empirical calibration could be made for a built-in Delrin ^{13}C signal, but that empirical approach would be reliable only if the rf field homogeneity and intensity were constant from one experiment to the next.

One of the reasons why the large-volume MAS system was developed was to provide a sufficient increase in the number of nuclei being observed to permit the observation of natural-abundance ^{13}C MAS spectra in single-pulse (SP) experiments for samples with low carbon content or samples giving broad lines. In this context, characterization of the ^{13}C spin-lattice relaxation behavior and time(s) (T_1^{C}) of the Delrin part of the spinner system is needed. Somewhat to our surprise, the 2.5-cm^3 MAS system was also found to be well suited to cross-polarization (CP) ^{13}C experiments (*1*). Hence, characterization of the Delrin proton spin-lattice relaxation behavior and time(s) (T_1^{H}), ^1H - ^{13}C cross-polarization behavior and time constant(s) (T_{CH}), and proton rotating-frame spin-lattice relaxation behavior and time(s) ($T_{1\rho}^{\text{H}}$) is also indicated. This paper characterizes these relevant spin relaxation behaviors and the use of hexamethylbenzene (HMB) for establishing the suitability of the built-in Delrin signal as a SP and/or CP ^{13}C intensity standard for ^{13}C MAS experiments.

It should be noted that the built-in Delrin standard does not qualify as an *internal* intensity or chemical shift reference. Indeed by the intrinsic polyphase nature of any nonsolution combination of solids, there cannot be an *internal* standard for solid samples, unless the reference is part of a single-phase solid (i.e., part of a solid solution or one portion of an actual compound of which signals from other portions of the compound require spin counting).

EXPERIMENTAL SECTION

^{13}C MAS spectra were obtained at 22.6 MHz on a Chemagnetics M-100/90S spectrometer, using the probe/spinner system described earlier (*1*). T_1^{H} values were measured through ^{13}C signals via cross polarization (*2*). T_1^{C} values were measured by inversion-recovery techniques, using a long delay time (at least $5T_1^{\text{C}}$) between repetitions and spin-lattice relaxation for generating the ^{13}C magnetization that is inverted. Values of T_{CH} and $T_{1\rho}^{\text{H}}$ were determined from variable contact time experiments, with ^{13}C magnetization generated by cross polarization; the data were

analyzed by eq 1, which is correct for the case $T_{1\rho}^H \gg T_{CH}$ (3),

$$M(\tau) = M^*(e^{-\tau/T_{1\rho}^H})(1 - e^{-\tau/T_{CH}}) \quad (1)$$

a condition validated by results obtained in this work (vide infra). In eq 1, $M(\tau)$ is the ^{13}C magnetization generated during a CP contact time τ , and M^* is the magnetization that would be generated if cross polarization were infinitely fast and rotating-frame spin-lattice were infinitely slow. All the NMR experiments reported in this paper were carried out with magic angle spinning at a speed of about 3.3 kHz; small corrections for spinning sideband intensities were included in the data analyses described below.

Hexamethylbenzene was obtained from Merck and used as obtained. Magnesium oxide was obtained from Aldrich (99+%) and used as received. The Delrin from which the plastic portion of the spinner was made was obtained from Afton Plastics Molding Co. (Lakeland, MN).

RESULTS AND DISCUSSION

1. Single-Pulse Results. (a) T_1 Measurements. ^{13}C inversion-recovery experiments were carried out on samples consisting of 18.3% HMB and 81.7% MgO in the 2.5-cm³ Delrin/zirconia spinner system. A repetition delay of 100 s was employed. Analysis of the data for the Delrin signals revealed that the inversion-recovery data could be fit well if three exponential decays are assumed. Because of the multiexponential character of these plots, a detailed error analysis is difficult and probably not warranted by the data. We estimate that the values reported here are accurate to within 10–40%. The slowly relaxing component (48%) manifests a T_1^C value of 9.2 s; the medium relaxation component (24%) manifests a T_1^C value of 2.7 s; and the rapidly relaxing component (28%) manifests a T_1^C value of 0.074 s. The relaxation data of the aromatic HMB peak were fit well by a single exponential decay, with $T_1^C = 1.65 \pm 0.04$ s. The aliphatic HMB peak displays a two-exponential fit, manifesting T_1^C values of 0.18 s (48%) and 0.87 s (52%). The origin of this multiexponential ^{13}C spin-lattice relaxation behavior in HMB is not understood; in any case, experimental conditions in our subsequent SP experiments were chosen to take this apparent behavior into account. The 100-s repetition delays employed in the SP experiments (vide infra) are an order of magnitude larger than the largest measured T_1^C values.

(b) *SP Calibrations.* In order to calibrate the built-in Delrin ^{13}C signal empirically for the single-pulse approach, SP experiments with 100-s repetition delays were carried out on a series of samples consisting of HMB/MgO mixtures of various compositions. Figure 1 shows a plot of the ratio of the integrated intensities of the aliphatic HMB peak and the Delrin peak for this set of mixtures. This plot is a straight line with a correlation coefficient of 0.9987. From this plot, we obtain the result (corresponding to the intensity ratio = 1) that the ^{13}C SP signal of the built-in Delrin corresponds to 0.265 ± 0.007 g of HMB. Taking the molecular formula, molecular weight, Avogadro's number, and the natural abundance of ^{13}C into account, this corresponds to $(0.265 \pm 0.007) \times (6/162.26)(1.108 \times 10^{-2})(6.022 \times 10^{23}) = (6.54 \pm 0.17) \times 10^{19}$ ^{13}C spins, a number that can be used in future experiments of ^{13}C counting that employ this particular spinner/coil combination. Figure 1 also shows the corresponding results for the aromatic carbon resonance of HMB. An analogous analysis, with a correlation coefficient of 0.9996, yields the result that the built-in Delrin resonance corresponds to 0.251 ± 0.004 g of HMB, or $(6.19 \pm 0.10) \times 10^{19}$ ^{13}C spins.

2. CP Results. (a) T_1^H , T_{CH} , and $T_{1\rho}^H$ Measurements. ^{13}C -monitored T_1^H inversion-recovery experiments (2) were carried out on the sample of 18.3% HMB and 81.7% MgO in the 2.5-cm³ Delrin/zirconia spinner. The computer fit of an exponential/inversion-recovery equation for each of the ^{13}C peaks in the spectrum yielded the following T_1^H values:

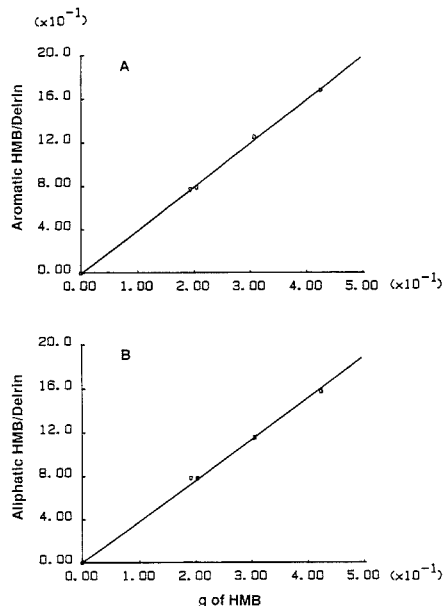


Figure 1. Plot of the ratio of the aromatic HMB ^{13}C intensity to the Delrin ^{13}C intensity (A) or the ratio of the aliphatic HMB ^{13}C intensity to the Delrin ^{13}C intensity (B), measured via single-pulse (SP) experiments (100-s repetition delay), vs grams of HMB in HMB/MgO mixtures.

Table I. Results of Variable Contact Time Experiments^a

^{13}C peak	recycle delay = 5 s		recycle delay = 1 s	
	T_{CH} , ms	$T_{1\rho}^H$, ms	T_{CH} , ms	$T_{1\rho}^H$, ms
Delrin	0.29 ± 0.03	77 ± 4	0.27 ± 0.07	80 ± 1
aliphatic HMB	1.98 ± 0.06	98 ± 2	1.88 ± 0.09	90 ± 4
aromatic HMB	2.50 ± 0.10	127 ± 4	2.27 ± 0.10	78 ± 15

^a Stated error limits represent the 95% confidence level.

Delrin, 0.412 ± 0.005 s; aromatic HMB, 0.104 ± 0.001 s, and aliphatic HMB, 0.104 ± 0.001 s. The relevance of these values is the fact that the ^{13}C magnetization that is generated by cross polarization is dependent upon the ^1H magnetization available at the beginning of the CP pulse sequence. This ^1H magnetization is in turn the steady-state magnetization established as a result of spin-lattice relaxation between the end of one CP sequence and the beginning of the next. From the point of view of the ^1H magnetization, this steady-state magnetization, M_{SS}^H , is analogous to what is obtained at the beginning of 90° pulses in a long series of 90° pulses, after each of which M_z^H is zero (as is also the case in CP). This steady-state magnetization is given by eq 2, where M_0^H is the equilibrium

$$M_{SS}^H = M_0^H(1 - e^{-\tau_d/T_1^H}) \quad (2)$$

magnetization and τ_d is the repetition delay between the end of the CP data acquisition period and the initiation of the next ^1H 90° pulse.

Variable contact time CP experiments were carried out on the sample of 18.3% MgO and 81.7% HMB in the 2.5-cm³ Delrin/zirconia spinner. For each ^{13}C peak, the computer fit of the data to eq 1 yielded values of T_{CH} and $T_{1\rho}^H$. Figure 2 shows a representative set of data (for the Delrin peak) together with the computer fit. Table I gives the T_{CH} and $T_{1\rho}^H$ values derived for the Delrin, aliphatic HMB, and aromatic

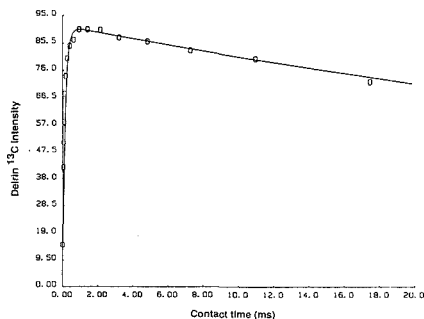


Figure 2. Plot of the Delrin ^{13}C intensity as a function of CP contact time, obtained with 1-s repetition delay.

HMB carbons from computer fits.

In the simplest view, values of T_{CH} and $T_{1\rho}^{\text{H}}$ should not depend on the recycle delay, τ_d , as the cross polarization simply works on whatever amount of ^1H magnetization is available at the beginning of the CP sequence. For the two HMB peaks one expects that, not only should the $T_{1\rho}^{\text{H}}$ values measured via the aromatic and aliphatic peaks be the same (the magnetization of both carbon types is obtained from the same set of protons, the methyls), but this common value should be independent of τ_d . The fact that substantial differences are measured may reflect the fact that the largest τ value employed in the $T_{1\rho}^{\text{H}}$ measurements is about one-third of the smallest $T_{1\rho}^{\text{H}}$ value measured; hence, only early parts of the $T_{1\rho}^{\text{H}}$ -determined decay were monitored, so the accuracy of those $T_{1\rho}^{\text{H}}$ measurements must be questioned. Thus, there may be systematic errors, in addition to random errors, in these determinations. In addition, the fact that all the T_{CH} and $T_{1\rho}^{\text{H}}$ values measured with $\tau_d = 1$ s are smaller than the corresponding values measured with $\tau_d = 5$ s probably implies an unintended change in the rf field strength from one set of measurements to the other. A shorter τ_d could result in higher temperatures in the rf circuits, which can detune these circuits. The fact that T_{CH} for the aliphatic HMB carbons is smaller than that of the aromatic HMB carbons reflects the fact that C-H coupling for aliphatic HMB carbons is stronger than C-H coupling for aromatic HMB carbons. In any case, all of the $T_{1\rho}^{\text{H}}$ values obtained here are at least an order of magnitude larger than the CP contact times of interest in this study, so the factor $e^{-\tau/T_{1\rho}^{\text{H}}}$ in eq 1 is effectively unity for all of the HMB carbon resonances.

(b) *CP Calibrations.* A series of CP calibration experiments analogous to the SP calibration experiments represented in Figure 1 was carried out on the same set of HMB/MgO mixtures. Before calculation of the $M_{\text{a}}/M_{\text{D}}^{\text{a}}$ and $M_{\text{ar}}/M_{\text{D}}^{\text{ar}}$ ratios to be used in CP plots analogous to the SP plots in Figure 1, correction factors $M^*/M(\tau)$ were applied to the raw ^{13}C intensity data according to eq 1, based on the T_{CH} and $T_{1\rho}^{\text{H}}$ values obtained from the variable contact time data. As indicated above, the first factor on the right side of eq 1 is in each case equal to unity in the cases of interest here. In addition, for experiments with the shorter delay (τ_d), correction factors $M_{\text{v}}^{\text{H}}/M_{\text{SS}}^{\text{H}}$ were computed from eq 2, using the $T_{1\rho}^{\text{H}}$ values reported above, and applied to the raw ^{13}C intensities.

A plot (not shown here) of the ratio of ^{13}C intensities, corrected according to eq 1, of the aliphatic HMB and Delrin resonances obtained with a 5-ms CP contact time (τ) and a 5-s repetition delay (τ_d) consists of a straight line with a correlation coefficient of 0.9997. From the slope of this plot we obtain the result that the built-in Delrin CP signal corresponds to 0.220 ± 0.004 g of HMB, or $(5.42 \pm 0.10) \times 10^{19}$ ^{13}C spins. An analogous analysis of the CP data of the ar-

omatic HMB peak yields a straight-line plot (not shown here) with a correlation coefficient of 0.9996. From the slope of that plot we obtain the result that the built-in Delrin CP signal corresponds to 0.219 ± 0.004 g of HMB, or $(5.40 \pm 0.10) \times 10^{19}$ ^{13}C spins, in good agreement with the result obtained from the aliphatic signal.

Analogous CP experiments were carried out on the same mixtures, using a 5-ms CP contact time and a 1-s repetition delay. Corrections were applied according to eq 1 and 2. The aliphatic HMB plot analogous to that of Figure 1B is a straight line with a correlation coefficient of 0.9960, yielding the result that the built-in Delrin CP signal corresponds to 0.214 ± 0.014 g of HMB, or $(5.28 \pm 0.35) \times 10^{19}$ ^{13}C spins. The aromatic HMB plot analogous to that of Figure 1A is a straight line with a correlation coefficient of 0.9972 and a slope that yields the value 0.214 ± 0.012 g of HMB, corresponding to $(5.28 \pm 0.30) \times 10^{19}$ ^{13}C spins.

The CP results for both the 5 ms/5 s and 5 ms/1 s parameter sets constitute calibrations that are within experimental error of each other, indicating *empirically* that the built-in Delrin CP signal of this particular MAS system reproducibly corresponds to about $(5.35 \pm 0.18) \times 10^{19}$ ^{13}C spins. This number is about 16% below the value obtained by the SP calibrations discussed above. The fact that consistent CP calibrations are obtained means that CP spin counting can be carried out reliably on an *empirical* basis. The fact that the empirical CP "HMB equivalent" is smaller than the corresponding SP "HMB equivalent" is understandable on the basis of the geometry of the $2.5 \text{ cm}^3/4.5 \text{ kHz}$ spinner system.

The HMB sample is contained within the active volume of the rf coil and is hence efficiently interrogated by either SP or CP approaches. However, a substantial fraction of the Delrin in the spinner falls outside the active volume of the rf coil. The ^{13}C rf field and tip angle experienced by the Delrin magnetization originating from any region of the spinner fall off with increasing distance from the rf coil. Nevertheless, for any region for which the tip angle is nonzero, there is a corresponding contribution to the Delrin SP signal, which is accounted for empirically in the SP calibration. Similarly, the fall-off of ^{13}C and ^1H rf fields with increasing distance from the *single* double-tuned rf coil affects CP efficiency. Presumably, the ^{13}C and ^1H rf fields fall off by the same factor for a given spatial region of the Delrin spinner, so the CP effectiveness does not abruptly fall to zero immediately outside the coil. However, the CP efficiency can fall off considerably faster than the $\cos \omega_1 t_p$ dependence of SP-generated magnetization (where ω_1 = the rf field in rad s^{-1} = Avis and t_p is the pulse duration), because of the requirement of a strong rf field to maintain the spin-lock condition, especially for protons. Hence, it is reasonable that the "corrected" ratio of the CP HMB aliphatic or aromatic signal intensity to the "corrected" CP Delrin intensity should be larger than what one would expect from comparisons with SP results.

The results described above show that within a variance of about $\pm 4\%$, the ^{13}C intensity of the built-in Delrin signal can be used as an intensity standard for ^{13}C absolute intensity or spin counting experiments, either by the single-pulse or cross-polarization approaches. It should be noted that some of the $\pm 4\%$ variance for each method may be due to variability in the detection sensitivity of the HMB signals, rather than errors or variations in the Delrin ^{13}C signal intensity. Hence, the precision and accuracy of the Delrin ^{13}C signals may be considerably better than $\pm 4\%$. One could argue that HMB, which has a CP match condition that is relatively sensitive to mismatch, is not an optimum choice for this purpose. Perhaps a better choice would be a compound with relatively rigid CH_2 groups; the strong ^1H - ^1H dipolar interactions in such

a system would result in a broader (less fragile) CP match condition.

It is worth emphasizing that the level of precision indicated above should be expected only if one's experiments are limited to a *specific spinner assembly*. Calibrations of the type represented by Figure 1 should be carried out for each spinner assembly (assuming reproducibility of spinner assemblies is not perfect) and periodically even for a specific unit (assuming some wearing of a spinner system with repeated usage). For the reasons discussed above, one should expect greater variability, or lower precision, due to variations in rf field strength or homogeneity in CP spin counting experiments than in SP spin counting experiments carried out by this approach.

The results presented in this paper offer major hope for a convenient strategy for the measurement of absolute ^{13}C intensities or ^{13}C spin counting in ^{13}C NMR studies of certain types of systems in which there has been substantial uncertainty in the significance of ^{13}C NMR intensities. Examples include cases in which paramagnetic centers in the sample may

interfere with the observation of ^{13}C intensity due to excessive broadening and/or paramagnetic shifts, cases in which certain carbon environments may preclude the existence of reasonably efficient ^{13}C spin-lattice relaxation, and cases in which the remoteness of certain carbon atoms from hydrogen may interfere with ^{13}C observation via ^1H - ^{13}C cross polarization. Applications of these types are under way in this laboratory.

Registry No. ^{13}C , 14762-74-4.

LITERATURE CITED

- (1) Zhang, M.; Maciel, G. E. *J. Magn. Reson.*, in press.
- (2) Sullivan, M.; Maciel, G. E. *Anal. Chem.* 1982, 54, 1615.
- (3) Mehring, M. *Principles of High Resolution NMR in Solids*; Springer-Verlag: New York, 1983; pp 152-154.

RECEIVED for review May 19, 1989. Accepted August 22, 1989. The authors gratefully acknowledge partial support of this research by National Science Foundation Grant No. CHE-8610151 and Department of Energy Contract No. DE-AC22-88FC88813.

TECHNICAL NOTES

Evaporation Device for Continuous Flow Liquid Secondary Ion Mass Spectrometry

Ming-chuen Shih,* Tao-Chin Lin Wang, and S. P. Markey*

Laboratory of Clinical Science, National Institute of Mental Health, Bethesda, Maryland 20892

INTRODUCTION

Continuous flow (CF) liquid secondary ion mass spectrometry (LSIMS) or fast atom bombardment (FAB) mass spectrometry has attracted considerable interest (1-4) because it offers several advantages in comparison to static LSIMS. First, new samples can be analyzed conveniently without breaking vacuum or changing instrument focus, facilitating automatic operation and rapid sample throughput. Second, samples dissolved in a variety of organic solvents may be admixed with glycerol to form a liquid matrix compatible with both chromatographic and LSIMS requirements. Third, spectra are characterized by lower chemical noise than that observed with static LSIMS. Finally, since samples elute discretely, chromatographic data processing techniques are applicable.

In the operation of a CF-LSIMS or FAB probe, one of the common handicaps for extended continuous stable operation is the accumulation of liquid around the probe tip region. This problem exists whether the liquid is delivered either internally or externally to the probe shaft to the target surface to form a thin film. The results are peak broadening from stagnancy of liquid flow, film instability from the freezing of mobile phase in the capillary, and instability of ion source pressure due to dripping and bubbling of mobile phase. Various efforts have been directed toward minimizing these undesirable effects [e.g., selection of mobile phase, variation of control parameters for mass and heat transfer and the use of fritted surfaces (1), all aiming at on-site evaporation, and the use of wicking material to remove liquid from the target surface and to provide a thin film and smooth flow (5, 6)]. We have demonstrated quantitative analyses of polar substances using CF-LSIMS (7, 8), and have consequently desired to operate in this mode continuously and routinely for 6-8-h periods for analytical assays, a requirement more rigorous than that reported previously by others. We have sought to extend the

time period of continuous operation by facilitating and sustaining liquid transport across the probe surface by channeling the liquid onto a large absorbent surface which could provide sufficient heat and fluid capacity to bring the flow system close to a state of mass transfer dynamic equilibrium (i.e., a state in which the rate of liquid steadily evaporated into the vacuum system equals the rate of mobile phase delivered to the probe tip). The idea was tested by using an evaporation device made of cellulose with an extended surface area, displaced from the LSIMS target surface, and in contact with a solid probe which serves as a large heat sink. We are able to operate in CF-LSIMS mode for periods longer than 8 h with only slight deterioration of performance.

EXPERIMENTAL SECTION

A tandem quadrupole mass spectrometer (TSQ-70, Finnigan Mat, San Jose, CA) was used with a prototype CF-LSIMS apparatus (Bioprobe, Finnigan MAT). This apparatus delivers liquid through a capillary tube which is positioned to contact a standard probe located near the ion extraction lens assembly (Figure 1a). An unfocused cesium ion gun (Phrasor, Duarte, CA) was the primary ion source. A solid, stainless steel probe shaft dimensionally identical with the standard heated commercial probe was machined for these studies in order to provide a rugged device with a large heat capacity. It was fitted with a standard copper FAB probe tip. Figure 1a shows the probe-evaporator assembly. The evaporator consisted of two layers of cellulose absorbent to maximize the evaporation surface area. The outer layer (shaded portion A in Figure 1b) was cut from a 10 mm \times 50 mm single thickness cellulose extraction thimble (Whatman, Inc., Clifton, NJ). The inner layer (shaded portion B in Figure 1c) was cut from a similar 25 mm \times 100 mm single thickness cellulose extraction thimble. A large hole (C in Figure 1b) and a small hole (D in Figure 1b) were cut in the outer layer to increase the pumping efficiency. Cutting with small surgical scissors minimized the generation of paper lint. The two cellulose layers were overlapped by rolling portion B into a tube and sliding it into portion A. The resulting evaporation assembly was then force-fitted onto

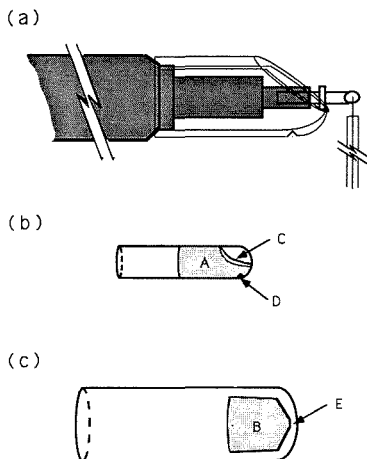


Figure 1. (a) Probe-evaporator assembly. (b) The outer layer of the evaporator. (c) The inner layer of the evaporator.

the probe shaft so that the lower edge of the probe tip collar touched the pointed end (E in Figure 1c) of the inner layer. To minimize the thermal load on the immediate vicinity of the probe tip and to maximize the evaporation surface area, the absorbent was in contact with the probe shaft only near the base of the evaporator. This contact provided a heat conduction pathway to the evaporator.

A pulse-dampened pump (Model 302, Gilson, Middleton, WI) delivered a 20% glycerol/ H_2O solution to a 0.5- μ L loop injector. The liquid flowed through a 75 μ m i.d. \times 90 cm fused silica tubing (Polymicro Technologies, Phoenix, AZ) to meet the probe tip (Figure 1a). The mobile phase flow rate was 8 μ L/min, and the ion source temperature was 40–45 $^{\circ}$ C. The probe was heated at the probe handle with a heating tape to maintain the temperature of the probe shaft at the entry port of the mass spectrometer at about 40 $^{\circ}$ C. The cellulose evaporator assemblies were withdrawn from the vacuum system and discarded after use. The performance of this device was evaluated by repetitive 0.5- μ L injections of mobile phase containing 10 ng of potassium salt of (3-methoxy-4-sulfatoxyphenyl)ethylene glycol (MOPEG-sulfate, Fluka Chemicals, Ronkonkoma, NY).

RESULTS AND DISCUSSION

Figure 2 shows the results of repetitive injections of mobile phase containing MOPEG-sulfate, a norepinephrine metabolite for which we desired a direct quantitative analysis method. While this example demonstrates stable operation in negative ion mode, we have obtained similar results monitoring positive ions in the routine analyses of 1-methyl-4-phenylpyridine and 2-amino-3-(methylamino)propanoic acid. For the analysis of MOPEG-sulfate, the continuous flow system was operated continuously for 9.5 h with only slight deterioration of performance. The size of the evaporator used was approximately 10 mm i.d. \times 28 mm length. With 20% glycerol/ H_2O mobile phase at 8 μ L/min flow rate, the retention of liquid in the evaporator after 9.5 h of continuous operation was 16.1% by weight.

There are two engineering principles that this system incorporates and that are applicable to all CF-LSIMS systems. First, the rapid flow of liquid across the probe tip surface and into another area reduced the thermal load at the probe tip (e.g., we have physically separated the site of secondary ion emission from the region of liquid evaporation). Thus, the requirement for careful monitoring and precise control of probe tip temperature in order to supply heat for mobile phase

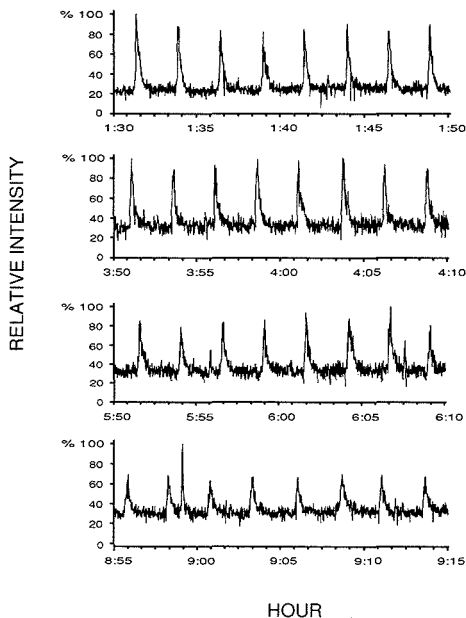


Figure 2. Negative ion selected ion recordings of m/z 263 ($M - H$) obtained by repetitive loop injections containing 10 ng of MOPEG-sulfate in 0.5 μ L of 20% glycerol/water during a period of more than 9 h demonstrating the stability of the CF-LSIMS system with an evaporation device.

evaporation has been eliminated. Instead, there is a heat conduction pathway, bypassing the probe tip, which transfers heat to the evaporator. Second, the use of an extended absorbent evaporation surface in contact with a large heat sink increases the rate of mobile phase evaporation at reduced temperature. As liquid begins to accumulate within this absorption medium, the wetted surface area starts to expand rapidly. The surface expansion increases the rate of evaporation and decreases the rate of liquid accumulation. As the rate of accumulation approaches zero, the flow system approaches a state of mass transfer dynamic equilibrium. Thus, if sufficient evaporation surface area is provided, a CF-LSIMS system can be operated for extended periods. We anticipate that with a balance of absorbent, evaporation surface, and heat sink, a wide range of mobile phase compositions and mobile phase flow rates should be accommodated in CF-LSIMS.

Registry No. Cellulose, 9004-34-6.

LITERATURE CITED

- Ito, Y.; Takeuchi, D.; Ishii, D.; Goto, M. *J. Chromatogr.* **1985**, *346*, 161-166.
- Caprioli, R. M.; Fan, T.; Cottrell, J. S. *Anal. Chem.* **1986**, *58*, 2949-2954.
- Ashcroft, A. E.; Chapman, J. R.; Cottrell, J. S. *J. Chromatogr.* **1987**, *394*, 15-20.
- de Wit, J. S. M.; Deterding, L. J.; Moseley, M. A.; Tomer, K. B.; Jorgenson, J. W. *Rapid Commun. Mass Spectrom.* **1988**, *2*, 100-104.
- Caprioli, R. M. *Proc. ASMS Conf. Mass Spectrom. Allied Top.*, **36th** **1988**, 729-730.
- Lin, S.; Caprioli, R. M. *Proc. ASMS Conf. Mass Spectrom. Allied Top.*, **36th** **1988**, 1000-1001.
- Markey, S. P.; Wang, T.-C. L.; Shih, M.; Boni, R.; Duncan, M.; Yang, S.-C.; Bradford, D. *Proc. ASMS Conf. Mass Spectrom. Allied Top.*, **36th** **1988**, 739-740.
- Wang, T.-C. L.; Shih, M.; Markey, S. P.; Duncan, M. *Anal. Chem.* **1989**, *61*, 1013-1016.

RECEIVED for review June 19, 1989. Accepted August 4, 1989.

Manual Headspace Method To Analyze for the Volatile Aromatics of Gasoline in Groundwater and Soil Samples

Valerie D. Roe, Michael J. Lacy, and James D. Stuart*

Department of Chemistry, U-60, 215 Glenbrook Road, University of Connecticut, Storrs, Connecticut 06269-3060

Gary A. Robbins

Department of Geology and Geophysics, U-45, 345 Mansfield Road, University of Connecticut, Storrs, Connecticut 06269-3045

Contamination of groundwater and soil by leaking underground petroleum storage tanks is an increasingly common environmental problem. The study of a gasoline-contaminated site involves the collection of a large number of soil and water samples. The use of on-site soil-gas monitoring equipment and portable gas chromatographs is proving to be very effective in screening sites (1, 2). However, there remains the need to corroborate the often variable field analyses with laboratory-based methods.

We were required to develop a rapid, 15–20 min, manual method to analyze primarily for the six important volatile aromatics, i.e., benzene, toluene, ethylbenzene, and the three xylene isomers (often collectively abbreviated BTEX), in gasoline-contaminated groundwater and soil samples. Rapid turnaround times were required so as to reduce the loss of the compounds to volatilization and bacterial degradation, thus providing a better comparison to the field data. A static headspace method was developed to be performed directly in the 40-mL screw-cap septum vial in which the sample had been collected in the field. The developed headspace method allowed for the analysis of trace volatile components as well as those present at much higher levels. This is not possible for the often used purge-and-trap methods.

In the past, static headspace methods have proven to be rapid and effective means of analyzing for various volatile pollutants in groundwater and soil samples. Static headspace involves a partitioning of volatile components between the aqueous and vapor phases enclosed in a gas-tight vial. Soil samples are enclosed in vials with distilled water, which serves to extract the contaminants. Thereupon, a partitioning of the volatile organics into the enclosed vapor phase occurs. The theoretical and practical considerations of such static headspace methods have been discussed in depth (3–11).

THEORETICAL DEVELOPMENT

To achieve representative and reproducible results, the static headspace method requires that chemical and thermal equilibrium be reached within the sampling vessel. Henry's law (eq 1) applies to the vapor–liquid system under these conditions. Henry's law constant H is related to the vapor

$$H = P_v / C_w \quad (1)$$

pressure of the gas over the solution, P_v , and to the concentration of the compound in the water phase, C_w .

When the volume of headspace to volume of aqueous phase is a constant ratio in all samples and standards, a standard curve can be plotted, and there is no need to utilize Henry's law for quantitative analysis. This is simple to achieve for aqueous samples, as a constant, known volume can be withdrawn from each vial. Soil samples, however, pose a more difficult problem. To avoid the loss of volatile constituents during handling, soils are collected in vials with a known mass of distilled water and immediately capped. The final headspace volume is variable, depending upon the volume occupied by the soil; therefore the headspace to water ratio varies from sample to sample. A correction factor based on

Henry's law must therefore be applied to the gas chromatographic results in order to make the analysis meaningful.

An effective Henry's law constant at the analytical condition can be determined by running the same standard solution at two different headspace to liquid volume ratios, as indicated by eq 2. The ratios (V_v/V_w) represent the volume ratios of

$$H = \frac{1 - (A_1/A_2)}{(A_1/A_2)[(V_v/V_w)_1 - (V_v/V_w)_2]} \quad (2)$$

headspace to aqueous phase in the two trials. A_1 and A_2 represent the peak areas for the compound of interest. Once Henry's law constant has been found for each compound, an unknown concentration of the compound in a soil sample can be calculated by using eq 3. Here the subscripts s and o

$$C_s = C_o \frac{V_w A_s (1/H + (V_v/V_w)_s)}{M_s A_o (1/H + (V_v/V_w)_o)} \quad (3)$$

indicate the soil and standard respectively, V_w is the volume of water added to the vial, and M_s is the mass of the soil.

EXPERIMENTAL SECTION

Instrumentation. Separations were performed with a capillary column gas chromatograph (Hewlett-Packard Model 5880A). A split/splitless injector was used in the splitless mode. Megabore capillary columns, 0.55 mm i.d., 30 m in length with 3.0- μ m film thickness of DB-1 (J&W Scientific) were used. The column's eluent was passed through a photoionization detector (PID) (HNU Systems, Model 52-02A) equipped with a 10.2-eV lamp, followed by a flame ionization detector (FID) (Hewlett-Packard). The PID was connected to one integrator while the FID output was monitored by the GC terminal (Hewlett-Packard, Model 5880A, Level 4). The following column oven temperature program was used: initial temperature, 40 °C; initial time, 3.0 min; temperature program rate, 8 °C/min; final temperature, 190 °C, with a variable final time to elute higher boiling components. The flow rate through the column was controlled at 5–7 mL/min. Manual injections of the headspace vapors were accomplished by using 250- or 500- μ L gas-tight, fixed needle microsyringes (Scientific Glass Engineering, Part No. 010508 or 010510). To prevent septum corings from entering the column because of the use of relatively wide-bore syringe needles, a plug about 1 cm long of silanized glass wool was packed into the glass injection port liner.

The gasoline-polluted soil or groundwater samples were collected in 40-mL glass vials (Supelco, Part No. 2-3299), with hole caps (Supelco, Part No. 2-3283) and Teflon-faced septa (Supelco, Part No. 2-3281). Each vial contained as a preservative 100 μ L of a 24 000 mg/L aqueous solution of HgCl₂. A final concentration of 60 mg/L HgCl₂ was obtained upon completely filling the vial with 40 mL of groundwater. This was found to be an effective method of preservation against microbial degradation. Immediately after sampling, the capped vials were inverted to reduce the loss of entrapped air and any volatile components and then packed on ice and returned to the laboratory where they were kept refrigerated at 4 °C if analysis could not be conducted immediately.

Twenty to sixty minutes before analysis, the vials were placed in a 25.0 °C constant temperature water bath. After about 15 min of temperature equilibration, a 1.5 in. long, 22-gauge needle was inserted through the septum to allow air to enter. Then a

Table I. Effect of Using Mercuric Chloride as a Preservative for Groundwater Samples

time, days	concentration, $\mu\text{g/L}$							
	unpreserved				preserved with 60 mg/L mercuric chloride			
	B	T	E	X	B	T	E	X
0	34	92	227	947	31	73	221	892
2	32	85	94	783	36	95	216	890
14	0	54	0	0	34	87	237	991
39	0	25	0	0	38	92	270	973

similar, second needle attached to a 30-mL Luer-Lock syringe was used to removed 10.0 mL of the aqueous phase. The vial was kept in an inverted position and shaken thoroughly for 1 min. The vial, with 10.0 mL of headspace, was then again placed in the 25.0 °C water bath and allowed to reach thermal and phase equilibrium. At the time of analysis, 200–500 μL of the headspace was withdrawn with a gas-tight syringe and injected into the gas chromatograph.

RESULTS AND DISCUSSION

This method has proven to be a rapid and effective means of analyzing environmental samples. Brief run times of 15–20 min and lack of sample work-up allow up to 20 samples to be analyzed in an 8-h work day. The PID has a useful analytical range for BTEX in water extending from about 1 $\mu\text{g/L}$ to at least 15000 $\mu\text{g/L}$ using this method. Thus, samples with a wide range of contamination can be analyzed without dilution or other sample-handling techniques.

It was found that chemical preservation of environmental samples was required in order to obtain meaningful results. Merely storing unpreserved soil or water samples at 4 °C, as discussed by EPA Method 503.1 (12), was not sufficiently to prevent biodegradation, even for short periods of time. In one of our studies, a groundwater sample from a gasoline spill site contained 221 $\mu\text{g/L}$ of ethylbenzene immediately after collection. After 2 days of refrigeration, only 43% of the initial concentration of ethylbenzene remained in an unpreserved sample. Other results from this study are presented in Table I. Preserved samples from the same location maintained initial concentrations of BTEX even after 39 days. The HgCl_2 was therefore effective at preventing biodegradation, and no volatile losses occurred from the sampling vials.

Headspace analysis has several clear advantages over the more conventional purge-and-trap methods. Rapid analyses' turnaround times, as mentioned above, are easily achieved. The lack of expensive purging equipment is also important. Another benefit is the ability to perform multiple runs on a single sample vial. Purge-and-trap is essentially a destructive method; the sample may only be purged and analyzed once. The removal of a sample of headspace vapors, however, does not significantly diminish the total mass of analyte within a sample vial, and equilibrium is reestablished within 2–5 min. Overall reproducibilities of between 2 to 8 per cent relative

standard deviation were obtained for repeated, manual injections of vapors from the same aqueous BTEX standards in the range from 440–2200 $\mu\text{g/L}$.

Purge-and-trap methods also suffer from the inherent problems associated with the use of adsorbents. The adsorbent trap may be selective, can be overloaded, may experience carryover, and may break down with repeated heating and purging cycles. Additionally, volatile losses can occur during transfer of the sample from the sampling vial to the instrumentation. The simplicity of the headspace method avoids these problems; there is no sample transfer and no sample work-up outside of the vial. This simplicity is what makes static headspace methods so useful and attractive, particularly for analyses conducted in the field.

ACKNOWLEDGMENT

We acknowledge the donation of the Model 5880A gas chromatograph by the Hewlett-Packard Corp. We also thank Dr. T. M. Spittler, Lab Director of USEPA Region I, for his assistance and valuable discussions.

LITERATURE CITED

- (1) Robbins, Gary A.; Roe, Valerie D.; Stuart, James D.; Griffith, J. Tyler *Proceedings of Petroleum Hydrocarbons and Organic Chemicals in Groundwater*; National Water Well Association: Houston, TX, 1987; pp 307–315.
- (2) Spittler, Thomas M.; Clifford, W. Scott; Fitch, Lester G. *Proceedings for the Characterization and Monitoring of the Veda (Unsaturated) Zone*; National Water Well Association: Denver, CO, 1985; pp 236–246.
- (3) Kiang, Patty, H.; Grob, Robert L. *J. Environ. Sci. Health* **1986**, *A21*, 71–100.
- (4) Friant, Stephen, L.; Suffet, Irwin H. *Anal. Chem.* **1979**, *51*, 2167–2172.
- (5) Kaiser, Klaus L. E.; Oliver, Barry G. *Anal. Chem.* **1976**, *48*, 2207–2209.
- (6) Dietz, Edward A., Jr.; Singley, Kenneth F. *Anal. Chem.* **1979**, *51*, 1809–1814.
- (7) Hachenberg, Horst; Schmidt, Adolph P. *Gas Chromatographic Headspace Analysis*; Heyden and Sons, Ltd.: London, 1977.
- (8) Croll, Brian T.; Sumner, Margaret E.; Leathard, David A. *Analyst* **1986**, *111*, 73–76.
- (9) Cowen, W. F.; Baynes, R. K. *J. Environ. Sci. Health* **1980**, *A15*, 413–427.
- (10) Umbreit, Gerald R.; Grob, Robert L. *J. Environ. Sci. Health* **1980**, *A15*, 429–466.
- (11) Wylie, Philip L. *J. Am. Water Works Assoc.* **1988**, *80*, 65–72.
- (12) Cotruvo, J. A.; Bellar, T. A.; Lichtenberg, J. J. *The Analysis of Aromatic Chemical Indicators of Industrial Contamination in Water by the Purge and Trap Method*; USEPA: Cincinnati, OH, 1981; EPA 600/4-81-057.

RECEIVED for review June 26, 1989. Accepted August 14, 1989. This research is funded through the cooperative agreement grant, No. CR-814542-01, with the Environmental Monitoring System Laboratory, U.S. Environmental Protection Agency, Las Vegas, NV. This article has not been subject to official Agency review and no endorsement should be inferred. Mention of trade names in the article does not indicate USEPA endorsement of any kind. A portion of this work was presented as Paper 800 at the Pittsburgh Conference on Analytical Chemistry and Applied Spectroscopy, Atlanta, GA, March 1989.

Comparison of Paraffin Oil and Poly(chlorotrifluoroethylene) Oil Carbon Paste Electrodes in High Organic Content Solvents

Neil D. Danielson,* Julie Wangsa, and Margaret A. Targove

Department of Chemistry, Miami University, Oxford, Ohio 45056

INTRODUCTION

Carbon-paste electrodes (CPEs) have been used as electrochemical (EC) detectors for liquid chromatography because

they are easy to fabricate, have a wide potential working range (1), and can be modified with electron mediators to lower the required applied electrode potential (2, 3). In addition, the

surface of the electrode can be easily renewed. The paste is usually composed of graphite and Nujol oil although other binders such as silicone oil, bromoform, and bromonaphthalene have been used (1). A Nujol CPE prepared by using the surfactant sodium lauryl sulfate in the binder was stable in nonaqueous solutions such as acetonitrile (4). A polymeric silicone oil CPE was recently demonstrated for LC detection at high acetonitrile and methanol concentrations (5). Even at high positive applied potentials, good electrode lifetime was achieved.

A Kel-F oil and a fluorocarbon oil (perfluorobutylamine) CPE have been used previously in aqueous voltammetric studies in the comparison of the properties of seven CPEs (6). Upon oxidation of ferricyanide, hydroquinone, or phenol, the peak currents were somewhat higher using either of these fluorocarbon-based electrodes as compared to the other hydrocarbon or silicone oil based electrodes. Although Kel-F particle-graphite composite electrodes have been used for high-performance liquid chromatography (HPLC) detection (7, 8), the potential of fluorocarbon oil CPEs as HPLC detectors has not been explored.

We have explored the use of Kel-F (poly(chlorotrifluoroethylene)) oil as a mulling liquid for the preparation of carbon paste electrodes for use in continuous-flow systems. By use of amperometric detection with flow injection analysis (FIA), the Kel-F oil CPE shows an enhanced response over the Nujol CPE with mobile phases of both low and high acetonitrile compositions. The responses of both electrodes are found to be dependent on the polarity of the organic solvent used in the mobile phase which affected the active surface area of the CPE.

EXPERIMENTAL SECTION

Chemicals. All chemicals were reagent grade or better. Kel-F oil no. 10 was obtained from Ohio Valley Specialty Chemicals (Marietta, OH) and the Nujol oil (paraffin oil) was purchased from Fisher Scientific (Fairlawn, NJ). The graphite powder was from BAS (West Lafayette, IN) or Fisher Scientific (Fairlawn, NJ). Particle size was determined to be about 10–25 μm by light microscopy. Triply distilled water was obtained from a Barnstead Nanopure distillation unit (Sybron/Barnstead; Boston, MA).

Equipment. The FIA arrangement consisted of a Beckman Model 110A pump modified with a pulse dampener (52 cm \times 4.6 cm i.d. stainless steel), a Rheodyne Model 7010 injector (Rheodyne; Berkeley, CA) with a 20- μL sample loop, and a Model LC-3A electrochemical detector employing a thin-layer transducer cell (Bioanalytical Systems, BAS; West Lafayette, IN). The electrochemical cell was composed of a stainless steel auxiliary cell half (MF-1018), a plastic Kel-F cell half (MF-1009), and a Ag/AgCl reference electrode (RE-3). The indicator electrode has a geometric area of 7.07 mm². Peaks were generated on a Fisher Recordall Series 5000 (Houston Instruments; Austin, TX) or a Linear Model (Linear Instruments, Reno, NV) strip chart recorder.

Cyclic voltammetry and chronocoulometry measurements were performed with a BAS-100 electrochemical analyzer (BAS; West Lafayette, IN). The electrochemical cell consisted of the BAS carbon-paste electrode, a Pt wire counter (auxiliary) electrode, and a saturated Ag/AgCl reference electrode. Cyclic voltammograms were obtained at the scan rate of 100 mV/s after the electrode was cycled 20 times. For the chronocoulometry, the potential was stepped from -100 to 400 mV at the pulse width of 250 ms. On the basis the Cottrell equation, the active surface area of the CPE can be calculated from the slope of a plot of charge Q vs $\text{time}^{1/2}$. The diffusion coefficient value of 7.6×10^{-6} cm²/s for K₃Fe(CN)₆ in 1 M KCl (9) was corrected for the change in viscosity of a 30/70 aqueous-acetonitrile (10) solution resulting in a diffusion coefficient of 12×10^{-6} cm²/s.

Procedure. The carbon paste was made in batches and stored for subsequent use. Graphite powder predried at 100 °C and the mulling oil (Kel-F or Nujol oil) were combined in the ratios of 1.25 to 1.7 (g of graphite to mL of mulling oil) and mixed thoroughly with a mortar and pestle. The carbon paste was tamped into the flow cell with a brass rod and then the surface was

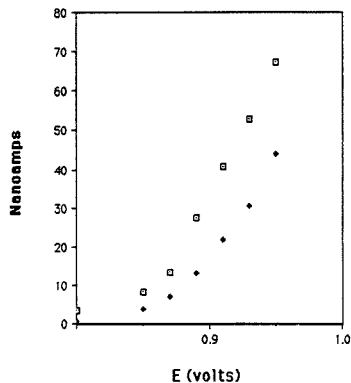


Figure 1. Hydrodynamic voltammogram for estriol using a Kel-F oil (\square) and a Nujol oil (\blacklozenge) carbon paste electrode: test solute, 10 ppm estriol; mobile phase, 80/20 acetonitrile–0.025 M phosphate buffer, pH = 3.2.

flattened by rubbing on finished white paper (11). Both the thin-layer cell and the voltammetric CPE were repacked by replacing approximately one-fifth of the previously used carbon paste. Equilibration of a new carbon paste electrode was carried out for at least 8 h at 0.3 mL/min by using 70/30 phosphate buffer-acetonitrile to reduce the background noise. After the electrode was resurfaced, equilibration time with the desired mobile phase was about 45 min. Estriol solutions were prepared in acetonitrile and ascorbic acid solutions in 0.08 M acetate buffer, pH = 4.8. Oxidation potentials vs Ag/AgCl were maintained at 0.95 V for estriol and 0.70 V for ascorbic acid. The flow rate was maintained at 1 mL/min.

Mobile phases were varied for estriol (0.025 M phosphate, pH = 3.2, organic content as stated), but isocratic for ascorbic acid (0.08 M acetate buffer containing 0.001 M trihexylamine, pH = 4.8, 20% acetonitrile). In all FIA experiments, at least five injections were made for each data point. Peak height was found to be satisfactory for quantitation.

Swelling of either Nujol or Kel-F oils by an organic solvent was determined by adding the solvent to the preweighed oil sample and allowing the mixture to sonicate for 1 h. The excess organic solvent was allowed to evaporate off by natural means for about 72 h and by a stream of N₂ for an additional 1 h. The weight of the organic solvent in the oil divided by the weight of the original Kel-F oil was percent gain. Determinations were done in triplicate.

RESULTS AND DISCUSSION

In order to test the electrodes under extreme conditions, estriol, a type of estrogen, was chosen as the test solute. This estrogen exhibits a high overvoltage, requiring a high applied potential for oxidation. A previous method reports an applied potential of 1.15 V vs Ag/AgCl using a glassy carbon electrode (12). Hydrodynamic voltammograms using estriol for both the Kel-F oil and Nujol oil CPEs are compared in Figure 1. The current generated for each potential was larger for the Kel-F oil CPE than that of the Nujol oil CPE. In the potential range of 0.80–0.95 V, the Kel-F oil CPE generated about twice the current. At lower potentials such as +0.80 V, the difference in background currents between the two electrode types was negligible. At +0.95 V, the background current for the Kel-F oil electrode was about 4 times higher. An applied potential of +0.95 V was used in subsequent LC-EC experiments. For an equivalent current response of the Nujol CPE, a potential of 0.99 V would be required.

Nujol oil and Kel-F oil carbon paste electrodes were compared by using mobile-phase combinations ranging from 0 to 80% acetonitrile (Figure 2). Each point represents at least five injections with a relative standard deviation (RSD) of no

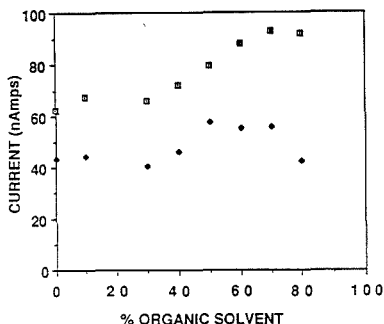


Figure 2. Effect of acetonitrile content on response of a Kel-F oil (□) and Nujol oil (◆) carbon paste electrode: test solute, 10 ppm estriol; aqueous portion of mobile phase, 0.025 M phosphate buffer, pH = 3.2; applied potential, +0.95 V.

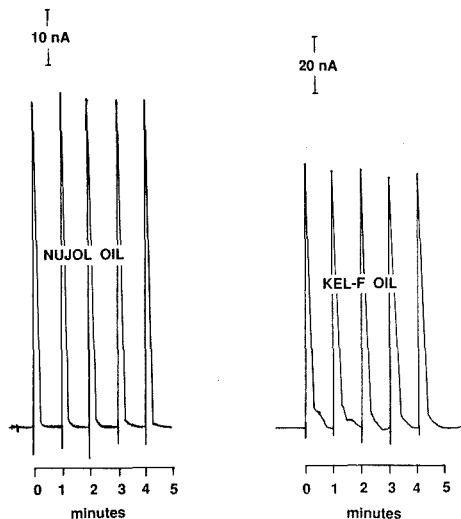


Figure 3. Sample peaks using a Kel-F oil and a Nujol oil carbon paste electrode: test solute, 10 ppm estriol; mobile phase, 70/30 acetonitrile–0.025 M phosphate buffer, pH = 3.2 for Kel-F oil CPE; 50/50 acetonitrile–0.025 M phosphate buffer, pH = 3.2 for Nujol oil CPE; applied potential, +0.95 V.

greater than 6%. In a 100% aqueous solution and low concentrations of up to 30% acetonitrile, the responses of both electrodes remained constant. However, the signals generated by the Kel-F oil CPE are about 1.5 times greater than the Nujol oil CPE. Larger peak currents were obtained with both electrodes as the acetonitrile content increased to 70%. From 70% to 80% acetonitrile, the Kel-F oil CPE responded about a factor of 1.7 better than the Nujol oil CPE. The diminished response of the Nujol oil CPE is likely due to the electrode instability (13) with mobile phases containing 70% and 80% acetonitrile. Representative FIA outputs for both electrodes are shown in Figure 3. Repetitive injections of 10 ppm estriol illustrate the enhancement observed for the Kel-F oil CPE and the equivalent reproducibility of both electrodes. Some broadening can be noted for the Kel-F electrode peaks. Detection limits for estriol were 180 and 200 ppb for the Kel-F oil and Nujol oil CPE, respectively. These values are comparable because the Kel-F oil CPE background was about 5

Table I. Comparison of Response for Kel-F Oil and Nujol Oil Carbon Paste Electrodes^a

estriol concn, ppm	current, nA	
	Kel-F	Nujol
0.1	0.96 ± 0.02	0.50 ± 0.02
0.5	4.62 ± 0.08	1.64 ± 0.01
1.0	6.09 ± 0.09	3.04 ± 0.13
2.0	12.26 ± 0.12	5.74 ± 0.27
4.0	34.91 ± 0.11	14.25 ± 0.14
8.0	53.74 ± 0.24	23.07 ± 0.33
10.0	71.02 ± 0.77	27.41 ± 0.31

^a Mobile phase, 80/20 acetonitrile–0.025 M phosphate buffer, pH = 3.2; applied potential, 0.95 V. ^b 0.264 mM $K_3Fe(CN)_6$ in 30/70 aqueous/acetonitrile (0.1 M KCl).

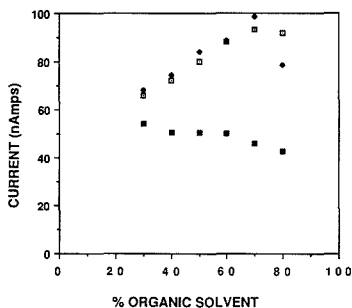


Figure 4. Effect of organic solvent polarity on response of a Kel-F oil CPE: (□) acetonitrile; (◆) 2-propanol; (■) methanol. Other conditions as in Figure 2.

times more noisy. Even after 8 h of use besides the initial equilibration period, a noise value of 0.50 nA was present. Linearity of both CPEs extended to about 50 ppm. Table I shows the current generated for 0.1–10 ppm estriol solutions with the standard deviation data using 80% acetonitrile. Correlation coefficients were 0.994 for both electrodes. The average relative standard deviations (RSD) for these data were 1.1% and 2.3% for the Kel-F oil and Nujol oil CPEs, respectively. In a study of five consecutively renewed carbon-paste surfaces, a 15 ppm estriol solution was injected six times for each electrode. The RSD for these data was 8%. Previous reports indicate RSD values of 5% (14) and 7% (2) for carbon paste electrodes.

The response of the Kel-F oil electrode is dependent on the polarity of the organic solvent in the mobile phase as well as the amount. Figure 4 shows the response of the Kel-F oil CPE as a function of methanol, 2-propanol, and acetonitrile composition. Increasing the concentration of solvents with lower solvent parameters (15), such as acetonitrile and 2-propanol ($\epsilon^o = 0.65$ and 0.82 , respectively), caused the enhanced electrode response. The decrease in response of the Kel-F oil CPE at high 2-propanol content was due to electrode instability. Methanol, which possesses a higher ϵ^o value of 0.95, did not improve the response of the Kel-F oil CPE. When methanol was used in the mobile phase, resurfacing of the electrode was required more frequently. Swelling experiments showed the Kel-F oil adsorbed organic solvents better than Nujol oil. The percent weight gains for Kel-F oil equilibrated with methanol, acetonitrile, and 2-propanol were 0.06, 0.13, and 0.21, respectively. The same results for Nujol oil were 0.02, 0.02, and 0.14. In general, it appears that moderately nonpolar solvents such as acetonitrile or 2-propanol are the desirable mobile phase modifiers. Solvents such as tetrahydrofuran (THF) are too nonpolar ($\epsilon^o = 0.57$) and will dissolve the Kel-F oil while

Table II. Cyclic Voltammetric and Chronocoulometry Data for Nujol and Kel-F Oil CPEs

electrode	solvent	current, μA		peak potential separation, mV	active surface area, cm^2
		cathode	anode		
Nujol	Aqueous ^a	3.4	4.3	117	0.079
Kel-F	aqueous	4.0	5.7	107	0.094
Nujol	70% ACN ^b	1.8	6.1	66	0.082
Kel-F	70% ACN	5.5	11.6	59	0.267

^a0.264 mM $\text{K}_3\text{Fe}(\text{CN})_6$ in 1 M KCl. ^b0.264 mM $\text{K}_3\text{Fe}(\text{CN})_6$ in 30/70 aqueous/acetonitrile (0.1 M KCl).

more polar solvents such as methanol do not show the enhanced current response.

The response of ascorbic acid was also tested in the FIA-EC system. About 1.5 times the signal was generated at a Kel-F oil CPE as compared to the Nujol oil CPE using a 1×10^{-5} M solution of ascorbic acid. Therefore, the greater response of the Kel-F oil CPE appears to be a general phenomenon, not just specific to one type of compound or functional group.

Cyclic voltammetry (CV) and chronocoulometry were carried out to ascertain the reason for the enhanced response of the Kel-F oil CPE. The same FIA flow cell was used for these measurements. Table II shows the CV data and active surface area measurements for Nujol and Kel-F CPEs in both aqueous and 70% acetonitrile solutions. In aqueous solutions, both electrodes show a 1.3–1.4 times higher anodic current and a large peak potential separation indicating nonreversibility. In 70% acetonitrile, the peak separation is more Nernstian; however, the ratio of peak currents has increased further for both electrodes. At a low scan rate of 8 mV/s, peak current ratios close to 1.0 and peak potential separations of 30–35 mV have been reported for Nujol and Kel-F oil CPEs using ferricyanide (6). Using a small voltammetry Kel-F oil CPE of shallower depth, current ratios of 1.0 and a peak separation of 64 mV at 10 mV/s were found in 70% acetonitrile. As evidenced by the y-intercept data of the chronocoulometry plots, the adsorbed surface area concentration is higher for the Kel-F oil CPE. This may contribute to the nonunity ratios of the peak currents. The surface area data in Table II do help explain the CPE response data as a function of acetonitrile content in Figure 2. The surface area of the Kel-F oil CPE is larger in both aqueous and 70% acetonitrile solutions than the Nujol oil CPE. The dramatic rise in the Kel-F oil CPE response in Figure 2 can be explained by the surface area change. In addition, the Kel-F oil may possess some functional groups, which contribute to the generated current and background current. A UV spectrum of a concentrated Kel-F solution (18% (w/v)) prepared in tetrahydrofuran showed absorbance peaks of 0.6 and 0.15 at 240 and 295 nm, respectively. However, the infrared spectrum showed only expected major absorbance peaks at 950 cm^{-1} for the C–Cl band and $1100\text{--}1400 \text{ cm}^{-1}$ for the C–F band. The modest increase in surface area of the Nujol oil CPE is also mirrored by a less substantial change in Figure 2.

Lifetimes of both the Nujol and Kel-F oil CPEs were surprisingly good in acetonitrile (Figure 5). Although a modest drop was observed after 5 h, the response of both electrodes plateaued out to at least 10 h. The enhanced response ratio

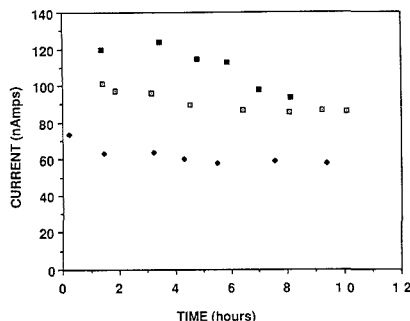


Figure 5. Lifetimes of Nujol and Kel-F oil CPEs in 70% solutions: (◆) Nujol, acetonitrile; (□) Kel-F, acetonitrile; (■) Kel-F, 2-propanol.

of the Kel-F oil CPE to the Nujol oil CPE was maintained. As expected, the lifetime of the Kel-F oil CPE in 70% 2-propanol was not as good, showing a constant drop in response of 30 nA over an 8-h period.

Future work will be directed at understanding the response and reproducibility of the Kel-F fluoropolymer CPEs under a wide variety of HPLC conditions. Because Kel-F polymers can be derivatized (16–18), the fabrication of a carbon-paste electrode with a chemically tailored binder should be feasible.

ACKNOWLEDGMENT

Assistance with the cyclic voltammetry and chronocoulometry measurements was provided by R. K. Jaworski and J. A. Cox of Miami University.

LITERATURE CITED

- (1) Dryhurst, G.; McAllister, D. L. In *Laboratory Techniques in Electroanalytical Chemistry*; Kissinger, P. T., Heineman, W. R., Eds.; Marcel Dekker: New York, 1984; pp 289–319.
- (2) Halbert, M. K.; Baldwin, R. P. *Anal. Chem.* **1985**, *57*, 591–595.
- (3) Santos, L. M.; Baldwin, R. P. *Anal. Chem.* **1986**, *58*, 848.
- (4) Marcoux, L. S.; Prater, K. B.; Prater, B. G.; Adams, R. N. *Anal. Chem.* **1985**, *57*, 1447.
- (5) Horvai, G.; Fekete, J.; Niegreis, Zs.; Toth, K.; Pungor, E. *J. Chromatogr.* **1987**, *385*, 25–32.
- (6) Lindquist, J. J. *Electroanal. Chem. Interfacial Chem.* **1974**, *52*, 37–46.
- (7) Tallman, D. E.; Weisshaar, D. E. *J. Liq. Chromatogr.* **1983**, *6*, 2157.
- (8) Anderson, J. L.; Whiten, K. K.; Brewster, J. D.; Ou, T.-W.; Nonidez, W. K. *Anal. Chem.* **1985**, *57*, 1366.
- (9) Freund, M. S.; Brajter-Toth, A. *Anal. Chem.* **1989**, *61*, 1048.
- (10) van der Wal, S. *Chromatographia* **1985**, *20*, 274.
- (11) Adams, R. N. *Electrochemistry at Solid Electrodes*; Marcel Dekker: New York, 1969; p 283.
- (12) LC-EC Application Note No. 35, Bioanalytical Systems (BAS).
- (13) Krstulovic, A. M.; Collin, H.; Guiochon, G. A. In *Advances in Chromatography*; Giddings, C., Gruschka, E., Cazes, J., Brown, P. R., Eds.; Marcel Dekker: New York, 1984; Vol. 24, Chapter 4.
- (14) Sawyer, D. T.; Roberts, J. L. *Experimental Electrochemistry for Chemists*; Wiley: New York, 1974; pp 69–113.
- (15) Snyder, L. R.; Kirkland, J. J. *Introduction to Modern Liquid Chromatography*; Wiley: New York, 1979; pp 257–260.
- (16) Danielson, N. D.; Taylor, R. T.; Huth, J. A.; Siergiej, R. W.; Galloway, J. G.; Paperman, J. B. *Ind. Eng. Chem. Prod. Res. Dev.* **1983**, *22*, 303.
- (17) Dias, A. J.; McCarthy, T. J. *Macromolecules* **1985**, *18*, 1826.
- (18) Beaver, L. G. Ph.D. Dissertation, Miami University, 1987.

RECEIVED for review February 13, 1989. Revised manuscript received July 3, 1989. Accepted August 17, 1989. This work was supported in part by a grant from the Miami University Faculty Research Committee.

Versatile Impedance Matching Network for Inductively Coupled Plasma Spectrometry

Akbar Montaser,* Izumi Ishii, and R. H. Clifford

Department of Chemistry, George Washington University, Washington, D.C. 20052

S. A. Sinex¹ and S. G. Capar

Division of Contaminants Chemistry, Food and Drug Administration, Washington, D.C. 20204

INTRODUCTION

Impedance matching network (IMN) is the essential component in generating and stabilizing inductively coupled plasmas (ICP) operated at fixed frequency. The chief functions of an IMN are to (a) facilitate plasma formation, in a smooth and rapid fashion, by minimizing the great difference in impedance as the gaseous environment in the plasma torch changes from the nonionized to the ionized stage, (b) ensure the efficient transfer of radio frequency (rf) power from the generator to the plasma, and (c) compensate for real-time variations in impedance as the composition of plasma gas or the sample is altered in spectrochemical measurements.

Only a few publications (1-11) have addressed IMN and its modification, probably because Ar ICP has been the most prominent discharge used in spectrochemical analysis (12, 13), and generally no change in IMN design was necessary. In the last decade, plasma discharges sustained in other gases have been investigated to an increasing extent due to certain economic and analytical advantages (14, 15). For most fixed-frequency ICP facilities in current use, IMNs possess limited tuning and loading ranges; therefore, either non-argon plasmas cannot be generated or a significant impedance mismatch would exist when the plasma is formed. Thus, it would be relevant to devise a versatile IMN that would allow formation of ICP discharges in gases such as argon, helium, nitrogen, air, and mixed gases by using a single facility. Desirable features for such a system are discussed in this report. The proposed IMN was implemented on two ICP facilities.

IMPEDANCE MATCHING NETWORKS

Figure 1A,B shows the circuit diagrams of typical IMNs used currently on almost all crystal-controlled generators. Figure 1C shows the proposed IMN used by us for a 5-kW (Model HFC-5000D generator, RF Plasma Products, Inc., Voorhees, NJ) and a 2.5-kW ICP system (Henry Electronics, Los Angeles, CA). The frequency for the crystal-controlled generators was 27 MHz, but the same IMN could also be used at 41 MHz. Incident power control for generators was provided with automatic power circuitry used commonly in ICP spectrometry. The matching networks for the 5-kW and the 2.5-kW generators were directed by Model AMN-PS-1 and Model AMN-PS-2A controllers (RF Plasma Products, Inc.), respectively. The latter was developed based on the requirements identified in this study and discussed below.

Both the conventional and the modified IMNs consisted of three major components: the shunt capacitor (loading capacitor), the series capacitor (tuning capacitor), and the load coil. This design, known as the L configuration, is used on most fixed-frequency ICP systems because of its wide tuning range. The shunt capacitor is normally adjusted manually while the series capacitor is directed by the IMN controller.

For the conventional IMN, the shunt capacitors consist of a fixed component, usually 250-500 pF made from four to five 50- to 100-pF ceramic capacitors rated at 5-15 kV (L. S. Jennings, San Jose, CA), and a variable air capacitor. Typical

air capacitors used on conventional IMNs have the range of 23-98 pF (rated at 7 kV, Type 153-11-1, Cardwell Condenser Corp., Long Island, NY) and 19-488 pF (rated at 2 kV, Type 154-3-1, Cardwell Condenser Corp.). Such ranges are sufficient to form and stabilize an Ar ICP. For He ICP discharges (16-23) and for mixed-gas plasmas (24-27) sustained in argon-nitrogen, argon-oxygen, and argon-air, shunt capacitance in the range of 400-1000 pF has been necessary to stabilize the plasmas. With the conventional IMN, fixed capacitors must often be inserted in or removed from the shunt circuit to form and stabilize the discharges. Such changes are not only time-consuming but difficult to implement because the free space in most commercial matchboxes is quite limited for mounting additional capacitors or the matchbox is not easily accessible. To eliminate these problems, we replaced the shunt capacitors with a single variable, 25-1000 pF ceramic-envelope vacuum capacitor (Type CVDD-1000-15S, L. S. Jennings). The shunt capacitance could be varied manually with its value tracked by a digital dial. Historically, it would be of interest to mention that in the early days of ICP spectrometry, RF Plasma Products, Inc., used a single capacitor for the shunt circuit to manufacture a few IMNs. The approach was subsequently abandoned because it was too costly and a wide tuning range was not necessary for the Ar ICP.

The main electrical stresses on the shunt and the series capacitors are normally current and voltage (4), respectively. Thus, we used a ceramic-envelope vacuum capacitor, rated for high-current usage, for the shunt circuit to prevent excessive heating of the capacitor and the consequent impedance mismatch. In addition, either the warm air inside the matchbox was exhausted with a fan or forced air was fed continuously into the matchbox. The ventilation process enhanced the stability of the forward power, especially for operation above 1.2 kW.

For the series circuit, a variable 10-300-pF, 15-kV ceramic-envelope vacuum capacitor was used, similar to that adopted in most commercial IMNs. At forward power levels greater than 2 kW or when the number of turns for the load coil had to be increased to facilitate formation of He plasmas (16-23), voltage on the capacitor was too high and, sometimes, arcing occurred inside the matchbox which could damage the capacitor. Again, proper ventilation for the matchbox reduced changes of overheating and electrical breakdown at high power.

For the Ar ICP, the typical load coil, fabricated from 1/8 in. copper tubing, has an inside diameter of 26-27 mm and consists of 3-3.5 turns. A 3- to 4-turn load coil has been used in studies of mixed-gas plasmas (24-27) at 27 MHz. For both the argon and the mixed-gas ICP discharges, the bottom turn of the load coil is normally grounded. In contrast, He ICPs are formed more easily when the load coil is grounded at the top turn (16-23). Because the ionization energy of helium is higher than that of argon, a higher voltage must be applied to the load coil to generate He ICP discharges (16-23). This may be accomplished either by increasing the number of turns for the load coil or by raising the forward power. The former method has been used by us to generate He ICP discharges (16-23). A coil with a larger number of turns (between 4 to

*To whom correspondence should be addressed.

¹Present address: Department of Physical Sciences, Prince George's Community College, Largo, MD 20772-2199.

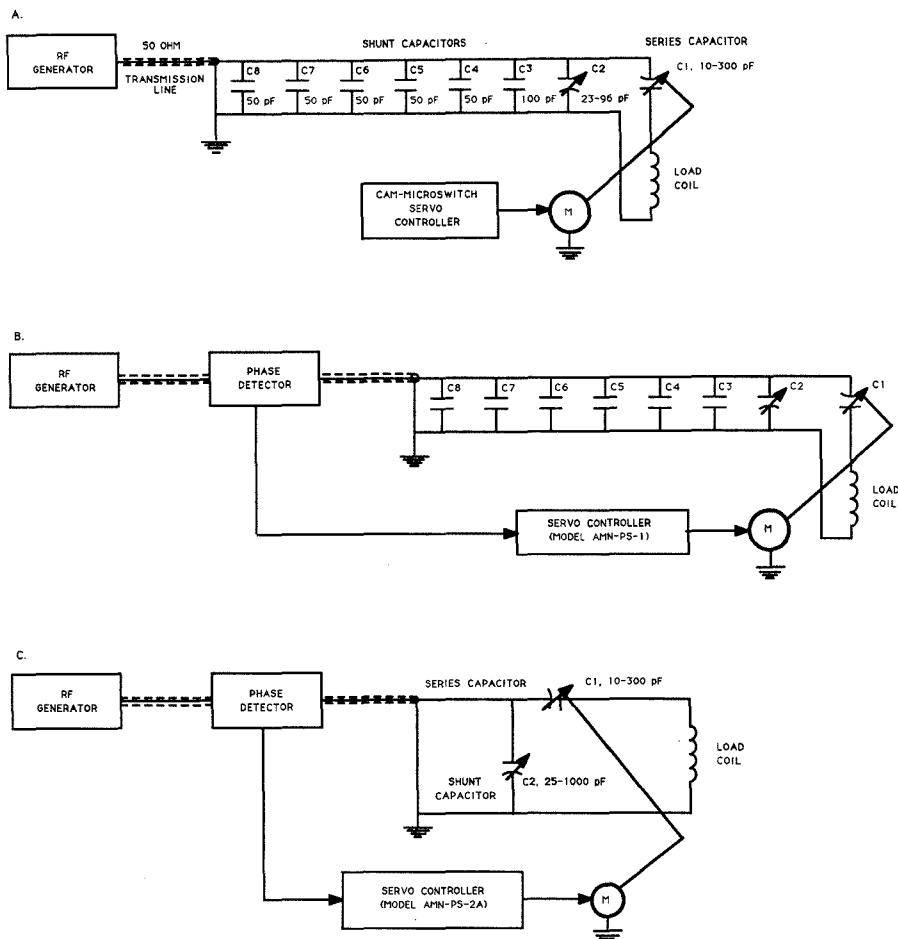


Figure 1. Simplified circuit diagram of an impedance matching network in L configuration: (A, B) systems used in most fixed-frequency generators, (C) proposed system.

5.5 turns) not only increases the voltage for easing plasma ignition but also enhances transfer of rf power to the plasma (4). This greater power transfer efficiency is particularly important for He ICP discharges because lower gas temperatures have been measured for helium vs argon plasmas (20). As the coil inductance increases, the magnetic flux density of the coil is enhanced (4) and a filament-type plasma is formed at the center of the He ICP torch. This filament-type plasma may be converted into an annular discharge by using the injector gas, yet the process can become very sensitive to the gas flow dynamics when coils with seven or more turns are used.

Aside from the matchbox, certain modifications are useful for the existing IMN controllers, or in manufacturing the future ones. To generate a variety of ICP discharges on a single facility, the IMN controller must be equipped with an electronic feedback circuit that samples the 50- Ω transmission line by a phase detector. The positive and negative error signals produced by the detector drive a servo system attached to the series capacitor. If the signal from the phase detector is zero, the system is matched, i.e., reactive impedances en-

countered during plasma operation are transformed to a resistive load.

Certain ICP manufacturers use a cam-microswitch mechanism to tune the ICP to preset conditions. Even if a matchbox is modified as suggested in this report, the settings for the cam-switch mechanism must be changed frequently to tune different plasmas for minimum reflected power. Such a task is extremely time-consuming and often frustrates ICP users. Figure 2 shows the general block diagram of one of the controllers (Model AMN-PS-2A) modified in this work for generating various ICP discharges. The general operation of the controller is discussed below.

The phase detector (A2) samples the transmission line at 50 Ω and generates an error signal that causes the servomotor to turn the series capacitor. The direction of the change depends on the polarity of the phase shift. The error signal is amplified by an operational amplifier (A3) which has a variable gain for adjusting the sensitivity of the feedback loop. This phase gain adjustment is crucial in suppressing plasma oscillation. At low gain, a mismatch is not rapidly compensated, thereby increasing the reflected power and drifts in

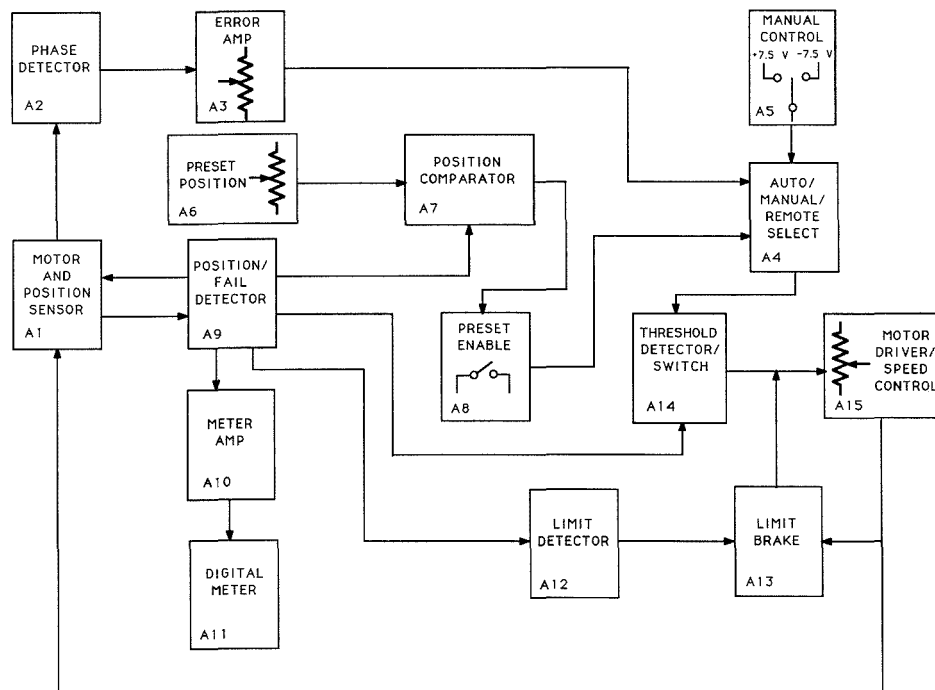


Figure 2. Block diagram of a controller for the impedance matching network used to generate various ICP discharges.

spectrometric signal. At high gain, plasma oscillations can be observed and stable plasma operation is not feasible.

The signal from the error amplifier (A3) is then directed to the mode selector unit (A4) which allows the operator to select one of the following operations: automatic mode using the phase detector (A2), manual control (A5) using the \pm switch on the controller, or the remote mode using a switch on the matching network. The preset potentiometer (A6) allows the tuning capacitor to be preset digitally for each plasma when the preset-enable switch (A8) is activated. With this provision, the difference between the tuning conditions under the plasma on/off stages can be minimized, thus facilitating plasma ignition.

The position comparator (A7) receives a signal from the motor position sensor (A1) processed by the position fail detector (A9). Should A9 receive no signal from A1, then a fail light will come on and the motor will not turn the series capacitor. The processed signal from A1 is also amplified by A10 and is directed to a digital meter (A11) to provide information on the capacitance of the series capacitor. To prevent damage to the series capacitor at the end of its travel, A9 also feeds the limit detector (A12) which in turn activates the limit brake (A13) for stopping the servomotor. The threshold detector switch (A14) detects the signals from A9 and A4 for activating the servomotor under satisfactory conditions. Finally, the motor driver (A15) provides a voltage control that permits adjustment of the speed of the servomotor. Proper adjustment of this control is necessary; otherwise the servomotor will drive the series capacitor past the match point, extinguishing a barely ignited plasma.

On the basis of our experience, an IMN not only should possess a matchbox with sufficient range to tune various ICP discharges but should be equipped with a controller that has provisions for presetting the tuning condition (A6), adjusting

the phase gain (A3), and controlling the speed of the servomotor (A15). Obviously, computer control of these parameters and rf power is desirable. Also, a small fan must be installed on the matchbox to prevent temperature variation. These features are not usually needed for an Ar ICP facility, but they are quite important if ICP users become interested in forming ICP discharges in other gases to extend the domain of samples that can be handled effectively in practice (14).

During the last two years, we have successfully used impedance matching networks described above for forming very stable ICP discharges in argon, helium, argon-nitrogen, argon-oxygen, and argon-air. The length of time required to switch over from one plasma to another has been reduced to a few minutes, rather than hours or days. Because plasma gas composition is among the parameters that must be optimized for certain applications, manufacturers of ICP-based instruments are encouraged to adopt the proposed impedance matching system in their future instruments.

ACKNOWLEDGMENT

We thank H. Tan of GWU, and W. B. Sisson, J. A. Easterling, and W. F. Syner of the Food and Drug Administration (FDA) for their assistance during this work. Special thanks are due to L. West, J. Ott, and R. Spangler of RF Plasma Products, Inc., Voorhees, NJ, for their contributions in implementing our design criteria.

LITERATURE CITED

- Schleicher, R. G.; Barnes, R. M. *Anal. Chem.* **1975**, *47*, 724-728.
- Allemand, C. D. *ICP Inf. News!* **1976**, *2*, 1-26.
- Montaser, A.; Fassel, V. A. *Anal. Chem.* **1976**, *48*, 1490-1499.
- Allemand, C. D.; Barnes, R. M. *Spectrochim. Acta* **1978**, *33B*, 513-534.
- Carr, J. W.; Blades, M. W.; Hieftje, G. M. *Appl. Spectrosc.* **1982**, *36*, 689-691.
- Monnig, C. A.; Koertyohann, S. R. *Appl. Spectrosc.* **1985**, *39*, 884-885.

- (7) Douglas, D. J.; French, J. B. *Spectrochim. Acta* **1986**, *41B*, 197-204.
- (8) Douglas, D. J. U.S. Patent Number 4 682 026, 1987.
- (9) Gagne, P. H.; Morrisroe, P. J. U.S. Patent Number 4, 629, 940, 1986.
- (10) Jakubowski, N.; Raeymaekers, B. J.; Broekaert, J. A. C.; Stuewer, D. *Spectrochim. Acta* **1989**, *44B*, 219-228.
- (11) Yang, P.; Ross, B.; Hieftje, G. M. *Appl. Spectrosc.* **1989**, *43*, 1093-1095.
- (12) *Inductively Coupled Plasmas in Analytical Atomic Spectrometry*; Montaser, A., Golightly, D. W., Eds.; VCH Publishers, Inc.: New York, 1987, 660 pp.
- (13) *Inductively Coupled Plasma Emission Spectroscopy*; Boumans, P. W. J. M., Ed.; Wiley: New York, 1987; Parts I & II.
- (14) Montaser, A.; Van Hoven, R. L. *CRC Crit. Rev. Anal. Chem.* **1987**, *18*, 45-103, and references therein.
- (15) Ohls, K. D.; Golightly, D. W.; Montaser, A. "Mixed-Gas, Molecular-Gas, and Helium Inductively Coupled Plasmas Operated at Atmospheric and Reduced Pressures. In *Inductively Coupled Plasmas in Analytical Atomic Spectrometry*; Montaser, A., Golightly, D. W., Ed.; VCH Publishers, Inc.: New York, 1987, and references therein.
- (16) Chan, S.; Montaser, A. *Spectrochim. Acta* **1985**, *40B*, 1467-1472.
- (17) Chan, S.; Van Hoven, R.; Montaser, A. *Anal. Chem.* **1986**, *58*, 2342-2343.
- (18) Chan, S.; Montaser, A. *Appl. Spectrosc.* **1987**, *41*, 545-552.
- (19) Montaser, A.; Chan, S.; Koppenaal, D. *Anal. Chem.* **1987**, *59*, 1240-1243.
- (20) Chan, S.; Montaser, A. *Spectrochim. Acta* **1987**, *42B*, 591-597.
- (21) Tan, H.; Chan, S.; Montaser, A. *Anal. Chem.* **1988**, *60*, 2542-2544.
- (22) Chan, S.; Tan, H.; Montaser, A. *Appl. Spectrosc.* **1989**, *43*, 92-95.
- (23) Chan, S.; Montaser, A. *Spectrochim. Acta* **1989**, *44B*, 175-184.
- (24) Montaser, A.; Chan, S.; Huse, G. R.; Vieira, P. A.; Van Hoven, R. L. *Appl. Spectrosc.* **1986**, *40*, 473-377.
- (25) Montaser, A.; Fassel, V. A.; Zalewski, J. *Appl. Spectrosc.* **1981**, *35*, 292-302.
- (26) Ishii, I.; Golightly, D. W.; Montaser, A. *J. Anal. At. Spectrom.* **1988**, *3*, 965-968.
- (27) Ishii, I.; Montaser, A. Radial Excitation Temperatures in Argon-Oxygen and Argon-Air Inductively Coupled Plasmas, *J. Anal. At. Spectrom.*, in press.

RECEIVED for review July 17, 1989. Accepted August 31, 1989. This research (at GWU) was sponsored in part by the U.S. Department of Energy under Grant No. DE-FG05-87-ER-13659. Partial support for A.M. and R.H.C. was provided by the FDA.

Here's Why Two Esteemed, Technical Societies Want *Your* Expertise...

The American Chemical Society & American Institute of Chemical Engineers
Announce their 1990 co-publication of

BIOTECHNOLOGY PROGRESS

Editor, Jerome S. Schultz, *University of Pittsburgh*

SUBMIT YOUR PAPERS NOW TO THIS IMPORTANT "NEW" PUBLISHING MEDIUM

Beginning January 1990 BIOTECHNOLOGY PROGRESS, a well-established journal of the American Institute of Chemical Engineers, will become a joint publication of the American Chemical Society and AIChE. As a collaborative effort, several significant changes will occur, *providing enhanced editorial coverage and expanded readership*. These include:

- **Accelerated frequency** — from quarterly to bimonthly issues!
- **A redesigned format** which will better meet the needs of both new and current subscribers.
- **A redefined editorial focus** guaranteed to attract:
 - 1) additional topical papers and primary research findings
 - 2) an audience comprising the very experts *you* want to reach!

ATTENTION CHEMISTS, LIFE SCIENTISTS, AND ENGINEERS!

In bimonthly issues, BIOTECHNOLOGY PROGRESS will provide the latest concepts — in genetics...microbiology and biochemistry...molecular and cellular biology...chemistry and chemical engineering — as they apply to the development of processes, products, and devices. Emphasis will be placed on the *application of fundamental engineering principles* to the *analysis* of biological phenomena involved.

BIOTECHNOLOGY PROGRESS will be of particular interest to *practitioners of R&D in process development, product development, and equipment/instrumentation design for the biotechnology/bioprocess industry*. Its coverage will encompass food, pharmaceutical, and biomedical arenas.

LOOK FOR HIGHLY TARGETED TOPICS LIKE THESE

- **Applied Biochemistry:** Equilibrium data, protein conformations in solution, mapping of molecular surfaces.
- **Applied Molecular Biology:** Cell physiology, gene expression, protein transport, metabolic engineering.
- **Bioreactor Technology:** Reactor engineering, mechanical engineering, materials science, process control, biosensors.
- **Biocatalytic Processes:** Site specific mutagenesis, enzyme mimetics, cofactor regeneration, applied pharmaceutical mimetics.
- **Formulation and Product Delivery.**
- **Bioanalysis:** Online monitoring, containment, containment monitoring, offline analysis, statistical analysis (nonlinear regression, multifactor analysis).
- **Bioseparations.**

ADDRESS YOUR MANUSCRIPT SUBMISSIONS & AUTHOR INQUIRIES TO:

Jerome S. Schultz
Editor, BIOTECHNOLOGY PROGRESS
Center for Biotechnology and Bioengineering
University of Pittsburgh
911 William Pitt Union
Pittsburgh, PA 15260
Telephone: 412/648-7956 Fax: 412/624-7145

To receive editorial updates please write:
American Chemical Society, Marketing,
BIOTECHNOLOGY PROGRESS, Room 609,
1155 Sixteenth St., N.W., Washington, D.C. 20036
FAX: 202/872-6005
Telex: 440159 ACSP UI or 89 2582 ACSPUBS

Finally, a real GC/MS for under \$50,000!

HP 5890 Series II GC sets new industry standards with high temperature operation, cool-on-column injection and pressure programming.

MS ChemStation (DOS series) is 386-based to provide speed and multitasking for highest lab productivity.

Sensitive, universal and specific, the HP 5971A MSD produces true EI spectra even from dirty, complex matrices.



Complete quadrupole GC/MS system actually fits on a five-foot lab bench.

Mouse interface simplifies operation.

Now any lab can afford a GC/MS with an HP mass selective detector (MSD). Our new PC-controlled system costs only \$49,770* yet gives you high performance.

There's multitasking for acquiring and analyzing data simultaneously. There's true, classical EI spectra that stand up to challenge. There's Microsoft® Windows software

for ease of use. Plus access to PC word processing, spreadsheets and desktop publishing. And for total automation, you can add an optional autosampler and barcode reader.

Put the system to work in *any* size laboratory. Even network it to other vendors' data systems. Then enjoy the highest uptime in

the industry because HP is consistently rated number 1 for reliability, service and support. For more, call **1 800 556-1234, Ext. 10218**. In CA, **1 800 441-2345, Ext. 10218**.

*U.S. list price.
Microsoft® is a U.S. registered trademark of Microsoft Corporation.



**HEWLETT
PACKARD**